

On the electrochemical exfoliation of graphene
materials *via* cation intercalation

A thesis submitted to The University of Manchester for the degree of

Doctor of Philosophy

in the Faculty of Engineering and Physical Sciences

2014

Adam John Cooper

School of Chemistry

Table of Contents

Abstract	9
Patents and publications.....	10
Declaration.....	11
Copyright	11
Acknowledgement	13
Symbols.....	17
Standard Constants	17
Standard Symbols.....	17
Electrochemistry Symbols.....	18
Greek Symbols.....	19
Abbreviations.....	20
List of Tables and Figures	24
 Chapter 1: Introduction	 46
1.1 Carbon	46
1.2 Graphene and its analogues	53
1.3 Electronic and mechanical properties of graphene	55
1.4 Electrochemical and chemical properties.....	57
1.5 Graphene synthesis overview	65
1.6 Solution phase exfoliation	68
1.7 Electrochemical synthesis of graphene materials.....	73
1.8 Thesis overview.....	80

Chapter 2: Electrochemical theory and experimental.....	84
2.1 Reference electrodes and the Nernst equation.....	84
2.2 Mass transport and the requirement for supporting electrolyte	87
2.3 Faradaic and non-Faradaic processes.....	90
2.4 Electrochemical techniques (diffusion limited).....	95
2.4.1 Voltammetry	95
2.4.2 Chronoamperometry	101
2.4.3 Chronopotentiometry and galvanostatic procedures	103
2.4.4 Electrical Impedance Spectroscopy (EIS)	105
2.4.5 IR drop	110
2.5 Physical analysis.....	111
2.5.1 X-ray diffraction (XRD)	111
2.5.2 Microscopy.....	114
2.5.2.1 Atomic Force Microscopy (AFM)	114
2.5.2.2 Electron microscopy	116
2.5.3 Spectroscopic techniques.....	118
2.5.3.1 Raman spectroscopy.....	118
2.5.3.2 Raman spectroscopy of few-layer graphene flakes.....	124
2.5.3.3 Raman spectroscopy <i>2D</i> peak fitting.....	129
2.5.3.4 Electron Paramagnetic Resonance spectroscopy	132
2.5.3.5 X-ray Photoelectron Spectroscopy	133
2.6 Experimental	134
2.6.1 Chemicals and materials.....	134
2.6.2 Equipment	134
2.6.2 Working electrodes	135
2.6.3 Counter electrodes (CE)	136
2.6.4 Reference electrodes (RE).....	136

Chapter 3: Electrochemical cathodic intercalation studies	140
3.1 Introduction	140
3.1.1 Introduction to lithium-ion (Li-ion) batteries	141
3.1.2 Graphite Intercalation Compounds (GICs)	145
3.1.3 Tetraalkylammonium reduction chemistry	147
3.2 Results	151
3.2.1 Reference electrode systems	151
3.2.2 Electrolyte decomposition: separate CE chamber	153
3.2.3 Primary voltammetry	155
3.2.4 Tetraalkylammonium voltammetry	160
3.2.5 Electrode size effects on voltammetry	166
3.2.6 Dimethylformamide (DMF) electrochemistry	167
3.2.7 Dimethyl sulfoxide (DMSO) electrochemistry	168
3.2.8 Implications of oxygen involvement	170
3.2.9 Anionic BF_4^- intercalation	171
3.2.10 Ionic liquid (IL) voltammetry	173
3.2.11 UV-Vis spectroscopy of electrolyte reduction	179
3.2.12 Electron Paramagnetic Resonance Spectroscopy (EPR)	184
3.3 Conclusions	192
Chapter 4: Graphite Intercalation Compound formation and stability	196
4.1 Introduction	196
4.2 Results	200
4.2.1 Lithium electrochemistry at a non-porous electrode	200
4.2.2 Lithium electrochemistry at a layered HOPG electrode	201
4.2.3 Lithium charge/discharge cycling	205
4.2.4 TMA^+ electrochemistry	209
4.2.6 TMA^+ Average Coulombic Efficiency (%ACE) testing	213
4.2.7 TEA^+ electrochemistry	225

4.2.8 TEA ⁺ Average Coulombic Efficiency (% _{ACE}) testing	228
4.2.9 TBA ⁺ electrochemistry	231
4.2.10 TBA ⁺ Average Coulombic Efficiency (% _{ACE}) testing.....	233
4.2.11 Average Coulombic Efficiency (% _{ACE}) comparisons.....	236
4.2.12 Quantitative electrochemical intercalation studies.....	242
4.2.13 Is the intercalation mechanism, diffusion controlled?.....	254
4.2.14 Quantitative GIC formation	267
4.3 Conclusions	272
 Chapter 5: Electrochemical cathodic expansion	 276
5.1 Introduction	276
5.2 Results	278
5.2.1 Optical expansion	278
5.2.2 SEM imaging of electrode expansion	279
5.2.3 Tetraoctylammonium (TOA ⁺) intercalation.....	285
5.2.4 X-ray diffraction studies	287
5.2.5 HK-graphite expansion	302
5.2.6 Impedance testing of expanded HOPG electrodes	304
5.3 Conclusions	318
 Chapter 6: Electrochemical cathodic exfoliation	 322
6.1 Introduction	322
6.2 Results	324
6.2.1 Methods and processes.....	324
6.2.2 Effects of gaseous liberation on exfoliation procedure.....	326
6.2.3 NMP exposure effects on graphene materials	328
6.2.4 Graphite cathode source materials.....	330
6.2.5 Selection of cathodic charging potentials	335
6.2.6 Sonication aided HOPG exfoliation	340

6.2.7 Raman spectroscopy of exfoliated graphite materials	341
6.2.7.1 HK-3 graphite Raman analysis	347
6.2.7.2 HK-7 graphite Raman analysis	348
6.2.7.3 HK-11 graphite Raman analysis.....	349
6.2.7.4 HK-800 graphite Raman analysis.....	350
6.2.8 Atomic Force Microscopy analysis of HK-graphite exfoliate....	352
6.2.9 Few-layer graphene concentration derived from UV-Vis.....	355
6.2.10 Electron microscopy of graphene materials	356
6.2.11 Assessing the degree of flake functionalization.....	358
6.2.12 Non-electrochemical exfoliation of graphite.....	361
6.3 Conclusions	365
Chapter 7: Overall thesis conclusions	370
7.1 Conclusions	370
7.2 Future work	374
Appendix A: <i>in situ</i> electrochemical studies and on-going investigations.....	378
A1 Introduction	378
A2 Results	381
A2.1 Graphite pellet electrode: Approach A.....	381
A2.2 HOPG support electrode: Approach A (continued)	383
A2.3 Inert atmosphere electrochemical cell: Approach B	385
A2.4 Approach B: HOPG working electrode	386
A3 Conclusions	391
References	392

Total thesis word count = 78,085

University of Manchester

Adam John Cooper

Doctor of Philosophy thesis

“On the electrochemical exfoliation of graphene materials *via* cation
intercalation”

Abstract

The controlled electrochemical intercalation of tetraalkylammonium species has been studied as a potential high purity, high yield, and scalable fabrication method toward graphene materials. In order to avoid any induced surface oxidation or chemical functionalization, necessary for the production of pristine and high quality graphene materials, cationic intercalation was favoured over anionic intercalation, which has hitherto dominated the literature regarding both chemical and electrochemical solution-phase graphene production routes.

The mechanism of the exfoliation process operates *via* the formation of graphite intercalation compounds, formed amid the interplanar graphene galleries during electrochemical cathodic load of a graphite electrode. The intercalation compounds are stabilised by the neighbouring graphene sheets, even during exposure to relatively large cathodic potentials. Crucially, the intercalation mechanism depends on the presence of an intercalating electrolyte to function, and although the exfoliated products have been shown to be relatively free of oxygenated functional groups, large flakes fall prey to spontaneous re-aggregation when in the presence of electrolyte; it is believed the materials exhibit a slight degree of surface charge and any resulting electrostatically-driven stability is sufficiently masked by the supporting electrolyte.

The route as a whole is presented over several investigative stages, probing the intercalation, cathode expansion and subsequent exfoliation processes of the graphite source in divisions, with the aid of both electrochemical and spectroscopic analysis techniques as well as a comprehensive characterisation of the produced exfoliated graphene materials.

Patents and publications

The findings herein formed the basis for a successfully filed patent by the University of Manchester in 2012 as well as publication in Carbon in 2014, of which featured in Carbon’s ‘most downloaded articles’ and also on the volume cover. In addition, a second manuscript, focusing on the mechanics of the intercalation process, was submitted to the Journal of Electroanalytical Chemistry for publication, and a third manuscript, of which the author’s contribution was in the form of Raman characterisation of few-layer graphene, was submitted for publication in ACS Nano in the latter stages of the studentship.

Patent no. WO2012120264-A1 “Production of graphene”

A. J. Cooper, N. R. Wilson, I. A. Kinloch, and R. A. W. Dryfe, “Single stage electrochemical exfoliation method for the production of few-layer graphene *via* intercalation of tetraalkylammonium cations”, Carbon 66 (0), 340-350 (2014).

A. J. Cooper, M. Velický, I. A. Kinloch, and R. A. W. Dryfe, “On the controlled electrochemical preparation of R_4N^+ graphite intercalation compounds and their host structural deformation effects”. *Submitted manuscript: Journal of Electroanalytical Chemistry*.

M. Velický, P. S. Toth, A. J. Cooper, S. D. Worrall, H. V. Patten, A. T. Valota, I. A. Kinloch, K. S. Novoselov, E. W. Hill, and R. A. W. Dryfe, “Electron transfer kinetics on graphene mono- and multi-layers supported on Si/SiO₂ substrate. *Submitted manuscript: ACS Nano*.

Declaration

I, the author Adam John Cooper, declare that no portion of the work referred to in this thesis has been submitted in support of an application for another degree or qualification in this, or any other, university or other institute of learning.

Copyright

- i. The author of this thesis (including any appendices and/or schedules to this thesis) owns certain copyright or related rights in it (the “Copyright”) and s/he has given The University of Manchester certain rights to use such Copyright, including for administrative purposes.
- ii. Copies of this thesis, either in full or in extracts and whether in hard or electronic copy, may be made only in accordance with the Copyright, Designs and Patents Act 1988 (as amended) and regulations issued under it or, where appropriate, in accordance with licensing agreements which the University has from time to time. This page must form part of any such copies made.
- iii. The ownership of certain Copyright, patents, designs, trademarks and other intellectual property (the “Intellectual Property”) and any reproductions of copyright works in the thesis, for example graphs and tables (“Reproductions”), which may be described in this thesis, may not be owned by the author and may be owned by third parties. Such Intellectual Property and Reproductions cannot and must not be made available for use without the prior written permission of the owner(s) of the relevant Intellectual Property and/or Reproductions.
- iv. Further information on the conditions under which disclosure, publication and commercialisation of this thesis, the Copyright and any Intellectual Property and/or Reproductions described in it may take place is available in the University IP Policy (see <http://documents.manchester.ac.uk/DocuInfo.aspx?DocID=487>), in any relevant Thesis restriction declarations deposited in the University Library, The University Library’s regulations (see <http://www.manchester.ac.uk/library/aboutus/regulations>) and in The University’s policy on Presentation of Theses.

Acknowledgement

The author would like to express his total gratitude and respect towards his supervisors, Prof. Robert Dryfe and Prof. Ian Kinloch, for their continued patience and guidance throughout the project, as well as helping the author develop his skills as a professional research scientist and electrochemist. Special thanks must also go to Dr. Chris Muryn and Dr. Patrick Hill, for their assistance with atomic force microscopy and scanning electron microscopy, respectively, and Dr. Neil Wilson, at the University of Warwick, for his contribution to the author's first publication in the form of atomic force microscopic analysis. Thanks to Mr. Chris Slann and the mechanical workshop, for their help in the design and fabrication of specialist electrochemical equipment, and to the Engineering and Physical Sciences Research Council for funding of the studentship.

To his friends, both past and present, in particular Dr. Matěj Velický, Dr. Briony Setterfield-Price, Mr. Andrew Norman John Rodgers and Miss. Deborah Lomax, for creating the most enjoyable working environment and offering encouragement in (several) times of need.

And finally, to his family, for their reassurance and understanding throughout, without which would have been extremely difficult, and in particular to Natalie, for her continued patience, specifically during the final twelve months, and her carefully chosen words “go and sit in a dark room”, which were sometimes offered in an attempt to restore his faith in science.

To my parents and Elsie

‘There is no more open door by which you can enter into the study of natural philosophy, than by considering the physical phenomena of a candle.’

Michael Faraday

Symbols

Standard Constants

c	Speed of light	299792458	m s^{-1}
e	Elementary charge	1.602×10^{-19}	C
F	Faraday's constant	96485.339	C mol^{-1}
h	Planck's constant	6.626×10^{-34}	J s
m	Mass of an electron	9.109×10^{-31}	kg
N_A	Avogadro's constant	6.022×10^{23}	mol^{-1}
R	Ideal Gas constant	8.314	$\text{J K}^{-1} \text{mol}^{-1}$
π		3.141592654	—

Standard Symbols

A	Area	cm^2
A_s	Surface Area	cm^2
d	Crystallographic d -spacing	nm
D	Diffusion coefficient	$\text{cm}^2 \text{s}^{-1}$
j	Imaginary component of impedance	—
J_i	Flux of species i	$\text{mol cm}^{-2} \text{s}^{-1}$
K/K'	Dirac Points	—
m	Mass	g
M	Molar mass	g mol^{-1}
p	Pressure	Bar
t	Time	s
T	Temperature	K
z	charge	—

Electrochemistry Symbols

$A_{\text{O/R}}$	Activity of O/R	—
c^\ominus	Unit concentration	mol dm^{-3}
C	Capacitance	F
C_s	Specific capacitance	F g^{-1}
C_{dl}	Double layer capacitance	F
CPE_{dl}	Pseudo capacitance	F
E	Electrode potential	V
E^0	Standard redox (or cell) potential	V
$E^{0'}$	Formal potential	V
E_{F}	Fermi energy	V
ΔE_{p}	Peak separation	V
E_{pa}	Anodic peak potential	V
E_{pc}	Cathodic peak potential	V
f	Frequency	Hz or s^{-1}
I	Electrical current	A
I_{c}	Capacitive current	A
I_{f}	Faradaic current	A
I_{lim}	Limiting current	A
I_{pa}	Anodic peak current	A
I_{pc}	Cathodic peak current	A
I_{s}	Steady state current	A
J	Current density	A cm^{-2}
k^0	Heterogeneous electron transfer rate constant	cm s^{-1}
k_{s}	Heterogeneous electron transfer rate	—
n	Number of electrons transferred	—
Q	Charge	C

r_e	Electrode radius	cm
R	Resistance	Ω
R_{ct}	Resistance to charge transfer	Ω
R_s	Resistance to charge transfer	Ω
V	Voltage	V
$x_{HP/OHP}$	Distance to inner and outer Helmholtz planes	cm
z	Ionic charge	—
Z''	Impedance (imaginary)	Ω
Z'	Impedance (real)	Ω
Z	Total impedance	Ω

Greek Symbols

α	Transfer coefficient	—
γ	Activity coefficient	—
Γ	Brillouin zone	—
δ	Diffusion layer thickness	cm
ϵ	Dielectric permittivity	$F\ m^{-1}$
ϵ_0	Permittivity of free space	$F\ m^{-1}$
λ	Wavelength	nm
η	Overpotential	V
ν	Kinematic viscosity	$cm^2\ s^{-1}$
ν	Scan rate	$V\ s^{-1}$
θ	Angle	Degrees ($^\circ$)
φ	Electrostatic potential	V
Φ	Phase angle shift	—
τ	Time constant	s
ω	Radial frequency	$Rad\ s^{-1}$

Abbreviations

[<i>Ox</i>]	Concentration of oxidised species
[<i>Red</i>]	Concentration of reduced species
% _{ACE}	Average Coulombic Efficiency (%)
A	Acoustic phonon
AFM	Atomic Force Microscopy
Ag/AgCl	Silver/silver chloride reference electrode
BDD	Boron doped diamond
BMIM	1-butyl-3-methylimidazolium
C	Capacitor
CA	Chronoamperometry
CE	Counter Electrode
CPE	Constant Phase Element
CNT	Carbon Nanotube
CV	Cyclic Voltammetry
CVD	Chemical Vapour Deposition
DMEU	1,3-dimethyl-2-imidazolidinone
DMF	Dimethyl Formamide
DMSO	Dimethyl Sulfoxide
DOS	Density of Electronic States
DR	Double Resonance
DSSC	Dye Sensitised Solar Cell
EDAX	Energy Dispersive X-ray Analysis
EDLC	Electrochemical Double Layer Capacitor

EG	Expanded Graphite
EIS	Electrochemical Impedance Spectroscopy
EPR	Electron Paramagnetic Resonance
ET	Electron Transfer
FET	Field Effect Transistor
FLG	Few-layer Graphene
FWHM	Full Width Half Maximum
GC	Glassy Carbon
GC	Galvanic Charge
GD	Galvanic Discharge
GIC	Graphite Intercalation Complex
GO	Graphene Oxide
rGO	Reduced Graphene Oxide
HK- n	Graphite rod (HK Grade), where n = grain size / μm
HOPG	Highly Orientated Pyrolytic Graphite
IHP	Inner Helmholtz Plane
IL	Ionic Liquid
iLO	In-plane Longitudinal Optical Phonon Mode
IPA	Isopropyl Alcohol
IPE	Ideal Polarized Electrode
iTO	In-plane Transverse Optical Phonon Mode
MWCNT	Multi Walled Carbon Nanotube
NMP	N-Methyl-2-Pyrrolidone
NMR	Nuclear Magnetic Resonance

O	Optical phonon
OHP	Outer Helmholtz Plane
PC	Polycarbonate
PVA	Polyvinyl Alcohol
R_4N^+	Tetraalkylammonium cation
R	Alkyl chain
R	Resistor
RE	Reference Electrode
R(RC)	Circuit: Resistor (series) Resistor + Capacitor (parallel)
SA	Surface Area
SCE	Saturated Calomel Electrode
SECM	Scanning Electrochemical Microscopy
SEI	Solid Electrolyte Interface
SEM	Scanning Electron Microscopy
SHE	Standard Hydrogen Electrode
Si/SiO ₂	Oxidised Silicon Substrate with 300 nm Oxide Layer
SPI	SPI Grade of HOPG
SPM	Scanning Probe Microscopy
TBA ⁺	Tetrabutylammonium
TBAClO ₄	Tetrabutylammonium perchlorate
TBABF ₄	Tetrabutylammonium tetrafluoroborate
TEA ⁺	Tetraethylammonium
TEAClO ₄	Tetraethylammonium perchlorate
TEABF ₄	Tetraethylammonium tetrafluoroborate

TEM	Transmission Electron Microscopy
TMA ⁺	Tetramethylammonium
TMAClO ₄	Tetramethylammonium Perchlorate
TMABF ₄	Tetramethylammonium tetrafluoroborate
TR	Triple Resonance
UHV	Ultra High Vacuum
UV-Vis	Ultra Violet-Visible
vdW	van der Waals
WE	Working Electrode
XRD	X-ray Diffraction
XPS	X-ray Photoelectron Spectroscopy

List of Tables and Figures

Figure 1.1) Schematic representation of HOPG showing five AB-stacked graphene layers and four 3.354 Å interplanar separations.....	49
Table 1) Table summarising the density, electrical resistivity and band gaps of graphene, diamond, GC, HOPG, silver and molybdenum disulphide.....	50
Figure 1.2) Molecular models depicting how layered graphite, rolled carbon nanotubes (CNTs) and wrapped Buckminsterfullerene (C60), can all be constructed from graphene sheets	54
Figure 1.3) DOS per unit cell for (a) (17,3) CNT exhibiting semiconductor behaviour, ⁵⁶ (b) (7,7) CNT exhibiting metallic behaviour, ⁵⁶ and (c) graphene exhibiting zero-band semiconductor behaviour ⁵⁷	58
Figure 1.4) Fermi level schematic describing heterogeneous electron transfer and the required energy of the Fermi level in order to permit electron donation to the reactant, according to the Marcus-Gerischer view	59
Figure 1.5) Schematic showing anionic and cationic intercalation between graphene layers	76
Table 2) Summary of relevant literature regarding electrochemical preparation of graphene materials through anionic and cationic intercalation mechanisms (blue: purely anionic, green: purely cationic)	77
Table 2 continued) Summary of relevant literature regarding electrochemical preparation of graphene materials which employ the use of both anionic and cationic control within procedures	78

Figure 2.1) Schematic representation of the electrolyte double layer for a positively polarised electrode, showing the inner-Helmholtz plane and the outer-Helmholtz plane constructed from electrolyte species	92
Figure 2.2) Potential profile across the double layer region indicating how the potential is distributed in solution	94
Figure 2.3) Schematic representation of a voltammetric sweep between two potential limits against time	96
Figure 2.4) Typical current response of a system containing a redox mediator, in which the mediator is reduced and oxidised during potential sweeping generating cathodic and anodic currents, respectively.....	97
Figure 2.5) CV showing the effect of varying the rate at which the potential is swept on the cathodic peak current (E_{pc}) and the anodic peak current (E_{pa}) for a reversible system	98
Figure 2.6) Schematic depicting the current lag and decay, of a system during the application of a potential step between E_1 and E_2 , where $E_1 < E_0 < E_2$. <i>N.B.</i> The current lag time is not quite to scale, and has been increased for the purpose of clarity.	101
Figure 2.7) Schematic depicting the potential behaviour under galvanostatic conditions used for charge/discharge cycling.....	104
Figure 2.8) Schematic of a R(RC) circuit used to record exemplary impedance measurements to determine the values of individual resistive and capacitive components in an experimental cell. WE, CE and RE denote the connections to the working, counter and reference electrodes, respectively.	107

Figure 2.9) Resulting Nyquist plot revealing the respective resistive and capacitive values of the circuit elements in the R(RC) circuit	109
Figure 2.10) Schematic showing X-ray diffraction of a crystal lattice with explanation as to the origin of the parameters employed in the Bragg equation	111
Figure 2.11) Schematic showing the underlying mechanism of an Atomic Force cantilever tip, and the manner in which morphology images are constructed.	114
Figure 2.12) Schematic indicating the different possible phonon modes in graphene's reciprocal space lattice, and their respective Raman spectroscopy signals specifically showing how it is possible to obtain <i>2D</i> Raman signals even in the absence of lattice defects (re-drawn from Malard <i>et al.</i> ¹⁸⁷)	120
Figure 2.13) Typical Raman spectrum (data obtained herein) of few-layer graphene material showing the common Raman signals associated with graphene materials	122
Figure 2.14) Comparative Raman spectra of graphite and graphene (single and multilayer) recorded at 514 nm and 633 nm excitation laser wavelengths, showing the 2D peak shape dependence upon the number of inherent graphene layers. Data acquired from published work by Ferrari <i>et al.</i> 2006 ¹⁹³	123
Figure 2.15(a) Optical images of a graphene flake at 10x magnification displaying different flake thicknesses. Points labelled indicate the points analysis <i>via</i> Raman spectroscopy and a mixture of edge sites, boundaries between different numbers of layers and basal plane.	125
Figure 2.15(b) Optical images of a graphene flake at 10x magnification displaying different flake thicknesses. Points labelled indicate the points	

analysis <i>via</i> Raman spectroscopy and a mixture of edge sites, boundaries between different numbers of layers and basal plane.	126
Figure 2.16(a) Raman spectra measured at various points (1 – 14) on micromechanically exfoliated graphene showing respective number of graphene layers determined from the varying shape and intensity of the <i>2D</i> band at <i>ca.</i> 2700 cm^{-1}	128
Figure 2.16(b) Raman spectra measured at various points (15 – 31) on micromechanically exfoliated graphene showing respective number of graphene layers determined from the varying shape and intensity of the <i>2D</i> band at <i>ca.</i> 2700 cm^{-1}	129
Figure 2.17) Raman <i>2D</i> band fitting to increasing number of Lorentzian functions displaying reasonable good fit with four Lorentzian components.....	131
Figure 2.18) 4-neck electrochemical cell schematic, as used for graphene synthesis procedures involving graphite rod electrodes, in this case purged with argon gas, but eventually conducted within a closed saturated argon atmosphere	138
Figure 3.1) Schematic illustrating the expansion of the interplaner graphene galleries induced by the intercalation of tetraalkylammonium cationic species, where R on the R_4N^+ cation represents the alkyl group.....	140
Figure 3.2) Schematic illustrating the staging phenomenon of GICs between graphene layers for stages $1 \leq n \leq 4$	145
Figure 3.3) Current response of the ferrocene/ferrocenium redox mediator at a GC working electrode, against various reference electrode systems, scanned at 100 mV s^{-1}	151

Table 3) Reference electrode stability data expressed as measured E_0 potential of the Fc^+/Fc reduction <i>vs.</i> reference and pseudo-reference electrodes, at increasing periods of time.....	152
Figure 3.4) Voltammetric responses for TBABF_4 (0.1 M) in NMP at a HOPG electrode using (a) a Pt CE in a separate chamber, and (b) Pt CE returned to the main cell, scanned at 50 mV s^{-1}	153
Figure 3.5) Image showing $10 \times 50 \text{ mm}$ platinum gauze CE placed surrounding the graphite WE	154
Figure 3.6) CVs showing (a) complete potential window of TMAClO_4 in NMP at a GC WE, and (b) effect of IR-compensation on the negative limit of the potential window, scanned at 50 mV s^{-1}	156
Figure 3.7) Repeatable CVs showing intercalation and de-intercalation of lithium into a HOPG electrode, recorded at a scan rate of 50 mV s^{-1}	157
Figure 3.8) CVs showing lithium intercalation/de-intercalation at a HOPG electrode exposed to a solution of LiClO_4 (0.1 M) in NMP; highlighting the effect of successive scanning, inset: photograph of a graphite rod with $\text{LiOH}/\text{Li}_2\text{O}$ deposit, recorded at a scan rate of 50 mV s^{-1}	159
Figure 3.9(a) CVs showing the resulting current responses at a HOPG electrode (coloured lines) and a platinum wire electrode (black line) in solutions of TMAClO_4 (0.1 M) in NMP recorded at a scan rate of 50 mV s^{-1}	162
Figure 3.9(b) CVs showing the resulting current responses at a HOPG electrode (coloured lines) and a platinum wire electrode (purple line) in solutions of TEABF_4 (0.1 M) in NMP recorded at a scan rate of 50 mV s^{-1}	163

Figure 3.9(c) CVs showing the resulting current responses at a HOPG electrode (coloured lines) and a platinum wire electrode (black line) in solutions of TBABF ₄ (0.1 M), recorded at a scan rate of 50 mV s ⁻¹	164
Figure 3.10) CVs showing the resulting current responses at a HOPG electrode when varying degrees of the electrode are exposed to the solution, recorded at a scan rate of 50 mV s ⁻¹	166
Figure 3.11) Voltammetric responses for TEAClO ₄ (0.1M) in DMF at a HOPG electrode showing (a) effect of successively more negative potential limit, (b) effect of halved electrolyte concentrations, and (c) effect of successive cycling, recorded at a scan rate of 50 mV s ⁻¹	168
Figure 3.12) Voltammetric responses for TEAClO ₄ (0.1 M) in DMSO at a HOPG electrode showing effect of a successively more negative potential limit, recorded at 50 mV s ⁻¹	169
Figure 3.13) (a) Current responses indicative of oxygen reduction despite argon saturation of solutions prior to CV analysis (scanned at 100 mV s ⁻¹) and (b) linear Randles-Ševčík plot displaying oxygen peak current dependence on square root of scan rate	170
Figure 3.14) CVs showing current response at HOPG WE for initial scan (blue), and subsequent scans (black to red), measured at 100 mV s ⁻¹ , across the whole available potential window of the system.....	171
Figure 3.15) CVs showing the current response at a HOPG WE in TEABF ₄ in NMP at the positive limit of the potential window, showing no faradaic processes and no BF ₄ ⁻ intercalation/de-intercalation, scanned at 100 mV s ⁻¹	173
Figure 3.16) Molecular structures of BMIM ⁺ , BF ₄ ⁻ , highlighting the relatively similar cationic sizes of BMIM ⁺ and TBA ⁺	174

Figure 3.17) Current responses obtained at a HOPG electrode in the presence of BMIM BF₄, indicating BMIM BF₄ intercalation and de-intercalation, as well as the introduction of an unknown anodic peak current after exploring cathodic potentials lower than -2.5 V, scanned at 100 mV s^{-1} 175

Figure 3.18) Current response at a HOPG working electrode in the presence of a 1:1 vol% mixture of NMP and 1-butyl-3-imidazolium tetrafluoroborate [BMIM][BF₄], recoded at a scan rate of 50 mV s^{-1} 177

Figure 3.19) Current response at a HOPG working electrode in the presence of a 1:1 volume ratio of NMP and [BMIM][BF₄] showing the non-permanent effects of potentiostatic waiting at the negative limit of the potential window, scanned at 50 mV s^{-1} 178

Figure 3.20) UV-Vis absorption spectra, recorded *ex situ*, of (a) a system containing 0.1 M TEABF₄/NMP, after increasing intercalation times, and inset (b) pure NMP 180

Figure 3.21) UV-Vis absorption spectra of system containing pure NMP, after increasing cathodic charging times of a GC electrode, indicating solvent decomposition 181

Figure 3.22) Schematic suggesting two likely mechanisms to the degradation of NMP: either *via* reaction with an alkyl carbanion produced from the reduction of R₄N⁺ or *via* the one-electron reduction and subsequent reaction of the produced pyrrolidone radical species with an alkyl radical. Both mechanisms ultimately lead to the ring opening of N-methylpyrrolidone to produce the amine species..... 182

Figure 3.23) Schematic of the *in situ* electrochemical EPR setup showing HOPG, acting as WE connected with platinum wire *via* a pinhole, Teflon-insulated platinum CE and RE with an EPR sample tube filled with electrolyte. 186

Figure 3.24) recorded EPR signals for (a) TBA^+ reduction performed at a bare Pt wire and (b) Li^+ reduction performed at a HOPG electrode, using applied potentials of -2.4 V vs. Ag for a period of 1000 s, and showing the absence of any EPR active species	187
Figure 3.25) EPR signals obtained from <i>in situ</i> electrochemistry in TBAClO_4 at a HOPG electrode, recorded at X band (9.8705 GHz)	188
Figure 3.26) Time dependence of the spectrum acquired in Figure 3.22 over a period of 4 minutes (limits of the magnetic field values 5320 to 5330 G), displaying a slight decrease in intensity of the observed signal of the 4 minute duration	189
Figure 3.27) Signal intensity dependence on the applied constant potential (-2.4 V), (limits of the magnetic field values 5320 to 5330 G), displaying an increased signal intensity on application of an electrical current	190
Figure 4.1) Voltammetric response at a GC working electrode in 0.1 M LiBF_4 in NMP, scanned at 100 mV s^{-1} vs. Ag/AgClO_4	201
Figure 4.2) Voltammetric responses at a HOPG working electrode in 0.1 M LiClO_4 in NMP, scanned at 100 mV s^{-1} vs. Ag/AgClO_4 showing SEI formation at the graphite electrode and the effects of decreased activity	202
Figure 4.3) Voltammetric responses at a HOPG working electrode in 0.1M LiClO_4 in NMP, scanned at 100 mV s^{-1} vs. Ag/AgClO_4 showing (a) the development of prominent lithium redox peaks on increasing the cathodic limit of the potential window with successive scanning, and (b) an enlarged portion of the lithium redox peaks showing Q_i and Q_d values determined from CV peak currents	204

Figure 4.4(a) Charge/discharge plots showing 5 cycles with decreasing E_c performed at a 8 mg HOPG electrode in LiBF_4 (0.1 M) in NMP, from which data was extracted from cycles two, three and four, and plotted in Figure 4.5	205
Figure 4.4(b) Charge/discharge (3^{rd} cycle) with decreasing E_c performed at a 8 mg HOPG electrode in LiBF_4 (0.1 M) in NMP showing gradient changes of transients with increasing E_c	206
Figure 4.5) Plot showing how the average (taken over cycles 2-4) lithium charge/discharge efficiency is affected by increasing E_c from values of -0.8 V to -4 V	208
Figure 4.6) Voltammetric response in 0.1M TMAClO_4 in NMP, scanned at 100 mV s^{-1} vs. AgAgClO_4 , at (a) GC WE, (b) HOPG WE showing successive increase of the negative potential limit, (c) HOPG small potential window (initial scans black) and (d) HOPG large potential window (initial scans black)	210
Figure 4.7) Voltammetric response of HOPG in 0.1 M TMAClO_4 in NMP, scanned at 100 mV s^{-1} vs. Ag/AgClO_4 , between -3 V and $+2$ V, showing the presence of oxygen reduction Faradaic processes as a result of perchlorate electrolysis at <i>ca.</i> $+1.5$ V.....	212
Figure 4.8(a) TMA^+ charge/discharge plots showing 5 cycles with decreasing E_c (from -0.8 V to -2.0 V) performed at a 10 mg HOPG electrode in TMAClO_4 (0.1 M) in NMP	214
Figure 4.8(b) TMA^+ charge/discharge plots showing 5 cycles with decreasing E_c (from -2.3 V to -2.8 V) performed at a 10 mg HOPG electrode in TMAClO_4 (0.1 M) in NMP	215

Figure 4.9(a) TMA^+ charge/discharge showing 5 repeated charge/discharge cycles with decreasing E_c performed at a 10 mg HOPG electrode in TMAClO_4 (0.1 M) in NMP, from which data was extracted from cycles two, three and four, and plotted in Figure 4.10	216
Figure 4.9(b) TMA^+ charge/discharge (3 rd cycle) with decreasing E_c performed at a 10 mg HOPG electrode in TMAClO_4 (0.1 M) in NMP showing gradient changes of transients with increasing E_c	218
Figure 4.10) Plots showing how TMA^+ charge/discharge efficiency is affected by the increasing E_c from values of -1 V to -5 V. (a) shows initial scans, (b) shows the effect of using data from extended cycling, (c) shows an example of ‘anomalous’ data (circled), and (d) shows the effect of using a thick (<i>ca.</i> 1 mm) HOPG sample	219
Figure 4.11) Schematic describing the effects of intercalation saturation, whereby further migrating cations (red) are unable to be stabilised by the neighbouring graphene sheets and are therefore subsequently irreversibly reduced to trialkylamine species and other by-products.....	221
Figure 4.12) CV showing current response at HOPG WE, measured at 100 mV s^{-1} , demonstrating the effect of holding at -2 V for increasing periods of time, on the anodic peak current.....	224
Figure 4.13) Voltammetric response in 0.1M TEABF_4 in NMP, scanned at 100 mV s^{-1} vs. Ag/AgClO_4 , at (a) GC WE, (b) HOPG WE showing successive increase of the negative potential limit and the effect on the anodic peak on the reverse sweep, (c) HOPG small potential window displaying CV repeatability and (d) HOPG large potential window displaying CV reproducibility.....	227
Figure 4.14(a) TEA^+ charge/discharge showing 5 repeated charge/discharge cycles with decreasing E_c performed at a 3.5 mg HOPG electrode in TEABF_4	

(0.1 M) in NMP, from which data was extracted from cycles two, three and four, and plotted in Figure 4.17 228

Figure 4.14(b) TEA⁺ charge/discharge showing a single cycle (3rd cycle) with decreasing E_c performed at a 3.5 mg HOPG electrode in TEABF₄ (0.1 M) in NMP 229

Figure 4.15) Plots displaying how TEA⁺ charge/discharge efficiency is affected by decreasing E_c from values of -1 V to -5 V for (a) original dataset, and (b) repeated dataset 230

Figure 4.16) Voltammetric responses in 0.1M TBABF₄ in NMP, scanned at 100 mVs⁻¹ vs. Ag/AgClO₄, at (a) a GC electrode scanned over the whole potential window, (b) a HOPG electrode displaying the voltammetric effects of successively increasing the cathodic potential limit, (c) and (d) an HOPG electrode showing eventual CV repeatability 232

Figure 4.17(a) TBA⁺ charge/discharge showing repeated charge/discharge transients for 5 cycles where $0.5\text{ V} \leq E_c \leq -5\text{ V}$ 233

Figure 4.17(b) Zoom of a TBA⁺ single cycle (3rd cycle) of 4.17(a) where $0.5\text{ V} \leq E_c \leq -5\text{ V}$ 234

Figure 4.18) plots displaying how TBA⁺ charge/discharge efficiency is affected by increasing E_c from values of -1 V to -5 V for (a) original dataset, and (b) repeated dataset with extended cycling for E_c values less than -2 V 235

Figure 4.19) Comparative %_{ACE} trends for different tetraalkylammonium cations and lithium at HOPG as well as a GC electrode. 236

Figure 4.20) Schematic highlighting the spatial restrictions incurred as a result of increasing cation size..... 240

Figure 4.21) Schematic showing the differences in degree of stabilisation provided by a) a surface adsorption mechanism, and b) a gallery-intercalation mechanism	242
Figure 4.22(a) CV at a HOPG disc electrode in TBABF ₄ in NMP, recorded at four different scan rates to highlight the effects of scan rate on the observed current responses, thereby indicating a staging phenomenon	245
Figure 4.22(b) CV at a HOPG disc electrode in TBABF ₄ in NMP, recorded at 0.1 mV s ⁻¹ highlighting current steps associated with intercalation staging ...	246
Figure 4.23) CVs showing the effects of varying scan rate on voltammetry between 20 mV s ⁻¹ and 100 mV s ⁻¹ , at a HOPG electrode in TEABF ₄ (0.1 M) in NMP	248
Figure 4.24) CVs showing the effects of increasing the negative limit of the potential window by 0.25 V on the anodic peaks during the reverse sweep, at a scan rate of 1 mV s ⁻¹ , at a HOPG electrode in TEABF ₄ (0.1 M) in NMP.....	250
Figure 4.25) CV showing the effect of slowing the scan rate to 0.1 mV s ⁻¹ revealing subtle current responses not previously observed, indicating the complex nature of the TEA ⁺ intercalation/de-intercalation process, at a HOPG electrode in TEABF ₄ (0.1 M) in NMP	251
Figure 4.26) Randles-Ševčík plot for both the intercalation and de-intercalation peak currents observed for the intercalation/de-intercalation of TEA ⁺ at a HOPG electrode submerged in a solution of TEABF ₄ (0.1 M) in NMP.....	252
Figure 4.27) Charge/discharge plots, obtained from the second cycle of a series, of ln(<i>I</i>) <i>vs.</i> time, for TMA ⁺ cycling at a HOPG working electrode in NMP. <i>E</i> _c was varied between -2 V and -4 V. Discharge was conducted at 0 V in all cases.	256

Figure 4.28) Charge/discharge plots, obtained from the second cycle of a series, of $\ln(I)$ *vs.* time, for TEA⁺ cycling at a HOPG working electrode in NMP. E_c was varied between -2 V and -4 V. Discharge was conducted at 0 V in all cases. 257

Figure 4.29) Charge/discharge plots, obtained from the second cycle of a series, of $\ln(I)$ *vs.* time, for TBA⁺ cycling at a HOPG working electrode in NMP. E_c was varied between -2 V and -4 V. Discharge was conducted at 0 V in all cases. 258

Figure 4.29(a) $\ln(I)$ *vs.* $\ln(t)$ plots, for lithium, showing charge/discharge cycling at a HOPG working electrode in NMP at varying E_c values between -2 V and -4 V. Discharge was conducted at 0 V in all cases. 261

Figure 4.29(b) $\ln(I)$ *vs.* $\ln(t)$ plots, for TMA⁺, showing charge/discharge cycling at a HOPG working electrode in NMP at varying E_c values between -2 V and -4 V. Discharge was conducted at 0 V in all cases. 262

Figure 4.29(c) $\ln(I)$ *vs.* $\ln(t)$ plots, for TEA⁺, showing charge/discharge cycling at a HOPG working electrode in NMP at varying E_c values between -2 V and -4 V. Discharge was conducted at 0 V in all cases. 263

Figure 4.29(d) $\ln(I)$ *vs.* $\ln(t)$ plots, for TBA⁺, showing charge/discharge cycling at a HOPG working electrode in NMP at varying E_c values between -2 V and -4 V. Discharge was conducted at 0 V in all cases. 264

Table 4) Tabulated gradient values for both charge and discharge transients, acquired from $\ln(I)$ *vs.* $\ln(t)$ plots (Figure 4.29(a-d)) for Li⁺, TMA⁺, TEA⁺, and TBA⁺ 265

Table 5) Tabulated TEA:C ratios determined from various intercalation times 268

Figure 4.30) 3D molecular structures of C_{44} and TBA^+ , drawn to scale, highlighting their relatively similar sizes. The 2D model (top-left) shows TBA^+ 's flattened conformation spanning nearly 14 benzene rings (C_{44}) 270

Figure 5.1) Photographs of (a) as prepared HOPG, (b) HOPG expansion after 1000 s TEA^+ intercalation, (c) HOPG expansion after 1000 s TBA^+ intercalation, (a–c scale in mm) (d) HOPG expansion after 10,000 s TBA^+ intercalation, and (e) SEM image of HOPG expansion after 6000 s TBA^+ intercalation 278

Figure 5.2) SEM micrographs of various portions of a TBA^+ intercalated (–0.5 mA, 1000s) HOPG sample displaying (a) micron-sized pores developing in the graphite structure attributed to ion intercalation, (b) fan-like expansion accompanied with micron sized pores, (c) portions of the graphite electrode not exposed (left) and exposed (right) to the electrolyte solution, and (d) zoom of (c) showing only expansion at edge sites and not deep into the graphite lattice 281

Figure 5.3) SEM micrographs showing TBA^+ intercalated HOPG (–0.5 mA, 1000s) highlighting (a) two distinct features of the expansion (macroscopic gallery expansion and microscopic flake expansion), (b–d) regions of the HOPG cathode showing both gallery expansion and flake expansion indicating that the two features are not dependent upon each other..... 283

Figure 5.4) SEM micrographs displaying (a) *ca.* 200 μm sized gallery expansion, and (b) microscopic expansion within the expanded segments shown in (a). TBA^+ intercalated HOPG (–0.5 mA, 1000s)..... 284

Figure 5.5) SEM micrographs showing (a) and (b) severe electrode deformation as a result of TOA^+ intercalation (1000 s –2.5 V), and (c) corresponding CV showing poor intercalation current response 286

Figure 5.6) Photograph of TBA⁺ expanded HOPG sample (10,000 s, −0.1 mA) showing the resulting fan structure expanding from the point of contact 287

Figure 5.7) Powder X-ray diffraction pattern for a) as prepared diffraction pattern between $2\theta = 10^\circ - 90^\circ$, (b) zoom of (a) between $2\theta = 10^\circ - 26^\circ$, and (c) TBA⁺ expanded HOPG (10,000 s, −0.1 mA) 290

Figure 5.8) Powder X-ray diffraction pattern for (a) TMA⁺ expanded HOPG (1000 s, −0.1 mA), and (b) zoom of small angle peaks produced from intercalation of TMA into HOPG (*ca.* $4 \times 10 \times 1$ mm, 0.1 mg) 292

Figure 5.9) Powder X-ray diffraction pattern for (a) TEA⁺ expanded HOPG (1000 s, −0.1 mA), and (b) zoom of small angle peaks produced from intercalation of TEA into HOPG (*ca.* $4 \times 10 \times 1$ mm, 0.1 mg) 293

Figure 5.10) Powder X-ray diffraction pattern for a TBA⁺ expanded HOPG measured at increasing intercalated time intervals, showing the effect of intercalation on the pre-existing sub-lattice diffraction peaks 295

Figure 5.11) Powder X-ray diffraction patterns for SPI-1 and SPI-3 grade HOPG showing sub-lattice *d*-spacings at small angles 297

Figure 5.12) SEM imaging of various segmented sections in an expanded portion of a HOPG electrode, intercalated with TBA⁺ for 1,000 s at −2.4 V 298

Figure 5.13) SEM imaging of a HOPG electrode intercalated with TEA⁺ for 1,000 s at −2.4 V 300

Figure 5.14) SEM imaging of various segmented sections in an expanded portion of a HOPG electrode, intercalated with TBA⁺ for 1,000 s at −2.4 V 301

Figure 5.15) Powder XRD of fresh non-intercalated HK-2 graphite (blue) and TEA ⁺ -intercalated HK-2 (graphite for 5,000 s at -2.4 V), showing a general loss of crystallinity; indicated by the disappearance of several crystallographic planes in the original as-prepared graphite as well as a broad band appearing in the region $2\theta = 15 - 25^\circ$	303
Figure 5.16) Equivalent Randle's circuit for that of an electrochemical cell, showing a CPE in place of a capacitor, representing the electrochemical double layer, R2 representing the resistance to charge transfer, R_{ct} , and the inclusion of a Warburg impedance element, Z_w , representing the resistance to mass transport, to the electrode in solution	306
Figure 5.17) Typical impedance data, expressed as a Nyquist plot, recorded at a HOPG electrode in the presence of TEABF ₄ (0.1 M) in NMP with annotation describing the inherent frequency dependant mechanisms in their respective frequency regions.....	308
Figure 5.18) EIS data showing an increase in the measured electrochemical capacitance of HOPG as a result of electrode expansion caused <i>via</i> intercalation of TBA ⁺ (-2.4 V)	310
Figure 5.19) EIS data of a stainless steel WE in TBABF ₄ (0.1 M) in NMP (red) showing comparative data obtained at a HOPG WE (blue/green)	311
Figure 5.20) Nyquist plot showing high frequency EIS data measured at a HOPG WE in TMAClO ₄ (0.1 M) in NMP at cumulative cathodic charging times (-2.4 V), showing an increase in measured capacitance and decrease in resistance to charge transfer	313
Figure 5.21) Nyquist plot showing EIS data over the entire frequency range, measured at a HOPG WE in TMAClO ₄ (0.1 M) in NMP at cumulative cathodic charging times (-2.4 V), showing an increase in the total impedance associated with diffusion control	314

Figure 5.22) Capacitance and R_{ct} trends as a function of cumulatively measured intercalation times, at a HOPG WE in TBABF ₄ (0.1 M) in NMP	316
Figure 5.23) Nyquist plot showing EIS data over a) the entire frequency range, and b) high frequency range, measured at a pair of stainless steel tweezers (WE) in TBABF ₄ (0.1 M) in NMP at cumulative cathodic charging times, showing no change in C, R_s , R_{ct} , and Z_w over intercalation times as large as 4000 s.....	317
Figure 6.1) Schematic showing the routes towards flake isolation from HK-graphite rod electrodes <i>via</i> filtration and drop casting methods	325
Figure 6.2) Schematic showing the effects of gaseous products on exfoliation procedures and unsharpened graphite electrodes.....	328
Figure 6.3) Optical micrographs showing (a) and (b) micromechanically cleaved few-layer graphene on Si/SiO ₂ substrate, (c) NMP dispersed graphene transferred to Si/SiO ₂ and (d) micromechanically cleaved graphene on Si/SiO ₂ substrate after exposure to pure NMP and oven drying	329
Figure 6.4) (a-c) HOPG expansion as a result of R_4N^+ intercalation with various procedures and systems, and (d) direct HK-graphite exfoliation as a result of R_4N^+ intercalation without the need for further processing.....	331
Figure 6.5) A typical TEA ⁺ intercalation/de-intercalation CV depicting the selected cathodic charging potentials used in the chronoamperometric procedure, showing different potentials of the intercalation peak (a) -2.2 V, (b) -2.3 V, (c) -2.4 V, (d) -2.6 V, (e) -2.8 V, and (f) -3 V.	336
Figure 6.6) Photographs of the electrochemical cell under two different potentiostatic conditions in which the graphite rod was (a) cathodically charged at -3 V in the presence of TEA ⁺ (<i>ca.</i> 2000 s), and (b) cathodically charged at -2.4 V in the presence of TEA ⁺ (<i>ca.</i> 4 h)	337

Figure 6.7) Photographs of (a) as prepared HOPG, (b) TEA^+ expanded HOPG after 48 h in NMP at -2.4 V, (c) expanded HOPG in pure NMP, and (d) HOPG after 24 h sonication in pure NMP 340

Figure 6.8) Photograph showing reshaped graphite rod to counter the hindering effects of bubble formation on the residing face of the graphite cathode..... 342

Figure 6.9) Optical images of exfoliated flakes on Si/SiO₂ substrates with corresponding Raman signal responses for each individual flake. 343

Figure 6.10) Raman spectrum of a possible tri-layer obtained from TEA^+ intercalation of HK-2 graphite, showing (a) full spectrum and (b) $2D$ peak only displaying reasonably good fit to four Lorentzian functions..... 344

Figure 6.11) Raman spectrum of typical a graphite flake, obtained from TEA^+ intercalation of HK-2 graphite, showing (a) full Raman signal, (b) optical image of flake, and (c) $2D$ band with reasonable peak fitting to four Lorentzians highlighting the two-peak nature of the $2D$ band 345

Figure 6.12) Raman spectrum of a possible 3/4 layer flake obtained from TEA^+ intercalation of HK-3 graphite, showing (a) full Raman signal, (b) optical image of flake, and (c) $2D$ band with reasonable peak fitting to four Lorentzians highlighting the two-peak nature of the $2D$ band 347

Figure 6.13) Raman spectrum of a possible 4 layer flake obtained from TEA^+ intercalation of HK-7 graphite, showing (a) full Raman signal, (b) optical image of flake, and (c) $2D$ band with reasonable peak fitting to four Lorentzians highlighting the two-peak nature of the $2D$ band 348

Figure 6.14) Raman spectrum of a possible bi-layer flake, obtained from TEA^+ intercalation of HK-11 graphite showing (a) full Raman signal, (b) optical image

of flake, and (c) 2D band with reasonable peak fitting to four Lorentzians highlighting the two-peak nature of the 2D band 349

Figure 6.15) Raman spectrum of a possible tri-layer flake, obtained from TEA⁺ intercalation of HK-800 graphite showing (a) full Raman signal, (b) optical image of flake, and (c) 2D band with reasonable peak fitting to four Lorentzians highlighting the two-peak nature of the 2D band 350

Figure 6.16) Optical image showing exfoliated material drop casted onto oxidised silicon wafers (300 nm oxide thickness) displaying both large ‘graphitic’ flakes and smaller ‘graphene’ materials..... 352

Figure 6.17) AFM images of flakes prepared *via* 12 h TMA intercalation (−2.4 V) and subsequent exfoliation of the graphite rod. (a) zoom in of representative 2.5 μm × 2.5 μm area showing AFM traces, (b) Micrograph of typical 20 × 20 μm area of Si/SiO₂ substrate supporting flakes, (c) corresponding height measurements of red traced path in Figure 6.17(a), (d) Flake thickness (nm) distribution of 456 graphene islands, (e) corresponding height measurements of green traced path in Figure 6.17(a), (f) flake area distributions (m², (20 × 10^{−15} m)^{1/2} corresponds to 140 nm) of 456 graphene islands. 354

Figure 6.18) SEM images of graphene exfoliation supported on holey carbon TEM grids showing, (a)-(c) typical few-layer materials similar in lateral size to those shown in previous AFM data (Figure 6.21), and (d) a larger flake exhibiting more graphitic morphology to the presented smaller flakes..... 357

Figure 6.19) XPS survey spectrum of as prepared HK graphite rod showing relative atomic percentage of oxygen and carbon present 359

Figure 6.20) XPS survey spectrum of electrochemically exfoliated graphite rod showing relative atomic percentage of oxygen and carbon present 360

Figure 6.22) Photograph of round bottomed flasks containing graphite powder post 24 h sonication (30% power, 37 kHz, 26 °C) in (a) NMP containing TBABF ₄ (0.1 M), and (b) pure NMP ²⁸²	362
Figure A1) Schematic showing Approach A: micromechanical injector setup .	378
Figure A2) Schematic of Approach B: <i>in situ</i> electrochemical cell obtained from EL-Cell GmbH, Hamburg, Germany, showing placement of WE between quartz window and copper current collector, lithium CE and lithium RE	380
Figure A3) Photographs of a) graphite (200 µm) pellet, b) graphite pellet supporting a solution of TMAClO ₄ (0.1 M) in NMP after initial deposition, and c) wetting effects of TMA ⁺ containing electrolyte solution on graphite pellet displaying instability after as little as 10 minutes.	382
Figure A4) Photograph of HOPG sample supporting electrolyte drop taken after ca. 30 minutes, showing successful HOPG-support of a solution of TMAClO ₄ (0.1 M) in NMP with no effects of wetting.	383
Figure A5) Schematic and photograph of HOPG support electrode using micromanipulator injector setup	384
Figure A6) (a) Raman spectrum of few-layer graphene material on pure silicon wafers, and (b) optical image of analysed flake faintly visible through solution	385
Figure A7(a) Consecutive CVs showing non-reversible Li ⁺ reduction at a HOPG electrode.....	387
Figure A7(b) CVs showing non-reversible TEA ⁺ intercalation/de-intercalation into a HOPG electrode after as little as three CV scans	388

Figure A8) CVs showing current response (current density) at a HOPG (14.8 mg) working electrode displaying prominent TEA⁺ redox peaks on the initial scan with significantly reduced intensities on the successive scans 390

Chapter one

Introduction

1 Introduction

1.1 Carbon

Carbon, first classified as an element by Antoine Lavoisier in 1789¹ and originally placed fifth in Mendeleev’s periodic table of the elements², is arguably one of, if not *the*, most well studied components of our world. Life as we know it is described as carbon-based and the majority of all scientific discoveries can be traced back to the little six-proton bearing nucleus. The fundamental reason for carbon’s significance in our universe lies within its ability to form two, three and four chemical bonds with neighbouring atoms and molecules, yielding an array of structural configurations and spanning a myriad of functions and applications in everyday life; from its importance in industrial stainless-steel alloys³, simple sugars and complex DNA coding⁴, to the forefront of the industrial revolution in the form of hydrocarbons, and not forgetting more recent troubles in relation to climate change. The importance of carbon in our world cannot be overstated, since it plays such a pivotal role in every aspect of historic and modern science.

With respect to carbon based chemical structures consisting of purely adjacent covalently bonded carbon atoms, is it possible to obtain several different carbon *allotropes*. The first and most common form is known as diamond (from the ancient Greek *adámas*, “unbreakable”). Here carbon’s four sp^3 orbitals are able to form four individual σ bonds in a tetrahedral configuration, resulting in a continuously extended and extremely rigid crystal structure yielding, as the ancient Greeks accurately assumed; the hardest known natural material to mankind. The extremely high inherent crystallinity results in good thermal conductivity, by allowing even and efficient energy dispersion throughout the crystal lattice. Conversely, diamond is a poor electrical conductor due to the

strong covalent bonding and large band gap, and therefore a free electron mobility deficiency; thus pure diamond has few applications in electrochemical techniques.

It would be a hasty introduction to diamond to ignore its fascinating visual characteristics and robustness which make it the most popular gemstone in jewellery. Pure diamond has an electronic band gap of 5.5 eV, corresponding to a deep ultraviolet wavelength of 225 nm. Because of this, the energy of visible light is insufficient to cause electron promotion from the electronic valance band to the conduction band, and as a result visible light is completely transmitted, yielding diamond's characteristic clear and colourless appearance. Coloured diamond is possible however, and is due to the presence of trace chemical impurities; nitrogen (yellow), boron (blue), hydrogen (violet) and vacancy defects located throughout the lattice (red).⁵ All of these chemical changes have the same effect: reducing the electronic band gap to energies sufficiently small to allow electron promotion, induced by visible light absorption. These effects of chemical doping have been exploited in the scientific world, and synthetic diamond doping is a relatively popular area of research in which a small proportion of carbon atoms (ppm, 10^{18} - 10^{21} atom cm⁻³)⁶ within the lattice are substituted with boron. The electron deficient boron, which reduces the band gap to permit the absorption of visible light, also permits electron mobility *via* the introduction of carrier holes through which electrons can move freely, allowing boron doped diamond (BDD) to be studied as an electrode material in electrochemistry.

Since the valence orbitals in carbon are similar enough in energy, it is possible to form another stable structure consisting of three planar σ bonds hybridised with a pair of delocalised π -electrons. This layered sp^2 structure is termed

graphite, and is a well-known electrical conductor and thermal insulator.⁷ Graphite consists of layers of hexagonally arranged carbon rings covalently bonded to one another, which are able to stack upon each other in various ways (section 2.5.1). Unlike diamond however, graphite is a soft material, a feature that is directly related to the layered nature of the crystal, allowing the layers to slide over one another with relative ease. More importantly with respect to this thesis, because of graphite's good electronic conductivity, it is a much more natural material for electrochemical applications than other carbon allotropes.

The planar C-C sp^2 bond length in graphite is 1.42 Å and this double bond-like character is fully responsible for the increased conductivity. This delocalised π -bond arises from the interaction of the neighbouring un-hybridised p-orbitals, and this degree of conjugation allows electrons to move freely throughout the entire plane. In contrast, the strength of the van der Waals (vdW) interactions holding the layers together can be reflected in the interlayer spacing. The distance between layers is approximately 3.354 Å and as a result graphite is easily cleaved parallel to the layers.⁷ The poor overlap of un-hybridised p-orbitals results in large electrical resistivity ($0.15 \times 10^{-3} \Omega \text{ cm}^{-1}$)⁸ in the direction perpendicular to the layers, making graphite structurally unique.

Highly orientated pyrolytic graphite (HOPG) is manufactured graphite with an exceptionally high degree of crystallographic orientation, typically achieving less than 1° of angular spread between the graphite sheets.⁹ HOPG is particularly useful as an electrode material due to its easily accessible edge planes and cleavable basal plane which on cleaving presents a new, chemically clean reactive substrate. In electrochemistry, HOPG is a suitable material for the investigation of both edge plane and basal plane activity in electron transfer and it has been suggested that electron transfer (ET) reactions proceed more

slowly on the cleaved surface (basal plane) than on the exposed edge plane of HOPG.¹⁰ HOPG is prepared by compression annealing of pyrolytic graphite at 2800 to 3600°C.⁷

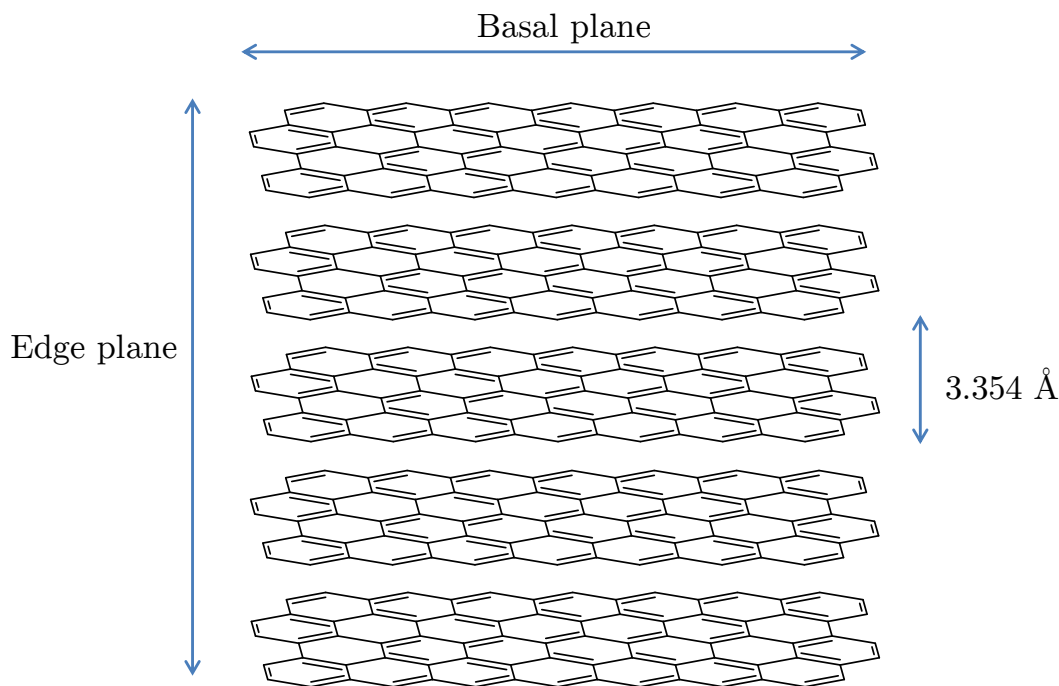


Figure 1.1) Schematic representation of HOPG showing five AB-stacked graphene layers and four 3.354 Å interplanar separations

Glassy carbon (GC) is another major form of carbon widely used as an electrode material. GC electrodes consist of sp^2 carbon-bonded sheets, similar to that of graphite, which are intertwined with one another resulting in a hard, amorphous material.¹¹ In addition to GC's good conductivity, other desirable properties for use as an electrode in voltammetry include its extremely low gas permeability and its high chemical inertness.

Table 1) Table summarising the density, electrical resistivity and band gaps of graphene, diamond, GC, HOPG, silver and molybdenum disulphide

Material	Density / g cm^{-3}	Electrical resistivity / $\Omega \text{ m}$	Band gap / eV
Graphene	7.7×10^{-8} (theoretical) ⁽¹²⁾	1×10^{-8} ^(13,14)	0 ⁽¹⁵⁾
Diamond	3.51 ⁽⁷⁾	10^{16} ⁽¹⁶⁾	5.5 ⁽¹⁷⁾
GC	1.3 – 1.6 ⁽¹⁸⁾	$3 - 8 \times 10^{-5}$ ⁽¹⁹⁾	1 – 4 ⁽²⁰⁾
HOPG	2.25 ⁽²¹⁾	$3.5 - 4.5 \times 10^{-7}$ (basal plane) ⁽⁸⁾ $0.15 - 0.25 \times 10^{-3}$ (edge plane) ⁽⁸⁾	0.04 ⁽²²⁾
Silver	10.49 ⁽²³⁾	1.58×10^{-8} ^(24,25)	0 ⁽²⁵⁾
MoS ₂	5.06 ⁽²⁶⁾	8.51 ⁽²⁷⁾	1.2 – 1.4 (bulk) ^(28,29) 1.9 (2D material) ^(28,29)

Although these forms of bulk carbon have significantly different structures, it should be noted that they only consist of carbon atoms in two different hybridised states, which are fundamental to the bonding that prevail. The values in Table 1 highlight this, and show how the density, electrical resistivity and band gap of several different carbon based structures vary as a result of the inherent carbon hybridisation, as well as comparative values for silver, and molybdenum disulphide; the latter being another 2D semi-conductor material. The most striking value presented is the electrical resistivity of graphene. Due to its high extent of electron delocalisation and extremely high intrinsic charge carrier mobility, graphene's electrical resistivity is even lower than silver metal; the least electrical resistive material known.²⁵

Because diamond is electrically insulating, focus is placed on structures with the delocalised system essential for the required electrical conductivity. GC and graphite are three dimensional structures and therefore can be split into lower dimensions.

In 1985, the first preparation and characterisation of C_{60} *via* laser radiation was reported by Kroto, Curl and Smalley.³⁰ C_{60} , or Buckminster fullerene, was the first completely spherical molecule consisting of 60 fully conjugated carbon atoms, as illustrated in Figure 1.2. This discovery presented the first reduced dimensionality carbon structure and represents a 0D configuration. C_{60} is fully sp^2 hybridised and thus has a large delocalised system made up of 20 hexagonal and twelve pentagonal rings. The five membered rings are required for the curved surface to exist and the structure is arranged such that no five membered rings are adjacent to one another. The inclusion of both five and six membered rings results in two different C–C bond lengths; bonds at the junctions of two hexagonal rings have a length of 139 pm whereas bonds between hexagonal and pentagonal rings have an increased length of 145.5 pm. This results in C_{60} (and all other members of the fullerene family) possessing localised single bond and double bonds throughout its structure and thus C_{60} cannot be said to have 100% aromaticity, due to the poor electron delocalisation in the five membered rings.³¹⁻³³

If we are to increase the idea of Buckminster fullerene in one geometrical direction, the resulting structure is the carbon nanotube (CNT), which has much more promising applications within electroanalytical chemistry. CNTs are generally divided into two groups; single-walled carbon nanotubes (SWCNTs) which consist of a single rolled up layer of graphite, and multiwalled carbon nanotubes (MWCNTs), which contain several rolled up sheets of

graphite illustrated in Figure 1.2. CNTs were first proposed as early as 1952 when Radushkevich and Lukyanovich obtained clear TEM images of 50 nm diameter tubes.³⁴ These findings were published in the *Soviet Journal of Physical Chemistry* and is perhaps the reason that the discovery did not catch the scientific world's attention until their 're-discovery' by Sumio Iijima in 1991.^{32,35}

As CNTs are essentially rolled up single/multilayer graphene sheets, perhaps the obvious solution to enable reliable electrochemical studies would be to unroll them into their corresponding sheets. This leads us onto the final sub-dimensional allotrope of graphite, the unique two dimensional layer; graphene.

1.2 Graphene and its analogues

Graphene was discovered at the University of Manchester in 2004 by Andre Geim and Konstantin Novoselov, who in 2010 were jointly awarded the Nobel Prize in Physics for their contributions to condensed matter physics and the isolation of graphene. It was previously assumed that graphene could not exist in the ‘free state’, as isolated 2D crystals were thought to be too thermodynamically unstable.³⁶⁻³⁸ However it has been found that, specifically for graphene, this is counteracted by the abundance of strong interatomic bonds preventing the degradation of the material *via* thermal fluctuations.³⁹⁻⁴¹

Graphene is a continuous single atomic plane of graphite with exceptionally high crystal quality which is “*sufficiently isolated from its environment to be considered freestanding.*”⁴² Although it is the last of the sub-dimensional carbon structures to be isolated, it can be considered the fundamental building block to which all others carbon structures are built upon; wrapped 0D fullerenes, rolled 1D CNTs and layered 3D graphite (Figure 1.2). This two-dimensional lattice is composed entirely of carbon sp^2 hybridisation arranged in a honeycombed network, thus it can be viewed as an “infinite” aromatic molecule since the unhybridised p_z orbitals on each carbon form an extensively conjugated π system. Consequently, graphene exhibits unique electrical and mechanical properties including excellent tensile strength, thermal and electrical conductivity and possesses fascinating electronic properties such as the Quantum Hall effect at room temperature.⁴²⁻⁴⁶

Additionally, since graphene, by definition, is two dimensional it yields an appreciable theoretical specific surface area of $2630 \text{ m}^2 \text{ g}^{-1}$, making it a contender as an electrode material for future supercapacitor research.⁴⁷

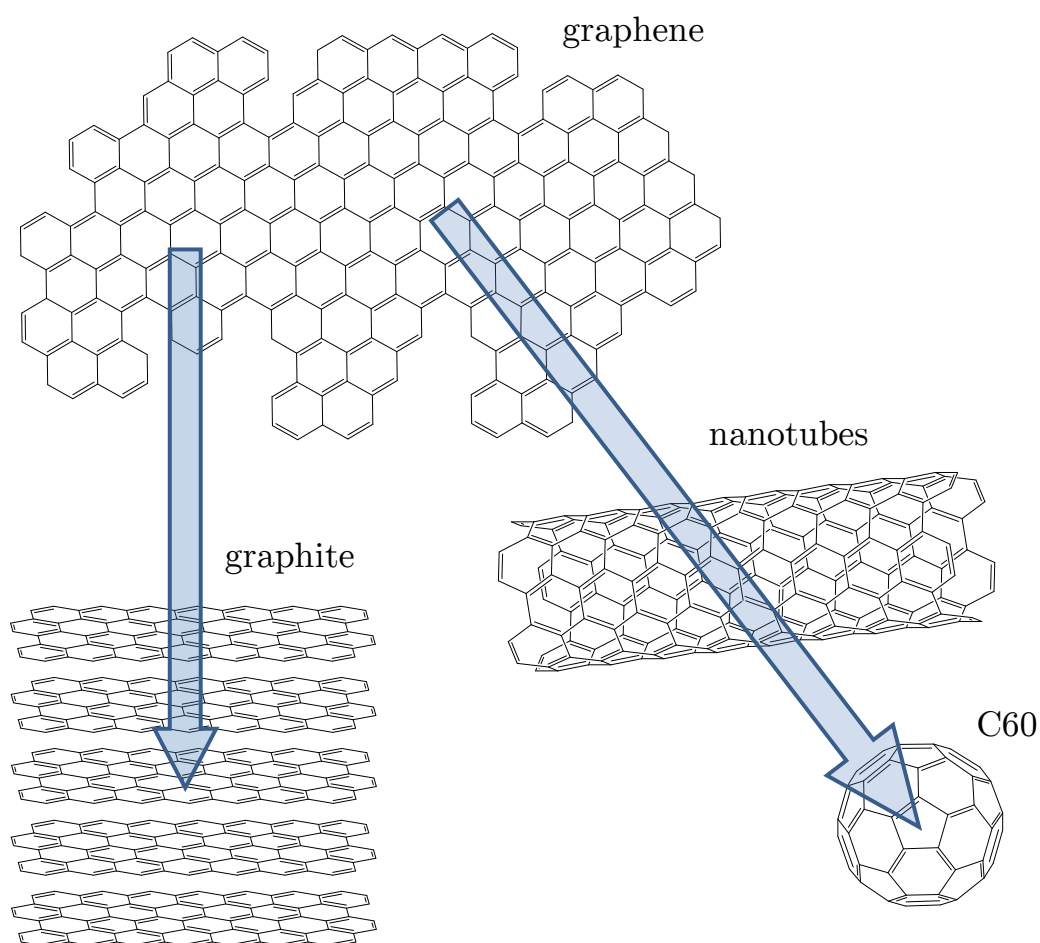


Figure 1.2) Molecular models depicting how layered graphite, rolled carbon nanotubes (CNTs) and wrapped Buckminsterfullerene (C60), can all be constructed from graphene sheets

1.3 Electronic and mechanical properties of graphene

Although there is a rapidly growing family of 2D crystals, graphene has remained in the spotlight of experimental and theoretical research, leaving all other 2D materials relatively unexplored. However, the primary reason for graphene's initial success is undoubtedly clear; its inimitable charge transport properties.

Each carbon atom in the lattice is able to form three strong covalent sp^2 bonds to adjacent carbons via the hybridisation of the s, p_x and p_y atomic orbitals. The available p_z atomic orbital is then able to overlap with the three neighbouring atoms to form a band of filled π orbitals, thus providing graphene (and graphite) the ability to conduct in the crystallographic xy plane. Essentially, the bonding π and antibonding π^* bands of graphene are indistinguishable at the Fermi energy level and thus there is no band-gap, hence graphene being categorised as *zero-gap semiconductor*. This is important with respect to electrochemistry and electron transfer (see later, section 1.4)

In electronics, field effect transistors (FETs) are used to control the flow of electrons (or holes) from the source to the drain, such that either an n-channel or p-channel (negative and positive, respectively) is employed; thus FETs are said to be unipolar.⁴⁸ However, graphene displays a large ambipolar electric field effect, in that charge carriers can be continuously tuned between electrons and holes, to concentrations, n , as large as 10^{13} cm^{-2} .^{38,49,50} Perhaps even more interesting is the way in which these charge carriers behave. In graphene, electrons propagating through the hexagonal carbon lattice lose their effective mass, resulting in relativistic particles more naturally described using the Dirac equation, rather than the Schrödinger equation more commonly associated with electrons at ambient conditions. These quasiparticles created by the interaction

with the periodic potential of graphene's honeycomb lattice (Dirac fermions) can be visualised as either electrons that have lost their rest mass, m , or neutrinos that have gained the electron charge, e .^{38,42} As a result of the high crystalline lattice having a minimal degree of structural defects, the electrons are said to behave ballistically, with mobilities, μ , exceeding $15,000 \text{ cm}^2 \text{ V}^{-1} \text{ s}^{-1}$ even under ambient conditions and can be improved to greater than $100,000 \text{ cm}^2 \text{ V}^{-1} \text{ s}^{-1}$ *via* reducing impurity scattering (*cf.* $1,000 \text{ cm}^2 \text{ V}^{-1} \text{ s}^{-1}$ for single crystal silicon.⁵¹) It has been shown by Chen *et al.*¹³ that at a carrier density of $1 \times 10^{12} \text{ cm}^{-2}$, scattering by the acoustic phonons in pristine graphene places an intrinsic limit of $200,000 \text{ cm}^2 \text{ V}^{-1} \text{ s}^{-1}$ on room temperature mobilities. However graphene supported on Si/SiO₂; the most commonly investigated experimental setup, has been shown to limit carrier mobilities to $40,000 \text{ cm}^2 \text{ V}^{-1} \text{ s}^{-1}$ as a result of optical phonon induced scattering of the Si/SiO₂ substrate. Moreover, electrons are able to travel unscattered with no decrease in velocity over a submicron scale, with the scale extending to as much as $0.3 \text{ }\mu\text{m}$ at 300 K .³⁸

Graphene's mechanical and thermal properties are in no way overshadowed by its electronic properties. It displays a tensile strength as high as $130,000 \text{ N/mm}^2$, has room temperature thermal conductivity of $5000 \text{ W m}^{-1} \text{ K}^{-1}$ and a Young's modulus of almost 1.0 TPa .^{42,52,53}

For a more comprehensive review on graphene physics, including its inherent quantum Hall effects, the reader is directed to a progress report by Geim and Novoselov.³⁸

1.4 Electrochemical and chemical properties

With respect to heterogeneous electron transfer, knowledge of the density of electronic states (DOS) within the system is essential to the understanding of ET reactions. Metals are highly conductive since there are a high number of atomic orbitals available to form bands with a large DOS, and thus electrons are able to move freely between atoms with minimum energy penalty. Marcus theory states that in the heterogeneous electro-reduction of O to R, there is a conservation of energy accompanied with the electron transfer, and thus, the energy of R must exactly equal the sum of O and the energy of the electron in its Fermi level.⁵⁴ Metals are therefore, usually, the best choice of electrode material, since there is a range (band) of energies available for heterogeneous electron transfer to redox species with different formal potentials. However, semiconductors possess zero DOS in the gap region (the band *gap*) and so for electron conduction *i.e.* promotion of an electron from the conduction band to the valence, there is an energy cost. Due to inherent defects within HOPG, there is actually a slight overlap between the conduction and valence bands⁵⁵ thus resulting in a low DOS at the Fermi level ($0.0022 \text{ states atom}^{-1} \text{ eV}^{-1}$ *cf.* $0.28 \text{ states atom}^{-1} \text{ eV}^{-1}$ for gold).³³ For semiconducting CNTs however, there is a band gap which electrons require sufficient energy to pass to permit conduction. Figure 1.3 shows how the DOS per atom varies for CNTs with semiconductor (a) and metallic (b) properties, and graphene (c); displaying the band gap more clearly.

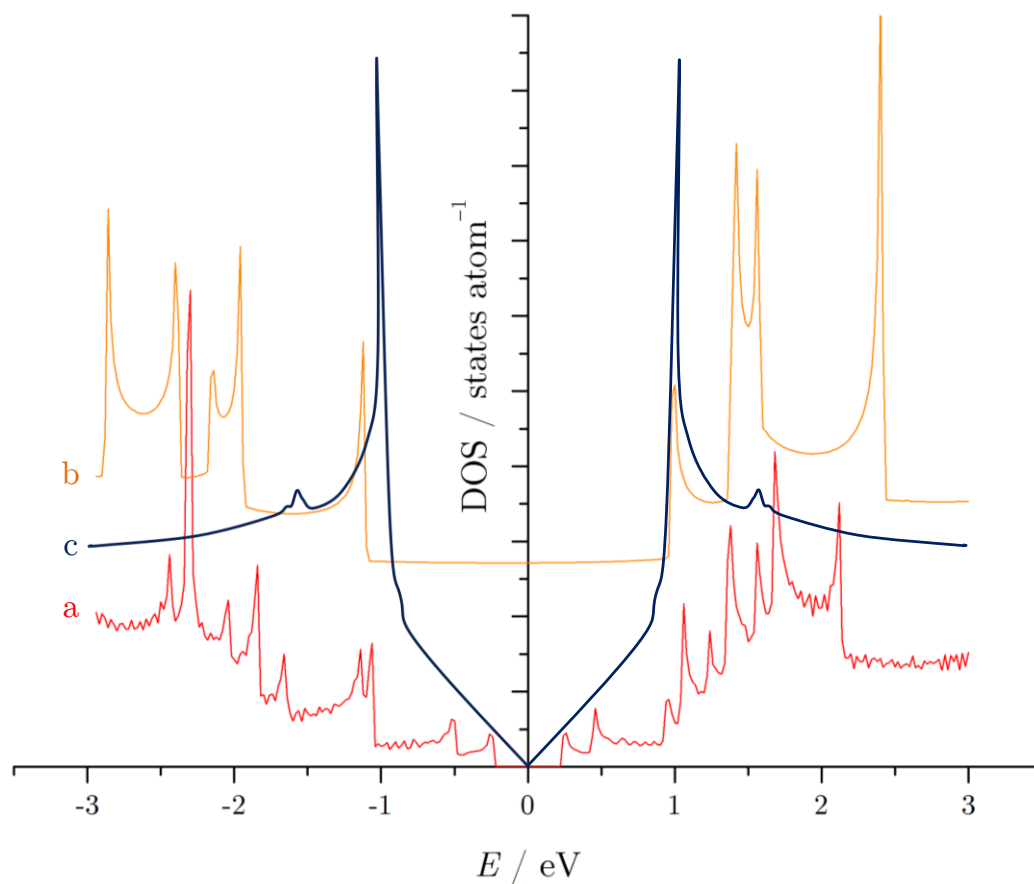


Figure 1.3) DOS per unit cell for (a) (17,3) CNT exhibiting semiconductor behaviour,⁵⁶ (b) (7,7) CNT exhibiting metallic behaviour,⁵⁶ and (c) graphene exhibiting zero-band semiconductor behaviour⁵⁷

With respect to heterogeneous ET, it follows that any redox couple with a formal potential in this region cannot undergo ET, though molecular energies will be broadened by thermal effects. For most carbon electrodes this is has significant importance, since it has been shown the DOS is directly dependent on the carbon structure (Figure 1.3).

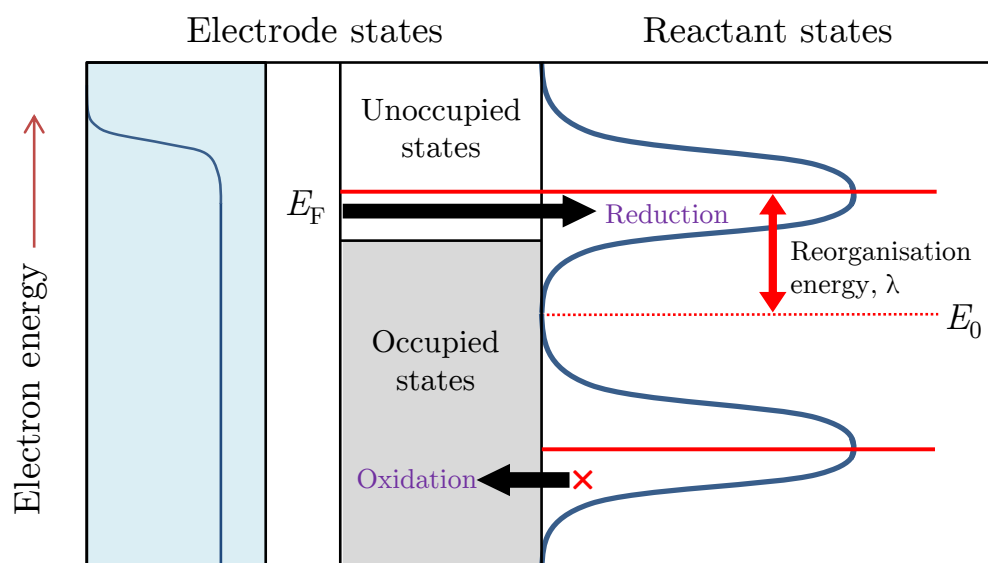


Figure 1.4) Fermi level schematic describing heterogeneous electron transfer and the required energy of the Fermi level in order to permit electron donation to the reactant, according to the Marcus-Gerischer view

Figure 1.4 describes how reduction and oxidation processes are able to occur within a system *via* control of the Fermi energy, or potential of the working electrode. If for example the potential of the working electrode is held at a potential that exceeds the standard potential (E_0) of the redox couple in solution, then the molecule is able to accept an electron and subsequently be reduced. In turn, oxidation can only occur if it is energetically favourable *i.e.* if $E_0 > E_F$. In HOPG there is a slight overlap in energy of the conduction band and the valence band and as such HOPG is often referred to as a semi-metal, with E_F lying in amongst accessible energy levels.

Carbon materials host a range of advantageous properties making them highly versatile electrode materials. They generally have large potential windows, are fairly inert with respect to species adsorption, are cheap and light, and can be manufactured in an array of shapes and sizes for use in different systems. Since CNTs are essentially rolled up graphene, it can be safely assumed that graphene materials utilise all the valuable properties of CNTs whilst omitting the most challenging aspects, such as the metal catalyst impurities that stem from the tubes' production. The 2D nature of graphene results in no volume difference between graphene's surface and bulk structure, giving a maximum surface area to volume ratio with a theoretical surface area of $2630 \text{ m}^2 \text{ g}^{-1}$.^{38,42,58,59} Moreover, graphene's ambipolarity means that chemical functionalization of either electron donating or electron withdrawing substituents can lead to chemical "gating" of the electrode, which can be easily monitored with the use of current detection methods.^{60,61} This high sensitivity is a key interest since it highlights the possibility of single molecule detection, *via* graphene functionalization to facilitate surface adsorption of gaseous molecules.

Depending on how one is to define 'graphene', it could be reasoned that there is currently very little published work on the electrochemistry of graphene. However if one were to search the available literature for 'graphene' and 'electrochemistry', Elsevier's Scopus search engine returns over 5000 results. This highlights how loosely the word 'graphene' is applied, resulting in an abundance of 'graphene research' papers in which graphitic materials are often studied. Graphene is, strictly speaking, a single layer material and is intuitively often termed 'single layer' graphene or 'mono-layer' graphene for the purpose of clarity. There are hundreds of papers on the electrochemistry of graphene nanosheets (GNS), multi-layer (MLG) and few-layer graphene (FLG), and thousands on CNTs alone.

Graphene, CNTs and HOPG can all be studied with respect to their structural geometries. HOPG is highly anisotropic with electrical resistivity perpendicular to the basal plane significantly larger than perpendicular to the edge plane, $1.7 \times 10^{-3} \text{ } \Omega \text{ m}$ *cf.* $4 \times 10^{-7} \text{ } \Omega \text{ m}$ respectively.⁷ This correlates with reports of the basal plane being much less electrochemically active than the edge plane, with much slower ET rates being quoted for typical redox mediation systems, for example the ferro/ferricyanide redox couple has been reported to exhibit an ET rate of $<10^{-9} \text{ cm s}^{-1}$ at the basal plane, and 0.022 cm s^{-1} at the edge plane of graphite.⁶² However, Lai and co-workers have reported evidence to suggest fast ET ($>0.5 \text{ cm s}^{-1}$) for $[\text{Ru}(\text{NH}_3)_6]^{3+}$ reduction at basal plane electrodes.⁶³ This basal plane *vs.* edge plane phenomenon has developed into a controversial topic, with some authors claiming that any basal plane activity is simply a result of ‘guaranteed’ surface defects/step edges⁶⁴ and that the true basal plane is completely inert.⁶⁵ Moreover, it has been reported that HOPG cyclic voltammograms provide poor fits to linear diffusion simulations and display increased peak-to-peak separations (ΔE_p). This is indicative of slow ET kinetics relative to other electrode materials and highlights the contribution of step edges and defects on basal plane HOPG.⁶²

The step edges of HOPG can be as little as one graphene layer to several layers thick and form a nucleation point for reactions to proceed from. These step edges have been exploited by Penner *et al.* who have reported selective electrodeposition of metal nanoparticles onto these step edges (electrochemical step edge decoration), demonstrating the reactivity difference of edge plane HOPG to basal plane HOPG.⁶⁶

Graphene’s credible charge transfer properties highlight its potential as an electrode material in electrochemical applications. Some examples include

graphene-based supercapacitors^{67,68,59}, utilising the absolute surface area (A_s) to volume ratio, and transparent counter electrodes in dye-sensitized solar cells DSSCs).^{69,70} In order to optimise these devices fully and to incorporate graphene into electrochemical devices and sensors, it is essential to attain a solid level of understanding regarding the nature of the charge transfer mechanism of graphene.

Fundamental graphene electrochemical studies, including contribution to the basal plane *vs.* edge plane argument, hinge on a universal problem experienced by all graphene researchers; the method by which a practical sized graphene flake is isolated, and successful implementation as the functioning working electrode in an electrochemical cell. Mechanically exfoliated flake sizes tend to be no larger than *ca.* 100 μm in diameter, yielding obvious size complications in the preparation of a monolayer flake as a working electrode. A similar hindrance has long prevailed in CNT electrochemical research, though this is more significant in CNT work, since the individual nanotubes are much smaller. Additionally, there is vast amount of literature regarding graphene-based electrochemical sensors constructed from GC-modified graphene nanosheets (GNS) and reduced graphene oxide/graphene oxide (rGO/GO, respectively) electrodes, however these ‘graphene’ electrodes are generally constructed in an uncontrolled and ill-defined manner, as is also often the case with CNTs, and the increased electrochemical sensitivity is often simply a measure of an increased electrode surface area.⁷¹⁻⁸⁸

Returning to the basal plane *vs.* edges debate, Davies *et al.* argue that any graphite basal plane activity is solely due to surface defects on the exposed basal plane. They conclude this by selectively isolating the edge terraces of step edges, *via* chemical masking of the basal plane, and show that the voltammetric

responses of the solution phase redox mediator $[\text{Ru}(\text{NH}_3)_6]^{3+/2+}$ displayed very little differentiation in peak currents from the original unmasked HOPG.⁶² However they also state that on decreasing the number of step edges, the peak separations increase, indicating slower ET kinetics. If the electrochemical response were solely due to step edges, step edge density would indeed be related to peak current but it is unclear why the number of step edges should have an effect on the reaction kinetics.

More recently, Lai and co-workers at the University of Warwick reported fast electron transfer at pristine basal plane graphite using scanning electrochemical cell microscopy (SECCM), in which the HOPG basal plane is studied directly in isolation from any present step edges.⁶³

The basal plane *vs.* edge plane argument for graphite can naturally be extended to that of graphene, and which could permit a better-defined study. Preparation of a defect free graphene sheet would provide a definite quantitative response to the debate, since a direct comparison between basal and edge plane could be made. The first reported electrochemical research on single layer graphene was published in 2011 by Li *et al.* and they state that the basal plane is indeed active for heterogeneous electron transfer.⁸⁹ They show how, by isolation of the graphene basal plane, it is possible to not only detect the oxidation of ferrocene methanol (FeMeOH), but present evidence of the system showing good reversible kinetics and behaviour typical of a diffusion controlled reaction. They obtained sigmoidal CVs and observed scan-rate-independent limiting steady-state currents, both consistent with radial diffusion to a microelectrode geometry. Additionally, currents on the order of nA were observed, which is within good agreement with theoretical currents obtained.

Even more recently, Valota *et al.* also confirm an electrochemically active basal plane, similarly acquiring currents on the order of nA for the ferricyanide reduction at basal plane graphenes. Additionally, they report values for the standard charge transfer rate constant (k_0) at defect-free monolayer graphene as $1.2 \times 10^{-3} \text{ cm s}^{-1}$ (twice that obtained for a defect containing multilayer sample, $7 \times 10^{-4} \text{ cm s}^{-1}$).⁹⁰

The main problems associated with correct assessment of basal plane electroactivity lie in the clear difficulties of isolating a defect-free, edge-site free, pristine graphene flake, that is sufficiently large for use as the working electrode in an electrochemical system. As such, the debate is still very active in the area of nano-carbon electrochemistry, and work remains to satisfy both views.

1.5 Graphene synthesis overview

There are naturally two approaches to the production of graphene: The first approach (or ‘*top-down*’ method) is *via* exfoliation of a larger precursor *i.e.* a bulk graphite source into individual graphene layers, whilst the second approach (‘*bottom-up*’) builds graphene *via* a growth mechanism from smaller carbon based constituents. As such, there are currently several accepted routes to graphene synthesis that lie within both of these general approaches.

For the purpose of this thesis, the term ‘exfoliation’ is only ever used to describe the complete removal of few-layer material from a bulk source. The term ‘expansion’ is reserved for the process by which an electrode physically expands, and the process by which large ‘graphitic’ material prematurely breaks off the electrode is termed ‘electrode fracture’.

The original and arguably finest method of graphene synthesis, in terms of structural purity and crystallinity, is the micromechanical cleavage of bulk graphite; the technique originally used in the discovery of graphene.⁹¹ The method uses Scotch tape pressed to both faces of a graphite flake where the unpeeling of the tape results in direct exfoliation of the graphite. This process is repeated typically 10 to 20 times and is able to produce high quality crystalline flake sizes up to 100 μm in diameter: sufficient for most research purposes. The problematic step does not lie within single layer production however, but the detection and isolation of any single layer products, which are effectively hidden in an overabundance of graphitic particles, since the process suffers from an extremely low throughput. Even with use of modern characterisation techniques, one can fail to successfully identify single layer flakes. For example Scanning Probe Microscopy (SPM) has too low throughput and Scanning Electron Microscopy (SEM) is unable to detect any clear

signatures from the different number of layers. AFM and Raman spectroscopy are poor large area mapping techniques and heavily rely on user familiarity with graphene materials for successful identification.

In truth, the initial discovery of graphene was particularly fortuitous. Graphene becomes visible under an optical microscope when placed on a silicon wafer with a 280 nm thick SiO₂ layer between the Si and the graphene flake; unknown at the time of discovery. Actually, Blake and co-workers found that with the use of filters, graphene is visible on any oxide layer thickness, with the exception of 150 nm and less than 40 nm, although 280 nm and 90 nm oxide layer thickness were most appropriate for use with green light.⁹² Remarkably, as little as a 5% deviation in the SiO₂ layer thickness from these optimum thicknesses can lead to graphene becoming completely optically transparent.³⁸ An additional advantage of micromechanical cleavage over all other routes presented here, with the exception of epitaxial growth, is that it is currently the only ‘dry’ process therefore minimising the risk of solvent related contamination and further processing, though residues from the tape may remain and require removal *via* washing. Micromechanical cleavage is a true one-step process and although produces the highest quality flakes for research purposes, is not a viable route for long term industrial synthesis due to the associated small lateral flake sizes, low throughput and the obvious scalability constrictions.

Alternatively, *bottom-up* epitaxial growth is the means of growing graphene either by chemical vapour deposition (CVD) using a hydrocarbon feed source or by the thermal decomposition of SiC.⁹³⁻¹⁰² CVD techniques employ a transition metal substrate, typically Fe or Ni, on which the graphene nucleation and growth occurs *via* exposure to a hydrocarbon feedstock under ultrahigh vacuum (UHV; base pressure 1×10^{-10} Torr) at typical temperatures of *ca.* 1400 °C.¹⁰³

CVD generally produces much larger flake sizes (limited by the grain sizes formed on the substrate, which can inter-grow to cover the entire substrate) than micromechanical cleavage but is an unfavourable route since it is expensive, due to the required high temperatures, produces low yields and has several processing limitations; such as the requirement of a growth substrate and subsequent transfer of grown flakes.¹⁰⁴ It generally does not form pristine graphene sheets as is the case with mechanical cleavage, introducing a large concentration of surface defects during the growth mechanism. However for the time being, the feasible large grain sizes (on the order of mm) make it a viable route of graphene production for research electronics; where a high degree of structural crystallinity is not necessarily demanded. This has been demonstrated with the production graphene sheets on 30 inch substrates¹⁰⁵ and the Samsung Group have produced the first flexible touch screen in 2010, exploiting graphene's flexibility and transparency (as well as its electrical conductivity) constructed using CVD grown graphene as the electrode component.¹⁰⁶

It has been reported that single and few-layer graphene (typically 100 layers) has been successfully produced *via* thermal decomposition of silicon carbide.¹⁰⁷ The method involves heating SiC wafers above 1100 °C, above which the Si atoms preferentially sublime and the carbons are left to self-assemble into a monolayer. This method is said to be the “champion” route to graphene for electronics applications, since the monolayer produced resembles the original dimensions of the SiC wafer, and the SiC substrate can act as an insulating base. However, this method still produces a significant amount of defects which hinder its use as a research material not to mention the high costs associated with scalability, and the inability to remove the graphene from the SiC substrate.^{42,103}

1.6 Solution phase exfoliation

In the solution phase preparation of graphene materials (the same principles apply for any exfoliated few-layer materials) the success not only depends on an effective exfoliation technique, but on the employment of an efficient dispersing solvent in which the graphene materials are exfoliated. Without such a solvent/dispersion medium, flake re-aggregation is quickly established, resulting in the sedimentation of graphitic materials. With respect to graphene exfoliation, N-methylpyrrolidone (NMP) and dimethylformamide (DMF) have been found to be the most efficient solvents for dispersibility, in terms of the obtained stable concentrations (as high as 25 mg mL^{-1})¹⁰⁸, and their investigation was based mainly on their previous success at dispersing CNTs.¹⁰⁸⁻¹¹⁶ However, it is possible to select other efficient solvents for graphene dispersibility by their Hildebrand and Hansen solubility parameters, as well as their surface tensions.^{114,115,117} It should be noted here that solvent selection cannot be solely determined by solvents/molecules exhibiting similar surface tensions, since solubility is governed by several solvent-solute interactions: dispersion forces/Van der Waals, dipole-dipole interactions, and hydrogen bonding.

Solubility theory states that a dispersion can be considered a solution when the free energy of mixing, ΔG_{mix} , is negative. The free energy of mixing is given by;

$$\Delta G_{mix} = \Delta H_{mix} - T\Delta S_{mix} \quad (1.1)$$

where ΔH_{mix} is the enthalpy of mixing, and ΔS_{mix} is the entropy of mixing. For most systems, mixing is driven by a large ΔS_{mix} ensuring a negative ΔG_{mix} . However for graphene and CNT systems, the ‘solute’ is particularly big (and rigid in the case of nanotubes), and therefore ΔS_{mix} is typically small.¹¹⁸ Because of this, it means ideal solvents for graphene/CNT dispersion likely

exhibit a small enthalpic term, in order to ensure a negative free energy of mixing.

Significantly, there are two main criteria towards efficient graphene dispersions; as addressed above, the first is by minimising the enthalpic cost of mixing, and is achieved through selection of solvents which exhibit similar surface energies to that of graphene. It has been shown that peak concentrations of graphene dispersions can be obtained for solvents with surface tensions close to 40 mJ m^{-2} ,^{108,110,112} corresponding to surface energies of *ca.* 70 mJ m^{-2} .¹¹⁹ The surface energy of graphene has been calculated to be *ca.* 68 mJ m^{-2} ,¹⁰⁸ and is consistent with that of graphite (53 mJ m^{-2}) obtained from recent contact angle measurements.¹²⁰ This dependence on surface energy indicates that dispersion stability is vdW driven, rather than chemically driven. However it is important to note that solvents simply exhibiting surface energies of *ca.* 68 mJ m^{-2} will not guarantee efficient graphene dispersion, since the solvents' Hildebrand and Hansen solubility parameters are equally as significant.

The second criterion for successful dispersion of graphene materials relies on the solvent's ability to stabilise the graphene sheets; either through steric or electrostatic stabilisation. Steric stabilisation operates *via* the presence of functionalization; physically restricting the aggregation of graphene sheets through steric hindrance.

Alternatively, in many colloidal systems, surfactant coated (or functionalised) graphene is electrostatically stabilised against aggregation, *via* formation of an electrical double layer surrounding each dispersed sheet. Indeed, Hong *et al.* show that GO undergoing further oxidation allows for successful electrostatic stabilisation in aqueous electrolytes;¹²¹ the same principles can be applied to graphene dispersions in non-aqueous electrolytes, if some residual surface charge

is present on the graphene sheets. The electric double layer is energetically sufficient to counteract the long range vdW attraction of neighbouring sheets, and effectively acts as a potential barrier, which stabilises against flake re-aggregation.¹¹² Due to its hydrophobicity, graphene does not disperse well in aqueous media without some degree of surface functionalization to prevent aggregation,^{116,122,123} whereas GO does.¹²⁴

There has been significantly more interest in graphene production *via* the reduction of graphene oxide (GO). This approach relies on the initial oxidation of graphite to GO followed by the exfoliation of the bulk graphite oxide to GO in a dispersing solvent such as NMP, DMF and even water.¹²⁵⁻¹²⁷ The GO is then reduced in several ways; *via* chemical reducing agents (such as hydrazine¹²⁸ and sodium borohydride^{129,130}), photocatalytic reduction¹³¹, electrochemical^{132,133} and thermal reduction.¹³⁴ However concerns lie within the chemistry of these steps; harsh reagents and conditions with multiple steps make this an unfavourable practice, especially for industrial scalability.¹³⁵ Issues with this route are also associated with the chemical modification of the graphene during production. The oxidation step causes significant disruption to the conjugated π -electron system and although it is subsequently reduced, it is generally accepted that all the modification processes result in irreversible changes to graphene's unique electronic properties.^{136,137} It is for this significant reason alone that GO routes prove to be an unlikely pathway for research-standard graphene, although it shows potential towards industrial applications which utilise graphene's transparency and flexibility, and where pristine graphene-grade electrical conductivity is not of utmost concern.

The unzipping of CNTs has also been explored with the aim to produce graphene nanoribbons. One solution based oxidative process exposes the MWCNTs to concentrated sulphuric acid followed by treatment with 500 wt% KMnO_4 for 1 h.¹³⁸ However the obvious ferocity associated with the harsh oxidising conditions make this an unattractive route for commerciality.

Finally, ultrasonic exfoliation has been explored by immersing graphite flakes in a dispersing solvent; typical non-aqueous solvents include NMP and DMF, and Ionic Liquids (ILs) such as 1-octyl-3-methyl-imidazolium hexafluorophosphate have been employed, which exhibit a surface energy matching that of graphene.^{139,140} Sonication allows intercalation of the solvent, forcing the constituent layers apart and the matching surface energies of graphene and the solvent molecules encourage dispersion of the exfoliated flakes in the solvent. Other media for graphene–solution stabilisation include perfluorinated aromatic solvents such as octofluorotoluene ($\text{C}_6\text{F}_5\text{CF}_3$), which acts *via* π – π stacking charge transfer of the electron rich graphene sheets and the electron deficient aromatic molecules adjacent to the electronegative fluorine atoms.^{141,142}

Hernandez *et al.* show that sonication at low power for 30 min in NMP is most promising in terms of number of average number of layers produced and highest number fraction of monolayer graphene (2.5 and 29% respectively) compared to 1,3-dimethyl-2-imidazolidinone (DMEU) (4.5 and 11%) and cyclopentanone (4.8 and 5%).¹¹⁵

Liquid phase exfoliation offers significant advantages over mechanical and CVD methods, since it is a relatively cheap method that produces flakes with minimal defects. However, this sonication method produces poor yields due to its rather uncontrollable nature, as well as typically small lateral dimensions,^{143,144} and as a result other liquid–phase procedures are still being pursued.¹⁴⁵

There are currently several processing limitations associated with all chemical and sonication-based routes to graphene materials. These include time-consuming laborious procedures, high operating temperatures, and aggressive solvents/reagents; all of which contribute to relatively high costs associated with the industrial scalability of the procedures. These unfavorable reaction conditions are required in order to overcome the cohesive vdW energy (5.9 kJ mol^{-1}) of the neighboring graphene sheets, necessary for successful graphene exfoliation. Furthermore, graphene sheets produced by these methods display relatively high sheets resistances, ranging from 1 to $70 \text{ k}\Omega \text{ sq}^{-1}$.¹⁴⁶ The reported high sheet resistances are associated with the lateral dimensions on the order of $<1 \text{ }\mu\text{m}^2$, and have been attributed to flake damage during the harsh exfoliation process.

1.7 Electrochemical synthesis of graphene materials

Electrochemical approaches to preparing graphene materials involve the use of a liquid solution (electrolyte), and an electrical current to encourage structural deformation of a graphite working electrode, either *via* reduction or oxidation of the graphite. The working electrode is typically a graphite rod/film/HOPG and is either anodically charged or cathodically charged, though the latter route is less common. Electrochemical approaches are considerably advantageous over other non-electrochemical solution-phase processing methods, since they typically take place *via* a single step, are relatively simple to operate, and can be performed under ambient conditions; making them industrially attractive. Furthermore, electrochemical approaches can be performed on the order of minutes-hours, in contrast to chemical/sonication routes which are typically run for several days.^{136,147} Despite these issues, electrochemical routes have led to reported yields of milligram and gram quantities of few-layer graphene materials,¹⁴⁸⁻¹⁵⁰ though both the quality and purity of these graphene materials is questionable, due to the highly defective sheets produced, and the high flake functionality.

There is large scope for investigation of the electrochemical methods of graphene production, which will be the main focus of this project. Since HOPG is constructed of $>10^6$ graphene layers with an interlayer spacing of 0.354 nm, it has been suggested that ion intercalation between these layers, and the physical expansion of the electrode which occurs as a result, could eventually lead to exfoliation of the graphite into its constituent layers.^{145,151,152} This is perfectly demonstrated with the principle of the lithium ion battery, in which lithium ions intercalate in and out of a negatively charged graphite electrode. However

the primary focus of lithium battery research is in prevention of graphite expansion during intercalation, with the use of an intercalating species (*i.e.* Li^+) of a smaller crystallographic diameter than graphite's interplanar spacing, allowing for repeated intercalation/de-intercalation cycling with minimal deformation effects.

So far this idea has been utilised in electrochemical research in which ions in an electrolyte solution are employed to intercalate, expand and exfoliate bulk forms of graphite, with different degrees of success being reported. Liu *et al.* claim to obtain yields as high as 80% of fluorescent carbon nanomaterials using IL assisted electrochemical exfoliation of HOPG, using 1-octyl-3-methylimidazolium hexafluorophosphate ($[\text{C}_8\text{mim}]^+[\text{PF}_6]^-$) as the IL. However the exfoliated products were found to be heavily functionalised with the IL and have detrimental effects on graphene's electrical properties.

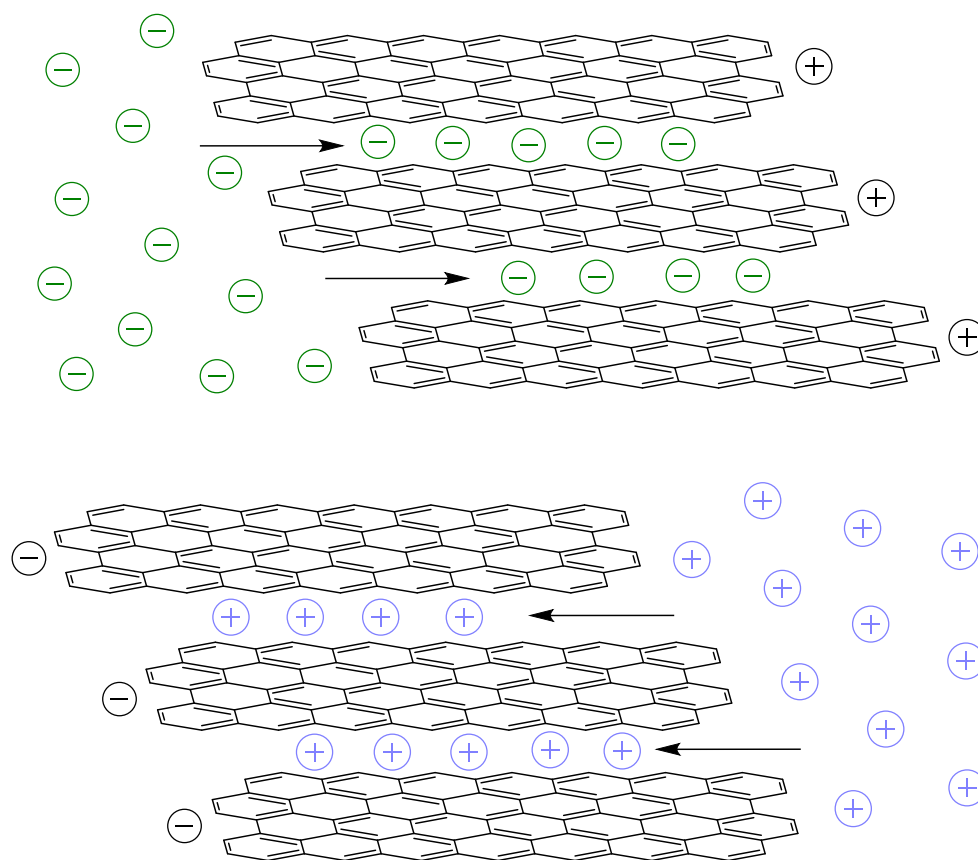
The process involved in the majority of literature utilises chronoamperometry, in which a two electrode system is used to apply a large potential difference, typically between 15 and 20 V, for a few minutes or times up to several hours. However, the chemistry of the exfoliation is somewhat unclear, not surprisingly due to the employment of extreme charging potentials, with authors offering different explanations for the resulting exfoliated nanomaterials. Lu *et al.* present an oxygen/hydroxyl radical method in which water is electrochemically oxidised, and the products attack the graphene edges facilitating tetrafluoroborate $[\text{BF}_4]^-$ anion intercalation¹⁵². However, both the above methods and the majority of intercalation/exfoliation research share a common feature in that they perform oxidation of the HOPG electrode through the use

of large anodic charging procedures, and thus inevitably produce oxidised/functionalised nanomaterials.

In contrast, the lithium insertion technique demonstrated by Wang *et al.*¹⁵³ is at the time of writing this thesis, one of only two published pieces of work demonstrating the use of pure cationic insertion, in which a Li^+ /propylene carbonate (PC) complex is intercalated between the graphene layers. However, this process requires an additional sonication step to produce electrode exfoliation and the potentials required are in excess of -15 V. It is unclear whether the intercalation or the sonication stage is the primary reason for observed exfoliation, although interestingly the authors state that lithium is necessary for successful exfoliation. They propose another mechanism in which NaOH is intercalated and found to improve exfoliation efficiency up to 20 times.^{133,145}

At the time this thesis was written, the only other report outlining a cathodic intercalation route towards graphene material production that did not heavily rely on other processing methods, such as sonication or microwave expansion was that of Yang and co-workers, who used N-butyl, methylpyrrolidinium bis(trifluoromethylsulfonyl)imide IL¹⁵⁴. The other reported work was that derived from this thesis; utilising R_4N^+ intercalation.¹⁵⁵ Both reports were available online September 2013, and the mechanisms only differ though the employed cation and the potentials required for operation; Yang and co-workers applied potentials as large as -30 V whereas the charging potentials required herein are (see Chapter 6) as little as -2.4 V. The reasons behind the selection of such cathodic potentials are not explained, however it could explain why Yang *et al.* successfully exfoliated HOPG, whereas only HOPG expansion (not exfoliation) was observed herein (shown later, Chapter 6).

anionic intercalation



cationic intercalation

Figure 1.5) Schematic showing anionic and cationic intercalation between graphene layers

Bourelle and co-workers¹⁵⁶ propose an intercalation mechanism involving formic-sulphuric acid mixtures. They present a two-step process in which initial electrochemical intercalation takes place followed by gas evolution from the intercalated species. The second stage involves the intercalation of HCOOH (facilitated by the formation of GO) and the reaction of H_2SO_4 and HCOOH between the graphene layers producing H_2O and gaseous CO . This interlayer gas evolution forces the layers apart, expanding the HOPG.

Table 2) Summary of relevant literature regarding electrochemical preparation of graphene materials through anionic and cationic intercalation mechanisms (blue: purely anionic, green: purely cationic)

Electrochemical procedure	Applied current / potential	Electrolyte	Working electrode	Exfoliation products	Comments	Ref
Anodic oxidation, edge plane attack, intercalation	+1.5 V to +8 V	[BMIM][BF ₄] / H ₂ O	HOPG	Oxidised FLG	0.002 g mL ⁻¹ in DMF, 200 nm × 500 nm	152
Anodic oxidation, IL intercalation	+15 V	[C8mim] ⁺ [PF ₆] ⁻ H ₂ O	Graphite rod	IL functionalised FLG	1 mg mL ⁻¹ 700 nm × 500 nm monolayer	151
Anodic oxidation	+5 V	Polysodium-4-styrene sulfonate	Graphite rod	Functionalised, defective FLG	-	150
Anodic oxidation, chemical reduction	+10 V	H ₂ SO ₄	Graphite flakes/HOPG	Few-layer GO	GO reduced	146
Anodic oxidation, sonication, chemical reduction	+10 V	H ₂ SO ₄	Graphite plate	Reduced GO	sonication, chemical reduction	157
Cathodic intercalation	-15 V +/- 5 V	Lithium propylene carbonate	Graphite	FLG (1-3 layers), 70% yield, 15 g	Requires sonication	153
Cathodic cation insertion and graphite exfoliation	-15 to -30 V	IL: N-butyl, methylpyrrolidinium bis(trifluoromethylsulfonyle)-imide	HOPG, graphite rods	Non-functionalised FLG (2–5 layers)	Single stage, re-dispersal in pure DMF	154
Cathodic cation insertion and graphite exfoliation	-2.4 V	R ₄ N ⁺	Graphite rod	Non-functionalised FLG (2–5 layers)	Single stage, 400 nm ² sheets, 0.012 mg mL ⁻¹	155

Table 2 continued) Summary of relevant literature regarding electrochemical preparation of graphene materials which employ the use of both anionic and cationic control within procedures

Electrochemical procedure	Applied current / potential	Electrolyte	Working electrode	Exfoliation products	Comments	Ref
Anodic oxidation followed by cathodic reduction	+0 V, +8 V, -8V	Triethylsulfonium bis(trifluoromethylsulfonyl) imide IL	Pencil	0.8 nm and 1.3 nm monolayer, FLG, GO	Functionalised materials, 0.02 g L ⁻¹ in DMF	158
Anionic oxidation/intercalation	+0 V to +10 V	FeSO ₄ + Na ₂ SO ₄ in H ₂ O	HOPG	30 - 40 nm Fe ₂ O ₃ "graphene hybrids"	Functionalised FLG	155
Anodic oxidation	+0.135 V, +1.5 V, +1.95 V	KNO ₃ , LiClO ₄ , (NH ₄) ₂ SO ₄ /H ₂ SO ₄ /KOH	HOPG	300 nm graphite layers	Oxidised graphite	159
Anodic exfoliation	+1.3 V	H ₂ SO ₄	HOPG	20 layers	Oxidised materials	156
Anodic oxidation/Cathodic reduction, potential cycling	-1 V to +3V	Aqueous Na ₂ SO ₄	Graphite	FLG (3 layers) (not Raman confirmed)	Inconclusive Raman analysis,	160
Anodic oxidation	+300 mA	Polysodium-4-styrene sulfonate	Graphite foil	Expanded graphite	Graphite foil covered in FLG	79
Anodic oxidation, edge plane attack, intercalation	-2V to +3V	[BMIM][BF ₄] IL / LiClO ₄	Flexible graphite	Flexible graphite	IL functionalised	104
Anodic oxidation, followed by cathodic reduction	+1.4 V to +2 V, then -1V to reduce	sodium dodecyl sulfate	Graphite rod	Monolayer	-	148
Cathodic reduction, microwave expansion, sonication	-1.5 V to +1.7 V	aqueous perchloric acid	Graphite foil	FLG	Microwave and sonication assisted exfoliation	149

A comprehensive review of all the literature regarding electrochemical preparation of graphene materials would take up the majority of this thesis, and therefore Table 2 has been constructed summarising many other various techniques, materials, electrolytes and solvents, as well as tabulated details regarding both the quality and concentrations of the produced graphene materials and any significant results of the reported procedure. The various procedures have been grouped according to the respective electrochemical procedure employed: where blue indicates purely anionic, green indicates purely cationic and un-highlighted entries (Table 2: continued) represent all other procedures which use a mixture of anionic and cationic procedures. A common feature throughout is the use of anionic intercalation for the purpose of expansion/exfoliation, followed by cathodic reduction to reduce the surface oxides created during the anodic process.

The vast majority of the tabulated procedures utilise anionic control to some degree, and as a result typically produce GO derivatives, as opposed to pristine graphene materials; for the problems associated with GO derivatives, please see the aforementioned discussion in section 1.6. It is thought that the reason for the commonly employed anodic oxidation is in the relative ease of the techniques, by which exfoliation is readily observed in solution.

In contrast to the popular anodic oxidation, cationic intercalation remains relatively unexplored and little success has been reported.

1.8 Thesis overview

This thesis is divided into seven chapters. Chapter one serves as an introduction to the project and acts as a summary of relevant literature relating to exfoliation methods of graphene (physical, chemical and electrochemical) as well as an introduction to graphene's electronic properties and its suitability as an electrode material in applied electrochemical systems. Chapter two is more specific to electrochemistry in general, addressing particularly relevant experimental techniques and specific experimental details including cell design, electrodes, chemicals and materials.

It is worth highlighting the main objective of this thesis; to investigate the potential towards a single stage production route for single layer graphene. The work naturally splits into three main stages; intercalation, cathode expansion and finally, electrode exfoliation. The work is therefore presented in three main Chapters correlating with the three main stages in the overall production method. Incidentally the late acquirement of a controlled atmosphere glove box resulted in the separation of the intercalation stage into two parts, which became Chapters three and four. Each Chapter will have its own individual introduction to the work, which in turn will correlate with the present introduction Chapter one.

Chapter three presents an overview of the electrochemical investigations performed prior to the acquisition of the glove-box, and investigates the uses of different reference electrode systems, solvents, electrolytes, electrolyte concentrations, and potential window limitations, as well as initial Li^+ and R_4N^+ (tetraalkylammonium) intercalation work in an open air (non-controlled) environment. The effects of oxygen involvement are addressed as well as the effects of electrode exposure on primary voltammetric cycling. The employment

of Ionic Liquids (ILs) is also investigated, alongside brief investigation with anionic intercalation processes. Finally UV-Vis spectroscopy has been used to investigate electrolyte/solvent decomposition at large cathodic potentials, and Electron Paramagnetic Resonance (EPR) to probe the presence of radical species on electrochemical reduction.

Chapter four highlights the importance of an oxygen-free working environment and all work within was conducted in an argon-saturated, pressurised glove box. The primary aim of this work is to quantitatively understand what is occurring on a molecular level in the intercalation stages with respect the intercalated species, using voltammetry and chronoamperometry as the main tools for investigation. It is of interest to determine how tetraalkylammonium cations interact with the internal basal planes of HOPG and other carbon sources under the influence of large cathodic charging potentials for prolonged periods of time and is heavily linked to current lithium ion battery work. The degree of recoverable charge on intercalation/de-intercalation has been studied for different R_4N^+ cations as well as lithium. This Chapter also investigates the potential for controlled electrochemical synthesis of GICs.

Chapter five concentrates on the irreversible volumetric expansion of the graphite cathode and how it is affected by various parameters. The main forms of characterization employed are scanning electron microscopy (SEM) and X-ray Diffraction (XRD) to determine the manner in which cation intercalation occurs with respect the host structure and how gallery expansion proceeds. Ultimately, it is of interest to control the degree of intercalation between graphene sheets in order to control the thickness of exfoliated graphene materials, therefore understanding of the expansion mechanism is imperative.

Finally, the specific capacitance and impedance of the expanded graphite electrodes has been

Chapter two

Electrochemical theory and experimental

2 Electrochemical theory and experimental

2.1 Reference electrodes and the Nernst equation

Reference electrode systems are best described with the aid of the Nernst equation (equation 2.1); which relates electrode potentials (E) to the relative concentrations of the oxidised and reduced species in solution.

$$E = E^{\theta} + \frac{RT}{nF} \ln \frac{[Ox]}{[Re]} \quad (2.1)$$

Where E^{θ} (V) is the potential for the redox couple which is measured experimentally, R is the ideal gas constant, T is temperature, n is the number of electrons transferred in the cell half-reaction and F is Faraday's constant. An example of a practical application of this equation in electrochemistry is exemplified by the construction of a stable reference electrode, to which all measured potential differences are recorded against.

In order to measure heterogeneous electron transfer, a minimum of two electrodes must be exposed to the electrolyte: the electrode of interest (working electrode, WE) and an additional electrode (counter, CE) in order to complete the circuit. This is the simplest demonstration in which the reference electrode (RE) is the CE. For accurate measurement at the working electrode, the reference electrode needs to maintain a constant electrode potential.

In order for the RE to remain stable, such that measured potentials can be accurately determined, the RE requires a constant current to pass through at all times. To permit this, the relative concentrations of the oxidised and reduced species at the electrode surface must remain constant under a range of applied working potentials. This is attained *via* chemical saturation of both contributors a suitable redox couple.

The universal standard RE, the standard hydrogen electrode (SHE), is based on the reduction of protons to form gaseous hydrogen. However, because of the impracticalities associated with the electrode, various secondary reference electrodes are commonly used and historically, the saturated calomel electrode (SCE) and silver/silver chloride (Ag/AgCl) have become the most frequently used secondary reference electrodes in aqueous media.

Ag/AgCl and SCE are commonly used aqueous electrodes and their stability is based on the surrounding saturated aqueous solution. Non-aqueous electrochemistry however poses a universal problem since there is currently no widespread practical standard RE in use. Although it is possible to use aqueous based REs in non-aqueous systems for short periods of time, it is not a reliable method for longer timescales. The problem arises as a result of undefined liquid junction potentials created by the phase boundary of the aqueous and non-aqueous media, as well as the different ionic compositions between the reference compartment and the rest of the cell. Different ionic compositions are unavoidable due to the generally poor solubility of chloride salts in non-aqueous media, where perchlorate salts may be more appropriate.¹⁶¹

In non-aqueous electrochemistry, various half cells containing silver salts have been developed for use as reference electrodes eliminating the phase boundary issue observed with alternative approaches. Additionally, the use of ferrocenium/ferrocene redox couple as an internal standard is another successful route to measuring stable electrode potentials. However organisation of data relative to various reference electrodes can be somewhat unclear, thus a universal non-aqueous standard is desirable. Contradictory to the previous statement, several non-aqueous reference electrodes have been used throughout

this work as the stability and reliability of the reference electrode was constantly improved. Eventually it was found that a Ag/AgClO₄ RE proved most reliable (section 3.2.1), and as such all potentials referred to herein have been converted such that they are *versus* Ag/AgClO₄.

2.2 Mass transport and the requirement for supporting electrolyte

The means by which molecules travel through a medium, has great impact on the electrochemical response at the electrode under inspection. There are three primary mechanisms by which species can be transported in solution to an electrode at which reaction occurs. The first of these is ion *diffusion*, which occurs as a direct result of concentration gradients present in solution. Ion *migration* occurs *via* the effect of electrostatic fields acting upon charged species; such fields drive the movement of ions in either the same or opposite direction of the field, depending on the respective charges of said ions. As such neutral species are unaffected by electrostatic forces and can therefore ignore the effects of externally applied electric fields. Finally, *convection* is the term used for species being transported *via* global movement of the solution, a primary example of convection is utilised in rotating disc electrodes by which stirring is employed to ensure a steady flux of species at the working electrode. For all work presented in this thesis, experiments were carried out on unstirred solutions and therefore no detail into convection will be presented. Nonetheless mass transport may occur in one or all forms; as such the total flux of species is a combined effect of all these routes.

$$J_i = f(\text{diffusion, migration, convection}) \quad (2.2)$$

For systems operating primarily under steady state diffusion, in the form of a controlled concentration gradient between the bulk electrolyte and electrolyte at the electrode surface, the flux of species arriving at the electrode can be adequately quantified using Fick's 1st law of diffusion, where J is the flux/mol cm⁻² s⁻¹, $\frac{\partial c}{\partial x}$ is the local concentration gradient at point x , and D is known as the diffusion coefficient (cm² s⁻¹)

$$J_{diffusion} = -D \frac{\partial c}{\partial x} \quad (2.3)$$

With respect to electroanalytical voltammetry, as described later, the assumption of purely diffusive control is applied. This assumption is permitted with the use of a supporting ‘background’ electrolyte to eliminate the transport of the electroactive species *via* ion migration. This is done by the supporting electrolyte not taking part in any electron transfer processes, but effectively carrying the majority of the current in the bulk solution due to the excess concentrations; typically $100 \times$ the electroactive redox species concentration. In addition, the supporting electrolyte increases the conductivity of the solution by minimising the effects of the Ohmic drop created by the solution. The supporting electrolyte chosen should be inert under the conditions chosen, and is sometimes referred to as the *inert electrolyte*.¹⁶² Similarly, mass transfer *via* convection can be completely neglected *via* the use of unstirred solutions.

However, for solutions where no electroactive redox species is present, (or in the bulk electrolyte phase, where concentration gradients are minimal) the effects of ion migration may be greater than ion diffusion, since the current is carried mainly in the form of migration. It should be noted that ion migration theory is of particular interest here, given its relevance to the work herein.

The flux, J , of species arriving at the electrode *via* migration can be described by the second term in the Nernst-Planck equation:

$$J_i(x) = -D_i \frac{\partial C_i(x)}{\partial x} - \frac{z_i F}{RT} D_i C_i \frac{\partial \phi(x)}{\partial x} + C_i v(x) \quad (2.4)$$

Where $J_i(x)$ is the flux of species i ($\text{mol s}^{-1} \text{ cm}^{-2}$) at distance x from the electrode surface, D_i is the diffusion coefficient, $\partial C_i(x)/\partial x$ is the concentration gradient at distance x , $\partial \phi(x)/\partial x$ is the potential gradient, z_i and C_i are the charge number (dimensionless) and concentration (mol cm^{-3}) of species i ,

respectively, and $v(x)$ is the velocity (cm s^{-1}) of the solution. The first term represents Fick's first law describing transport *via* diffusion, whereas the second term can be related to migration only.¹⁶² Finally, the third term is the convection term, and is therefore negligible in a non-stirred system. Note that equation 2.3 applies to one dimensional, or linear, diffusion.

2.3 Faradaic and non-Faradaic processes

Two forms of current are capable of being generated at electrodes in solution. The first term is reserved for the form associated with the transfer of electrical charge (or electron transfer) at the electrode-solution interface. Electron transfer, either to or from a molecule at the electrode surface, results in reduction or oxidation of the species, respectively. This type of current is known as Faradaic current, since the redox reactions involved in these processes are governed by Faraday's law. Faraday's law of electrolysis states that the amount of substance chemically altered at an electrode during electrolysis is directly proportional to the quantity of electric charge transferred at the electrode, and can be measured quantitatively:

$$Q = \frac{nFm}{M} \quad (2.5)$$

Where Q is the total electric charge transferred (C), n is the number of electrons transferred in the reaction, m is the total mass of the substance involved (g), F is Faraday's constant (C mol^{-1}) and M is the molar mass of the substance (g mol^{-1}). Consequently, it follows that the total charge transferred is directly proportional to the concentration of the species involved.

Alternatively, an electrode-solution interface can display a range of potentials at which no charge-transfer occurs due to the thermodynamically or kinetically unfavourable nature of the reaction. Nonetheless, current may still flow due to the charging of the electrode|solution interface and the consequent rearrangement of ions in solution. In addition adsorption/desorption processes may also occur whereby the electrode surface does chemically change; these processes are termed non-Faradaic. When electrode reactions take place, both forms of current occur, however Faradaic currents are generally of greater

interest in terms of electroanalysis. Nonetheless, with respect to systems where charge transfer is undesirable, such as electrochemical capacitors, understanding of non-Faradaic currents is imperative.

An Ideal Polarised Electrode (IPE) is an electrode, at which no charge transfer occurs across the metal-solution interface. In theory this phenomenon would occur regardless of the externally applied potential difference, however in practice this is not the case, since all electrodes will eventually permit charge transfer if a large enough driving force, or potential difference, is applied. However, there will be a region within the potential window of the solution by which no charge transfer takes place, and it is within these potentials that the electrode-solution interface is analogous to an electrical capacitor. Whereas an electrical capacitor is comprised of two conducting sheets separated by a dielectric material, an electrochemical capacitor is comprised of ‘layers’ of conducting ions in solution and is commonly referred to in electrochemistry as the ‘electrochemical double layer’.

In the presence of no charge transfer, at a given potential, corresponding charges will exist at the electrode, q_e , and in solution, q_s , where $q_e = -q_s$. Experimentally, two electrodes would need to be employed to permit the flow of charge, thus two electrode-solution interfaces would need to be considered.

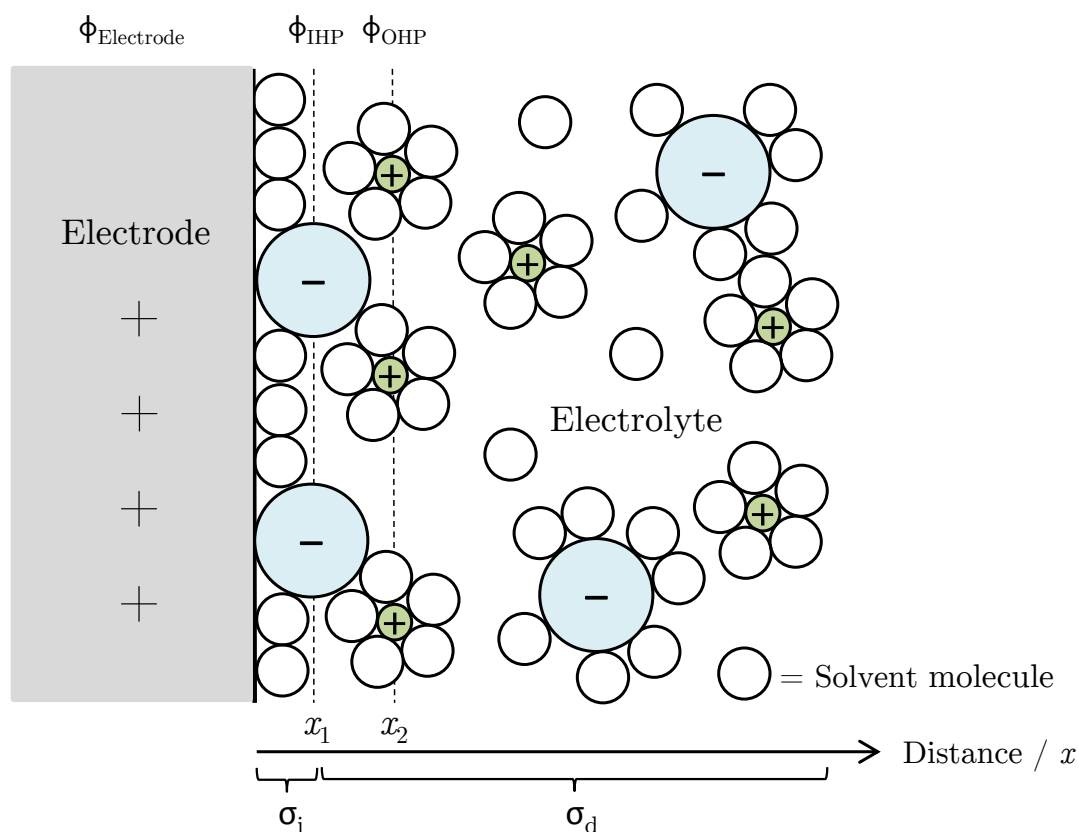


Figure 2.1) Schematic representation of the electrolyte double layer for a positively polarised electrode, showing the inner-Helmholtz plane and the outer-Helmholtz plane constructed from electrolyte species

The charge on the electrode represents an excess or deficiency of electrons; Figure 2.1 depicts an electrode with a deficiency of electrons, hence its positive charge. In particular, the charge on metal electrodes resides in a region less than $<0.1 \text{ \AA}$ from the electrode surface.¹⁶² The solution-phase charge is more complicated, whereby electrical neutrality is maintained *via* an excess of anions or cations neighbouring the electrode surface. The solution effectively forms layers of which the nearest to the electrode, the *inner Helmholtz layer*, is made up of specifically adsorbed ions/molecules. These adsorbed species are naturally neutral or oppositely charged to the electrode's polarisation. The *inner Helmholtz plane* is determined by the distance from the electrode surface, to the

foci of said adsorbed ions, x_1 , and is therefore defined by the ionic radius of the adsorbed electroactive species. The total charge density as a result of the adsorbed ions in the Helmholtz layer is σ_i ($\mu\text{C cm}^{-2}$). In addition, solvated ions are able to travel to the electrode surface only to a distance x_2 , and this distance is referred to as the *outer Helmholtz plane* (OHP). Finally, the bulk solution, not including the IHP region, is termed the diffuse layer and the total charge density associated with this region is σ_d . Subsequently:

$$\sigma_s = \sigma_i + \sigma_d = \sigma_e \quad (2.6)$$

The potential profile (Figure 2.2) across the double layer region gives an indication of the potential experienced by some electroactive species at distance x , as it is transported to the electrode surface from the bulk solution. The potential plateau, ϕ_s , is the potential the species experiences in the bulk solution and is constant throughout the diffuse layer. The electroactive species is able to approach the electrode surface only to the OHP where the potential decreases, and is equal to $\phi_2 - \phi_s$: the *potential drop* across the diffuse layer. Naturally, ϕ_1 is the potential experienced by a species at x_1 : the IHP.

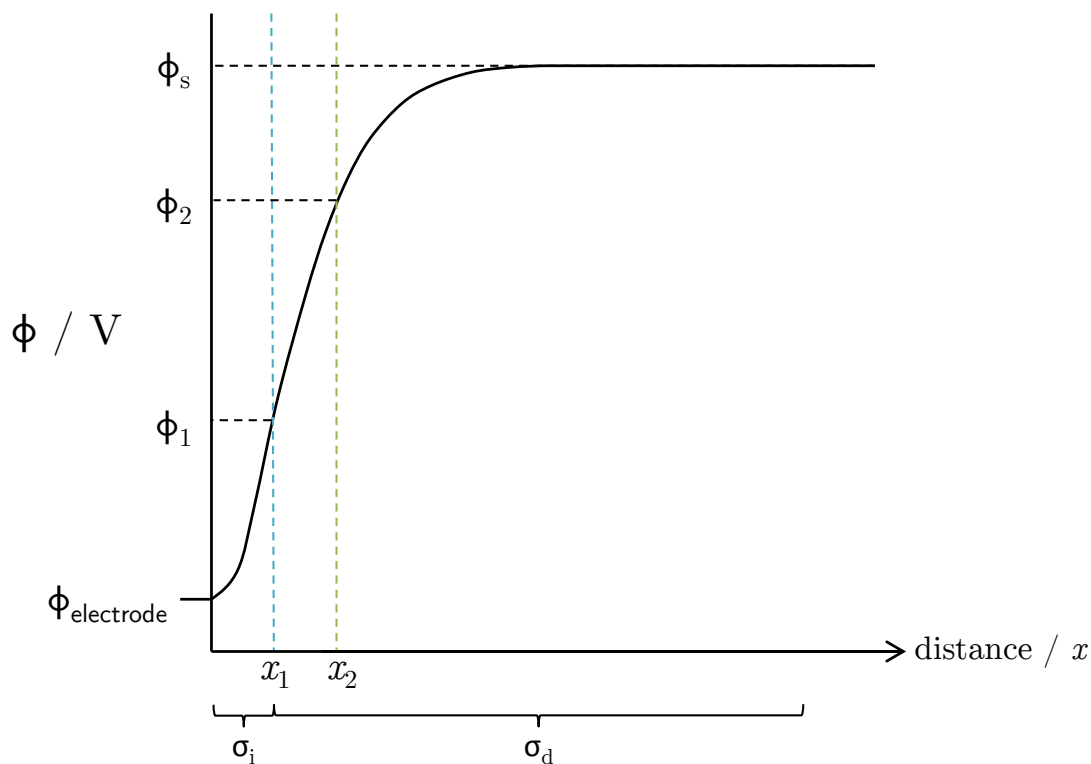


Figure 2.2) Potential profile across the double layer region indicating how the potential is distributed in solution

Specifically, double layer capacitance is of interest in the use of high surface area and/or high porosity electrodes, since electrodes with these properties are the basis of energy storage in electrochemical double layer capacitors (EDLCs). A more in depth review regarding electrochemical capacitance is provided in section 2.4.3.

2.4 Electrochemical techniques (diffusion limited)

2.4.1 Voltammetry

Voltammetry is the measurement of specific current flowing through the working electrode as a function of an externally applied potential difference, and is an indispensable tool for the analysis of electron transfer reactions at an electrode-solution interface. The most commonly used variant is the technique of Cyclic Voltammetry (CV) where an applied potential to a working electrode is swept, in a linear manner, from one limit, E_1 , through to another, E_2 , and back again. The rate at which this sweep is undertaken is the *scan rate*, ν (V s^{-1}) (Figure 2.3). It is common for E_1 to take the value of negligible current flow, although this is not a requirement, and for the investigation of an electroactive species, E_1 and E_2 are ideally selected such that the reduction potentials of the species in question lie somewhere in-between the two potential limits. This ensures that on sweeping the potential, the species undergoes oxidation or reduction.

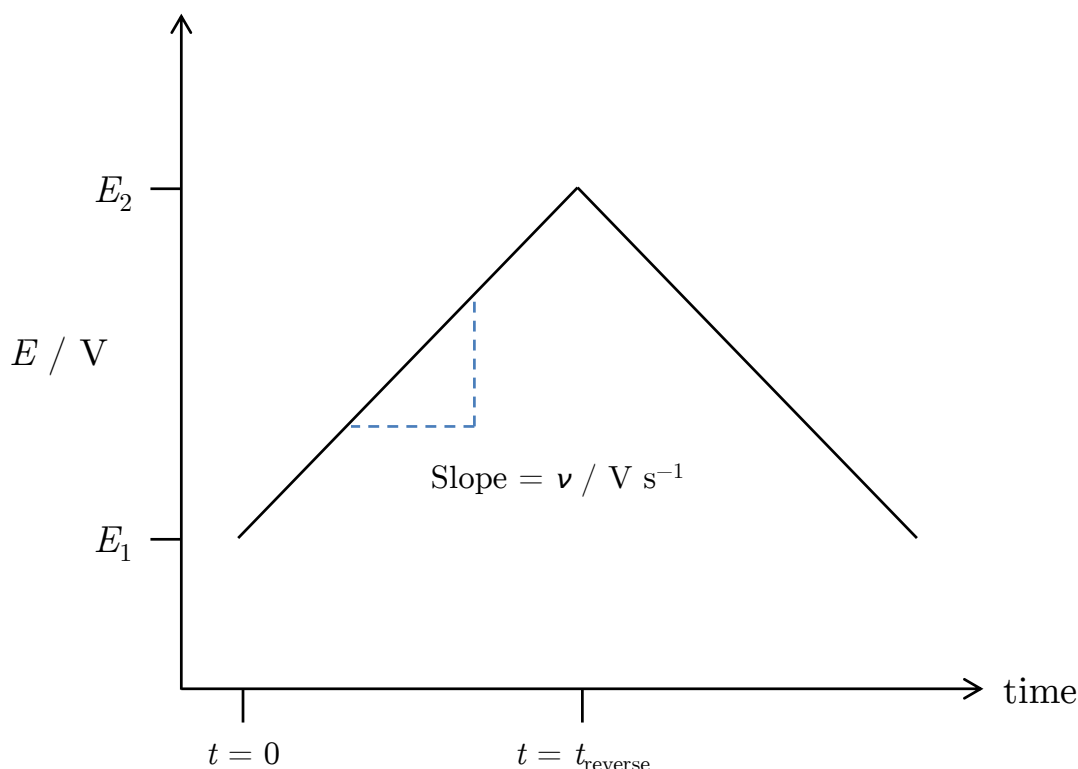


Figure 2.3) Schematic representation of a voltammetric sweep between two potential limits against time

CVs are constructed by plotting the measured currents for the forwards and backwards sweep on the same plot. The region between the two selected potentials, E_1 and E_2 is referred to as the potential window, the limits of which are defined by the electrochemical stability of the solvent and electrolyte. As such, aqueous electrochemistry has a relatively small potential window to work with due to the electrolysis of water at small potentials. Non-aqueous solvents offer an advantage in this respect, since the use of organic solvents permits the scanning over large potential windows, making the analysis of several reduction/oxidation processes possible. Potential step techniques are invaluable when considering diffusion limited electron transfer processes and CV enables the mechanistic assessment of electrochemical behaviour including evaluation of the number of electron transfer stages and number of electrons transferred.

Figure 2.4 depicts a typical CV representing the cycling of an oxidation/reduction process of an electroactive species, such as the ferrocene/ferrocenium redox couple, at a macroelectrode. Ferrocene undergoes a reversible one electron transfer oxidation/reduction at relatively low potentials: *ca.* 0.5 V *vs.* Ag/AgCl.

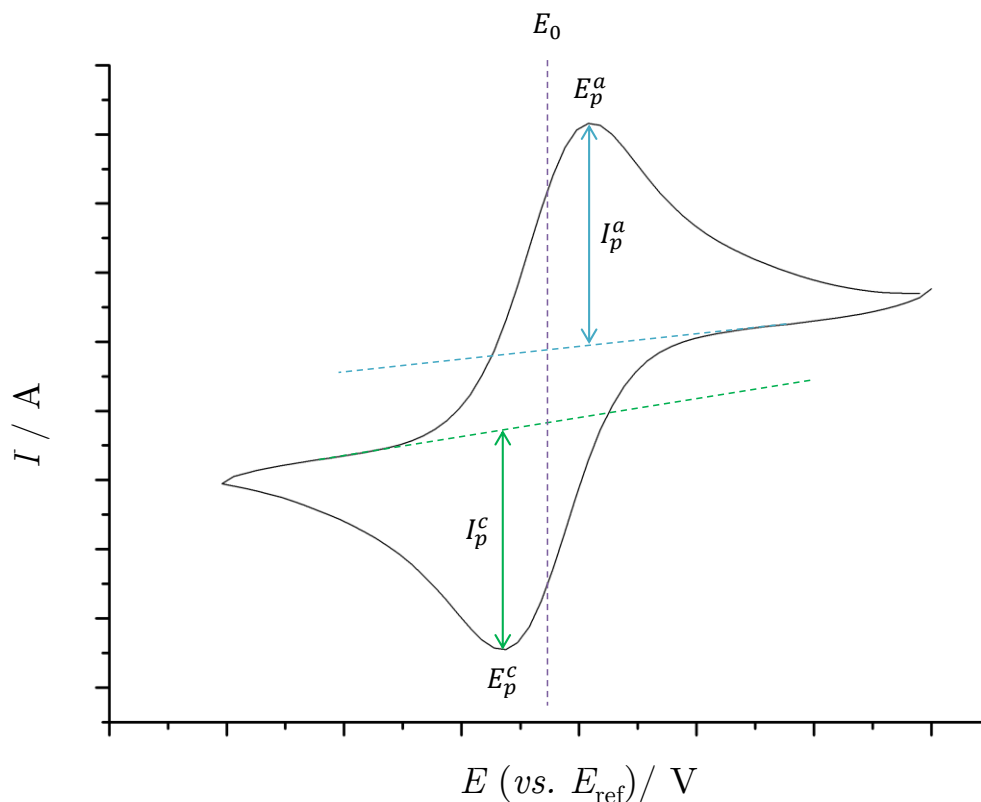


Figure 2.4) Typical current response of a system containing a redox mediator, in which the mediator is reduced and oxidised during potential sweeping generating cathodic and anodic currents, respectively

By cycling within this potential window it is possible to produce a voltammogram displaying an oxidative peak current, I_p^a , at potential E_p^a , corresponding to the oxidation of ferrocene to ferricenium, and an associated re-reduction of ferricenium on the reverse sweep to neutral ferrocene, at E_p^c , with a

corresponding cathodic peak current, I_p^c . Specifically, for a reversible, one electron transfer reaction, the peak separation between E_p^a and E_p^c is 59 mV.

$$\Delta E = E_p^a - E_p^c = \frac{59}{n} \text{ mV} = 2.303 \frac{RT}{nF} \quad (2.7)$$

Where n is the number of electrons transferred in the charge transfer process. The 59 mV peak separation is governed by the Nernst equation which includes a conversion factor of 2.303 for natural log to \log_{10} .

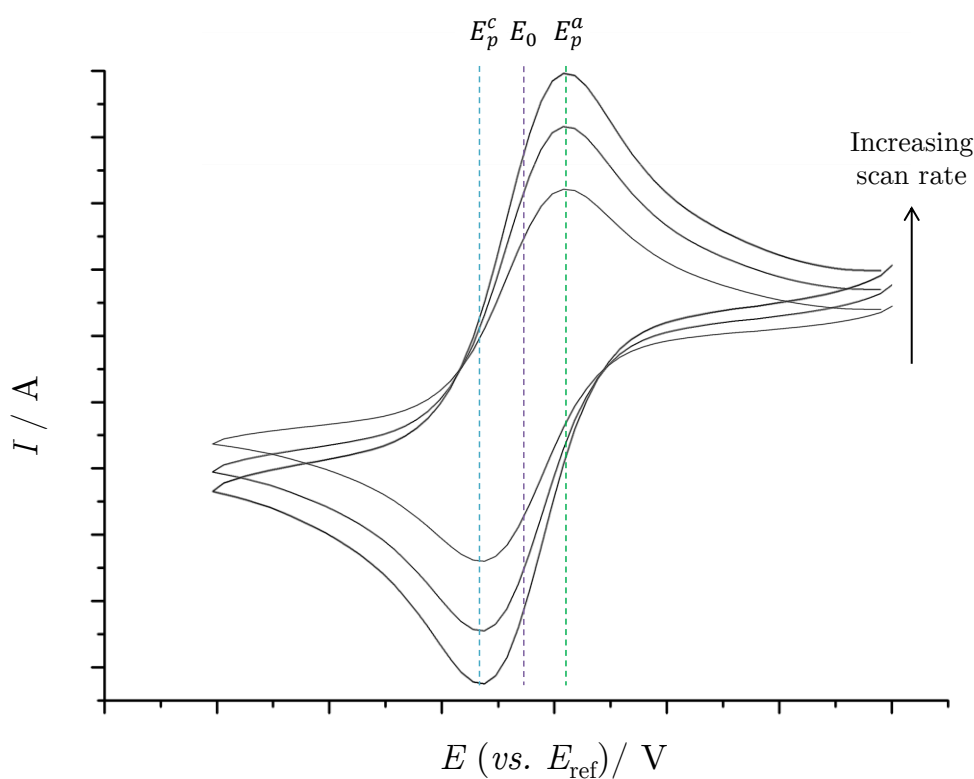


Figure 2.5) CV showing the effect of varying the rate at which the potential is swept on the cathodic peak current (E_p^c) and the anodic peak current (E_p^a) for a reversible system

Importantly, for an electrochemically reversible process, the peak positions do not alter as a function of voltage scan rate and the ratio of the peak currents is equal to 1. However, the peak currents are directly proportional to the square root of the scan rate, and this relationship is exploited in CV to determine

diffusion coefficients of electroactive species. By running CVs at various scan rates, and recording the relative peak currents for the oxidation and reduction process, it is possible to determine the value of the redox active species' diffusion coefficient *via* plotting of I_p^a (or I_p^c) against $\nu^{1/2}$. This relationship is known as the Randles-Sevcik relationship.

$$I_p^a = 0.4463nFAc \left(\frac{nFD\nu}{RT} \right)^{1/2} \quad (2.8)$$

Where n is the number of electrons transferred in the charge transfer process, F is Faraday's constant (C mol^{-1}), A is the working area of the electrode (cm^2), c is the concentration of the electroactive species (mol cm^{-3}), D is the diffusion coefficient of the electroactive species ($\text{cm}^2 \text{s}^{-1}$), ν is the scan rate (V s^{-1}), R is the ideal gas constant ($\text{J mol}^{-1} \text{K}^{-1}$) and T is temperature (K). Thus, a plot of i_p^a (or i_p^c) against $\nu^{1/2}$, for a reversible electrochemical system, should yield a linear relationship from which D can be determined. Additionally, the linearity of the plot is often used as an indication of how electrochemically reversible the system is.

Reversible/irreversible voltammetry is a term used to describe the electrode kinetics of the electroactive species. If a system is truly reversible, then the reverse scan will display an identical waveform to the original forward scan, where $I_p^a = I_p^c$, albeit with reverse polarity. A good example of this is presented in Figure 2.4.

Reversible voltammograms have several identifiable characteristics, all of which must be satisfied for the reaction to be considered truly reversible. As mentioned previously, ΔE must equal $59 \text{ mV } n^{-1}$ (for an n electron redox couple) and is independent of scan rate. Additionally, I_p^a and I_p^c must be proportional to $\nu^{1/2}$.

By definition, reversible electrode processes are indicative of fast electron transfer kinetics, in relation to mass transport of the electroactive species to the electrode. Consequently, less reversible voltammetry suggests slow electron transfer with respect to mass transport. The rate of electron transfer kinetics is measured by the standard electrochemical rate constant, k^0 , and the rate of mass transport is measured by the mass transport coefficient, m_T ,

$$m_T = \frac{D}{\delta} \quad (2.9)$$

where δ is the diffusion layer distance. Significantly, since the diffusion layer distance is affected by the scan rate then so is the rate of mass transport to the electrode surface. As the potential is swept from E_1 to E_2 , the thickness of diffusion layer surrounding the electrode increases, therefore the longer the time taken to scan the thicker the diffusion layer.

Essentially, if $k^0 \gg m_T$ then the voltammetric response is symmetrical about E_0 and the reaction is said to be *reversible*. Consequently, the system is said to be *irreversible* if $k^0 \ll m_T$, and is confirmed by an asymmetrical CV centred about E_0 .

Strictly speaking, since it is possible to control the rate of mass transport to the electrode *via* the scan rate, it follows that greater electrochemical irreversibility is encouraged by faster scan rates and as such, we can say that *all reactions* can be deemed irreversible at sufficiently fast scan rates.¹⁶³

2.4.2 Chronoamperometry

In chronoamperometry (CA), the applied potential is stepped and held constant over a period of time: the resulting faradaic current is recorded and plotted as a transient. It is a useful technique for metal deposition reactions, of which a constant ‘deposition’ or ‘growth’ potential is required to generate the reduction of metal ions from solution to form metal coatings and films. Although it is possible to determine the total charge passed for an electron transfer process voltammetrically, it may be more convenient to simply measure the total current using chronoamperometry. CA is commonly used technique for the determination of diffusion coefficients.

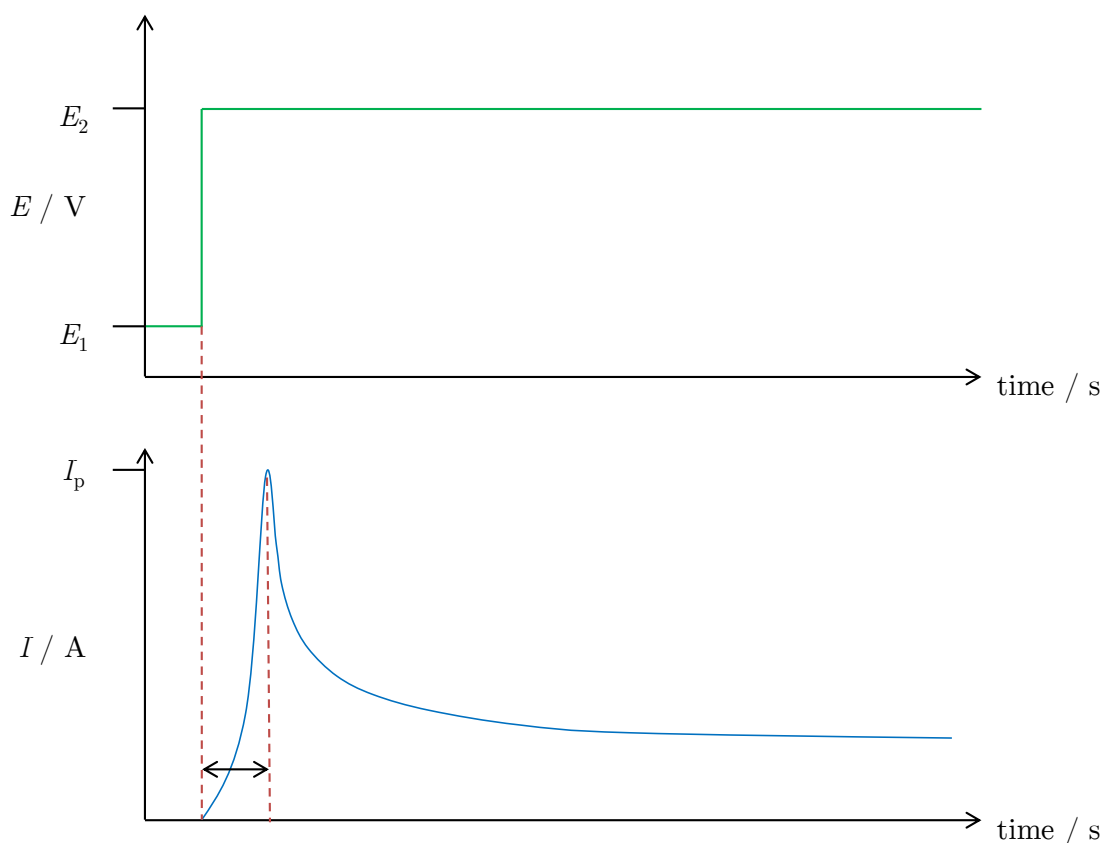


Figure 2.6) Schematic depicting the current lag and decay, of a system during the application of a potential step between E_1 and E_2 , where $E_1 < E_0 < E_2$. *N.B.* The current lag time is not quite to scale, and has been increased for the purpose of clarity.

In Figure 2.6, a potential E_1 is stepped to E_2 , where E_1 and E_2 take values smaller and larger than the standard reduction potential of a species respectively. The peak current, I_p , associated with E_2 is attributed to the system reaching diffusion control and is not obtained instantaneously. Instead there is a time period during which the current increases exponentially with time until I_p is reached. This time interval is a result of polarisation of the electrode-solution interface and reorganisation of the ions to form the electrochemical double layer. This time is therefore proportional to the size and charge of the electrolyte species, as well as the concentration, but can be as large as milliseconds.¹⁶³ Figure 2.6 is therefore not quite to scale, and the lag time has been increased for the purpose of clarity.

Once I_p is reached and the system attains diffusion control, the signal decays with $t^{-1/2}$ dependence, as a result of electroactive species depletion at the electrode surface. Because the flux of electroactive species to the electrode is proportional to the concentration gradient at the electrode surface, and the concentration gradient diminishes with time as a result of the increasingly thickening region of depleted species, the current signal decays with time.

The decay process is described by the Cottrell equation:

$$I = \frac{nFAc\sqrt{D}}{\sqrt{\pi t}} \quad (2.10)$$

Since the decay is proportional to the diffusion coefficient of the species, diffusion coefficients are determinable *via* plotting of current against $t^{-1/2}$. Significantly, CA is a more precise tool than CV for the measurement of diffusion coefficients, since it utilises the data recorded over the whole timescale rather than individually obtained peak currents.

2.4.3 Chronopotentiometry and galvanostatic procedures

Controlled current techniques are popular in testing of energy storage devices such as batteries and electrochemical double layer capacitors (EDLCs). Unlike previous described techniques, where the current is recorded as a function of the applied potential or time, here the potential is measured as a function of applied current over a period of time. Figure 2.7 shows a constant current example (green), with the corresponding potential response below (purple/blue) for both a single step and multi-step CA procedure. The steady current causes the electroactive species at the electrode to be oxidised or reduced at a constant rate, and the potentiometer responds by controlling the potential of the electrode such that it conforms to the standard potential of the redox couple. The potential of the electrode changes with time in order to counteract the effects of a concentration gradient created by depletion of the reactant. Once the concentration of the species at the electrode surface approaches zero, the flux of the redox couple to the electrode is insufficient to provide the current applied and as such, the potential is ramped in an attempt to maintain the constant current. If another redox process is available to the system at greater potentials than the initial process, then the potential response will eventually plateau out when it reaches the standard potential, since the secondary process will liberate electrons to contribute to the constant current.

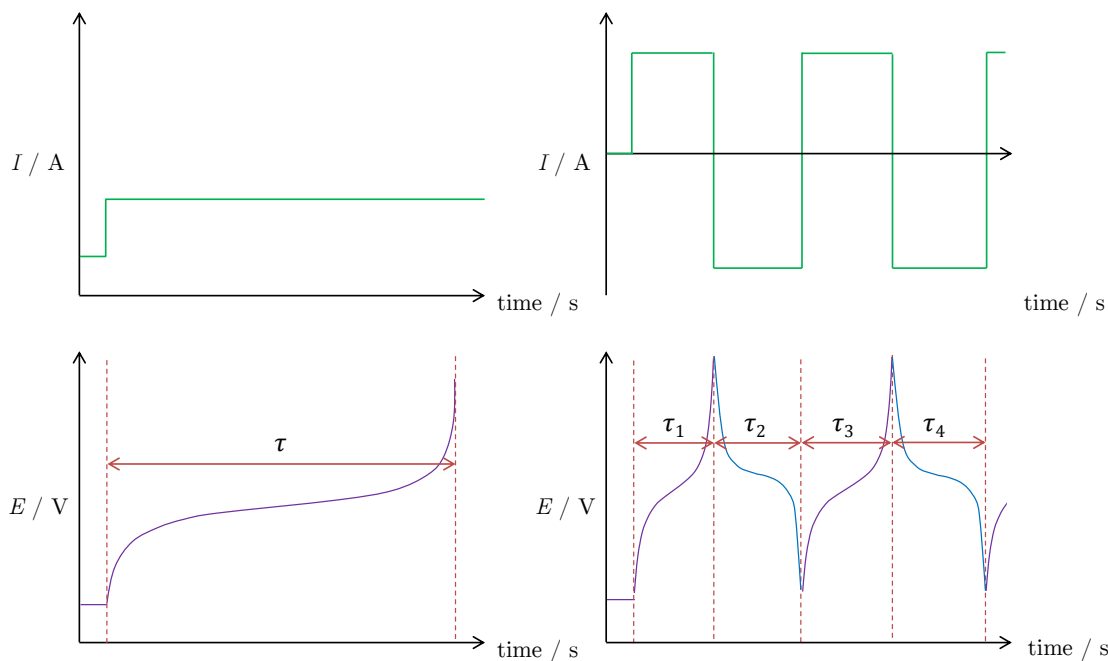


Figure 2.7) Schematic depicting the potential behaviour under galvanostatic conditions used for charge/discharge cycling

Galvanostatic charging and discharging (or cycling) is common in battery testing in which systems are repeatedly switched between anodic and cathodic currents. A practical analogy of this is a common mobile phone battery, in which the electrodes in the battery are constantly charged and discharged when the phone is being recharged and used unplugged, respectively. Significantly, with respect to the galvanostatic transients, the plateaus represent a region of which constant current and almost constant potential is achieved. The stability of these plateaus is therefore essential for batteries, which must supply an even and constant operating voltage to the external circuit. Subsequently, non-linear plateaus indicate undesirable varying charge/discharge potentials.

2.4.4 Electrical Impedance Spectroscopy (EIS)

The previous diffusion limited techniques utilise large fluctuations made to the system, including potential sweeps, potential steps and current steps. The result of these ‘macro-perturbation’ techniques is such that the system can be forced into a non-equilibrated state and the response of the system is monitored, typically in the form of a transient signal response. The alternative approach for electrochemical analysis is on a ‘micro-perturbation’, and employs the use of tiny alternating fluctuations and monitoring how the system follows these fluctuations at steady state.

For a simple circuit containing a sole resistor, the ability of the resistor to resist electrical current is independent of the frequency of the applied current, and therefore the resistance value is a simple function of the voltage, V , and the electrical current, I , more commonly expressed as Ohm’s law:

$$V \equiv IR \tag{2.11}$$

The resistor follows Ohm’s law for all voltage and current levels, and significantly the current and voltage signals are *in phase with one another*.

However, electrical circuits typically contain additional circuit elements that exhibit much more complex behaviour, and cannot be simplified using Ohm’s law. Therefore the term impedance is employed, which describes the ability of a circuit to resist the flow of electrical current throughout the entire system. In a more complex cell, the current response to an applied sinusoidal potential will also be a sinusoid at the same frequency, however capacitive elements have a phase-shifting effect upon the measured current response and it is this measured phase shift that allows the reverse determination of the total cell impedance.

$$Z = \frac{E_t}{I_t} = \frac{E_0 \sin(\omega t)}{I_0 \sin(\omega t + \Phi)} = Z_0 \frac{\sin(\omega t)}{\sin(\omega t + \Phi)} \quad (2.12)$$

Where Z is the total system impedance, E_t is the potential at time t , E_0 is the amplitude of the applied signal, I_t is the current response at time t , I_0 is the current amplitude and ω is the radial frequency of the current response in rad s^{-1} . The conversion factor between radial frequency, ω , and frequency f (expressed Hz) is 2π .

The impedance of the system is therefore expressed in terms of a magnitude, Z_0 , and a phase shift, Φ .

The total impedance, Z_0 , is given by:

$$Z = Z' - j \cdot Z'' \quad (2.13)$$

$$\text{where; } Z' = R \text{ and } Z'' = \frac{1}{\omega C}$$

Where, as shown, Z' and Z'' are the real (resistive, R , in-phase) and imaginary (capacitive, $1/\omega C$, out-of-phase) components of the impedance, respectively. Finally, the phase angle shift is given by:

$$\tan \Phi = \frac{Z'}{Z''} = \frac{1}{\omega RC} \quad (2.14)$$

For a comprehensive mathematical derivation of these relationships, including the proof regarding the imaginary impedance component, the reader is directed to *Electrochemical Methods: Fundamentals and Applications* by Allen J. Bard and Larry R. Faulkner, 2001.¹⁶²

EIS is typically used in electrochemical analysis to measure the total electrical impedance of a system over a range of frequencies, thus probing the frequency response of the system. Significantly, EIS is superior to both charge/discharge and CV methods for the determination of capacitance and resistance of an

electrochemical system, and allows the user to determine the resistance to charge transfer, the double layer capacitance, as well as the ohmic resistance of the cell.¹⁶⁴

In alternating current (AC) potentiostatic impedance measurements, the electrical impedance of the cell is monitored *via* the application of constant potential, which is modulated at a small amplitude, typically 0.01 V. The frequency of this signal is decreased from a characteristically large frequency (*e.g.* 1 MHz) to a comparatively small frequency (*e.g.* 0.1 Hz), and the frequency of the current response is monitored *via* a frequency response analyser. Although less common and not employed here, galvanostatic EIS is also possible, in which the current modulated and the voltage response monitored.¹⁶⁴

The data obtained is often expressed as a Nyquist plot, in which the real and imaginary impedance components acquired for different frequencies are plotted against one another. How quickly the circuit components are able to respond to the change in applied frequency signal, governs whether the current flows *via* the capacitive or resistive components.

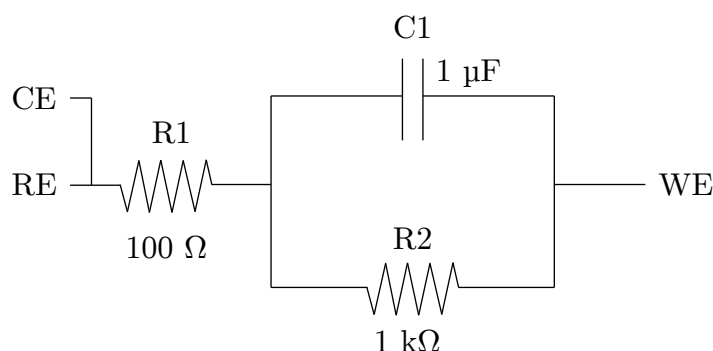


Figure 2.8) Schematic of a R(RC) circuit used to record exemplary impedance measurements to determine the values of individual resistive and capacitive components in an experimental cell.

WE, CE and RE denote the connections to the working, counter and reference electrodes, respectively.

Figure 2.8 shows a common R(RC) circuit, consisting of a $100\ \Omega$ resistor connected in series, and a $1\ \text{k}\Omega$ resistor and $1\ \mu\text{F}$ capacitor connected in parallel. This equivalent circuit is a good first approximation to an experimental cell. 0 V was applied to the working electrode terminal using a “dummy cell”, *i.e.* the collection of resistors and capacitors given in Figure 2.8, and the frequency of the modulation potential was decreased from 100 kHz to 0.1 Hz over a period of approximately five minutes. The determined Z' and Z'' impedance components were plotted against one another, and the resulting Nyquist plot is presented in Figure 2.9. A Nyquist plot typically displays a semi-circular behaviour depending on the behaviour of the components in the circuit. At high frequencies, all of the current is capacitive, I_c , therefore the imaginary component's (C1) contribution falls to zero, since it offers no impedance, and the only impedance that the current experiences arises due to the ohmic resistance of the cell. In this case it is the $100\ \Omega$ in-series resistor (R1). As the frequency decreases, R2 is able to respond, and faradaic current, I_f , is able to pass *via* R2 as well as the original I_c *via* C1, hence the current experiences impedance from both components and is presented on the Nyquist plot as a decrease in Z'' component to counter the increase in Z' . Eventually, at sufficiently slow frequencies the capacitor offers high impedance to the current, and the current is seen to flow *via* R1 and R2, reflected in the increase in measured Z'' . The values for R1 and R2 can be instantly determined from the Z' -axis interception; whereas, since the magnitude of the capacitive component is a function of the radial frequency (ω , rad s^{-1}) of the current response, $C = 1/Z''\omega$, measured in Farads, and requires modelling of the impedance curve to allow calculation. Again, details of this modelling function can also be found in

Electrochemical Methods: Fundamentals and Applications by Allen J. Bard and Larry R. Faulkner, 2001.¹⁶²

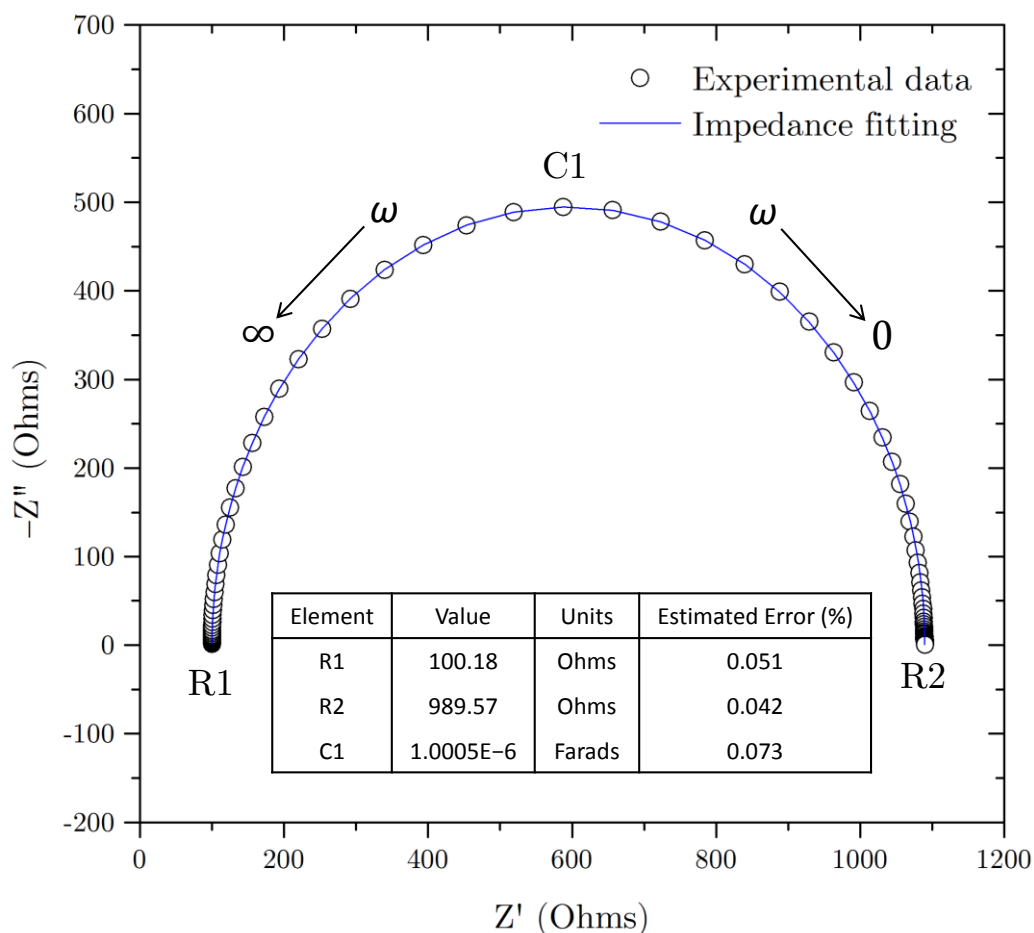


Figure 2.9) Resulting Nyquist plot revealing the respective resistive and capacitive values of the circuit elements in the R(RC) circuit

An electrochemical cell can be simplified to an electrical circuit analogy, where R1 represents the total ohmic resistance (R_{Ω}) of the cell and consists of the electrical resistance of the electrodes, cables, clips, solution, etc., R2 represents the resistance to charge transfer (R_{ct}) between a redox mediator and the electrode surface, and C1 is analogous to the electrochemical double layer capacitance (C_{dl}) at the electrode|solution interface, which forms the basis of an electrochemical supercapacitor. Finally, there is another feature that occurs in

electrochemical impedance measurements, as we will see later, termed the Warburg impedance, and is related to the resistance to mass transport of the electrolyte to the electrode interface. However since there is no electrolyte present in this introductory example, the Warburg impedance does not feature in the above simulated Nyquist plot.

2.4.5 IR drop

It is worth noting the significance of a commonly encountered problem when considering electrochemical diffusion limited analytical techniques. The problem of the IR drop arises as a result of the resistance in the cell. For voltammetric techniques, it is essential that the contribution of the IR drop is considered when measuring peak separations, since an increase in cell resistance will inherently increase the peak separation of the redox signals. The issue arises directly as a result of Ohm's law; since $V = IR$ the total recorded potential is a function of the current and the resistance in the cell. The ohmic current acts against the Faradaic current, thereby creating a drop in the potential. Naturally, electrolyte solutions are significantly more resistive than a metal wire, and in practice, this is corrected with the use of high concentrations of background electrolyte, as mentioned previously in section 2.2.

Further steps can be taken to ensure a minimum contribute of resistance in the cell, one being the placement of the working and reference electrodes as close together as possible with the aid of a Luggin capillary to minimises the solution path. Additionally, IR compensation is a mathematical feature incorporated into all potentiostats and may be employed to counteract the effects of IR drop on current transients.

2.5 Physical analysis

2.5.1 X-ray diffraction (XRD)

X-ray diffraction (XRD) is a powerful and non-destructive analytical tool for the investigation of crystallographic planes, chemical composition and molecular structure of crystals. For graphitic materials in particular, the ability to probe the crystal structure is relatively straight forward, since graphite is constructed of layers of equidistant graphene sheets and does not have a complicated crystal lattice as found in zeolites and other highly porous materials, for example.

The principle of XRD relies on the scattering of X-ray beams from crystallographic planes and measures the intensity of the scattered beam as a function of the incident and scattered angles, as well as the initial wavelength of the X-ray beam.

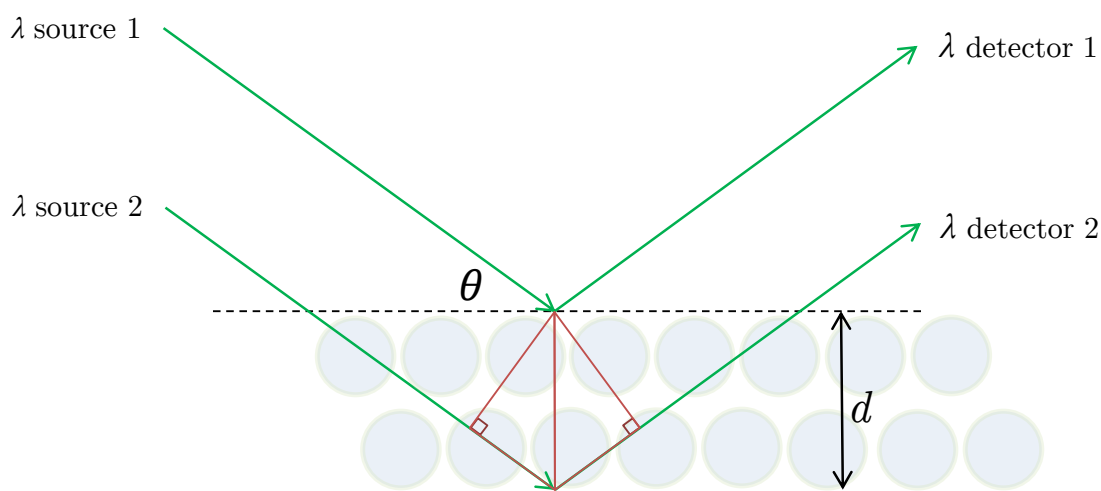


Figure 2.10) Schematic showing X-ray diffraction of a crystal lattice with explanation as to the origin of the parameters employed in the Bragg equation

The parameters are combined in the form of the well-known Bragg equation;

$$n\lambda = 2d\sin\theta \quad (2.15)$$

relating the number of crystallographic planes, integer n , with the wavelength of the incident X-ray radiation (in this case $\lambda = 1.5418 \text{ \AA}$) and the interplanar spacing of the crystallographic planes, d (nm).

Essentially, the Bragg equation dictates that the lower beam of radiation must travel an extra distance of $2d\sin\theta$ to the upper beam. This extra distance dictates the additional distance that must be travelled for the two beams to arrive at the detector in-phase with one another. Crucially, it is the distance between the crystallographic planes that govern the angles at which greatest intensities will be observed (Figure 2.10).

For graphite in particular, the crystal is made up from repeated graphene planes with an interplanar spacing (d spacing) of 0.345 nm. The graphene layers in graphite can be stacked in one of two stable configurations: Bernal (ABA) stacking, and Rhombohedral (ABC) stacking, though ABA is much more common; it is believed ABA is slightly more thermodynamically stable.¹⁶⁵ The different electrical properties governed by these two configurations are of interest: ABA stacked tri-layer graphene behaves as a semimetal¹⁶⁵⁻¹⁶⁸, exhibiting an electrically tuneable band overlap; however ABC stacked FLG is a semi-conductor with an electrically tuneable band gap.^{165,167-169} Despite the differences in electrical properties, the interplanar spacing remains unchanged; where the crystallographic d -spacing is the measured 0.354 nm interplanar graphene spacing. Because graphite/FLG does not have any other crystallographic planes, its XRD pattern is constructed entirely of diffraction signals from these graphene d spacings. The diffraction signal associated with the ABA stacking nature is called the (002) peak, and arises at a 2θ value of *ca.*

26 ° in powder X-ray diffraction patterns. Overtones, albeit of lower intensities, of this angle appear at $2\theta = ca. 55^\circ$ and $ca. 87^\circ$. Crucially, graphene displays no powder XRD pattern, since it is two dimensional and therefore has no three-dimensional crystal lattice. Subsequently, powder XRD analysis of single layer graphene is not possible however it may serve as a useful tool to probe bi-layer and tri-layer materials. Although not covered here, single crystal X-ray diffraction can be a valuable tool to study the crystal structure of single layer graphene materials.¹⁷⁰⁻¹⁷²

2.5.2 Microscopy

2.5.2.1 Atomic Force Microscopy (AFM)

AFM is an extremely high resolution microscopic technique, on the order of nanometres and is often employed as a tool to probe surface morphologies. Unlike spectroscopic techniques, which use light as the primary analytical tool, AFM imaging is undertaken by physically sensing the surface of the material with the use of a cantilever and contact tip. A laser is focused on the rear surface of the cantilever tip such that, on moving the cantilever over the sample, the change in height ‘felt’ by the cantilever tip induces a change in the reflection of the laser on the reverse of the cantilever, which is monitored by a photodiode (Figure 2.11). By mapping the entire surface it is possible to obtain high resolution images in extraordinary detail.

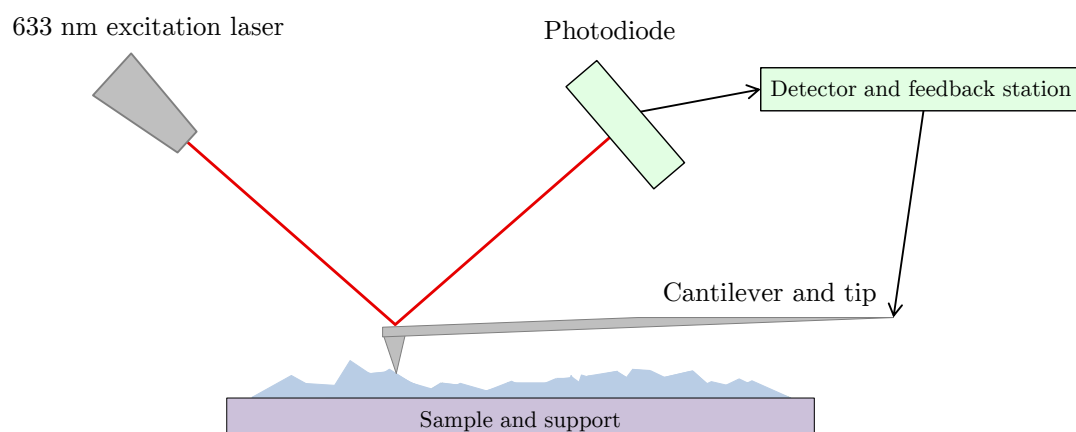


Figure 2.11) Schematic showing the underlying mechanism of an Atomic Force cantilever tip, and the manner in which morphology images are constructed

AFM performed in tapping mode is particularly useful in the mapping of nanocarbon materials and, more specifically, graphene flakes, where when

combined with Raman spectroscopy, serves as an ideal complimentary method to determine the number of graphene layers present in multi-layer graphene samples.

AFM can be conducted in two manners: *contact force mode* and *tapping mode*. As the name suggests, contact force mode ensures the cantilever tip is constantly in contact with the sample surface, and the tip is ‘dragged’ across the sample, thereby constantly mapping the surface. Constant force mode is more accurate than tapping mode, since the tip is always in contact with the substrate, however for delicate nanometre-scale morphologies, this approach can be too aggressive, and samples may be subsequently damaged. This is certainly the case with graphene samples, especially monolayer, where contact force can scratch and pierce the atom-thick surface. To address this, tapping mode can be employed, in which the cantilever tip is oscillated at a constant frequency on the sample surface, thus minimising surface damage.

Unfortunately, when determining height profiles and surface topographies of materials on the atomic scale, the degree of measurement error becomes increasingly significant, as reflected by the varying values of AFM-deduced graphene thicknesses by different research groups. Measured thicknesses of monolayer graphene on oxidised silica range by more than 1 nm, with Nemes-Incze *et al.* measuring 0.4 nm¹⁷³, Gupta and co-workers determining thicknesses of 0.68 nm¹⁷⁴ and finally Novoselov *et al.* reported thicknesses of as large as 1.6 nm.¹⁷⁵ Other authors have also reported differing values.¹⁷⁶⁻¹⁷⁸ Given that the vdW radius of carbon is 0.17 nm, these measured thicknesses may appear relatively large for a monolayer material and it is suspected that one reason for this increase is due to interactions between the graphene sheet and the substrate; it should be noted that the aforementioned differences were all found

on oxidised silicon substrates of same oxide-layer thickness, however. In addition, surface conditions of sub-nanometre thick materials will also complicate measured readings. This highlights the requirement for a secondary characterisation technique.

2.5.2.2 Electron microscopy

Like AFM, electron microscopy is an analytical technique enabling extremely high resolution imaging. Depending on the accelerating voltage, electrons can have wavelengths 100,000 times shorter than those of visible light photons, and electron microscopy is able to reveal detail on the order of tens of picometres.¹⁷⁹

Electron microscopy exists in two main forms, transmission electron microscopy (TEM) and scanning electron microscopy (SEM), the latter being employed throughout this work. In TEM, electrons are generated, typically with the use of a tungsten filament cathode, and accelerated using relatively high energy (approximately 40-400 keV with respect to the cathode) toward the sample. The electron beam is focused with the use of electrostatic/electromagnet lenses and transmitted through the specimen of interest; the information gathered is magnified *via* an objective lens and the image is recorded. TEM's resolution is mainly limited by spherical aberration and can be partially corrected with the use of additional hardware.^{180,181} This leads to high resolution TEM (HRTEM) of which modern instruments have a maximum resolution of 0.47 Å. TEM's main disadvantage is in its requirement for extremely thin samples (<100 nm); this disadvantage naturally does not hinder graphene research.¹⁸²

Alternatively SEM utilises a comparatively low energy electron beam (*ca.* 0.2 keV to 40 keV), though beam focus operates in the same manner as TEM. Instead of penetrating the sample however, the low energy beam is scanned

across the sample surface and the image recorded relies on the energy lost from the electrons on interaction with the sample. When the electron beam interacts with the sample, energy is lost in a variety of mechanisms in the form of heat, low energy secondary electron emission, high energy backscattered electrons, light emission and X-ray emission. The types of which are dependent on the sample material composition and topography. Although the resolution of SEM is typically lower than TEM, analysis of bulk material (up to tens of mm) is possible since the SEM image relies on surface processes rather than transmission.

An additional and popular feature of SEM is energy dispersive X-ray analysis (EDAX) where the energy of the emitted X-rays is monitored. Since the energy of the X-rays is proportional the chemical identity of the specimen, it is possible to determine the elemental composition of the sample of interest.¹⁸³

2.5.3 Spectroscopic techniques

2.5.3.1 Raman spectroscopy

Bulk graphite, GC, CNTs, and HOPG all absorb light over a wide range of wavelengths and thus light absorption techniques are not well suited for the detection and characterisation of low dimensional forms of carbon. The most commonly employed technique for characterisation of low dimensional carbon materials is Raman spectroscopy. This light scattering technique involves photon absorption; in the resonant case this promotes electrons from a valence state to a virtually excited one (or to a virtual state, in the case of non-resonant excitation). On loss of this energy to lattice vibrational modes, called phonons, the solid relaxes to a different vibrational state, and this difference in energy is seen as a shift in the emitted photon's frequency away from the excitation wavelength. This shift is conventionally termed Stokes or anti-Stokes depending on whether the emitted photon is of a lower or higher frequency respectively, and is an example of inelastic scattering due to the energy transfer involved.¹⁸⁴

Graphene, having two inequivalent adjacent carbon atoms in its unit cell, displays both acoustic (A) and optical (O) phonons. The result is a total of six possible phonon branches comprising of both in-plane (i) and out-of-plane (o) vibrations, as well as longitudinal (L) and transverse (T) vibrational directions with respect to the carbon lattice.¹⁸⁵⁻¹⁸⁷

With respect to the acquired Raman spectrum of (*pristine*) graphene, there are (*two*) three main phonons corresponding to (*two*) three intense peaks. The most prominent peaks include the *G* band appearing at 1582 cm^{-1} , and another band appearing at *ca.* 2700 cm^{-1} historically named the *G'* band.¹⁸⁷ The *2D* band has conventionally been known as the *G'* band, since it is the second most

prominent signal observed in graphite/graphene material. However, it should be noted that the G' band is chemically unrelated to the G band, and is in fact due to second order (or double resonance, DR) phonons. These DR phonons are the reason for another prominent spectral feature, the D band; appearing at 1350 cm^{-1} which is effectively the breathing modes of sp^2 rings due to the presence of structural defects present in the lattice. For this reason the D band has become known as the ‘defect’ peak.

Since the G' band’s Raman shift is approximately double that of the D band (2700 cm^{-1} and 1350 cm^{-1} , respectively), it has become commonplace to refer to the G' band as $2D$. However, caution must be used since the $2D$ band is a two phonon mode that can occur independently of the structural defects required for the D band’s existence. The $2D$ band is therefore always present in graphitic Raman spectra, regardless of the presence of any defects, whereas pristine monolayer graphene will display no D peak and an intense $2D$ peak. Authors tend to use both labels for this same peak, which can cause some confusion and the remainder of this work, the label $2D$ will be used for the band at *ca.* 2700 cm^{-1} .

The G band is the only band that arises from a normal first order Raman scattering process and arises due to the doubly degenerate phonon mode at the Brillouin zone (Γ) of graphene’s reciprocal space lattice. This G band is associated with the two in-plane vibrational components; iTO and iLO , which are degenerate at Γ , and can be visualised more simply as the vibrations between sub-lattice A, and sub-lattice B.

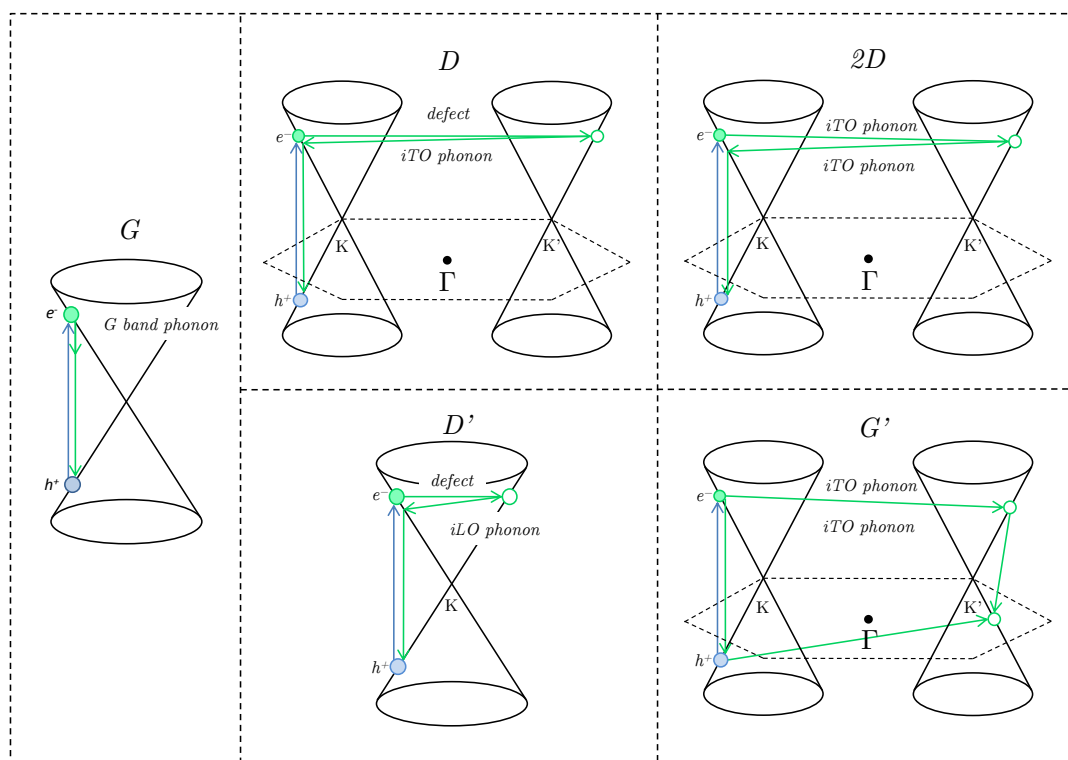


Figure 2.12) Schematic indicating the different possible phonon modes in graphene's reciprocal space lattice, and their respective Raman spectroscopy signals specifically showing how it is possible to obtain $2D$ Raman signals even in the absence of lattice defects (re-drawn from Malard *et al.*¹⁸⁷)

The G band is characteristic of in-plane sp^2 carbon bond vibrations and is often referred to as the 'graphite-like' mode, since it is present in all bulk forms of graphitic carbon due to the large extent of hexagonal sp^2 , covalently bonded carbon atoms.¹⁸⁸

Figure 2.12 shows a schematic of the possible phonon modes expressed in graphene's reciprocal space lattice; it is important to note that this is not in real space and the inequivalent Dirac points (K/K') are not positioned, as one would expect, at the carbon atoms in the graphene lattice. For a detailed description of graphene's real space reciprocal space translation, and for the advantages of working in reciprocal space, the reader is referred to reference 188.¹⁸⁹

Unlike the G band, the D and $2D$ bands are not normal first order Raman scattering processes and arise as overtones; proceeding *via* DR scattering routes as depicted in Figure 2.14. The $2D$ band involves two phonons centred around the K/K' Dirac points but significantly the D band requires a path *via* a phonon and a defect site. This is the reason why a $2D$ band will still be present even in completely defect free graphene. Both of these double resonance mechanisms are energy conserving and are known as *inter-valley* processes, as they connect the points (or valleys) around inequivalent K/K' points.¹⁸⁶

In contrast, the D' band process is known as an *intra-valley* process, since it connects points within the same cone. Again, the D' band proceeds *via* a structural defect and therefore, the D' band only arises due to the presence of defects, however this is a less prominent peak than the other bands.

Finally, in the special case of monolayer graphene, where the valence and conduction bands are so freely accessible, it is possible that a triple resonance (TR) scenario can occur in the form of hole scattering, as well as electron scattering as the DR process allows. The result is depicted in Figure 2.12, where instead of the electron being scattered back *via* the reverse phonon, the hole is scattered in the opposite direction adding a further step in this resonance mechanism.^{190,186} It is thought that this TR is a reason for the observed large intensity of the $2D$ band relative to the G band in monolayer graphene.¹⁸⁷

Additionally there is another overtone band named the $D+G$ which appears above 3000 cm^{-1} . Figure 2.13 shows the typical Raman spectrum for a bulk sample of few-layer graphene, illustrating the positions of the relative bands.

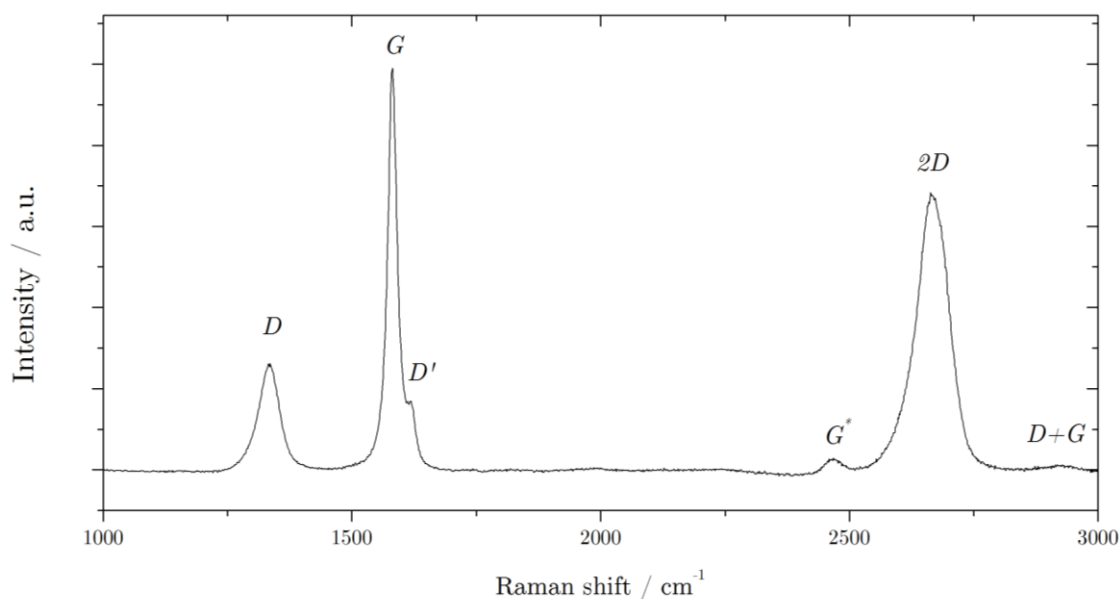


Figure 2.13) Typical Raman spectrum (data obtained herein) of few-layer graphene material showing the common Raman signals associated with graphene materials

For graphene/graphite, the D band is typically found at approximately 1350 cm^{-1} , the G at 1582 cm^{-1} and the $2D$ at 2680 cm^{-1} , as presented in Figure 2.13. Disorder in the structure is reflected by broadening and overlapping of the D and G bands thus making individual interpretation difficult. In such cases, the I_D/I_G intensity ratio is employed as a measure of crystallinity where a small ratio suggests a greater degree of sp^2 vibrations; indicating a more graphitic like structure.¹⁹¹ Pristine monolayer graphene displays no D peak, unless flake edges are exposed to the laser. Ion intercalation of graphite can also be observed spectroscopically with the splitting of the G peak into two bands and an increase in the D band as the ions split the graphene layers apart.^{185,186,192-195}

Raman spectroscopy is especially powerful for the characterisation of graphene and graphene derivatives, and it is well known that the number of layers of graphene can be distinguished *via* the change in shape of the $2D$ peak; as a shoulder develops with increasing number of layers.^{177,185,186,192-199} As detailed

previously, the $2D$ band is the result of a DR phonon process and for monolayer graphene, as shown in Figure 2.14, this band appears as a single Lorentzian and can be successfully modelled with a single Lorentzian curve, having a full width at half maximum (FWHM) of $ca. 24 \text{ cm}^{-1}$.^{187,200,201}

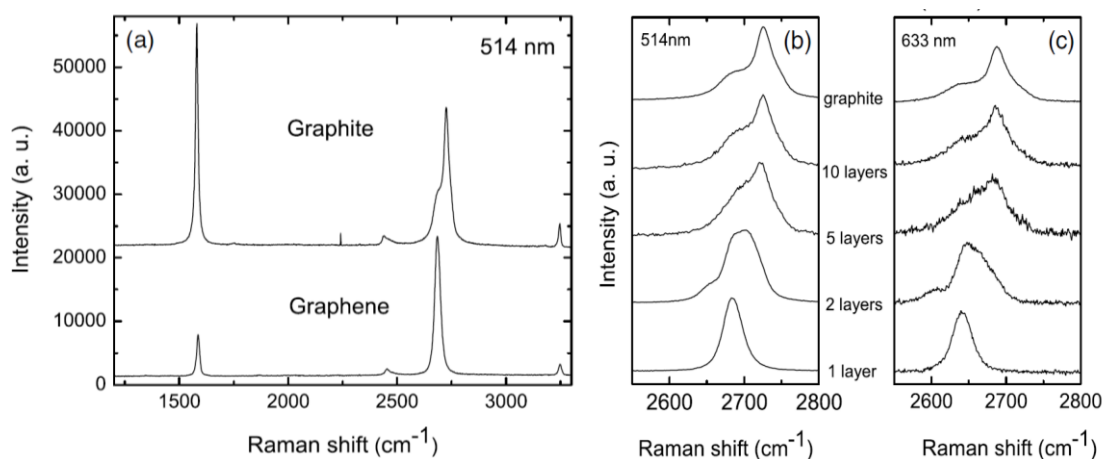


Figure 2.14) Comparative Raman spectra of graphite and graphene (single and multilayer) recorded at 514 nm and 633 nm excitation laser wavelengths, showing the $2D$ peak shape dependence upon the number of inherent graphene layers. Data acquired from published work by Ferrari *et al.* 2006¹⁹³

The $2D$ peak in bulk graphite has two components: the $2D_1$ and $2D_2$ which are approximately $\frac{1}{4}$ and $\frac{1}{2}$ the intensity of the G peak, respectively. These individual peaks become more visible the more layers graphene has, and although the Raman spectra for graphene with more than $ca. 5$ layers becomes indistinguishable from bulk graphite, it is a powerful technique for differentiating single layer, bi-layer and tri-layer graphene.^{185,187,193,200}

2.5.3.2 Raman spectroscopy of few-layer graphene flakes

This piece of work was part of an investigation not included within this thesis, in which the electron transfer of various redox couples was measured at the basal plane of graphene electrodes with varying numbers of inherent graphene layers, to probe the relationship between electron transfer kinetics and the number of graphene layers. However, the post-electrochemistry Raman analysis serves to demonstrate the power of Raman spectroscopy in graphene materials characterisation; primarily highlighting the relationship between number of graphene layers and the resulting Raman spectra.

Micromechanically exfoliated graphene was prepared on a Si/SiO₂ substrate and Figure 2.15(a) and 2.15(b) show selective points on a multi-layer graphene flake, of which were analysed with the use of a Witec alpha300 Raman spectrometer equipped with a 488 nm excitation wavelength laser at <1 mW power intensity, in order to avoid any laser damage of the graphene sample. Different coloured points represent the three different forms of surface: basal plane (red), edge sites (blue) and boundaries between different numbers of graphene layers (yellow).

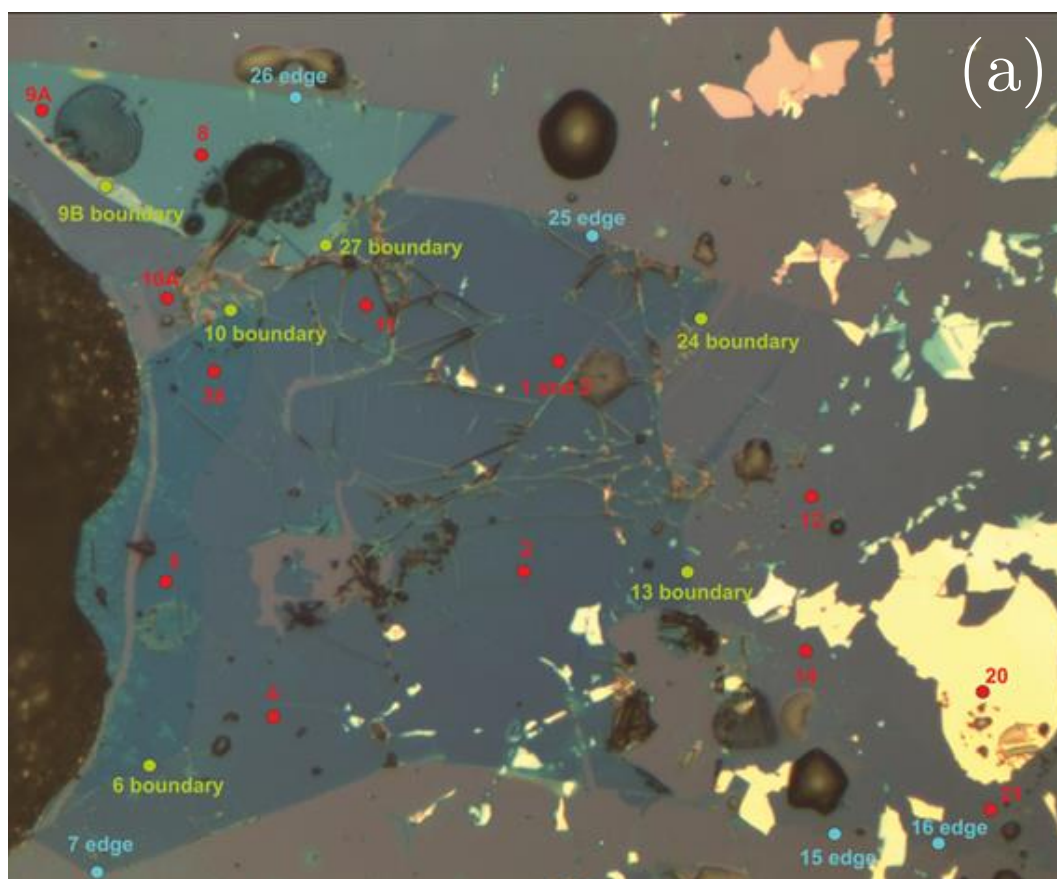


Figure 2.15(a) Optical images of a graphene flake at 10x magnification displaying different flake thicknesses. Points labelled indicate the points analysis *via* Raman spectroscopy and a mixture of edge sites, boundaries between different numbers of layers and basal plane.

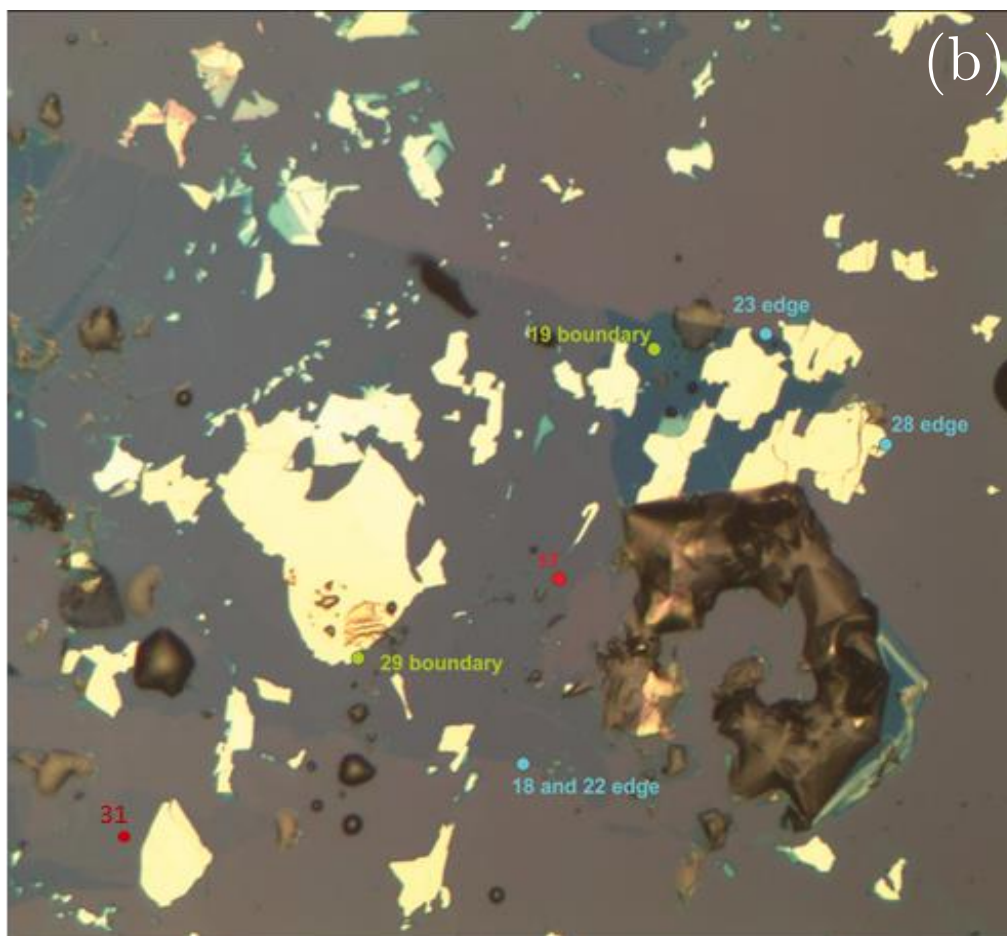


Figure 2.15(b) Optical images of a graphene flake at 10x magnification displaying different flake thicknesses. Points labelled indicate the points analysis *via* Raman spectroscopy and a mixture of edge sites, boundaries between different numbers of layers and basal plane.

The recorded spectra (Figures 2.16(a) and 2.16(b)) have been plotted for each point (point number shown to left of each spectrum) and the estimated number of graphene layers (red numbers in parentheses on right hand side) were determined from the shape and position of the $2D$ bands at *ca.* 2700 cm^{-1} . Analysis was based on several shape and positional features of the $2D$ band: a strong signal at *ca.* 2750 cm^{-1} alongside a prominent shoulder peak at 2700 cm^{-1} is characteristic of graphitic materials corresponding to a minimum of 10 layers.¹⁸⁵ The $2D$ band characteristics were coupled with the $G:2D$ peak

intensities; with fewer-layer materials exhibiting smaller $G:2D$ ratios, and monolayer graphene exhibiting $G:2D$ ratio < 1 .²⁰² Flakes between 5 and 10 layers can be difficult to correctly identify to the nearest 1 layer using Raman spectroscopy alone, however confident estimation between 1 and 5 layers is possible with practise, though the use of a secondary characterisation technique is highly desirable. As the number of layers decreases, the sub-peak at 2750 cm^{-1} becomes less prominent and the whole $2D$ band becomes more symmetrical about $ca. 2700\text{ cm}^{-1}$, exemplified by point 10(a). Bi-layer samples are instantly recognisable by the introduction of a small but noticeable peak at 2675 cm^{-1} and a relatively wide ('flat') region at the tip of the $2D$ band (point 29). Finally, monolayer graphene is instantly identifiable with its single sharp lorentzian peak at $ca. 2700\text{ cm}^{-1}$ (point 31). Typically, the $2D$ band also increases in intensity with respect to the G band, and although the $2D$ band of pristine monolayer graphene is significantly more intense than graphene's G band, the I_G/I_{2D} ratio can be heavily affected by chemical doping in the graphene lattice from different supporting substrates,^{195,202} as is likely the case for point 31. However even heavily doped monolayer graphene exhibits a single Lorentzian fitted $2D$ band.

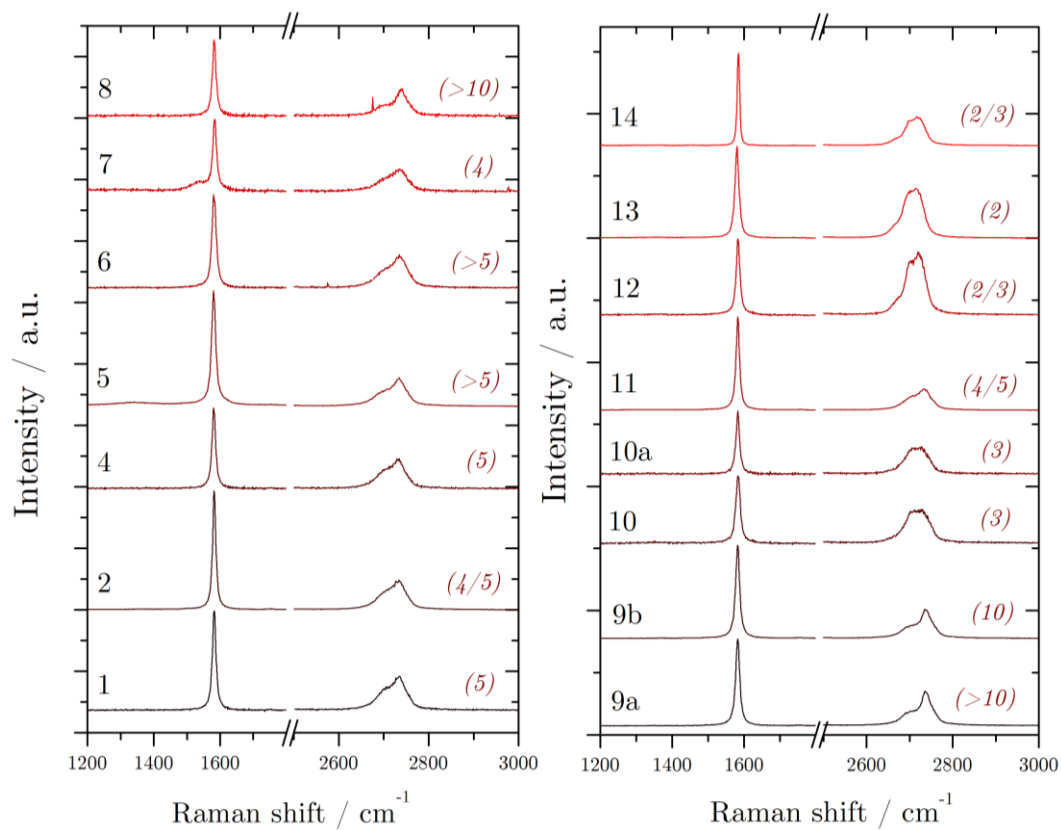


Figure 2.16(a) Raman spectra measured at various points (1 – 14) on micromechanically exfoliated graphene showing respective number of graphene layers determined from the varying shape and intensity of the 2D band at *ca.* 2700 cm^{-1} .

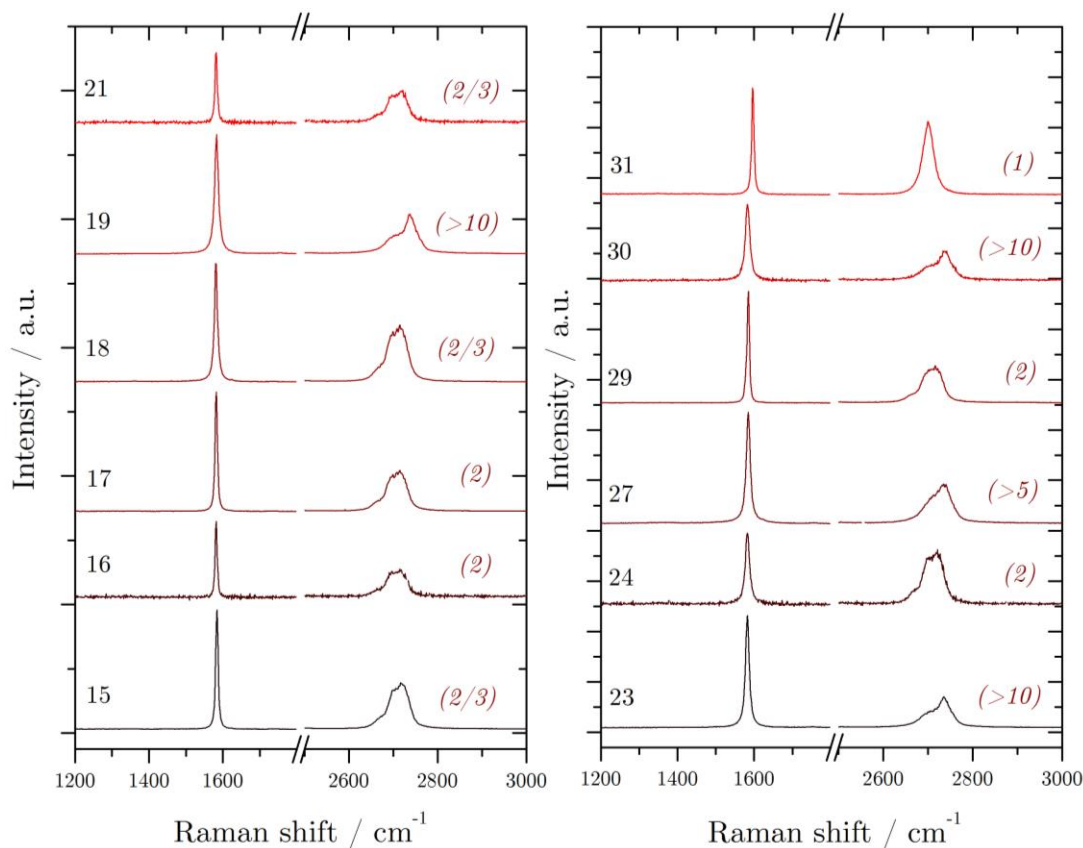


Figure 2.16(b) Raman spectra measured at various points (15 – 31) on micromechanically exfoliated graphene showing respective number of graphene layers determined from the varying shape and intensity of the *2D* band at *ca.* 2700 cm^{-1} .

2.5.3.3 Raman spectroscopy *2D* peak fitting

In order to aid flake characterisation, Raman *2D* peak fitting was conducted using a multiple-peak fit program in OriginPro 8.5 software, in order to assess the number of graphene layers more accurately. As mentioned previously, single layer graphene can be fitted to a single Lorentzian function centred at 2700 cm^{-1} , however fitting becomes increasingly difficult for two or more layers, since the *2D* band splitting suddenly comprises of four sub-peaks for bi-layer graphene due to overlap of the Dirac cones between adjacent graphene layers and the resulting additional possible Raman phonons.^{177,185,186,193}

Figure 2.17 shows the Raman $2D$ peak for a typical few-layer flake with various fitting options undertaken, where 2.19(a), 2.19(b), 2.19(c) and 2.19(d) are fitted to one, two, three and four Lorentzian components, respectively. It is well-known that monolayer graphene's $2D$ band can be fitted to a single Lorentzian, and lesser-known that bi-layer graphene can be fitted to four Lorentzian components.^{185,202} However, peak fitting to three, four, and five layers is not so clear since the Raman peak shapes and sub-components are sensitive to the graphene stacking order.¹⁹⁹ Consequently the number of graphene layers between three and five is difficult to determine using Raman spectroscopy alone, and a secondary techniques is required, commonly AFM or TEM.

It can be seen in Figure 2.17 by that increasing the number of sub-peak Lorentzian components, a better overall fit is obtained, although the improvement from three to four Lorentzian components is negligible. Clearly the peak cannot be fitted to a single peak, so it can be safely assumed that the flake is not a monolayer sample. A fair evaluation of the number of layers in this flake would be 3-5, however without the use of AFM or TEM further estimation is not completely reliable.

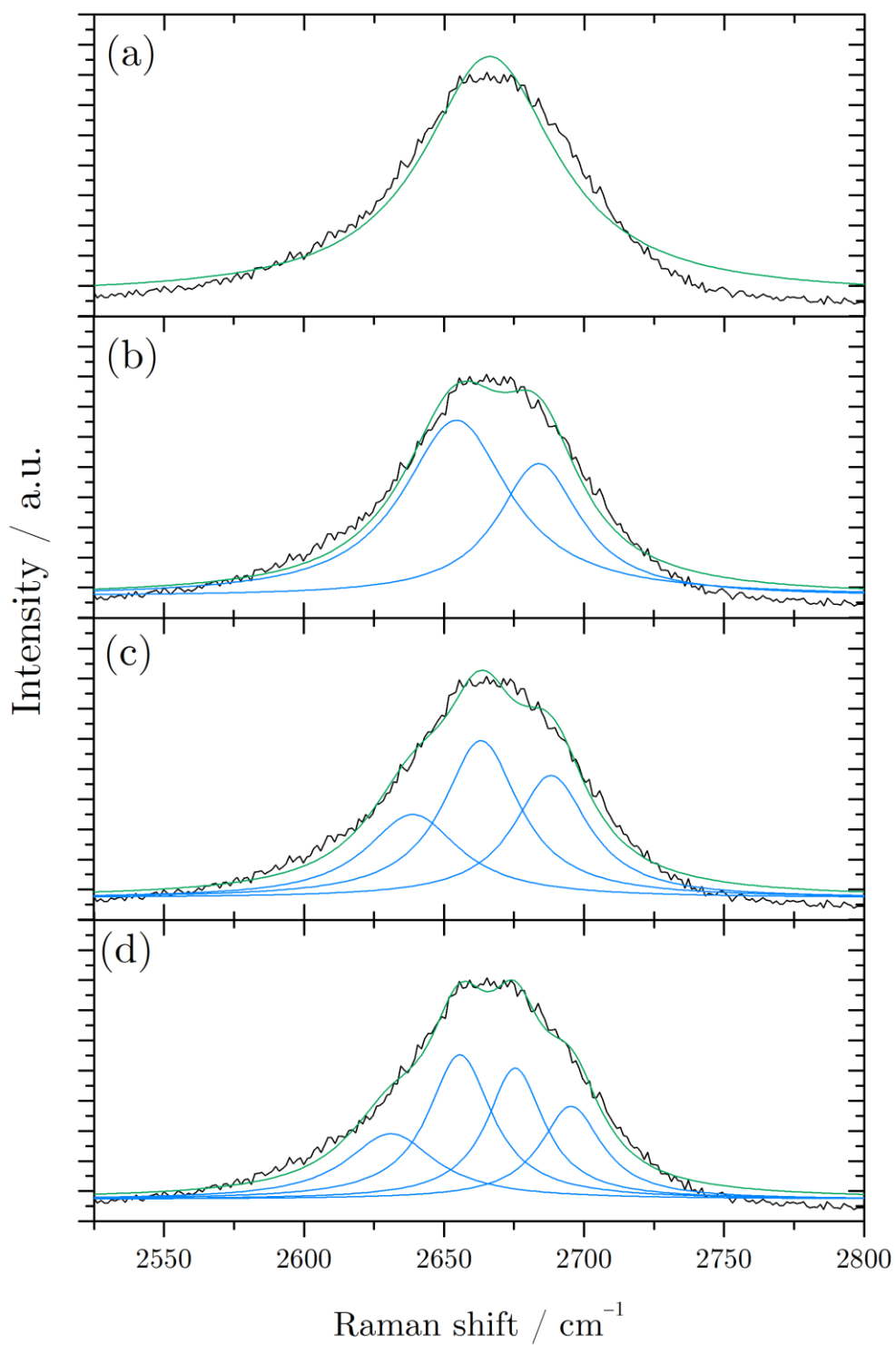


Figure 2.17) Raman $2D$ band fitting to increasing number of Lorentzian functions displaying reasonable good fit with four Lorentzian components

2.5.3.4 Electron Paramagnetic Resonance spectroscopy

EPR enables the study of paramagnetic species such as free radicals, electrons in unfilled conduction bands, bi-radicals and species in triplet states, amongst others. The basic principles of EPR are analogous to those of Nuclear Magnetic Resonance, in which a sample is placed within a magnetic field and a pulse of electromagnetic radiation (usually microwave) is applied for the purpose of inducing transitions between spin states. However whereas in NMR the decay relaxation of the excited atomic nuclei is measured, EPR is concerned with the relaxation decay from excited spin states of excited unpaired electrons. Because the majority of stable molecules have their electrons paired, EPR is not as widely applicable as NMR as an analysis technique, however because of this it does enable the use of many conventional solvents which do not contribute to the resonance spectrum, as is the case in NMR.

In this work EPR was employed to probe the presence of radicals formed *in situ* within a solid graphite electrode to probe the nature of the resulting reduced cation.

2.5.3.5 X-ray Photoelectron Spectroscopy

X-ray Photoelectron Spectroscopy (XPS) is a spectroscopic technique, which enables compositional information on solid samples, particularly solid surfaces, to be found. It is a particularly useful tool in graphene exfoliation work to determine the extent of chemical functionalization/oxidation of exfoliated flakes. The basic mechanism of XPS involves the use of specific energy photons to excite the electronic states of core atoms at/near the surface of a sample. The resulting ejected electrons are filtered and specific energies are monitored and recorded. This is essentially the opposite mechanism to EDAX (see section 2.6.2.2). Resonance peaks are observed in the resulting energy spectra correlating to specific energies, characteristic of the atomic structure at the sample surface. Although the penetration of X-rays is relatively deep within the sample, the analysis depth is limited by the ability of the electrons to escape from the sample without losing the photon-acquired energy. As such, for excitation energies *ca.* 1400 eV, electrons greater than 10 nm below the surface have only a small probability of reaching the surface without any loss of energy.²⁰³ As a result, these electrons only end up contributing to the background signal rather than contributing to well-defined photoelectric resonances.

In this work, as is the case in most solution-phase graphene production work, XPS was used to characterise the degree of flake oxidation.

2.6 Experimental

2.6.1 Chemicals and materials

HOPG (SPI-1, SPI-2, and SPI-3 grade, $10 \times 10 \times 1$ mm and 3 mm discs) was obtained from SPI supplies (West Chester, PA, USA). Graphite rods and Madagascar graphite were acquired from Graphexel Ltd, UK and contained no adhesive binder. The following chemicals were ordered from Sigma-Aldrich and used without further purification: 1-Methyl-2-pyrrolidone (NMP, biotech. grade $\geq 99.00\%$), NMP (anhydrous, 99.5%), lithium tetrafluoroborate (LiBF_4 , 99.99%, melting point 297°C), tetramethylammonium perchlorate (TMAClO_4 , 99.99%, melting point 300°C), tetramethylammonium tetrafluoroborate (TMABF_4 , 99.99%, melting point $>300^\circ\text{C}$), tetraethylammonium tetrafluoroborate (TEABF_4 , 99.99%, melting point $365 - 368^\circ\text{C}$) and tetrabutylammonium tetrafluoroborate (TBABF_4 , 99.99%, melting point $159 - 162^\circ\text{C}$), dimethyl sulfoxide (DMSO, anhydrous, grade $\geq 99.9\%$), N,N-Dimethylformamide (DMF, anhydrous, grade 99.8%), silver perchlorate (AgClO_4 , anhydrous, 97%), platinum gauze (52 mesh, 99.9% trace metal basis). Platinum wire (0.5 mm diameter) was ordered from Fischer Scientific, UK.

“Anodisc” 13 mm Alumina ($0.02\ \mu\text{m}$ pore size) membranes were supplied by Whatman (Maidstone, UK).

2.6.2 Equipment

All potentials were controlled by a PGSTAT100 potentiostat (Autolab, Utrecht, The Netherlands) using Autolab GPES software and Autolab NOVA software. Electrochemical measurements were undertaken in specially designed glass cells to accommodate all necessary electrodes and argon syringe.

Sonication was conducted in an Elma ELMASONIC P70H 100% power (220 W) for a range of times (between 1 min and 12 h). Electrochemical cell temperatures were controlled *via* a Grant GD100 water bath. Sonicated samples were centrifuged in SIGMA 2-16, SIGMA Laborzentrifugen, (Osterode am Harz, Germany) at 13,500 rpm for 30 min.

Raman spectroscopy was performed using a 633 nm excitation wavelength (Renishaw RL633 Class 3B 20 mW HeNe laser) at 10% intensity. The Raman spectrometer was a Renishaw Mk1 System 2000 RM controlled with Wire software on a Windows 95 operating system, and fitted with an Olympus BH2 microscope. Powder X-ray diffraction was conducted on a D8 Discover diffractometer with a CuK-Alpha X-ray source ($\lambda = 1.5405 \text{ \AA}$). AFM data was obtained on an Asylum Research MFP3D-SA microscope. XPS data was collected on a Thermo Scientific K-Alpha spectrometer, using a monochromatic AlK α X-ray source operated at 100W. The analysis diameter was 300 μm and charge neutralisation was used for all analysis. SEM images were obtained on a FEI Quanta 200 (E) SEM equipped with energy dispersive X-ray analysis. Karl-Fischer titration was conducted using a C20 Coulometric KF Titrator (Mettler Toledo).

2.6.2 Working electrodes

Various forms of graphite were used as the working electrode material, including HOPG, graphite rods (various grades), graphite flakes, Madagascar graphite, few-layer graphene. Platinum wire was also used as a comparison, along with glassy carbon (GC, CHI 104 electrode, 3 mm diameter, CH Instruments, Austin, USA). Glassy carbon electrodes were polished with Kemet diamond suspension prior to use.

HOPG and graphite rods were contacted using self-closing tweezers. For graphite support electrodes, HOPG was contacted using copper wire and silver conductive adhesive epoxy (Alfa Aesar) on the reverse basal plane of the HOPG.

In the case of *in situ* Raman and XRD investigations, HOPG was placed in a dedicated cell (ECC-Opto, EL-CELL GmbH, Hamburg).

2.6.3 Counter electrodes (CE)

In all experiments, the CE was constructed from a platinum gauze, spot welded to a platinum wire support (Advent Research Materials, UK). An additional platinum mesh (10×25 mm) was wrapped around the gauze to increase the surface area of the CE for long CA procedures. It was important to ensure the working area of the CE was sufficiently larger than the working electrode in order to pass the desired current with minimal resistance issues. Prior to every experiment, platinum CEs were cleaned in a Bunsen burner flame to ensure complete removal of any contamination.

2.6.4 Reference electrodes (RE)

Due to the use of non-aqueous media throughout, there was no obvious choice of reference electrode. Electrolytes employed typically contained either perchlorate (ClO_4^-) or tetrafluoroborate (BF_4^-) anions. *Saturated BF_4 and ClO_4* reference electrodes, in the form of a silver wire oxidised to form a coating of $\text{Ag}^0/\text{Ag}^+\text{BF}_4^-$ and $\text{Ag}^0/\text{Ag}^+\text{ClO}_4^-$ respectively, were not suitable due to attack from NMP and subsequent stripping of the $\text{Ag}^+\text{BF}_4^-/\text{Ag}^+\text{ClO}_4^-$ layer from the silver wire. However, a *saturated silver* system ($\text{Ag}^0/\text{Ag}^+\text{ClO}_4^-$) in the

form of a silver wire in contact with 0.01 M AgClO_4 , where the system is sensitive to silver ions rather than perchlorate/tetrafluoroborate ions was possible.²⁰⁴ The Ag/AgClO_4 RE was found to be stable for approximately two weeks of experiments and was therefore freshly reconstructed on a weekly basis. The saturated silver Ag/AgBF_4 system was not possible due to the poor solubility of AgBF_4 in NMP however because of its sensitivity towards silver ions it was found that it was also stable for tetrafluoroborate containing electrolyte.

Other pseudo-reference electrodes chosen throughout the project included Pt wire, Ag wire, and elemental mercury.

A mercury RE electrode was constructed by placing Hg in a 3 mm inner diameter glass tube of which a silver wire was inserted and the glass tube sealed. The other end was sealed using a Vycor[®] glass frit (Scientific and Medican Products Ltd., Cheadle, UK) *via* heat shrink. This tube was placed within a larger glass tube, filled with the electrolyte of use and sealed in the same manner.

The $\text{Ag}^0/\text{Ag}^+\text{ClO}_4^-$ electrode was constructed in a similar manner to the Hg electrode; by placing a silver wire in a 3 mm diameter glass tube sealed at one end with a Vycor[®] glass frit. The tube was filled with 0.01 M AgClO_4 in 0.1 M of chosen electrolyte and sealed.

The typical electrochemical cell employed for the majority of the work was as described in Figure 2.18.

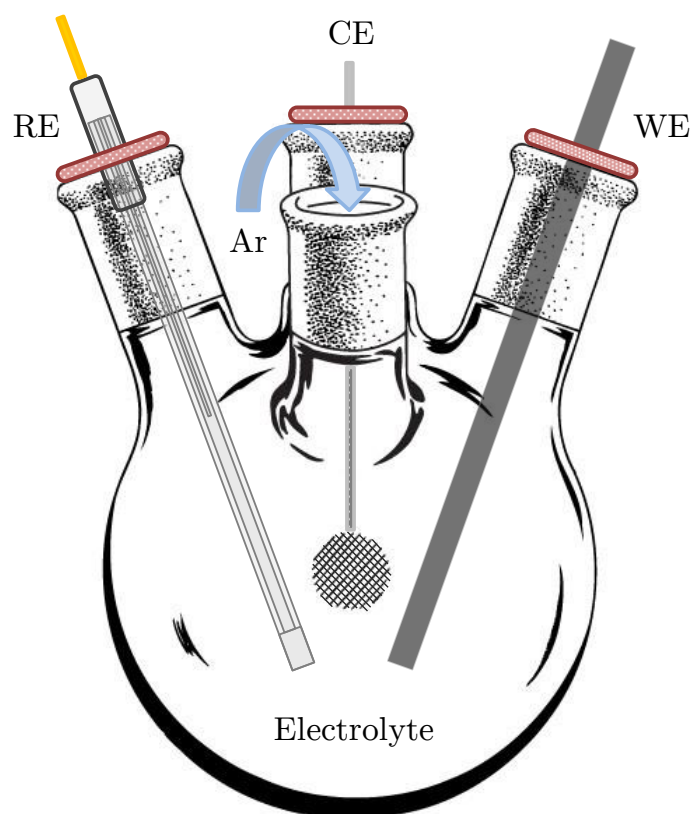


Figure 2.18) 4-neck electrochemical cell schematic, as used for graphene synthesis procedures involving graphite rod electrodes, in this case purged with argon gas, but eventually conducted within a closed saturated argon atmosphere

Chapter three

Electrochemical cathodic intercalation studies

3 Electrochemical cathodic intercalation studies

3.1 Introduction

Within this Chapter, investigations including primary electrochemical intercalation and subsequent electrolyte reduction will be addressed; this Chapter could be alternatively viewed as the ‘preliminary electrochemistry’ Chapter. The initial stage for the production of graphene utilises the controlled electrochemical intercalation of tetraalkylammonium cations into a bulk graphitic cathode, in an aim to exfoliate the graphite cathode.

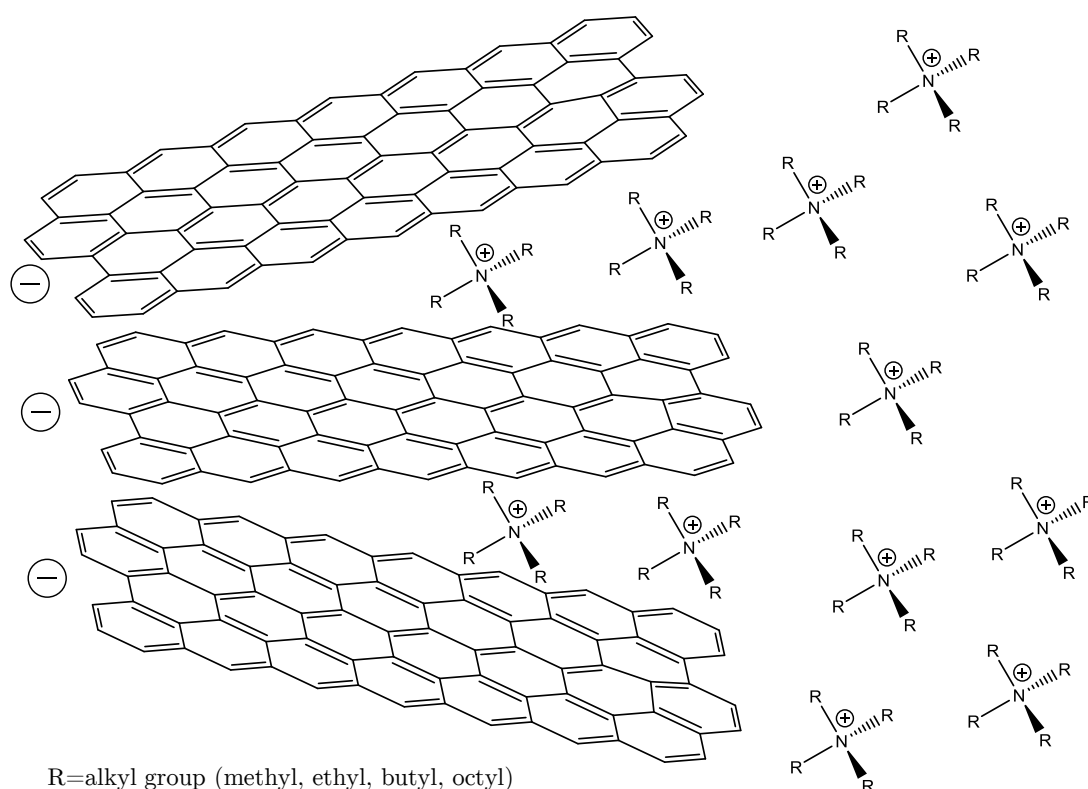


Figure 3.1) Schematic illustrating the expansion of the interplanar graphene galleries induced by the intercalation of tetraalkylammonium cationic species, where R on the R_4N^+ cation represents the alkyl group

The goal of this work is to understand to what extent a graphite cathode interacts with the intercalating species, and whether the graphite can be broken down into its constituent graphene layers with the use of this mechanism; does intercalation form a graphite intercalation compound (GIC) and does this hinder or facilitate the process in any way? Investigated are the effects of different cationic species and solvents on recorded voltammetry, and the effect of oxygen involvement has on the system, as well as work to determine the nature of the GIC formed as well as electrolyte/solvent decomposition effects observed at significantly large cathodic potentials.

A brief background on lithium ion battery chemistry, graphite intercalation compounds and tetraalkylammonium reduction chemistry is covered prior to presentation of results.

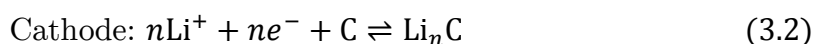
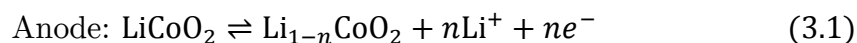
3.1.1 Introduction to lithium-ion (Li-ion) batteries

The significance of Li-ion batteries in this work cannot be ignored. This class of rechargeable batteries exploits the mobility and intercalation of lithium cations into a graphitic anode/cathode on charge/discharge, respectively. The lithium ion cell is comprised of a lithium containing electrolyte such as lithium hexafluorophosphate (LiPF_6), lithium tetrafluoroborate (LiBF_4) or lithium perchlorate (LiClO_4) and since the potentials produced by the Li-ion cell are typically larger than those at which aqueous solutions are electrolysed, and due to lithium's high affinity to react with water; non-aqueous or aprotic solvents are employed, such as ethylene carbonate and dimethyl carbonate. This electrolyte solution is in contact with an anode (usually graphitic carbon) and a cathode (lithium containing compound such as lithium cobalt oxide).²⁰⁵⁻²¹⁴ *N.B.* the terminology for electrodes can be misleading, since in a galvanic cell (in

which reactions occur spontaneously when the terminals are connected externally with the use of a conductor, such as primary batteries) the two terminals are reversed (cathode is positive, electrical current flows from the cathode to the anode). For all intents and purposes, we will continue with our aforementioned definition for electrolytic cells, as defined by Michael Faraday; where the cathode is negatively charged, and which cations migrate towards under an applied potential difference¹⁶², and note that ‘anode’ and ‘cathode’ in equations 3.1 and 3.2 have been swapped in order to match this definition: *cation intercalation occurs at the cathode.*

Non-aqueous solvents are susceptible to decomposition on cathodes during charging; however the use of appropriate aprotic solvents facilitates the deposition of a solid layer (known as the solid electrolyte interface, SEI)²¹⁵⁻²²⁴ on the electrode surface which prevents further decomposition of the electrolyte on successive cycling. Although SEIs do prevent further solvent decomposition and maintain high ionic conductivity, continued growth as a result of fresh electrode exposure from lithiation causes a significant, continued loss of electronic conductivity and a steady decrease in battery life.²²⁵

Both the anode and cathode are constructed from materials with layered crystal structures, enabling the intercalation and storage of Li^+ between layers *via* the following half reactions;



Lithium is the ideal choice of intercalating species since its crystallographic diameter (0.146 nm) is smaller than the interplanar spacing of both graphite and LiCoO_2 (0.354 nm and 0.24 nm, respectively).^{7,226} On charging, lithium flows from the anode to the cathode where it intercalates between the graphene

layers and is reduced; forming a Li_nC graphite intercalation compound (GIC). Simultaneously at the LiCoO_2 anode, cobalt is oxidised from Co^{3+} to Co^{4+} , completing the electrical circuit and allowing current flow.

During discharge, in which lithium spontaneously de-intercalates from the graphite cathode and migrates to the anode, power is harnessed from the cell *via* the electrons liberated during the corresponding cobalt reduction and lithium oxidation reactions.

The cell does unfortunately have its limits; overcharging of the cell causes the formation of cobalt(IV) oxide at the cathode, and over-discharge supersaturates the lithium cobalt oxide leading to the irreversible production of lithium oxide. Both of these processes eventually cause a decrease in life cycle and ultimately prevent the battery from functioning at all.

The key aspect of this system lies within the employment of lithium as the intercalating species to avoid physical anode deformation. Whereas in Li-ion battery research focus is on maintaining the structure of the graphite electrode to allow for improved life cycles, in graphene synthesis the exact opposite is desired in the expansion and exfoliation of the graphite electrode.

Not too distantly related, and certainly worth mentioning are electrochemical double layer capacitors (EDLCs); the future graphene-based energy storage application to challenge Li-ion batteries. Energy storage in double layer capacitors is based on the charge separation at an interface between the electrode surface and an electrolyte solution with ionic conductivity and the energy is stored in the electric field fashioned by the electrochemical double layer.^{227,228} (See Chapter 1)

Energy storage directly from charging/discharge processes offers great advantages over the alternative Li-ion intercalation mechanism, since the

lifetimes of the EDLCs are considerably greater than that of Li ion batteries. This is particularly due to undesirable side reactions occurring parallel to the ion intercalation mechanism, such as the formation of SEIs, resulting in the poisoning and degradation of the carbon electrode. However, the main disadvantage associated with EDLCs is their relatively small energy densities (*ca.* 1–10 Wh kg⁻¹) when compared to conventional batteries (*ca.* 20–100 Wh kg⁻¹).^{229,228} One problem associated with graphene based EDLC construction lies in prevention of graphene sheet re-aggregation, since sheet re-aggregation significantly decreases the electrode surface area and has detrimental effects on the total capacitance. One particularly ambitious solution to this problem is to use CNTs as supporting pillars between graphene sheets allowing for maximised surface area for double layer capacitance storage; this methodology has been developed into practice, producing a pseudo-capacitive material delivering an energy density of *ca.* 35 Wh kg⁻¹ at a high power density (*ca.* 8 kW kg⁻¹).²³⁰

3.1.2 Graphite Intercalation Compounds (GICs)

Graphite intercalation compounds are complexes with formula XC_n , where an element or molecule X is intercalated between the graphene sheets of the graphite lattice and n is the number of carbon atoms in the stoichiometric formula.²³¹⁻²³³ The degree of intercalation is the most important characteristic ordering property of GICs and is denoted in terms of a staging index n , where n is the number of graphene layers between adjacent intercalated layers; for example a stage-1 GIC comprises of alternating graphene layers and intercalating layers, stage-2 GICs consist of two non-intercalated graphene layers alternate with an intercalated layer, and so forth as shown in Figure 3.2.

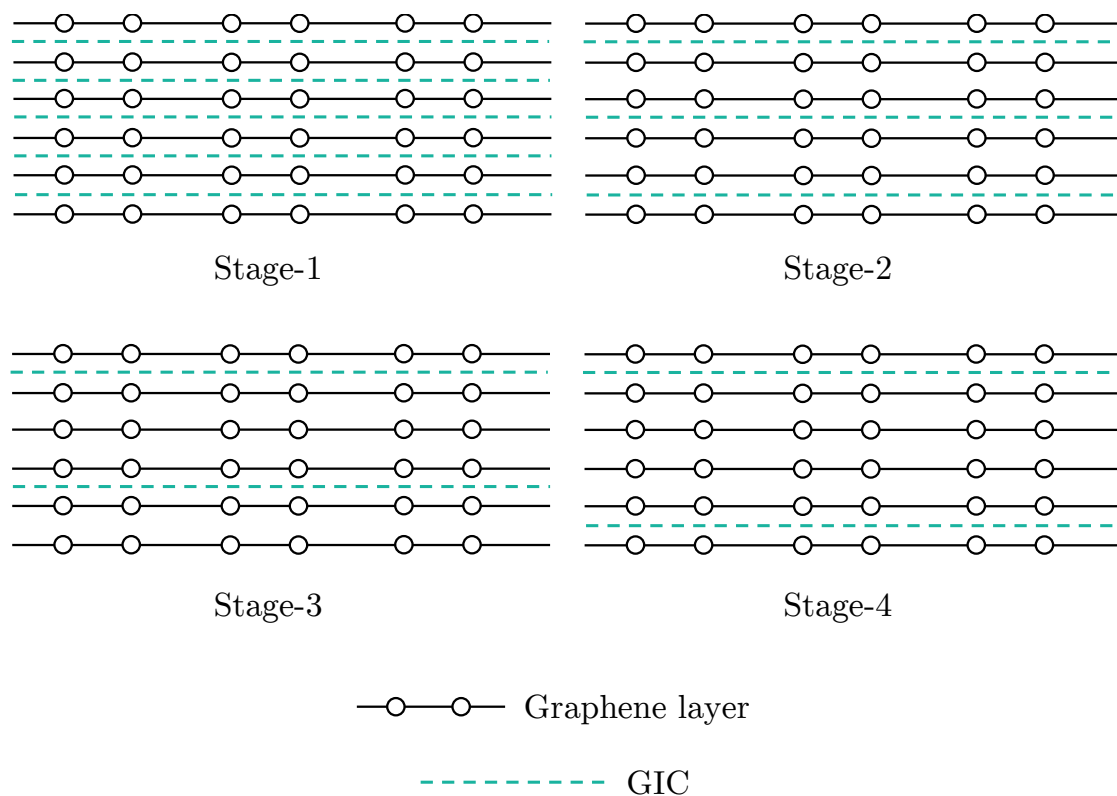


Figure 3.2) Schematic illustrating the staging phenomenon of GICs between graphene layers for stages $1 \leq n \leq 4$

GICs are able to control the variation of properties of the graphite over wide ranges *via* the control of the total free carrier concentration. The free carrier host of graphite is typically very low (on the order of 10^{-4} free carriers/atom at room temperature²³⁴) and intercalation of different species and concentrations allows for the controlled increase in electrical, thermal and magnetic properties.

Synthetically there are several routes to the production of GICs, including liquid-phase ion intercalation, electrochemically controlled ion intercalation and co-intercalation techniques as well as two-zone vapour transport.^{232,235-239} More specifically, the preparation of tetrabutylammonium GICs have been reported²⁴⁰, where synthesis takes place *via* a cationic displacement reaction in which a sodium-ethylenediamine Na(en)_y^+ , where ‘en’ represents ethylenediamine, complex within graphene galleries is rapidly displaced by TBA^+ cations. The formed stage-1 GIC compound with formula C_{44}TBA exhibited a gallery expansion of 0.47 nm. The sodium-ethylenediamine was prepared by reacting sodium metal with graphite powder in a solution of ethylenediamine. The subsequent displacement reaction was performed by reacting with TBABr in DMF. It is perhaps surprising that the TBA^+ cation, with a crystallographic diameter of 0.89 nm^{241,242} is able to intercalate at such a high stage-degree since it is almost thrice the size of the graphite interplanar spacing. Even the interplanar spacing reported for the sodium-ethylenediamine GIC complex is 0.671 nm. The explanation toward TBA’s stage-1 intercalation ability is due to the flexibility of the alkyl (butyl) chain lengths, allowing the cation to be compressed to a measured 0.47 nm (*d*-spacing of GIC). Amongst others, this particular piece of work has inspired the thinking behind the use of electrochemical TBA^+ -graphite intercalation as a possible route to graphene synthesis *via* the exfoliation of the produced TBA GIC. Indeed, this was

perhaps the original aim of Sirisaksoontorn and co-workers; however no subsequent work regarding this has since been reported.

For a full, comprehensive review on the formation and stability GICs, the reader is directed to an excellent report entitled 'Intercalation compounds of graphite' by M. S. Dresselhaus and G. Dresselhaus, 1981.²³⁴

3.1.3 Tetraalkylammonium reduction chemistry

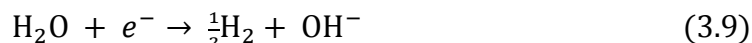
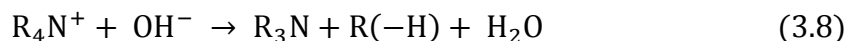
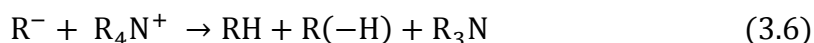
The cathodic behaviour of tetraalkylammonium cations has been reported at different electrode materials including GC, graphite, and platinum; proposing significantly different mechanisms for the cation reduction, depending on the electrode material it proceeds by.

Dahm and co-workers²⁴³ investigated TEA^+ and TBA^+ tetrafluoroborate reduction in DMF at a GC electrode, and propose that TEA/TBA^+ reduction at the cathode proceeds *via* several steps initiated by the single electron reduction of the tetraalkylammonium cation to an ethyl or n-butyl radical, reaction (3.3). They propose that the reactive radical species spontaneously decomposes to form a trialkylamine and an alkyl radical in reaction (3.4) but since the latter is reduced at potentials more positive than those of the original R_4N^+ cation, is reduced further to yield an alkyl carbanion, reaction (3.5).

The alkyl carbanion can go on to abstract a proton from either a parent tetraalkylammonium cation (reaction 3.6), or if there is residual water present in the solvent; *via* reaction with water (reaction 3.7). Both of these routes yield a stable alkane; of which is dependent on the original R group.

Reaction 3.7 ultimately gives rise to a hydroxyl-initiated tetraalkylammonium cation reduction, to an alkane and a trialkylamine plus the recycling of water.

Simultaneously, at the potentials required to reduce tetraalkylammonium species any residual water will certainly undergo electrolysis at such negative potentials, regenerating hydroxyl and yielding the production of hydrogen gas (reaction 3.9).



These processes are described at a GC electrode, which does not possess a layered/porous structure that allows ion intercalation. Simonet *et al.* propose similar findings using a GC electrode and suggest R_4N^+ reduction *via* reactions (3.3) and (3.4) for heterogeneous ET in DMF.²⁴⁴ They expand on the work of Dahm and co-workers by introducing HOPG as the working electrode, noting that intercalation of the cations takes place prior to reaction. Like Dahm, they report voltammograms with a continuous current increase at potentials more negative than -2.5 V *vs.* saturated calomel electrode (SCE) and they relate this feature to the reduction of residual water and/or acidic impurities within the solvent, though offer no mechanistic detail. They also report that on drying of the solvent, the accessible negative limit of the potential window decreased to -2.7 V *vs.* SCE and a well-defined cathodic step appeared close to the negative limit. They observed an anodic peak on the reverse scan which they claim to be

associated with the cathodic step, since its I_p increases proportionally with time, with respect to chronoamperometry performed after the cathodic step. Finally they report a large peak separation, ΔE_p , between the anodic and cathodic current responses of 0.85 V and 1.06 V with TMA^+ and TBA^+ respectively,²⁴⁵ although do not offer any in depth explanation towards the large peak separation.

However arguably most significant of their findings, is their proposition of the idea of graphite intercalation compounds (GICs), in which the tetraalkylammonium cations are stabilised by the graphite electrode and can be regarded as an electron reservoir that has potential to act as a solid reducing agent:



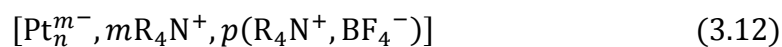
Additionally, this reservoir can act as an efficient reducing agent towards organics, donated RX^{244} :



However there is uncertainty regarding the nature of the graphite lamellar compound, specifically the location of the generated charge. A valid question, and one to be tackled herein, is whether the negative charge bases itself on the graphene layers, or whether the cation is reduced to some radical species which is stabilised by the graphene layers.

Finally, it is worth mentioning another interesting piece of work by Simonet in which they investigate tetraalkylammonium tetrafluoroborate reduction chemistry at a platinum working electrode.²⁴⁵ They show that under dried solvent conditions, decomposition of the ammonium cation does not take place,

and instead the formation of an adsorption-like complex occurs at the platinum surface which they write as:



The accompanying voltammograms to support this theory are of similar shape to those shown for the formation of tetraalkylammonium GICs and SEM-assisted surface imaging revealed the presence of crystals containing nitrogen, boron and fluorine. Finally, these crystals exhibited strong reducing reagent abilities established by intense blue colourisation, characteristic of benzophenyl ketyl radical anions, when exposed to a solution of benzophenone and fluorenone in DMF.²⁴⁵

3.2 Results

3.2.1 Reference electrode systems

The ferrocene/ferrocenium (Fc^+/Fc) redox couple was employed to test the suitability of various reference electrodes for this work. Ferrocene (1 mM) was dissolved in a 0.1 M solution of TEABF_4 in NMP and voltammetry measured at a GC WE. Since the majority of this work was undertaken in non-aqueous media, there is no suitable standard reference electrode to use. The use of ferrocene as an internal reference would be suitable at the beginning and end of procedures, but is impractical for the duration of long CA procedures. Pt, Ag and Hg pseudo-reference electrodes were investigated using Fc^+/Fc as well as a saturated Ag^+ electrode. The CVs were conducted at scans rates of 100 mV s^{-1} .

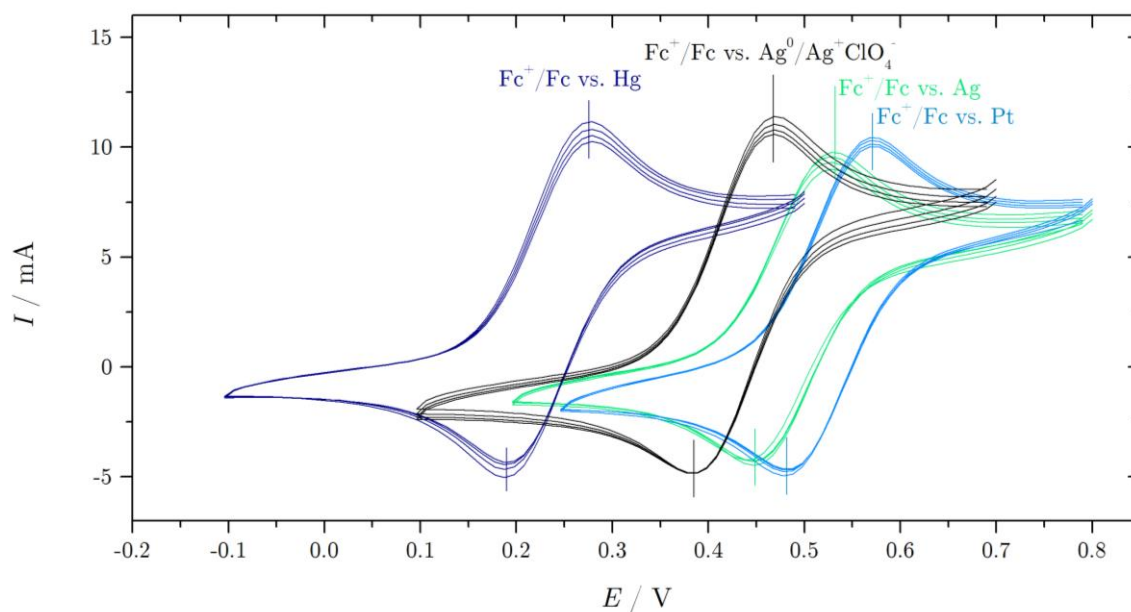


Figure 3.3) Current response of the ferrocene/ferrocenium redox mediator at a GC working electrode, against various reference electrode systems, scanned at 100 mV s^{-1}

Pt and Ag wires, as well as Hg, were used as REs initially, however these were eventually replaced with a $\text{Ag}^0/\text{Ag}^+\text{ClO}_4^-$ RE, since it was found to be stable for longer periods of time. For CA procedures where potentials as large as -6 V were applied, the Ag and Pt REs were not suitable. Table 3 shows the degree to which the determined redox potential (E_0) of Fc^+/Fc drifts with time for different reference electrodes.

Table 3) Reference electrode stability data expressed as measured E_0 potential of the Fc^+/Fc reduction *vs.* reference and pseudo-reference electrodes, at increasing periods of time

time / h	E_0 <i>vs.</i> Hg / V	E_0 <i>vs.</i> Ag / V	E_0 <i>vs.</i> Pt / V	E_0 <i>vs.</i> Ag/AgClO ₄ / V
0	+0.238	+0.488	+0.528	+0.428
24	+0.053	+0.562	+0.518	+0.413
48	+0.024	+0.661	+0.507	+0.406
72	+0.011	+0.727	+0.494	+0.401

Potential drifts as large as *ca.* 250 mV were observed for $E_{\text{Fc}/\text{Fc}}^0$ when referenced against Ag, whereas drifts of only *ca.* 30 mV were observed for Pt wire and Ag/AgClO₄. From these results it was determined that the Ag/AgClO₄ reference electrode was the most stable of the four reference systems for the longest period of time, and consequently used for all subsequent work.

3.2.2 Electrolyte decomposition: separate CE chamber

During electrochemical procedures, particularly when a HK-graphite rod was employed as the WE, the solution was found to colourise from clear to yellow/brown and was accompanied with an amine odour. This has been attributed to solvent decomposition in the cell and it is suspected that the colourisation occurs at the platinum CE, since at large measured currents a dark brown stream was often seen falling from the Pt CE.

Various techniques to further determine the origin of solvent colourisation during prolonged voltammetry were implemented. One method included sectioning the platinum gauze CE in a separate compartment to the rest of the cell such that any colouring as a result of electrolyte oxidation at the CE would be clearly visible in the separate chamber.

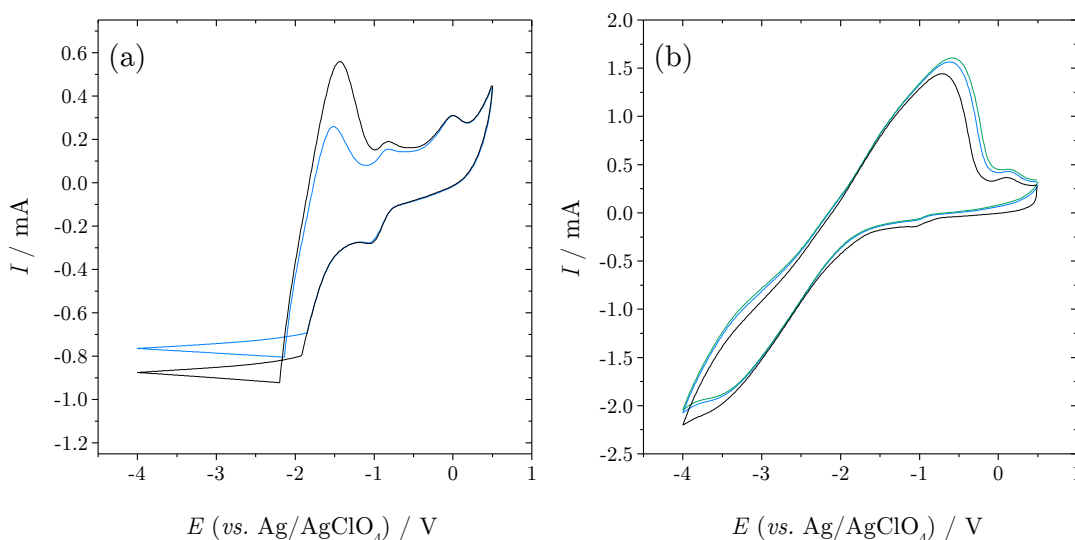


Figure 3.4) Voltammetric responses for TBABF_4 (0.1 M) in NMP at a HOPG electrode using (a) Pt CE in a separate chamber, and (b) Pt CE returned to main cell, scanned at 50 mV s^{-1}

Figure 3.4(a) shows the voltammetric responses using this cell setup and it can be seen the potentiostat was unable to pass a large enough current through the cell as a result of the high resistance caused by the glass frit/separate counter

cell. It was not possible to conduct the procedure long enough to determine the source of solvent colourisation. Once the CE was returned to the same cell (Figure 3.4(b)), it was clear that the separation caused the observed resistance.

To minimise the extent of solvent colourisation, a large CE (10 mm \times 50 mm platinum gauze) shaped around the working electrode was employed in order to allow the passage of larger currents with minimal solvent decomposition, as shown in Figure 3.5. This was found to reduce the degree of solvent colourisation, when using a graphite rod working electrode (immersed to give an electrode area of *ca.* 400 mm²) and during measurement of large currents (mA).

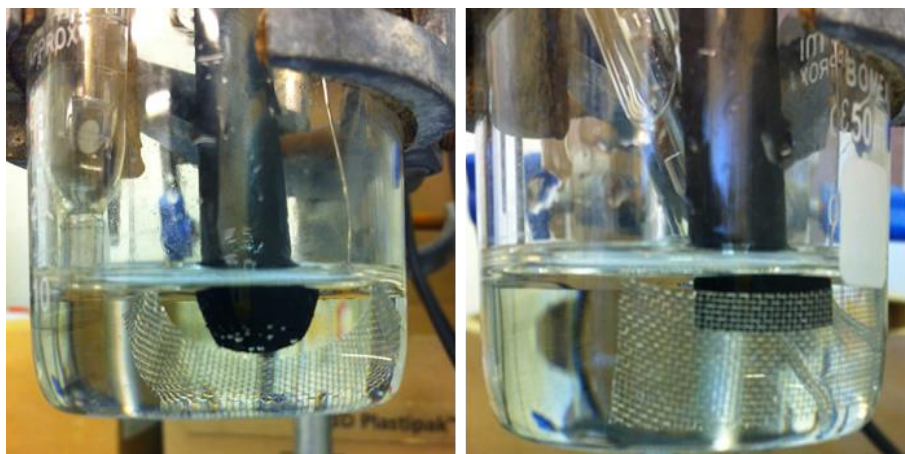


Figure 3.5) Image showing 10 \times 50 mm platinum gauze CE placed surrounding the graphite WE

3.2.3 Primary voltammetry

NMP was the solvent of choice for the procedure, for the reasons outlined previously (large potential window for cation intercalation/good graphene dispersion properties). To establish the accessible potential window of NMP, TMA ClO_4 (0.1 M) was dissolved in pure NMP and a GC working electrode was employed in a three electrode setup alongside a Pt CE and Ag/Ag ClO_4 RE. The potential was swept initially between +0.5 V and -0.5 V at a scan rate of 50 mVs $^{-1}$ and these two limits were increased sequentially until the CV in Figure 3.6(a) was obtained. The maximum potential window obtainable with tetraalkylammonium containing electrolytes was approximately 6 V, from +2 V to -4 V, although the negative limit was pushed further in some experiments to -5 V. The ideal working potential window can be seen to be between *ca.* +2 and -2 V which is the region in which very little Faradaic activity occurs, though small currents can be observed associated with residual oxygen/water in the system. Outside these limits, a steady increase in background current is observed corresponding to irreversible electrolyte reduction. Despite this, an ideal working potential window of *ca.* 4 V is good, even for a non-aqueous solvent. Due to the nature of the work being primarily focused on cationic intercalation, it is the negative region of the potential window that is of greater interest.

Figure 3.6(b) displays how the current response is affected by varying amounts of applied IR compensation. CVs were often skewed clockwise; often an indication of high resistance throughout cell, and is likely a result of the non-aqueous solvent. In an attempt to correct for this, IR-compensation was applied between 800 Ohms and an IR limit (potentiostat limit) of 2000 Ohms. It can be seen that the IR-compensation does have the desired effect, but the 2000 Ohms was insufficient to correct for currents as large as *ca.* 1 mA. To

address the issue of high resistance, electrodes were placed in close proximity to one another for all future experiments (within 0.5 cm).

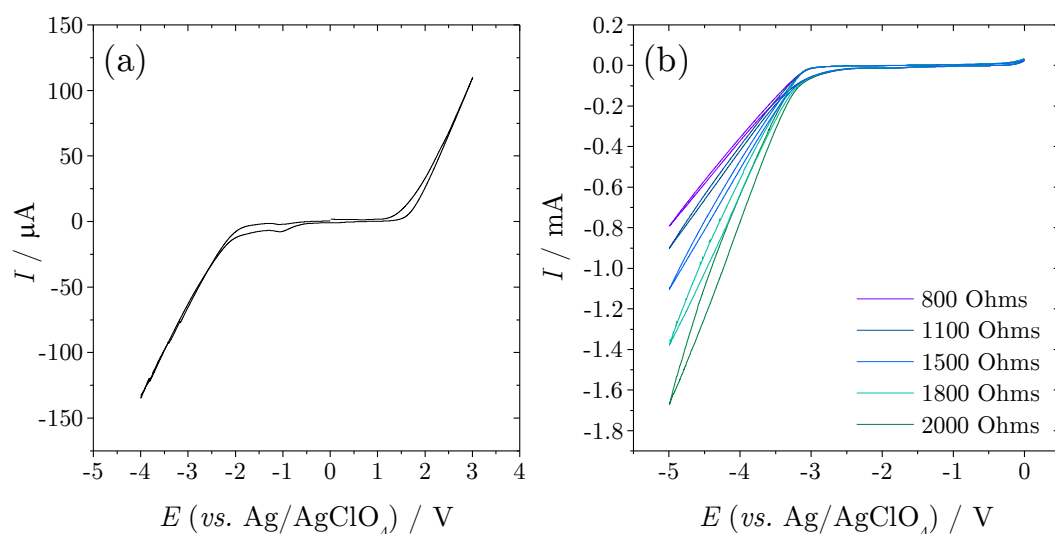
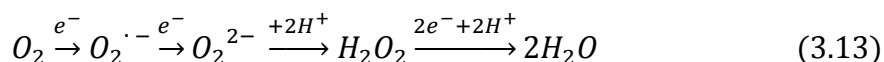


Figure 3.6) CVs showing (a) Full potential window of TMAClO_4 in NMP at a GC WE, and (b) effect of IR-compensation on the negative limit of the potential window, scanned at 50 mV s^{-1}

To mimic lithium ion battery chemistry at a graphite cathode, LiClO_4 (0.1 M) was dissolved in NMP and HOPG (sample size: $2 \times 10 \times 0.5 \text{ mm}$) was employed as the working electrode. The system was purged with argon for 20 minutes prior to investigation *via* CV cycling between +1 V and -4.5 V; the resulting voltammogram is presented in Figure 3.7. The two most prominent features are a) the sudden current increase at *ca.* -3 V corresponding to the intercalation of lithium into the graphite host electrode, and b) on reversal of the potential sweep the current is retrieved and a broad oxidation peak is observed corresponding to the subsequent de-intercalation of lithium ions. The CV is analogous to the repeated charging/discharging of a lithium ion battery.

The two peaks visible on the cathodic sweep at *ca.* -1 V and -2 V are attributed to the 2-electron reduction of molecular oxygen to superoxide ($\text{O}_2^{\cdot -}$) and oxide (O_2^{2-}):



In aqueous media, the current responses would be attributed to the complete 4-electron reduction of oxygen to hydrogen peroxide and water, however because NMP is aprotic, spontaneous protonation to peroxide and water is not easily achieved, and the following 2-electron reduction/protonation does not occur, if water is excluded.

Despite purging with argon in a sealed cell, removal of all oxygen from the system was not possible. However, the presence of dissolved oxygen and subsequent electrolysis did not prevent relatively reproducible voltammetry from being obtained. The reason for the repeatable CVs is due to the position of the negative limit of the potential window; the lithium intercalation peak was only partially explored.

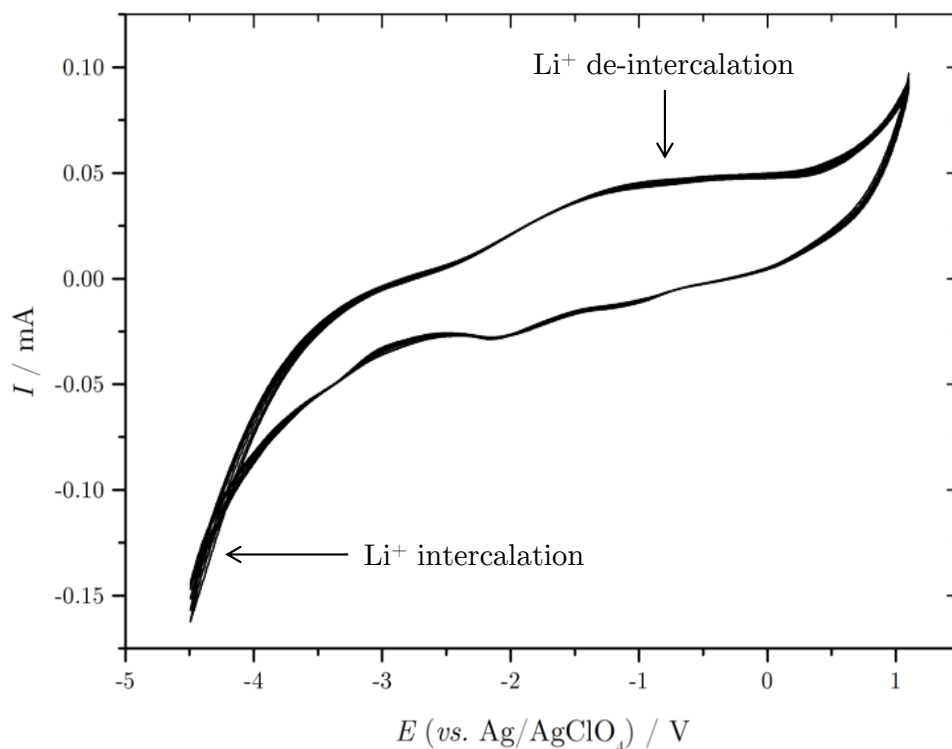
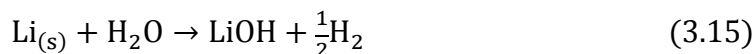
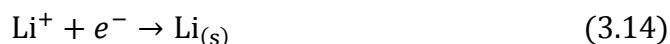


Figure 3.7) Repeatable CVs showing intercalation and de-intercalation of lithium into a HOPG electrode, recorded at a scan rate of 50 mV s^{-1}

In order to investigate the entire lithium reduction peak it was established that an extension of the CV negative limit to -6 V was necessary. Figure 3.8 shows the resultant CV, scanned over a potential window totalling a remarkable 7 V. On the reverse anodic scan a broad peak is evident over the region of *ca.* -2 V and 0.5 V. These peaks are associated with lithium reduction to lithium metal (on the cathodic scan) and the resulting re-oxidation on the anodic scan. However there is more to this reaction than the CV alone suggests; small peaks associated with water hydrolysis/oxygen reduction are visible despite argon purging prior to analysis.

Lithium rapidly reacts with residual water and oxygen to form LiOH and Li₂O, respectively, as well as hydrogen gas:



A white deposit was visible on the graphite electrode after multiple CV (>10) scans; this was more easily visible on a graphite rod (shown, inset Figure 3.8) than a HOPG electrode, though a small degree of white deposit was visible on the edge planes of HOPG (not shown). No deposit was noticeable on the basal plane of HOPG, however. This again highlights the difference in reactivity between basal plane and edge plane graphite electrodes, and can explain why deposit was more readily formed on graphite rods, since graphite rods have a larger degree of edge plane exposure as a result of their comparatively low anisotropy. The white solid is consistent with the formation of a lithium

compound, and in addition a traditional flame test produced the characteristic intense red flame of lithium.

During uninterrupted CV scanning, the peak currents of the intercalation and de-intercalation procedures can be seen to decrease substantially from *ca.* 150 μA to 50 μA and *ca.* 75 μA to 20 μA , respectively. This is a result of the observed lithium-compound deposition on the electrode surface, effectively poisoning the electrode thus reducing its effective working area. What this does highlight though is the degree to which a changing working area of an electrode has on the voltammetry.

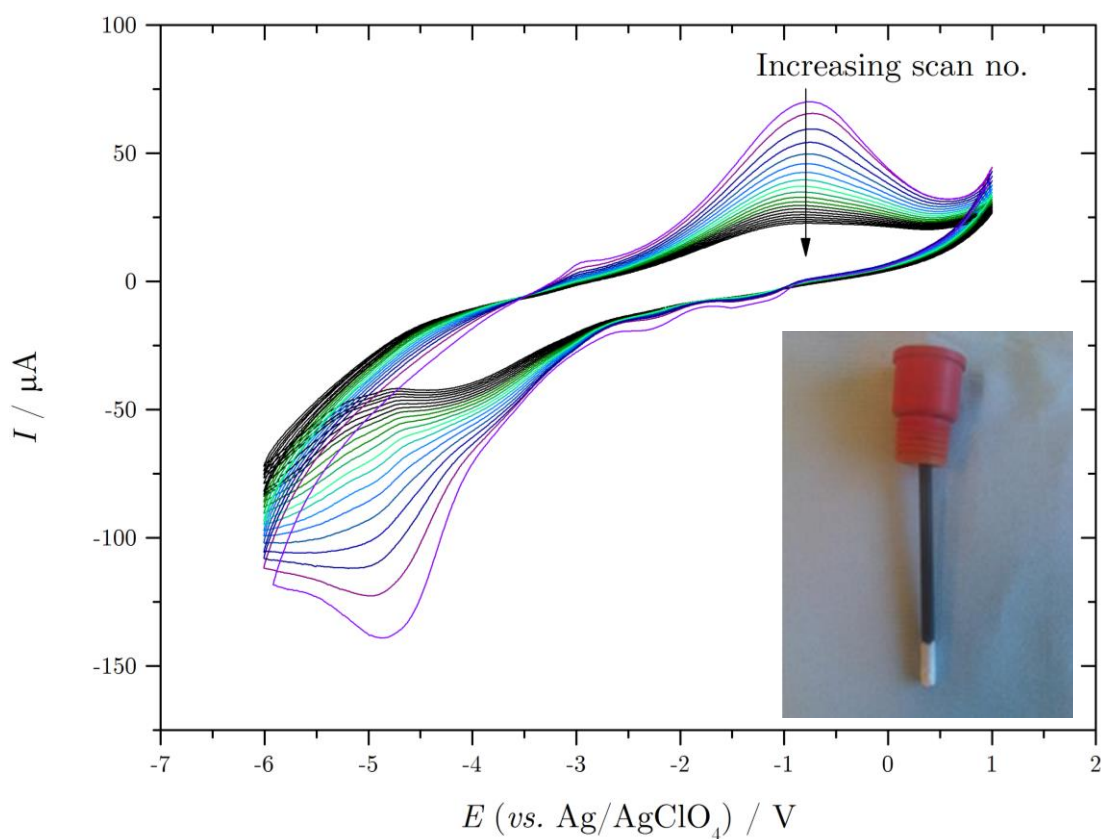


Figure 3.8) CVs showing lithium intercalation/de-intercalation at a HOPG electrode exposed to a solution of LiClO_4 (0.1 M) in NMP; highlighting the effect of successive scanning, inset: photograph of a graphite rod with $\text{LiOH}/\text{Li}_2\text{O}$ deposit, recorded at a scan rate of 50 mV s^{-1}

3.2.4 Tetraalkylammonium voltammetry

TMA⁺, TEA⁺ and TBA⁺ containing electrolytes were investigated independently in the same manner as lithium. Both perchlorate and tetrafluoroborate counter ions were employed throughout the work since sole use of a single counter-ion was not possible due to solubility issues. On a side note, it was interesting to note that TMABF₄ was insoluble in NMP at 0.1 M concentrations, despite achievable NMP-solubility with lithium and TEA⁺ containing electrolytes of the same concentration. As a substitute for tetrafluoroborate, perchlorate was employed as the counterion for all TMA⁺ studies. However despite the obvious desirability for one type of counterion for experimental consistency, voltammetry was unaffected by different counter ions since general analysis was conducted in the cathodic region of the potential window. The only occasions where notable differences were observed were when anodic potential regions (more positive than +1 V) were explored, where anionic electrolysis occurred. In this case, when using perchlorate, oxygen reduction peaks were observed during successive scans as a result of oxygen abstraction from the perchlorate electrolysis at *ca.* +2 V (section 4.2.5). Conversely, no oxygen is abstracted from tetrafluoroborate electrolysis and this was reflected in the absence of oxygen reduction currents in successive scans (see section 3.2.9).

Except when probing the effects of concentration dependence on voltammetry, electrolyte concentrations were kept at a maximum of 0.1 M; larger concentrations than this caused solubility problems in NMP. This maximum concentration value (0.1 M) was initially selected on the basis of maximising the degree of intercalation/expansion, by providing more available cation species to intercalate.

Figures 3.9(a-c) show the resulting voltammetry recorded at HOPG electrodes (coloured lines) and platinum wires (black lines) in solutions of (a) TMA ClO_4 (0.1 M), (b) TEABF $_4$ (0.1 M), and (c) TBABF $_4$ (0.1 M). The three cations show similar voltammetry at a HOPG working electrode; with cation intercalation and de-intercalation peaks centred on *ca.* -2 V. The intercalation peak on the cathodic scan begins at *ca.* -2 V, almost an entire volt higher than lithium, and does not peak until *ca.* -3 V (for TMA $^+$). The peak separation between the cathodic and anodic peak currents, ΔE_p , was found to increase slightly with increasing cationic diameter, although the position of the anodic peak current remains relatively unchanged for the three cations. This is attributed to the mechanics of the intercalation process; since TBA $^+$ requires conformational flattening in order to intercalate and thereby overcome the space limitation incurred by the neighbouring graphene sheets. Thus it is logical to think of TBA $^+$ requiring additional energy to permit intercalation (*cf.* TMA $^+$). This also explains why the anodic peak current position is *ca.* -1.5 V for all the R $_4\text{N}^+$ cations, since there is no additional energetic cost associated with the de-intercalation of any specific cation. At the very least this observed increase in ΔE_p with increasing cationic diameter is in agreement with Simonet *et al.*²⁴⁵

Perhaps the most notable feature of the HOPG cycles is the increasing intercalation and de-intercalation peak currents (I_p) on successive scanning. The peak current of the cathodic currents (and the anodic currents, although to a lesser extent) was found to increase with successive scanning and eventually after upwards of 100 scans CVs evolved to a constant, reproducible current response. However these eventual current responses were found to be significantly less prominent than initial currents, with CVs resembling little in the way of distinguishable Faradaic current features due to an increased background current.

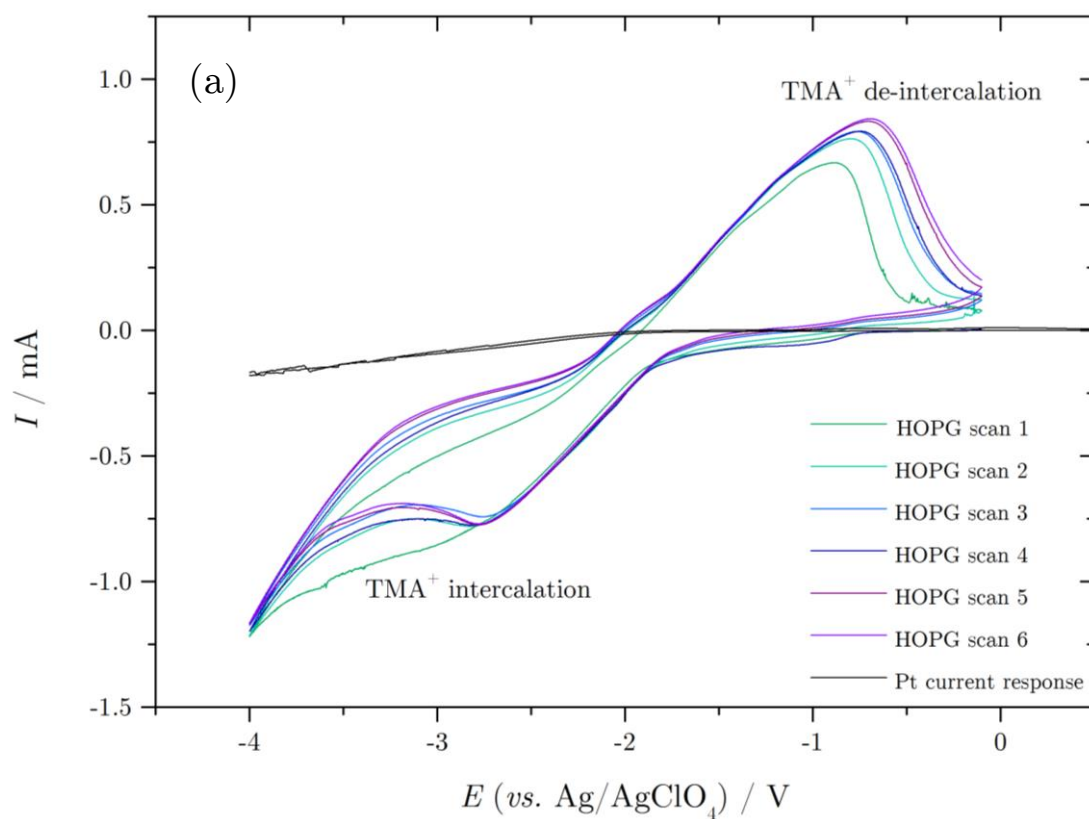


Figure 3.9(a) CVs showing the resulting current responses at a HOPG electrode (coloured lines) and a platinum wire electrode (black line) in solutions of TMAClO_4 (0.1 M) in NMP recorded at a scan rate of 50 mV s^{-1}

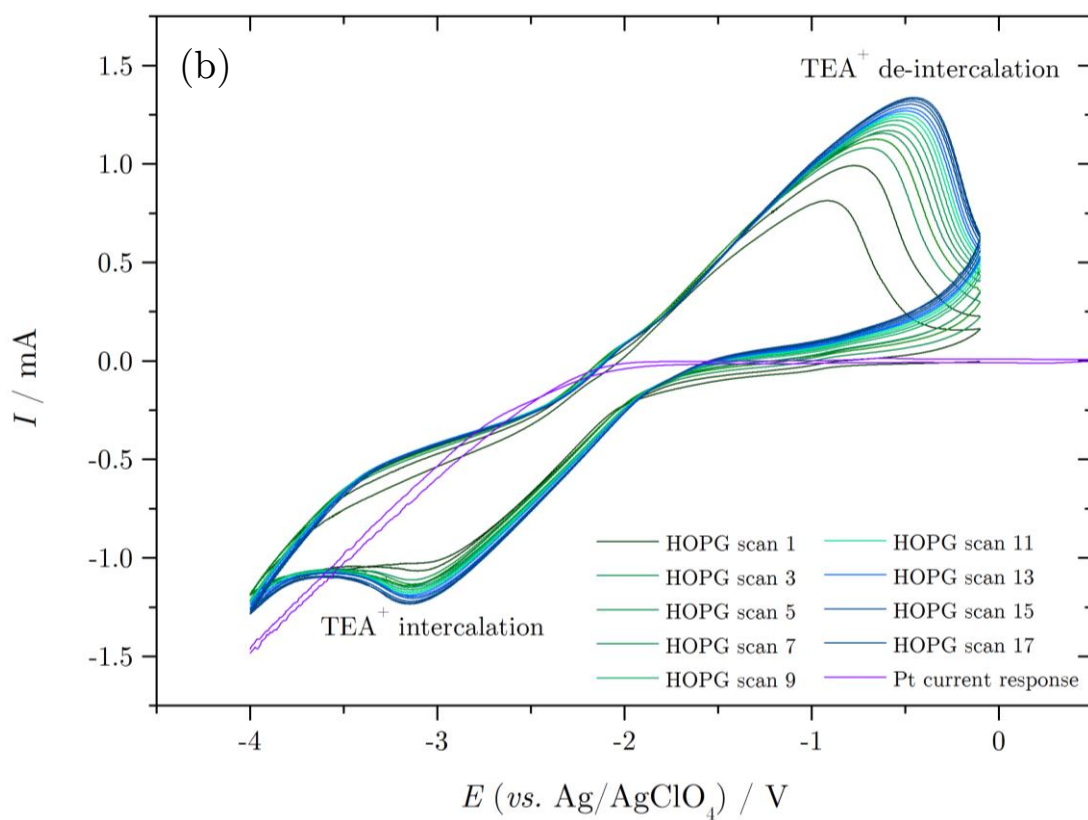


Figure 3.9(b) CVs showing the resulting current responses at a HOPG electrode (coloured lines) and a platinum wire electrode (purple line) in solutions of TEABF₄ (0.1 M) in NMP recorded at a scan rate of 50 mV s⁻¹

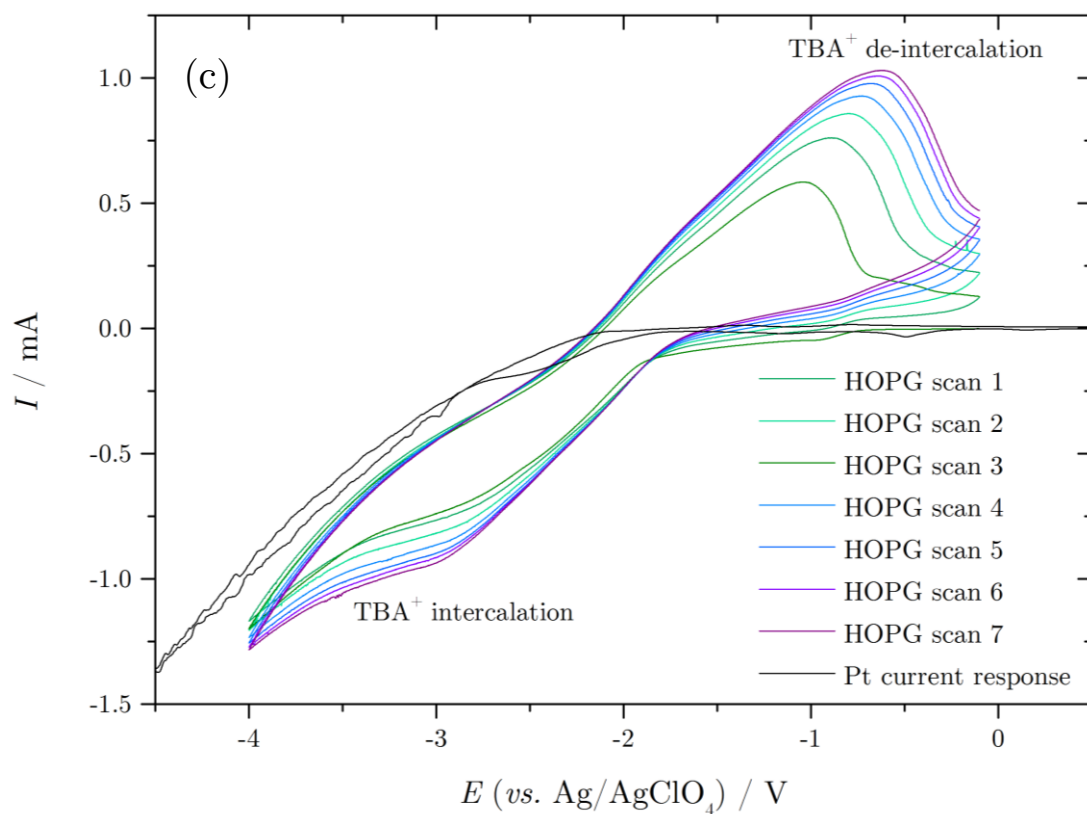


Figure 3.9(c) CVs showing the resulting current responses at a HOPG electrode (coloured lines) and a platinum wire electrode (black line) in solutions of TBABF₄ (0.1 M), recorded at a scan rate of 50 mV s⁻¹

Voltammetry at a Pt wire working electrode has also been included in the CVs in Figure 3.9 (a-c), and for all cations the current response is featureless other than the steady increase in background current at potentials below *ca.* -2 V. No peak currents are visible that can be attributed to intercalation/formation of a stable GIC, in contrast to work by Simonet at platinum electrodes also performed under inert atmospheric conditions.²⁴⁵ This was originally attributed to the presence of residual water in the electrolyte reacting with reduced R₄N⁺. However it was found later on (revisited, Chapter 4) that staging currents are only visible when the potential is scanned at a sufficiently slow rate.

Also accompanied with extended CV cycling, particularly with TBA^+ and TEA^+ , was visible expansion of the HOPG working electrode. Expansion caused during CV scanning was found to be irreversible (application of 0 A resulted in no collapse of the electrode back to original size) resulting in permanent deformation. Electrode expansion is covered in detail in Chapter 4.

When scanning the potential in extremely cathodic regions, typically more negative than -4.5 V, gaseous liberation at the graphite cathode was observed. The degree of bubble formation was proportional to the magnitude of the applied potential, and indicates the complete breakdown of some species and the possible evolution of hydrogen gas as a result of proton reduction. For this reason, such negative potentials were avoided since it is difficult to identify what is occurring mechanistically under such extreme conditions.

3.2.5 Electrode size effects on voltammetry

The CV in Figure 3.10 shows the visible voltammetric effects associated with increasing the exposed working area of a HOPG working electrode. It is clear that peak currents associated with intercalation/de-intercalation increase as the proportion of HOPG exposed to the electrode is increased.

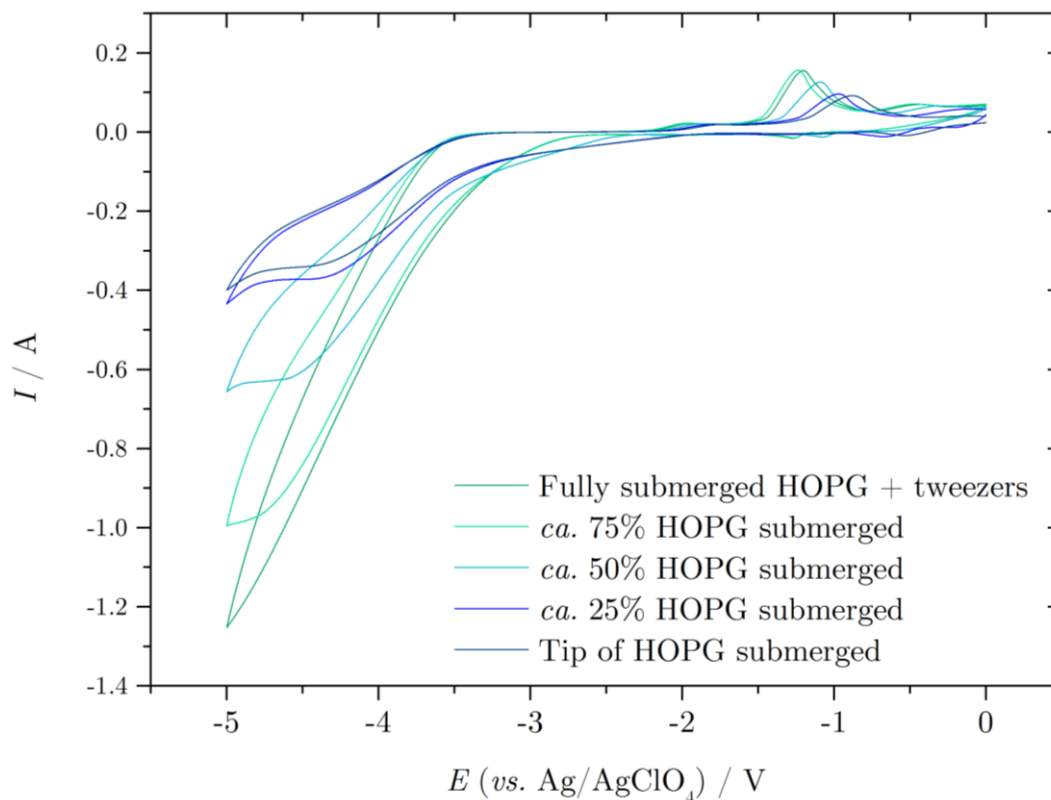


Figure 3.10) CVs showing the resulting current responses at a HOPG electrode when varying degrees of the electrode are exposed to the solution, recorded at a scan rate of 50 mV s^{-1}

Though the degree of varied exposure was only approximate, it can be seen that there is a definite relationship between peak current magnitude and the degree of electrode exposure. This is due to the increased degree of edge plane exposure of the HOPG electrode, allowing more accessible galleries for ion intercalation; thus more current is produced from the reduction of more cationic species (Faraday's law). However, it is not so clear why the background current should also increase, which eventually has the effect of masking the

intercalation current response completely. One feasible explanation is the substantial uncompensated resistance within this system (section 3.23), since the potential of the reduction peak current can be seen to shift negatively on each consecutive scan; this could also account for the negative shift of the anodic peak current at *ca.* -1 V on consecutive scans.

3.2.6 Dimethylformamide (DMF) electrochemistry

NMP was replaced with DMF as the electrochemical solvent, in which TEAClO_4 (0.1 M) was dissolved. DMF was used in order to probe the solvent dependence of the familiar voltammetric peaks situated towards the negative limit of the potential window. HOPG was used as the working electrode to simulate previous intercalation work (in NMP).

The voltammetric response obtained in DMF was similar to that in NMP, indicating that the large reduction/oxidation current responses frequently seen with graphitic working electrodes are a result of electrolyte reduction/oxidation and not solvent decomposition. Figure 3.11(a) shows the anodic peak dependence on the cathodic sweep limit and presents almost exact current responses to NMP voltammetry. The anodic peak can be seen to increase proportionally with increasing negative potential limit. Further confirmation that the observed peaks are related to electron transfer between the graphite and electrolyte is presented in Figure 3.11(b); halving the electrolyte concentration to 0.05 M had the effect of reducing the intensities of the respective cathodic and anodic peak currents by half. The black CV in Figure 3.11(b) shows the response at a GC electrode; no peaks are observed. Figure 3.11(c) shows the effect of successive cycling within the presented potential

window and shows the change in the magnitude and position of the cathodic peak with time.

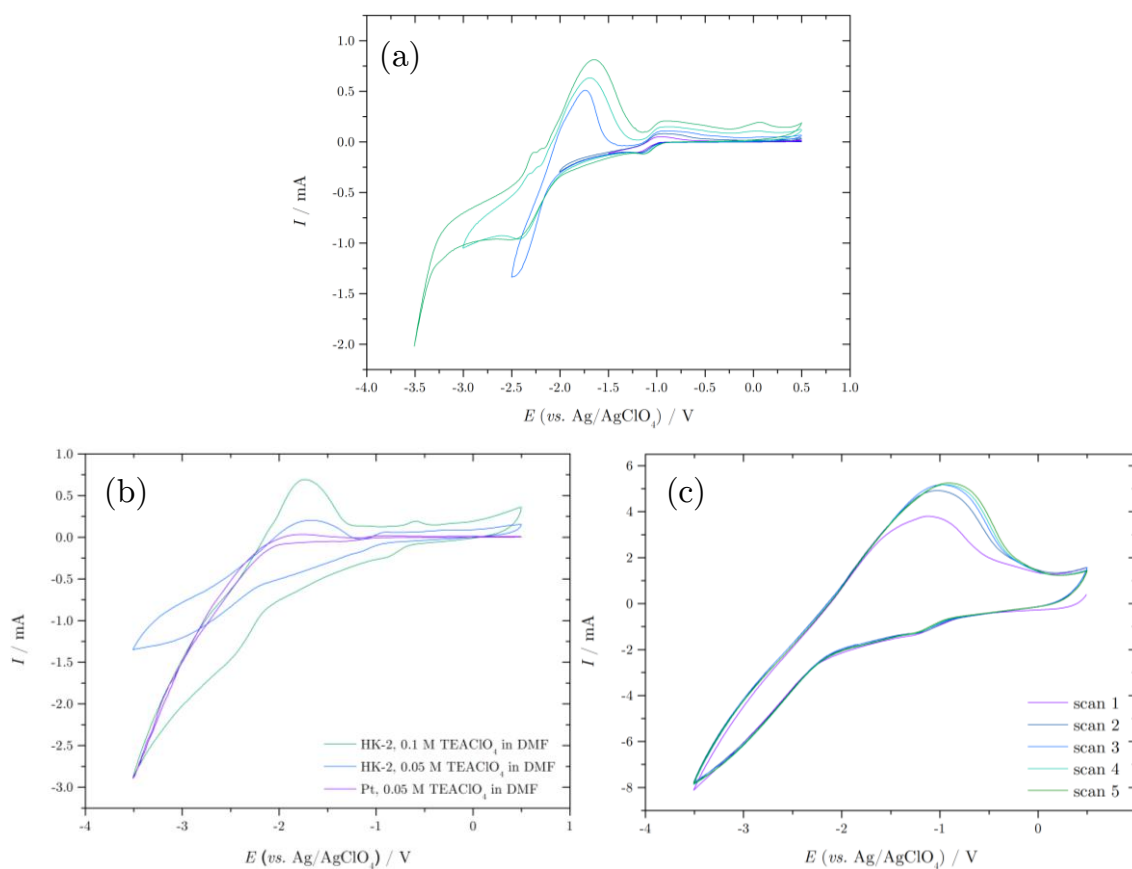


Figure 3.11) Voltammetric responses for TEAClO₄ (0.1M) in DMF at a HOPG electrode showing (a) effect of successively more negative potential limit, (b) effect of halved electrolyte concentrations, and (c) effect of successive cycling, recorded at a scan rate of 50 mV s⁻¹

3.2.7 Dimethyl sulfoxide (DMSO) electrochemistry

DMSO was employed as the electrochemical solvent and the process repeated with a HK-2 graphite rod. The CV in Figure 3.12 shows the familiar cathodic and anodic current responses as seen with NMP and DMF. This confirms that the currents observed are a function of electrolyte intercalation, an argument strengthened by the effect of electrolyte concentration, employment of a Pt wire working electrode, and the result of subtly different voltammetric shapes with the use of different electrolytes.

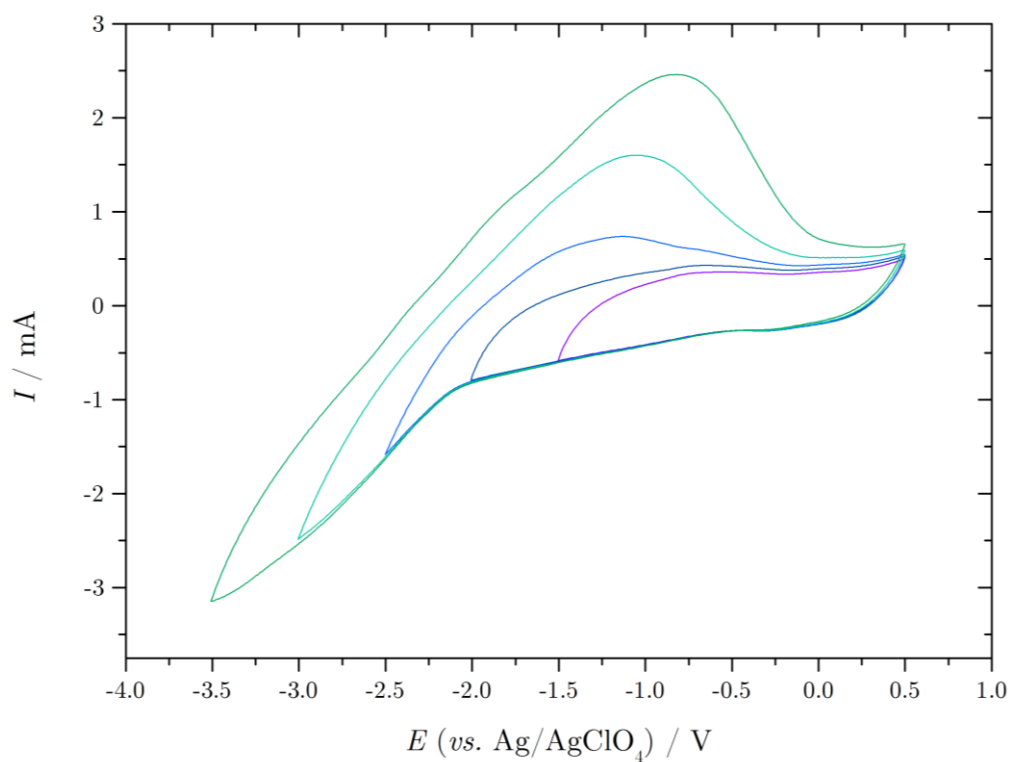


Figure 3.12) Voltammetric responses for TEAClO_4 (0.1 M) in DMSO at a HOPG electrode showing effect of a successively more negative potential limit, recorded at 50 mV s^{-1}

3.2.8 Implications of oxygen involvement

Argon saturation of electrochemical cells was performed for 30 minutes prior to measurement, followed by continual degassing of the cell headspace during measurement. However significant Faradaic current responses attributed to oxygen reduction were still present in the region of *ca.* -1 V to -2.5 V after argon saturation procedures, as presented in Figure 3.13. It is thought that, in these cases, solution bubbling has little effect on solution degassing.

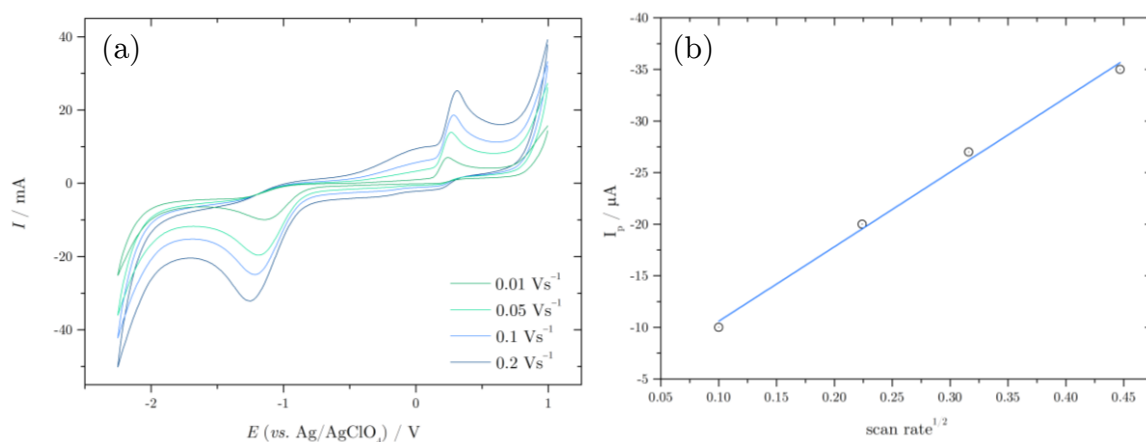


Figure 3.13) (a) Current responses indicative of oxygen reduction despite argon saturation of solutions prior to CV analysis (scanned at 100 mV s^{-1}) and (b) linear Randles-Ševčík plot displaying oxygen peak current dependence on square root of scan rate

Because of the presence of oxygen in solution, the reduction mechanism can proceed *via* alternate routes, and this complicates the probing of specific steps.

3.2.9 Anionic BF_4^- intercalation

In order to investigate BF_4^- intercalation, a solution of 0.1 M TEABF_4 in NMP was prepared under inert (argon) atmosphere. Voltammetry was measured at a HOPG electrode *vs.* Ag/AgClO_4 (Figure 3.14) and the potential window pushed to the upper and lower limits.

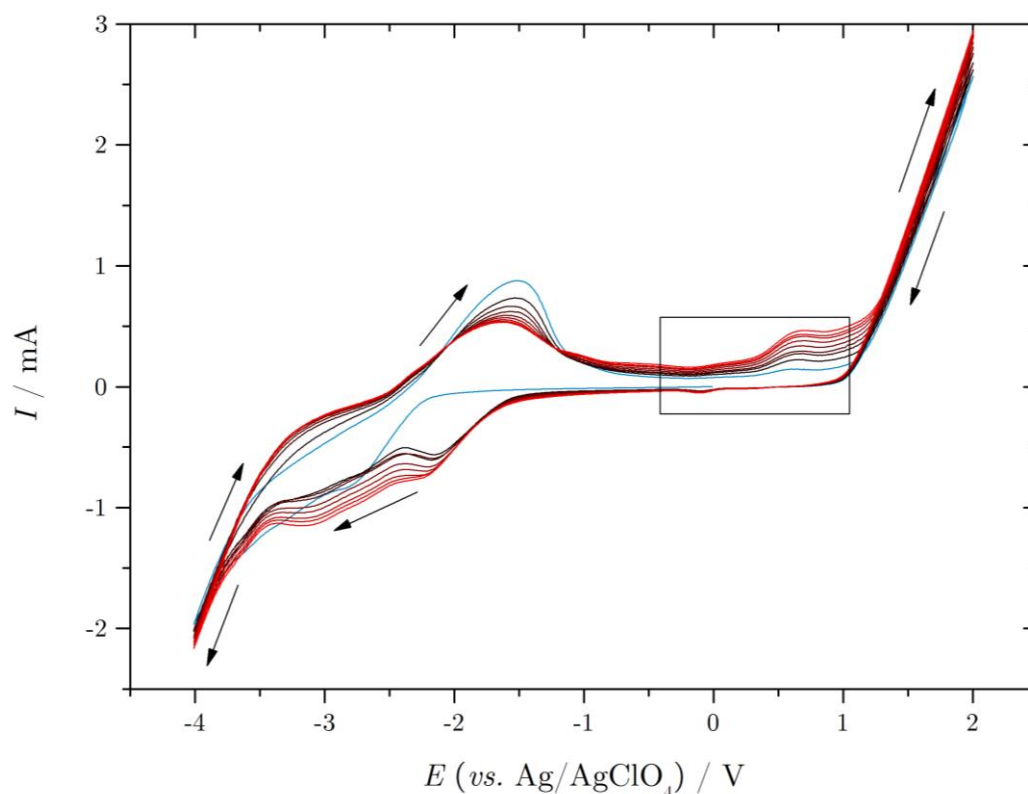


Figure 3.14) CVs showing current response at HOPG WE for initial scan (blue), and subsequent scans (black to red), measured at 100 mV s^{-1} , across the whole available potential window of the system.

During the initial scan (blue line) the familiar cation intercalation/de-intercalation current response is visible, centred on *ca.* -2.5 V . It can be seen that from the second scan onwards (once the potential has been swept to the anodic limit) that new peaks at $E < -2 \text{ V}$ are visible and are clearly related to the positive potential region previously scanned, since they only appear once the anodic region has been explored, and their peak currents decrease in the same

manner during consecutive scanning. The new current features are a result of anodic scanning and are attributed to the reduction of a new species. It can be seen that the oxidation of BF_4^- is not totally reversible (there is no *significant* corresponding reduction peak on the reduction scan, highlighted on the graph with a black box). However, it could be argued that it is not totally clear whether the new reduction peak at *ca.* -2.0 V is related to the BF_4^- oxidation at $+0.5$ V, or from scanning the potential to $+2.0$ V.

Voltammetric cycling was performed between 0 V and $+1.5$ V (Figure 3.15) to restrict intercalation activity to BF_4^- only, however the CV shows very little peak currents in the selected regions. Slight ‘bumps’ can be made out at *ca.* 0.8 V (anodic scan), and at *ca.* 0.7 V (on the cathodic scan). These small peaks are associated with BF_4 oxidation and subsequent re-reduction. These peaks were not as clear as BF_4 intercalation peaks found by Hardwick *et al.*²²⁷ Hardwick *et al.* used acetonitrile as the solvent and it might be the case that NMP does not facilitate the intercalation of BF_4^- as efficiently as acetonitrile. Alternatively, the use of slower scan rates might reveal more voltammetric detail (see later, Chapter 4).

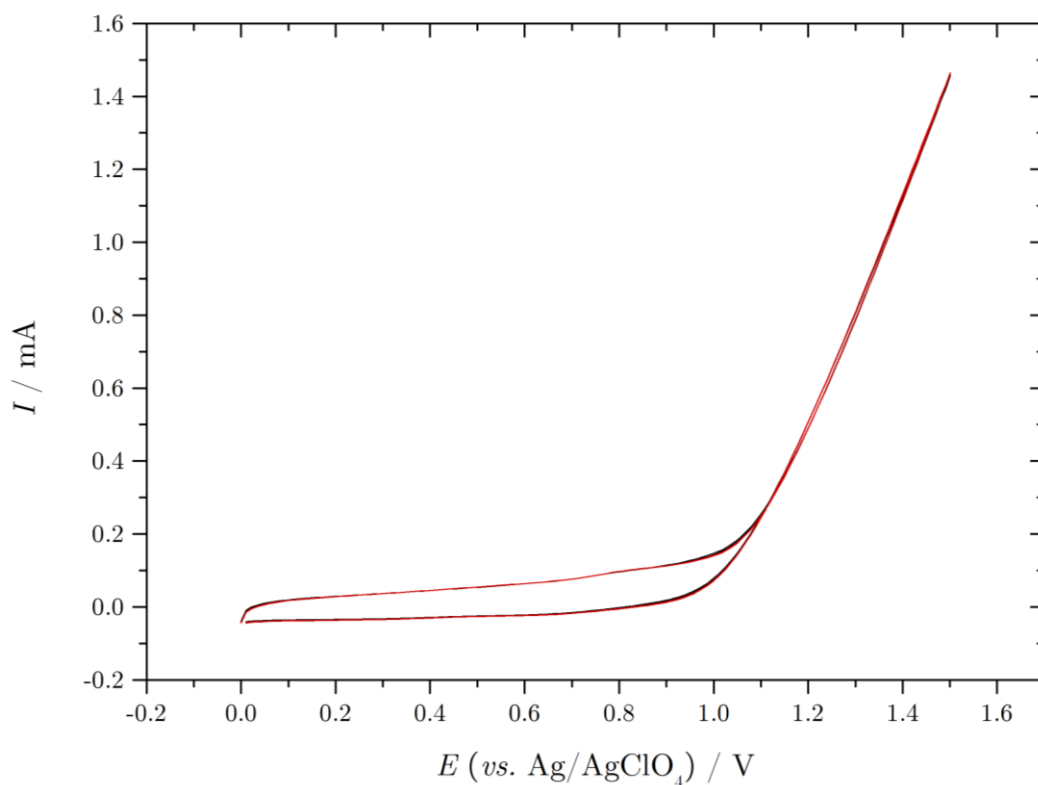


Figure 3.15) CVs showing the current response at a HOPG WE in TEABF₄ in NMP at the positive limit of the potential window, showing no faradaic processes and no BF₄[−] intercalation/de-intercalation, scanned at 100 mV s^{−1}

3.2.10 Ionic liquid (IL) voltammetry

It was found by co-workers that a 1:1 mixture of NMP and 1-butyl-3-imidazolium tetrafluoroborate [BMIM][BF₄] was stable as a droplet for *in situ* electrochemical analysis at the micro scale. If this electrolyte is suitable for use as an intercalating species, then *in situ* analysis of the procedure would be possible, allowing a more detailed and accurate study of the intercalation mechanism.

To begin, pure [BMIM][BF₄] was employed as the solvent/electrolyte for intercalation; the molecular structure is given in Figure 3.16.

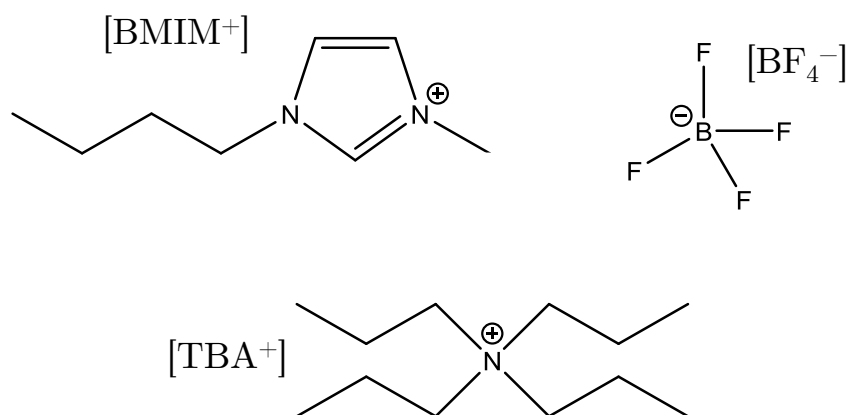


Figure 3.16) Molecular structures of BMIM^+ , BF_4^- , highlighting the relatively similar cationic sizes of BMIM^+ and TBA^+

The vdW radius of BMIM^+ has been approximated to *ca.* 0.46 nm using the known radius of EMIM^+ (0.303 nm),²⁴⁶ and is therefore of comparable size to the R_4N^+ cations employed herein. However the significant difference here lies in the ability to approximate R_4N^+ cations to spherical species, whereas the BMIM^+ cation will exhibit relative planarity, making it a suitable candidate to study the effects of cation planarity on intercalation observations.

The same three electrode system as previous work was employed for the intercalation of $[\text{BMIM}^+]$ into HOPG and the resultant CVs are presented in Figure 3.17.

Voltammograms were initially scanned between 1 and -1 V, with the negative limit being steadily decreased to -3.5 V *via* potential steps of 0.5 V. It can be seen in Figure 3.16 that as the negative limit is decreased to -2 V, the current increases sharply indicating reduction of BMIM^+ to BMIM at the graphite cathode. On the reverse sweep, a small anodic current response is visible at *ca.* -1.5 V which has been attributed to the re-oxidation of BMIM to BMIM^+ . On decreasing the negative limit further to -2.5 V, the peak magnitudes of the respective cathodic and anodic process can be seen to become more prominent,

with the anodic peak current at *ca.* -1.5 V increasing by an order of magnitude. This shape resembles a similar voltammetric shape to previous R_4N^+ work. However, decreasing the negative limit to -3 V induces a new unfamiliar anodic peak at *ca.* -0.5 V. This peak can be associated with the increase in current at *ca.* -2.5 V on the cathodic scan. It is unclear at present what the origin of this new peak is.

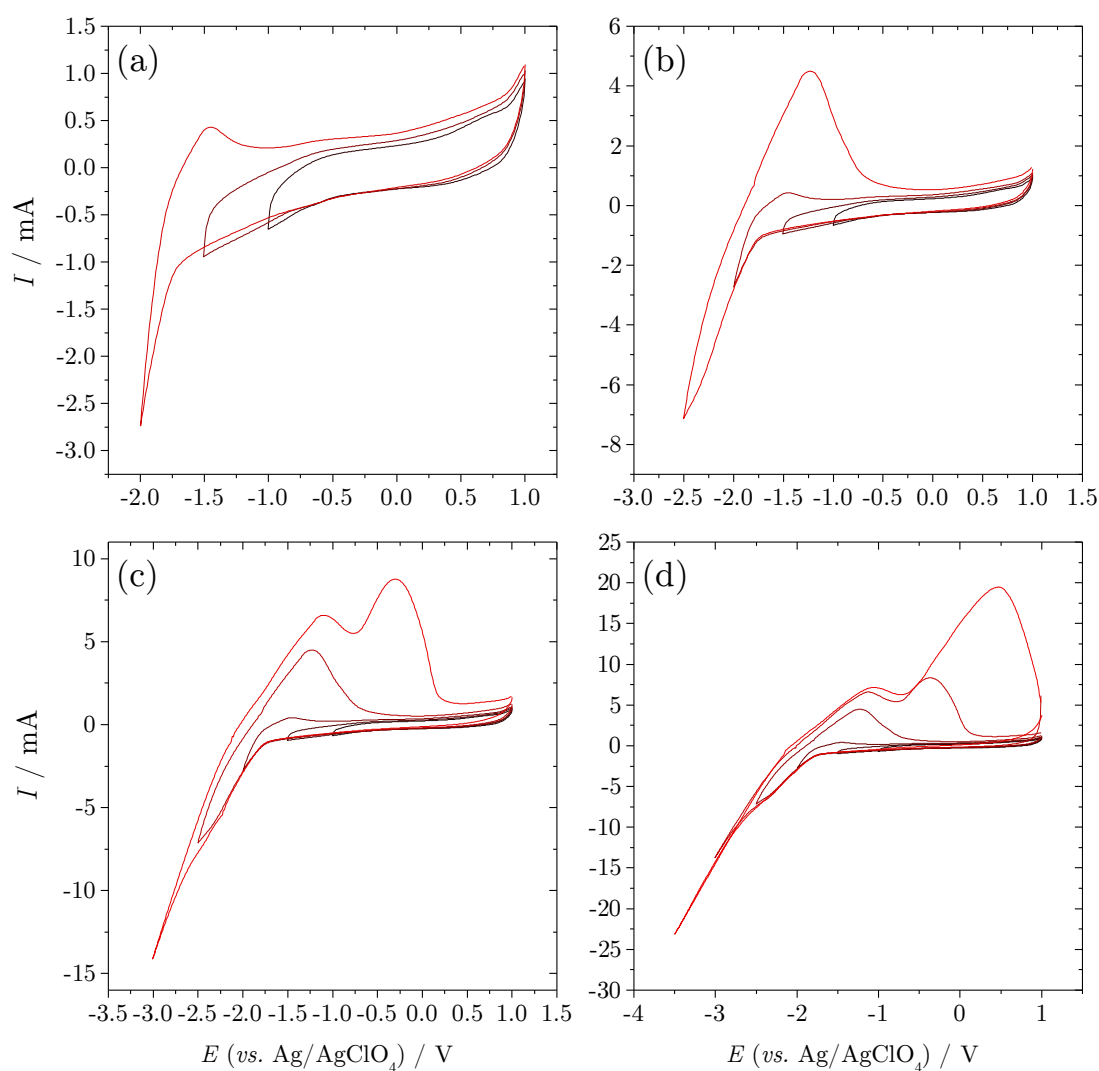


Figure 3.17) Current responses obtained at a HOPG electrode in the presence of BMIM BF_4 , indicating BMIM BF_4 intercalation and de-intercalation, as well as the introduction of an unknown anodic peak current after exploring cathodic potentials lower than -2.5 V, scanned at 100 mV s^{-1}

Despite the use of a HK-11 graphite electrode, no visible expansion of the electrode accompanied the voltammetry, even under the application of potentials as low as -2.5 V for 6000 s. Additionally, no bubbles were formed on the graphite surface or the Pt CE during the voltammetric sweeps or the CA procedure.

Alternatively, the new peak could represent the oxidation of the BF_4^- anion, although this is unlikely to produce such a prominent peak since the anion has been used extensively previously, and showed no significant visible re-oxidation peak on the following cathodic scan. No electrode expansion was visible with the pure $[\text{BMIM}][\text{BF}_4]$ electrolyte, however voltammetry indicates that re-oxidation of the cation is possible. It is suspected that the relatively high viscosity of the $[\text{BMIM}][\text{BF}_4]$ IL hinders the efficient intercalation of the solvent between the graphene galleries, however the planarity of the cation may act as a play-off to this hindrance, allowing intercalation due to its narrow dimension. Indeed, no electrode deformation was witnessed, and after extended charging times the solvent was seen to decompose in a similar manner to NMP (solvent colourisation, brown/black) after prolonged charging.

In order to reduce the viscosity of the electrolyte and encourage intercalation/expansion, a 1:1 volume ratio of NMP and 1-butyl-3-imidazolium tetrafluoroborate $[\text{BMIM}][\text{BF}_4]$ was prepared. The voltammogram in Figure 3.18 shows a quite different current response at a HOPG electrode and the absence of initial de-intercalation peak (*ca.* -2 V) as seen in Figure 3.18 is clear, showing that one can exist without the other and that the two cathodic peaks must be independent of one another.

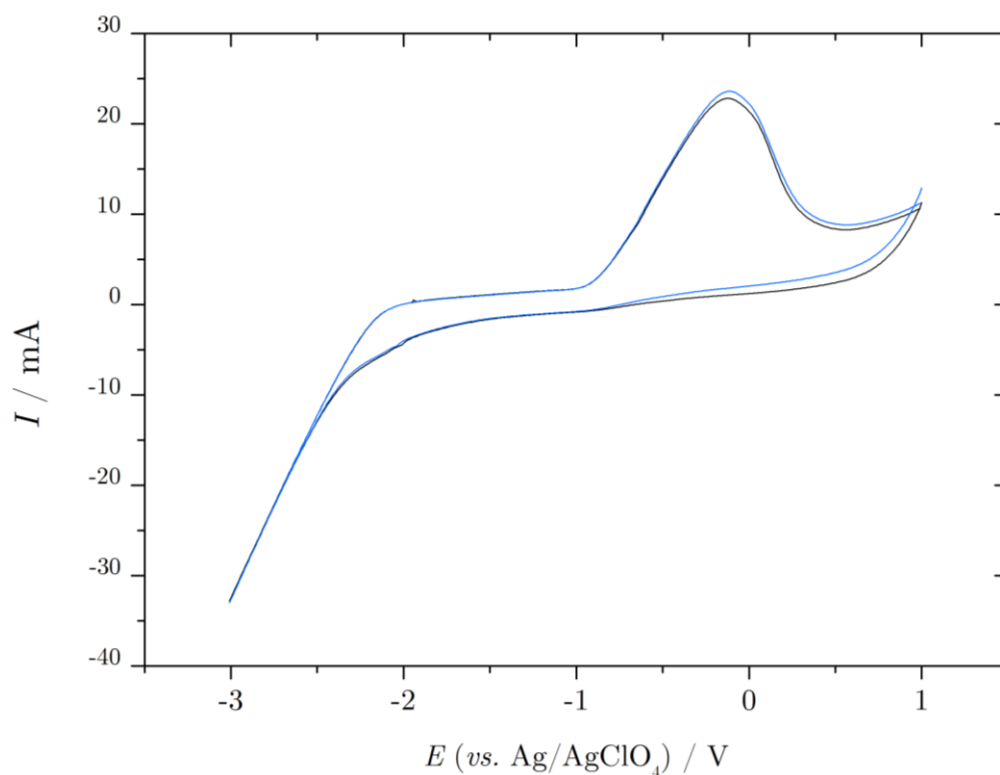


Figure 3.18) Current response at a HOPG working electrode in the presence of a 1:1 vol% mixture of NMP and 1-butyl-3-imidazolium tetrafluoroborate [BMIM][BF₄], recorded at a scan rate of 50 mV s⁻¹

Although CV did not cause any visible electrode exfoliation during scanning, CA procedures (−3 V, 2000 s) did cause electrode fracture to occur, though this was on comparable timescales as solvent decomposition, and the viscous nature of the solvent caused the exfoliate to be suspended within the IL.

Finally, potential holding experiments were conducted using the BMIM BF₄:NMP electrolyte. By pushing the negative limit to less extreme potentials than previously, and by experimenting with the duration of time spent at the cathodic limit, it became clear that the anodic peak actually comprises of two peaks. As in Figure 3.18, the familiar anodic response at *ca.* −2 V is again not present. By increasing the time at which the potential was held at −2.5 V on the cathodic scan, the anodic peak currents at −1 V increase in size accordingly.

Eventually, at 120 s potential holding, the two peaks begin to mask one another and show a resemblance to the anodic peak current observed in Figure 3.18. On the final scan, no potential hold was conducted and the current response can be seen to mimic the initial scan relatively well. This shows that by charging at -2.5 V for periods for less than 120 s, the system is allowed to relax to its original state, shown with relatively reproducible initial and final CV scans. This indicates that by only slightly exploring the cation reduction peak, the system displays good reversibility (in terms of the degree of recoverable charge associated with the de-intercalation and oxidation of BMIM to BMIM^+). The origin of these two peaks is currently not understood, since the oxidation of BMIM is a one electron oxidation and therefore should produce a single current response, though it could be related to the planarity of the cation.

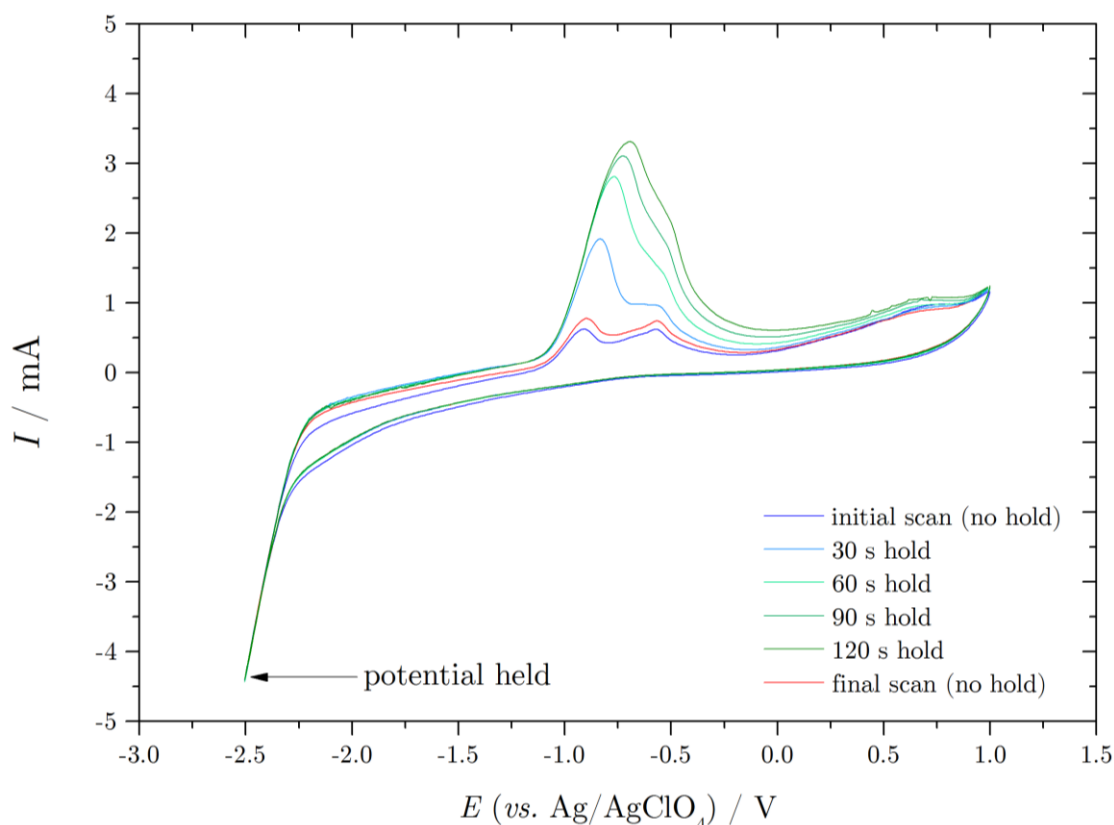


Figure 3.19) Current response at a HOPG working electrode in the presence of a 1:1 volume ratio of NMP and $[\text{BMIM}][\text{BF}_4]$ showing the non-permanent effects of potentiostatic waiting at the negative limit of the potential window, scanned at 50 mV s^{-1}

3.2.11 UV-Vis spectroscopy of electrolyte reduction

UV-Vis spectroscopy was employed to probe the nature of reduction products in more detail. To ensure no oxygen was involved in the procedure or analysis stages, experiments were performed in an argon-saturated ($[\text{O}_2] = 0.1$ ppm, $[\text{H}_2\text{O}] = 0.1$ ppm) glove box pressurised to 0.3 mbar. 2 mL aliquots of the electrolyte in the region of the GC electrode were removed and stoppered under the controlled atmosphere prior to external analysis, whereby UV-visible spectra were measured between 200 and 800 nm using a quartz cell of 2 mm path length.

The potential of a GC working electrode in 0.1 M TEABF₄/NMP was held at -4 V; well into the region of electrolyte reduction. After successive periods of time, aliquots of the electrolyte in close proximity to the GC electrode were analysed and the spectra in Figure 3.20 show how the absorbance changes with increasing charging times.

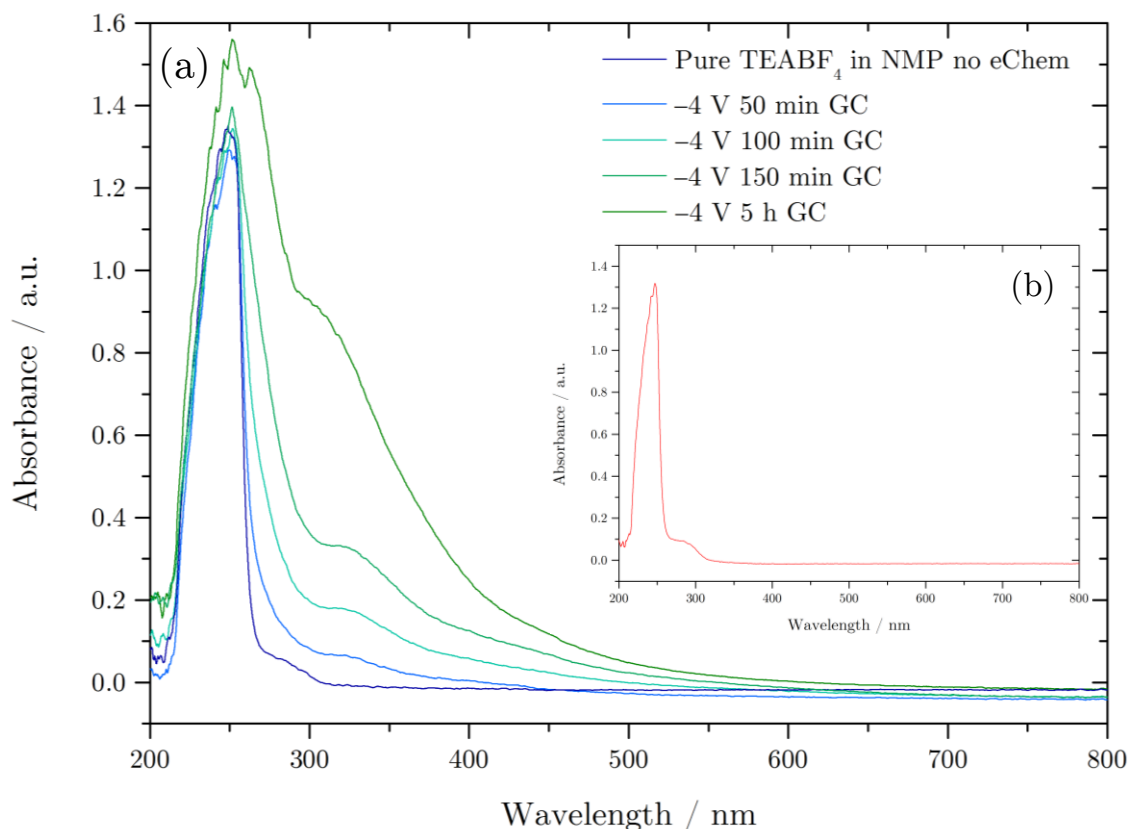


Figure 3.20) UV-Vis absorption spectra, recorded *ex situ*, of (a) a system containing 0.1 M TEABF₄/NMP, after increasing intercalation times, and inset (b) pure NMP

The inset (b) in Figure 3.20 shows the absorbance spectrum of pure NMP and shows a peak at *ca.* 240 nm and a smaller intensity absorbance shoulder at *ca.* 290 nm. TEABF₄ therefore does not absorb in the wavelength range shown, as shown in Figure 3.20 (purple line), or if it does, it is masked by the NMP. Application of -4 V for increasing periods of time resulted in the formation of a new peak at *ca.* 325 nm, which increases in intensity with increased application time and is attributed to the formation of a new compound.

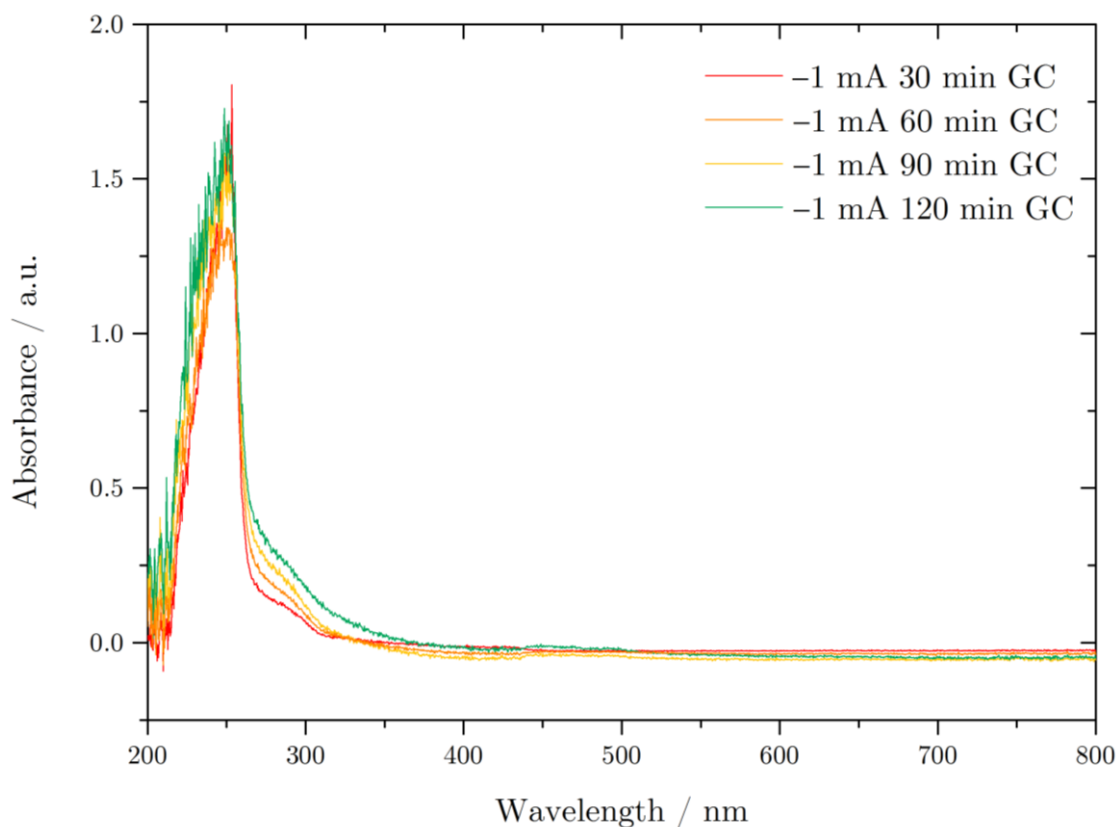


Figure 3.21) UV-Vis absorption spectra of system containing pure NMP, after increasing cathodic charging times of a GC electrode, indicating solvent decomposition

As a control, current was passed through a GC electrode in a solution of NMP containing no electrolyte. Unsurprisingly, because of the omission of conducting electrolyte, nearly -11 V was required to pass a current of -0.1 mA. The resultant UV-Vis spectra, recorded every 30 minutes for a total period of 2 hours, are presented in Figure 3.21 and it can be seen that a similar pattern follows, with the development of an absorption peak at *ca.* 300 nm over the duration of the applied potential. However the increase in absorbance is clearly less significant than with the inclusion of electrolyte, and solvent colourisation was much less noticeable in the pure NMP system.

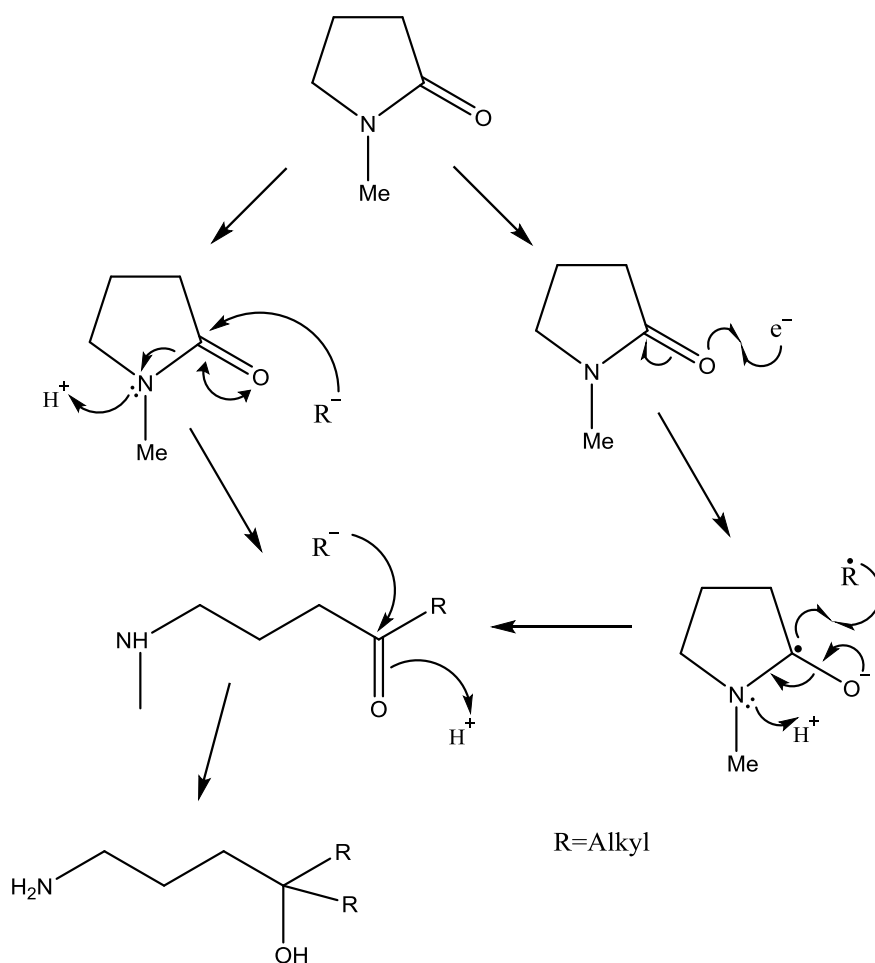


Figure 3.22) Schematic suggesting two likely mechanisms to the degradation of NMP: either *via* reaction with an alkyl carbanion produced from the reduction of R_4N^+ or *via* the one-electron reduction and subsequent reaction of the produced pyrrolidone radical species with an alkyl radical. Both mechanisms ultimately lead to the ring opening of N-methylpyrrolidone to produce the amine species

The decomposition mechanism of NMP can proceed *via* several routes, however two of the more likely paths have been presented in Figure 3.22. The simplest mechanism follows the straight 1-electron reduction of NMP at the graphite cathode, to produce a pyrrolidone radical species, which preferentially couples with an alkyl radical species produced from R_4N^+ reduction (see Equation 3.3). The alternative mechanism proceeds *via* nucleophilic attack of an alkyl carbanion on the carbonyl group of N-methylpyrrolidone. Both of these

approaches result in the ultimate ring-opening of NMP to produce the amine species presented, which is thought to produce the absorption at *ca.* 300 nm.

It is thought that the electro-reduction of R_4N^+ facilitates the reduction of NMP due to the presence of the R^- and R^\cdot products, which react with NMP as nucleophiles. NMP is therefore much more stable when no electrolyte is present, since the possible reduction paths are restricted to the single-electron reduction at the cathode. This increased NMP-stability was evident during the control experiment, since barely any degree of colourisation was visible to the eye after 2 h charging. It can be confirmed that the solvent colourisation is a result of NMP decomposition, and the developing absorbance peak at *ca.* 300 nm is due to the NMP decomposition products.

There are of course an array of possible mechanisms towards NMP reduction, since NMP molecules will be exposed to a number of different reactive species; namely those resulting from R_4N^+ reduction (presented in equations 3.3 to 3.8). The presented mechanisms therefore assume decomposition *via* the most reactive species; R^- , R^\cdot , and direct electron reduction. Additionally, the two mechanisms assume the absence of residual oxygen and water in the system, which if present, will cause several other decomposition routes. Since for further work, the use of an argon saturated glove box was employed, oxygen/water related decomposition schemes have not been covered.

3.2.12 Electron Paramagnetic Resonance Spectroscopy (EPR)

On reduction of the cation during the intercalation process, it is believed that a graphite intercalation complex (GIC) is formed and subsequently stabilised by the neighbouring graphene sheets. It is evident that electron transfer takes place, since a reduction peak in the voltammetry is present, and it is also established (shown later, Chapter 4) that the use of a porous graphite electrode facilitates the re-oxidation of the reduced cation.

There are two possible mechanisms by which graphite can facilitate the recovery of the reduced form of the cation: it may catalyse the re-oxidation process in a way in which platinum cannot, thus physically permitting the re-oxidation, though this is unlikely. More likely it stabilises the cation against subsequent decomposition, allowing the re-oxidation of the species with relative ease. Whichever mechanism, it is the large surface area of the graphene sheets that plays the pivotal role, shown by the effect of an expanded graphite electrode in coulombic efficiency work in Chapter 4. It is proposed that the role in which the graphite/graphene prevents cation reduction to an ‘unrecoverable’ state, is through the formation of a ‘partial’ reduction state, or GIC.

Despite GIC formation, charge transfer still occurs between the cathode and the cation, as shown voltammetrically. Mechanistically however, it is unclear where this residual charge lies; on the graphite as a negative charge or in the form of a tetraalkylammonium anion radical stabilised by the neighbouring graphene sheets.

Tetraalkylammonium reduction at GC electrodes has been presented in section 3.1.3 and the general consensus from literature points towards the production of a tetraalkylammonium anion radical, which then proceeds to spontaneously react with neighbouring species. However, this mechanism occurs on the surface of GC, where no intercalation or GIC formation can occur; the mechanism at a layered graphite electrode, in which ion intercalation takes place, could presumably be significantly different.

To investigate the nature of the formed GIC, an *in situ* EPR spectroscopic experiment was employed. A pinhole was drilled through a HOPG sample ($5 \times 2 \times 1$ mm), through which the wire was threaded and wrapped tightly to ensure electrical contact. The CE and RE were Teflon-insulated platinum wires to prevent electrical short circuiting when the electrodes were placed in a quartz EPR sample tube. The electrodes were inserted into the tube prior to filling with LiClO_4 (0.1M) (and later TBAClO_4 , 0.1 M) in NMP (Figure 3.23).

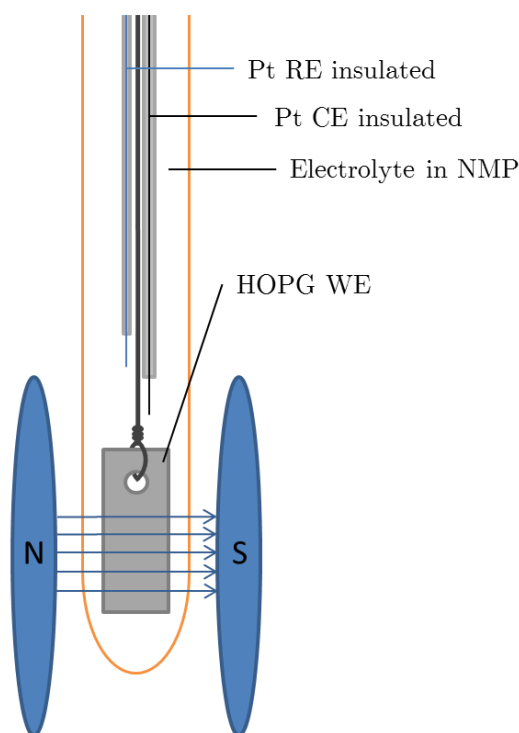


Figure 3.23) Schematic of the *in situ* electrochemical EPR setup showing HOPG, acting as WE connected with platinum wire *via* a pinhole, Teflon-insulated platinum CE and RE with an EPR sample tube filled with electrolyte.

Prior to electrochemical reduction of TBA^+ at a HOPG electrode, two control measurements were undertaken; a) TBA^+ reduction was performed at a bare Pt wire and b) Li^+ reduction was performed at a HOPG electrode, using applied potentials of -2.4 V vs. Ag for a period of 1000 s. The duration of applied potential was kept to a minimum so as to reduce the degree of expansion, since size limitation was a concern in the EPR sample tube. The EPR signal responses for both of these controls are presented in Figures 3.24(a) and 3.24(b), and it can be seen that no signal response was generated for either control. This indicates that TBA^+ reduction at a platinum cathode, and Li^+ reduction at a HOPG electrode, did not produce any detectable species with paramagnetic activity, at least on a measureable timescale.

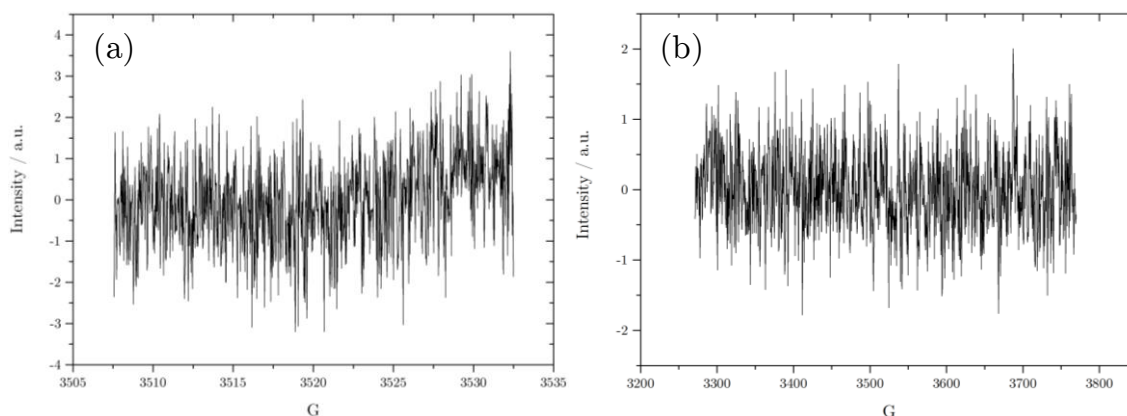


Figure 3.24) recorded EPR signals for (a) TBA⁺ reduction performed at a bare Pt wire and (b) Li⁺ reduction performed at a HOPG electrode, using applied potentials of -2.4 V *vs.* Ag for a period of 1000 s, and showing the absence of any EPR active species

TBA⁺ reduction was then performed at a HOPG working electrode, and the EPR signal measured in the same manner. The resulting EPR signal is presented in Figure 3.25 and a clear asymmetrical EPR singlet at 3525 Gauss is presented. This EPR signal was found to decrease in intensity over a period of approximately 24 h, as presented in Figure 3.25.

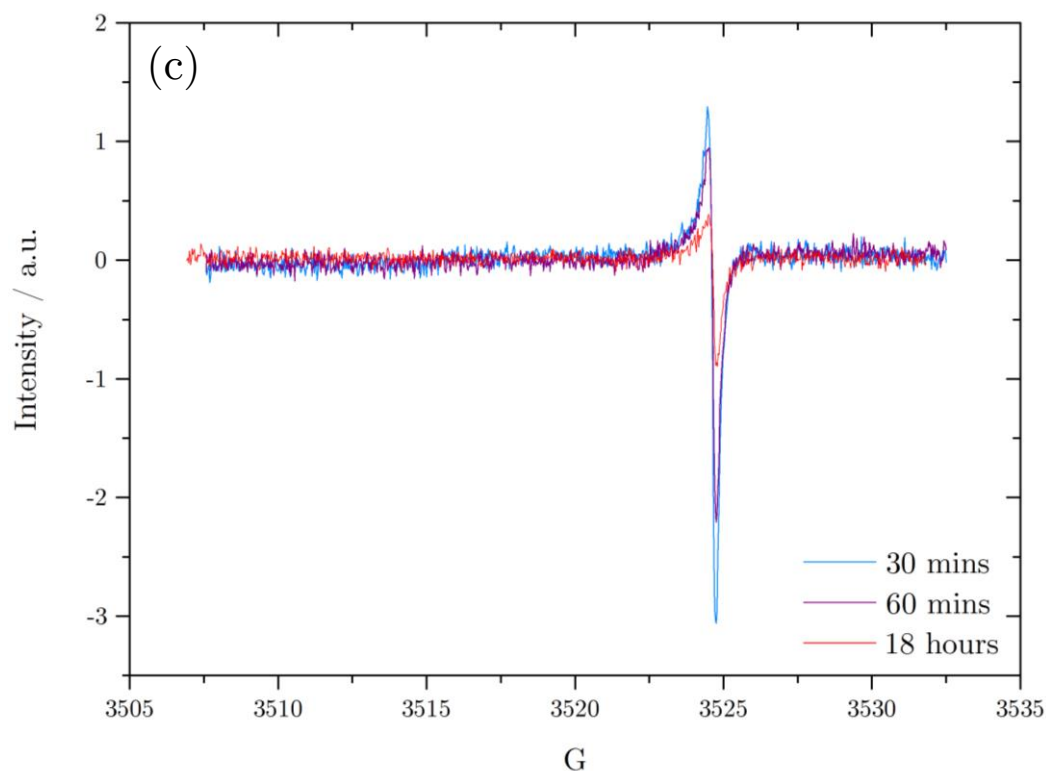


Figure 3.25) EPR signals obtained from *in situ* electrochemistry in TBAClO₄ at a HOPG electrode, recorded at X band (9.8705 GHz)

Once the applied potential was ceased, the signal intensity can be seen to decrease slightly on the timescale of minutes (Figure 3.26), and after a total period of 24 h, the signal was seen to have disappeared completely. The software was set up to record continuous spectra, of which were been plotted one after the other, allowing distinguishability between the separate signals.

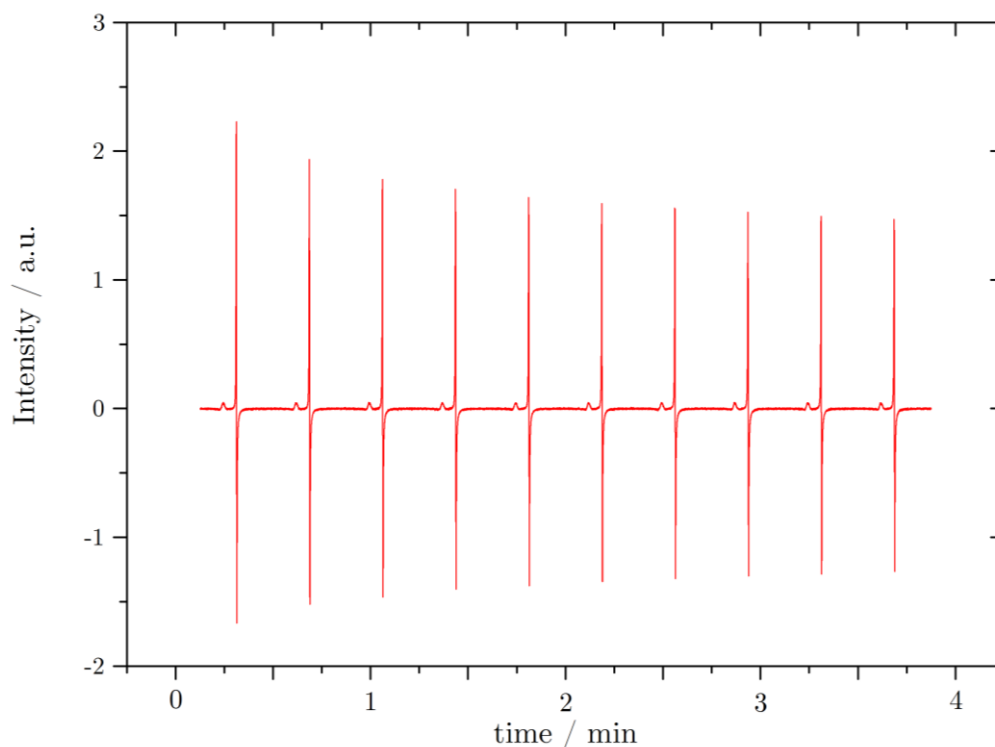


Figure 3.26) Time dependence of the spectrum acquired in Figure 3.22 over a period of 4 minutes (limits of the magnetic field values 5320 to 5330 G), displaying a slight decrease in intensity of the observed signal of the 4 minute duration

Finally, -2.4 V was applied to the HOPG WE for *ca.* 5000 s and Figure 3.27 shows an overlay of the recorded current on top of the recorded EPR signal (again, recorded every 500 s and plotted one after the other to show a time lapse effect) and the signal intensity can be seen to increase for as long as the potential is applied to the working electrode. Because of the CA procedure, a corresponding current decay is associated with the constantly applied potential due to the depletion of cations at the electrode surface (see section 2.4.2)

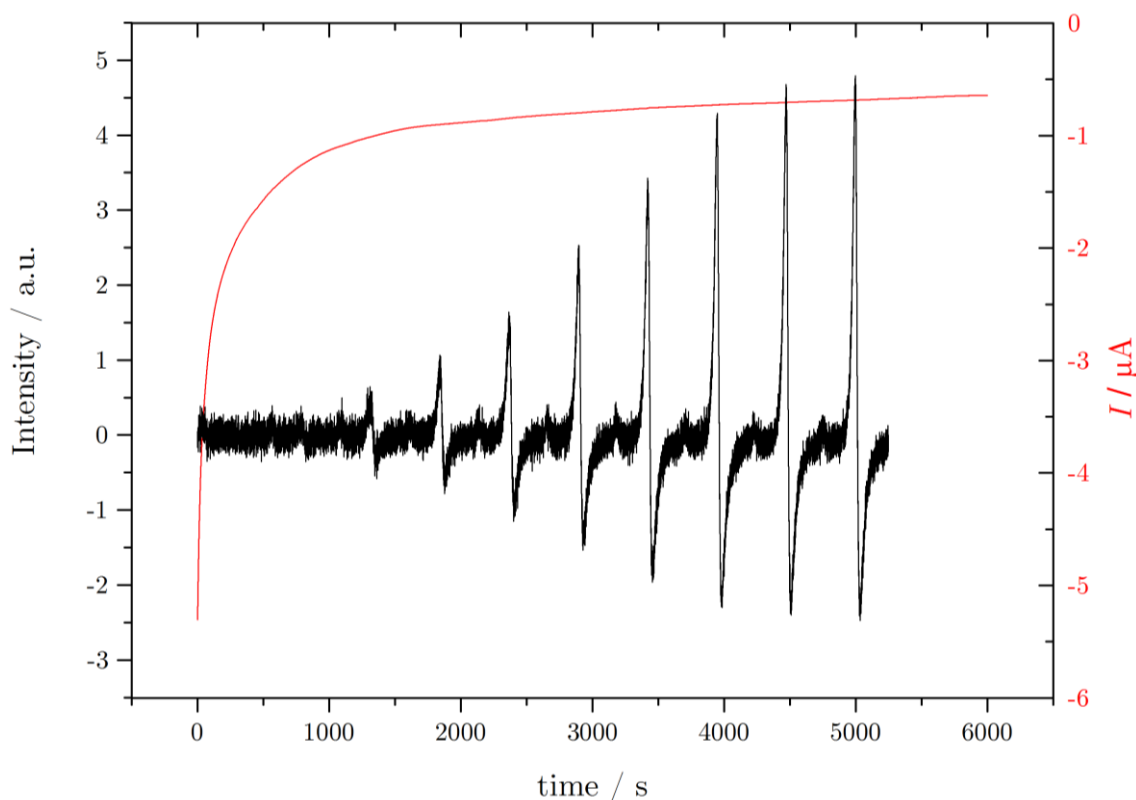


Figure 3.27) Signal intensity dependence on the applied constant potential (-2.4 V), (limits of the magnetic field values 5320 to 5330 G), displaying an increased signal intensity on application of an electrical current

The EPR results presented herein are admittedly, not totally conclusive as towards an ET mechanism. The singlet observed attributed to the generated radical is not suggestive of a nitrogen-centred radical. Nitrogen (^{14}N) has spin $= 1$ and therefore using $2MI + 1$, where M is the number of equivalent nuclei, and I is the nuclear spin, calculating the number of expected EPR spectral lines yields three, or a triplet, for a nitrogen centred radical species. However the spectrum clearly shows a singlet response; oxygen (both ^{12}O and ^{14}O) has spin $= 0$, ($\therefore 2MI + 1 = \text{singlet}$) therefore it is plausible that the signal could be oxygen related in the form of a superoxide radical species. This is plausible, since the experiment was not performed under inert conditions and any residual oxygen present in solution could easily be reduced to superoxide at potentials as

low as -2.4 V. However it is interesting that no EPR signal is observed for the control measurements, which should also produce oxygen containing radical species. It could be valuable to repeat this system in an argon saturated glove-box so as to exclude the possibility of oxygen involvement, though the complications of this setup make it an unattractive practice. Although the EPR study is inconclusive, and generally points the formation of superoxide *via* oxygen reduction, it is interesting to note that no nitrogen-like triplet is observed for any of the studies. The absence of any EPR signal associated with a nitrogen-containing species suggests that the negative charge produced by the intercalation/reduction mechanism does not lie on the reduced R_4N^+ species, but rather remains on the graphene sheet within the electrode:



where; $[\text{graphite}^{n-}-(R_4N^+)_n]$ represents the GIC which is stabilised by neighbouring graphene sheets.

3.3 Conclusions

Primary voltammetric analysis of lithium and tetraalkylammonium containing electrolytes in NMP at Pt, GC and HOPG working electrodes has shown differing results. With the use of non-porous GC and Pt electrodes, CVs typically displayed a steady increase in background current at potentials more negative than *ca.* -2 V, which is associated with the decomposition of the electrolyte and/or solvent. It is suspected that solution colourisation is actually a result of NMP decomposition, although irreversible electro-reduction of R_4N^+ does begin to occur at cathodic potentials more negative than -2.0 V and it is thought the reduction products of R_4N^+ facilitate the breakdown of NMP. Furthermore, prolonged scanning periods within these large negative potential regions (for example, when scanning at relatively slow scan rates) was accompanied with solvent colourisation and gaseous liberation at the graphite cathode. Though the employment of extremely large surface area CEs did reduce the degree of decomposition (deduced from a decreased amount of solvent colourisation) and bubbling, it was not possible to eradicate this problem.

CV at HOPG electrodes in the presence of both lithium and tetraalkylammonium (methyl, ethyl and butyl) based electrolytes, clearly displayed broad cathodic peaks on the initial scan, and a subsequent anodic peaks on the reverse sweep. These peaks have been attributed to the intercalation and de-intercalation of the lithium/tetraalkylammonium cationic species into and out of the porous graphite cathode, during which there is an electron transfer reaction associated with the partial reduction of the intercalated species. However the voltammetry and relative charges for the two respective processes were found to be both irreproducible and unpredictable, since control of the electrode size/geometry, as well as oxygen involvement

proved challenging. Argon saturation of the electrolyte solution followed by degassing of the cell headspace was ineffective, as shown by the presence of oxygen reduction current responses in the voltammetry directly afterwards. It has been shown that the intercalation/de-intercalation peaks are independent of solvent, and peak currents were found to be proportional to electrolyte concentration; allowing us to conclude that the voltammetric features are associated with the cation.

Probing the reduction mechanism using UV-Vis and EPR spectroscopic techniques proved challenging, without the ability to completely remove the effects of oxygen involvement, since the EPR spectra simply indicate the production of an oxygen radical species formed *via* the electrochemical reduction of residual water. However UV-Vis spectroscopy did confirm the presence of solvent decomposition as a result of the applied the cathodic load.

Finally, despite the general consensus for the non-existence of a universal standard reference electrode for use in non-aqueous media, it was found that a $\text{Ag}^0/\text{Ag}^+\text{ClO}_4^-$ system, employing the use of a conventional perchlorate counterion, was stable for several weeks and provided reliable stable potential measurements. Additionally, it has been found that NMP is an excellent solvent choice for non-aqueous electrochemistry and exhibits an ideal working potential window of *ca.* 4 V, extended to *ca.* 7 V for short term analysis. Since NMP has been found to be an excellent solvent for graphene dispersion, it follows that NMP would be an ideal choice for graphene electrochemistry work, in which the use of non-aqueous media is desired; for example in the study of battery/supercapacitor applications.

Chapter four

Graphite Intercalation Compound formation and stability

4 Graphite Intercalation Compound formation and stability

4.1 Introduction

As has been described in detail earlier, ionic intercalation is a process by which insertion of an ionic species takes place into the lattice of a host structure. In the case of graphite, this can result in the formation of graphite intercalation complexes (GICs) and irreversible structural deformation of the graphitic lattice.^{234,247} Various chemical routes to tetraalkylammonium (R_4N^+) and alkali metal GIC synthesis have been presented^{248,249,250,240} taking place *via* cationic displacement reactions. Electrochemical procedures are less common^{251,252} despite the relative simplicity of cathodically charging a graphite electrode in the presence of a R_4N^+ based electrolyte.

In aqueous media graphite cathodes are relatively inert, since the potentials associated with working in aqueous systems are restricted to the potential limits of water electrolysis.²⁴⁵ In aprotic media however, where the solvent is cathodically sufficiently stable, graphite cathodes can be susceptible to attack by electron transfer between the electrolyte cations and the graphite cathode at sufficiently negative potentials.²⁵² R_4N^+ salts, with formula $R_4N^+X^-$ where R represents the alkyl group and X the counterion, are commonly employed electrolytes in electrochemistry due to their extremely negative reduction potentials and good solubility in aprotic media. As such the negative potential limit of many metallic electrodes has previously been assigned to the potential at which R_4N^+ degradation occurs.²⁴⁵ In an oxygen free environment, it has been proposed that R_4N^+ reduction at GC proceeds *via* an alkyl radical mechanism producing an alkyl carbanion, which is prone to reaction with a parent R_4N^+ , yielding various stable alkanes (see section 3.1.3).²⁴³ However, by performing the reduction at a layered graphite electrode (HOPG) with

electrochemical control, work within this Chapter shows it is possible to prevent the complete reduction of R_4N^+ based electrolytes, and the resultant GIC can be de-intercalated and retrieved from the host structure using potentiostatic control.

In the case of R_4N^+ reduction at graphite cathodes, the formation of a GIC has been found to occur accompanied by a significant irreversible volumetric expansion of the host graphite, irrespective of whether intercalation is electrochemical^{244,253} or non-electrochemical.^{240,248}

Besenhard and co-workers have described Li^+ and TMA^+ reduction at both graphite foil and platinum electrodes and presented similar findings to those within this Chapter.^{251,252} It has also been shown by Simonet and co-workers that under dry solvent conditions, decomposition of R_4N^+ at platinum electrodes can be prevented and a platinum insertion complex is achievable in a similar manner to GIC formation.²⁴⁵

The results presented in this Chapter expand on the previously reported work, by showing that GIC formation can be reversible or irreversible depending on the magnitude of the applied electrochemical charging load. Larger tetraalkylammonium cations (TEA^+ and TBA^+) have also been studied herein at HOPG working electrodes as well as at GC electrodes, to investigate the charge recovery behaviour over a range of cathodic loading potentials.

The non-electrochemical preparation of tetrabutylammonium GICs has been reported²⁴⁰ (section 3.1.2) where a stable GIC of formula $C_{44}TBA$ was achieved, inducing an interplanar expansion from 0.35 nm to 0.47 nm. This separation is smaller than the cationic diameter of TBA^+ (0.826 nm), and is attributed to the flexibility of the TBA^+ alkyl chain lengths. Electrochemical production of R_4N^+ GICs presents a more controlled route, and allows for the de-intercalation of the

GIC from the host structure if desired,^{251,252,254} as well as offering control over the degree of intercalation and therefore the R_4N^+ GIC composition. Additionally, optimization of controlled electrochemical intercalation into graphite could offer a tunable production route towards monolayer, bi-layer and tri-layer graphene materials.²⁵⁵

This chapter primarily investigates electrochemical formation of a GIC in the layered graphite cathode *via* the use of lithium and R_4N^+ charge/discharge cycling at various working electrodes and conditions. Average cycling efficiencies ($\%_{ACE}$) have been used as a tool to measure the degree of recoverable charge during intercalation at sufficiently large negative potentials, causing irreversible electrolyte reduction, and these studies were found to be both cathode material and cationic species dependant. More quantitative electrochemical studies have been employed to probe the diffusion related attributes of the intercalation mechanism, presenting evidence to support the hypothesis for a relatively complex mechanism for GIC formation including several ‘staging’ steps. Finally, the degree of generated charge during intercalation/de-intercalation of R_4N^+ species has been used as an estimate to determine preliminary formulaic GIC formation.

Unless otherwise stated, all studies here forth were conducted in an argon-saturated ($[O_2] = 0.1$ ppm, $[H_2O] = 0.1$ ppm) pressurised glove box (+0.3 mbar *vs.* atmospheric pressure) in order to probe the effects of oxygen and water in the graphite intercalation/electrolyte reduction mechanism. To ensure the exclusion of residual water from the system, compounds were weighed outside the glove box and left open in the glove box for a period of time to ensure removal of atmospheric air from powders. Solutions were then prepared in the glove box where they remained throughout the duration of the work. Additionally, a fresh $Ag^0/Ag^+ClO_4^-$ reference electrode was prepared in the

glove box and sealed. Between experiments, any apparatus that required cleaning was removed from the glove box and washed externally with ethanol, after which it was reintroduced to the glove box and allowed to stand for an equilibrium period prior to reuse.

4.2 Results

4.2.1 Lithium electrochemistry at a non-porous electrode

Lithium was investigated as the initial intercalating species. LiClO_4 (0.1 M) was dissolved in anhydrous NMP (10 mL) ($<0.005\%$ H_2O). It should be noted here that Karl-Fischer titration yielded a residual water content of 61.6 ppm, or 0.0065%, highlighting the requirement for independent analysis of chemicals obtained from commercial sources. CV was used to scan potentials between 0.5 V and -6 V at a GC working electrode, at a scan rate of 100 mV s^{-1} . Figure 4.1 displays the resultant current response over a potential window of *ca.* 7 V, and as well as the absence of oxygen reduction and water hydrolysis, there was also no $\text{LiOH}/\text{Li}_2\text{O}$ deposition present on electrodes after CV procedures. As seen in previous open-air voltammetry (Chapter 3), the familiar sharp and steady increase in background current is observed when the voltammetry is swept to extreme cathodic potentials, although the potential can be pushed to more negative potentials (-4 V) before Faradaic processes begin to occur, indicating that oxygen involvement facilitates solvent breakdown.

The background current observed here is also not associated with the deposition of $\text{LiOH}/\text{Li}_2\text{O}$ on the working electrode as seen previously at graphite rod electrodes, since there are no peak current responses to suggest such a reaction and no deposit was visible to the eye on the electrode. In addition, it can be assumed that the possibility of any $\text{LiOH}/\text{Li}_2\text{O}$ deposition masked by the large background current can be excluded, since there is no corresponding anodic peak current associated with the oxidation of the deposition on the reverse anodic scan. The ‘background’ current observed can therefore be attributed to the irreversible reduction of NMP and Li^+ .

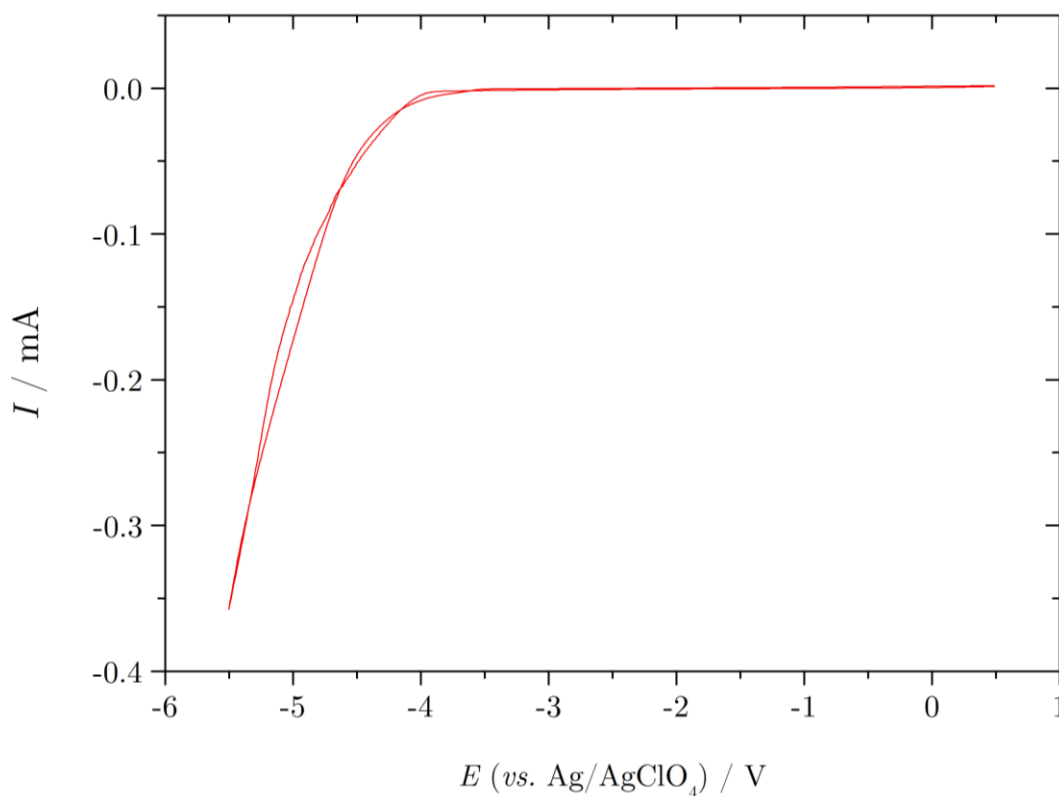


Figure 4.1) Voltammetric response at a GC working electrode in 0.1 M LiBF₄ in NMP, scanned at 100 mV s⁻¹ vs. Ag/AgClO₄

4.2.2 Lithium electrochemistry at a layered HOPG electrode

CV was performed at a HOPG electrode in the presence of LiClO₄ (0.1 M) in NMP (Figure 4.2) and the effect of decreasing the cathodic limit of the potential window for consecutive scans is shown. It can be seen that the lithium reduction peak positions (between *ca.* -2.5 V and -3.5 V) remain relatively unchanged when the cathodic limit is kept below *ca.* -3 V, although naturally a greater proportion of the reduction peak is exposed on extending the cathodic limit. However the reduction peaks then begin to decrease in magnitude when the potential exceeds -3 V until *ca.* -3.5 V where the reduction peak is no longer present.

The CVs show the formation (or deposition) of a stable SEI layer during consecutive scanning, where on each successive scan the SEI layer is built up, and as can be seen, is not stripped off on the anodic scans, shown with the absence of a corresponding oxidation peak in the voltammetry.

Eventually the SEI acts as a barrier to further lithium reduction, and the full effect of this barrier is visible on the last scan: when the potential is swept to -4 V, no further current responses associated with complete lithium deposition are observed. Instead the fully-formed SEI layer allows the intercalation and de-intercalation of lithium, as shown with the lithium de-intercalation current feature on the anodic scan.^{121,225,256}

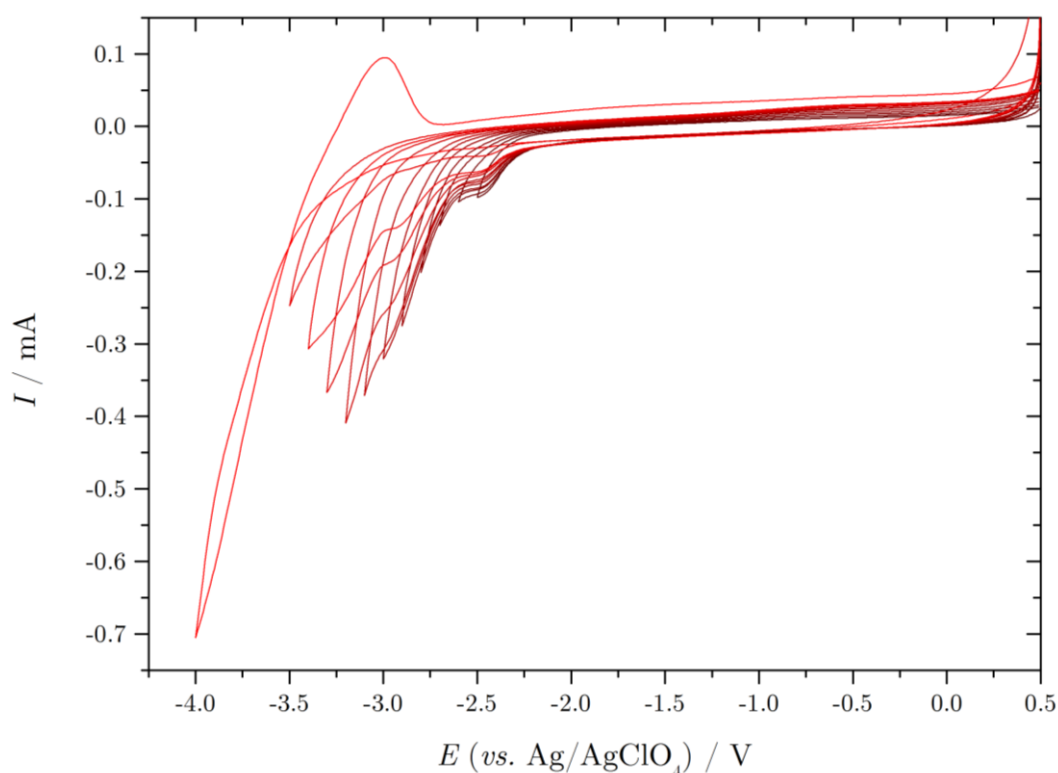


Figure 4.2) Voltammetric responses at a HOPG working electrode in 0.1 M LiClO_4 in NMP, scanned at 100 mV s^{-1} vs. Ag/AgClO_4 showing SEI formation at the graphite electrode and the effects of decreased activity

The HOPG working electrode was then replaced with a freshly cleaved HOPG electrode measuring approximately 4 mm \times 4 mm \times 0.5 mm. As shown previously this pair of redox peaks are associated with the intercalation and de-intercalation of lithium in and out of the graphite structure.^{257,258} Though SEI formation will preferentially take place at freshly exposed graphite edge planes, reversible lithium reduction can occur *via* pre-formed SEI coverage since the SEI layer is penetrable to Li^+ but not electrolyte molecules.^{259,260} This leads to unpredictable voltammetry, since both irreversible SEI formation and Li^+ intercalation/de-intercalation can occur autonomously, depending on the degree of pre-formed SEI coverage and the degree of lithium penetration.

As can be seen in Figure 4.3(a), scanning to -4.5 V has the effect of increasing the corresponding anodic peak current on the reverse scan, showing that the two peaks are interrelated.

Figure 4.3(b) shows an enlarged region of the most prominent lithium peaks, observed when the voltammetry was scanned to -4.5 V. From this scan, the associated charges for the intercalation and de-intercalation processes were calculated to measure the efficiency of the charge transfer process. The generated charge associated with the intercalation of lithium into HOPG was found to be 0.46 mC whereas the de-intercalation charge measured 0.35 mC, corresponding to *ca.* 78% charge efficiency. This *ca.* 20% charge loss has two main contributions: the first is a relatively large degree of measurement error, since the magnitude of charges obtained are derived from the use of tangential lines constructed from human judgement. Secondly, there is expected to be some degree of unrecoverable charge in the reverse scan, since the redox peaks are present in the region of increasing background current and therefore irreversible reduction of solvent and/or electrolyte, or SEI formation, actually contributes to the measured intercalation charge Q_I , which is not re-oxidised on

the reverse scan. As a result of the peak positions relative to the region of solvent breakdown, it is not possible to calculate the relative proportions of these two roles which contribute with the use of cyclic voltammetry.

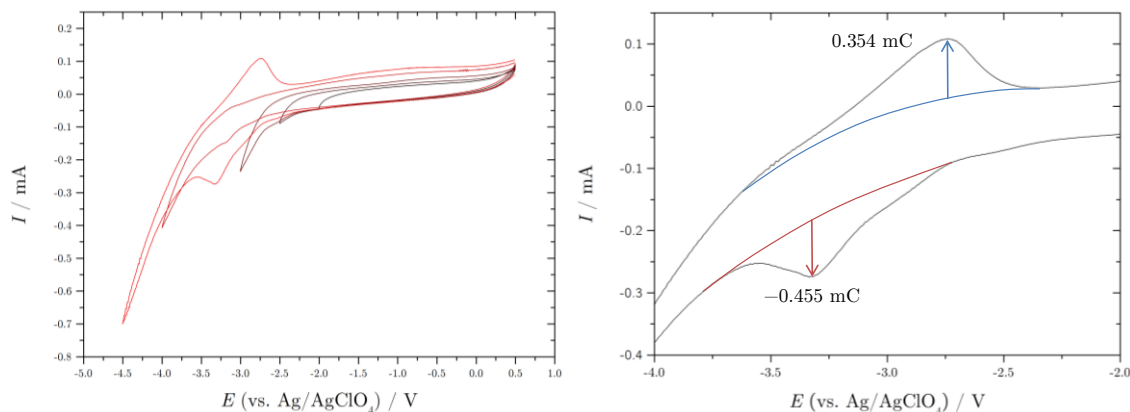


Figure 4.3) Voltammetric responses at a HOPG working electrode in 0.1M LiClO₄ in NMP, scanned at 100 mV s⁻¹ vs. Ag/AgClO₄ showing (a) the development of prominent lithium redox peaks on increasing the cathodic limit of the potential window with successive scanning, and (b) an enlarged portion of the lithium redox peaks showing Q_i and Q_d values determined from CV peak currents

Finally, in addition to recorded 0.1 ppm O₂ and H₂O concentrations in the system, no reduction peaks associated with the presence of oxygen in solution are visible in the potential range 0 to -1.6 V, providing evidence to suggest the solution was free of residual oxygen. However the presence of intercalation peaks centred on -3 V do show that the presence of oxygen is not necessary for the intercalation/reversible reduction of lithium at a HOPG cathode.

4.2.3 Lithium charge/discharge cycling

CA was employed to probe the degree of generated charge associated with intercalation and de-intercalation of lithium into HOPG, since CV proved to be unsuitable. Initially, LiBF_4 was investigated in parallel with the effect of intercalating potential. The charging potential, E_c , was varied from -0.8 V through to -4 V, and discharge, E_d , was conducted at 0 V in all cases. Charge and discharge was performed for 20 s and data was extracted from the transients of the second, third and fourth cycles to produce Figure 4.4. Data from the first cycle transients was not used in the analysis to avoid any non-equilibration effects often observed during initial scans.

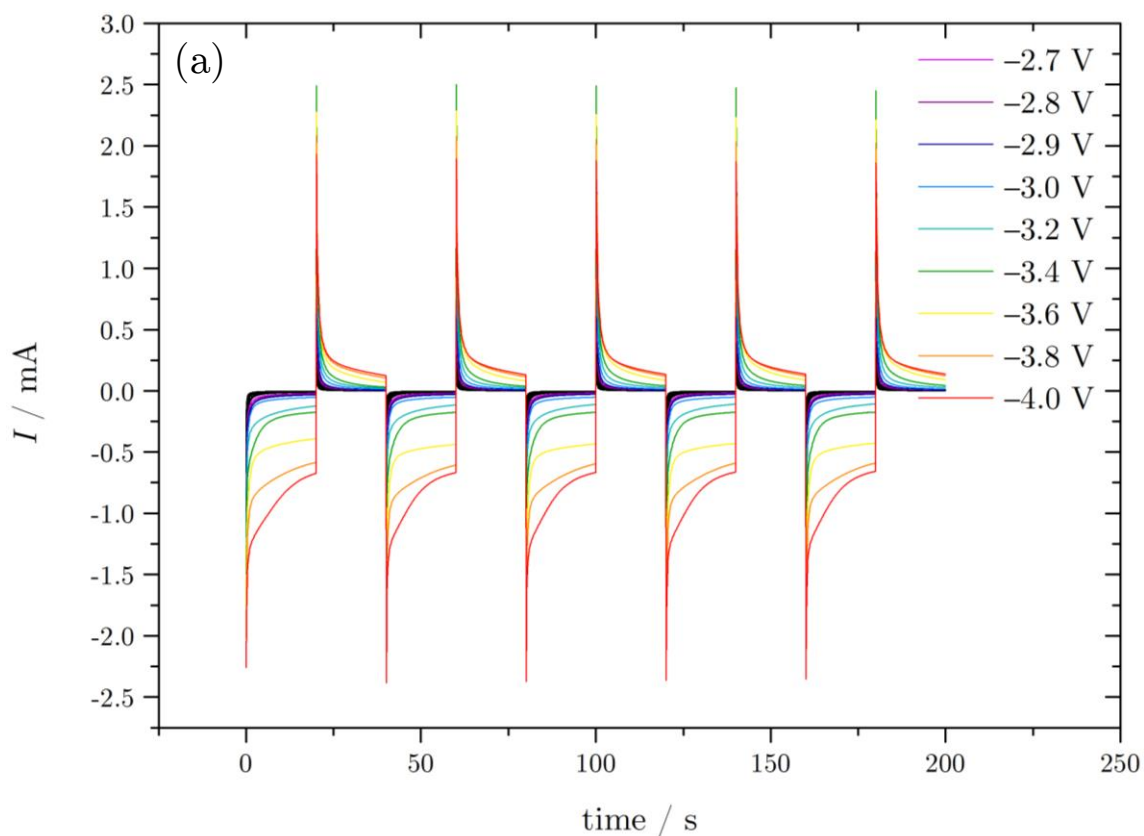


Figure 4.4(a) Charge/discharge plots showing 5 cycles with decreasing E_c performed at a 8 mg HOPG electrode in LiBF_4 (0.1 M) in NMP, from which data was extracted from cycles two, three and four, and plotted in Figure 4.5

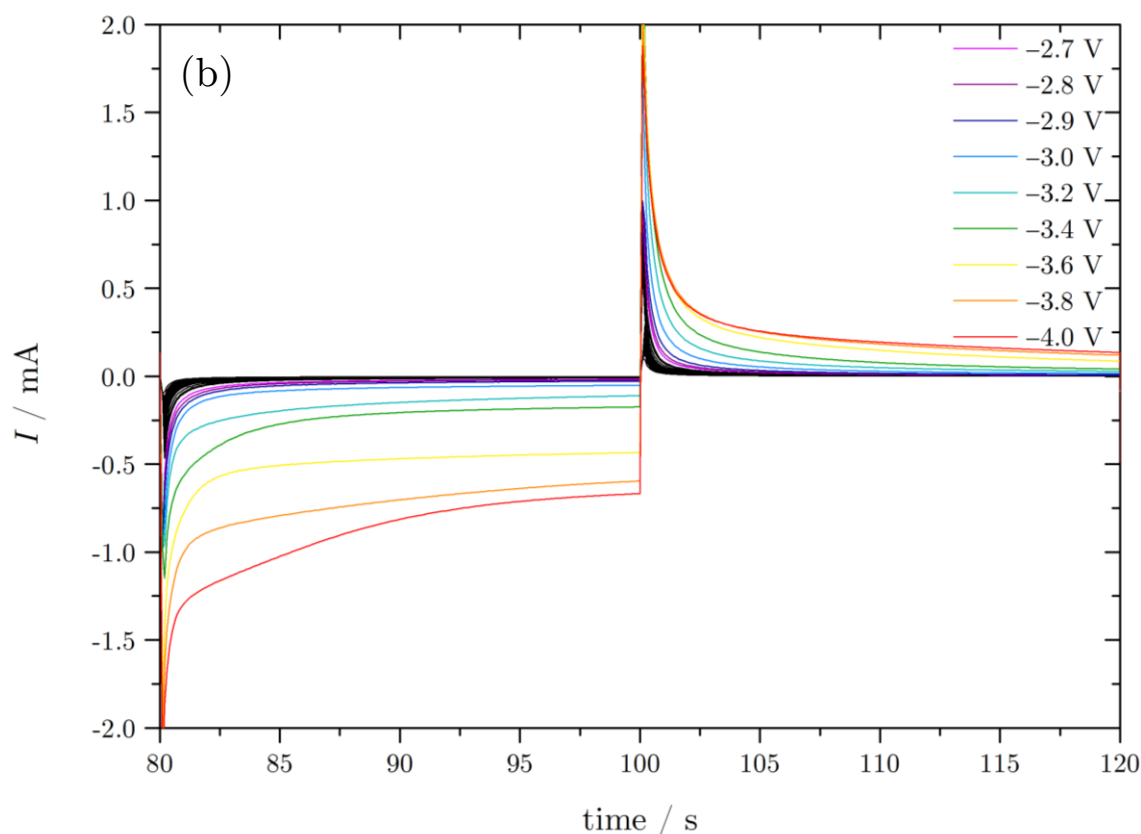


Figure 4.4(b) Charge/discharge (3rd cycle) with decreasing E_c performed at a 8 mg HOPG electrode in LiBF_4 (0.1 M) in NMP showing gradient changes of transients with increasing E_c

The ‘amount of recoverable charge’ is defined here as the ratio between the *total intercalation charge* and the *total de-intercalation charge* for individual charge/discharge cycles. This ratio, expressed as a percentage, has been termed the average coulombic efficiency ($\%_{\text{ACE}}$) since the data presented was an average taken from four charge/discharge cycles.

In addition, the term ‘reversibility’ is often used throughout this work to describe the degree of charge recovery during charge/discharge. This term should not be confused with systems being ‘electrochemically reversible’ (see Chapter 2), which is also used within this chapter.

Figure 4.5 shows how the recorded coulombic efficiency ($\%_{ACE}$) varies as a function of the applied charging load: as E_c is initially decreased from -0.5 V to *ca.* -2 V, the coulombic efficiency remains relatively stable at *ca.* 100%. There is a slight decrease to *ca.* 95%; since the charging potentials are well within the region in which little Faradaic activity occurs, electrochemical reduction of surface oxide groups present on the HOPG basal/edge planes could account for the slight loss in recoverable charge within this region, additionally this decrease could be associated with initial SEI layer formation (as presented in Figure 4.2) though this should not begin to appear until *ca.* -2 V. However the coulombic efficiency rapidly decreases to *ca.* 30% when the charging potentials are decreased to potentials lower than -2 V. This transient is similar in shape to the lithium CVs, and the sharp decrease in coulombic efficiency has been attributed to the irreversible formation of the SEI formation, which is deposited on the charging process but cannot be removed on the discharge procedure. The steady decrease in the coulombic efficiency can also be attributed to other irreversible chemical processes, such as solvent breakdown and SEI breakdown. It would appear that the formation of the SEI layer does not allow for reversible lithium intercalation/de-intercalation. This could be the result of two different mechanisms; a) that a sufficiently stable SEI layer (one that can protect from further lithium reduction) cannot form on comparative timescales to the charge/discharge cycling, and/or b) that the SEI layer is not chemically stable at such cathodic conditions, thus is reduced as well. Whatever the mechanism, it is clear that there is no protective process to allow the reversible intercalation of lithium, reflected by the steadily decreasing degree of charge recovery.

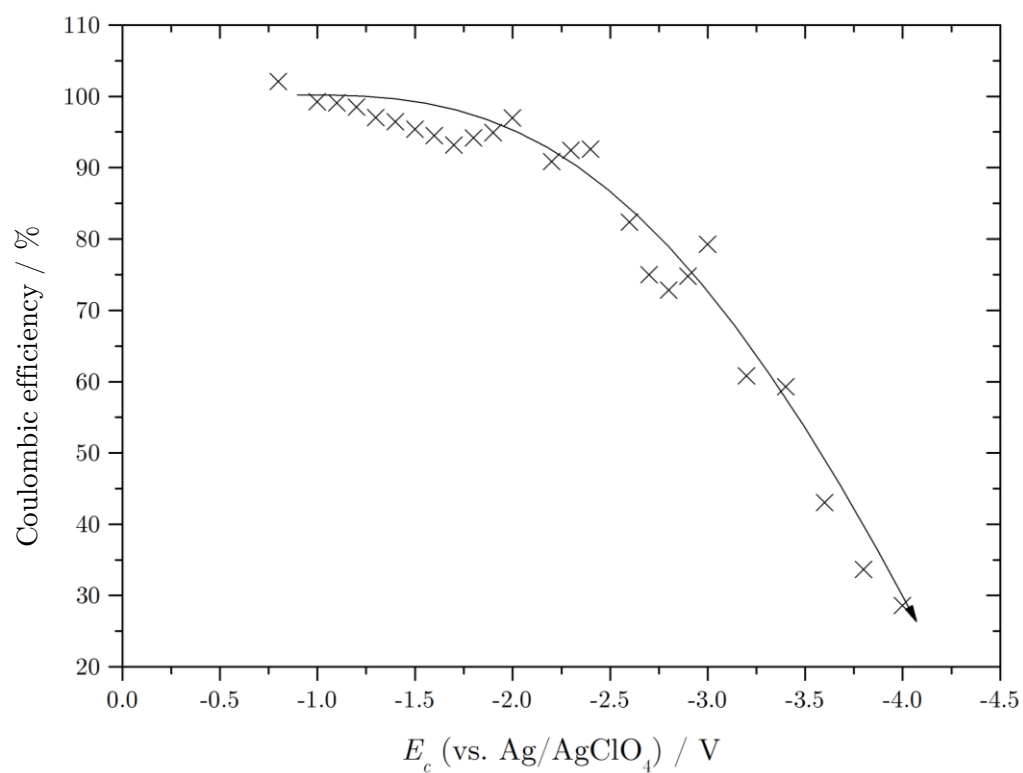


Figure 4.5) Plot showing how the average (taken over cycles 2-4) lithium charge/discharge efficiency is affected by increasing E_c from values of -0.8 V to -4 V

4.2.4 TMA⁺ electrochemistry

Focus was switched to R₄N⁺ cation intercalation. The first of these, TMA⁺, has a crystallographic diameter of 0.558 nm,²⁴² therefore slightly greater than the interplanar spacing of HOPG. In addition, it is not too physically dissimilar from Li⁺ in terms of its flexibility because of its relatively short alkyl chain lengths, nonetheless it should still exhibit a small degree of flexibility. Figure 4.6(a) shows the current response at a GC electrode and displays the familiar background current. As shown previously, intercalation/de-intercalation peaks were observed when employing HOPG as the working electrode (Figure 4.6(b)) and the effect of decreasing the negative limit of the potential window on the observed anodic peak current is visible. Figure 4.6(c) shows repeated cycling between 0.5 and -2.5 V and displays reproducible voltammetry. Here the potential window only slightly explores the cathodic region at which electron transfer occurs, as is confirmed with the reverse scan anodic current. By cycling in this small window relatively reproducible CVs are obtained. It was expected that cycling over a much larger potential window would result in irreversible voltammetry in contrast to cycling in a small potential region, as shown previously in oxygenated voltammetry.

The irreproducible CVs seen in previous work have previously been attributed to a constantly expanding electrode as a result of intercalation, thereby producing constantly increasing working area. Unexpectedly this was not observed in the controlled atmosphere work, and it was found that even voltammetric cycling deep into the cathodic region (-3.5 V) eventually allowed for the recording of initially repeatable voltammograms (Figure 4.6(d)). Naturally, as shown previously the anodic peak currents (and associated charges) are much greater than in the ‘small’ potential window cycling. This highlights the importance of an oxygen free environment, since consecutive CVs

(at least for the initial few) are seen to be reproducible. CV analysis over extended periods of time would still be expected to produce CVs with less pronounced features, since electrode expansion would inevitably dominate the process. Nonetheless, this serves as an interesting result, since it directly attributes previous CV irreproducibility to the presence of residual oxygen/water in the system.

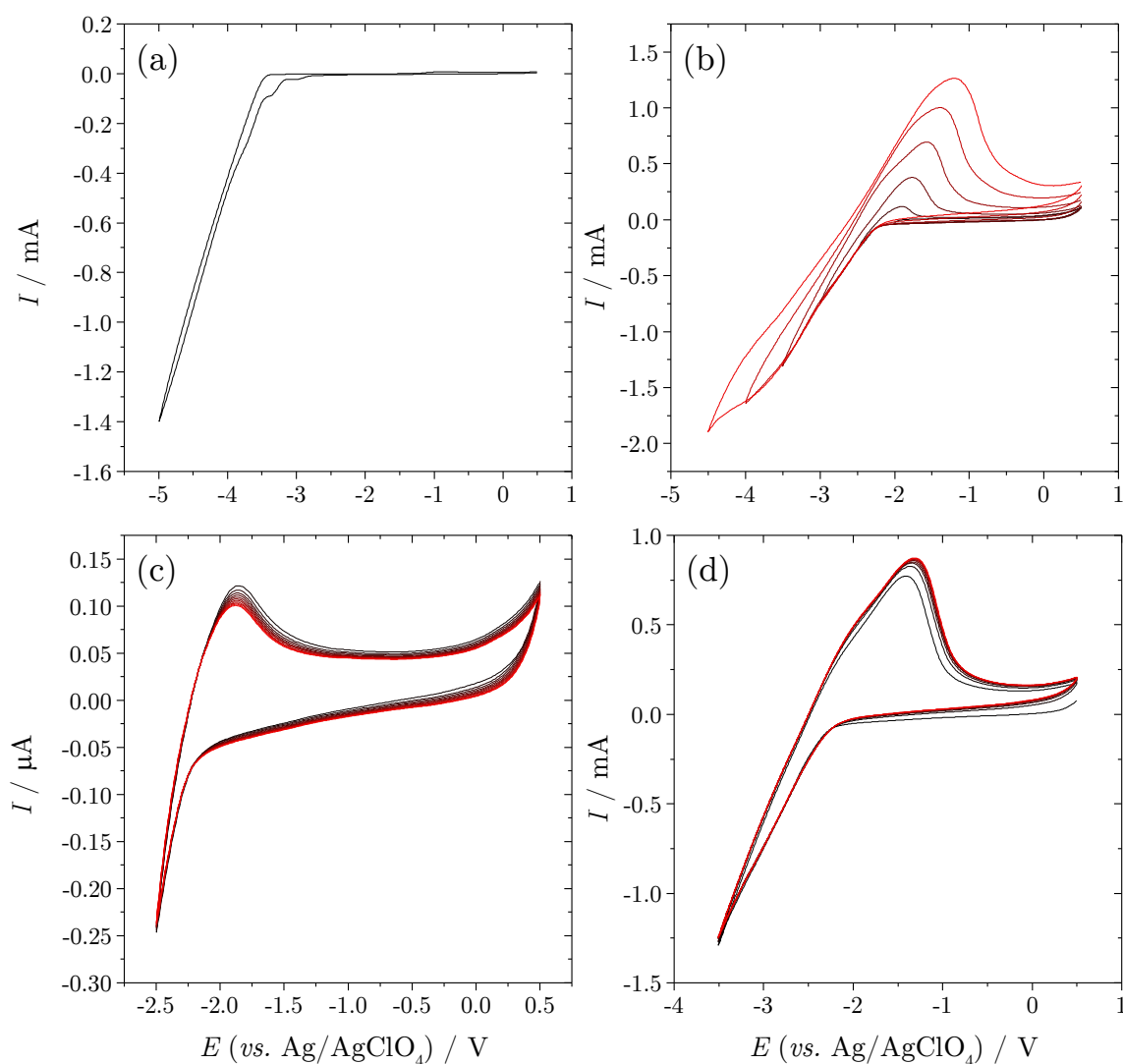
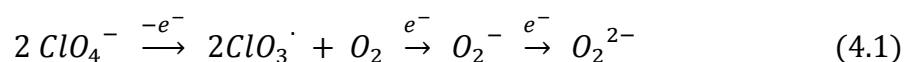


Figure 4.6) Voltammetric response in 0.1M TMAcClO_4 in NMP, scanned at 100 mV s^{-1} *vs.* AgAgClO_4 , at (a) GC WE, (b) HOPG WE showing successive increase of the negative potential limit, (c) HOPG small potential window (initial scans black) and (d) HOPG large potential window (initial scans black)

The positive limit of the potential window was increased to probe the effects of anionic intercalation. Large enough positive potentiostatic conditions are expected to provide the driving force to successively intercalate perchlorate between the graphene galleries in the graphite anode, resulting in oxidation of the anion and associated Faradaic responses. The potential limit was increased to +2 V and cycling was performed, beginning at 0 V, through -3 V and continued to +2 V. This cycle was repeated several times (Figure 4.7). On the second scan and every scan thereafter, directly after the potential has been swept into the large positive region, two new peaks are observed. Peak no 1 lies at *ca.* -1.5 V whereas peak 2 lies at *ca.* 0.2 V. These new reduction peaks are due to the presence of oxygen and correspond to the double-step electro-reduction of oxygen to superoxide (1) and oxide (2). This oxygen does not arise from atmospheric dissolution, since the experiment was performed in an oxygen free environment; this is confirmed by the oxygen-featureless first CV scan. The presence of oxygen occurs due to irreversible perchlorate electrolysis at large positive potentials, generating oxygen and chlorine.



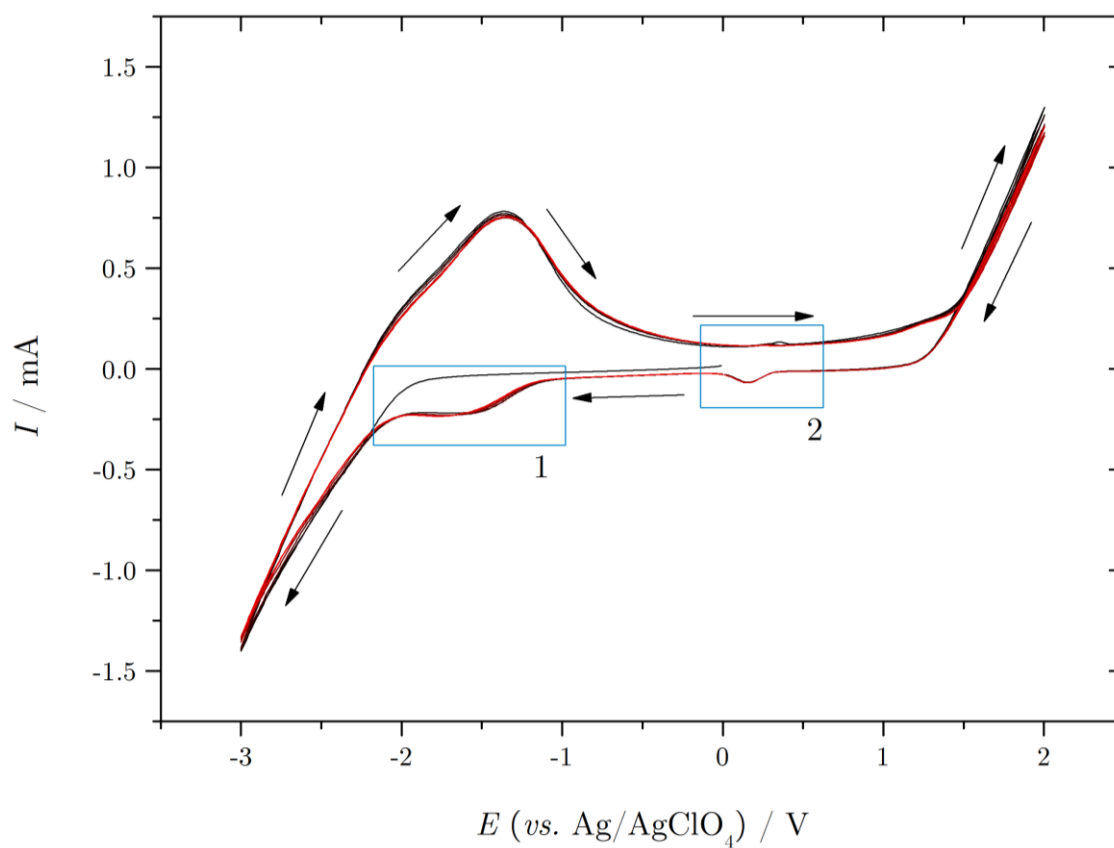


Figure 4.7) Voltammetric response of HOPG in 0.1 M TMAcClO₄ in NMP, scanned at 100 mV s⁻¹ vs. Ag/AgClO₄, between -3 V and +2 V, showing the presence of oxygen reduction Faradaic processes as a result of perchlorate electrolysis at *ca.* +1.5 V.

4.2.6 TMA⁺ Average Coulombic Efficiency (%ACE) testing

As for the aforementioned lithium work, CA was employed to probe the degree of generated charge associated with intercalation and de-intercalation of TMA⁺ into HOPG. A 10 mg HOPG sample (*ca.* 0.1 mm thickness) was submerged by *ca.* 50%, exposing *ca.* 5 mg HOPG to the electrolyte solution. Initially, TMA⁺ClO₄⁻ was investigated in parallel with the effect of intercalating potential. The charging potential (E_c) was varied from -1.5 V down to -4 V, and again, discharge (E_d) was conducted at 0 V for all cases. Charge and discharge was performed for 20 s, from which data was extracted from the second, third and fourth cycles, and averaged.

The initial charge/discharge transients have been presented in Figures 4.8(a) and 4.8(b) prior to presentation of data over the entire E_c range, and show the measured current response with increasing E_c . Figure 4.8(a), shows current responses for E_c values between -0.8 V and -2.0 V and it is clear that the peak currents for both the charge and discharge procedures are approximately equal (*ca.* 20 μ A). The transients are also featureless (with respect to Faradaic processes). This is sensible, given the magnitude of the charging potentials applied; within the region of non-Faradaic activity (see preceding voltammetry in Figure 4.6).

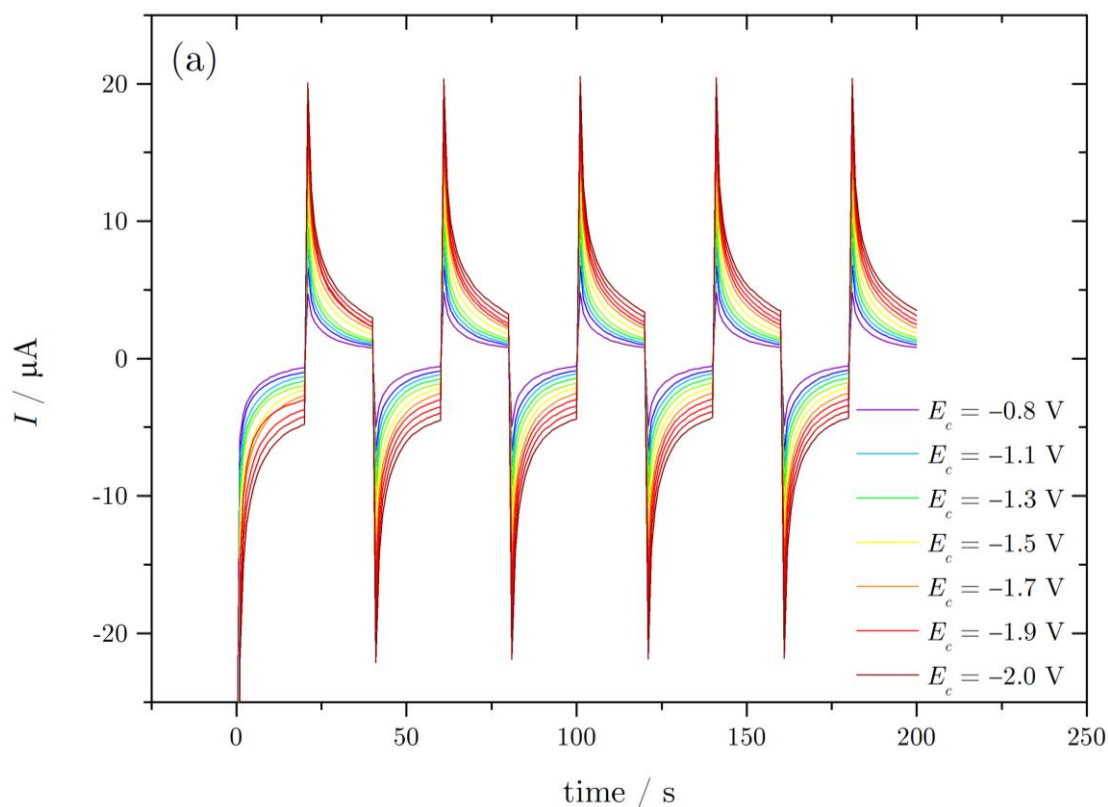


Figure 4.8(a) TMA^+ charge/discharge plots showing 5 cycles with decreasing E_c (from -0.8 V to -2.0 V) performed at a 10 mg HOPG electrode in TMAClO_4 (0.1 M) in NMP

However there is a clear change in the shape of the transients when the charging potential is decreased to -2.3 V (Figure 4.8(b)), and this change persists for charging potentials as low as -2.8 V: whereas in Figure 4.8(a) show approximately equal peak currents, and similar decay transients, the charging transients for the more negative E_c values exhibit substantially smaller peak currents (*ca.* -1.25 mA) than their corresponding discharge transients (*ca.* $+3.5$ mA). Since this difference becomes apparent at the onset of intercalation, it indicates that it takes longer for cations to intercalate than it does for them to de-intercalate (the charge takes longer to be generated during intercalation than during de-intercalation). It follows that cation intercalation into the graphite structure is much slower than during de-intercalation, because of the spatial restrictions put in place by the graphene galleries as well as neighbouring

cations as they effectively ‘queue’ to intercalate. The cations experience no spatial restrictions when de-intercalating into the bulk solution, the opposite in fact, hence the must faster discharge rate.

However, despite exhibiting larger peak currents on the discharge transients, it should be noted that the total charge associated with the discharge (Q_d) was not larger than that of the charging transient (shown later in coulombic efficiency data: Figure 4.9).

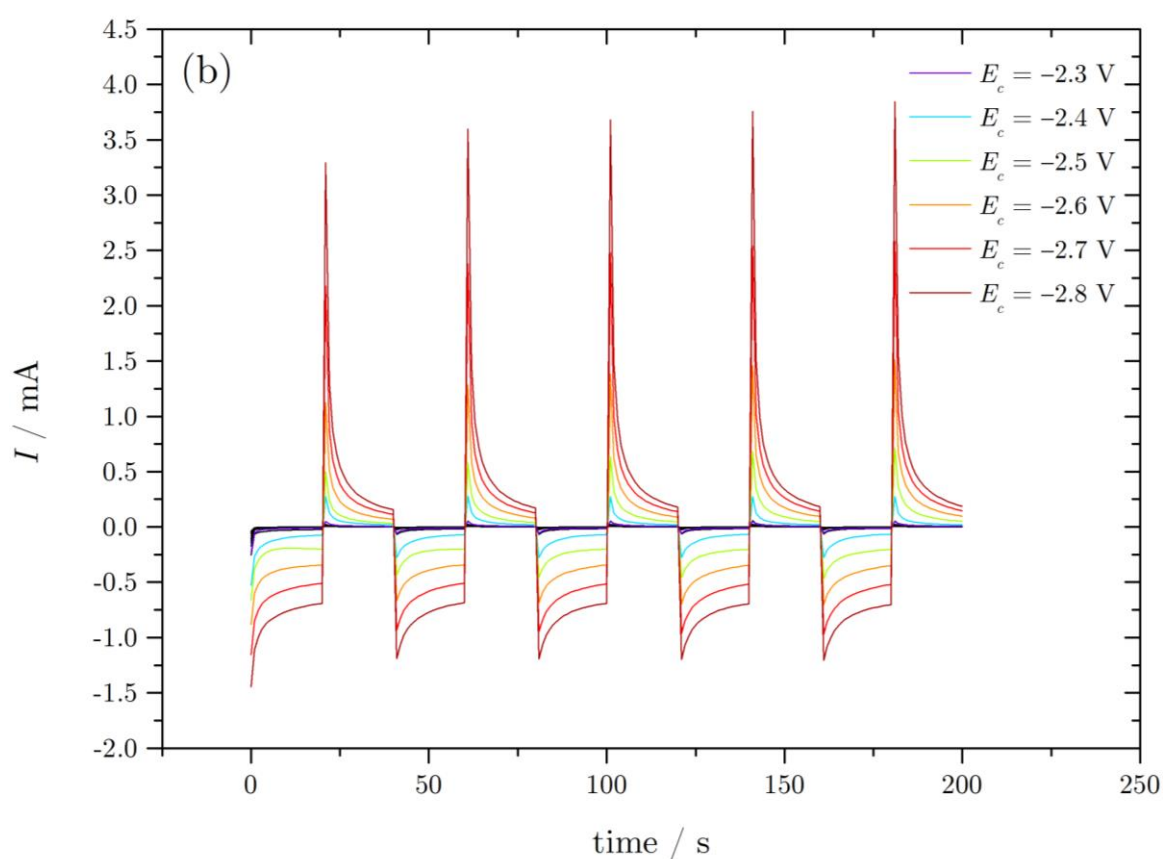


Figure 4.8(b) TMA^+ charge/discharge plots showing 5 cycles with decreasing E_c (from -2.3 V to -2.8 V) performed at a 10 mg HOPG electrode in TMAClO_4 (0.1 M) in NMP

Figure 4.9(a) shows the data acquired over the entire range of E_c values tested, though for the purpose of clarity only the more negative E_c values, which have not been presented yet, have been labelled. It can be seen that the unequal peak currents persist, since the cations are still experiencing the effects of an overcrowded, spatially restricted lattice during intercalation, followed by unhindered de-intercalation freely back into the bulk solution.

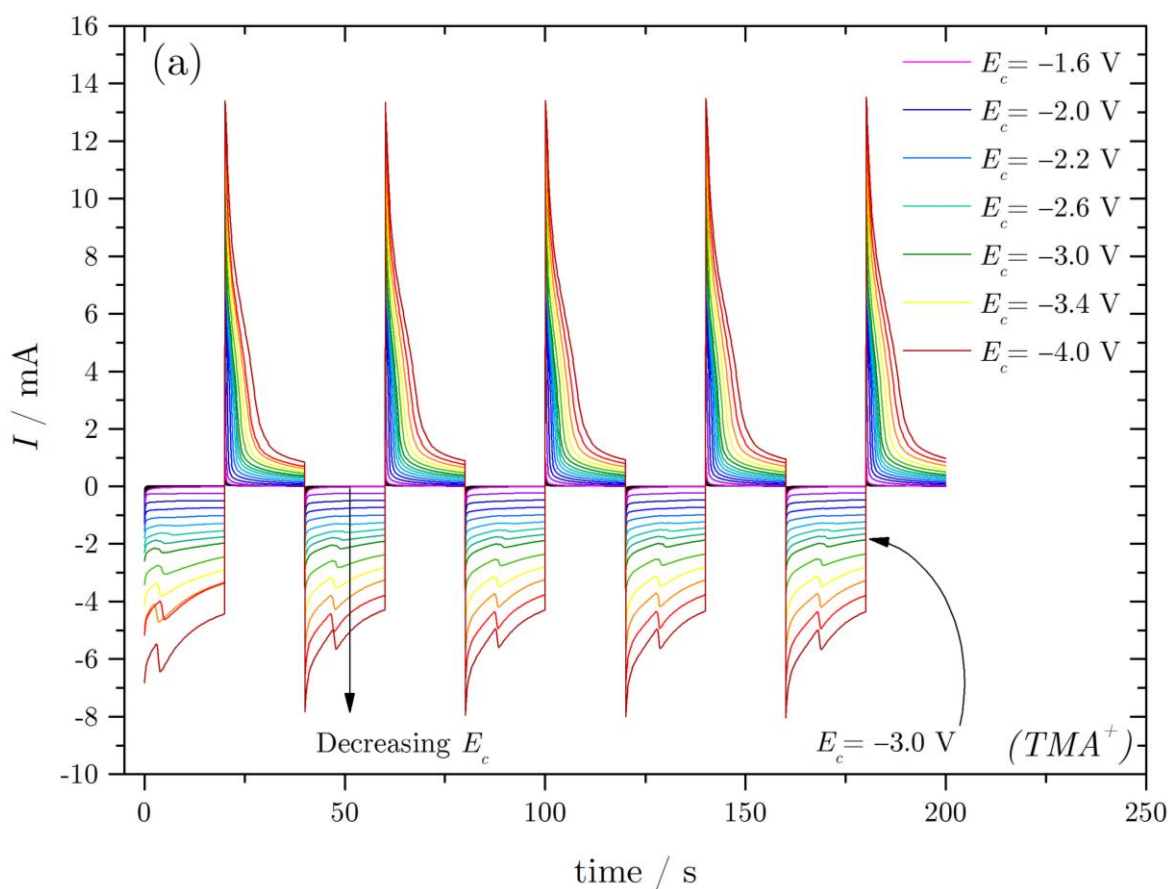


Figure 4.9(a) TMA^+ charge/discharge showing 5 repeated charge/discharge cycles with decreasing E_c performed at a 10 mg HOPG electrode in $TMAClO_4$ (0.1 M) in NMP, from which data was extracted from cycles two, three and four, and plotted in Figure 4.10

Over the course of the charge/discharge investigation, the HOPG electrode was found to expand in a typical ‘fan’ structure (shown in more detail in Chapter 5), though over the course of 5 cycles the degree of expansion was negligible, at least to the naked eye, and expansion can be assumed to occur only on the micro-scale for initial cycling.

It can be seen in Figure 4.9(a) that the transients are relatively reproducible between cycles 2 to 5, indicating that the same process occurs each time once the system has been allowed to reach some equilibrium state (first cycle does appear to be different, attributed to initial double layer charging effects at the electrode). This suggests that the degree of expansion during each negative charging cycle is either negligible or reversible; though it is thought that this degree of expansion, which will be on the micro/nano-scale at such short charging times, would not contribute significantly to the voltammetry over such small timescales. The reproducibility of cycles 2-5 is noteworthy, indicating a reliable source of data to average.

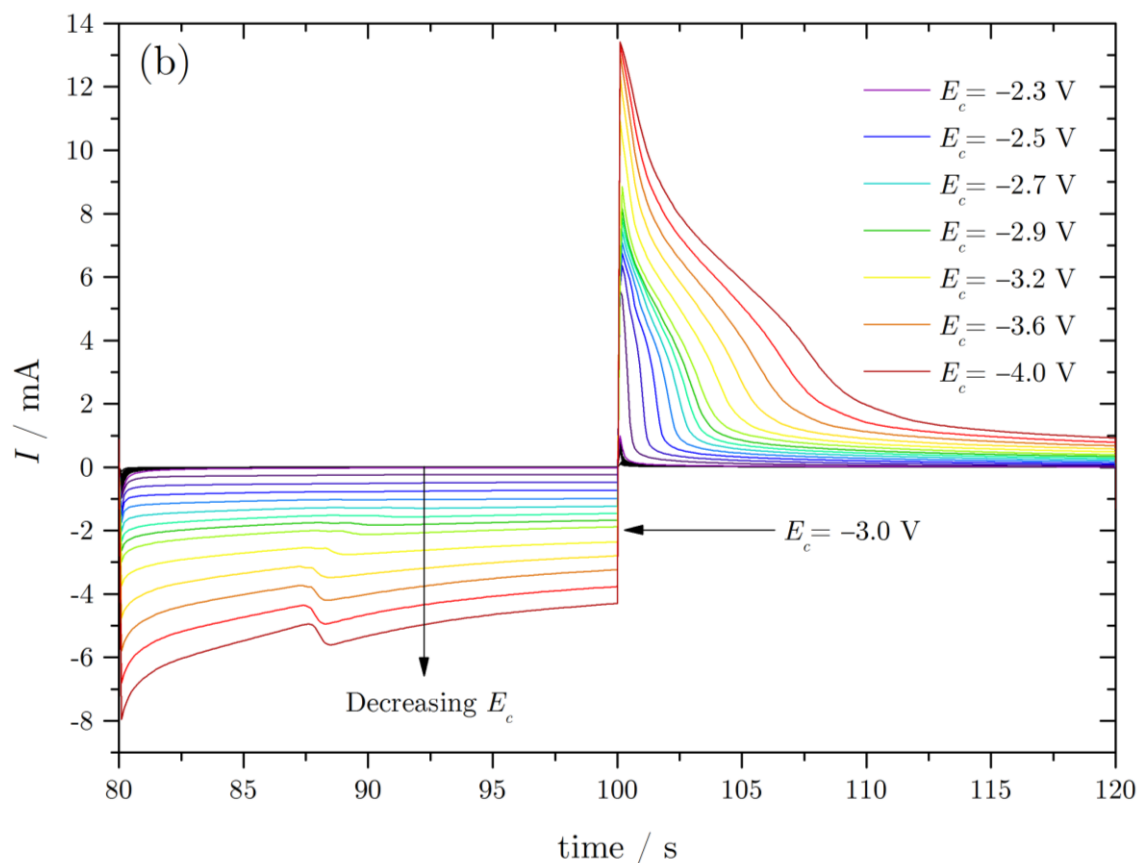


Figure 4.9(b) TMA^+ charge/discharge (3rd cycle) with decreasing E_c performed at a 10 mg HOPG electrode in TMAClO_4 (0.1 M) in NMP showing gradient changes of transients with increasing E_c

Figure 4.9(b) shows the fourth cycle only, displaying the transient shape more clearly. It can be seen that when $E_c < -3\text{ V}$ the charging transients' shapes change and a sharp increase, or 'hiccup', in the recorded current is observed approximately half way through the charge (*ca.* 85 s). The reproducibility of this feature in the successive cycles is clear, and also increases in intensity with decreasing E_c . The reason for this 'hiccup' is thought to be associated with the nucleation phase of the formation of a staged GIC.^{261,262} The consequence of the 'hiccup' is clearly present in the larger than expected anodic peak current (*ca.* 13 mA) at $t = 0$ of the discharge transient, as well as an obvious shoulder on the discharge transient. This 'hiccup' doesn't begin to appear until $E_c <$

ca. -3 V which is the same point the trends (charge) begin to steadily increase. These two phenomena are likely to be linked, though the implications were not inherently clear at this stage.

As for lithium, the $\%_{\text{ACE}}$ of TMA^+ was calculated for the four cycles (Figure 4.8(a)) and plotted against varying E_c as presented in Figure 4.10(a-d). Every $\%_{\text{ACE}}$ plot presented herein, unless otherwise stated, is the third in a series of plots, which were considered sufficiently repeatable. Due to the high sensitivity of the measurements it was necessary to conduct multiple dataset repeats to establish reliable data.

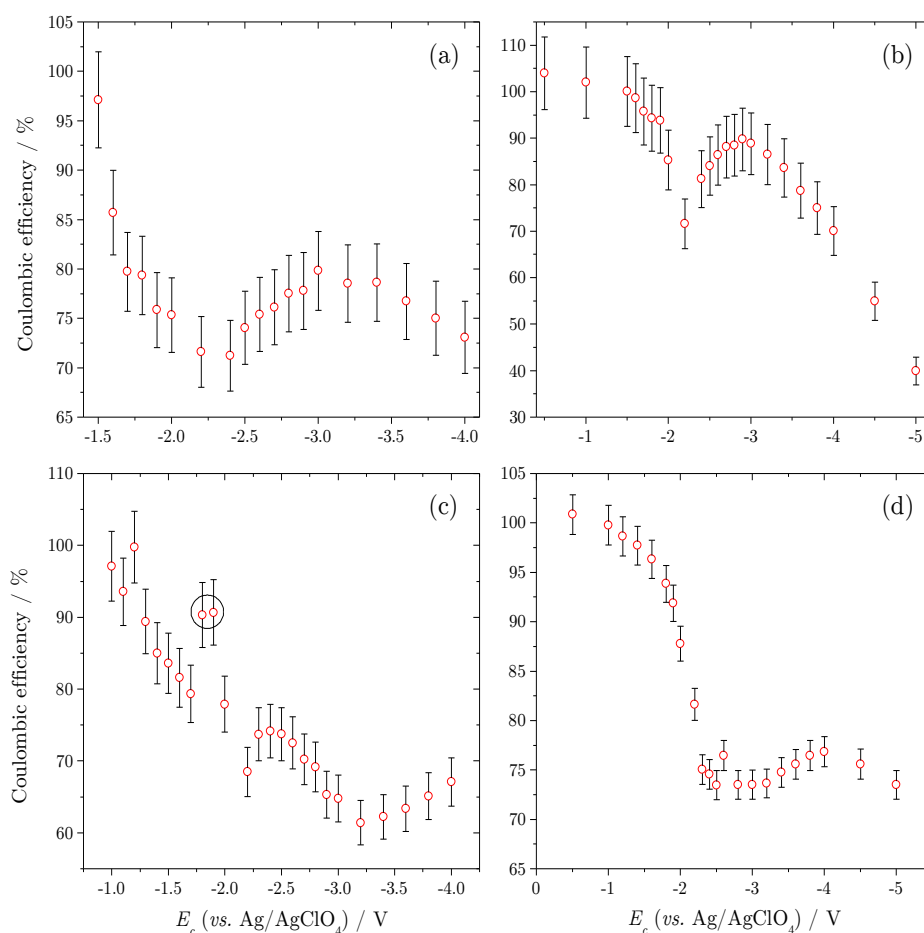


Figure 4.10) Plots showing how TMA^+ charge/discharge efficiency is affected by the increasing E_c from values of -1 V to -5 V . (a) shows initial scans, (b) shows the effect of using data from extended cycling, (c) shows an example of ‘anomalous’ data (circled), and (d) shows the effect of using a thick (*ca.* 1 mm) HOPG sample

Figure 4.10 shows a selection of coulombic efficiency relationships derived from TMA^+ charge/discharge cycling data. Typical data sets obtained from the initial four cycles generally displayed variable charge ratios as large as *ca.* 15%; shown with the inclusion of error bars on each plot.

Figure 4.10(a) shows a clear trend as E_c is decreased from -1.5 V to -4 V . In the initial ‘Stage I’, where $-1.5\text{ V} \leq E_c \leq -2\text{ V}$, the $\%_{\text{ACE}}$ can be seen to decrease from *ca.* 100% to 75%. Here E_c values are within the potential region of little Faradaic activity, and therefore a large decrease in the $\%_{\text{ACE}}$ seems illogical. However the steady decrease can be attributed to small measureable changes in non-Faradaic current. To probe this, 25 cycles were recorded in an attempt to allow the system to reach some degree of stability, and data was extracted from the final four cycles. The resulting plot is presented as Figure 4.10(b). It can be seen that the $\%_{\text{ACE}}$ can be recovered to nearly 100% by using data from longer periods of potentiostatic cycling. It is thought that this initial decrease in the charge recovery is a result of surface oxide groups present on the graphite’s edge and basal planes. This effect was previously seen with lithium, and can explain why after prolonged cycling or ‘electrochemical cleaning’, the system is allowed to behave in a more reversible fashion, since the surface oxide groups have been sufficiently reduced and charge is not subsequently ‘used up’ reducing these surface species.

In 4.10(b) a sharp decrease in the $\%_{\text{ACE}}$ is observed at potentials around *ca.* -2 V . It should be noted that this phenomenon is real, and not simply a result of reduced cycling times since repeated cycling (25 cycles) was unable to completely recover coulombic efficiency to 100% at these potentials. The decrease in $\%_{\text{ACE}}$ could be attributed to partial intercalation without resulting in sufficient electrode expansion, in which ions cannot fully de-intercalate from the host structure due to spatial restrictions. This hindrance to de-intercalation

would be reflected in a decrease in total Q_d , since charge would remain at the electrode solution interface. In addition, and perhaps more likely, saturation of the electrode|solution interface with partially reduced TMA^+ would result in no subsequent stabilisation of reduced cations: resulting in complete irreversible reduction of these newly arriving species (Figure 4.11). The charge passed to reduce these species is consequently not recovered on the discharge process, since the un-stabilised species are completely reduced, and this is reflected in a decrease in the coulombic efficiency.

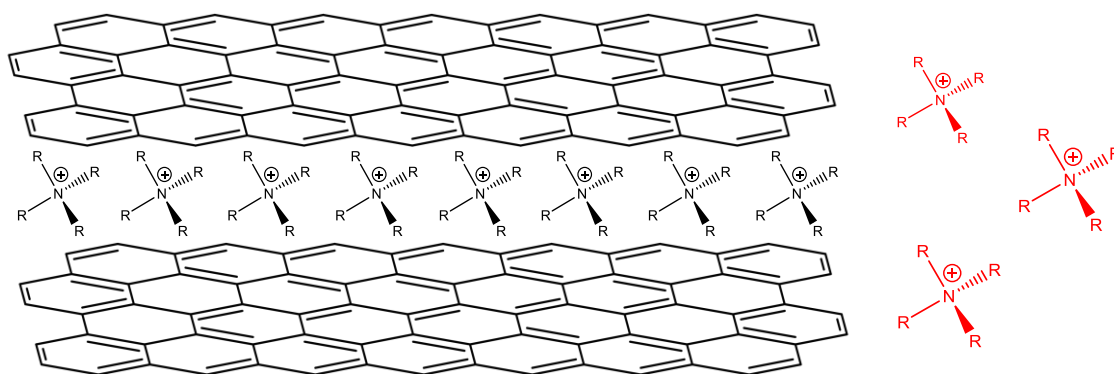


Figure 4.11) Schematic describing the effects of intercalation saturation, whereby further migrating cations (red) are unable to be stabilised by the neighbouring graphene sheets and are therefore subsequently irreversibly reduced to trialkylamine species and other by-products

Interestingly, the $\%_{ACE}$ does not continue to decrease steadily and in Stage II, where $-2\text{ V} \geq E_c \leq -3\text{ V}$, the trend begins to increase. -2.4 V has been found to be the potential at which noticeable intercalation and electrolyte reduction occurs, and is also associated with the minimal potential required to result in observable electrode expansion of a HOPG electrode: this correlates with the gradient change of the plot.

Often during cycling in Stage I, occasional data points were recorded corresponding to cycling efficiencies in excess of 90%, (Figure 4.10(c), circled). These points were initially labelled anomalous; though they actually carry

significant importance. These ‘anomalous’ points were only observed between E_c values of -1.5 V and -2 V which is telling of their nature; the sudden increase is attributed to a net increase in flux of ions de-intercalated during the discharge process. The excess number of ions is thought to be present due to the previous charging cycles in which some ions become trapped within the graphite pores. These points were observed most often with TMA^+ and it is logical that TMA^+ may be more susceptible to ion-trapping, due to its size compared to the graphene interplanar spacing and the cation’s relative inflexibility. It is not until electrode expansion becomes sufficient, that these ions are allowed to de-intercalate freely, contributing positively to Q_d and observed as larger than expected efficiencies.

Finally, it was found that slightly different masses and thicknesses of initial HOPG samples had drastic implications on recorded data. Figure 4.10(d) shows the resulting $\%_{\text{ACE}}$ plot obtained when employing a relatively large mass of HOPG (13.6 mg) as the WE, approximately $10\times$ the thickness of samples generally used (1 mm *cf.* 0.1 mm). In Stage I of the plot, the trend is unchanged, but in Stage II charge is not recovered to the same extent as with thinner HOPG samples (75% *cf.* 90%). In addition, the $\%_{\text{ACE}}$ does not decrease at $E_c < -2$ V, but continues to produce cycling efficiencies greater than 70% even at E_c values as low as -5 V. Since Stage I is related to double layer charging, it follows that increasing the degree of accessible intercalation sites (thickness) has no effect on the double layer charging at the electrode. This is sensible, since intercalation is not required in order to charge the electrode|solution interface. It is unclear at this stage why the coulombic efficiency does not peak to near 100% efficiencies, as in the case of the *ca.* 0.1 mm study, given the introduction of more intercalation galleries in the *ca.* 1 mm study. However it can explain why the coulombic efficiency remains high

(*ca.* 70%) even at charging potentials as low as -5 V, since a greater degree of GIC stabilisation can help the electrolyte ‘cope’ with the cathodic conditions.

Finally, potential-holding voltammetry was conducted with TMA^+ intercalation into HOPG. As before with lithium work, the negative limit of the potential window was fixed for increasing periods of time to demonstrate the effect on the anodic peak current on the reverse scan. Figure 4.12 shows that fixing the potential at -2 V on each scan for increasing periods of time (0 s, 30 s, 60 s, 90 s, 120 s) resulted in an increase in the anodic peak current on the reverse scan. It should be noted that eventually, increasing the time period has little effect on the anodic peak current, indicating that a maximum amount of charge can be generated from intercalation at -2 V. Since this charging potential is relatively positive, it might be assumed that these are simply non-Faradaic charging processes occurring; however the potential is clearly probing the intercalation peak, and does have the effect of causing (and altering) a corresponding anodic peak current on the reverse scan.

The black dashed line in Figure 4.12 shows that on the final scan, where the potential was swept freely without interruption between the two potential limits, the current response is almost identical to the initial scan, demonstrating that the system is able to return to its original state. This shows that the application of -2 V does not cause permanent damage to the system.

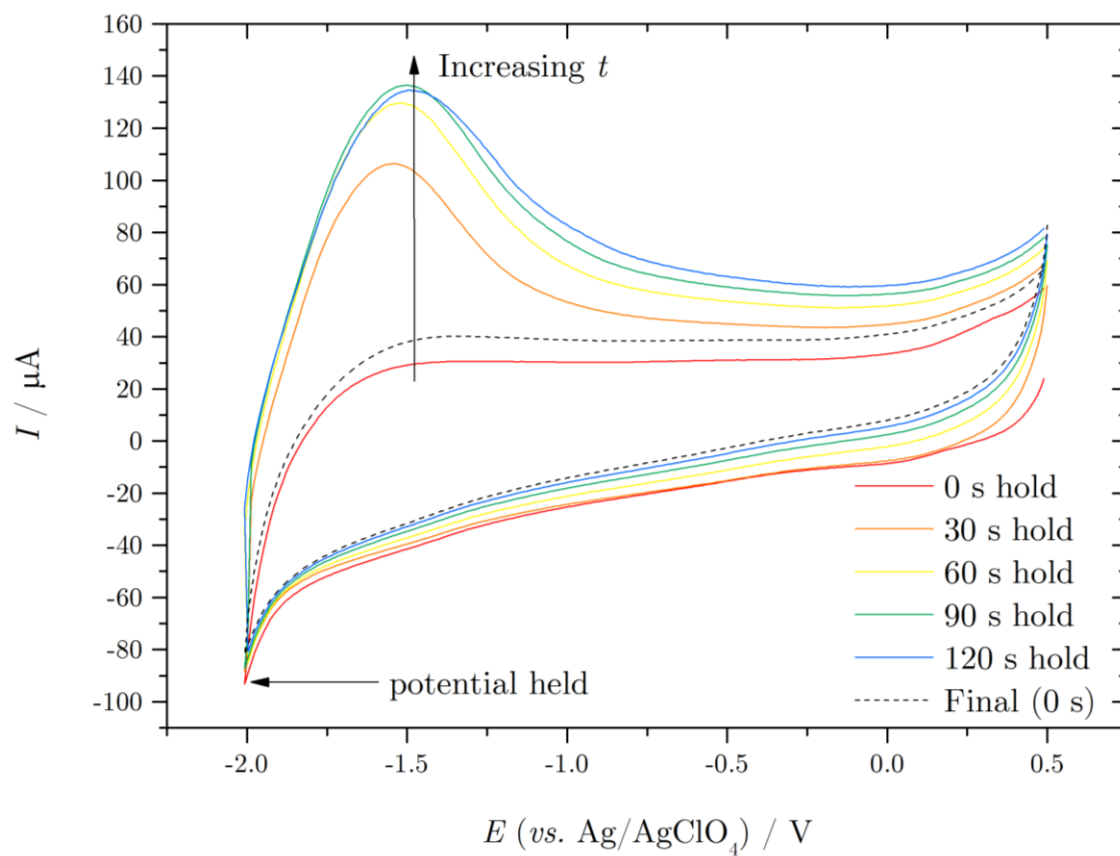


Figure 4.12) CV showing current response at HOPG WE, measured at 100 mV s^{-1} , demonstrating the effect of holding at -2 V for increasing periods of time, on the anodic peak current.

4.2.7 TEA⁺ electrochemistry

As with TMA⁺, voltammetry of TEABF₄ was investigated at both GC and HOPG electrodes. The crystallographic diameter of TEA⁺ is 0.674 nm,²⁴² almost double that of the interplanar spacing of HOPG; however the ethyl-alkyl chain lengths of the TEA⁺ cation permit a greater degree of flexibility than that associated with TMA⁺. This flexibility rationalises the reasons for cation selection; at nearly double the interplanar spacing of graphite one might assume a maximum of Stage-2 intercalation possible with such a relatively large cation. However, because of what has been shown with TBA⁺ under non-electrochemical conditions²⁴⁰, TEA⁺ flexibility might allow for intercalation with a higher degree of staging.

Figure 4.13(a) shows the current response obtained at a GC electrode in TEABF₄ (0.1 M). As shown previously with TMA⁺, the familiar increase in background current from *ca.* -3 V is observed. As expected from earlier work, no other voltammetric features are present in the CV. Figure 4.13(b) shows the current response at a HOPG electrode (2.1 mg, 0.1 mm thickness) and shows the effect of successively decreasing the negative limit of the potential window. It shows that the magnitude of the anodic peak on the reverse sweep is proportional to the cathodic sweep magnitude. Figures 4.13(c) shows reproducible voltammetry when the cathodic peak is only partially explored and again displays that the anodic peak current observed is a result of scanning within the potential region of the cathodic peak, and Figure 4.13(d) shows successful CV reproducibility even over a large potential window (*ca.* 4 V). This is quite remarkable since it shows, at least for the initial 10 CVs, that reproducible voltammetry is possible even in the presence of irreversible solvent decomposition. This is due to the fact that at relatively fast scan rates (100

mV s⁻¹), the period of time spent in harsh reducing conditions ($E < -3.5$ V) is kept to a minimum, and the system is able to recover.

Finally, Figure 4.13(d) shows a slight oxidative current response in the anodic sweep at *ca.* -2.5 V. This peak has sometimes been observed previously in TMA⁺ and TEA⁺ voltammetry, although not as prominently as observed here. The peak only becomes visible once the potential is swept below *ca.* -3.5 V, entering the potential region of significant current increase. The peak was not observed in TBA⁺ voltammetry presented herein (section 4.2.9). This new peak could be the re-oxidation of the species being reduced at -3.5 V, though it is hard to say conclusively at this stage; this small peak is covered again in section 4.2.12.

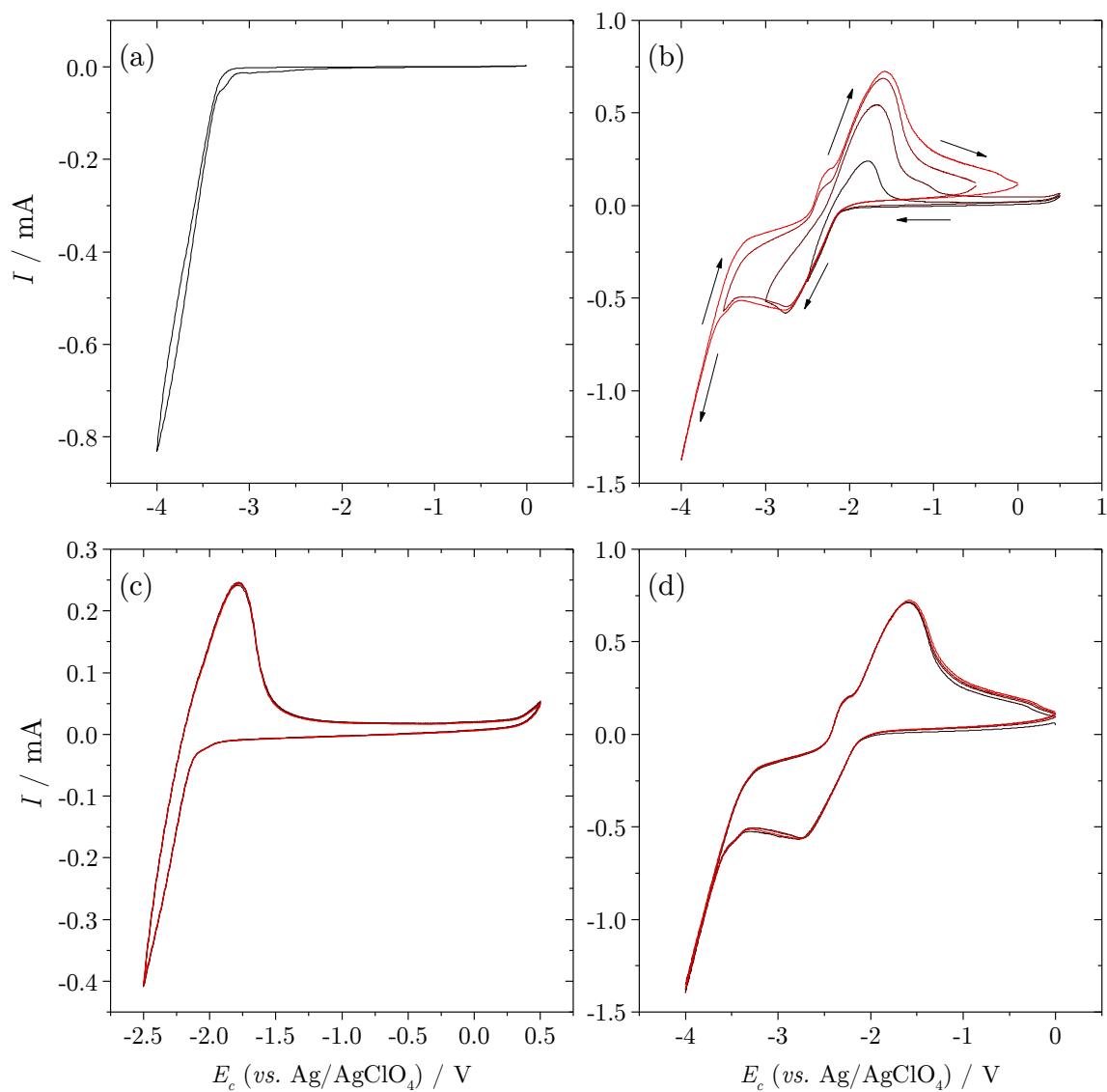


Figure 4.13) Voltammetric response in 0.1M TEABF_4 in NMP, scanned at 100 mV s^{-1} vs. Ag/AgClO_4 , at (a) GC WE, (b) HOPG WE showing successive increase of the negative potential limit and the effect on the anodic peak on the reverse sweep, (c) HOPG small potential window displaying CV repeatability and (d) HOPG large potential window displaying CV reproducibility

4.2.8 TEA⁺ Average Coulombic Efficiency (%_{ACE}) testing

In the same manner as with previous galvanic cycling, charge/discharge was performed on a HOPG working electrode (3.5 mg, 50% submerged) in a solution of TEABF₄ (0.1 M) in NMP, from which the coulombic efficiency was determined and plotted as a function of E_c . Figure 4.14(a) shows the resulting five charge/discharge transients as E_c is decreased from -0.5 V to -5 V.

In a similar manner to TMA⁺ studies, albeit not as prominent, the presence of a current ‘hiccup’ in the charging transients is visible, specifically for E_c values more negative than -2.8 V, and again this ‘hiccup’ exhibits good reproducibility.

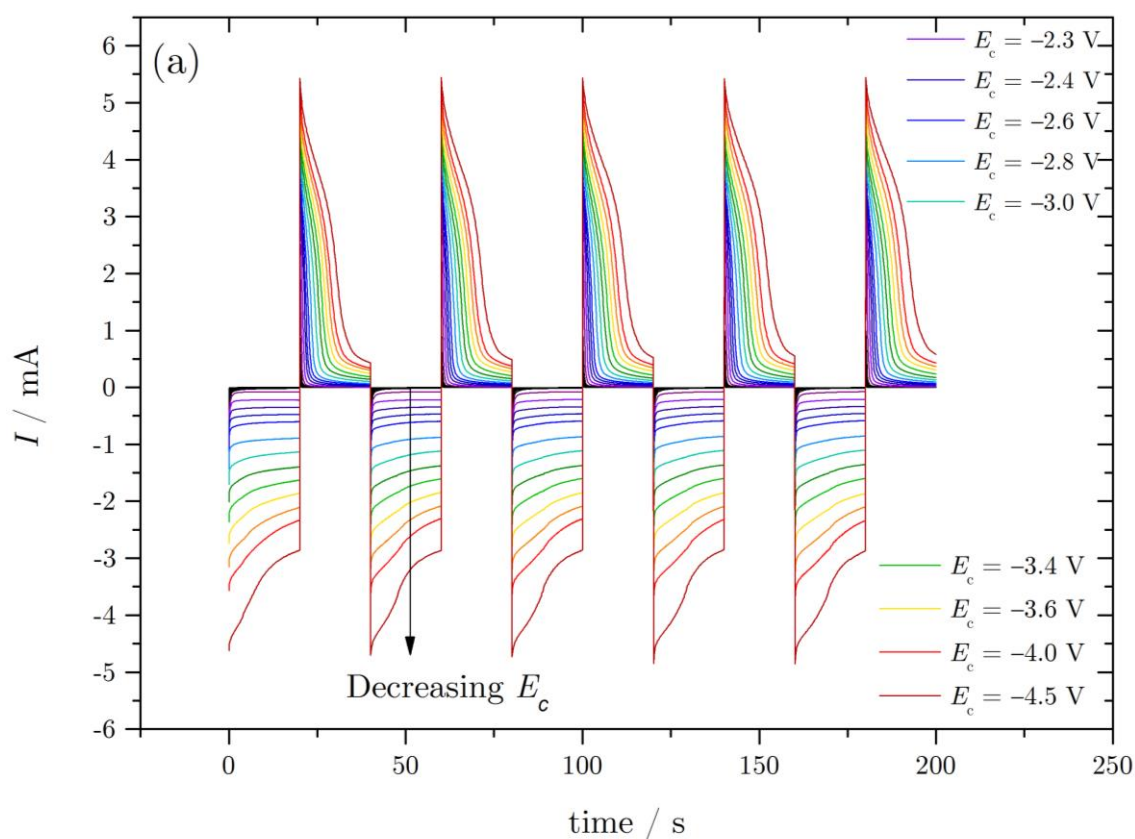


Figure 4.14(a) TEA⁺ charge/discharge showing 5 repeated charge/discharge cycles with decreasing E_c performed at a 3.5 mg HOPG electrode in TEABF₄ (0.1 M) in NMP, from which data was extracted from cycles two, three and four, and plotted in Figure 4.17

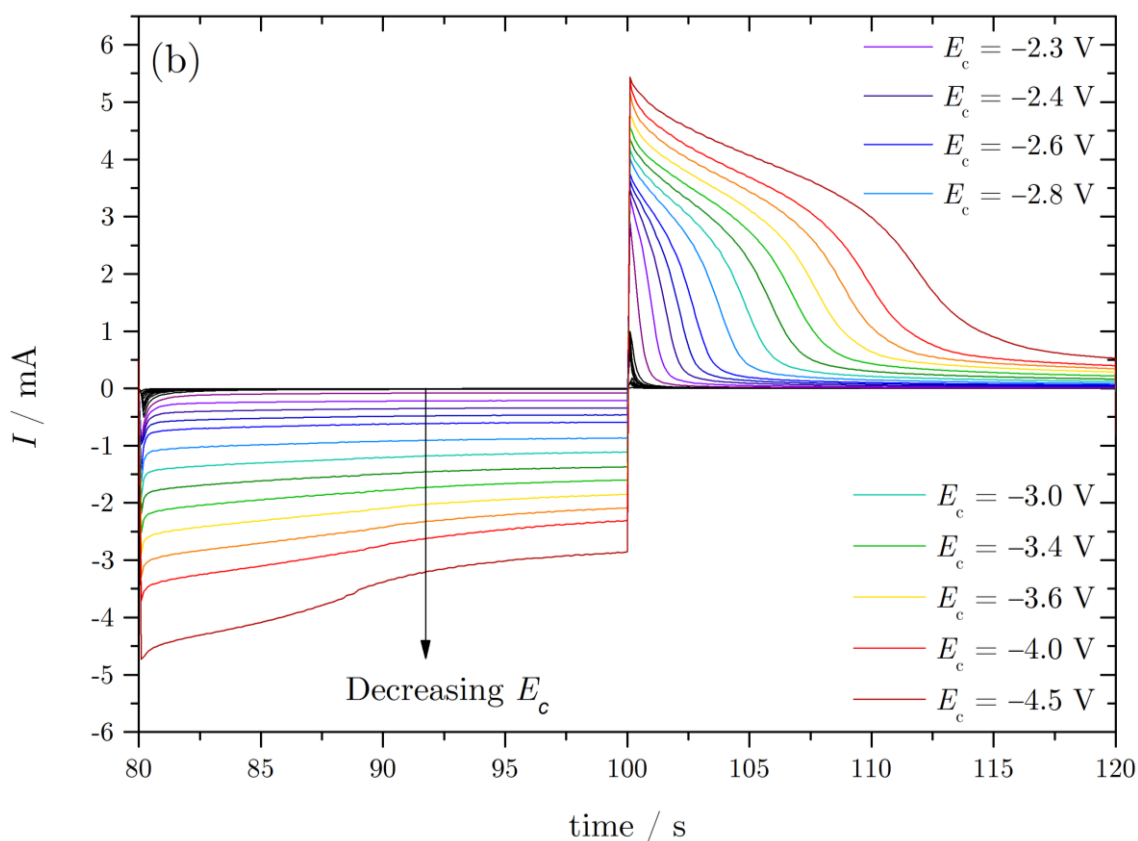


Figure 4.14(b) TEA⁺ charge/discharge showing a single cycle (3rd cycle) with decreasing E_c performed at a 3.5 mg HOPG electrode in TEABF₄ (0.1 M) in NMP

As previously, the data from these transients was used to construct average coulombic efficiency plots. Figure 4.15 shows the first run (4.15(a)) and a complete repeat of the system (4.15(b)) displaying the good reproducibility of this data. As with TMA⁺, the coulombic efficiency plot exhibits three stages: a sharp decrease in %_{ACE} is initially observed, followed by %_{ACE} recovery, until Q_d eventually becomes completely unrecoverable. This trend is explained in the same manner as with TMA⁺, and it would appear the cation size has no significant effects; however extended cycling at less negative potentials was again necessary in order to obtain 100% efficiencies, though the original dataset (Figure 4.15(a)) does show near-100% efficiencies already; possibly because of a smaller degree of surface oxide groups present than in the TMA⁺ study. To avoid potential damage to the gloves of the glove box during cutting of HOPG

samples, HOPG samples were always prepared outside of the glove box and, and the amount of time spent exposed to atmospheric conditions was not controlled between samples. Although samples were left for an equilibration time in the glove box prior to use, the required electrochemical ‘cleaning’ in TMA^+ (and TBA^+ , later) systems suggests that this equilibration time was not sufficient, or indeed possible, to remove all surface oxides for all samples.

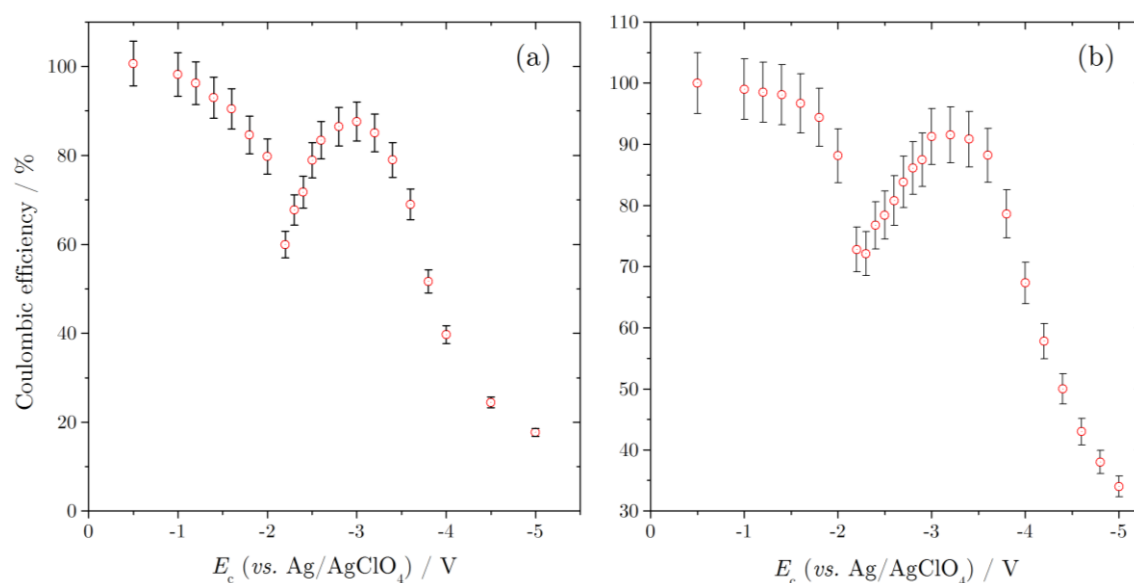


Figure 4.15) Plots displaying how TEA^+ charge/discharge efficiency is affected by decreasing E_c from values of -1 V to -5 V for (a) original dataset, and (b) repeated dataset

4.2.9 TBA⁺ electrochemistry

Finally, voltammetric analysis was repeated for the TBA⁺ system. Tetrabutylammonium has a crystallographic diameter of 0.826 nm,²⁴² significantly larger than HOPG's interplanar spacing, however has been shown to successfully intercalate between graphene sheets as a result of its flexibility and ability to form a flattened conformation.²⁴⁰ As with previous cations a GC electrode was employed as a comparative system. Figure 4.16(a) shows the resultant CV at a GC electrode, and like all other previous R₄N⁺ electrolytes studied, there is no intercalation current response observed at a GC electrode. However, there is a small current feature at *ca.* +0.5 V which is attributed to the oxidation of BF₄⁻.

On switching the WE for HOPG, the familiar intercalation/de-intercalation peaks are instantly visible, as seen with previous R₄N⁺ cations. Figure 4.16(b) shows that the resulting anodic peak current is related to the cathodic peak current, and figure 4.16(c) shows eventual CV reproducibility when only just exploring the intercalation potential region, here as expected the resulting de-intercalation peak current is relatively small (*ca.* 0.1 mA). Finally, Figure 4.16(d) shows that CV repeatability is possible even when scanning at potentials well within the intercalation region.

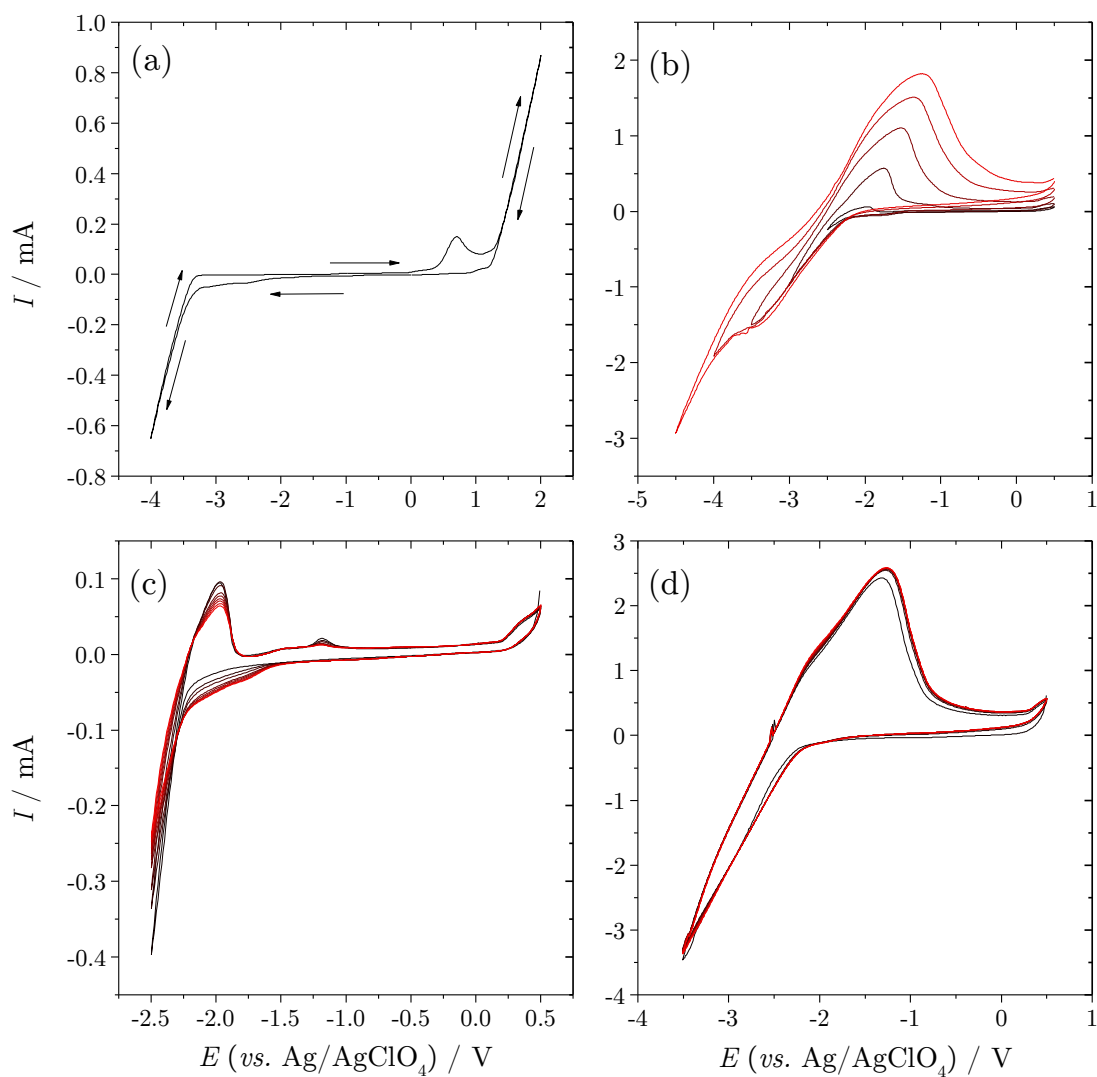


Figure 4.16) Voltammetric responses in 0.1M TBABF₄ in NMP, scanned at 100 mVs⁻¹ vs. Ag/AgClO₄, at (a) a GC electrode scanned over the whole potential window, (b) a HOPG electrode displaying the voltammetric effects of successively increasing the cathodic potential limit, (c) and (d) an HOPG electrode showing eventual CV repeatability

4.2.10 TBA^+ Average Coulombic Efficiency ($\%_{\text{ACE}}$) testing

In the same manner as previous galvanic cycling, charge/discharge was performed at a HOPG working electrode (2.2 mg, 50% submerged) in a solution of TBABF_4 (0.1 M) in NMP, from which the coulombic efficiency was determined and plotted as a function of E_c . Figure 4.17(a) shows the resulting transients over the entire E_c range. It can be seen that as E_c is decreased, the transients become less stable and increasingly unrepeatable with respect to successive cycles. Figure 4.17(b) shows the third cycle in more detail. Unlike TMA^+ and TEA^+ , no current ‘hiccup’ was observed with TBA^+ .

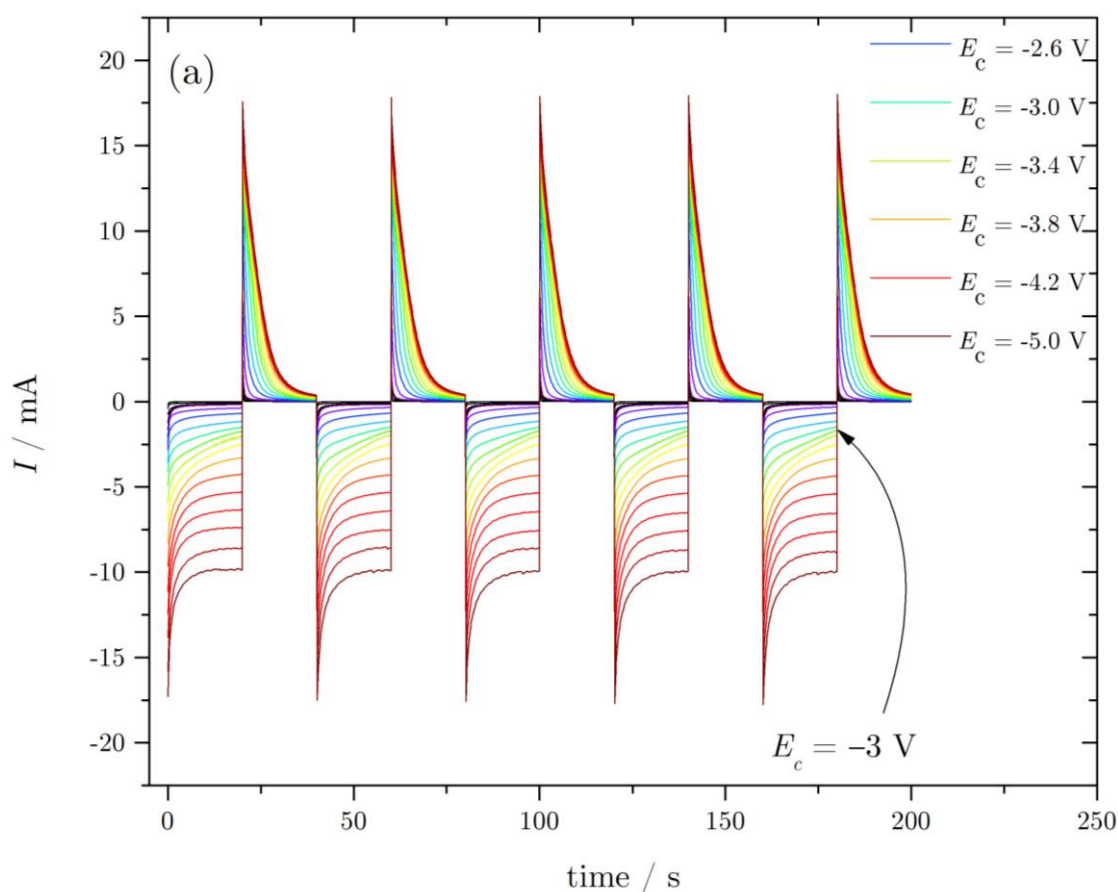


Figure 4.17(a) TBA^+ charge/discharge showing repeated charge/discharge transients for 5 cycles where $0.5 \text{ V} \leq E_c \leq -5 \text{ V}$

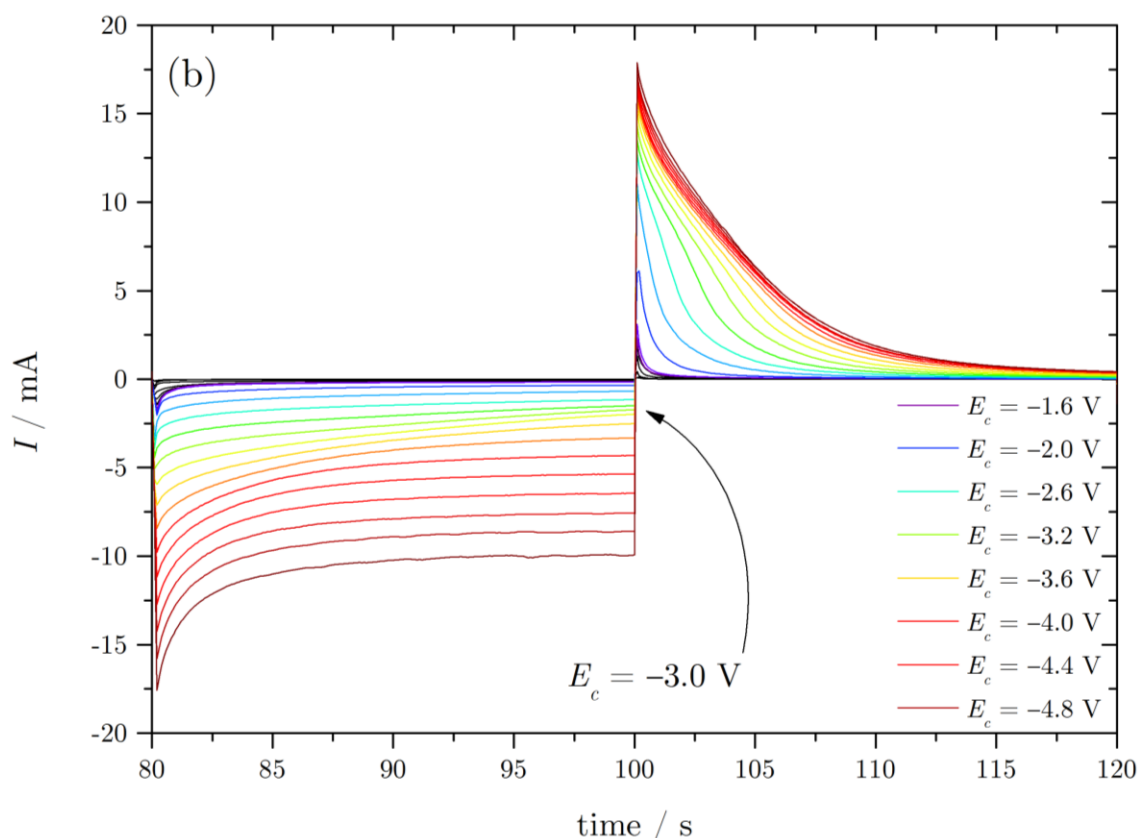


Figure 4.17(b) Zoom of a TBA^+ single cycle (3^{rd} cycle) of 4.17(a) where $0.5 \text{ V} \leq E_c \leq -5 \text{ V}$

From all the data in Figure 4.17(a) a coulombic efficiency plot was constructed (Figure 4.18(a)) and all data repeated in a fresh system with cleaned/prepared electrodes to construct Figure 4.18(b). The reproducibility of the data is again of a high degree and the familiar three trends are obvious in the plot. In Figure 4.18(a) the coulombic efficiency is unexpectedly high at less negative values of E_c : exceeding 100% efficiency, however as shown with other cations, prolonged cycling and data extraction from the 20^{th} - 25^{th} cycle produced coulombic efficiency values of the expected *ca.* 100% (Figure 4.18(b)). It was concluded from this, and from similar findings with TMA^+ and TEA^+ studies, that the extending cycling within this potential region facilitated the reduction of surface oxide groups on the graphite electrode, through electrochemical ‘cleaning’, allowing a chemically clean surface at which non-Faradaic charging processes could occur on future charge/discharge cycling.

Aside from the initial Stage I difference; where $E_c \geq -1.6\text{ V}$, the two plots not only display a high degree of reproducibility but also resemble the trends found previously with TMA^+ and TEA^+ .

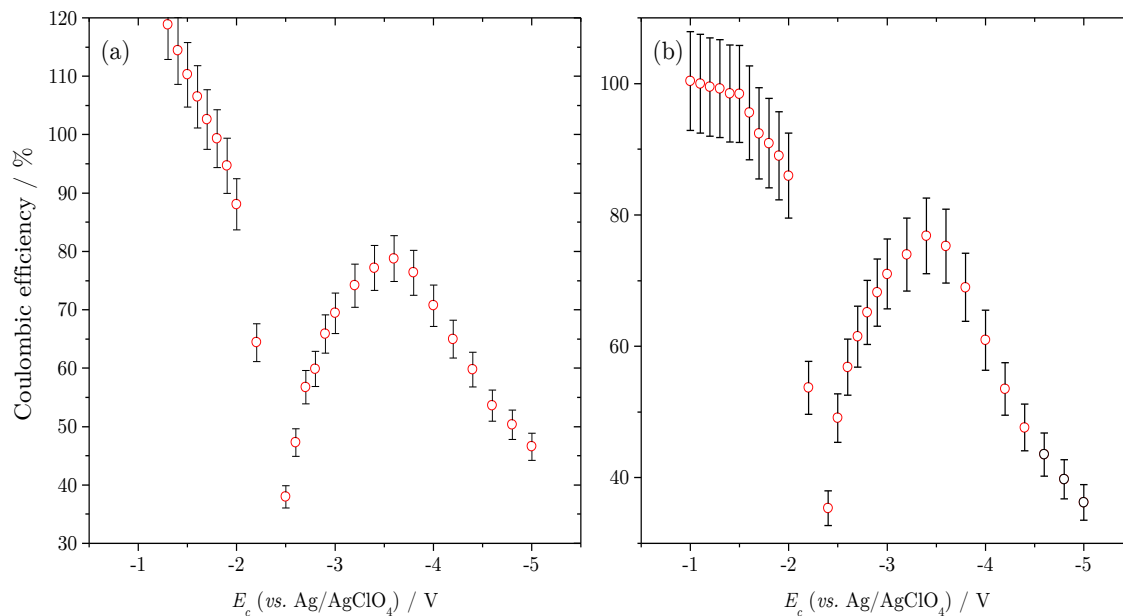


Figure 4.18) plots displaying how TBA^+ charge/discharge efficiency is affected by increasing E_c from values of -1 V to -5 V for (a) original dataset, and (b) repeated dataset with extended cycling for E_c values less than -2 V

4.2.11 Average Coulombic Efficiency ($\%_{ACE}$) comparisons

For graphical comparison, $\%_{ACE}$ plots for all R_4N^+ cations and lithium have been presented on the same plot, as well as the result from testing at a GC (non-porous, non-expandable) electrode. (Figure 4.19) Error bars have not been included in this plot for the purpose of clarity, though there is *ca.* 10% error estimated to be present within the data.

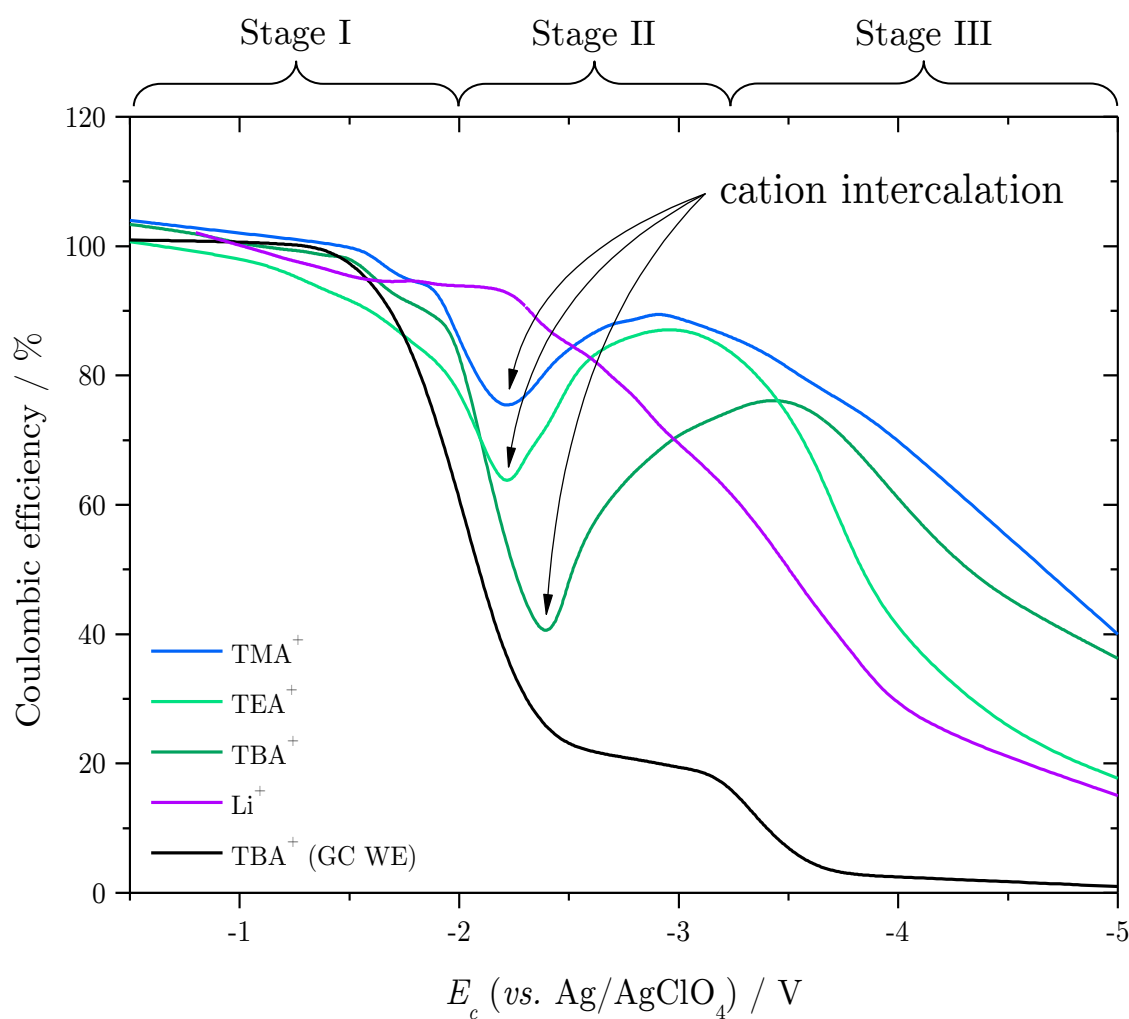


Figure 4.19) Comparative $\%_{ACE}$ trends for different tetraalkylammonium cations and lithium at HOPG as well as a GC electrode.

The most apparent detail of Figure 4.19 is the similar trends shown by all three tetraalkylammonium cations. The R_4N^+ trends exhibit three clear stages in the coulombic efficiency; the first stage is the relatively stable 100% coulombic efficiency until E_c reaches *ca.* -2 V. Stage I is when $0\text{ V} > E_c > -2\text{ V}$ and is associated with two processes: a) the electro-reduction of surface oxide groups present on the graphite cathode, which can eventually, with the use of prolonged charge/discharge electrochemical cleaning, be completely removed from the surface allowing near-100% cycling efficiencies to be achieved, and b) double layer charging of the electrode/solution interface, which resembles 100% coulombic efficiency once the electrode surface is chemically clean and absent of any surface oxidation.

Stage II, when $-2\text{ V} > E_c > -3\text{ V}$, initially shows a sharp decrease in the coulombic efficiency; indicating the onset of cation intercalation into the layered graphite structure. It is not totally clear why the coulombic efficiency should decrease at this point, since it is being proposed that intercalation has a stabilising effect upon the cations. However, it is believed that at these relatively positive potentials, either ion-trapping occurs *via* intercalation without significant electrode expansion, or a R_4N^+ -equivalent of Li^+ -SEI formation occurs. Whichever mechanism holds, the plot indicates that charge is lost somewhere, and therefore some irreversible process occurs.

However, in the latter stages of Stage II, a sudden recovery of $\%_{ACE}$ at *ca.* 2.2 V (TBA^+ at *ca.* 2.4 V) begins. This feature is significant and has been attributed to permitted *reversible* intercalation, as a result of the onset of irreversible electrode expansion.

It is thought that electrode expansion has two implications; it allows cations trapped in the host structure from Stage I to de-intercalate freely back into the bulk electrolyte, contributing positively to Q_d . Secondly, and more

significantly, it provides additional surface area at which the electrolyte double layer can form, allowing for additional Q_c storage at the electrode/electrolyte interface.

Eventually, in Stage III, the stabilisation effects provided by the graphite expansion cannot compete with the extreme cathodic conditions, and both the solvent and electrolyte are irreversibly reduced. This is reflected by the steady decrease in the coulombic efficiency at potentials more negative than *ca.* -3 to -3.5 V.

These three stages have been labelled on Figure 4.19, though it is important to note that although Stage I is relatively easy to define with the onset of intercalation, there is a comparatively large degree of overlap between Stage II and Stage III due to the competing electrode expansion and electrolyte/solvent breakdown processes, as well as the elongation of potential observed with TBA^+ .

Importantly, Figure 4.19 shows that different maximum recoveries are achievable for the three R_4N^+ species, and this maximum recovery (between *ca.* -3 V and -3.5 V) is related to increasing cation size. However it should be noted that there is a relatively large degree of error (between 5 – 10%) associated with the trends. The peak efficiency of the three cations is within a similar potential region, though that of TBA^+ is *ca.* 0.5 V more negative than that of TMA^+ and TEA^+ . It should be noted that the potential at which charge recovery begins is *ca.* 0.25 V more negative for TBA^+ than for TMA^+ and TEA^+ . This implies that TBA^+ intercalation requires slightly more negative potentials than the smaller cations, which could be attributed to the greater crystallographic diameter of TBA^+ requiring more energy to force the cation between the graphene galleries, indeed this is in agreement with the voltammetry (Figures 4.13(b) and 4.16(d)) in which the peak current of TEA^+

reduction is at *ca.* -2.75 V and the peak current of TBA^+ reduction is at *ca.* -3.5 V. However, though the peak of the coulombic efficiency for TEA^+ and TBA^+ agrees with the respective CVs, the same cannot be said for TMA^+ , though the current responses in the TMA^+ CVs are not as well-defined as those for the larger cations.

The decreasing peak efficiency with crystallographic diameter is counter-intuitive, since we are relating increasing degree of electrode expansion with increase in charge recovery, and as TBA^+ offers a greater degree of expansion it would be reasonable to assume TBA^+ should offer the greatest degree of recovery. However the opposite trend is observed and, with respect to reaching 100% efficiency, the coulombic efficiency peaks sooner for TBA^+ than TEA^+ and TMA^+ . One explanation might be that TBA^+ is simply more easily reduced than the smaller cations, however since the peak efficiency of TBA^+ charge recovery occurs at more negative potentials than the smaller cations, and because TBA^+ reduction occurs at more negative potentials on the voltammetry, this would appear to be an unlikely explanation.

Alternatively, if we consider the spatial constrictions offered by the layered structure on the different cations, the graphene galleries should accommodate more TMA^+ species than TBA^+ species, simply as a result of spatial restrictions (Figure 4.20).

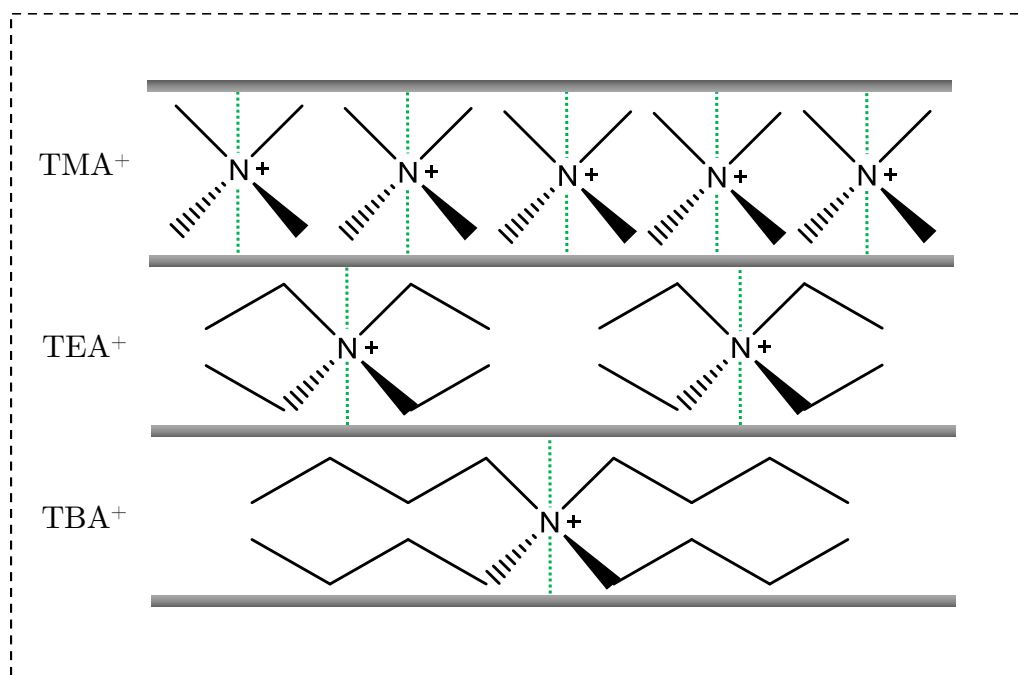


Figure 4.20) Schematic highlighting the spatial restrictions incurred as a result of increasing cation size

This effect could explain why it appears TBA⁺ requires greater energy (more negative potentials) to be completely reduced, since the stabilisation energy from the neighbouring graphene sheets is delocalised over a greater area, offering effectively greater stabilisation.

The combination of improved TBA⁺ stability (because of fewer intercalated species) along with a greater degree of TBA⁺-trapping due to the comparatively lengthy alkyl groups, could be the underlying reasons for the elongated coulombic efficiency curve of TBA⁺.

Finally, although the system is still competing with unrecoverable solvent breakdown at large cathodic potentials, it is thought that the aforementioned cation stabilisation effects help prevent solvent breakdown. Since it has been suggested that the products of R_4N^+ reduction can cause ring-opening of NMP (Figure 3.20), prevention of R_4N^+ reduction could in turn prevent some decomposition of NMP. This could help explain why the coulombic efficiency for TBA^+ remains higher than TMA^+ and TEA^+ at larger values of E_c .

Perhaps equally striking are the lithium and GC trends, exhibiting very little to no charge recovery mechanism thus strengthening the hypothesis that electrode expansion as a result of intercalation into a layered structure, has the direct consequence of stabilising GICs: shown by the increase in coulombic efficiency recovery. The lithium trend shows a steady decrease in the coulombic efficiency with E_c , as a result of continuous non-recoverable SEI formation on timescales too short for sufficient coverage to allow for reversible lithium intercalation. Finally the TBA^+ trend at a GC electrode exhibits a slight plateau of the coulombic efficiency, in the same potential region as the layer HOPG trends. This indicates that a degree of charge recovery (or TBA^+ stabilisation) is occurring, though no intercalation is possible at GC electrodes. This recovery occurs due to surface adsorption and subsequent stabilisation; naturally the degree of stabilisation from the adsorption mechanism is significantly less than that of the intercalation mechanism, since there is only one stabilisation ‘surface’ provided by adsorption stabilisation (Figure 4.21(a)) in contrast to the ‘two surfaces’ provided by the graphene galleries during intercalation (Figure 4.21(b)). Furthermore, the intercalation mechanism provides significantly more surface area than the adsorption mechanism, therefore allowing for a much greater degree of cation stabilisation.

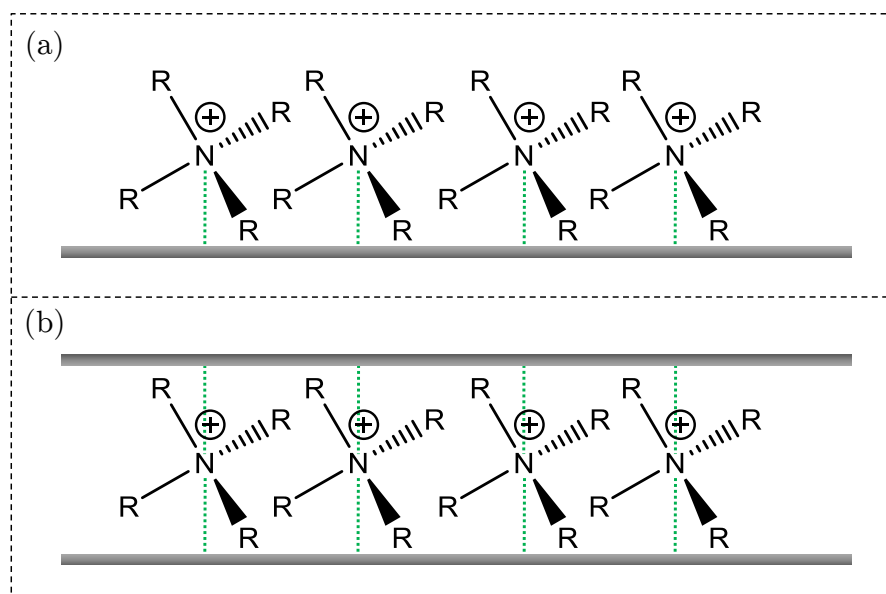


Figure 4.21) Schematic showing the differences in degree of stabilisation provided by a) a surface adsorption mechanism, and b) a gallery-intercalation mechanism

4.2.12 Quantitative electrochemical intercalation studies

Truly reversible electrochemical systems, such as those exemplified with the use of the classical ferrocene/ferricenium redox couple, require fast enough electron transfer kinetics to maintain chemical equilibrium, *i.e.* the concentrations of both O and R are equal, at the values required by the Nernst equation, at the electrode surface. Symmetrical CV shapes about E^0 , where the redox couple remains in equilibrium throughout the entire potential sweep are a characteristic trait of reversible processes. Conversely, non-symmetrical or skewed CV shapes are typical of slow electrode kinetics or quasireversible electrochemical processes.

Since true reversibility requires fast enough electron transfer rates to maintain equilibrium, it must also depend on the standard heterogeneous electron transfer (ET) rate (k_s) and the rate of change of the applied potential (the scan

rate, ν). The system is said to be quasireversible if the ratio of k_s/ν is sufficiently small such that equilibrium surface concentrations cannot be maintained.¹⁶² As mentioned in section 2.4.1 reversible systems are characterised by a peak separation of $\Delta E_p = 59/n$ mV. ΔE_p values > 59 mV are typical of quasi-reversible kinetics, with ΔE_p increasing with ν .¹⁶² Therefore, it is possible to obtain true reversibility at slow enough scan rates, at which the slow ET becomes comparable to the rate at which the surface concentrations can adjust. However, an increase in ΔE_p with ν is not just limited to quasi-reversible behaviour, and can also be attributed to the presence of uncompensated solution resistance in the cell.

Despite the use of Randles-Ševčík analysis being restricted to truly reversible systems,¹⁶² it has been initially employed here to probe the diffusion related phenomena observed during the intercalation process and later compared to the Cottrell equation describing current dependence on time for a chronoamperometric experiment. The Randles-Ševčík equation relates the recorded peak current (I_p) of the reduction and oxidation processes to the rate at which the voltammetry is swept, as detailed in section 2.4.1 (Equation 2.22), and when systems are diffusion limited, is a useful tool to determine diffusion coefficients of redox active species at the electrode interface.

As has so far been presented here, CV of R_4N^+ on HOPG is not symmetrical about E^0 , typically displaying quasireversible type CVs with large peak separations (*ca.* 500 mV – 1 V). The observed quasireversibility of the intercalation process is thought to be a result of the several simultaneous processes occurring, involving both GIC formation and complete R_4N^+ reduction, as well as occurring close to the negative limit of the NMP potential window.

However it has been found that with TEA^+ containing electrolytes, it is possible to obtain more reversible voltammetry when employing much smaller 2 mm HOPG discs (only partially submerged); decreasing the working area of the electrode allows the retrieval of better-defined peak currents from the background non-Faradaic current, since it decreases the degree of storable charge at the electrode but has no effect on the concentration of R_4N^+ electrolyte. Interestingly, it was not possible to obtain such voltammetry with either TMA^+ or TBA^+ . Figure 4.22(a) shows the current response at a HOPG disc electrode in 0.1 M TBABF_4 in NMP, at various scan rates. It can be seen that at scan rates of 2 mV s^{-1} , the familiar broad ‘intercalation’ and ‘de-intercalation’ peaks are observed. However it can be seen that by scanning over a longer period of time reveals greater voltammetric detail, and scanning at 0.1 mV s^{-1} results in voltammetry with clear distinct peaks. Figure 4.22(b) indicates the complex nature of the intercalation/de-intercalation process, scanning at 0.1 mV s^{-1} , and it is clear that ‘intercalation’ and ‘de-intercalation’ previously shown are actually a cumulative effect of several current responses which are indistinguishable at sufficiently fast scan rates. Since it is a reasonable assumption that the electro-reduction of TBA^+ (or indeed any of the R_4N^+ cations studied) is a 1-electron transfer, these multiple current responses are attributed to different stages of the intercalation (section 3.1.2), in which increasing degrees of intercalation staging occurs, rather than several reduction steps associated with multi-electron steps, such as that of $\text{Au}^{(\text{III})}$ to $\text{Au}^{(0)}$.²⁶³

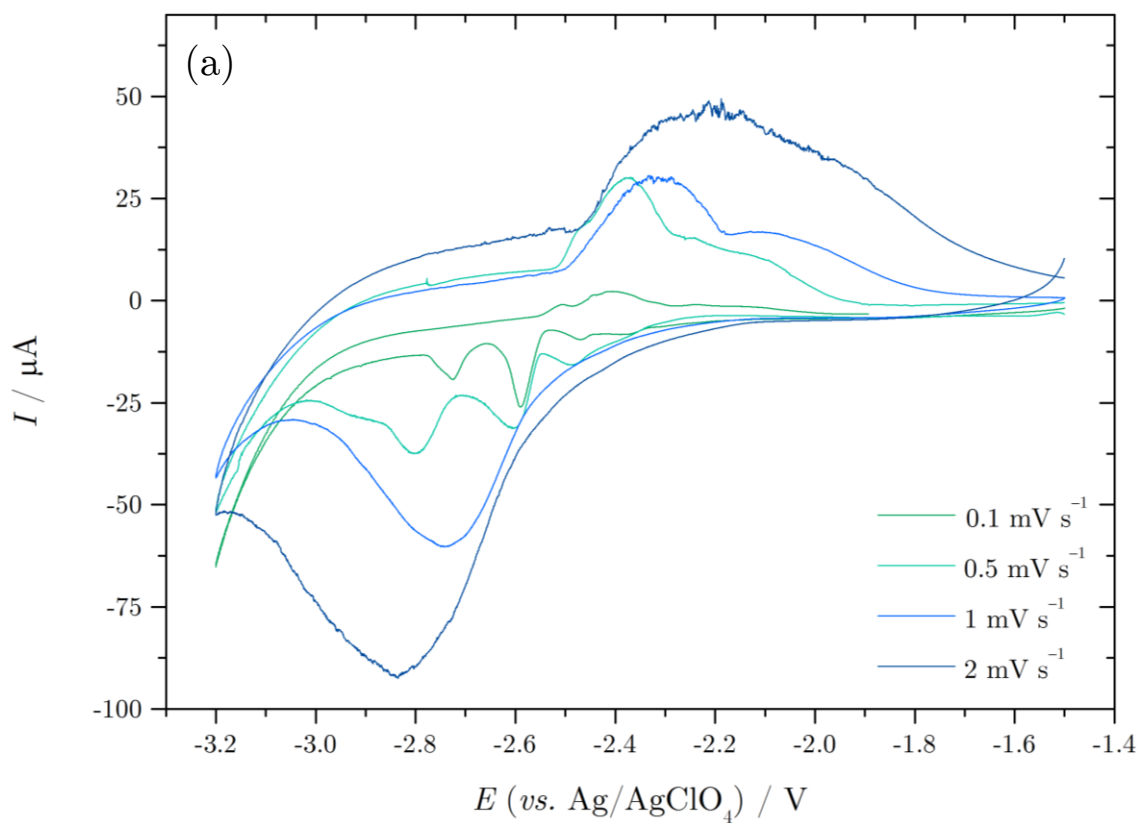


Figure 4.22(a) CV at a HOPG disc electrode in TBABF_4 in NMP, recorded at four different scan rates to highlight the effects of scan rate on the observed current responses, thereby indicating a staging phenomenon

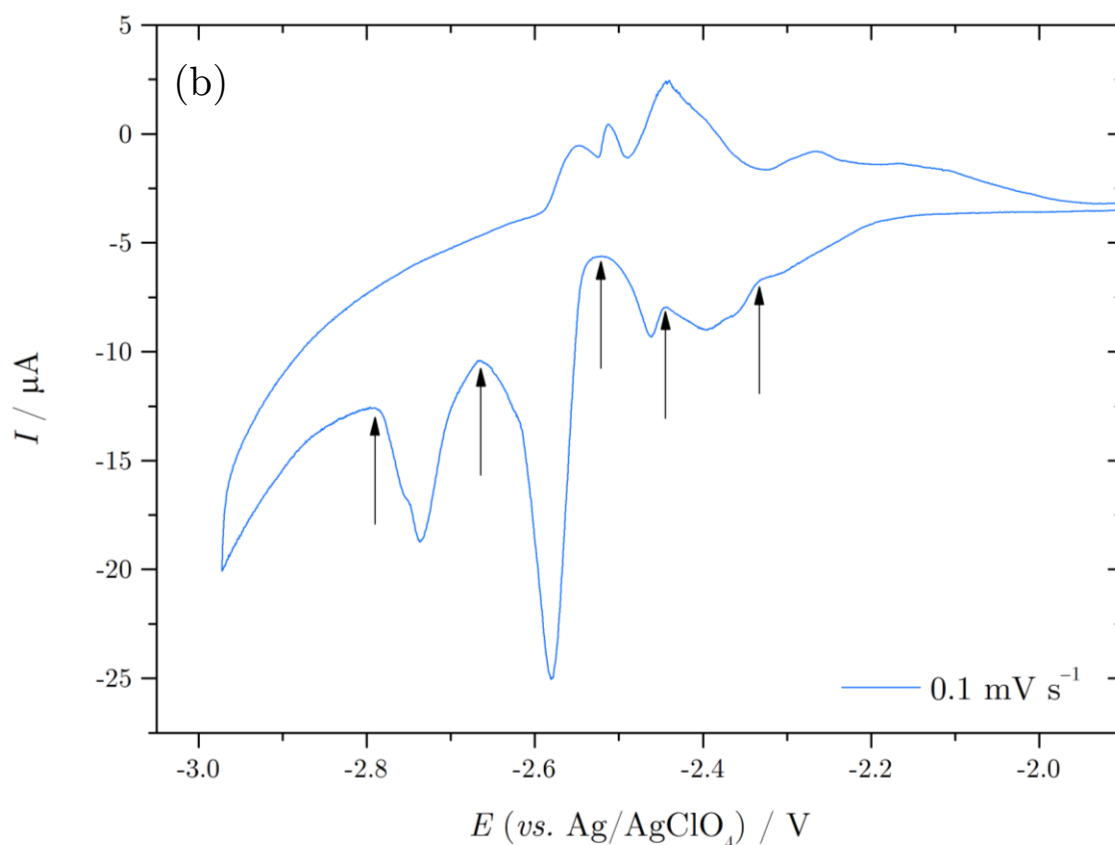


Figure 4.22(b) CV at a HOPG disc electrode in TBABF₄ in NMP, recorded at 0.1 mV s⁻¹ highlighting current steps associated with intercalation staging

The current steps (Figure 4.22(b), arrows) indicate the reduction of one stage to the next stage (indeed, de-intercalation staging is visible on the oxidative scan indicating oxidation of one stage to the next); Schoderböck *et al.* reported similar current steps in the intercalation of lithium into Madagascar graphite, and attributed these current features different degrees of stoichiometric staging.²⁶⁴ However staging has also been observed by other authors during electrochemical discharge and de-intercalation of the staged compounds.²⁶⁵

Incidentally over the course of the project, more reversible voltammetry was typically obtainable with the use of TEA⁺ containing electrolytes. This is within agreement with Simonet²⁴⁴ who also found similar voltammetry with TEA⁺, the reasons for which are currently unknown.

The dependence of the measured I_p and the ΔE_p , of both the associated TEA^+ intercalation and de-intercalation, on scan rate was investigated. (Figure 4.23)

Figure 4.23 shows the effect of varying the scan rate, between 20 mV s^{-1} and 100 mV s^{-1}) when cycling between -1 V and -3.5 V at a HOPG electrode (SPI-1, 3 mm disc) in TEABF_4 (0.1 M). Increasing scan rate was performed successively at the same HOPG sample, in the order: 20, 40, 60, 80, 100 mV s^{-1} . At fast scan rates (100 mV s^{-1}), the peak currents can be seen to reach a maximum of *ca.* 200 μA and a small peak ‘hump’ is visible at *ca.* -2.5 V on the reverse scan. On slowing the scan rate to 20 mV s^{-1} through intervals of 20 mV s^{-1} , the intercalation/de-intercalation current responses can be seen to decrease in magnitude and become better defined. The aforementioned unknown peak ‘hump’ can be seen to become much better defined, forming a small peak with a shoulder at *ca.* -2.4 V .

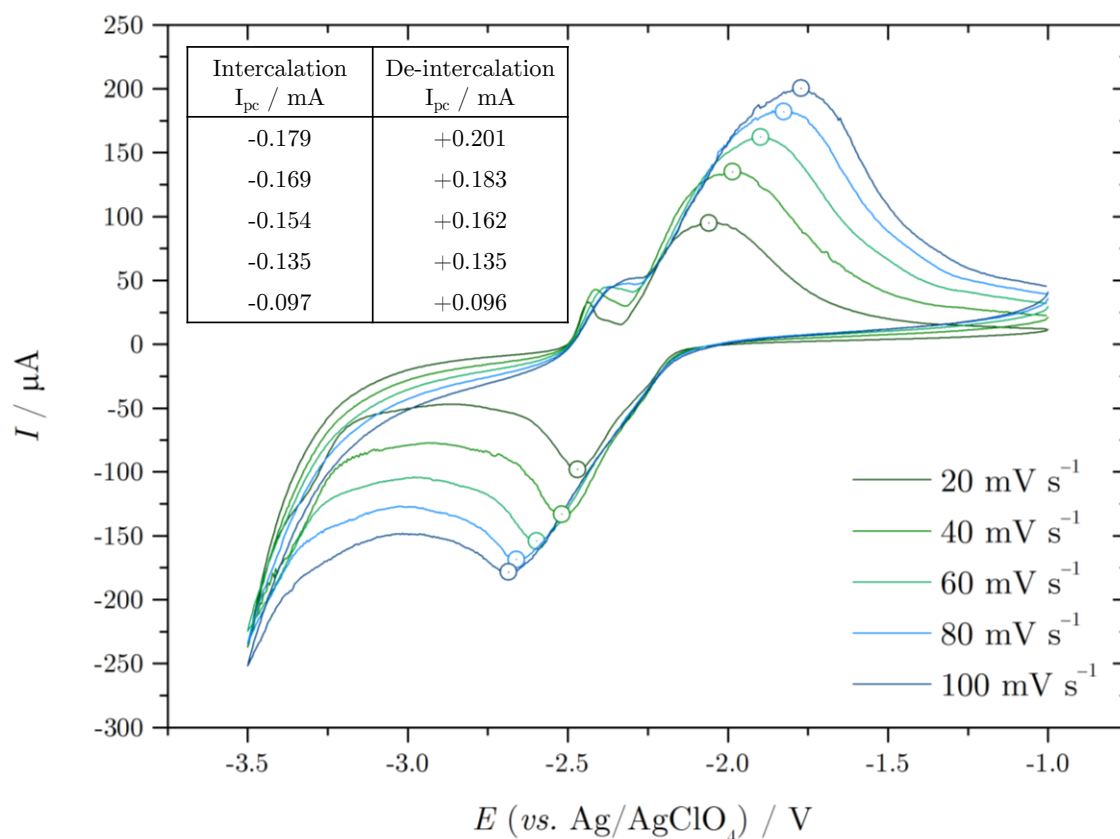


Figure 4.23) CVs showing the effects of varying scan rate on voltammetry between 20 mV s^{-1} and 100 mV s^{-1} , at a HOPG electrode in TEABF_4 (0.1 M) in NMP

Two other distinctive features arise from decreasing the scan rate of the recorded CVs, include a significant ΔE_p decrease from *ca.* 1 V to *ca.* 0.5 V on reducing the scan rate by nearly a factor of 10, and better defined peak currents are visible, implying that charging currents are more significant at faster scan rates and therefore, at slower scan rates, Faradaic processes are better resolved from the background current. Additionally, slower scan rates allow the graphene sheets more time to “open up”, thus allowing voltammetric analysis on a more comparable timescale. Although the rate of electron transfer is fast, the rate of intercalation/exfoliation is comparably slow; therefore hinders the rate of which the potential can be scanned.

The small peak at *ca.* -2.5 V that arises on the reverse anodic scan can be seen to become more prominent at slower scan rates, and actually shifts slightly to more negative potentials.

Figure 4.24 shows the current response when swept at a scan rate of 1 mV s^{-1} and a further decrease in the peak separation of the respective processes is visible. Interestingly, when the negative limit of the potential window is increased from -3.25 to -3.5 V, a clear reduction peak is surpassed and the magnitude of the unknown peak can be seen to increase by *ca.* 100 %, whereas the magnitude of the main de-intercalation peak is unaffected. This shows that the two peaks are related, and occur independently of the main intercalation/de-intercalation current features. At present the origin of this small peak is unknown, but is thought to be the re-oxidation of the species reduced at *ca.* -3.25 V.

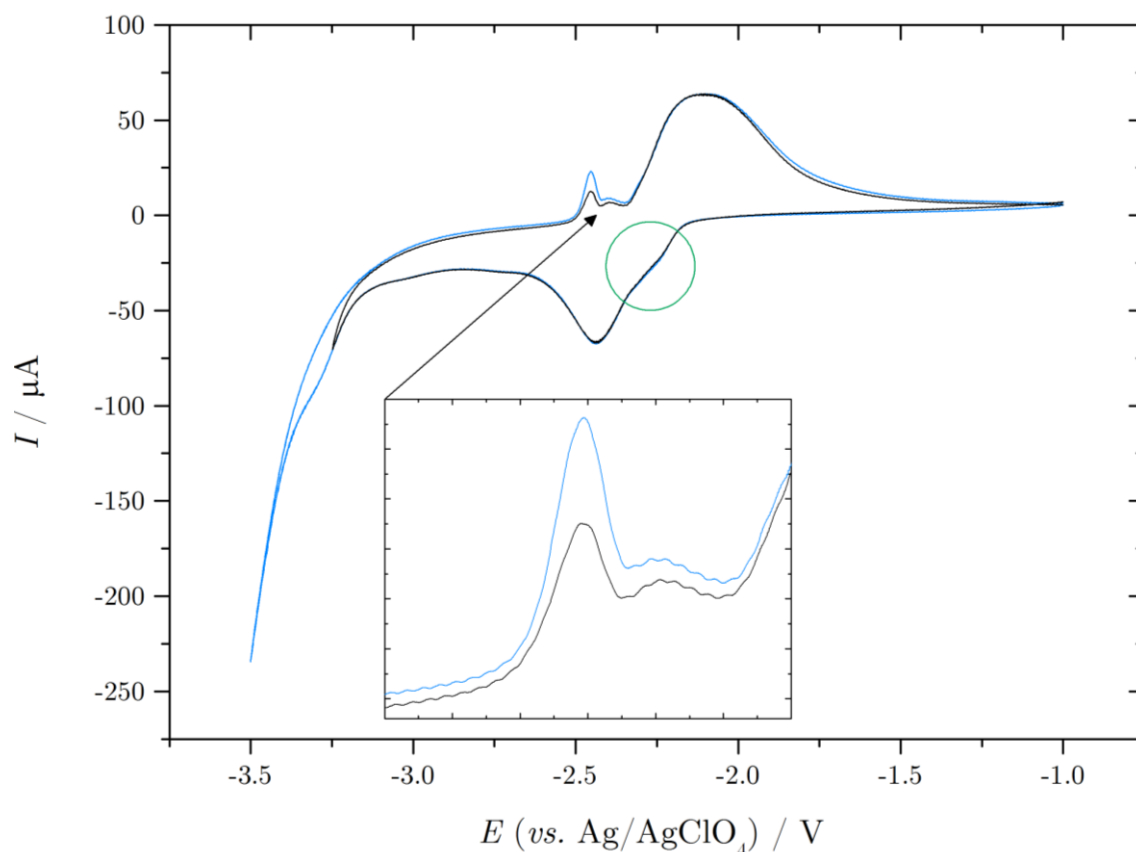


Figure 4.24) CVs showing the effects of increasing the negative limit of the potential window by 0.25 V on the anodic peaks during the reverse sweep, at a scan rate of 1 mV s^{-1} , at a HOPG electrode in TEABF_4 (0.1 M) in NMP

Finally, the scan rate was decreased to 0.1 mV s^{-1} and the resultant CV is presented in Figure 4.25. It can be seen that scanning over a prolonged time period reveals a significant number of subtle current responses previously unobservable at more practical scan rates, as well as decreasing the ΔE_p of the most prominent current features to 136 mV. Simonet observed electrolyte concentration dependant step like features in TBA^+ voltammetry at graphite electrodes, though an explanation as to the origin of these steps is not provided.²⁴⁴

Despite the 136 mV peak separation, the assumption of a 1-electron reduction is valid; since the oxidation state of R_4N^+ decreases by one integer once reduced

to the neutral R_3N species. However, it is unlikely that the peak separation should reach 59 mV, since mass-transport for diffusion/intercalation would presumably be sufficiently different from diffusion in the bulk solution.

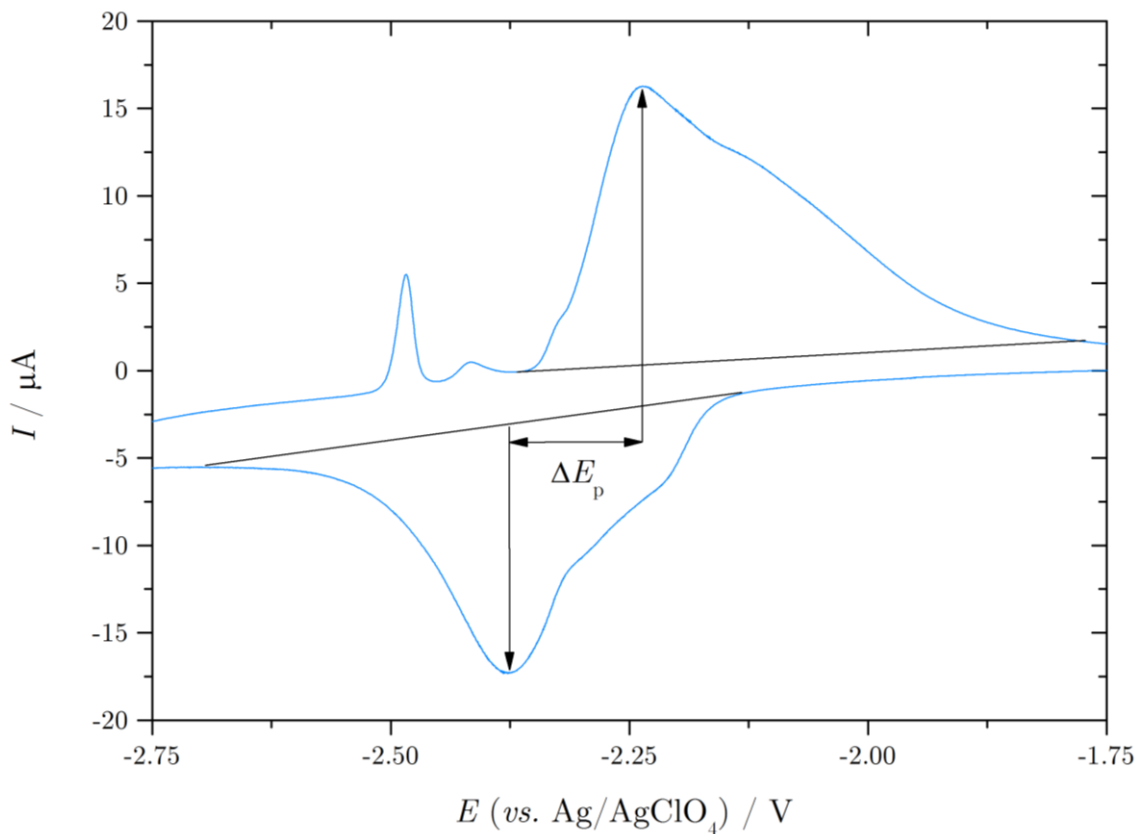


Figure 4.25) CV showing the effect of slowing the scan rate to 0.1 mV s^{-1} revealing subtle current responses not previously observed, indicating the complex nature of the TEA^+ intercalation/de-intercalation process, at a HOPG electrode in TEABF_4 (0.1 M) in NMP

Figure 4.23 shows the peak currents (circled) of the respective intercalation and de-intercalation peaks, and these values were used to construct a typical linear Randles-Ševčík plot, presented in Figure 4.26 relating recorded I_p to the square root of scan rate.

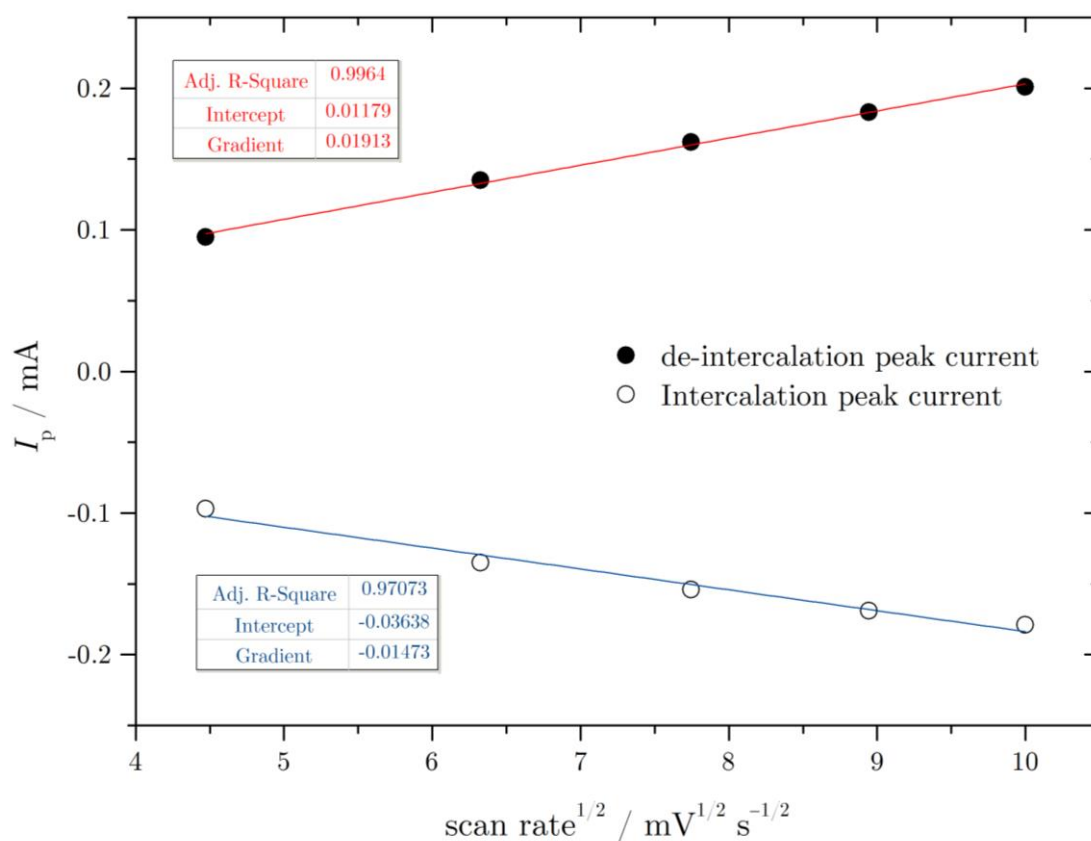


Figure 4.26) Randles-Ševčík plot for both the intercalation and de-intercalation peak currents observed for the intercalation/de-intercalation of TEA^+ at a HOPG electrode submerged in a solution of TEABF_4 (0.1 M) in NMP

Figure 4.26 shows the linear relationship between square root of scan rate and the I_p of the respective processes, and the two differing gradients are attributed to the quasireversible nature of the system. It should be noted that the gradients are of a similar magnitude, $-0.015 \text{ A mV}^{-1/2} \text{ s}^{1/2}$ for intercalation *cf.* $-0.019 \text{ A mV}^{-1/2} \text{ s}^{1/2}$ for de-intercalation, indicating that relatively equal amounts of current are generated on the forward and backwards scans, and the system is close to reversible when scanning in potential regions not extending below the cathodic limit of -3.5 V . This is in good agreement with $\%_{\text{ACE}}$ plots as shown in 4.2.11.

Usually Randles-Ševčík plots are employed to determine the diffusion coefficient of the redox couple in question; however this model assumes a freely diffusing redox couple in dilute solution. This analysis was attempted for the intercalation system using the gradient of the plot above and Equation 2.22.

From equation 2.22 we can establish that the gradient is a function of D , the diffusion coefficient, in the form of $0.4463nFAc\left(\frac{nFD}{RT}\right)^{1/2}$. The clear problem with this is the inclusion of surface area of the working electrode, which in the case of HOPG has been found to expand on exposure to R_4N^+ based electrolytes under applied cathodic potentials, thereby resulting in an unknown active area. For this reason, diffusion coefficients calculated in this manner can only be expressed in terms of an unknown area, and therefore cannot be explicitly defined. The same problem arises in employment of the Cottrell equation, as described in section 2.4.2, since the known electrode area is also required.

It would be interesting to determine whether the diffusion of the R_4N^+ cation in the bulk solution is the same as during intercalation between the graphene galleries. The diffusion coefficients of TMA^+ , TEA^+ and TBA^+ in water are $1.07 \times 10^{-5} \text{ cm}^2 \text{ s}^{-1}$,²⁶⁶ $0.87 \times 10^{-5} \text{ cm}^2 \text{ s}^{-1}$,²⁶⁷ and *ca.* $0.45 \times 10^{-5} \text{ cm}^2 \text{ s}^{-1}$,²⁶⁸ respectively. Therefore by correcting for the viscosity of NMP (1.7 mPa s) we obtain diffusion coefficients with respect to NMP; $6.29 \times 10^{-6} \text{ cm}^2 \text{ s}^{-1}$, $5.12 \times 10^{-6} \text{ cm}^2 \text{ s}^{-1}$ and $2.65 \times 10^{-6} \text{ cm}^2 \text{ s}^{-1}$, respectively.

Although the Randles-Ševčík plot displays a good linear correlation, the process cannot be strictly diffusion controlled since the absence of a masking supporting electrolyte results in transport of R_4N^+ to the electrode *via* migration as well as diffusion.

Secondly, the formation of the GIC could proceed *via* a combination of surface adsorption and deposition processes, as well as the possible staging phenomenon

addressed previously, involving several reduction steps. Thirdly, Randles-Ševčík assumes planar diffusion at the electrode interface, and whereas this is true near the electrode surface, it is an invalid assumption given the complex nano-scale layered structure of the graphite cathode, especially on volumetric expansion as a result of ion intercalation. Finally, the peak separation cannot solely be a function of the scan rate since the system is likely exhibit a certain degree of solution resistance. All these limitations, as well as the ever expanding electrode area as a result of R_4N^+ intercalation, make detailed analysis of the intercalation mechanism challenging.

4.2.13 Is the intercalation mechanism, diffusion controlled?

During double layer capacitance charging at potential E , the behaviour of the current, I , with time, t , is analogous to that of an electrical circuit consisting of a resistor and capacitor connected in series, and follows an exponential relationship:

$$I = \frac{E}{R_s} e^{-t/R_s C_d} \quad (4.2)$$

Where R_s is the resistor representing the solution resistance, and C_d is the capacitor representing the double layer capacitance. $R_s C_d$ is often simplified to the time constant τ .¹⁶² Since I is proportional to e^{-t} in double layer charging processes, plotting $\ln(I)$ against t should yield a linear relationship if the system proceeds *via* totally non-Faradaic processes.

Figure 4.27 shows the resulting $\ln(I)$ *vs.* t plot calculated from TMA^+ charge/discharge transients for decreasing values of E_c at a HOPG electrode in NMP. From looking at the charging transients for all three R_4N^+ species, it is clear that there are definite features which correlate the three stages identified

earlier in the coulombic efficiency data. The different stages are more noticeable with TMA^+ , than with the larger cations. However, when E_c is less negative than -2.4 V, the charging transients do not exhibit linear gradients as one would expect; these potentials being within the region of double layer charging. The reason for this is not understood at present. However, despite the non-linear transients obtained for less negative charging potentials, the charge and discharge transients for all the cations are relatively similar in shape; indicating that reversible charge/discharge is occurring within this potential region, or that the processes occur at the same rate and magnitude.

However, there is a significant change in the transient shape when the charging potential reaches -2.4 V, the potential at which intercalation begins, and interestingly the transients exhibit a clear increase in the degree of linearity. This is counterintuitive; since it has been shown this is the region in which Faradaic processes begin to occur. This linearity is most prominent when $E_c = -2.4$ V/ -2.6 V, but is soon disrupted when E_c is decreased to -2.8 V/ -3 V, and the familiar current ‘hiccup’ appears during TMA^+ charge/discharge since the logarithm analysis does not completely remove this feature from the original dataset completely, though little evidence of the blip remains in the TEA^+ case. Despite this hiccup, the gradients before and after this feature appear similar in magnitude and the hiccup was not included in calculation of gradient values.

The discharge transients, on the other hand, begin to exhibit a shoulder as soon as the ‘intercalation potential’ is reached, and this shoulder becomes more prominent with increasingly negative values of E_c . As can be seen from Figures 4.27 and 4.28, corresponding to TEA^+ and TBA^+ charge/discharge, respectively, the shoulder observed on the discharge transient is not dependent upon the current blip observed in the charging transient, since TEA^+ and TBA^+ cycling does not exhibit this feature. Perhaps more significant however,

is the fact that the degree of shoulder prominence is inversely related to the size of the cationic species; with TMA^+ cycling displaying a more prominent shoulder at more negative E_c values than observed with TEA^+ , which in turn displays enhanced prominence over TBA^+ .

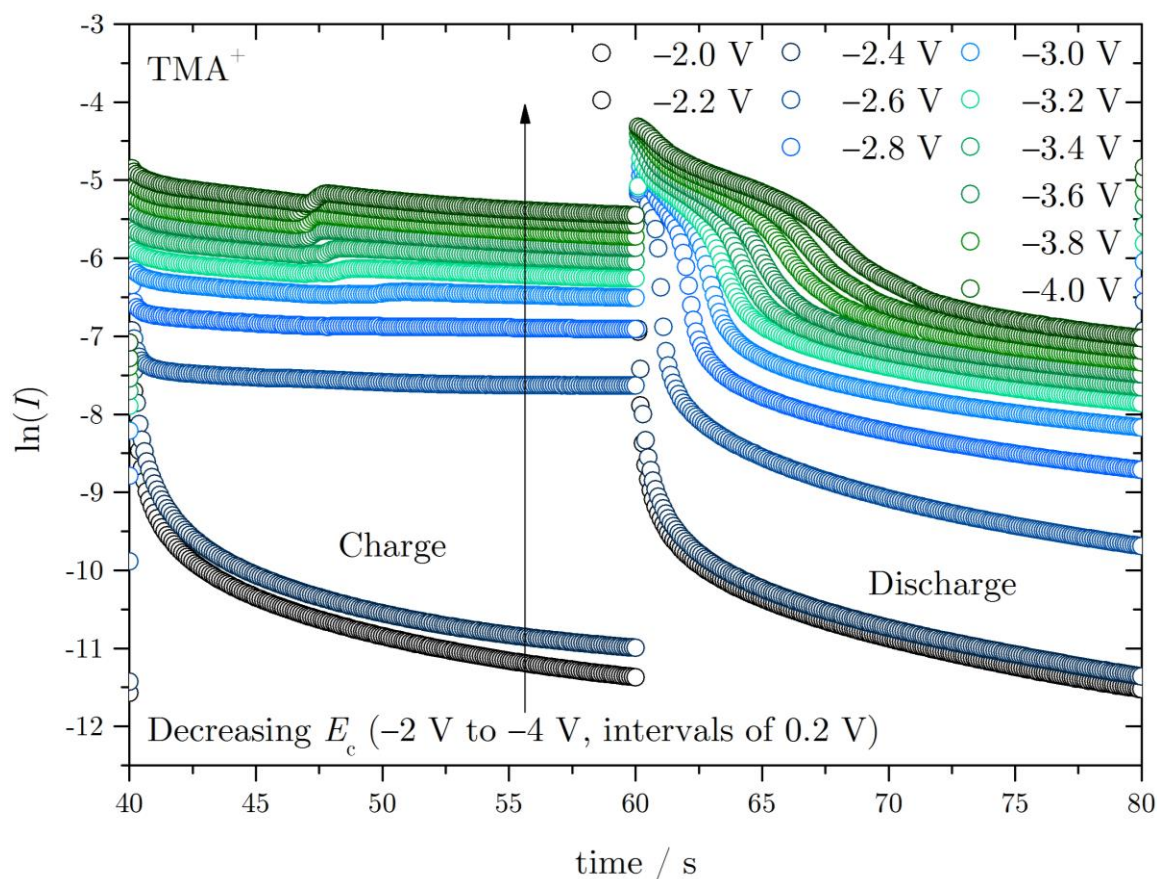


Figure 4.27) Charge/discharge plots, obtained from the second cycle of a series, of $\ln(I)$ *vs.* time, for TMA^+ cycling at a HOPG working electrode in NMP. E_c was varied between -2 V and -4 V. Discharge was conducted at 0 V in all cases.

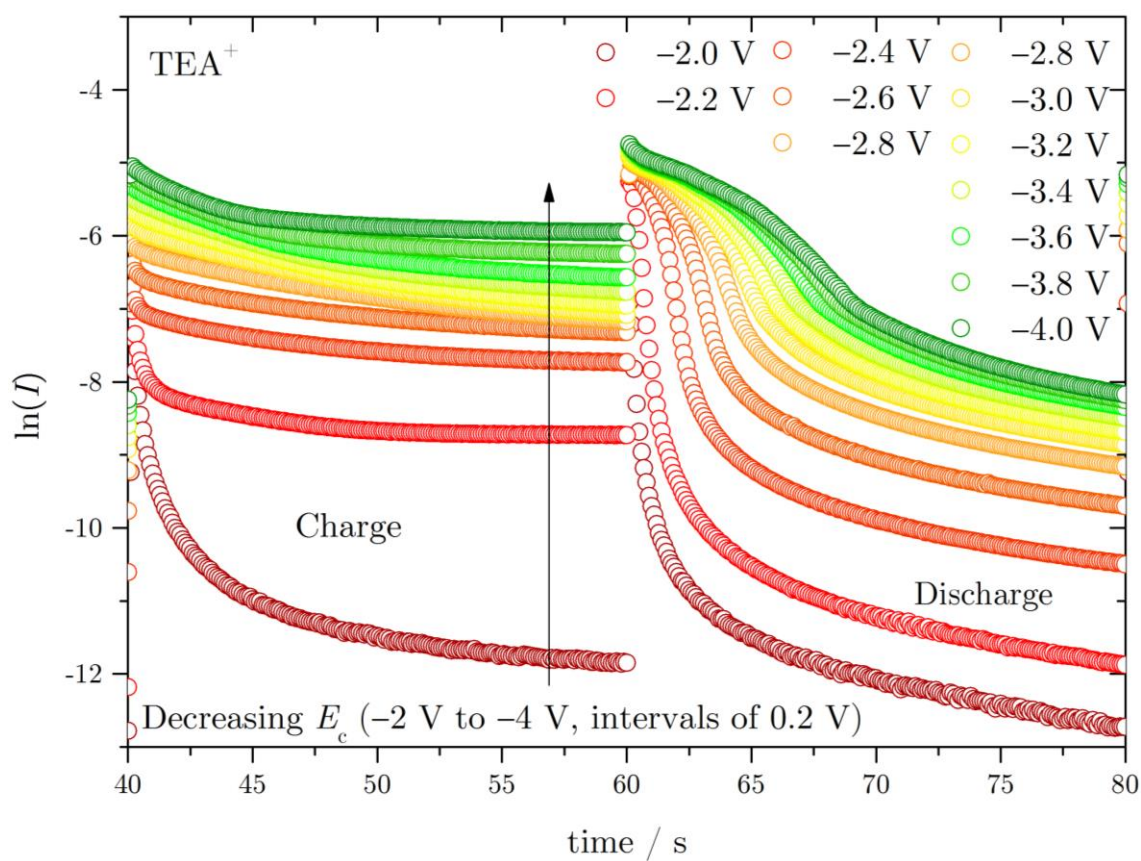


Figure 4.28) Charge/discharge plots, obtained from the second cycle of a series, of $\ln(I)$ *vs.* time, for TEA⁺ cycling at a HOPG working electrode in NMP. E_c was varied between -2 V and -4 V. Discharge was conducted at 0 V in all cases.

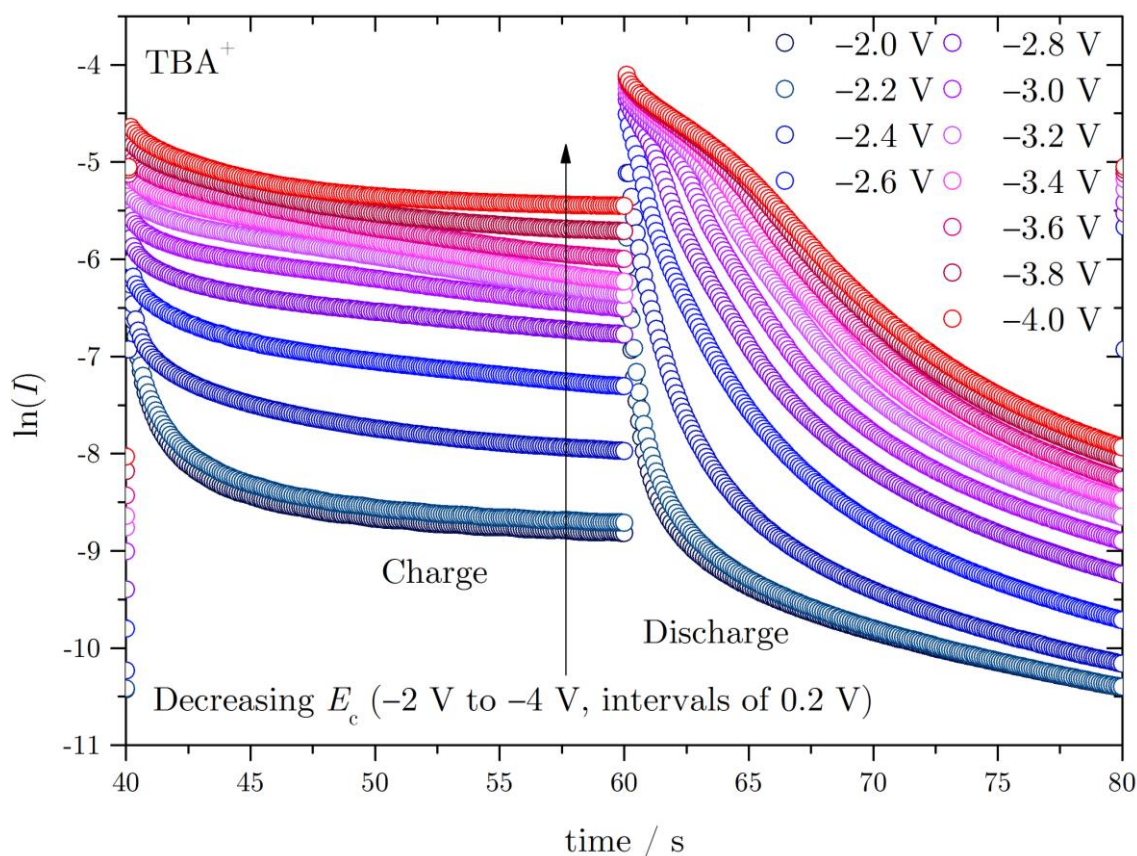


Figure 4.29) Charge/discharge plots, obtained from the second cycle of a series, of $\ln(I)$ *vs.* time, for TBA^+ cycling at a HOPG working electrode in NMP. E_c was varied between -2 V and -4 V. Discharge was conducted at 0 V in all cases.

The reasons for these observed transient shoulders during discharge are not clear at present, though the introduction of the shoulder actually increases the degree of linearity exhibited by the discharge transients, thereby suggesting that the de-intercalation eventually behaves more akin to a capacitor at more negative charging potentials. This seems unlikely, since unrecoverable charge loss has been shown to occur at such negative potentials, though electrode-expansion could facilitate diffusional-discharge, since fewer steric restrictions will occur.

These plots really only indicate that the intercalation and de-intercalation processes are not totally analogous to those of electrochemical double layer

capacitance charging, which is perhaps not overly surprising. However, interestingly the system appears to behave more akin to an electrochemical capacitor when experiencing large cathodic load, specifically when in the potential region of intercalation/GIC formation.

Since purely diffusion-limited current processes must follow a $t^{-1/2}$ relationship, because $I = kt^{-1/2}$, where k is equal to a constant of proportionality, or $nFAC\sqrt{D}/\sqrt{\pi}$ in the Cottrell equation¹⁶², intercalation/de-intercalation diffusion dependence can be assessed using natural logarithmic plots of $\ln(I)$ vs. $\ln(t)$, where a purely diffusion limited process should yield a linear gradient of $-1/2$ with intercept $\ln(k)$.

As can be seen in the $\ln(I)$ vs. $\ln(t)$ plots for charge/discharge using lithium and the three familiar R_4N^+ species (Figures 4.2(a-d)), the charging transients display relatively linear trends, with the respective measured gradients presented in Table 4. For all the cationic species studied here, the gradients of the charging transients decrease steadily from *ca.* -0.8 to *ca.* -0.1 . Even at E_c values more negative than the intercalation/GIC threshold, the gradients remain relatively linear indicating that the charging process is diffusion limited.

As can be seen from the discharge data ($4 > \ln(t) > 3$), none of the studied cations exhibit linear transients. The gradients of the discharge transients typically increase with decreasing E_c , and the familiar current shoulder can be seen on the R_4N^+ discharge transients (again, increasing prominence with decreasing R_4N^+ diameter), in contrast to Li^+ discharge where no shoulder feature is present and exponential decay is evident. This is the most surprising feature of all, since one would assume application of 0 V to the intercalated

system would have a purely diffusion limited effect, as the intercalated species are no longer potentially ‘held’ in their intercalation galleries and instead are permitted to diffuse out of the host structure. The explanation for this could be that the species are indeed ‘held’ in their intercalation galleries, and there is an activation barrier to their removal. In addition, mass transport *via* migration must also contribute to the intercalation/de-intercalation.

The shoulder on the R_4N^+ discharge transients only appears on the $E_c = -2.6$ V and more negative transients, and incidentally is the first transient exceeding the potential required for intercalation/GIC formation (-2.4 V). This suggests that the observed transient shoulder is related to the formation of a R_4N^+ GIC, and on de-intercalation the GIC cannot simply be expelled from the graphite cathode under diffusion control. Other than a possible activation barrier to the GIC oxidation and subsequent de-intercalation, the spatial restrictions of the graphite galleries could also prohibit diffusional mass transport.

From Figures 4.29(a-d) it can be seen that at less negative potentials the discharge transients are relatively similar in shape for all the cations studied; indicating that the same de-intercalation process occurs for all of the cations, though the non-linearity of the transients indicate the process is not diffusion controlled. However it is clear that when the charging potential is decreased to cathodic potentials more negative than *ca.* -2.6 V, the rate of current decay decreases with increasing cation diameter, showing greater shoulder prominence for TMA^+ than TBA^+ .

Finally, the de-intercalation shoulder is not simply a result of mathematical treatment, since it appears on the original charge/discharge transients (Figures 4.9(a,b) and 4.14(a,b)) albeit not quite as clear, and the shape dependence on

cationic species is unlikely to be a coincidence. The shoulder represents a decrease in the rate of current decay at initial discharge times, though quickly increases and plateaus towards the end of the discharge transient, resembling similar discharge rates (gradients) to those obtained from discharge transients where $E_c < -2.6$ V. The decreased rate of discharge decay is attributed to a slower rate of de-intercalation from the graphite cathode.

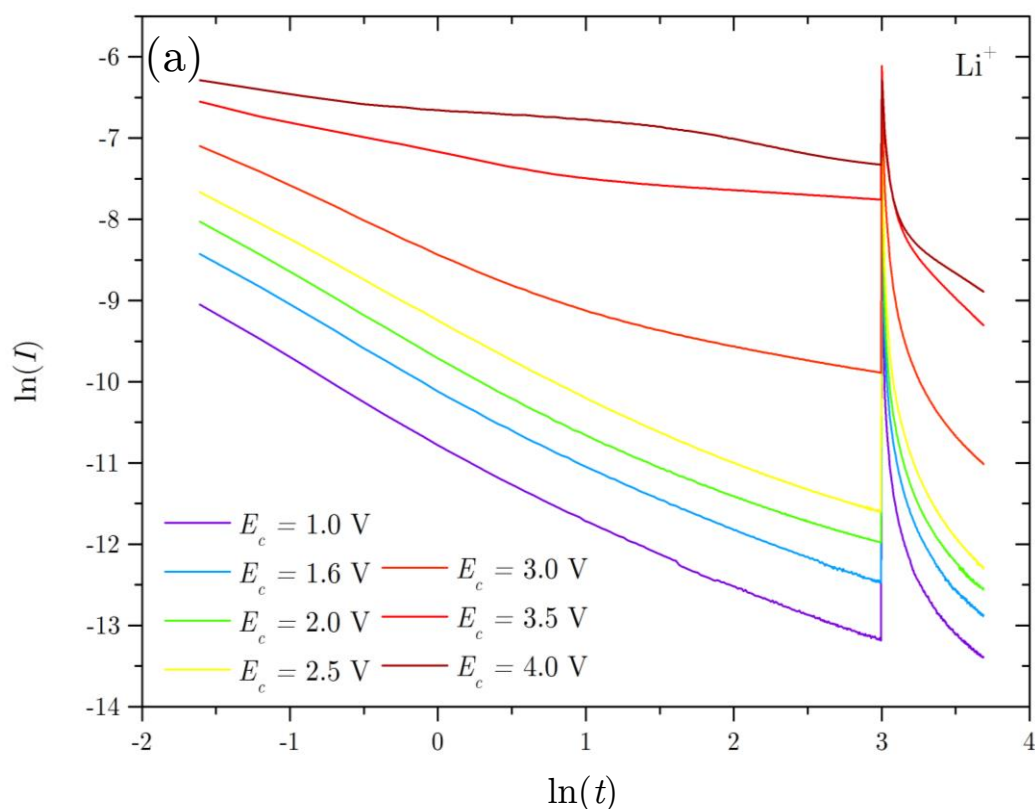


Figure 4.29(a) $\ln(I)$ vs. $\ln(t)$ plots, for lithium, showing charge/discharge cycling at a HOPG working electrode in NMP at varying E_c values between -2 V and -4 V. Discharge was conducted at 0 V in all cases.

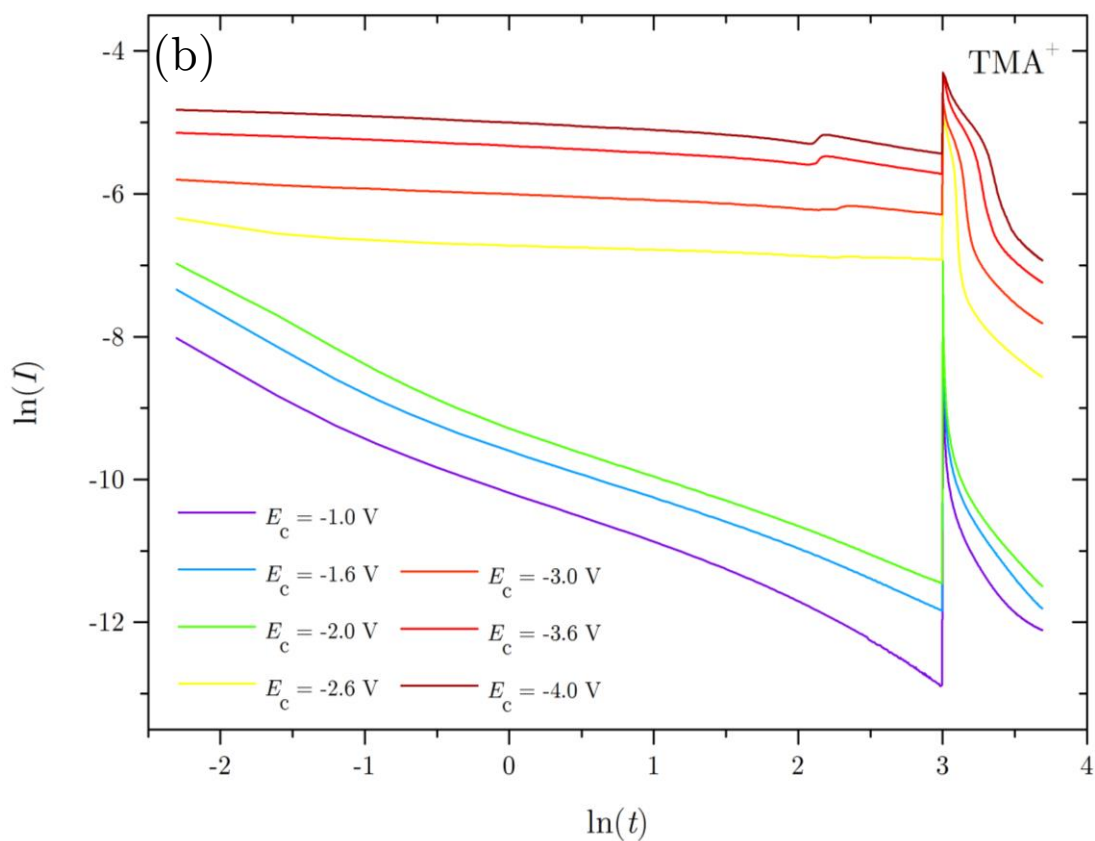


Figure 4.29(b) $\ln(I)$ vs. $\ln(t)$ plots, for TMA^+ , showing charge/discharge cycling at a HOPG working electrode in NMP at varying E_c values between -2 V and -4 V. Discharge was conducted at 0 V in all cases.

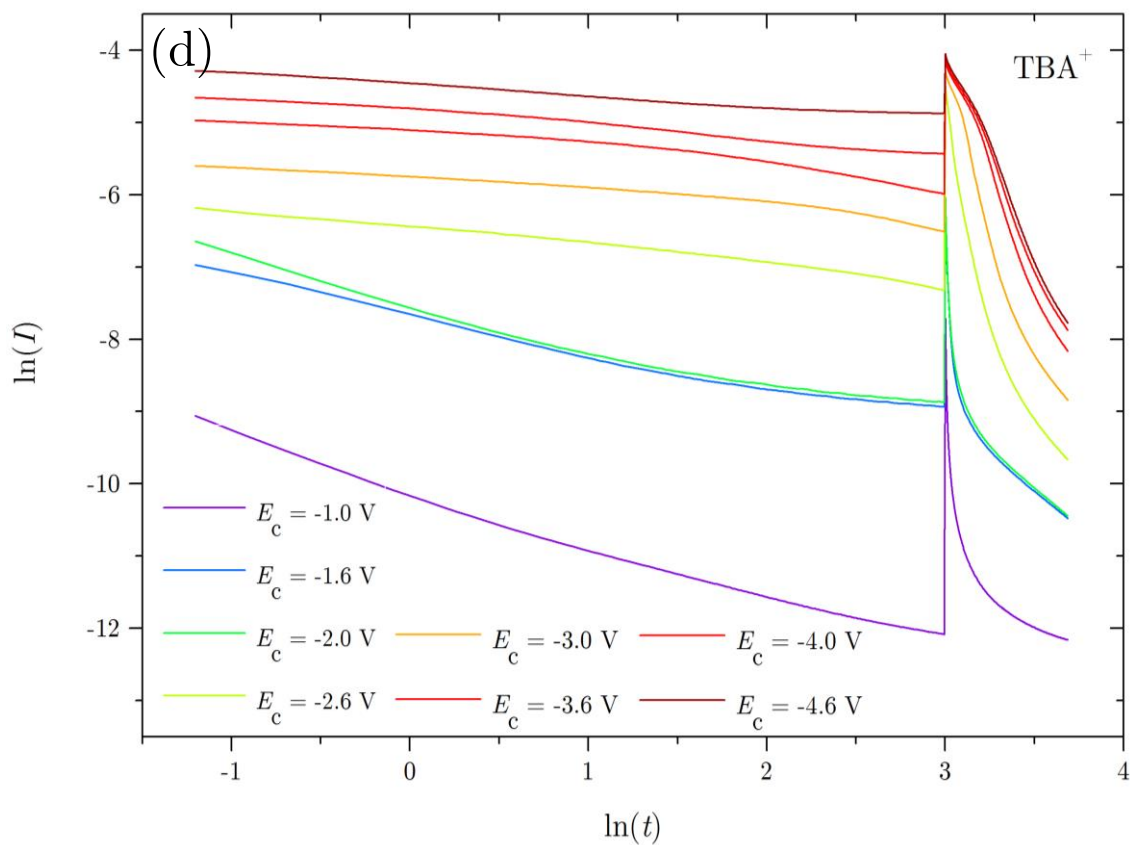


Figure 4.29(c) $\ln(I)$ vs. $\ln(t)$ plots, for TEA⁺, showing charge/discharge cycling at a HOPG working electrode in NMP at varying E_c values between -2 V and -4 V. Discharge was conducted at 0 V in all cases.

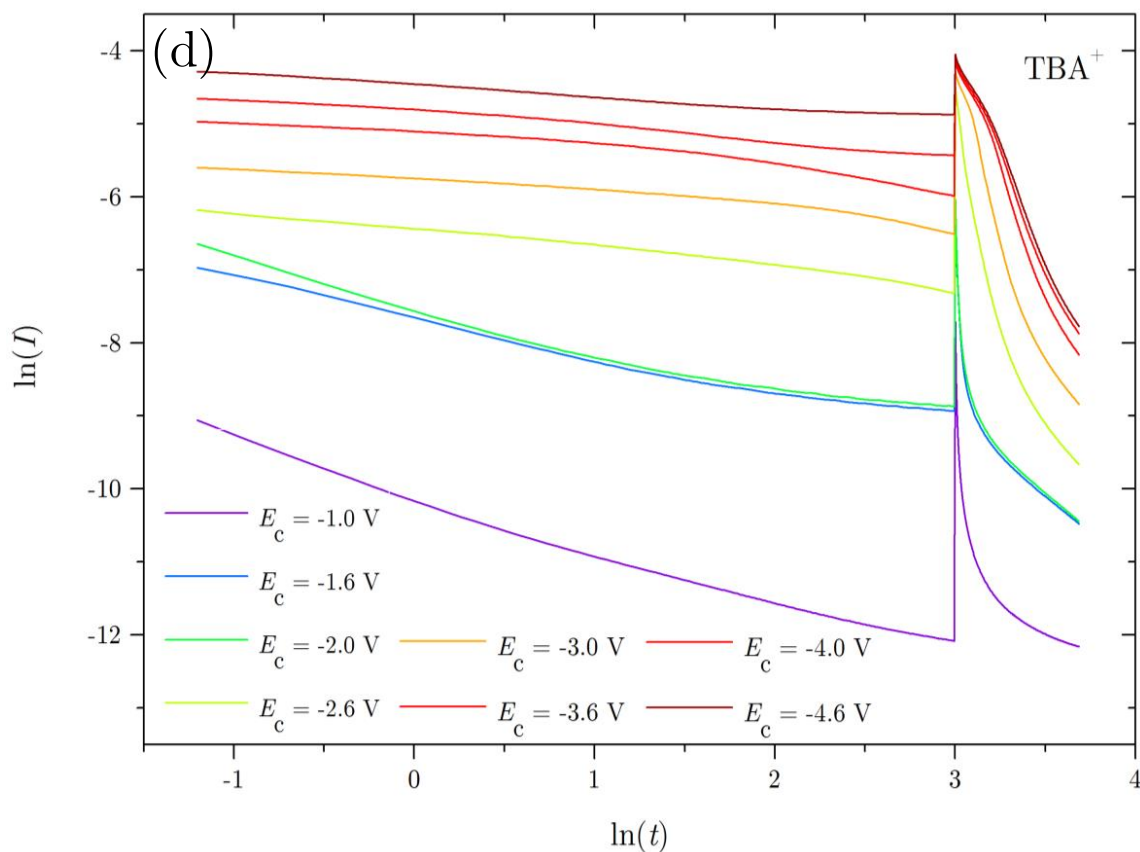


Figure 4.29(d) $\ln(I)$ vs. $\ln(t)$ plots, for TBA^+ , showing charge/discharge cycling at a HOPG working electrode in NMP at varying E_c values between -2 V and -4 V. Discharge was conducted at 0 V in all cases.

The gradients of the charge and discharge transients have been measured and presented in Table 4. To account for transients exhibiting complex exponents, *i.e.* including a shoulder, the gradients were calculated from an average of the main tangential gradients. It can be seen that the exponent of lithium charge remains relatively constant until the system is exposed to larger cathodic conditions; after which we see a decrease to -0.2 . The discharge exponent does measure *ca.* -0.5 at -3 V, indicating -3 V is close to the diffusion limit for lithium, however this may be coincidence since mass transport *via* migration cannot be omitted from the system and therefore it would be surprising to

observe $t^{-1/2}$ dependence. The discharge exponents remain relatively constant throughout however.

Table 4) Tabulated gradient values for both charge and discharge transients, acquired from $\ln(I)$ vs. $\ln(t)$ plots (Figure 4.29(a-d)) for Li^+ , TMA^+ , TEA^+ , and TBA^+

	Li^+		TMA^+		TEA^+		TBA^+	
E_c / V	charge	discharge	charge	discharge	charge	discharge	charge	discharge
-1	-0.84	-1.54	-0.85	-2.80	-0.92	-3.27	-0.67	-0.80
-1.6	-0.82	-1.66	-0.73	-3.04	-0.90	-3.18	-0.44	-2.01
-2	-0.82	-1.67	-0.75	-2.90	-0.91	-3.32	-0.46	-2.09
-2.5	-0.83	-1.94	-	-	-	-	-	-
-2.6	-	-	-0.07	-3.58	-0.24	-5.37	-0.28	-2.75
-3	-0.52	-1.76	-0.08	-3.80	-0.35	-5.81	-0.22	-3.00
-3.6	-0.20	-1.74	-0.10	-4.26	-0.38	-5.77	-0.28	-3.59
-4	-0.23	-1.22	-0.11	-4.19	-0.24	-5.64	-0.23	-3.73
-4.6	-	-	-	-	-0.15	-5.45	-0.14	-3.85

Though the data is not conclusive, it is clear that the charging exponent tends towards zero for all the cations. Conversely, the discharge exponents for the R_4N^+ cations become increasingly negative for decreasing E_c . This increase in the discharge exponent for more negative E_c values translates to a faster rate of current decay; which could occur *via* decomposition of the electrolyte or through electrode expansion; facilitating the expulsion of ions from the structure. The fact that electrode expansion is not observed for lithium intercalation, and that the lithium discharge exponents remain relatively constant through lithium

discharge, suggests that the increase in rate of current decay is related to the electrode expansion.

As highlighted in Section 2.2, the use of a supporting electrolyte, of typically 100x concentration, is used in order to restrict mass transport to purely diffusion control. However, because of the nature of the system, in which the supporting electrolyte acts as both the intercalating and electro-active species, mass transport of R_4N^+ species to the graphite cathode occurs *via* both diffusion and migration. Therefore it is not possible to improve the accuracy of the aforementioned diffusion data, while migration is an operative mechanism. It could be possible to minimise the effects of ion migration by employing lithium as a supporting electrolyte in which R_4N^+ is dissolved at smaller concentrations, and could be an interesting future study.

It is stressed here, that the previous discussion is based solely on the system behaving under laws of Fickian diffusion, and does not consider diffusion by other mechanisms such as Knudsen (diffusion of species within pores/channels where the channels are comparable in size to the species diameter) and Activated diffusion (diffusion across a potential barrier). These further mechanisms will undoubtedly play a significant role in the case of ion intercalation, where geometrical spatial restrictions are unavoidable within the pores of the graphite cathode.

4.2.14 Quantitative GIC formation

For electrode expansion experiments, HOPG samples were completely submerged in the electrolyte in order to maximise the degree of intercalation at all four edge planes of HOPG. The implication of this set up unavoidably exposes the electrical contact formed by the stainless steel self-closing tweezers to the electrolyte, thereby affecting measured currents. For post expansion analysis, where analysis is primarily non-electrochemical, this is of little concern. However for quantitative electrochemical-intercalation analysis this electrode setup is impractical and the current generated at the tweezers needs to be determined.

In order to omit the effect of the steel tweezers on current measurements samples were submerged such that approximately 50% of the HOPG sample was exposed to the electrolyte. This allowed only analysis of the graphite electrode and effects of the tweezers' contact were therefore removed. However a 50% exposure estimate is at best approximate, and often judged from outside a chemical glove box; therefore any work that requires the known mass or surface area of electrode exposed to the electrolyte cannot produce reliable results.

For example if the exact mass of electrode exposed to the electrolyte were known, then we can calculate, using Faraday's law of electrolysis, the degree of intercalation required to generate a specific charge.

In order to determine the exact mass of HOPG exposed, a HOPG sample was split as thin as practically possible (*ca.* 0.1 mm) and weighed by difference. The sample was then totally immersed in electrolyte and -3.0 V applied for 1000 s in an oxygen free environment. The electrode was then removed from the tweezer setup, and the electrochemical procedure repeated for the stainless

steel tweezers; subtracting the charge accumulated at the tweezers to determine the charge solely at the HOPG electrode. For example, the charge accumulated at a 2.3 mg HOPG electrode as a result of TMA^+ intercalation was calculated to be -116.9 mC. By conducting the experiment in an oxygen free atmosphere, it can be assumed that a negligible current is generated as a result of water hydrolysis/oxygen reduction in the system. It wasn't possible to eliminate the effects of solvent reduction on measured currents, however.

Since 2.3 mg HOPG contains *ca.* 1.15×10^{20} carbon atoms, using $Q = -116.9$ mC, -3 V applied for 1000 s generates a TEA^+ GIC with formula C_{158}TEA , reasonably assuming a one electron reduction of TEA^+ .

The number of TEA^+ cations intercalated, as well as the resulting GIC formulae were calculated for intercalation times of 4000 s and 10,000 s into freshly prepared HOPG samples of similar masses and dimensions, yielding calculated GIC compositions of C_{87}TEA and C_{39}TEA , respectively.

Table 5) Tabulated TEA:C ratios determined from various intercalation times

Time / s	M_{HOPG} / g	Q_{HOPG}	M_{TEA} / mg	No. of R_4N^+ ions	No. of C atoms	TEA : C ratio
1,000	0.0023	-0.1169	0.263	$7.2961\text{E}+17$	$1.15\text{E}+20$	1 : 158
2,500	0.0016	-0.1596	0.359	$9.9613\text{E}+17$	$8.03\text{E}+19$	1 : 81
4,000	0.0035	-0.3246	0.730	$2.0260\text{E}+18$	$1.76\text{E}+20$	1 : 87
10,000	0.0021	-0.434	0.976	$2.7088\text{E}+18$	$1.05\text{E}+20$	1 : 39

A total intercalation time of 10,000 s yields a calculated molecular ratio of 39 carbon atoms to every TEA^+ molecule. It was also found that by roughly halving both the intercalation time and HOPG sample mass resulted in a similar calculated TEA:C ratio.

Indeed, the total number of intercalated TEA^+ ions may not necessarily remain stabilised in the form of a GIC and therefore the calculated ratio is more accurately described as an *initial* ratio; whether these GICs are stable or spontaneously de-intercalate remains to be established. This could be probed by quantitative discharge, arguably a more reliable method of determining the GIC formula, or *via* thermal gravimetric analysis (TGA) to measure the mass loss of the GIC compound during heating. .

It is also possible to determine the amount of time it would take to saturate (or fully intercalate/charge) a HOPG sample with tetraalkylammonium cations. Sirisaksoontorn and co-workers²⁴⁰ prepared C_{44}TBA *via* displacement reaction; in which they found TBA^+ to adopt a flattened conformation, of diameter 0.47 nm²⁴⁰, in order to successfully intercalate into the graphite structure. It is important to stress that the conformational flattening only reduces the diameter of the cation in one dimension; the overall size of the cation is not reduced during intercalation and the size in the XY (graphene) plane spans nearly 14 benzene rings in its flattened conformer.

This is an example of considerably high intercalate content, *cf.* $\text{C}_{400-100}\text{NR}_4$ by Simonet *et al.*²⁴⁴

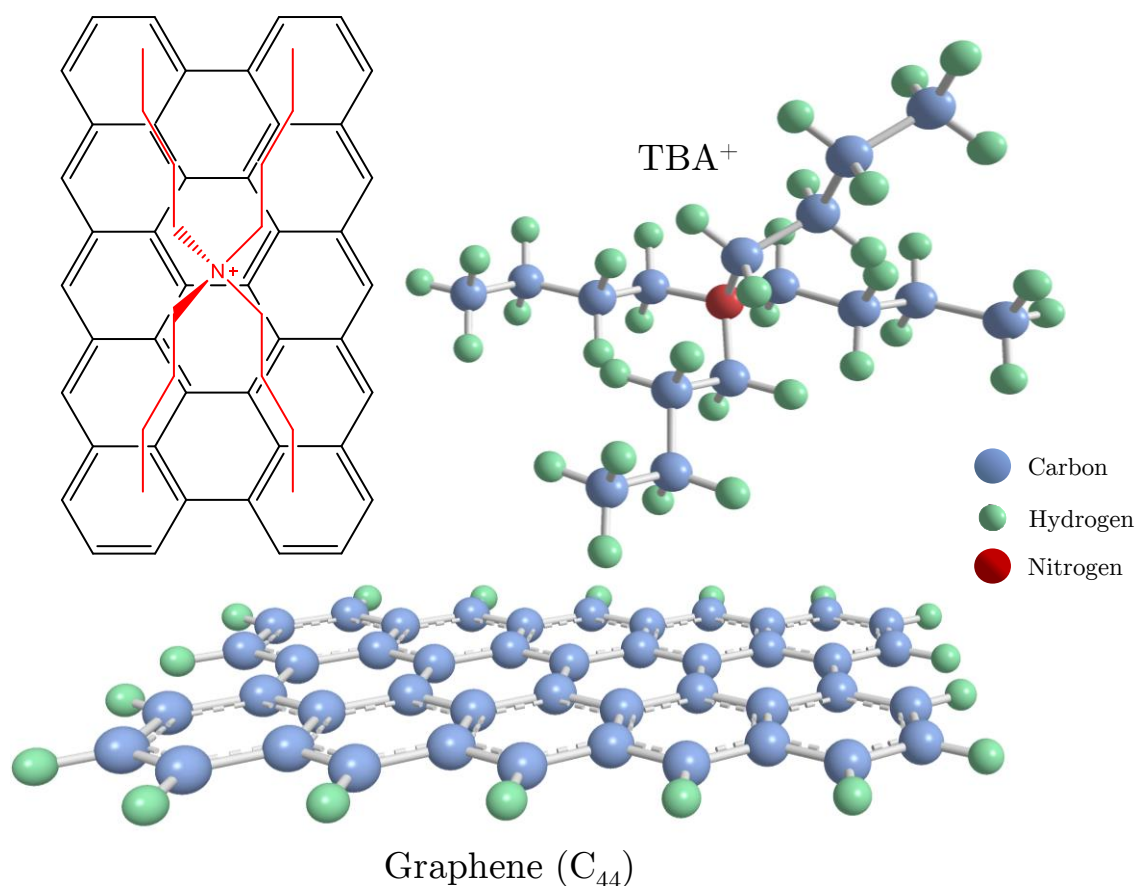


Figure 4.30) 3D molecular structures of C_{44} and TBA^+ , drawn to scale, highlighting their relatively similar sizes. The 2D model (top-left) shows TBA^+ 's flattened conformation spanning nearly 14 benzene rings (C_{44})

Since the flattened- TBA^+ is of a similar size to C_{44} in the xy plane (Figure 4.30), space limitations as well as TBA^+ - TBA^+ electrostatic repulsions point towards a TBA^+ : 44 C ratio being considered to reside near the upper limit of the possible degree of intercalation. If we assume $C_{44}TBA$ is at the near-saturation limit, and there are *ca.* 1×10^{20} carbon atoms in 2 mg graphite, then there are approximately $10^{20}/44 = 2.27 \times 10^{18}$ TBA^+ ions per 2 mg sample.

Finally we have 3.769×10^{-6} moles of TBA^+ and if we assume TBA^+ reduction is a one electron transfer process, we know that *ca.* 10^5 C is required to reduce

one mole of TBA^+ at the electrode. We therefore require *ca.* 0.364 C to reduce 3.769×10^{-6} moles of TBA^+ .

Therefore to achieve maximum intercalation of a 2 mg HOPG sample using a constant current of 1 mA, would take (using $Q = It$, where Q is 0.364 C, I is 1 mA, and t is time) approximately 6 minutes. Intercalation times used for graphite exfoliation were typically on the order of tens of minutes to hours (see Chapter 5 and 6), so it can be safely assumed that intercalation saturation occurs before expansion. A proposed mechanism is that electrode expansion occurs as a result of saturating the cathode with R_4N^+ species, where the energy associated with $\text{R}_4\text{N}^+ - \text{R}_4\text{N}^+$ electrostatic repulsion is greater than the energy cost of gallery expansion (overcoming the vdW forces of the neighbouring graphene sheets).

4.3 Conclusions

The electrochemical intercalation/reduction of tetraalkylammonium electrolytes, and associated formation of GICs, has been studied quantitatively at HOPG electrodes. It has been found that potentiostatically controlled R_4N^+ intercalation, using tetraalkylammonium species with different alkyl chain lengths, results in the formation of GICs between neighbouring graphene sheets within the graphite electrode, and allows for the controlled de-intercalation with the use of applied anodic potentials. TMA^+ , TEA^+ and TBA^+ all show charge recovery ability during potentiostatic cycling, even at charging potentials as low as -3 V *vs.* Ag/AgClO₄. The observed charge recovery is possible because of the GIC stabilization induced by neighbouring graphene sheets and associated graphite expansion, as shown by the poor charge recovery properties of TBA^+ reduction at a GC electrode. At sufficiently negative potentials it is thought that the stabilizing energy provided by the GIC conformation is overcome, resulting in unavoidable, irreversible reduction of the electrolyte. Interestingly, lithium intercalation studies did not exhibit the same degree of charge recovery as observed for R_4N^+ intercalation. This is partially due to the lack of GIC formation, but also due to the formation of an SEI layer on the graphene sheets.²⁶⁹ The SEI layer is irreversible, and acts as a barrier towards future solvent breakdown during successive voltammetric cycling.

In agreement with Simonet,²⁴⁴ it has been shown here that the intercalation of TEA^+ and TBA^+ results in significant irreversible structural deformation of the graphite cathode. However despite the observed irreversible deformation, the charge cycling remains relatively stable, and R_4N^+ intercalation yields high (80%) charge recoveries at charging potentials as low as -3 V. This feat cannot be performed to the same extent at GC electrodes due to the non-porous nature of the electrode, and the maximum degree of charge recovery is found to be

related to the crystallographic diameter of the R_4N^+ species, as well as the initial thickness of the host graphite cathode. In addition, lithium intercalation processes resulted in the expected formation of a protective SEI layer, though the timescales required for complete deposition exceeded those of the charge/discharge cycling, therefore no charge recovery was observed for lithium intercalation. Conversely, the short-timescales associated with near-100% R_4N^+ charge recovery during intercalation indicates the absence of a SEI deposition process.

Charge discharge cycling, and voltammetric cycling at sufficiently slow scan rates have been used to investigate the intercalation/de-intercalation-diffusion dependence. Clearly species intercalation requires the movement of ionic species between the graphene galleries, and the voltammetric measurement of this transportation has been found to be heavily dependent upon the speed at which the voltammetry is scanned.

During the investigation of the electron transfer mechanism of the GIC formation, the use of extremely slow scan rates revealed the complex nature of the intercalation, revealing evidence to support an intercalation staging phenomenon as a result of filled galleries. It has been proposed that observed electrode expansion accompanies R_4N^+ intercalation because the crystallographic diameter of the cations exceeds that of the interplanar spacing. Even through conformational flattening, thereby decreasing the diameter of TBA^+ , this diameter is still greater than the interplanar spacing forcing gallery expansion.²⁴⁰ However it is also thought that as a result of saturation of the graphene galleries with intercalated species, the neighbouring graphene sheets expand in an attempt to overcome the large electrostatic repulsion associated with neighbouring R_4N^+ cations in close-proximity to one another, resulting in the observed electrode expansion.

Chapter five

Electrochemical cathodic expansion

Electrochemical cathodic expansion

5.1 Introduction

This chapter focuses on electrochemically controlled cathodic expansion from the intercalation of tetraalkylammonium cationic species. Unlike Chapter 3, in which HOPG was mainly investigated as the working electrode material, a compressed graphite rod has here been introduced for the purpose of investigating the manner by which expansion occurs. Whilst HOPG offers advantages in terms of crystallite size (*ca.* <1mm) and its highly orientated nature (see Chapter 1), the graphite rods comprise of graphite flakes of various lateral crystallite sizes (*ca.* 2 μm – 800 μm depending on graphite rod grade) compressed into a cylindrical shape; no adhesive binder was used in the manufacturing process. As will be shown the electrode setup of HOPG introduces significantly different results to that of graphite rods. Graphite pellets, formed in a similar manner to graphite rods but made in-house have also been investigated, as well as natural Madagascar graphite flakes.

To electrochemically expand graphite electrodes, the potentials observed in the CV responses were used to define those set in chronoamperometric mode to control the intercalation processes. Chronoamperometry was employed to cathodically charge the graphite over extended periods of time and the effects of the charging potential, intercalating species, temperature and oxygen on the cathode expansion have been probed, as well as constant potential charging *vs.* battery-type cycling procedures. In order to measure degrees of graphite expansion, both SEM and XRD have been employed as the primary investigative tools as well as electrochemical capacitance testing, and some

Raman spectroscopy to probe the exfoliation of graphene sheets from the bulk electrode.

Interest is still placed on the nature of the intercalation stage formed and knowing the ‘degree of intercalation’ that is obtained after specific periods of time is valuable; achieving both a maximum and controlled intercalation staging is more likely to produce as few-layer materials as possible during exfoliation of flakes.

5.2 Results

5.2.1 Optical expansion

HOPG expansion yielded visibly intriguing results, expanding in a fashion resembling that of an accordion or fan. By totally immersing HOPG in tetraalkylammonium containing electrolytes in an open system, and applying a potential of sufficient magnitude it was possible to ease the structure apart as described, fanning out from the point of contact made by the steel tweezers. Figure 5.1(b) and 5.1(c) show the effects of intercalating TEA^+ and TBA^+ , respectively, into HOPG for 1000 s, and the expansion is clear even after such a small period of time. *N.B.* this was not carried out in a glove box. Lithium, being used as a comparison electrolyte, unsurprisingly yielded no electrode expansion even after prolonged intercalation times, only producing a white deposit on the HOPG electrode surface as described in section 3.2.3.

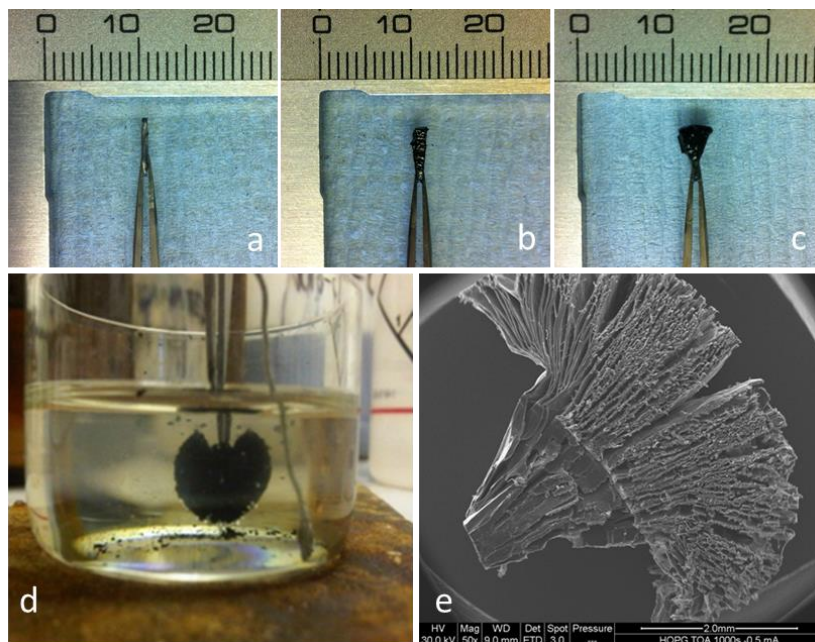


Figure 5.1) Photographs of (a) as prepared HOPG, (b) HOPG expansion after 1000 s TEA^+ intercalation, (c) HOPG expansion after 1000 s TBA^+ intercalation, (a–c scale in mm) (d) HOPG expansion after 10,000 s TBA^+ intercalation, and (e) SEM image of HOPG expansion after 6000 s TBA^+ intercalation

To confirm that electrode expansion is reliant upon ion intercalation and not simply electrostatic repulsion of neighbouring graphene sheets with the same electrostatic charge, cathodic potentials were applied to HOPG sample submerged in pure NMP containing no electrolyte and no electrode expansion was observed, even after prolonged charging times exceeding 4 h.

5.2.2 SEM imaging of electrode expansion

Expanded graphite cathodes were imaged using SEM to probe the microscopic deformation effects of intercalation using cations sufficiently large to cause electrode expansion. Figure 5.2 shows the micrographs obtained from a HOPG electrode intercalated with TBA^+ for extended periods of time and various different forms of structural deformation are visible as a result. Figure 5.2(a) shows the smallest observable feature in the form of micron sized pores, formed as a result of the cathodic charge. It can be seen that instead of a uniform expansion as one might hope for, the graphene layers appear to expand in the form of pores. These pores could be attributed to the fact TBA^+ is sufficiently large to hinder further TBA^+ intercalation, and this could be supported if the three tested cationic species revealed a trend in the measured intercalation charges for identical masses and dimensions of HOPG, since TBA^+ intercalation would yield a smaller charge than TMA^+ if fewer TBA^+ molecules were electrochemically reduced. However, without the use of a specially designed cell which enables the exact mass of graphite electrode to be calculated, this hypothesis has not been investigated. Figure 5.2(b) shows a portion of the graphite cathode which has been electrochemically expanded and multi-layer graphene sheets can be seen separated by the induced micron sized pores. Remarkably, this expansion occurs over a relative large range (*ca.* 50 μm) and the expansion can be seen to fan-out from a single region. This is essentially a

microscopic equivalent of the macroscopic fan-like optical expansion observed for HOPG, and is attributed to the high defect-dependence on the intercalation route. Ion intercalation is believed to occur *via* the lowest energy pathway, in the form of lattice defects and pre-existing submicron galleries present as a result of the fabrication process. However the manner in which the graphite lattice appears to ‘cling’ together is a reflection of the cumulative vdW interplanar interactions between the graphene sheets.

Figure 5.2(c) shows comparative portions of the HOPG electrode of which the left hand side has not been exposed to the electrolyte solution whereas the right hand side has. This SEM image confirms the requirement for exposure to electrolyte solution in order for successful expansion. Additionally, it would seem that the electrolyte is unable to migrate deep into the graphite cathode without the aid of significant expansion, resulting in exfoliation on the order of 10 μm depth as presented in Figure 5.2(d).

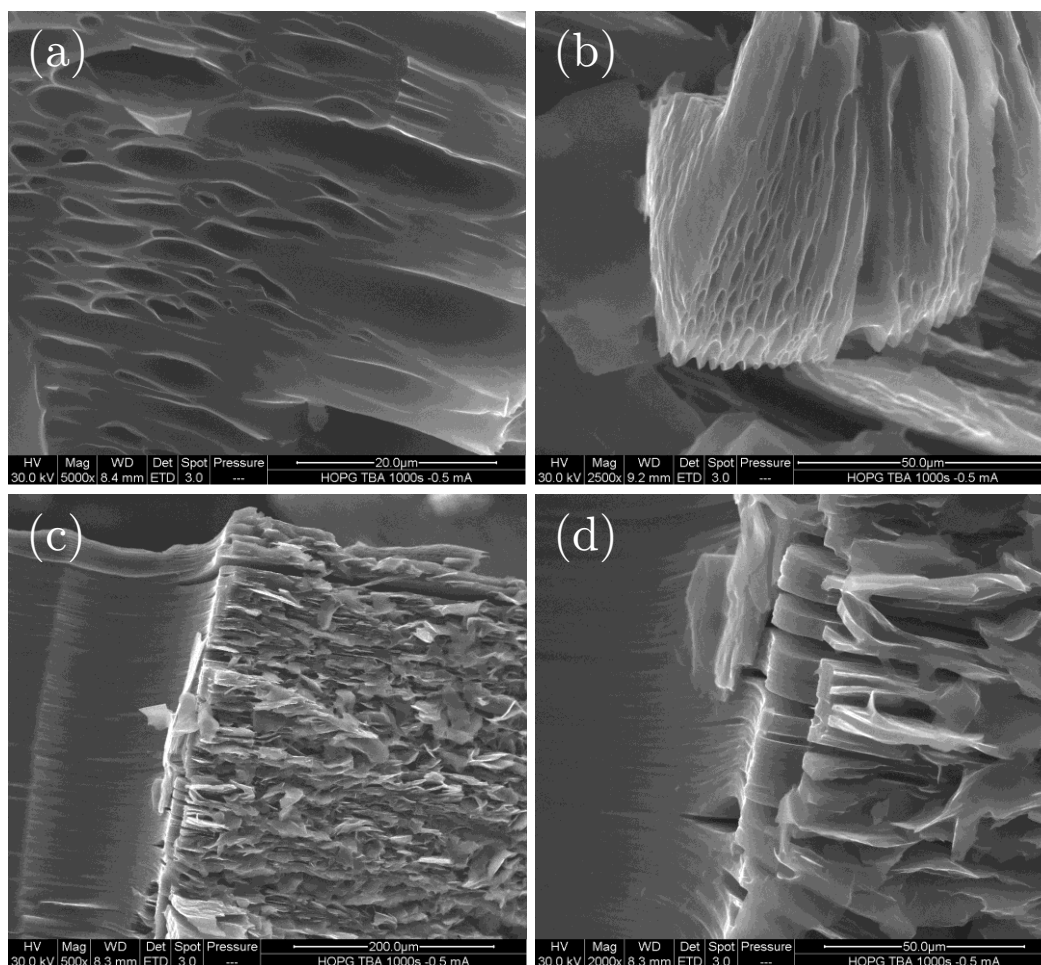


Figure 5.2) SEM micrographs of various portions of a TBA⁺ intercalated (−0.5 mA, 1000s) HOPG sample displaying (a) micron-sized pores developing in the graphite structure attributed to ion intercalation, (b) fan-like expansion accompanied with micron sized pores, (c) portions of the graphite electrode not exposed (left) and exposed (right) to the electrolyte solution, and (d) zoom of (c) showing only expansion at edge sites and not deep into the graphite lattice

Figure 5.3 shows further SEM imaging of TBA⁺ expanded HOPG (−0.5 mA, 1000s), and shows various portions of the expanded graphite displaying two distinct structural features. It can be seen in Figure 5.3(a) that there is a clear degree of structural segmentation present, where the graphite does not expand uniformly throughout all of the interplanar graphene galleries. The regularity of this segmentation is surprising, and can be attributed to either the size of the intercalated species limiting the intercalation to these ‘segments’ and thereby

preventing intercalation at more regular intervals, or regularly spaced lattice defects present within the HOPG structure by which intercalation preferentially occurs *via*. It is plausible that both of these possibilities contribute to the observed segmentation. Accompanying the structural segmentation is what appears to be flake ‘exfoliation’ at the edges of sheets (Figures 5.3(a) and 5.3(b)). It would seem reasonable that these portions of the electrode are more prone to exfoliation, since they are exposed to the electrolyte more so than the deep internal portions of the electrode. In addition, they will experience the largest degree of disruption during intercalation and de-intercalation of cations, since they are placed at the ‘entrance’ (and ‘exit’) of the intercalation pathway.

However, Figures 5.3(c) and 5.3(d) show a different portion of the electrode at which the segmentation is unaccompanied by the aforementioned flake ‘exfoliation’, indicating that the two features are not dependent upon one another. It also highlights that the two features are not sample or condition dependent, since they both appear on the same sample. Both features appeared at several locations on the expanded HOPG sample, and these positions could not be related to the positioning of the electrode relative to the electrochemical cell; for example, there was no noticeable increase in deformation on the side nearest the counter electrode.

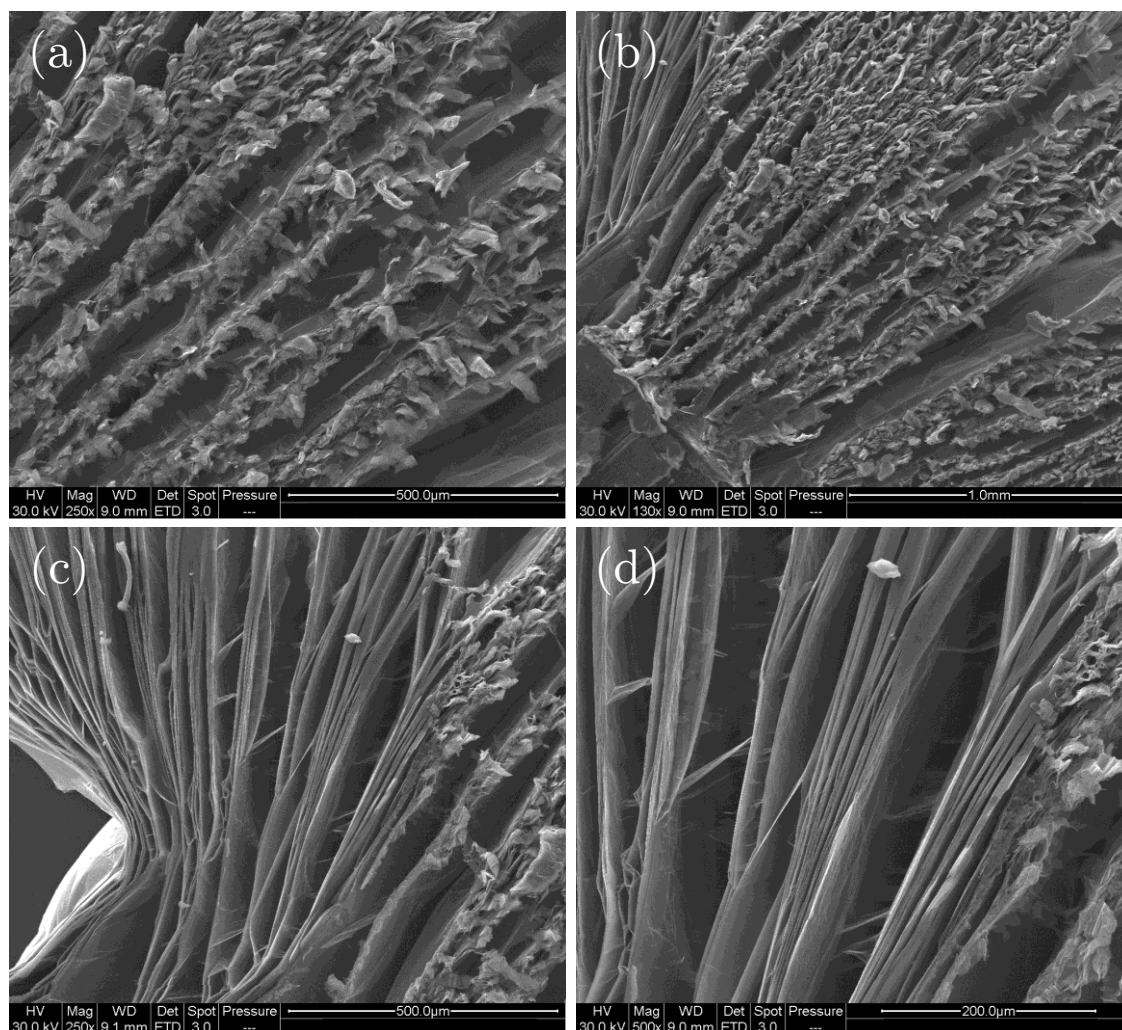


Figure 5.3) SEM micrographs showing TBA⁺ intercalated HOPG (−0.5 mA, 1000s) highlighting (a) two distinct features of the expansion (macroscopic gallery expansion and microscopic flake expansion), (b–d) regions of the HOPG cathode showing both gallery expansion and flake expansion indicating that the two features are not dependent upon each other

More detailed segmentation was visible on other parts of the electrode, and these regions were imaged at a higher resolution, allowed segment ‘widths’ of *ca.* 300 μm to be approximated (Figure 5.4(a)). Moreover, these graphitic segments appeared to contain further regular segmentation on the sub-micron scale (Figure 5.4(b)).

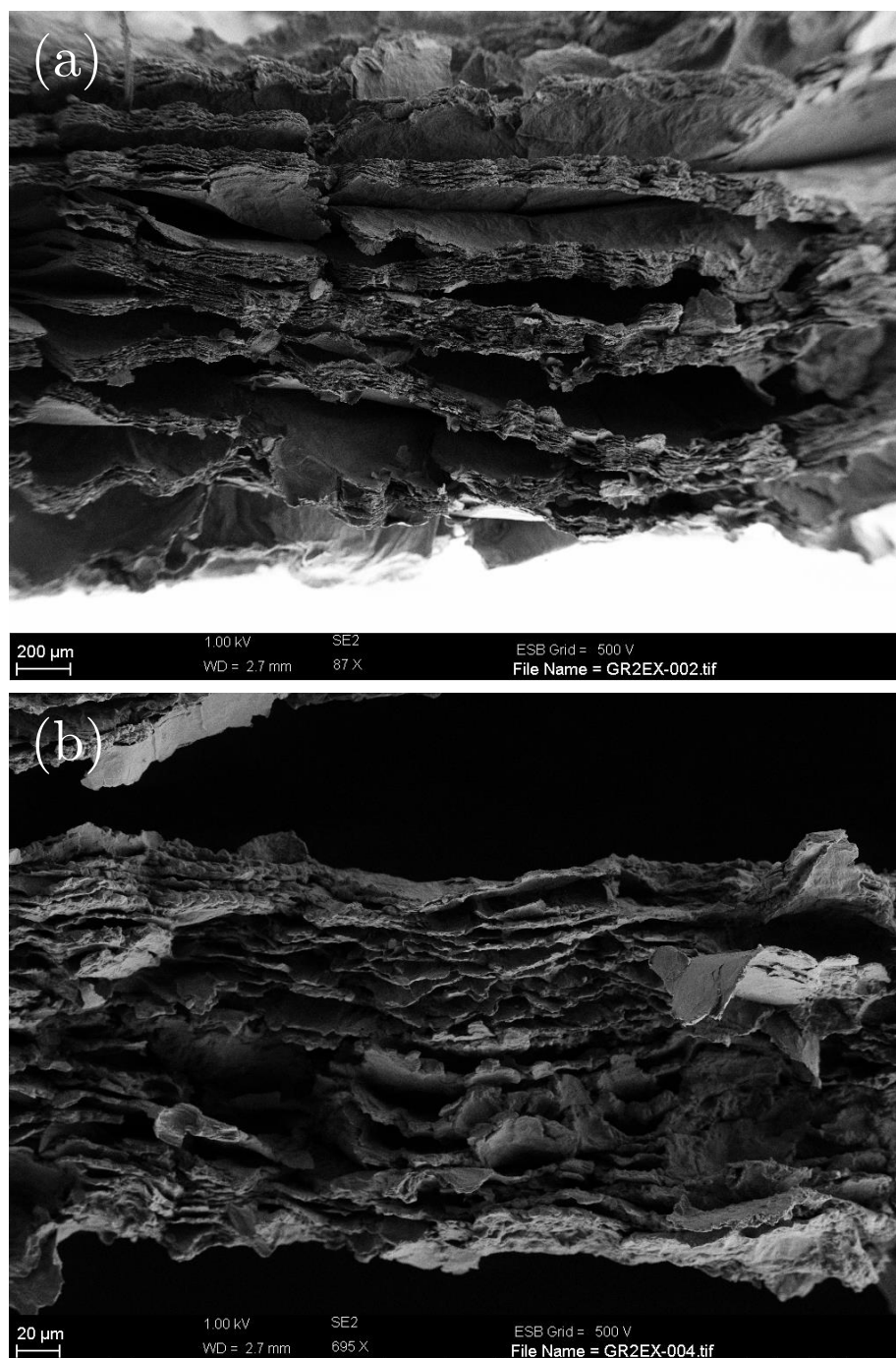


Figure 5.4) SEM micrographs displaying (a) *ca.* 200 μm sized gallery expansion, and (b) microscopic expansion within the expanded segments shown in (a). TBA⁺ intercalated HOPG (-0.5 mA , 1000s)

It would seem reasonable to imagine intercalation occurs *via* the most energetically favourable pathway, and once planes begin to expand this route

becomes the most favourable path since steric hindrance is not a concern until intercalation of enough species results in significant cation-cation electrostatic repulsions. However it is not so obvious why the segmentation appears regular in ‘thickness’, since any defects that facilitate intercalation are unlikely to be placed at regular intervals within the structure. This segmentation is revisited later on in this Chapter, when investigating changes in the crystal lattice in greater detail.

5.2.3 Tetraoctylammonium (TOA^+) intercalation

Since it was found that the rate of expansion, and degree of deformation (expansion) was related to the cationic species diameter, it seemed logical to investigate further R_4N^+ species with greater alkyl chain lengths than those of TBA^+ . Tetraoctylammonium (TOA^+) was chosen since it was easy to obtain: it has an alkyl chain consisting of eight carbon atoms, and has an approximate crystallographic diameter of 2 nm; calculated from the alkyl chain consisting of 8 carbon-carbon bonds having length 0.154 Å, with a sp_3 bond angle of 109.5° .

As can be seen from Figure 5.5(c) it was difficult to obtain voltammetry from which reliable data could be retrieved. Scanning of the potential into the negative regions associated with R_4N^+ intercalation produced noisy current responses, with no observable intercalation peak, though did follow the expected background. Interestingly, the familiar de-intercalation current feature was visible on the reverse scan. However the effects of such a large intercalation species were instantly noticeable during CV; exhibiting noisy current responses in the potential region corresponding to intercalation and significant electrode fracture occurring after as little as 5 CVs and large segments of the graphite electrode breaking off into solution with minimal effort. The SEM images

(Figure 5.5(a) and (b)) show the extent of deformation after as little as 1000 s intercalation (-2.5 V), and detailed features were not recoverable from the ‘mushy’ appearance of the electrode. These results lead to the discontinuation of TOA^+ , since it was established that TOA^+ was too large to cause ‘gentle’ intercalation and therefore exfoliation on the nanometre thickness scale, instead resulting in harsh electrode destruction.

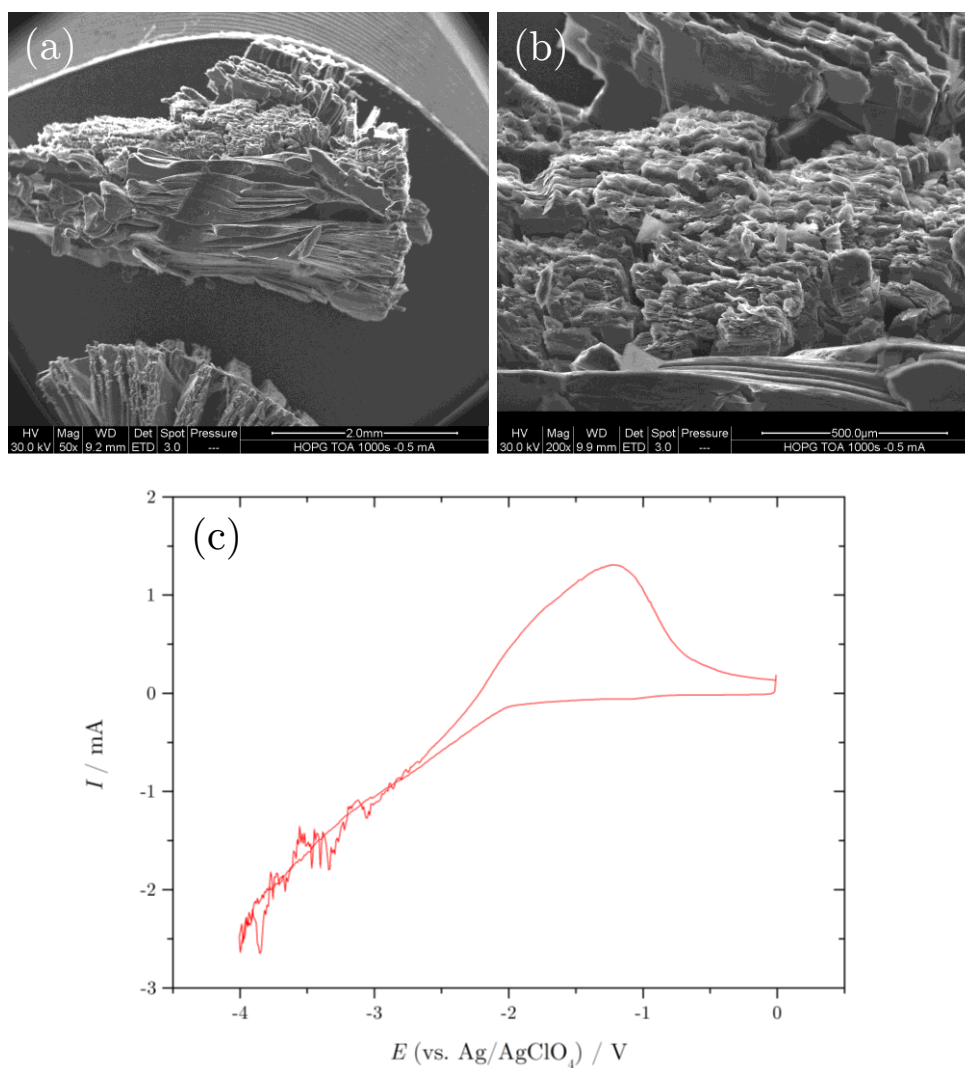


Figure 5.5) SEM micrographs showing (a) and (b) severe electrode deformation as a result of TOA^+ intercalation (1000 s -2.5 V), and (c) corresponding CV showing poor intercalation current response

5.2.4 X-ray diffraction studies

Powder X-ray diffraction was conducted on pre-expanded samples of HOPG intercalated with various R_4N^+ cations for various intercalation times. In order to obtain a maximum degree of intercalation, samples were submerged such that 100% of the HOPG sample was exposed to the electrolyte by also exposing the steel tweezers to the electrolyte. The implication of this setup being that currents measured cannot be solely attributed to activity at the graphite electrode, since the steel tweezers are also electrically conductive. It was found that due to the nature of the setup, samples expanded in a fan shape; expanding from the point held in contact by the tweezers (Figure 5.6). As a result of this fan-like expansion, the triangular shaped expanded samples could not be placed horizontally on the X-ray diffractometer sample stage. The consequence of this is that only a fraction of the entire expanded sample was in the correct orientation for XRD analysis, and therefore a large portion of the sample was not observed; providing only a sample analysis of the entire lattice.

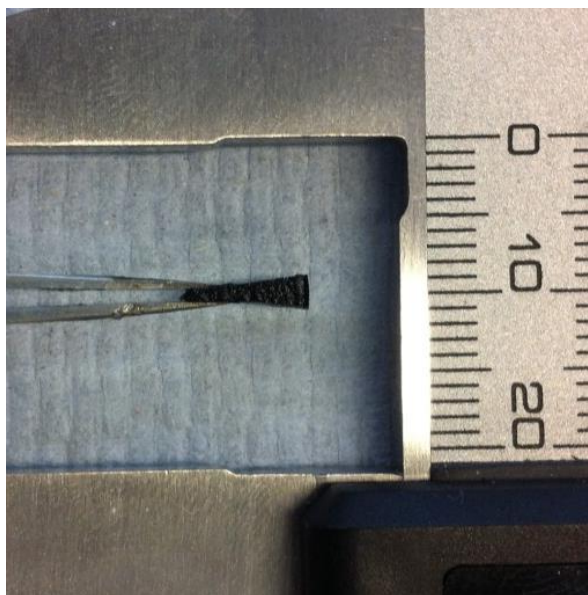


Figure 5.6) Photograph of TBA^+ expanded HOPG sample (10,000 s, -0.1 mA) showing the resulting fan structure expanding from the point of contact

Figures 5.7(a) and 5.7(b) show the powder XRD pattern for a HOPG sample (SPI-2 grade) prior to any electrochemical intercalation. The (002) diffraction peak at *ca.* $2\theta = 27^\circ$ corresponds to the regular *d*-spacing between graphene planes; 0.354 nm (Chapter 2). The (004) and (006) peaks are regular overtones of this (002) peak, which is why they exhibit smaller intensities. Figure 5.7(b) shows a zoom of the smaller angle diffractions corresponding to larger *d*-spacings than the (002) peak. Though little is visible in the way of features within this region, there is a small diffraction feature at *ca.* 24° .

Figure 5.7(c) shows the diffraction pattern for a heavily TBA^+ -expanded HOPG sample (-0.1 mA, 10,000 s) orientated as detailed above and counted continuously over a period of 10 minutes. The most noteworthy feature is the decrease in intensity of the (002) peak by approximately three orders of magnitude, accompanied with significant broadening of the signal. Both these features are known to be attributed to a loss of structural crystallinity^{153,270,271}; reasonable since the cation intercalation causes galleries to enlarge, resulting in a decrease in the abundance of (002) *d*-spacings. Since the (004) and (006) peaks are overtones, their intensities also decrease in the same manner; the (006) becomes indistinguishable since its intensity in the original non-expanded HOPG sample is relatively weak. However, as much as these diffraction changes correlate well with a loss of structural crystallinity, they actual tell us very little else. Since small 2θ angles correspond to large *d*-spacings, (and *vice versa*), the region of interest is where $2\theta = \text{ca. } 10 - 25^\circ$, since diffraction signals in this region will correspond to graphite interplanar expansion. It can be seen in Figure 5.7(c) that the background signal intensity steadily increases at $2\theta < 40^\circ$, (*d*-spacings > 0.225 nm), corresponding to a general gallery expansion (> 0.354 nm). This is due to the intercalation of TBA^+ opening up pores and sheets; thereby creating new *d*-spacings of larger *d* than the original 0.354 nm of

the (002) planes. The reason for the ‘general’ loss in crystallinity, as oppose to the appearance of new well-defined diffraction signals as specific galleries are formed, indicates the relative uniform nature of the intercalation, resulting in no ‘net’ creation of new d -spacings. This is perhaps not so surprising, since the graphite cathode is continuously losing all of its crystallinity during expansion of its crystallographic planes.

However, Figure 5.7(c) shows the clear introduction of another diffraction feature at $2\theta = ca. 45^\circ$ and this signal is associated with a new d -spacing measuring 0.198 nm; smaller than the 0.354 nm interplanar spacing of graphite. The appearance of this new diffraction signal, at larger angles (and smaller d) is attributed to the graphene galleries into which TBA^+ does not intercalate. These galleries are compressed by the neighbouring expansion of adjacent galleries, thereby producing smaller d -spacings. Unfortunately the high degree of expansion causes limited extraction of useful data.

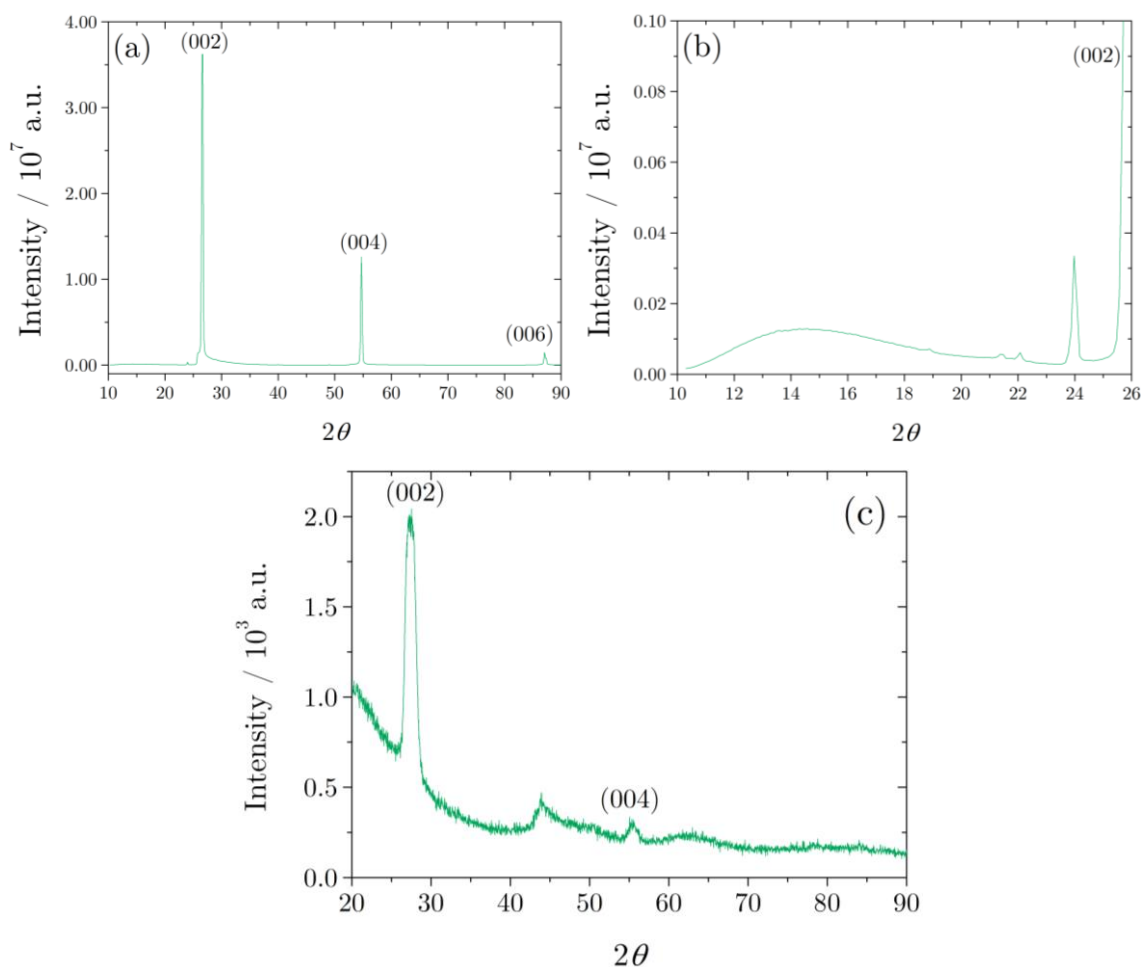


Figure 5.7) Powder X-ray diffraction pattern for a) as prepared diffraction pattern between $2\theta = 10^\circ - 90^\circ$, (b) zoom of (a) between $2\theta = 10^\circ - 26^\circ$, and (c) TBA⁺ expanded HOPG (10,000 s, -0.1 mA)

In order to obtain a more useful diffraction pattern, HOPG was expanded to a lesser extent, using TMA⁺ and TEA⁺ to obtain a more controlled, subtle expansion and for short periods of time. Expanded samples were then split into sections (cut parallel to the basal plane) measuring *ca.* <0.1 mm in thickness, and arranged randomly on the X-ray platform, which was rotated at a speed of 60 revolutions per minute. The X-ray counting time was increased from 10 minutes to 1 h, and eventually overnight recording was deemed necessary in order to increase sensitivity and sufficiently enhance peaks from the background signal.

Figure 5.8 shows the full diffraction pattern between $2\theta = 10 - 100^\circ$ of a TMA^+ expanded HOPG sample (-0.1 mA , 1000 s) prepared in the aforementioned manner. The (002) peak can be seen to have decreased in intensity along with the (004) and (006) features, and there is the emergence of a new peak at *ca.* 28° , corresponding to a d -spacing of 0.313 nm . This peak, is a direct contraction of neighbouring (002) planes, and its regularity throughout the lattice with respect to the (002) peak is indicated by an overtone at *ca.* 57° .

By expanding the HOPG to only a small degree, it was possible to determine distinguishable peaks at 2θ values below 25° . For a TMA^+ expanded sample, there are several peaks indicating new gallery expansions formed from the TMA^+ intercalation process; one might expect the new d -spacings to be of similar size to the crystallographic diameter of TMA^+ , since graphene sheets that have been successful intercalated between should be separated by the diameter of a TMA^+ molecule, *i.e.* 0.558 nm . However this was not the case, and several small diffraction signals become intense enough to allow differentiation from the background signal.

At first this was translated into the theory that intercalation does not occur homogeneously, but occurs *via* several intercalation routes and is relatively unpredictable. The four peaks labelled are clearly broad and not well-defined; their regularity throughout the lattice is therefore minimal but sufficient to produce the observed signals.

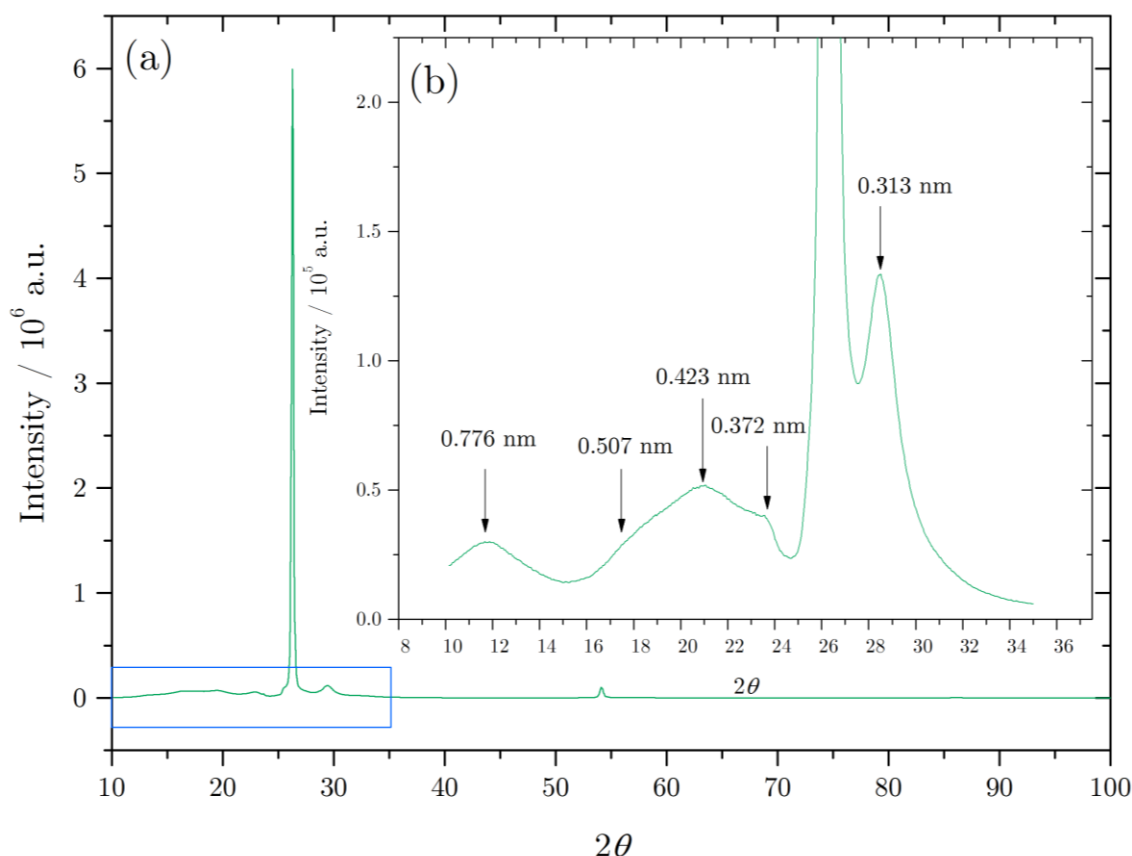


Figure 5.8) Powder X-ray diffraction pattern for (a) TMA⁺ expanded HOPG (1000 s, −0.1 mA), and (b) zoom of small angle peaks produced from intercalation of TMA into HOPG (*ca.* 4 × 10 × 1 mm, 0.1 mg)

Figure 5.9 shows the same procedure using a TEA⁺ intercalated sample. The observed low angle diffractions are again similar to TMA⁺ expanded graphite; peaks are broad and therefore overlap with one another resulting in difficult peak identity. However the peaks are better defined, and five calculable *d*-spacings are identifiable. Most prominent is a *d*-spacing at 13.5° which corresponds to a *d*-spacing of *ca.* 0.663 nm: the crystallographic diameter of TEA⁺. Again as with TMA⁺ gallery contraction is observed at 29.5°. This corresponds to a calculated *d*-spacing of 0.303 nm, slightly smaller than that induced by TMA⁺ intercalation. This seems logical since TEA⁺ should cause a greater degree of expansion than TMA⁺ due to its greater crystallographic

diameter and would thereby cause a greater degree of inter-plane contraction at pores not subjected to ion intercalation.

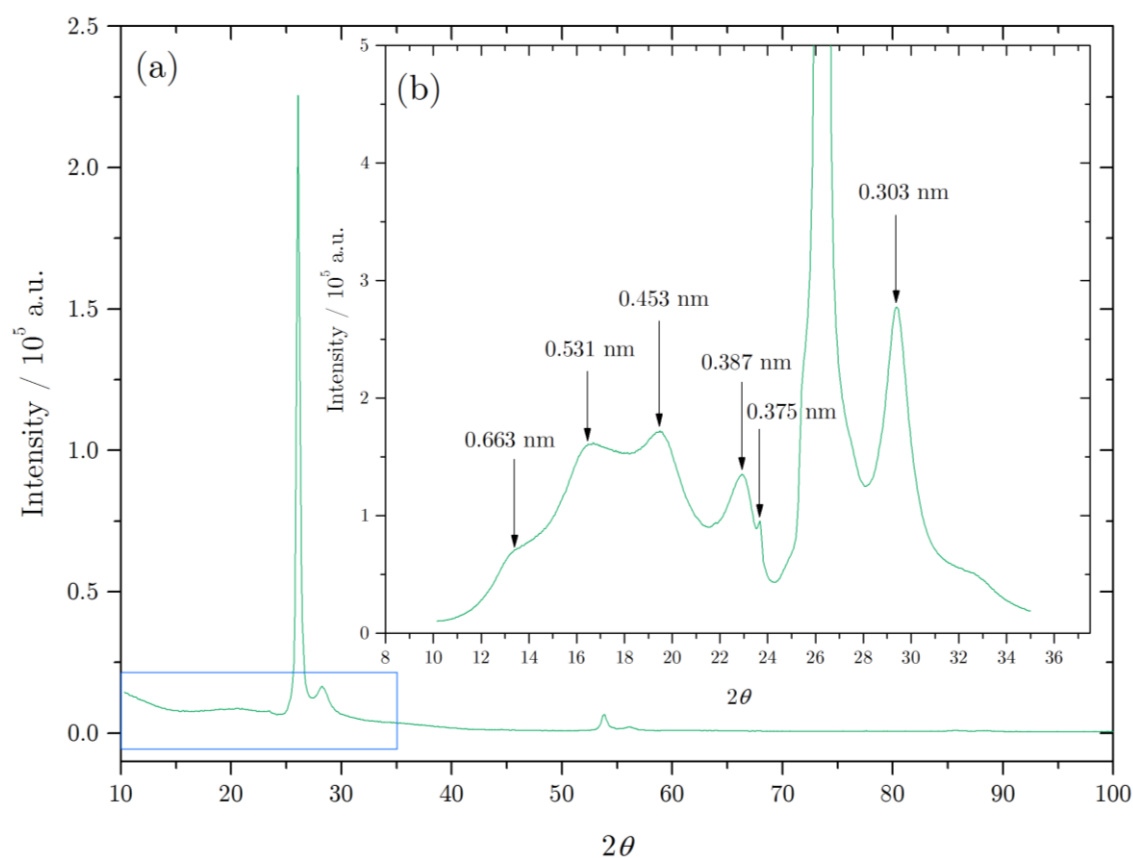


Figure 5.9) Powder X-ray diffraction pattern for (a) TEA^+ expanded HOPG (1000 s, -0.1 mA), and (b) zoom of small angle peaks produced from intercalation of TEA into HOPG (*ca.* $4 \times 10 \times 1$ mm, 0.1 mg)

Since TMA^+ and TEA^+ exhibit a certain degree of flexibility, albeit TEA^+ more than TMA^+ , it seems unsurprising that there are several preferential gallery expansions rather than a single expansion; corresponding to the crystallographic diameter of the respective cations. At the time, this was the best explanation towards the additional new diffraction signals; however it would seem there are other underlying reasons.

XRD analysis was repeated with TMA^+ , TEA^+ and TBA^+ intercalated HOPG samples, focus was solely placed on the small angle diffractions ($2\theta < 25^\circ$). Samples for intercalation were prepared as small and thin as possible (*ca.* $2.5 \times 4 \times 0.1$ mm), since Dresselhaus states that small, thin samples intercalate more quickly; generally producing higher staged and more homogenous intercalated compounds.²³⁴

TBA^+ intercalated HOPG (SPI-3 grade) for successive periods of time yielded the XRD patterns presented in Figure 5.10. For the purpose of graphical comparison, the XRD diffraction patterns have been scaled to one another and therefore their relative intensities are presented rather than their absolute intensities. The 0 s pattern corresponds to the XRD pattern of the as prepared, non-intercalated HOPG sample, and shows the presence of crystallographic *d*-spacings in the range $2\theta = \text{ca. } 18 - 25^\circ$. These diffractions are not prominent features, and are hidden well within the background signal, requiring several hours counting to reveal, however their presence is undeniable and is significant to the intercalation mechanism. The peak at $2\theta = \text{ca. } 24^\circ$ should not be confused with the (002) peak which appears at *ca.* 26° , which is not shown on Figure 5.10.

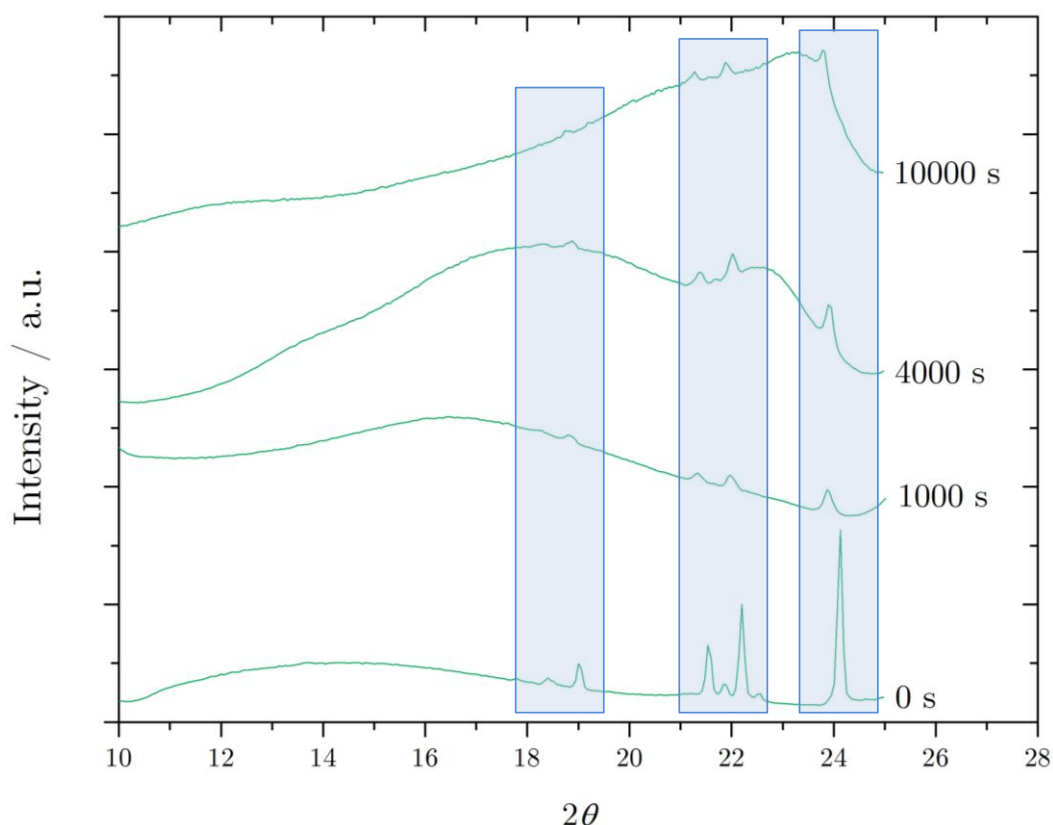


Figure 5.10) Powder X-ray diffraction pattern for a TBA^+ expanded HOPG measured at increasing intercalated time intervals, showing the effect of intercalation on the pre-existing sub-lattice diffraction peaks

The sub-lattice diffraction peaks are attributed to sub-lattice d -spacings created during the HOPG fabrication process, whereby gallery d -spacings are created between neighbouring graphite particulates as well as neighbouring graphene sheets. Theoretically these d -spacings might be expected to be of greater d than the 0.354 nm interplanar spacing of graphene sheets, since they are effectively artificial planes. It can be seen that these diffraction signals become less prominent with intercalation time, because the uniform expansion of the whole electrode begins to dominate, and the broad ‘background’ signal eventually masks the sub-lattice d -spacings (Figure 5.10). Additionally, the peaks can be seen to shift slightly to smaller 2θ angles, indicating that their d -spacings are increasing.

These sub-lattice d -spacings clearly have an effect on the intercalation mechanism, since as the intercalation time increases; the broad diffraction signal (*i.e.* the bulk exfoliation) begins to reside in the region of the pre-formed d -spacings. This is due to significant expansion of these artificial planes, causing overlap of their diffraction peaks and thereby adding to the general ‘background’ expansion. It is believed that these pre-existing galleries effectively act as energetically-favourable intercalation routes, by which intercalation preferentially occurs, since there are fewer steric restrictions associated with these galleries than intercalating between the narrower 0.354 nm galleries. However as shown by the ‘background signal’ increase, intercalation is not restricted to these pre-existing galleries, and expansion still occurs *via* the 0.354 nm galleries.

The presence of these sub-lattice crystallographic planes may be a result of the lower quality SPI-3 grade HOPG being used, and to test this, two different grades of HOPG (non-intercalated) were probed using XRD. Figure 5.11 shows the small angle diffraction patterns ($2\theta = 10 - 26^\circ$) for both SPI-1 and SPI-3 grade HOPG samples; the small angle peaks are clearly present in both samples, but a clear difference is seen between the two samples. Again, these peaks are not prominent signals and required extended analysis times to reveal clearly. Unsurprisingly the sub-lattice d -spacings are much more prominent in the lower grade SPI-3 HOPG than SPI-1 grade, and this is attributed to SPI-3 grade’s lower degree of intrinsic structural anisotropy. Additionally, both samples do show equally as intense broad signals in the 2θ region 10 - 20°.

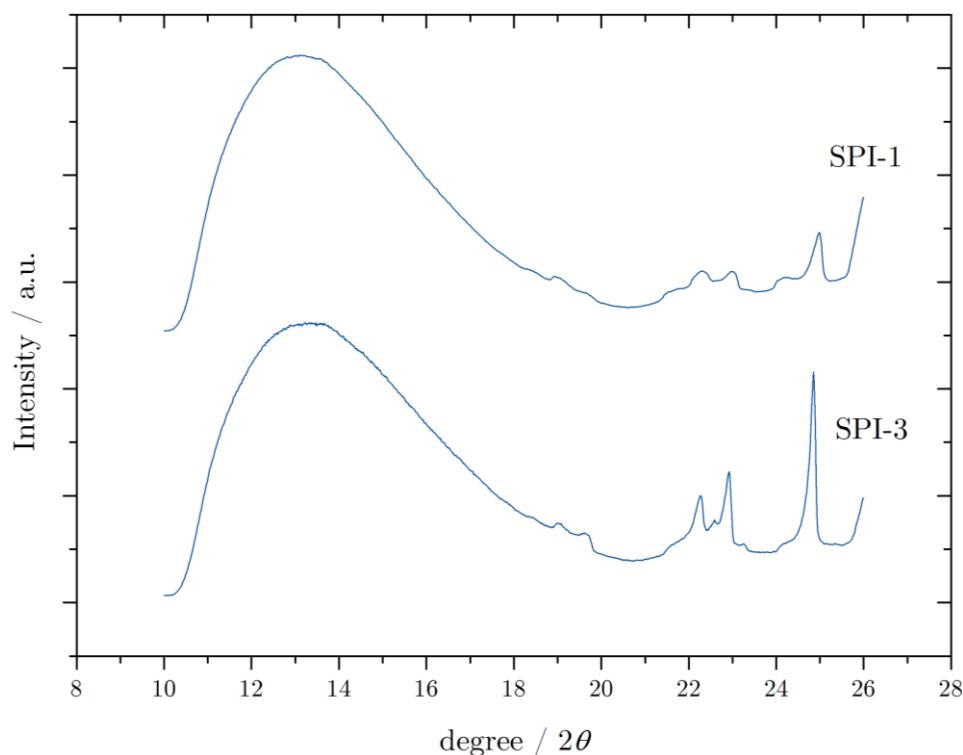


Figure 5.11) Powder X-ray diffraction patterns for SPI-1 and SPI-3 grade HOPG showing sub-lattice d -spacings at small angles

It is thought that the diffraction signals presented in Figures 5.8 and 5.9, which were originally thought to be solely related to the cation diameter, are actually also the result of intercalation *via* pre-formed galleries, which are greater than the ‘normal’ 0.354 nm spacing. The diffraction peak in Figure 5.9 that corresponds to a d -spacing of 0.663 nm, may indeed be due to ‘true’ TEA^+ separation, but since TEA^+ is relatively flexible, and because of the aforementioned pre-formed galleries by which intercalation can occur, it is no surprise that several diffraction features arise in the region of interest.

The same HOPG sample analysed with XRD after 10,000 s TBA^+ intercalation (Figure 5.10) was imaged using SEM. Samples were placed vertically such that the edge planes were contacted to a carbon sticky pad and samples were gold sputtered in order to maximise conductivity of the delicately contacted HOPG. The SEM images in Figure 5.12 show four areas of particular interest which

were representative of the entire HOPG sample. All the images shown are relatively low magnifications (250-1000 X) of the regular segmented expansion. The segmentation regularity is actually quite remarkable, where expansion occurs in groups rather than uniformly throughout the structure. These ‘large’ groups are on the order of tens of microns thick and run for lengths as large as 1 mm. Closer inspection of these groups reveals that the ‘large’ micron groups are comprised of further subgroups.

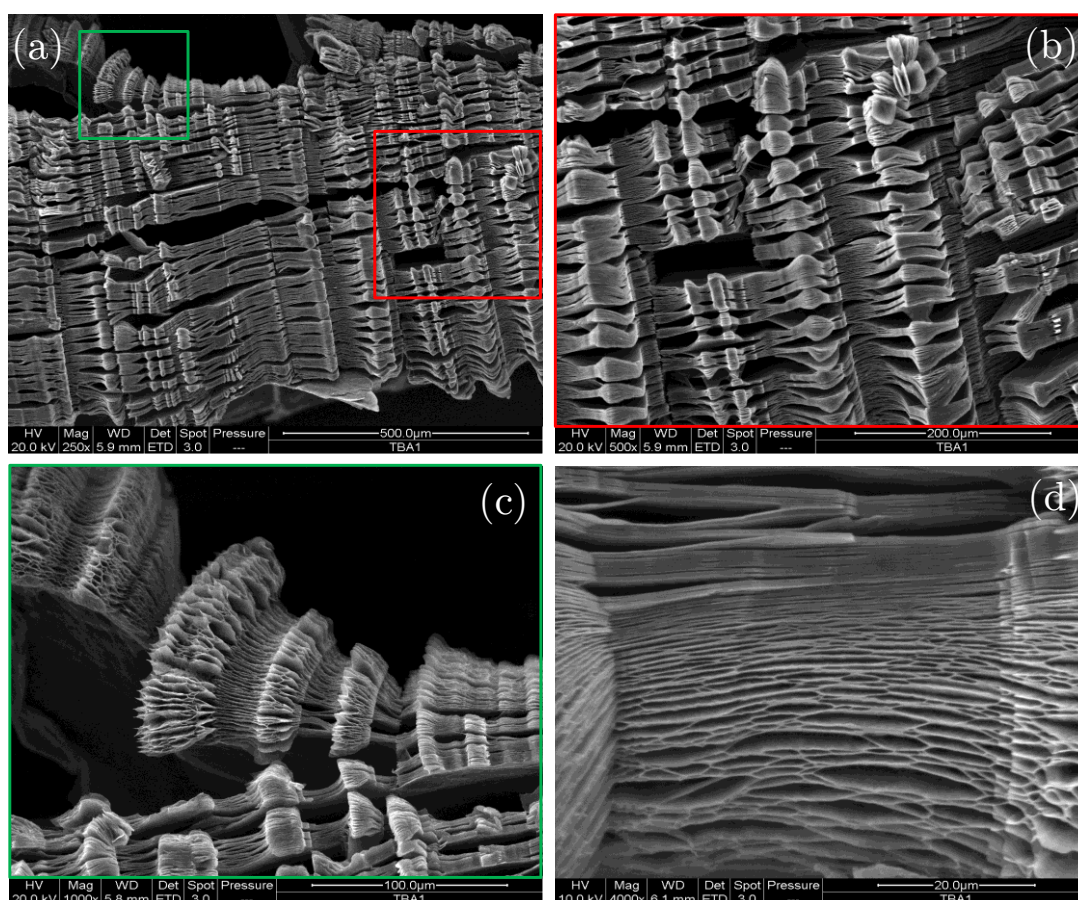


Figure 5.12) SEM imaging of various segmented sections in an expanded portion of a HOPG electrode, intercalated with TBA⁺ for 1,000 s at -2.4 V

Figure 5.12(a) shows a section of the expanded HOPG nearly 1 mm thick, and it is clear that within this section the edge planes are separated in groups; though there are heavily opened ‘pores’ on the structure, the dominating feature

is the regular sectioning. Figure 5.12(b) shows a zoom portion of 5.12(a) (red square) highlighting sections of splaying of planes at the edge of the sample, which same planes appear to ‘cling’ together deeper into the structure, after which they begin to splay once more. This ‘clinging’ of the sheets was observed in previous SEM imaging, and it would appear the ‘clinging’ has the effect of creating a porous network within the graphite.

Figure 5.12(c) shows an example of microscopic splaying, as seen previously on the macro scale, in which the graphite electrode splays out from a central point. This single point is always present at the point of contact from the tweezers, however microscopic versions of this were visible throughout the structure. These points reside deep within the graphite structure, which are not exposed to the intercalating species or the solvent, as such there is no reason for these points to expand, thus remaining unaffected. Finally 5.12(d) shows a further example of sheet ‘clinging’, this time on the submicron scale, though the effect is the same as previously reported. The sheets can be seen to be expanded in some regions, yet unaffected by the intercalation in other areas. It is thought that this occurs because of the bulky nature of the TBA^+ cation, since segmentation was not observed as frequently in samples intercalated with TEA^+ and TMA^+ . (Figure 5.13) Instead, a more homogenous expansion was visible, though this observation was not supported by XRD analysis, and it is possible that that this observed difference is a result of HOPG sample heterogeneity.

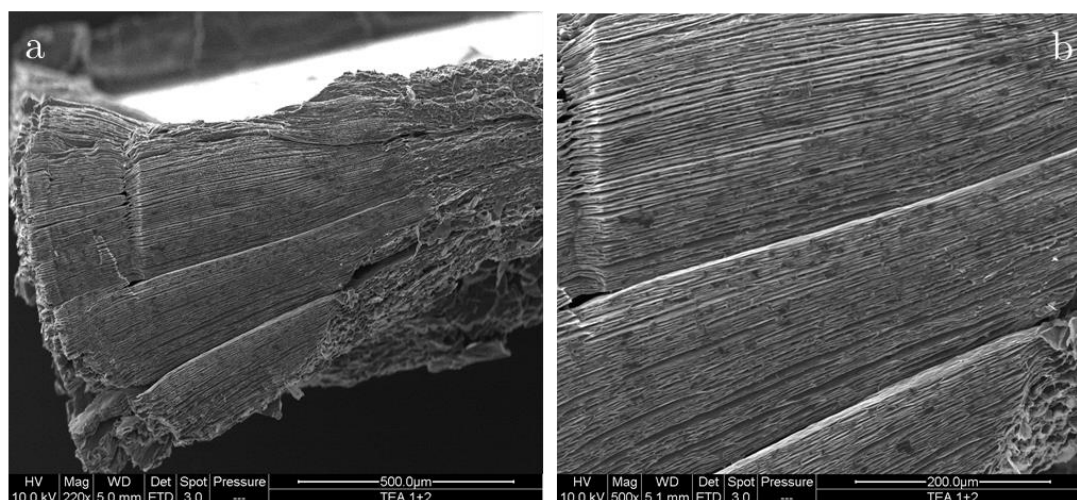


Figure 5.13) SEM imaging of a HOPG electrode intercalated with TEA⁺ for 1,000 s at -2.4 V

Finally, additional high resolution SEM micrographs have been included (Figure 5.14) showing enhanced detail of the segmentation produced from TEA⁺ intercalation of HOPG electrodes. It is clear that TBA⁺ intercalation results in severe segmentation, and it is therefore possible that TBA⁺ is too large, even when considering its flattened conformation, to intercalate with a high enough staging calibre to exfoliate materials thin enough to be considered graphene materials.

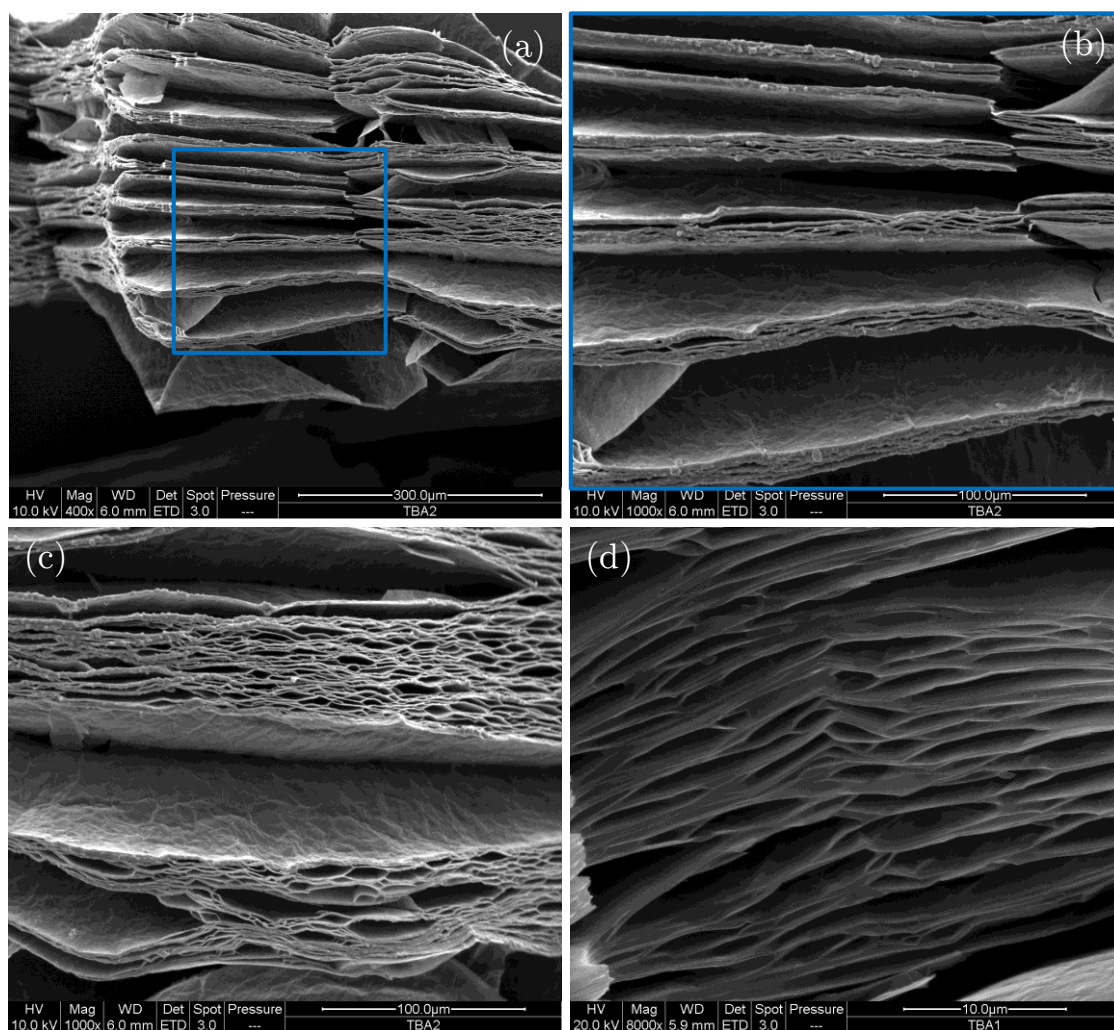


Figure 5.14) SEM imaging of various segmented sections in an expanded portion of a HOPG electrode, intercalated with TBA^+ for 1,000 s at -2.4 V

5.2.5 HK-graphite expansion

XRD was performed on fresh, non-intercalated HK-graphite and TEA^+ expanded HK-graphite (for 5,000 s at -2.4 V). It can be seen in Figure 5.15 that there are significantly more diffraction peaks than observed for HOPG, likely arising as a result of the fabrication process. Significantly, the (002) dominates (though not as prominently as in HOPG because of the relatively low anisotropy associated with the flakes in the rod), and although the expected decrease in magnitude for the intercalated sample is not as intense as observed for HOPG, a slight broadening is observed. This is attributed to a) the relatively random orientation of the inherent flakes contributing to a less intense initial (002) peak, and b) a generally smaller degree of intercalated sample, since the graphite rod was found to exfoliate readily into solution (see later, Chapter 6) thereby leaving an electrode of less mass than at the start of the procedure. It can be seen that the sharp diffraction peaks in the as-prepared sample disappear completely, accompanied with the formation of a broad band in the region $2\theta = 15 - 25^\circ$ attributed to the intercalation and *expansion* of the 0.354 nm interplanar graphene galleries. This is significant, since it shows that gallery expansion does occur with HK-graphite, and the electrode does not simply fracture. It is important to cause exfoliation of the flakes, but equally important to achieve a significant degree of gallery expansion prior to exfoliation, otherwise the entire procedure is an overcomplicated route of fabricating graphite flakes into a rod, only to break it apart again into the original graphite flakes.

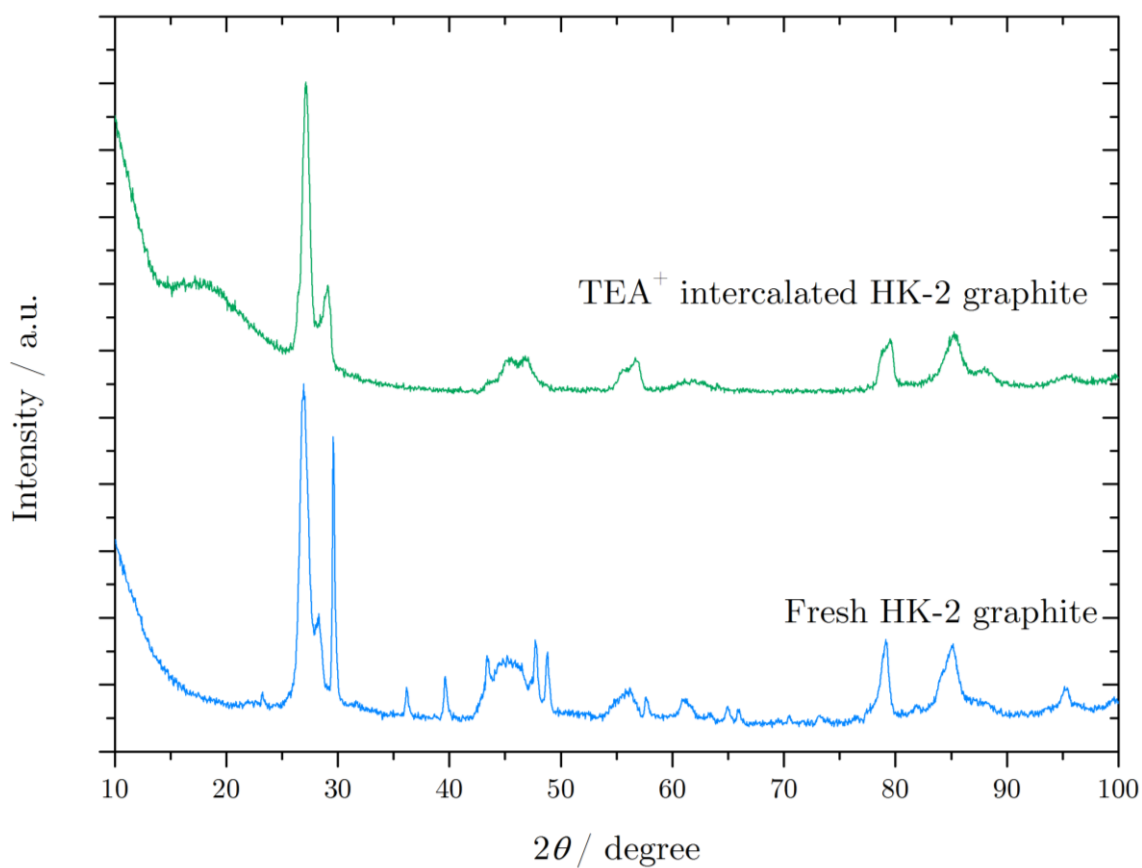


Figure 5.15) Powder XRD of fresh non-intercalated HK-2 graphite (blue) and TEA⁺-intercalated HK-2 (graphite for 5,000 s at -2.4 V), showing a general loss of crystallinity; indicated by the disappearance of several crystallographic planes in the original as-prepared graphite as well as a broad band appearing in the region $2\theta = 15 - 25^\circ$

5.2.6 Impedance testing of expanded HOPG electrodes

The following investigations are part of a preliminary study towards the measurement of electrochemical capacitance of the expanded graphite electrodes, and hints at further diffusion-limiting phenomena of the system. It should be noted, however, that the following discussion is based solely on Fickian diffusion. In reality the system is extremely complex, specifically with regard to diffusion in the bulk system and that during intercalation, not to mention the complications of measuring electrochemical impedance in non-aqueous media which generally exhibit an appreciable resistance in electrochemical cells. Nonetheless it serves as a valuable introduction to measuring the specific capacitance of electrochemically expanded graphite electrodes.

As described in 2.4.4, EIS is a sensitive probe for assessing the capacitive and resistive properties of an electrochemical system. This is possible because the system can be simplified to an electrical circuit analogy, consisting of individual resistive and capacitive circuit elements. In the example presented in 2.4.4, an electronic dummy cell was employed in order to determine the values of each electrical component through EIS. The dummy cell is an example of an ideal case, since the circuit of interest is already known, and the Nyquist plot is easily modelled to an exact circuit, rather than an equivalent one. In real experiments, specifically with electrochemical cells, the exact determination of the equivalent electronic circuit can be challenging. In principle, there are four major contributors to the total Z in an electrochemical system; the first three have already been addressed; a series resistance (R_s), a resistance to charge transfer (R_{ct}), and an electrochemical double layer capacitance (C_{dl}). The fourth component is known as the Warburg impedance, and is a measure of the impedance to mass transport of the electrolyte, of which exhibits both resistive

and capacitive properties. In practice however, real systems are not successfully modelled by these sole four parameters, and additional circuit elements are required for the accurate modelling of more complex systems. As a result, other equivalent circuits have been devised for more complex systems, such as adsorption processes and multi-step electron transfer processes. It should be noted that, the distribution of the generated capacitance at an electrochemical double layer in real-life experiments is often more accurately modelled with the use of a constant phase element (CPE_{dl}), Q , rather than an ideal electrical capacitor, C . Factors such as surface-roughness, inhomogeneous surface reaction rates, non-uniform surface coating, and unequal current distributions can lead to non-ideal capacitive behaviour, and this can be corrected for when modelled using a CPE_{dl} . For a more comprehensive description of CPEs and their mathematics surrounding their corrective capabilities, the reader is directed to *Impedance Spectroscopy: Theory, Experimental, and Applications* by Evgenij Barasoukov, 2005.¹⁶⁴ Three electrode electrochemical systems are often modelled to an equivalent Randle's circuit, in which the capacitor element is replaced with a CPE, as shown in Figure 5.16. Figure 5.16 also shows an additional circuit element, which represents the Warburg impedance of the cell. Because the Warburg impedance is mass transfer dependent, its presence is reliant on whether the process is diffusion or kinetically controlled. Thus, if the system is kinetically sluggish, then a relatively large R_{ct} will be observed, and may result in a very limited frequency range in which mass transport is a significant contributor. Conversely, R_{ct} may be comparatively small with respect to the Ohmic resistance, R_s , and in this case the Warburg impedance dominates a large proportion of the observed frequency range. In cases akin to the latter example, the system is so kinetically facile that the diffusion limitation can often result in poorly defined semicircle regions at the high frequencies.¹⁶⁴ The frequency dependence of the Warburg impedance can be

rationalised in terms of the diffusion distance travelled by the reactant species. As ω increases, the Warburg contribution becomes negligible, since reactants are not required to diffuse over large distances. In contrast, low frequencies, where the reactants must diffuse further through the electrolyte, species experience increased impedance from the electrolyte, hence why the Warburg impedance is only observed when ω approaches 0.

Because of this, a linear portion at *ca.* 45° is present on the Nyquist plot at frequencies approaching zero, since it consists of both real and imaginary Z components. Furthermore, the Warburg impedance behaves less like a capacitor and more like a resistor with decreasing frequency, reflected in the increasing real component and decreasing magnitude of the imaginary component, in the Nyquist plot.

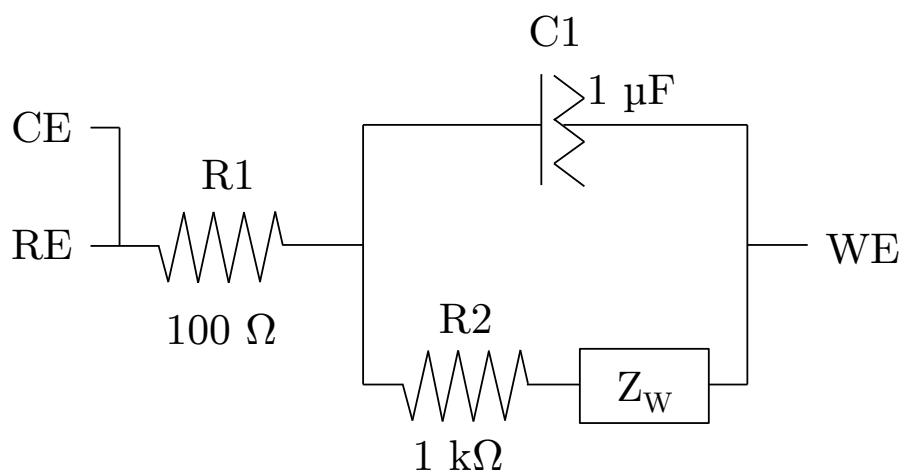


Figure 5.16) Equivalent Randle's circuit for that of an electrochemical cell, showing a CPE in place of a capacitor, representing the electrochemical double layer, R2 representing the resistance to charge transfer, R_{ct} , and the inclusion of a Warburg impedance element, Z_w , representing the resistance to mass transport, to the electrode in solution

Figure 5.17 shows a typical Nyquist plot obtained from EIS measurements at a HOPG working electrode in a solution of TBABF₄ (0.1 M) in NMP, over a

frequency range of 500 kHz to 10 Hz, and indicated are the approximate frequency regions of which relate to the different kinetic and diffusion limiting processes. In Li-ion battery research, in which the formation of an SEI layer is observed, impedance associated with this insulating layer is observed in impedance data at high frequencies (>100 kHz). However, no such SEI behaviour has been observed as a result of R_4N^+ intercalation, neither previously *via* voltammetry nor here, spectroscopically, as can be confirmed by the absence of any such feature at frequencies approaching 500 KHz. Additionally, the data in the frequency region corresponding to diffusion limitation (Warburg) can be clearly extrapolated to two different gradients. It is thought that this is a result of different diffusion processes occurring in the bulk, b , and at the surface (intercalation between layers) of the electrode, s . The diffusion of species in the bulk solution is expected to be much less restricted to that of species during intercalation, since the geometrical restrictions provided by neighbouring electrolyte species as well as the graphene galleries will hinder the movement of ions more so than the bulk solution. Similar Warburg observations have been reported for other intercalation studies²⁷²⁻²⁷⁵, and been attributed to different diffusion processes in the bulk electrolyte to that of ion intercalation.

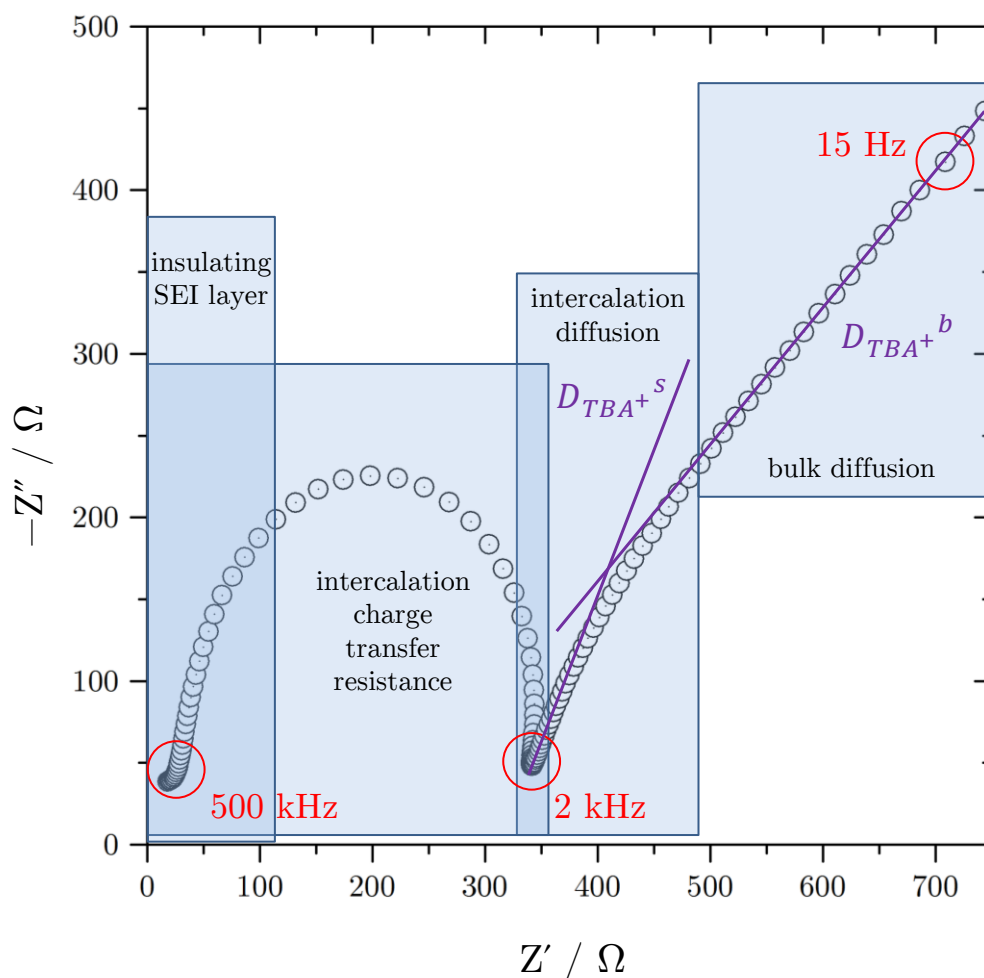


Figure 5.17) Typical impedance data, expressed as a Nyquist plot, recorded at a HOPG electrode in the presence of TEABF_4 (0.1 M) in NMP with annotation describing the inherent frequency dependant mechanisms in their respective frequency regions

EIS was employed as a tool to measure the degree of expansion of graphite cathodes, as a function of capacitance. Reliable qualitative data regarding cathode expansion was challenging, since the standardisation of measured surface area/volume was not cross-comparable between different systems. The sole hindrance to these investigations occurred in the form of the high dependence upon system conditions; degree of electrode exposure, initial electrode mass/area, and the inability to measure surface area and volume of the continuously changing graphite cathode, *in situ*. For these reasons, *in situ* electrochemical analysis was the only reliable and readily available technique,

and determination of the electrode's capacitance as a function of expansion time was probed, primarily in order to quantitatively compare the effects of cation size on electrode deformation.

Potentiostatic EIS was performed at HOPG electrodes of known mass, in order to determine their specific capacitances, C_s . 0 V was applied to the working electrode with modulation amplitude of 0.01 V over a frequency range of 500 kHz to 0.1 Hz and maximum integration time was set to 0.125 s. It should be noted that the R_4N^+ containing electrolyte solutions, in NMP, are not conventionally employed systems for EIS data acquisition. However since the degree of initial expansion is relatively small, and in order to maintain a high level of consistency between expansion and measurement, it was essential to complete both procedures in 'one pot', since the incurred error introduced during the electrode transfer between separate 'expansion' and 'analysis' systems would mask the measurement.

Figure 5.17 shows the measured EIS data for an HOPG electrode (19.8 mg) completely submerged in $TBABF_4$ (0.1 M) in NMP and expanded for successive periods of time *via* the application of -2.5 V. 0 V discharge of the electrode was performed for an equal amount of time between cathodic load and EIS measurement, in order to allow the system to relax to an equilibrated state prior to EIS measurement. It can be seen that the determined capacitance of the expanded HOPG increases as a function of intercalation time, and is attributed to the increased surface area caused by the intercalation/expansion process. During intercalation, the inter-planer graphene gallery expansion permits a greater degree of electrochemical double layer capacitance, since fresh portions of the electrode are continually exposed to the electrolyte. It can be seen that, with the aid of TBA^+ intercalation, the degree of capacitance increases by almost an order of magnitude, after approximately 1 h expansion.

A strange feature in the Nyquist plot shows a steady decrease in the $R_{ct} + R_s$ of *ca.* 20 ohms with expansion. However, because of the observed data scattering at high frequencies on expanded samples, it is unclear whether this pattern also occurs for values of R_s .

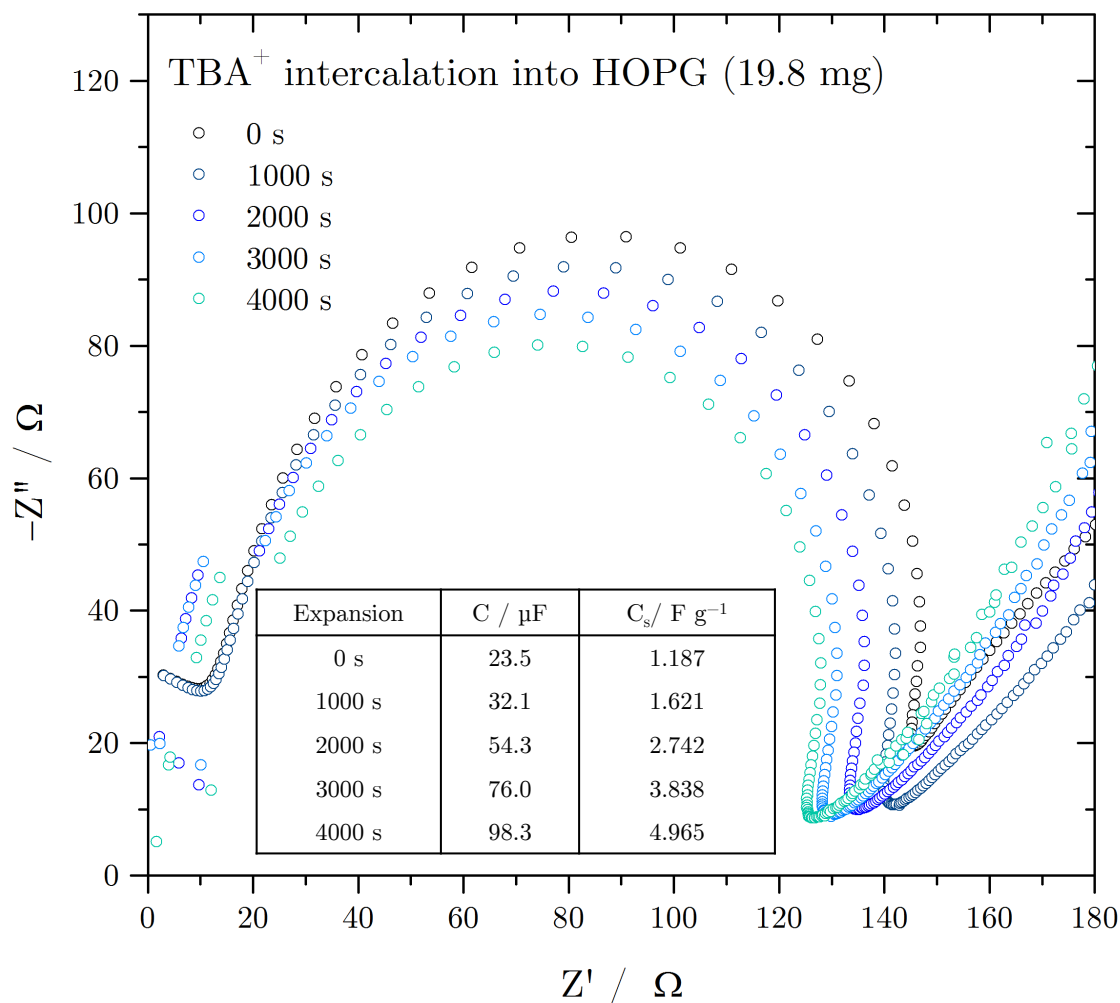


Figure 5.18) EIS data showing an increase in the measured electrochemical capacitance of HOPG as a result of electrode expansion caused *via* intercalation of TBA⁺ (−2.4 V)

In order to know the exact mass of exposed HOPG in contact with the electrolyte, it was unavoidable to omit the stainless steel tweezers in the previously presented EIS results. To account for the tweezers' electroactivity,

and to determine what proportion of the measured capacitance was governed by double layer charging at the metal|solution interface, the HOPG sample was disconnected from the setup and EIS was performed solely at the stainless steel tweezer WE. The measured impedance is presented in Figure 5.19 (red data set) and a capacitance of $0.978 \mu\text{F}$ was determined in the same manner as above. This value is surprisingly small; nonetheless it reveals that the tweezers contribute a negligible amount to the electrochemical double layer charging, and procedure/analysis conducted in the same cell should be possible.

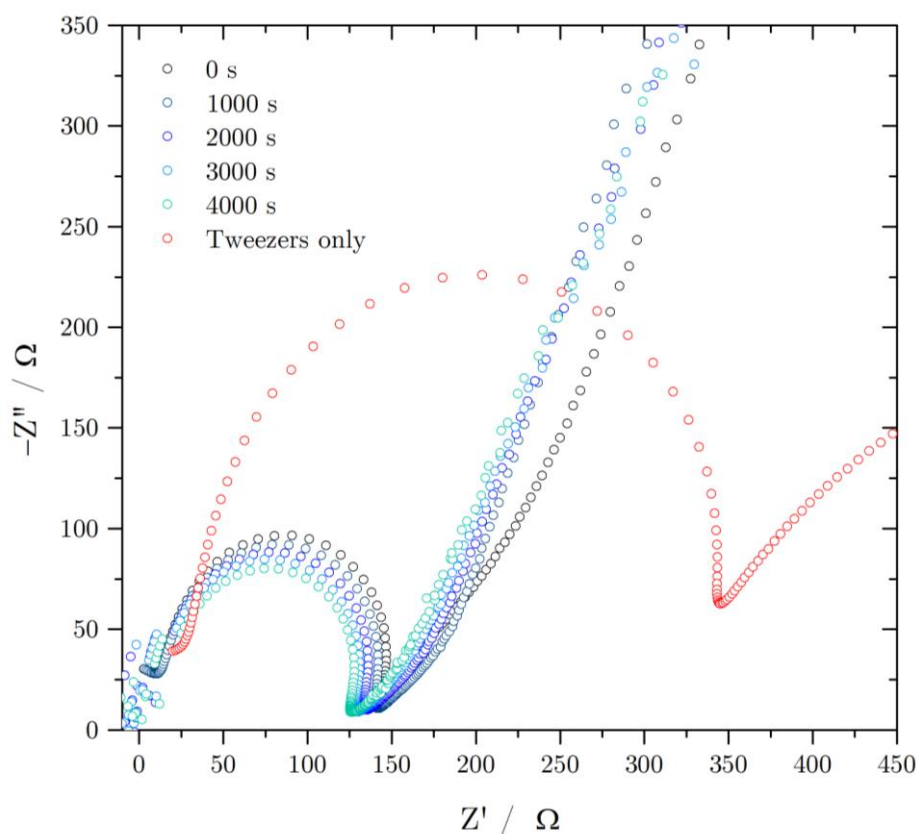


Figure 5.19) EIS data of a stainless steel WE in TBABF_4 (0.1 M) in NMP (red) showing comparative data obtained at a HOPG WE (blue/green)

The system was repeated with HOPG electrode exposed to TMA^+ -containing electrolyte, using the original method of submerging the entire sample of HOPG + tweezers. The Nyquist plot presented in Figure 5.20 shows a much smaller

magnitude to the previous TBA^+ setup; though this is explained by the much smaller working electrode area than previously, it highlights how sensitive the system is to different conditions. However the TMA^+ intercalation only increases the measured capacitance by *ca.* 10% after 4000 s intercalation, compared to nearly 500% increase as a result of TBA^+ intercalation.

The smaller change in measured capacitance is the instinctive result; TMA^+ intercalation should cause a smaller degree of capacitance increase than TBA^+ intercalation, because TMA^+ causes a smaller degree of electrode expansion. This makes sense, however an increase in the ‘degree of expansion’ is surprisingly large. In addition, the significant difference in magnitude between the original sample impedance’s should not go unnoticed, and it is possible this contributes to the increase.

Finally, the results are not particularly conclusive, since intercalation of TMA^+ should theoretically generate more charge at the electrode|solution interface, because more TMA^+ can be surface bound than TBA^+ because of fewer spatial restrictions and both cations have the same valence. This is not reflected in the measured capacitance of the two systems, and further questions the reliability of the 50 X increase.

The Z' axis intercept of the Nyquist curve indicates a solution resistance of *ca.* 25 Ω and this resistance appears to be unaffected by the charging process, despite colourisation of the electrolyte and suspected electrolyte decomposition. The total mass of the HOPG sample (4.7 mg) has been used to determine approximate specific capacitance values for the expanded HOPG samples, and are on the order of $\mu\text{F g}^{-1}$. Impedance measurements obtained purely at a HOPG electrode exposed to the electrolyte were found to be much less noisy than those including the tweezers in the measurement, however this was

preferred to removal of the tweezers and therefore not knowing the exposed mass of electrode.

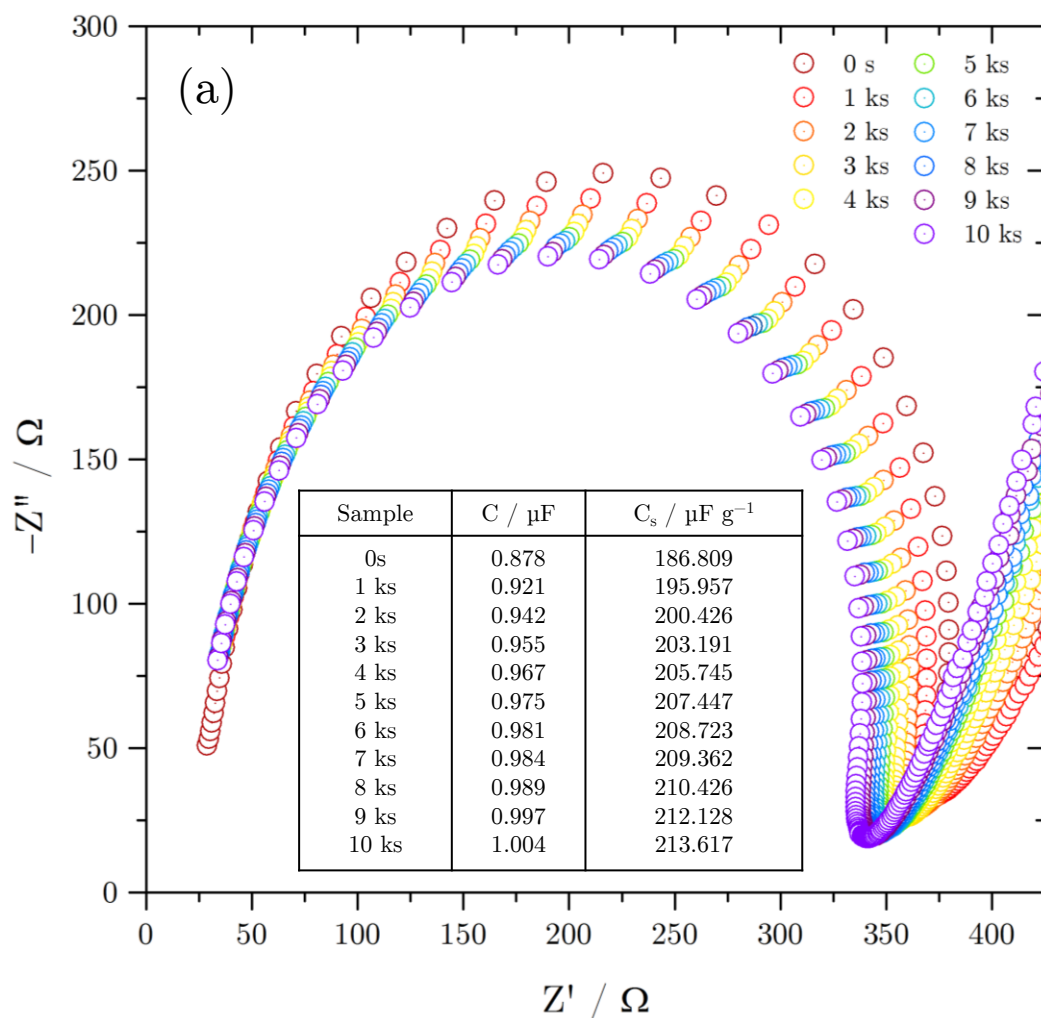


Figure 5.20) Nyquist plot showing high frequency EIS data measured at a HOPG WE in TMAClO_4 (0.1 M) in NMP at cumulative cathodic charging times (-2.4 V), showing an increase in measured capacitance and decrease in resistance to charge transfer

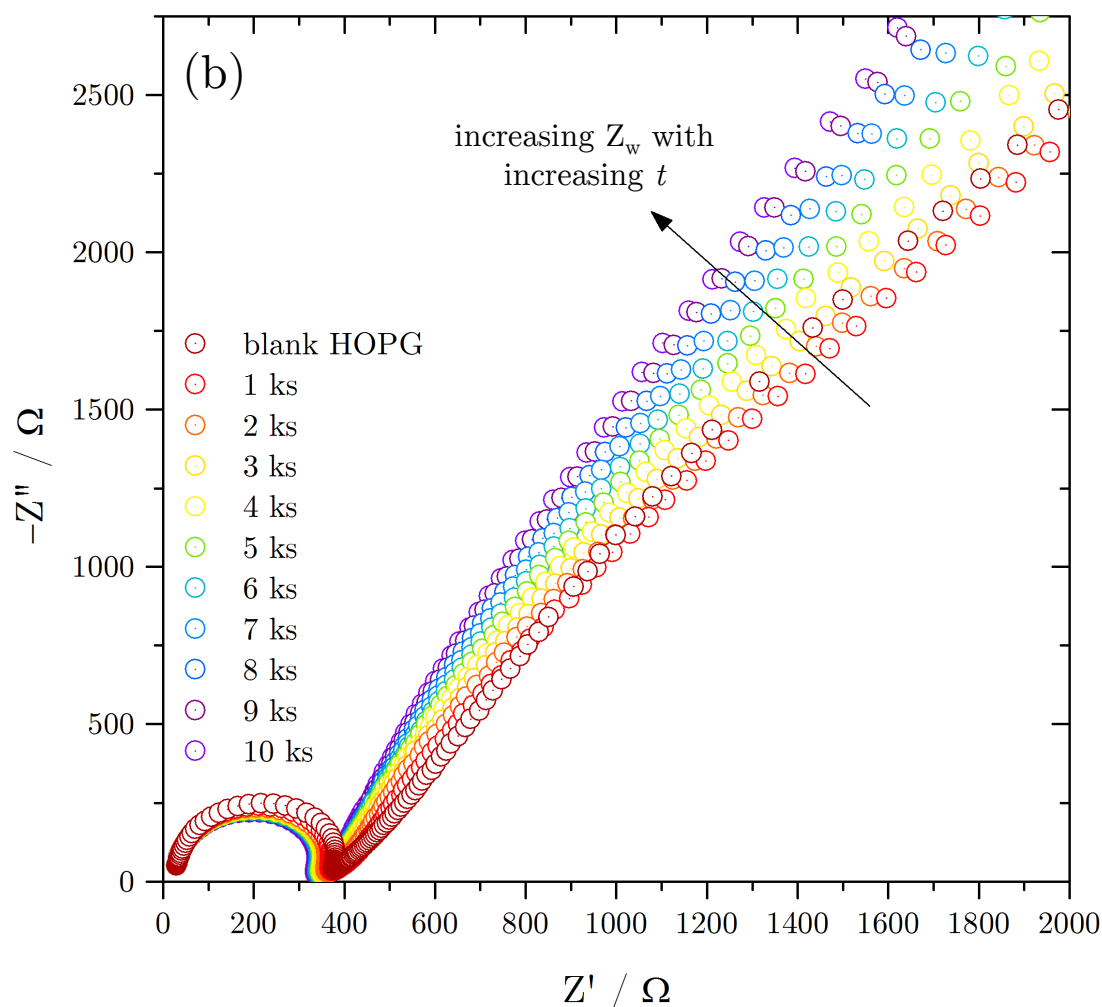


Figure 5.21) Nyquist plot showing EIS data over the entire frequency range, measured at a HOPG WE in TMAClO_4 (0.1 M) in NMP at cumulative cathodic charging times (-2.4 V), showing an increase in the total impedance associated with diffusion control

As well as an increase in the measured electrochemical capacitance of the expanded HOPG, the total Warburg impedance associated with diffusion behaviour appears to increase steadily with expansion time. Since the Warburg impedance is a measure of resistance to mass transport of the electrolyte, it can be safely assumed that this feature is solvent/electrolyte related, and probably associated with solvent decomposition, since solvent breakdown would naturally result in decreased ionic conductivity *via* a decrease in transport efficiency. As in Figure 5.17, there are two clear observable gradients in the Warburg

impedance, and these two gradients are preserved throughout the expansion process.

The angle of the Warburg impedance, initially measuring *ca.* 45° to the Z' axis, is indicative that the mass transport of species to the electrode is behaving like that of semi-infinite linear diffusion.²⁷⁶ However during the intercalation process, the Warburg angle to the Z' axis increases steadily, indicating that the R_4N^+ species are experiencing greater impedance towards diffusion. There are several reasons why this might be; firstly, any decomposition of NMP would increase the resistance in the cell, and the diffusion of electrolyte would become more difficult. Since discharge was performed prior to EIS measurements, it seems unlikely that the increased impedance is a result of gallery saturation; thus causing spatial restrictions to ion diffusion. In addition, the Warburg ‘double-gradient’ observation in initial measurements is preserved during cathodic load. If the increase in Z_w with cathodic load is due to solvent breakdown, it would seem sensible that the solvent breakdown would increase impedance to diffusion in both the bulk solution and during intercalation, and thereby maintaining the double gradient feature in the Nyquist plot.

Additionally, R_{ct} also appears to decrease steadily with increased expansion time, at approximately the same rate as ΔC_s ; however it is currently unclear as to why this trend is observed.

Figure 5.22 shows how the measured specific capacitance and charge transfer resistance of the expanded HOPG vary with electrode expansion, expressed as cumulative intercalation time, as a result of TBA^+ intercalation/expansion.

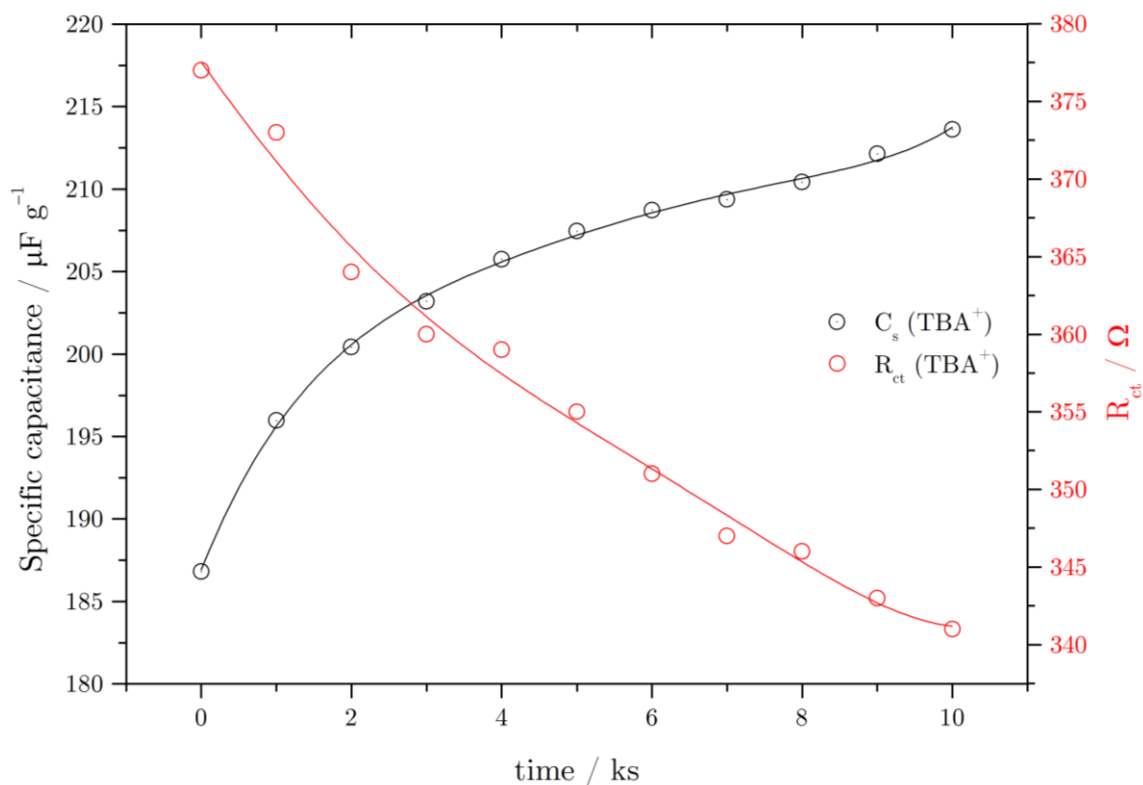


Figure 5.22) Capacitance and R_{ct} trends as a function of cumulatively measured intercalation times, at a HOPG WE in TBABF₄ (0.1 M) in NMP

Admittedly, the measured specific capacitance values on the order of $200 \mu\text{F g}^{-1}$ are drastically small in comparison to representative supercapacitor values, typically on the order of several hundred F g^{-1} , indeed the theoretically obtained value for graphene-based supercapacitors in which the entire surface area of graphene is utilised produces a value of 550 F g^{-1} .^{277,278,279,280} However, this example highlights the observed increase in capacitance as a result of cation intercalation, and although the measured values are typically small because the surface area change is not very large, this is only a preliminary study towards the use of expanded graphite electrodes for use in energy storage: the intercalation mechanism would need to be performed on comparative few-layer graphene samples which could prove to be an interesting study.

To confirm the observed EIS trends' dependence on an intercalation/expansion mechanism, the procedure was conducted at the stainless steel tweezers where no graphite was included, representing a system in which no ion intercalation or subsequent electrode expansion is possible. Figure 5.23 shows the obtained Nyquist plot, and it is clear that no change in the impedance occurs over the course of cathodic loading. The increase in observed C_s can therefore be attributed to an increased working area of the graphite cathode, allowing for a greater degree of electrochemical double layer charging at the electrode|solution interface.

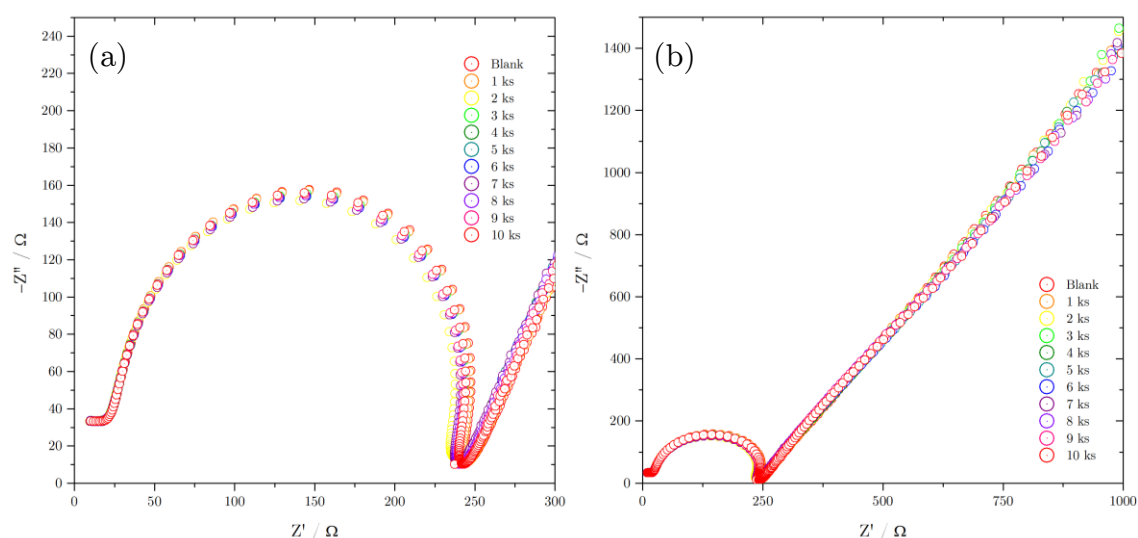


Figure 5.23) Nyquist plot showing EIS data over a) the entire frequency range, and b) high frequency range, measured at a pair of stainless steel tweezers (WE) in TBABF₄ (0.1 M) in NMP at cumulative cathodic charging times, showing no change in C , R_s , R_{ct} , and Z_w over intercalation times as large as 4000 s

5.3 Conclusions

The optical images and SEM micrographs presented herein, show that as a direct result of applied cathodic potentials to graphite electrodes in the exposure of R_4N^+ containing electrolytes, irreversible expansion of the graphite electrode is observed. However because of the increased flexibility associated with the increasing length of the alkyl chain lengths, there was not an obvious difference in the rate of observable expansion with the use of TEA^+ over TMA^+ , though TBA^+ intercalation did produce a greater degree of expansion over smaller charging timescales. TEA^+ is not significantly larger than TMA^+ (crystallographic diameters 0.674 nm and 0.558 nm, respectively), and the flexibility of TEA^+ allows the cation to intercalate without causing much more deformation than through the intercalation of the smaller TMA^+ . However the much larger TBA^+ cation (0.826 nm), is over twice the diameter of the interplanar graphite galleries and the flexibility of the cation cannot compensate for the sheer size of the cation, resulting in significant expansion effects.

Although macroscopic imaging of the electrodes exhibits uniform expansion of the electrodes, microscopic segmentation was revealed through the use of microscopic imaging techniques. The regularity of the observed segmentation was quite remarkable, and was revealed during powder XRD studies in the form of sub-lattice planes in the as-prepared graphite samples at 2θ values in the region $10^\circ - 25^\circ$. Indeed, the degree of the inherent sub-lattice spacing was more prominent in lower-grade HOPG, with higher grade HOPG unsurprisingly exhibiting much weaker signals associated with planes other than the prominent (002) crystallographic plane. The presence of these sub-lattice planes is thought to have a significant effect on the intercalation mechanism, whereby intercalating species preferentially intercalate *via* these pre-formed galleries due to a smaller energy cost. The implication of this sub-lattice-preference on the

exfoliated materials will be presented in the following Chapter, though it is believed to be significant.

Powder XRD revealed evidence to support the presence of sub-lattice planes in the HOPG electrodes, and generally showed an unsurprising loss in lattice crystallinity of HOPG during expansion. Additionally, the prominent (002) signal was seen to decrease and broaden with expansion, indicting a loss of this crystallographic feature, and the appearance of a small peak at slightly large 2θ values indicated the introduction of a new interplanar spacing as a result of graphene gallery contractions.

Finally, EIS was employed to probe effects of electrode expansion on measured specific capacitance and measured impedance. It has been shown that the specific capacitance increases as a function of HOPG intercalation, and although the values recorded were only on the order of $\mu\text{F g}^{-1}$, it might offer an introduction to a study towards R_4N^+ expanded few-layer graphene materials for employment in supercapacitor applications.

Because standardisation of measured surface area/volume was not cross-comparable between different systems, it could be beneficial to measure the degree of expansion, either using XRD or EIS, as a function of the total charge passed to the system, rather than the expansion time, and could provide a better study towards the expansion effects of the different R_4N^+ species. Other future work ideas developed from this Chapter include investigating the R_4N^+ electrolyte concentration dependence upon the degree of expansion, either with the aid of SEM, XRD or EIS. The electrolyte concentration dependence is revisited in section 6.6, and could prove to be an interesting study.

Chapter six

Electrochemical cathodic exfoliation

6 Electrochemical cathodic exfoliation

6.1 Introduction

The ensuing goal of this project was to investigate the employment of R_4N^+ cation intercalation for the exfoliation of a bulk graphite cathode into its individual constituent graphene sheets. This Chapter therefore focuses on the methods employed for direct exfoliation of graphite cathodes alongside the isolation and characterisation of the exfoliated products.

In principle, R_4N^+ cations were intercalated for time t by cathodically charging a graphite electrode, such that the graphite cathode exfoliated in solution and exfoliated products were dispersed in the solvent. The influence of oxygen was investigated in the exfoliation process alongside different source electrode materials; the employment of a HOPG cathode did not directly yield visible exfoliation, nor any identifiable flakes from solution processing, without the employment of an undesirable subsequent sonication stage to encourage exfoliation of expanded HOPG electrodes. In contrast, such post-treatment was not necessary for the exfoliation of HK-graphite electrodes, and graphite rods were found to exfoliate with minimal effort, driven using applied potentials as high as -2.4 V. As has been highlighted in previous Chapters, the need for a high intercalation stage is unprecedented, since low staging degrees result in graphitic exfoliation and eventual electrode fracture (described later). Arguably there is a fine line and a measure of personal opinion on the definition of graphitic material and few-layer graphene. Geim and Novoselov show that the electronic structure of graphite significantly changes for flakes consisting of less than ten graphene layers,³⁸ therefore for the purpose of this work any exfoliate material established to be greater than *ca.* 10 layers has been considered ‘graphitic’. Graphene/graphite terminology has become an increasing

controversial topic within graphene literature, and the author has laid a strict ‘ten-layer’ limit to avoid contributing to this issue.

6.2 Results

6.2.1 Methods and processes

The electrochemical intercalation method of graphene production naturally yields graphene material dispersions from which the graphene material needs to be isolated. Although this has not proved problematic in sonication-only routes, in which the pure solvent is easily removed *via* evaporation, the presence of electrolyte in graphene dispersions is currently not well studied. Indeed, the effects of R_4N^+ based electrolytes on graphene dispersion stability have certainly not been reported, and the potential to cause flake re-aggregation should be highlighted. Furthermore, the simple process of solvent evaporation leaves residual salt crystals on the sample surface, thus requiring a careful washing procedure in order to successfully remove electrolyte whilst retaining any graphene materials.

Electrochemically prepared graphene dispersions contain NMP, R_4N^+ based electrolyte and any reduced/decomposed forms of electrolyte and/or solvent. To isolate material of interest, graphene dispersions were centrifuged between 8,000 and 13,500 rpm for a maximum period of 30 min in order to remove large graphitic particulates, a *ca.* 2 mL aliquot was removed from the supernatant and allowed to rest for 24 h. Flakes were extracted using two methods: filtration, and solution drop casting onto oxidised silicon substrates. In earlier work, filtration was performed *via* alumina membranes (0.01 μm pore diameter) since filtration naturally offered increased yields due to the higher throughput. However flake identification on alumina substrates was challenging, due to the poor contrast offered by the alumina substrate and alumina membranes were naturally not suitable for AFM analysis, due to their softness and roughness.

The natural substrate for graphene identification by optical methods is Si/SiO₂ (see section 1.5) and therefore flake isolation for Raman characterisation was obtained by drop casting <1 mL graphene dispersion onto a Si/SiO₂ wafer and washing with pure NMP, ethanol and isopropylalcohol (IPA) to remove salt residue. Si/SiO₂ also proves to be the optimum substrate for AFM analysis since the hard surface was not disturbed by the AFM tip.

Care when undertaking substrate washing was essential, where placing the substrate under an already soft-flowing stream of cleaning agent was found to be the most effective washing procedure, since this offered a more gentle alternative to direct rinsing. The yield of the deposited flakes was found to improve on repeated washing and re-depositing. However, this process was repeated no more than three times to avoid potential re-aggregation of the deposited flakes.

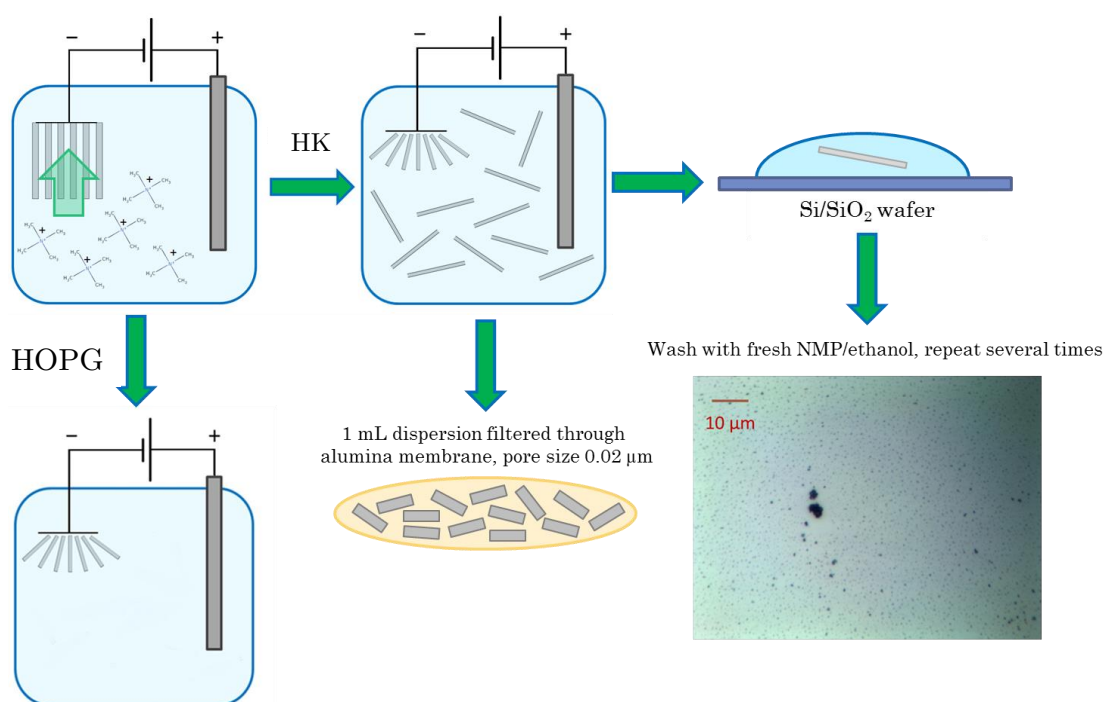


Figure 6.1) Schematic showing the routes towards flake isolation from HK-graphite rod electrodes *via* filtration and drop casting methods

Figure 6.1 presents a schematic highlighting the flake isolation procedure when exfoliating HK-graphite rods. It also shows the effects of intercalating HOPG with R_4N^+ species; this was found to produce no exfoliation (see later, section 6.2.4). For HOPG studies, electrodes intercalated for varying periods of time at different potentials were then sonicated for varying times at 30 % power, 37 Hz, in order to break apart the lattice. However, since the total omission of any secondary processing stage was desirable, focus was placed on electrochemically exfoliating HOPG rather than the employment of sonication techniques and, as such, little sonication work is included in this thesis. The optical image in Figure 6.1 shows a Si/SiO₂ wafer deposited with NMP/electrolyte/graphene dispersion and washed with pure NMP and ethanol/IPA. This washing and deposition procedure was repeated several times in order to improve flake yield and to increase the probability of few-layer graphene materials present on the silica substrate. The exact flake isolation procedure will be shown prior to presentation of the respective results.

6.2.2 Effects of gaseous liberation on exfoliation procedure

During CV, gaseous evolution at the graphite electrode was noticeable whilst exploring very negative potential regions (*ca.* < -4 V), however not noticeable during scanning of regions of smaller negative potentials (*ca.* > -3 V). During CA procedures however, at potentials which did not previously yield gaseous evolution during CV, gaseous evolution was observed streaming from the graphite cathode after extended periods of time.

Bubbling was observed to greater degrees in oxygenated systems and less so in work under a controlled inert atmosphere, likely due to hydrogen evolution *via*

oxygen reduction and water hydrolysis, however bubbling was not completely absent in glove box studies.

In systems where a large portion of the graphite electrode was submerged, as described in Figure 6.2(a), gaseous coverage of the reverse face of the electrode quickly reached 100% and remained covered, thereby obstructing contact between the solution and inverse face of the electrode. Bubble formation at the vertical electrode|solution interfaces were able to rise unhindered, and therefore a large proportion of the electrode remained in direct contact with the electrolyte. In this system therefore, bubble formation on the reverse face was not problematic. However, this electrode arrangement causes complications in data comparison, since maintaining consistency with respect to the active electrode working area was difficult to manage.

To address the issue of quantitative determination of electrode working area, a graphite electrode was placed in contact with the solution such that a meniscus formed between the electrode face and solution, as described in Figure 6.2(b), thereby ensuring the working area of the electrode equalled area of the rod's face. It was assumed that the degree of electro-wetting from the solvent on the vertical face of the electrode was negligible.

This meniscus arrangement proved problematic during CA procedures since the only active area (accessible to ion intercalation) of the electrode was the reverse face, and as a result, the total surface gas coverage on the electrode was found to increase steadily; hindering the exfoliation rate of a graphite electrode. Eventually bubble coverage reached 100%, acting as a barrier between the electrolyte and the graphite (Figure 6.2(c)). This was reflected in the decreased rate of exfoliation, which was observed to eventually cease along with the measured current. This was significant, since it demonstrates that solution contact is necessary for successful exfoliation of the electrode, and it is possible

to further conclude that electrode exfoliation isn't simply a result of electrostatic charging. In order to progress and permit species intercalation, the electrode was sharpened slightly to allow the unhindered escape of bubbles (Figure 6.2(d)).

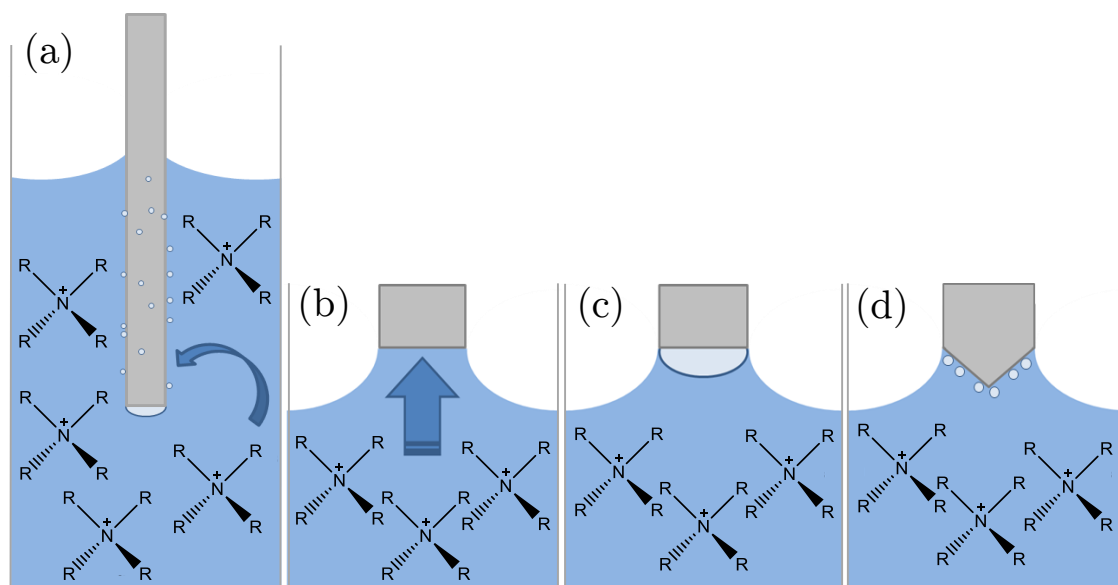


Figure 6.2) Schematic showing the effects of gaseous products on exfoliation procedures and unsharpened graphite electrodes

6.2.3 NMP exposure effects on graphene materials

To probe the effects of NMP masking of few-layer graphene on Si/SiO₂ substrates with 300 nm oxide layer thickness, and to determine whether or not exfoliated graphene materials would be visible after NMP exposure/deposition, few-layer graphene was prepared using micromechanical cleavage using high-tack, low-stain scotch-tape (BT-150E-KL, TELTEC GmbH, Germany) and transferred directly onto a Si/SiO₂ wafer (Figure 6.3(a) and 6.3(b)). Figure 6.3(c) shows an optical micrograph of a few-layer graphene flake transferred to a Si/SiO₂ wafer *via* dissolution in pure NMP. Scotch-tape supporting micromechanically cleaved graphene was submerged in NMP and sonicated for 4

h to allow transfer of graphene from tape to solution. The solution was then dropped onto a Si/SiO₂ wafer and oven dried at 200 °C for 12 h. Remaining solvent was removed by washing with ethanol/IPA and further oven baking. Finally Figure 6.3(d) shows graphene directly transferred to Si/SiO₂ from scotch-tape on which pure NMP was dropped and oven dried. In all the procedures it can be seen that aside from a slight difference in hue and a slight decrease in contrast, flakes remain identifiable on Si/SiO₂ wafers after exposure to NMP and it can be established that flakes exposed to NMP are still identifiable on 300 nm oxide covered Si/SiO₂ substrates.

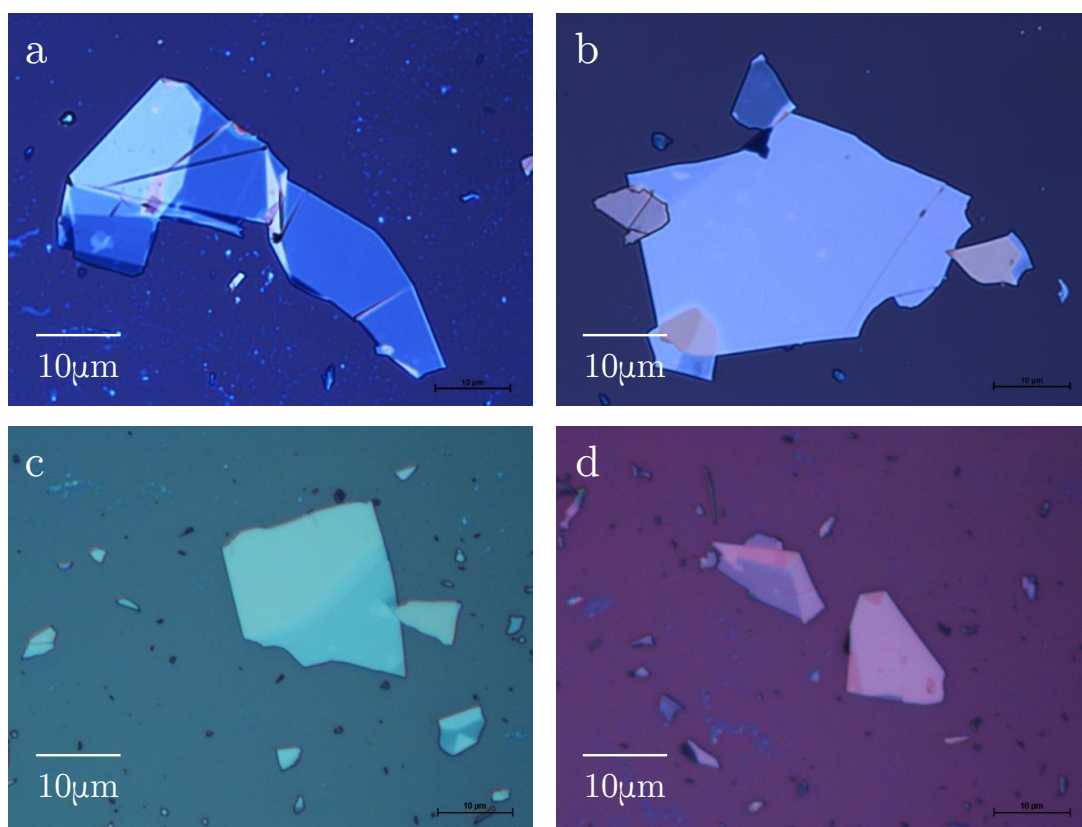


Figure 6.3) Optical micrographs showing (a) and (b) micromechanically cleaved few-layer graphene on Si/SiO₂ substrate, (c) NMP dispersed graphene transferred to Si/SiO₂ and (d) micromechanically cleaved graphene on Si/SiO₂ substrate after exposure to pure NMP and oven drying

6.2.4 Graphite cathode source materials

The two main graphite source materials employed for cathode exfoliation were HOPG (SPI-1, SPI-2, and SPI-3 grades) and HK-grade graphite rods of various grain sizes (2 μm –800 μm). Other graphite sources investigated included natural Madagascar graphite and graphite powder, each requiring adapted electrode setups.

As shown previously in cathodic expansion studies, HOPG was found to expand as a direct result of cationic intercalation. This expansion was found to depend on the size of the cation employed, the timescale over which the cathodic potential was applied as well as the magnitude of the applied potential. Excessively negative applied potentials (less than *ca.* -4 V) had significant solvent/electrolyte decomposition effects. Figure 6.4(a), 6.4(b), and 6.4(c) show expansion using TMA^+ , TEA^+ and TBA^+ , respectively, for extended periods of time, however none of which directly yielded exfoliation into solution. The solution was retained, centrifuged (though this step was later removed in an attempt to recover larger particulates) and analysed using optical microscopy and Raman spectroscopy. After drop-casting solutions, in which HOPG was electrochemically expanded, onto Si/SiO₂ wafers; Si/SiO₂ substrates appeared ‘blank’, showing no presence of flakes regardless of the chosen R_4N^+ species, the potentials applied in the CA procedure, centrifugal speed (0 – 13,500 rpm), temperature (up to 80°C), solvent, or SPI grade of HOPG.

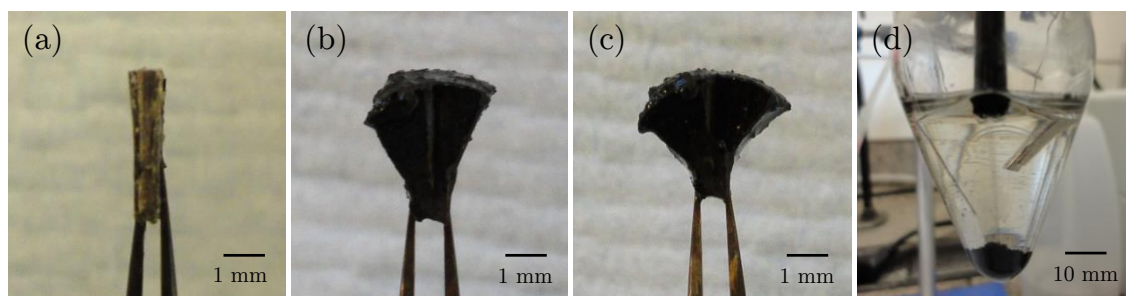


Figure 6.4) (a-c) HOPG expansion as a result of R_4N^+ intercalation with various procedures and systems, and (d) direct HK-graphite exfoliation as a result of R_4N^+ intercalation without the need for further processing

Figure 6.4(d) shows the effects of cathodically charging a graphite rod in the presence of R_4N^+ based electrolytes, in this case TEA^+ (0.1 M) in NMP, -3.0 V after 2000 s, though similar observations were recorded with all the R_4N^+ species at potentials equal to or more negative than -2.3 V. On the application of potentials more negative than -2.3 V, the graphite electrode was observed to disintegrate into solution, with varying visible particle sizes. Larger exfoliate slowly settled to the bottom of the electrochemical cell, however smaller flakes remained suspended for several hours and even remained in solution after centrifugation at 8,000 rpm for 30 minutes.

The reasons behind the differing results have been assigned to several structural differences of the two graphite sources. HOPG is synthesised by annealing pyrolytic carbon at 3300 K under compressive stress, and has a relatively large degree of anisotropy with respect to the crystallographic orientation of the graphene planes, with an angular spread between the graphene sheets of less than 1° .²⁸¹ Conversely, HK-graphite was produced by the high pressure compression of graphite powder, the result being a rod (in this case) of graphite, with a comparatively random orientation of graphite flakes. It is thought that the highly ordered nature of HOPG allows for cumulative vdW attraction

between neighbouring graphene sheets, making the electrode resistant towards exfoliation. This is observed in the impressive expansion effect of the HOPG lattice and its reluctance to exfoliate, in contrast to HK-graphite's small observable expansion. This cumulative sheet attraction is not observed in HK-graphite for the converse reasons, with the degree of total vdW attraction being significantly smaller due to the random orientation of flakes. The effect of the structural differences is both advantageous and a hindrance to the exfoliation process; the tendency not to exfoliate in the case of HOPG allows for a greater degree of intercalation and increased staging: essential for the exfoliation thinner materials. However, the obvious disadvantage lies in HOPG's inability to exfoliate at all under cathodic load in the presence of R_4N^+ . In contrast a decrease in the amount of cumulative attractive force permits premature exfoliation of HK-graphite, resulting in electrode fracture of large, and sometimes non-expanded graphitic particulates. However, despite the arguably premature exfoliation, HK-graphite does show some evidence of undergoing electrode expansion (XRD, Figure 5.15) prior to exfoliation, and this is supported by the isolation of few-layer graphene materials (see later, section 6.2.9 and 6.2.10).

As mentioned in section 1.7, Yang and co-workers employed extremely negative potentials (between -15 V and -30 V) to exfoliate HOPG electrodes into few-layer graphene materials.¹⁵⁴ Though they offer no explanation as to the use of such extreme conditions, and especially since they report cation intercalation occurs at potentials as little as -2.5 V, it is suspected that the requirement of such potentials was in order to overcome the strong cumulative vdW attraction of neighbouring graphene sheets in HOPG electrodes. However, the use of such negative potentials is unattractive for industrial scalability and has been avoided herein.

Admittedly, HOPG offers a more desirable route, since a more chemically pure source material is employed, and a higher degree of staging is theoretically obtainable. In addition the prevention of premature electrode fracture in HK-graphite is challenging. Nonetheless both graphite sources have been investigated, albeit with more effort being placed on HOPG exfoliation and to encourage the exfoliation of expanded HOPG, sonication processing has been employed. This is an undesirable route, since the industrial scalability of sonication production routes is unattractive due to the high associated energy requirements; sonication was tested only briefly. For HK-graphite electrodes, no further exfoliation processing was necessary: dispersions were centrifuged and flakes isolated directly onto Si/SiO₂ for characterisation as described in section 6.2.1.

HK graphite rod electrodes were available in several various grain sizes; 2, 3, 5, 7, 11, and 800 μm . For reference, the grain size of HOPG (in all SPI grades) was between 0.5–1 mm.⁸

To investigate grain sizes between 11 μm and 800 μm , graphite ‘pellet’ electrodes were constructed using natural graphite flakes; grades “2369”, “9842”, and “RFL 99.5” with grain sizes between approximately 500 and 700 μm , and were compressed with the use of a steel pellet press and standard workshop vice, into graphite pellets both with and without the aid of a polyvinyl alcohol (PVA) binding adhesive. However, in-house prepared graphite pellet electrodes were found to be very unstable when exposed to NMP, both with and without applied charging conditions, and the electrodes were seen to disintegrate with relative ease yielding premature electrode fracture and producing non-dispersible large graphitic particulates. Voltammetry obtained from the use of compressed graphite electrodes was typically quite resistive, and displayed little features in the way of Faradaic current processes. The resistance was attributed to the

PVA adhesive binder, however decreasing the amount of binder used simply resulted in delicate electrodes. Because of this, graphite pellet electrode studies were not continued, and because of the inability to purchase graphite rods with inherent grain sizes between 11 μm and 800 μm , there remains scope to investigate the effects of grain size on exfoliation success.

6.2.5 Selection of cathodic charging potentials

The potentials of the current features observed during CV were used to define those set in chronoamperometric mode to control the intercalation processes. To investigate the effects of applied cathodic load, the applied potential was varied over the entire range of the intercalation peak using potentials of (a) -2.2 V, (b) -2.3 V, (c) -2.4 V, (d) -2.6 V, (e) -2.8 V, and (f) -3 V, for periods of up to 24 h. These selected potentials are depicted in Figure 6.5, showing a typical TEA⁺ CV to which these potentials correspond. The intercalation peak obtained from various R₄N⁺ containing electrolytes differed slightly in terms of potential, and therefore the selected potentials were altered accordingly. However, it was found that despite the different R₄N⁺ cations used, the same general relationship was observed: the rate at which exfoliation occurred was observed to be faster for more negative potentials, with potentials near point (a) producing little observable exfoliation even after prolonged intercalation times of over several hours. Applied potentials below -3 V typically resulted in colourisation of the electrolyte from clear and colourless, through yellow to eventually dark brown/black accompanied with an intense amine aroma, associated with decomposition of the solvent (Figure 3.20) and an observed expansion of the electrode after timescales of only a few minutes.

Solvent colourisation was always accompanied by bubbling at the graphite cathode, and was found to become more vigorous with decreasing potential. A slight degree of bubbling was observed at potentials as high as -2.3 V, though it was only visible after several hours of cathodic charging.

To minimise the effects of solvent decomposition and bubbling, though resulting in slow rates of expansion (and subsequent exfoliation in the case of graphite rods), charging potentials were selected at potentials more positive than the measured I_{pc} , *i.e.* between -2.2 V and -2.5 V. Avoiding the use of extreme

potentials was necessary in order to understand the processes involved, since applied potentials exceeding several current responses can induce all the mechanistic steps simultaneously.

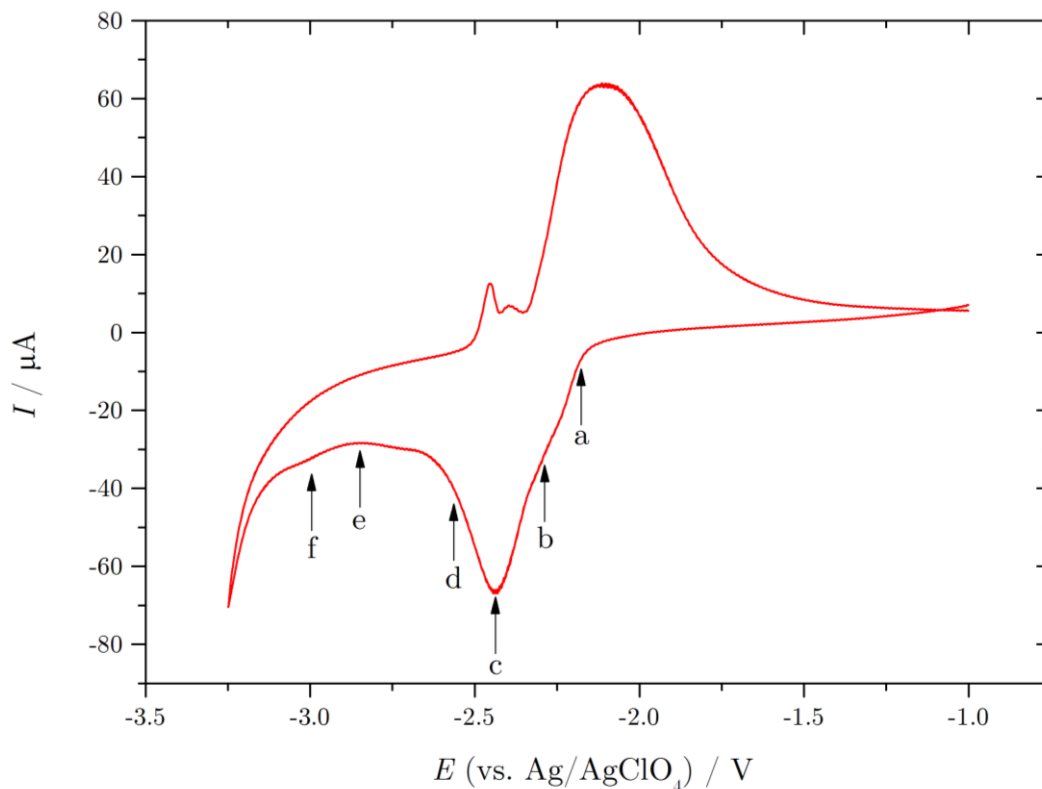


Figure 6.5) A typical TEA^+ intercalation/de-intercalation CV depicting the selected cathodic charging potentials used in the chronoamperometric procedure, showing different potentials of the intercalation peak (a) -2.2 V, (b) -2.3 V, (c) -2.4 V, (d) -2.6 V, (e) -2.8 V, and (f) -3 V.

The selected potential for the charging process had dramatic effects on the exfoliation and Figure 6.6 shows the two extremes of this selection. Figure 6.6(a) shows the immediate effects of a more negative cathodic charging potential (-3 V). On application of such a low charging potential, the electrode was found to exfoliate immediately, and the photograph clearly shows the exfoliation of the graphite rod electrode and subsequent settling of large particulates in the bottom of the flask with remarkable clarity. This degree of

exfoliation was found to be amplified, in terms of both visible size of the particulates and rate of exfoliation, with the use of even more negative cathodic potentials and with larger cationic species.

Figure 6.6(b) shows the alternative result, in which the graphite rod was charged at a less negative charging potential (-2.4 V). Indeed a greater period of time (*ca.* 4 h) was required until the electrolyte appeared as that of Figure 6.6(b). The significance of this image lies in the clear grey layer of exfoliation formed (Figure 6.6(b), highlighted with red box), which appears to be self-supporting in the region of electrolyte in close proximity to the working and counter electrodes. This band of exfoliation was found to eventually settle, over a period of 24 h, after removal of the external potentials from the system. Large graphitic particulates, as in the case of Figure 6.6a, were found to be produced, though the exfoliation was not limited to these large, graphitic flakes.

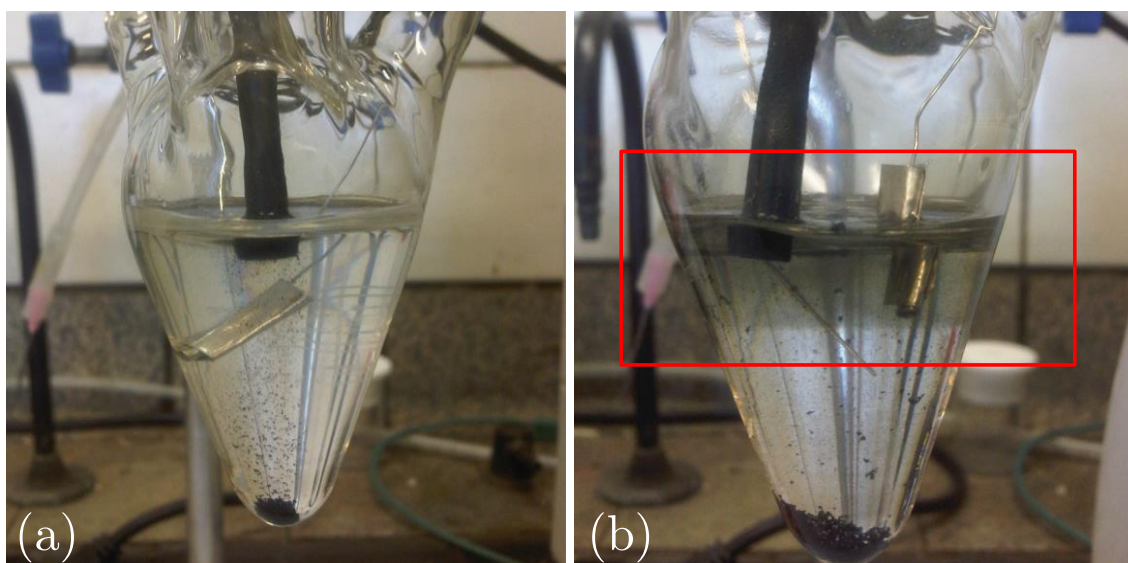


Figure 6.6) Photographs of the electrochemical cell under two different potentiostatic conditions in which the graphite rod was (a) cathodically charged at -3 V in the presence of TEA^+ (*ca.* 2000 s), and (b) cathodically charged at -2.4 V in the presence of TEA^+ (*ca.* 4 h)

The most obvious explanation for this observation lies within the timescales of the intercalation mechanism. In order to produce fewer-layer material, the intercalation must occur *via* maximum staging, i.e. with a maximum ratio of intercalated layers to graphene layers and one would expect that to intercalate 10 layers would take longer than to intercalate a single layer. There is a clear hindrance to this setup; once the degree of intercalation becomes significant enough to completely exfoliate part of the graphite cathode, whether this particulate is graphitic or few-layer, the particulate cannot undergo further exfoliation once it becomes completely detached from the electrode, i.e. intercalation and exfoliation can only occur when the particulate is able to conduct the flow of charge by being part of an electrode. This is significant, since it follows that the most efficient mechanism towards single layer graphene exfoliation would be to exfoliate the graphite cathode layer-by-layer. This is clearly challenging, since it is not possible to control the intercalation of the cations with such a degree of precision. However it may be possible to maximise the intercalation-staging through the use of longer intercalation times into the bulk cathode, which can be controlled through the use of less negative charging potentials; this conclusion is drawn from the dispersions shown in Figure 6.6 in which finer particulates remained suspended in solutions prepared using less negative potentials (no grey, self-suspended band was formed using more negative potentials). This also results in less solvent decomposition of the system, since less extreme potentials are required. Furthermore, to avoid the associated costs with the use of larger absolute potentials and frequent solvent/electrolyte replenishment, not to mention organic media waste disposal, eventual industrial scalability would require minimum operating potentials and less organic waste materials for this process to attract industrial interest.

Nonetheless, this play-off between a) maximum intercalation/expansion and b) exfoliation is extremely significant. If one could control the two stages independently, by permitting intercalation and forbidding exfoliation until the desired point, then this would be a major advantage to the fabrication process; since every graphene gallery could be intercalated and expanded to yield a maximum proportion of single layer exfoliation. As of yet, there is no known practical solution to this problem, and therefore the process relies on maximising the degree of intercalation before exfoliation proceeds.

6.2.6 Sonication aided HOPG exfoliation

HOPG was electrochemically expanded in TEABF₄ (0.1 M) for a total period of 48 hours at -2.4 V. During this time, the electrolyte was replaced with fresh electrolyte every 6 h to counter the detrimental effects of NMP reduction and maximise the degree of expansion. After 48 h and *ca.* 200 fold expansion, the HOPG was placed in a solution of pure NMP and sonicated at 100% power (220 W) for a period of 24 h.

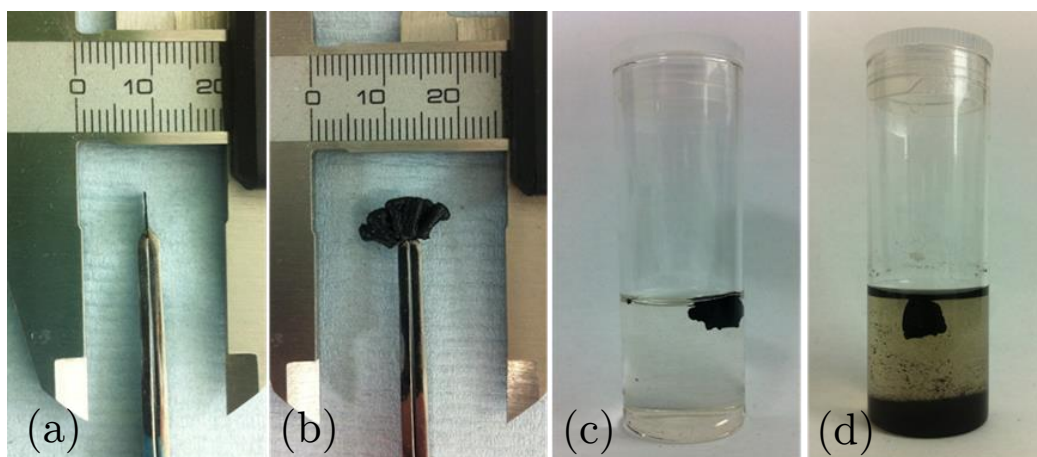


Figure 6.7) Photographs of (a) as prepared HOPG, (b) TEA⁺ expanded HOPG after 48 h in NMP at -2.4 V, (c) expanded HOPG in pure NMP, and (d) HOPG after 24 h sonication in pure NMP

The sonicated solution was centrifuged for 30 min at 8,000 rpm and a 1 mL aliquot drop cast onto an oxidised silicon wafer with 300 nm oxide layer, which was used as a substrate for subsequent Raman spectroscopy and AFM. No flakes were observed on the substrate surface post centrifugation and as a result smaller centrifuge speeds and times were experimented with in order to obtain isolated few-layer materials. The solution was also allowed to rest for 48 h with no centrifugation applied, yet still yielded no isolated materials on the oxidised silicon substrate, with the graphitic materials settling in the vial. Despite the excessive volumetric expansion observed for HOPG electrodes, successful

exfoliation to few-layer materials proved challenging, since the exfoliation produced by sonication of the expanded graphite yielded only graphitic materials of which was not stable as dispersion. There are currently no reported studies on the sonication of *expanded graphite* for the production of graphene materials.

6.2.7 Raman spectroscopy of exfoliated graphite materials

Before progressing, it should be noted that all the Raman spectra presented herein generally show a typical flake obtained from different respective processes. A ‘typical flake’ is defined as ‘a flake which frequently (over 50%) presented a Raman spectrum as shown.’ This is admittedly a rather loose definition, however without the use of automated Raman mapping, it was impossible to obtain reliable statistical data regarding flake thicknesses without manually selecting and analysing hundreds of flakes and incorporating human judgement into the analysis. It was decided that gathering ‘typical’ data would be better suited, such that more time could be spent investigating other parameters and controls. Nonetheless, the use of Raman mapping for this work would have been significantly advantageous, and would have allowed accurate statistical data regarding flake production; when producing thousands of flakes, automated statistical analysis is essential.

The exfoliation procedure was performed at various grades of HK-graphite using TEA⁺ for 24 h in NMP. Although it was suspected that less negative potentials were required for better staging, in order to increase the throughput of experiments, -3 V was applied for the duration in chronoamperometric mode, with a comparatively large Pt CE to counter solvent decomposition effects, and normal atmospheric conditions. After long charging procedures, bubbles were

seen to form on the residing surface of the graphite cathode, and to counter this effect the graphite was sharpened such that bubbles were able to escape easily (Figure 6.8).



Figure 6.8) Photograph showing reshaped graphite rod to counter the hindering effects of bubble formation on the residing face of the graphite cathode

Material produced *via* this process was removed from solution and deposited onto Si/SiO₂ wafers for Raman analysis.

HK-2 graphite (2 μm grain size) was initially employed as the starting material, and six flakes were identified and subsequently analysed; their Raman spectra are presented in Figure 6.9. In Figure 6.9, the laser spot has been included to illustrate the size of the spot relative to the analysed flake, for the purpose of clarifying the origin of visible *D* peaks in the obtained Raman spectra. Since the spot size is typically smaller than the analysed flake it is unlikely that the relatively intense *D* peak is associated with edge sites of the analysed flake and more likely to be associated with lattice defects present in the flakes and/or boundaries and edge sites between layers in few-layer flakes. All of the flakes (a)-(f) have lateral diameters on the order of 10 μm , but more significantly have graphitic-like optical appearances. The corresponding Raman spectra indicate

the presence of both graphitic-like and fewer-layer materials, with flakes (c) and (f) displaying spectra typically associated with fewer layer materials. For the purpose of clarity the spectrum of flake f has been enlarged and presented again in Figure 6.10 including a more detailed copy of the $2D$ peak.

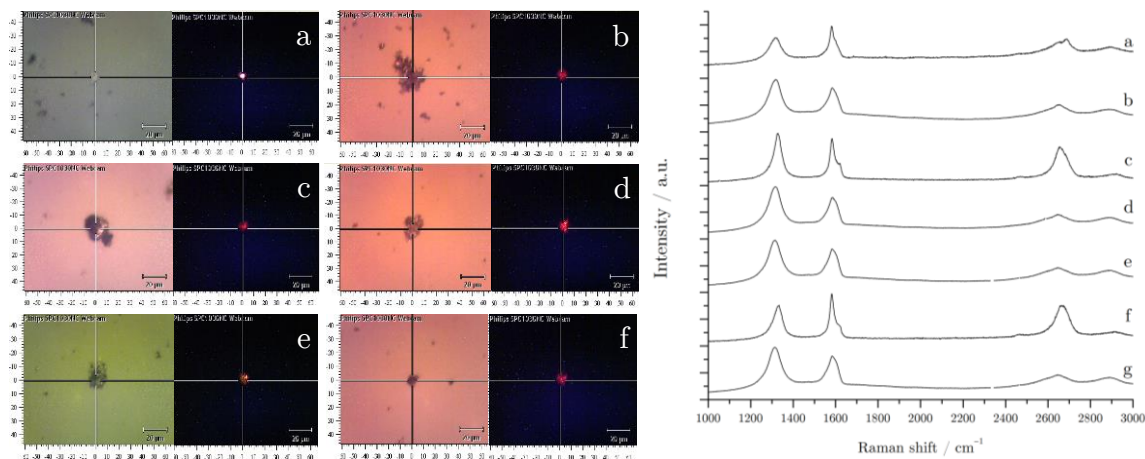


Figure 6.9) Optical images of exfoliated flakes on Si/SiO₂ substrates with corresponding Raman signal responses for each individual flake.

The Raman spectrum of flake f presents a possible tri-layer flake, indicated by the intensity of the $2D$ band and centred on *ca.* 2550 cm⁻¹. The $2D$ band can be fitted reasonably well to four Lorentzian functions, showing a flattened peak often associated with few-layer graphene materials. What is clear from this spectrum is that the flake is certainly few-layer, in contrast to the graphitic-like material observed in the optical image inset.

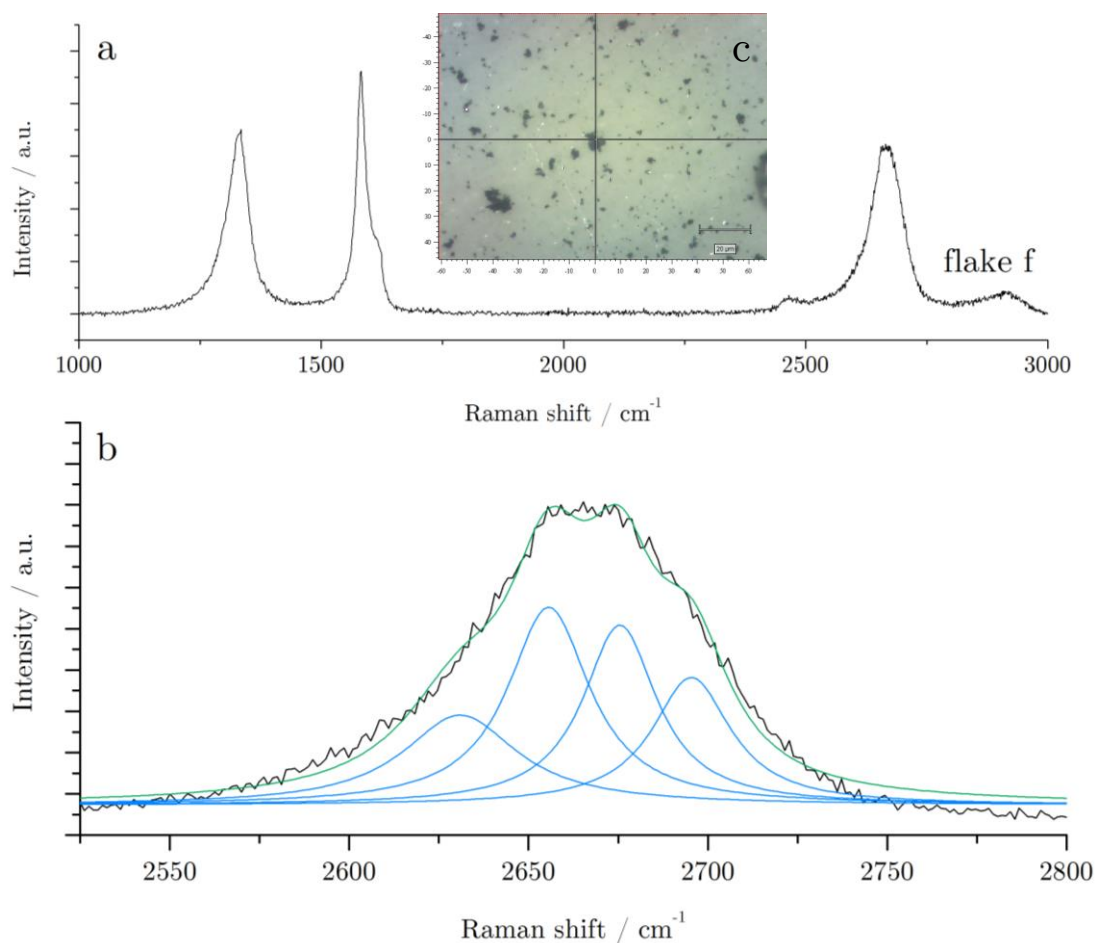


Figure 6.10) Raman spectrum of a possible tri-layer obtained from TEA^+ intercalation of HK-2 graphite, showing (a) full spectrum and (b) 2D peak only displaying reasonably good fit to four Lorentzian functions

In general, visibly larger materials produced obvious graphite-like spectra (Figure 6.11) and to obtain fewer-layer materials it was necessary to focus on as small a flake as practically possible; typically less than 5 μm in lateral diameter.

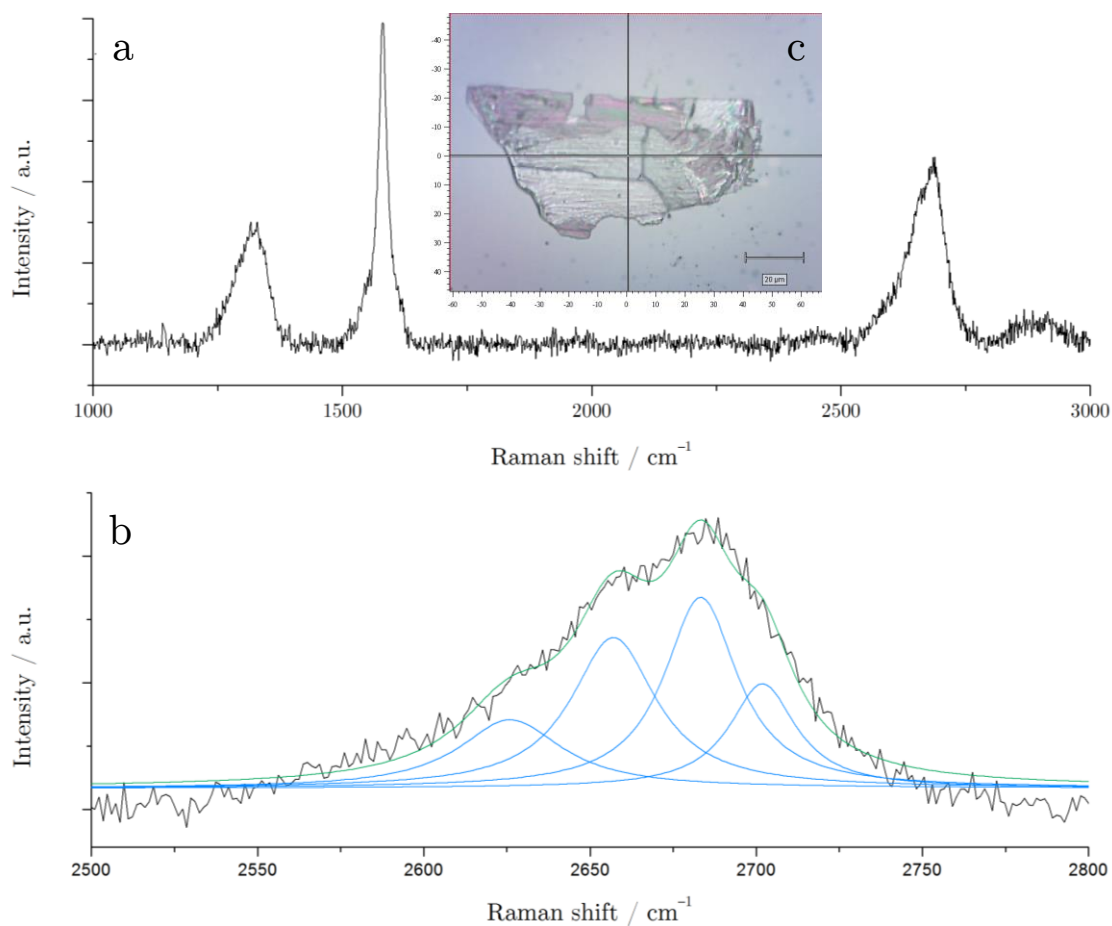


Figure 6.11) Raman spectrum of typical a graphite flake, obtained from TEA^+ intercalation of HK-2 graphite, showing (a) full Raman signal, (b) optical image of flake, and (c) 2D band with reasonable peak fitting to four Lorentzians highlighting the two-peak nature of the 2D band

Graphite rods, constructed from graphite flakes of increased grain size, were investigated to probe whether larger flakes could be produced from graphite sources with larger initial grain sizes. The following spectra show *typical examples* of flakes obtained from various graphite rod grades: HK-3 graphite (Figure 6.12), HK-7 graphite (Figure 6.13), HK-11 graphite (Figure 6.14), and HK-800 (Figure 6.15), where the number, n , denotes the average size of the graphite grain sizes (in microns) used for the rod's construction. It was found that; overall, the difference in grain size had little effect on the size of the exfoliated flakes, and that typically the isolated flakes produced Raman signals characteristic of few-layer graphene materials. It is not overly surprising that varying the grain size of the graphite resulted in no significant difference in the size of exfoliated materials, since the 'starting materials' only differed by less than 10 μm (with the exception of HK-800).

However, in all cases, flakes appeared graphitic-like in the optical CCD camera, as can be seen in the optical insets for each of the examples.

6.2.7.1 HK-3 graphite Raman analysis

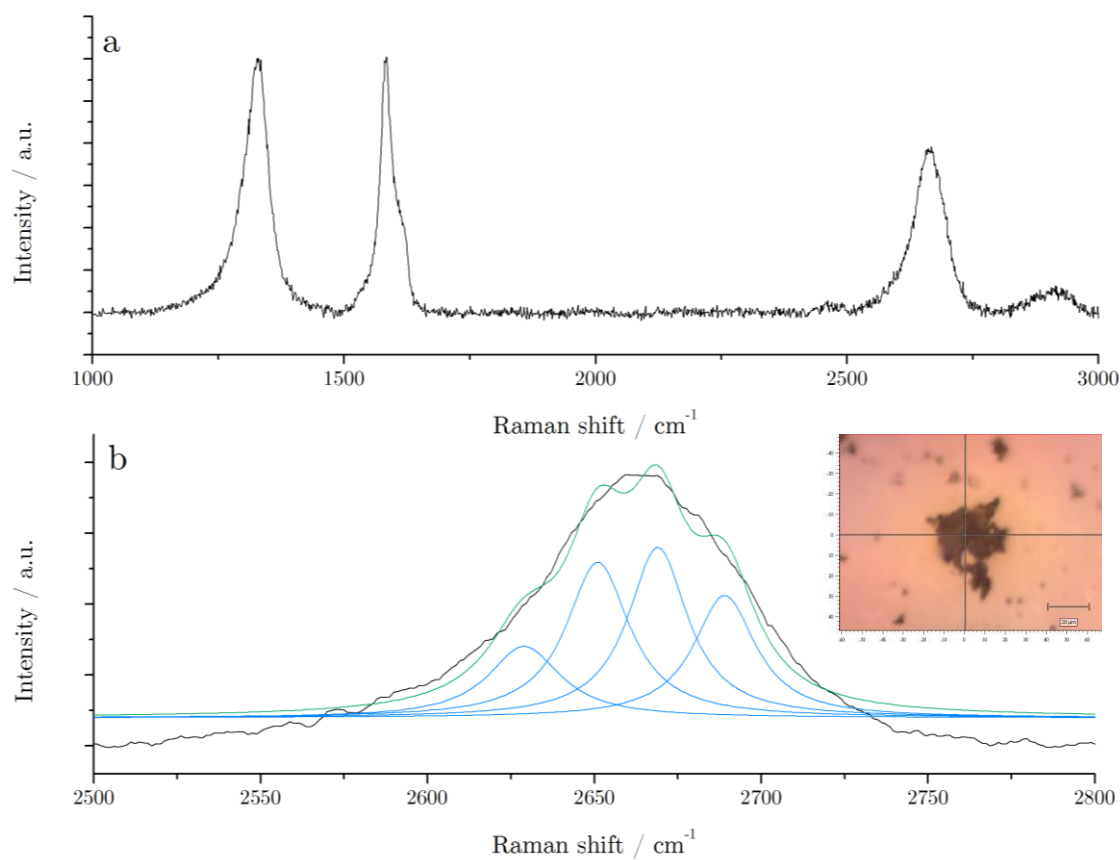


Figure 6.12) Raman spectrum of a possible 3/4 layer flake obtained from TEA^+ intercalation of HK-3 graphite, showing (a) full Raman signal, (b) optical image of flake, and (c) 2D band with reasonable peak fitting to four Lorentzians highlighting the two-peak nature of the 2D band

6.2.7.2 HK-7 graphite Raman analysis

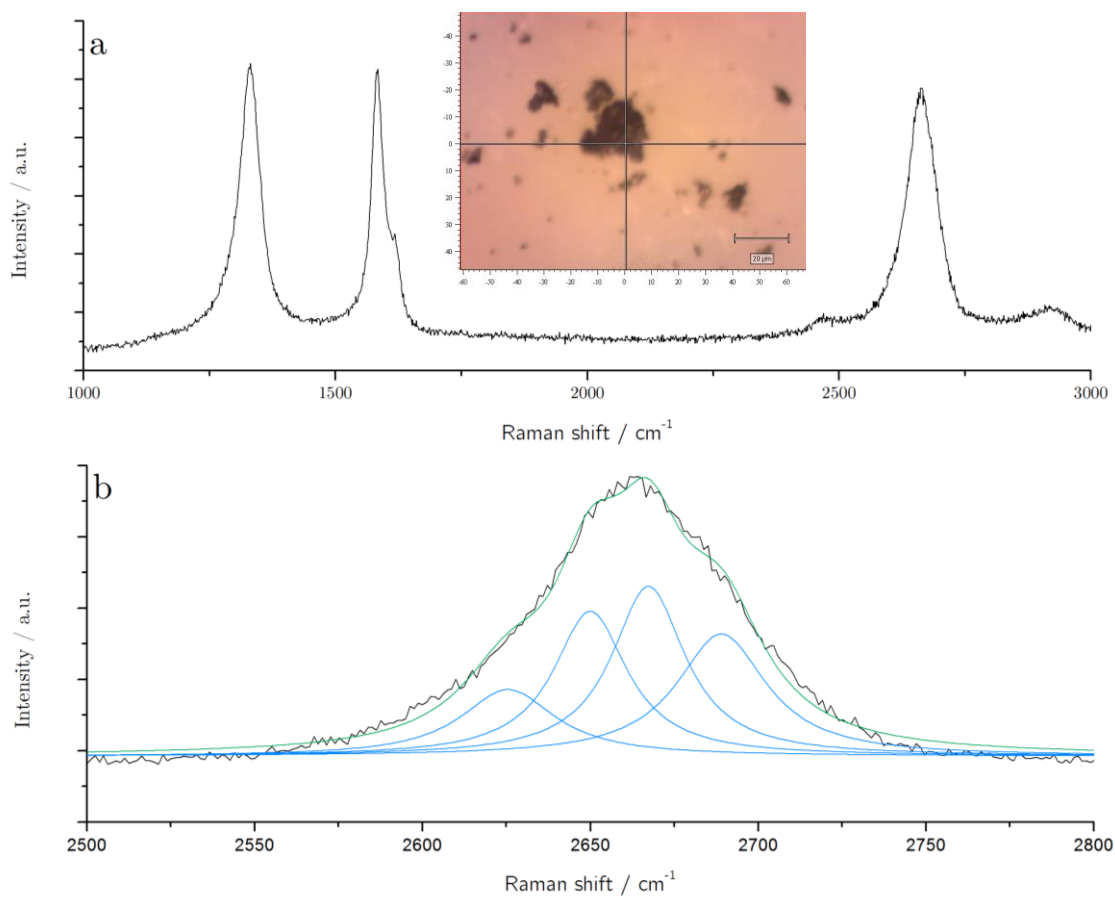


Figure 6.13) Raman spectrum of a possible 4 layer flake obtained from TEA⁺ intercalation of HK-7 graphite, showing (a) full Raman signal, (b) optical image of flake, and (c) 2D band with reasonable peak fitting to four Lorentzians highlighting the two-peak nature of the 2D band

6.2.7.3 HK-11 graphite Raman analysis

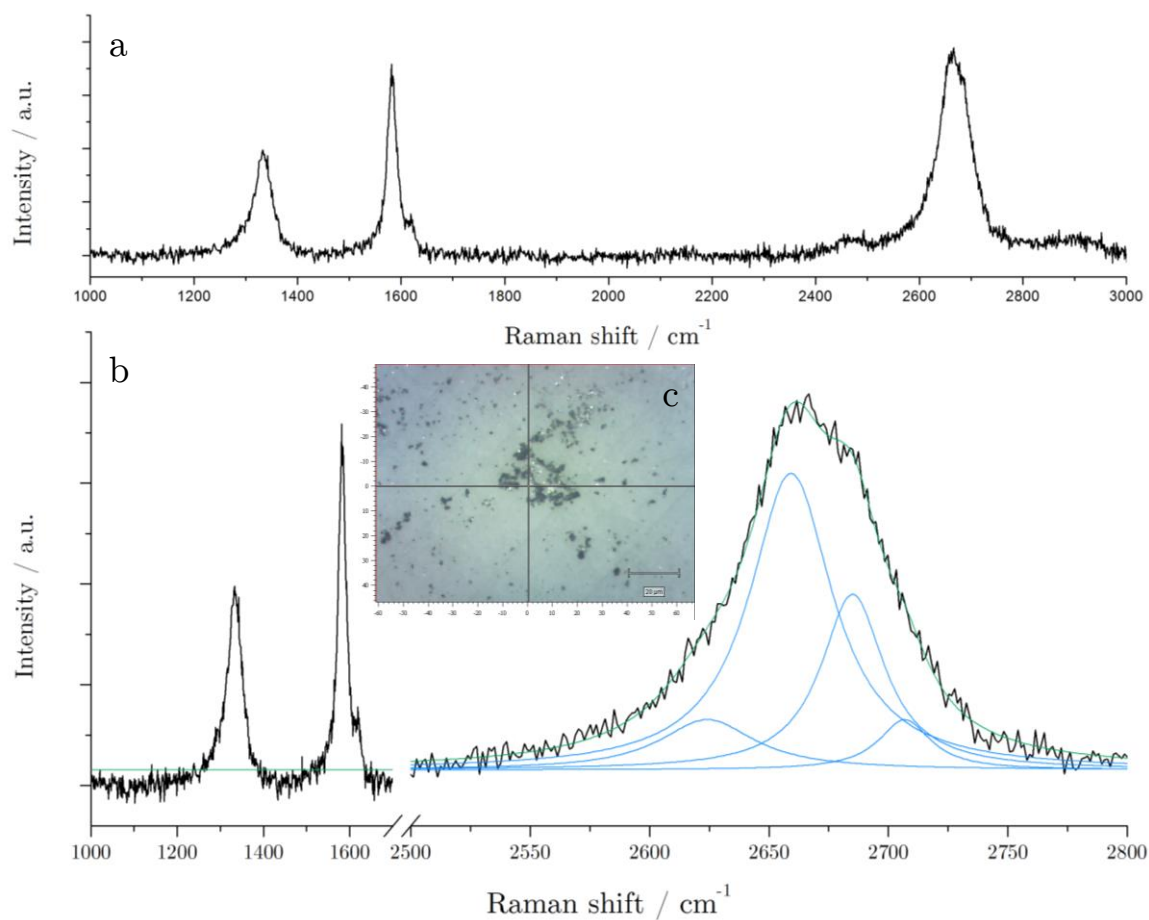


Figure 6.14) Raman spectrum of a possible bi-layer flake, obtained from TEA^+ intercalation of HK-11 graphite showing (a) full Raman signal, (b) optical image of flake, and (c) 2D band with reasonable peak fitting to four Lorentzians highlighting the two-peak nature of the 2D band

6.2.7.4 HK-800 graphite Raman analysis

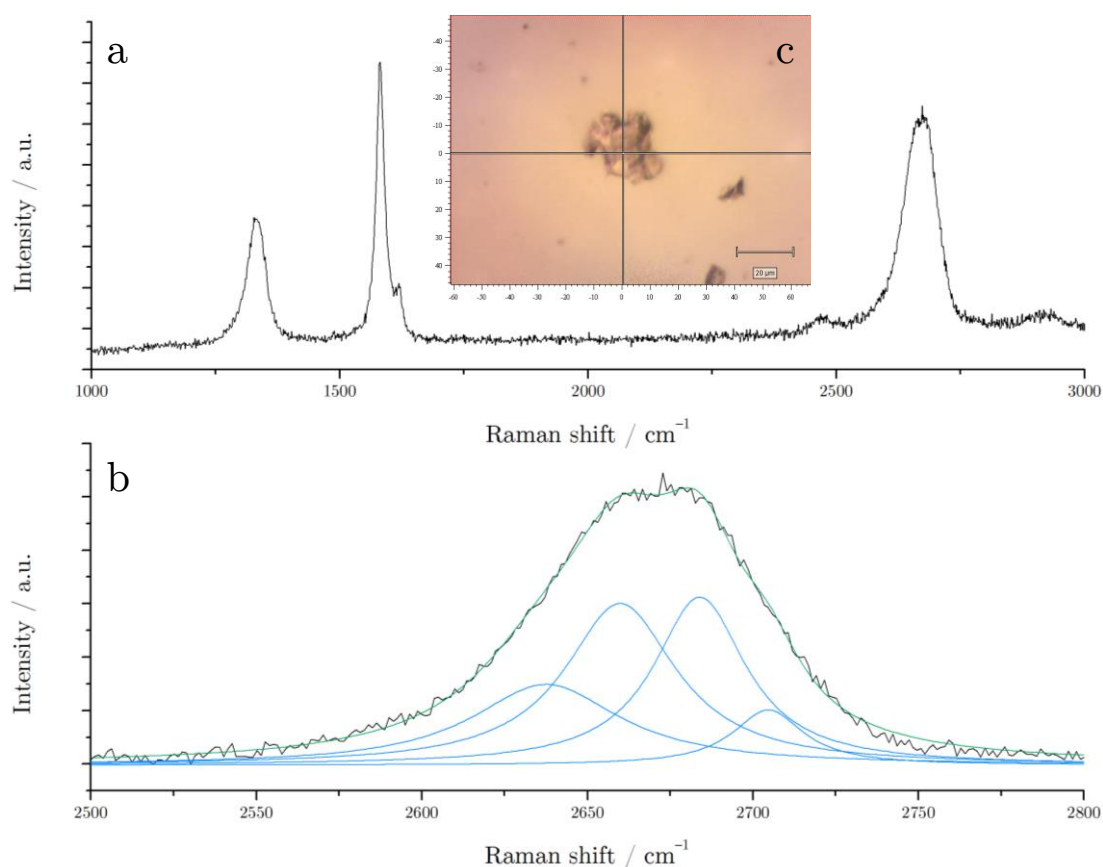


Figure 6.15) Raman spectrum of a possible tri-layer flake, obtained from TEA⁺ intercalation of HK-800 graphite showing (a) full Raman signal, (b) optical image of flake, and (c) 2D band with reasonable peak fitting to four Lorentzians highlighting the two-peak nature of the 2D band

Selected flakes were typically on the order of 10 μm, since any smaller than this made focusing of the Raman laser difficult resulting in little to no recordable signal. Typically, for all graphite grades, it was not difficult to locate flakes producing few-layer spectra despite appearing optically graphitic. By considering that both observations are true, then there are two possible explanations for this; the presence of electrolyte may facilitate partial flake re-stacking in solution, by which graphene flakes partially aggregate to form re-stacked sheets. The ‘partial’ re-stacking is important, since significant

separation is required to produce the few-layer graphene Raman signal; if no separation then a characteristic graphitic spectrum would be observed.

However alternatively, and more likely, is that the flakes observed are only partially exfoliated, and possibly separated by a GIC. The aid of previously shown SEM micrographs from electrode expansion (Figures 5.12 and 5.14) can help to visualise this effect. For example, if a monolayer separated from bulk graphite by a sufficiently large d -spacing created by a GIC complex, the excitation light of the Raman laser would ‘see’ a monolayer sheet rather than the true underlying graphitic structure. This highlights the need for a secondary characterisation technique.

6.2.8 Atomic Force Microscopy analysis of HK-graphite exfoliate

Flake isolation on sufficiently flat substrates for AFM analysis was obtained *via* drop casting graphene dispersions onto 300 nm oxidised silicon wafers. In this example, HK-2 graphite was employed as the cathode and cathodically charged at -2.4 V for 12 h, in a solution of TMAClO_4 (0.1 M) and the resulting solution analysed without the use of centrifugation. Figure 6.16 is an optical image of the Si/SiO₂ substrate after drop casting, showing the presence of both large and small flakes.

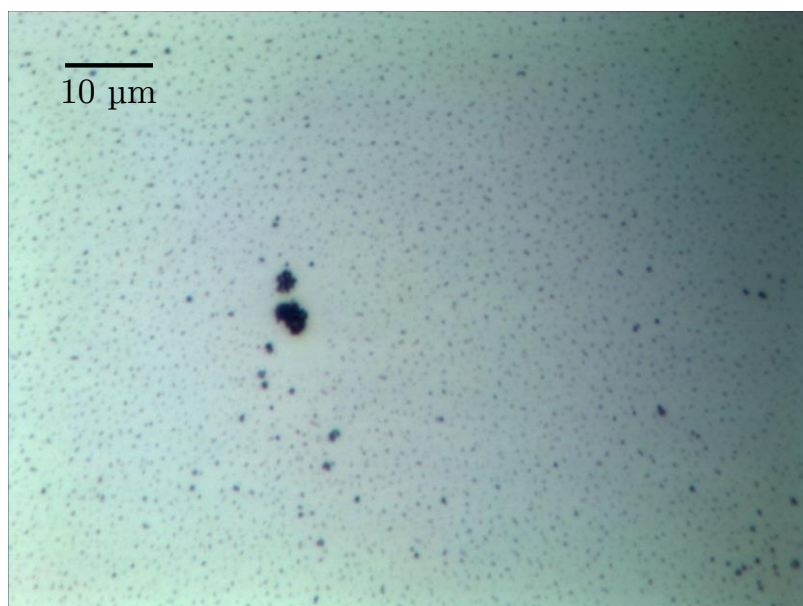


Figure 6.16) Optical image showing exfoliated material drop casted onto oxidised silicon wafers (300 nm oxide thickness) displaying both large ‘graphitic’ flakes and smaller ‘graphene’ materials

The following AFM images show isolated graphene flakes, with Figure 6.17(a) depicting a flake of similar visual characteristics as previously analysed using Raman spectroscopy, though it should be noted that it is not the same flake. The flake’s lateral diameter measures approximately $1\ \mu\text{m}^2$ and can be seen to be surrounded by much smaller flakes measuring *ca.* $200\ \text{nm}^2$. These smaller flakes are visible in Figure 6.16 as faint ‘dots’ and are a similar lateral size to

those observed, though not analysed, with Raman spectroscopy. However whereas resolution of the accessible Raman optics was insufficient to gather spectroscopic data for these flakes, AFM's higher resolution allowed the analysis presented in Figure 6.17.

Figures 6.17(a) and 6.17(b) show a $2.5 \mu\text{m}^2$ area scan, and $20 \mu\text{m}^2$ scan, respectively, and illustrate the distribution of graphene material flake sizes. The flakes are of a variety of shapes and sizes but, as the height profiles Figures 6.17(c) and 6.17(e) show, they are of fairly uniform thickness. Statistical analysis of the *ca.* 500 graphene flakes visible within this region, show that the typical thickness of the graphene flakes is around 1.8 nm (Figure 6.17(d)). Most of the few-layer graphene flakes have a diameter of 100 - 200 nm (corresponding to an area of 10000-40000 nm²) (Figure 6.17(f)). A few larger, micrometre size flakes are observed, but these are typically thicker corresponding to thicknesses of *ca.* 6 nm. These typically larger flakes are intriguing, since the previously shown Raman data of similar flake sizes provides contrasting results. The Raman spectra indicate these larger flakes consisting of *ca.* < 5 graphene layers (section 6.2.9) yet AFM height profiling indicates much thicker materials (6 nm heights indicate > 10 layers), since graphite's interplanar spacing alone (0.354 nm) yields nearly 17 interplanar spacings per 6 nm. The height profiles do offer some agreement with the previous optical properties (CCD camera) of the flakes, and suggest graphitic particulates; again highlighting the possibility towards incomplete exfoliation or possible flake re-stacking.

Simple flake counting revealed a yield of *ca.* 16 flakes per square micron; however the relatively small 200 nm lateral diameters of these few layer flakes restricts their realistic use in future commercial applications. Finally hardness testing was employed to confirm the observed materials to be carbon based.

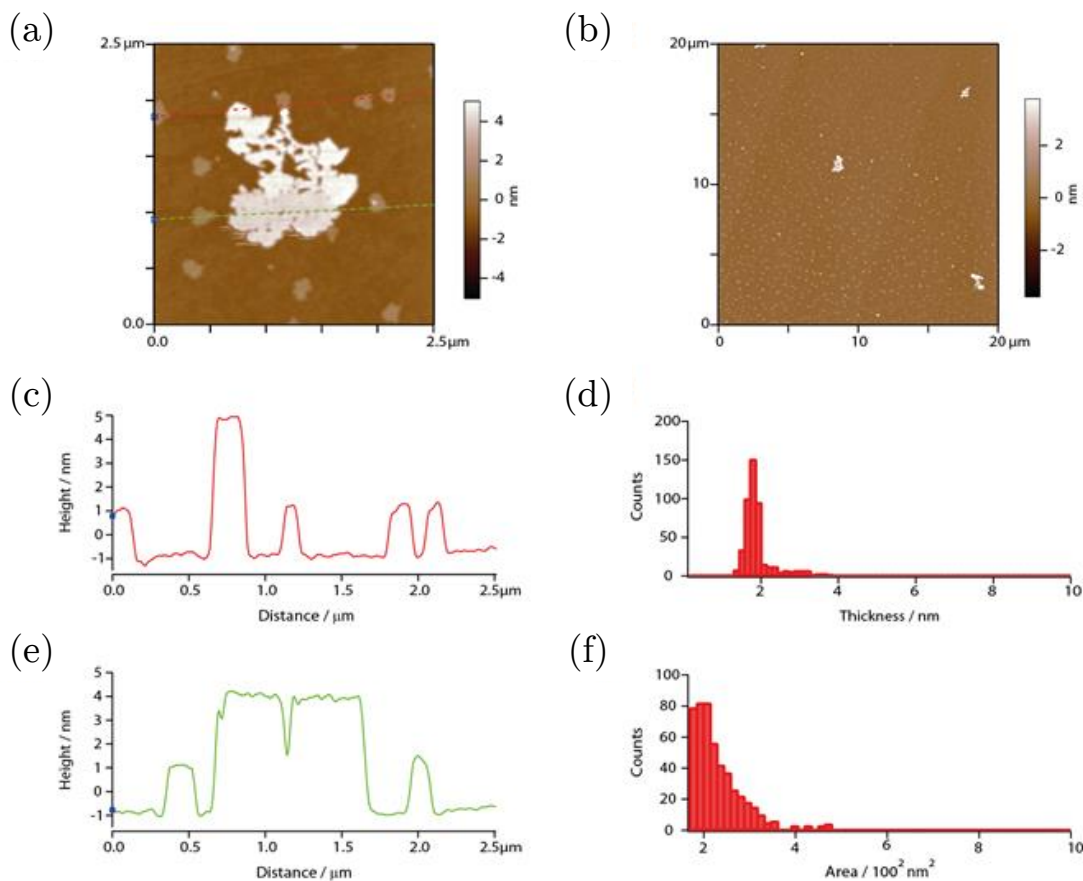


Figure 6.17) AFM images of flakes prepared *via* 12 h TMA intercalation (-2.4 V) and subsequent exfoliation of the graphite rod. (a) zoom in of representative $2.5\ \mu\text{m} \times 2.5\ \mu\text{m}$ area showing AFM traces, (b) Micrograph of typical $20 \times 20\ \mu\text{m}$ area of Si/SiO₂ substrate supporting flakes, (c) corresponding height measurements of red traced path in Figure 6.17(a), (d) Flake thickness (nm) distribution of 456 graphene islands, (e) corresponding height measurements of green traced path in Figure 6.17(a), (f) flake area distributions (m^2 , ($20 \times 10^{-15}\ \text{m}$)^{1/2} corresponds to 140 nm) of 456 graphene islands.

6.2.9 Few-layer graphene concentration derived from UV-Vis

The concentration of few-layer graphene in these dispersions was estimated using UV-Vis absorption spectroscopy. The concentration of few-layer graphene prepared *via* intercalation of a HK-2 graphite rod with TMA^+ (-2.4 V, 12 h), was estimated to be on the order of 0.01 mg mL^{-1} as calculated with the use of the Lambert-Beer relationship;

$$A = \epsilon cl$$

Where; A is the absorbance, ϵ is the absorption coefficient, and l is the cell length of the cuvette. The dispersion was placed in a quartz cuvette with a 2 mm cell length and the absorbance measured at 660 nm^{114} *vs.* a reference solution of TMAClO_4 (0.1 M) electrolyte in NMP. The absorption coefficient, $2.46 \times 10^3 \text{ L g}^{-1} \text{ m}^{-1}$, was the same value previously quoted by Coleman *et al.*¹¹⁴, for few-layer graphene dispersions (<5 layers) and an absorbance of 0.058 was recorded, corresponding to a concentration of $11.8 \text{ } \mu\text{g mL}^{-1}$, and this figure is of a similar order magnitude to concentrations reported electrochemical intercalation routes ($0.02 - 1 \text{ mg mL}^{-1}$)^{151,152,158} though it should be noted that these reported concentrations are not totally comparable, since they are obtained from anionic intercalation procedures; there being no reported concentrations obtained from purely cationic, electrochemically controlled, intercalation routes.

6.2.10 Electron microscopy of graphene materials

To accompany the AFM data collected for the exfoliated flakes, a < 0.1 mL sample was drop cast onto a holey carbon TEM grid, to act as both a filtration device and a support for the exfoliated graphene materials. By using holey carbon grids, with pore sizes measuring *ca.* 100 nm, it was proposed that HR-TEM would have the resolution required to probe the diffraction properties of the flake lattice, as well as detailed morphology and information regarding number of layers. TEM at 80 kV proved unsuccessful, since the small lateral sizes of the flakes caused agglomeration towards the edges of the holey carbon supports, and failure to span over the entire carbon pores, resulting in poor flake detection. Instead, the holey carbon grids were analysed using SEM, and the acquired SEM micrographs are presented in Figure 6.18. Images (a)-(c) show flakes typical of those observed with AFM-determined areas and thicknesses of *ca.* 400 nm² and 2 nm, respectively. Figure 6.18(a) shows a particular few-layer sample, indicated by its relative transparency to the electron beam. Flakes in Figures 6.18(b) and 6.18(c) are evidently thicker, and display a more roughened surface morphology. Finally, Figure 6.18(d) shows a typical larger flake, and exhibits more graphitic characteristics, albeit arguably partially exfoliated.

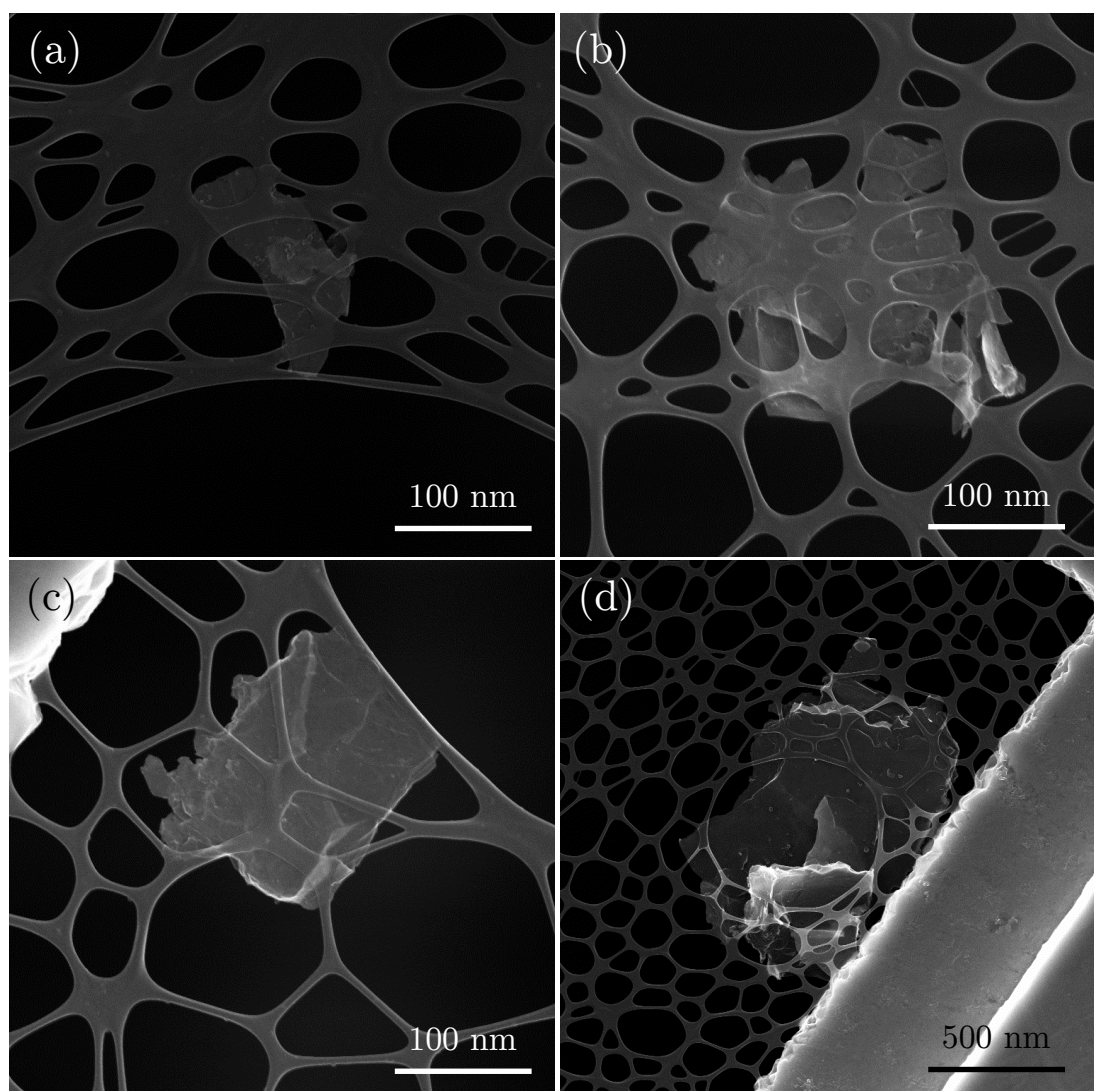


Figure 6.18) SEM images of graphene exfoliation supported on holey carbon TEM grids showing, (a)-(c) typical few-layer materials similar in lateral size to those shown in previous AFM data (Figure 6.21), and (d) a larger flake exhibiting more graphitic morphology to the presented smaller flakes

6.2.11 Assessing the degree of flake functionalization

X-ray photoelectron spectroscopy (XPS) was employed to probe the degree of chemical functionality of the exfoliated products. Any evidence of flake functionalization would be problematic at least, since the underlying theory supporting cathodic intercalation was to avoid the use of oxidising anodic potentials, and therefore preventing any flake functionalization. To assess this, a HK-graphite source was analysed prior to intercalation, and compared directly to electrochemically exfoliated material. For XPS analysis, NEXUS required a film, or compressed powder, with a minimal thickness of 50 nm. For graphene flake analysis this was unsuitable, and therefore the analysed exfoliate was not restricted to the few-layer materials, but also included graphitic materials in the analysis. A HK-2 graphite rod was exfoliated with TBA^+ , held at -2.5 V for 24 h in an open system (not in glove box allowing oxygen involvement), and the resulting dispersion was centrifuged at 13,500 rpm for 30 min. After which the exfoliate was collected *via* filtration through an alumina membrane, washed with ethanol and acetone and vacuum dried for 1 h prior to storage in a membrane box. The sample was stored for approximately 24 h prior to XPS analysis, unexposed to atmospheric conditions.

Figure 6.19 shows the survey spectrum of the as prepared graphite source, prior to any electrochemical treatment, and shows approximately 1.8% relative atomic % oxygen content. This amount of oxygen in nano-carbon materials is unsurprising and could have been introduced in the graphite synthesis stage, or simple atmospheric oxidation during exposure to normal atmosphere. Graphite is known to oxidise fairly easily in open air, a phenomenon witnessed by Lai and co-workers when analysing graphene electron transfer responses at basal plane electrodes.⁶³ Therefore, oxygen containing functional groups are expected to be present on the graphite material to a small degree, at least.

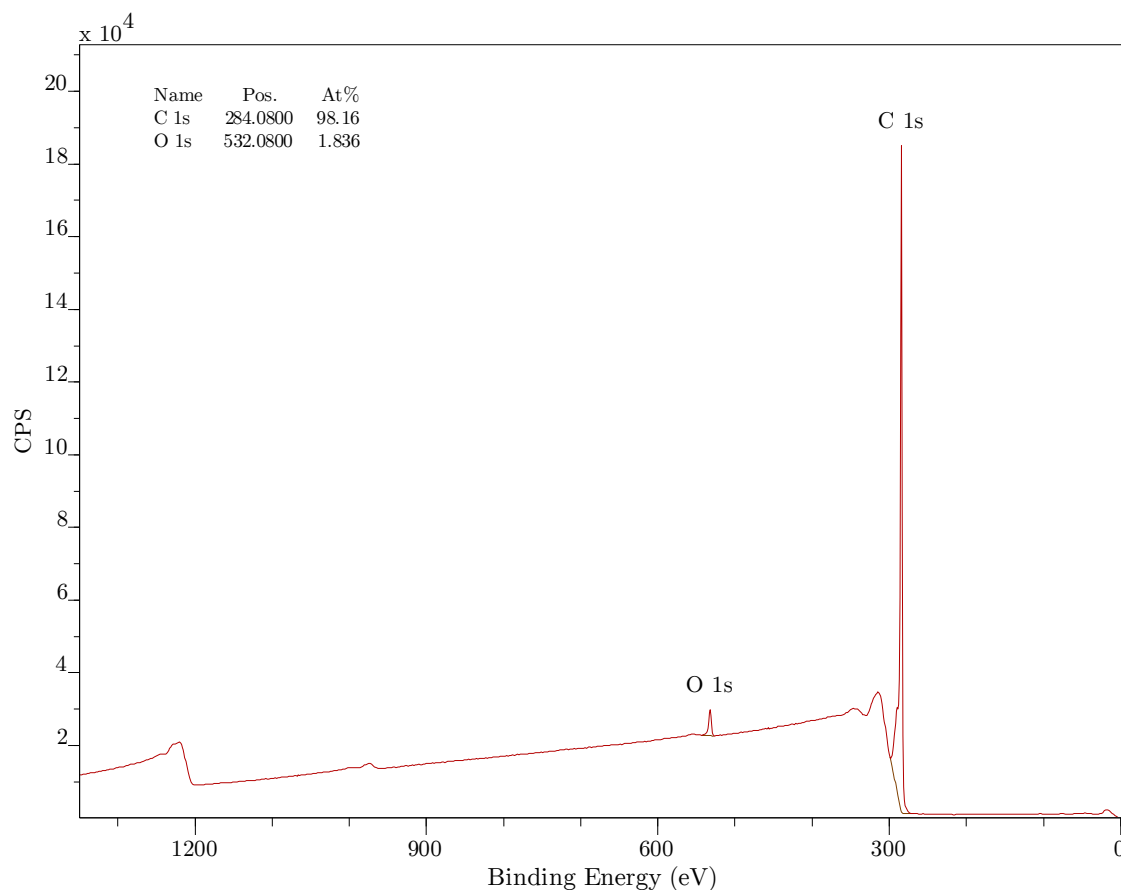


Figure 6.19) XPS survey spectrum of as prepared HK graphite rod showing relative atomic percentage of oxygen and carbon present

Figure 6.20 shows the XPS survey spectrum of the exfoliated material and indicates an increase of *ca.* 3% oxygen in the sample. This 1% increase is unlikely to have been introduced during electrochemical exfoliation, since the cathodic potentials are well out of the region at which graphite oxidation can occur; the oxygen is more likely to arise from the washing procedure or from exposure to atmospheric air. The surface area of the exfoliation is significantly larger than that of the compressed graphite rod source, so oxidation does not seem an unlikely option. However, it can be sensibly assumed from the XPS data that the electrochemical procedure as a whole can be described as non-oxidative since a 1% increase can be considered negligible, especially since the electrochemistry was performed in an open air system, and reduction of this 1%

may be possible with an optimized washing/storing procedure, or being conducted under controlled atmospheric conditions.

In addition, XPS did not reveal the presence of fluorine or nitrogen in the exfoliated materials; indicating a successful electrolyte-washing procedure and that no electrolyte-functionalization takes place on the graphene sheets, as is often the case with anionic methods.

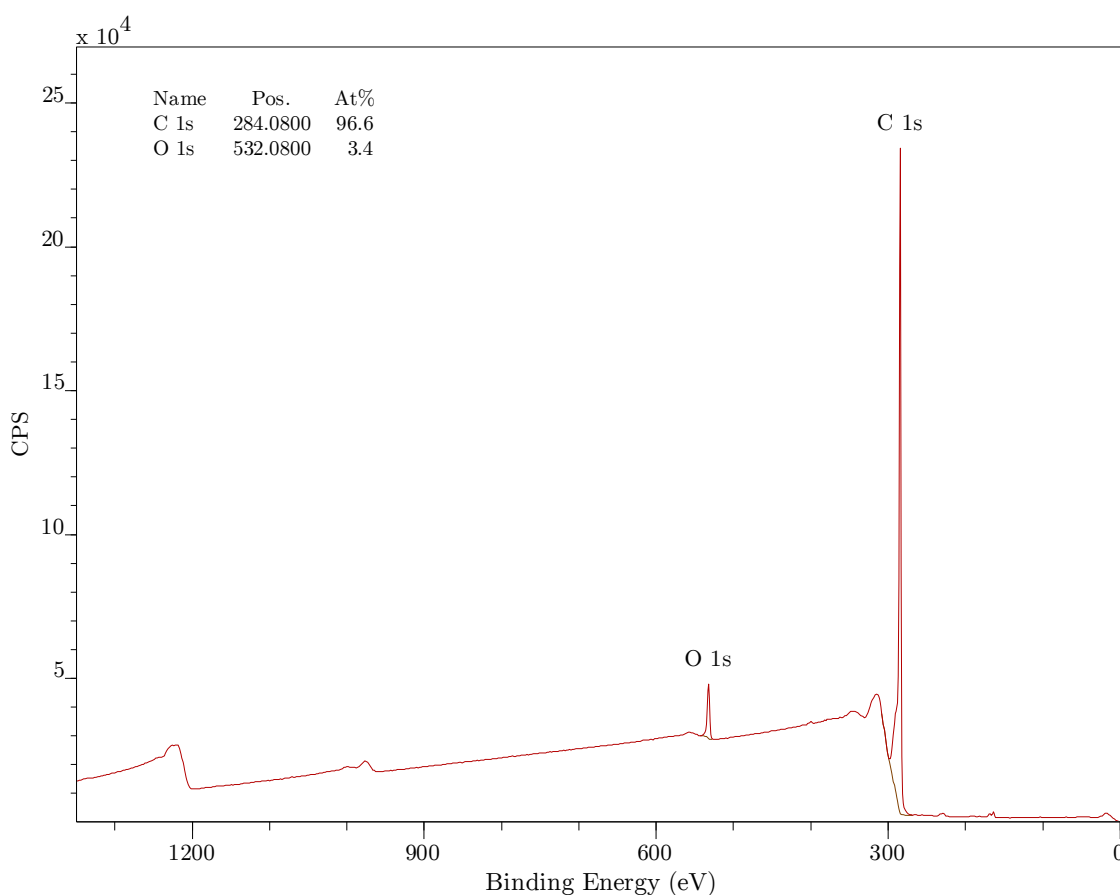


Figure 6.20) XPS survey spectrum of electrochemically exfoliated graphite rod showing relative atomic percentage of oxygen and carbon present

Finally, XPS showed no signs of nitrogen or fluorine present in the exfoliated materials, indicating products with relatively good purity and a successful washing method for electrolyte removal. However these results rest on the assumption that the surface chemistry of the exfoliated graphene materials is

similar to that of the exfoliated graphitic materials, since XPS analysis of isolated few-layer flakes was not possible.

6.2.12 Non-electrochemical exfoliation of graphite

Towards the end of this project, it was discovered by a co-worker that despite pure NMP being a good solvent for graphene dispersibility, the inclusion of electrolyte limited the effectiveness of NMP to disperse few-layer graphene materials successfully.²⁸² The result was determined through the investigation of sonication-based routes to graphene fabrication. Graphite powder (Grade-2369, Graphexel, UK) was sonicated in two separate systems; one containing pure NMP and the other containing NMP and electrolyte (TBABF₄) at 0.1 M concentration, for 24 h (30 % power, 37 kHz). The resulting dispersions prepared by Miss. Tania Campos-Hernandez are pictured in Figure 6.22, and a clear difference is observed: the presence of electrolyte dramatically decreases the degree of graphene dispersion, resulting in visible agglomeration and settling of graphite particulates.



Figure 6.22) Photograph of round bottomed flasks containing graphite powder post 24 h sonication (30% power, 37 kHz, 26 °C) in (a) NMP containing TBABF₄ (0.1 M), and (b) pure NMP²⁸²

The implications of this discovery on this thesis are overwhelming, and credit is given to Miss. Tania Campos-Hernandez for the provision of this information. The finding indicates that ultimate graphene exfoliation is inhibited by R₄N⁺-containing solvents, or at least at R₄N⁺ concentrations as large as 0.1 M, hence the large portion of un-exfoliated graphite present in the bottom of the flask.

It is believed that the presence of electrolyte causes the sonication-driven exfoliation to rapidly re-aggregate in solution, with the possibility of electrolyte inclusion between layers, forming the observed sedimented and un-dispersible graphite particulates. This mechanism can be rationalised in terms of surface energies between the graphene sheets and the NMP molecules; as we have seen earlier (section 1.6) the absence of electrolyte permits successful graphene dispersion in pure NMP, because the surface energies of graphene and NMP are relatively similar,^{110,139,283} and any surface charges, in the form of surface oxides

or functionalities are able to electrostatically stabilise the flakes against aggregation.

However, dissolution of R_4N^+ -containing electrolyte within the system will increase ΔH_{mix} substantially, since the surface energy of the charged electrolyte species will be significantly larger than the graphene sheets and NMP molecules. It follows that relatively large graphene sheets especially, are unable to be dispersed under entropic control; large sheets already exhibit a small ΔS_{mix} , and flake-aggregation ultimately occurs as a result of there being some degree of flake functionality. Flakes must possess a slight degree of surface charge here, either in the form of oxide groups (though XPS suggests that this is not the case) or from cathodic treatment, since the presence of electrolyte facilitates their aggregation; if the flakes were neutral, then the presence of electrolyte would not affect their ability to be dispersed.

Because of the inclusion of electrolyte, the repulsive charges of neighbouring flakes are able to be masked sufficiently, thereby effectively cancelling out the electrostatic stabilisation caused by the surface charges. There is therefore no long range repulsion to compensate the vdW attraction of neighbouring flakes, and flake aggregation preferentially proceeds. Dispersion of small flakes however, may be possible since ΔS_{mix} may be large enough to dominate ΔH_{mix} , thus permitting a negative ΔG_{mix} .

Solution B, containing electrolyte (0.1 M concentration) and sedimented graphite, is similar in appearance to solutions obtained *via* the electrochemical exfoliation procedure presented herein, and could explain why the lateral sizes of isolated flakes, retrieved through solution drop casting, are small. It also means that, regardless of the efficiency of an optimised R_4N^+ intercalation mechanism, in terms of the production of monolayer graphene, the presence of R_4N^+ electrolyte at this concentration (0.1 M) would inevitably encourage the

re-aggregation of large graphene materials in NMP solutions. It is possible to indirectly test this hypothesis, *via* the washing of sonicated/electrochemically exfoliated graphene materials with pure NMP, for the purpose of electrolyte removal, followed by the collection and re-dispersal of the graphene materials in pure NMP. This is arguably quite a laborious process for industrial viability, though re-dispersal of materials in pure DMF was reported by Yang *et al.*¹⁵⁴, presumably for this purpose.

There is clearly a play off between a) the requirement for electrolyte in order to permit ion intercalation thereby causing graphene sheet expansion/exfoliation, and b) the hindering effects of the electrolyte *via* the flakes' energetic preference toward aggregation due to the presence of electrolyte. By keeping the concentration of electrolyte to below that of the critical coagulation concentration, but still allowing intercalation/expansion, the minimal concentration could allow for successful flake dispersion in NMP. Additionally, it might be the case that although the presence of electrolyte inhibits the good dispersion properties of NMP, other solvents may not be affected in the same manner. As such, a simple solution to improve the degree of flake dispersion would be to find alternative solvents of which their dispersion properties are unaffected by electrolyte dissolution. Alternatively, it might be the case that an already tested solvent does not exhibit good graphene dispersibility when pure, but the addition of a specific electrolyte may enhance the solvent's dispersion properties allowing it to be a potential candidate for electrochemical exfoliation studies. This is clearly an extensive study, and due to the late discovery of the results has not been included in this thesis.

6.3 Conclusions

The suitability of tetraalkylammonium intercalation has been investigated for the direct exfoliation of a graphite cathode into graphene related materials, and it has been found that although the process is severely dependent upon the exact experimental conditions and materials, few-layer graphene production is possible. However the concentration of the produced dispersions is not an improvement over other reported works, though is in close agreement with reported values. The lateral flake sizes on the other hand, are probably too small to have any real application value. Few-layer graphene materials obtained from HK-graphite exfoliation were found to have lateral flake areas of *ca.* 400 nm² but with AFM determined flake thicknesses of *ca.* 2 nm, and Raman spectroscopy indicating less than five graphene layers. Most interestingly, it was found that under no experimental conditions was graphene material directly obtainable *via* cationic intercalation into HOPG, and only huge irreversible volumetric expansion of the HOPG cathode was observed. The differences between HOPG and HK-graphite lie in the anisotropy of the graphite lattice and the grain size of the constituent graphite flakes, and it is thought that both these factors contribute to the resistance of HOPG toward exfoliation, with neighbouring graphene sheets having a cumulative vdW attraction exhibiting increased stability. This cumulative effect is so strong, that even sonication aid was insufficient to exfoliate expanded HOPG into graphene-like material. However it is thought that the use of extremely cathodic potentials can facilitate the exfoliation of HOPG.

The effect of graphite particle grain size on exfoliation has been demonstrated using HK-graphite rods with varying grain sizes. It was found that varying the lateral grain size of the flakes within HK-graphite rods had little effect upon the sizes of the respective exfoliated graphene materials, except when the inherent

grain sizes were substantially large (800 μm) and a comparable size to those of HOPG (1 mm). In this case, HK graphite displayed a preference for expansion and eventual electrode fracture over exfoliation, exhibiting volumetric electrode expansion in a similar manner to that of HOPG.

This proves that grain size is an important factor in successful exfoliation, and this is attributed to the longer intercalation times required to exfoliate flakes with larger grain sizes. Additionally, exfoliation of HK-graphite with comparatively similar grain sizes to HOPG was successful whereas HOPG was not. This strengthens the hypothesis that anisotropy also takes an important role.

The main problem associated with the exfoliation of a graphite electrode (either under anionic or cationic control) lies in desirable high-stage intercalation prior to electrode exfoliation. HOPG's reluctance to exfoliate readily from R_4N^+ intercalation might actually be beneficial, since in order to obtain thinner materials, a higher degree of expansion is required prior to electrode exfoliation.

Despite the acceptable flake yields (0.012 mg mL^{-1}) and small lateral dimensions (200 nm^2), graphene material produced from HK-graphite exhibited relatively impressive purity; displaying narrow size and height distributions associated with the above size and thickness values.

XPS revealed *ca.* 1% oxygen introduction during the entire graphene production process, supporting the primary reasoning behind the employment of cationic intercalation rather than anionic; anionic always results in significant surface oxidation of the exfoliated materials and few authors actually report the oxygen content.¹⁵² The involvement of at least a small degree of oxygenation is inevitable, due to unavoidable exposure to an open atmosphere and various washing procedures in order to remove residual electrolyte. This result, at the

time of publication was one of only three examples of preparing non-functionalised graphene *via* electrochemical intercalation, and unlike the two other works; by Wang and co-workers¹⁵³ and by Morales *et al.*¹⁴⁹ does not require the use of sonication (if the HK material is employed) to prepare the exfoliated material: an industrially attractive option due to the associated low energy costs.

The clear detrimental effects of electrolyte presence are particularly damaging for the route's viability. The presence of electrolyte within the system, although required for the intercalation process, has clear implications on the efficient and successful graphene dispersion properties of which pure NMP has become known for. However, further work is required with regard this work, since the payoff between exfoliation and dispersion must be controllable to some extent through the use of an optimised electrolyte concentration. This electrolyte concentration must be sufficient to permit successful exfoliation, yet small enough to not hinder dispersion of the graphene materials; we now know that 0.1 M is too large to allow stable graphene dispersions.

Finally, since it was not practicable to obtain both complimentary AFM and Raman data for the same flakes, the lack of acquired Raman statistical data, like that presented for AFM, supporting flake analysis is extremely regrettable, but totally out of the authors control since the specialist equipment was unavailable.

The results presented so far highlight the clear differences between anionic and cationic intercalation techniques; where anionic intercalation has been reported to successfully produce few-layered materials, independent of the graphite source anode, which are always functionalised in some respect, or exhibit a relatively large degree of surface oxidation (see table 2). The difficulties associated with cationic intercalation have been presented, including small

lateral flake sizes, and in the case of HOPG; no exfoliation at all. The yields obtained from R_4N^+ intercalation are acceptable, but do not improve on other reported works, however the degree of flake functionality/oxidation appears to be extremely low, exhibiting better quality flakes than those prepared from any of the reported anionic routes (again, see table 2). The difficulties associated with cationic intercalation, with respect to obtainable yields and small flake sizes was initially suspected by the relative proportions of published work; 14 research papers reporting anionic techniques and only two pieces of work addressing cationic mechanisms^{153,149}; both of which required the use of a secondary exfoliation technique; sonication and microwave-assisted expansion, respectively, for successful FLG exfoliation.

There is currently very little published work relating the degree of graphene surface oxidation, to graphene dispersibility in both pure solvents and those containing electrolyte, though electrolytes are known to affect dispersion of CNTs very strongly, and it has been shown here that the inclusion of electrolyte on the flakes causes severe aggregation of larger flakes due to inherent surface charges of the graphene sheets. Despite this, it appears that if flakes are small enough (*ca.* 400 nm²), dispersion is possible at concentrations on the order of 0.01 mg mL⁻¹ even in the presence of R_4N^+ electrolyte at 0.1 M concentration.

Chapter seven

Overall thesis conclusions

7 Overall thesis conclusions

7.1 Conclusions

The primary focus of this PhD thesis was to investigate and develop an electrochemical fabrication method for the production of graphene materials, based on the controlled cationic intercalation of tetraalkylammonium species into a bulk graphite source electrode. The underlying rationale behind the project relies on the undesirable oxidation of graphene materials resulting from other electrochemical and chemical methods of production, due to either acidic conditions or the oxidative potentials applied. R_4N^+ intercalation, *via* the application of cathodic control, has been found to indeed cause direct exfoliation of graphene materials albeit of relatively small lateral sizes, but does appear to avoid significant oxidation or functionalization of the produced materials; a feat not reported for anionic methods (again, please see table 2 for specific references). However, significantly the process relies on the presence of an intercalating electrolyte, and it appears that the electrolyte presence causes significant re-aggregation of flake dispersions because of surface charges present on the materials and their inability to provide significant electrostatic stability towards re-aggregation.

Additionally, N-methylpyrrolidone has been employed as the solvent for studies, based on its relatively good graphene dispersion properties. However it was also found to be a good non-aqueous solvent for electrochemical purposes, due to its exceptionally large accessible potential window (4 to 7 V) and low toxicity,²⁸⁴ although NMP's high boiling point did hinder solvent removal.

The formation of a solid electrolyte interfacial layer on graphite electrodes as a result of lithium intercalation is a well-studied phenomenon in Li-ion battery

work, however no such SEI formation was witnessed during R_4N^+ intercalation studies. Indeed, the R_4N^+ reduction at the graphite electrode is believed to form a graphite intercalation compound at *ca.* -2.4 V *vs.* Ag/AgClO₄, stabilised *via* possible deposition on the graphene layers, however GIC formation was found to be reversible on the application of more positive potentials. Furthermore the GIC formation was found to be relatively stable even under the influence of large cathodic load (-3 V), and impressive charge recovery was observed. The nature of the charge transfer mechanism associated with the formation of a R_4N^+ containing GIC was probed with the use of EPR and UV-Vis spectroscopy, however given that analysis was performed under oxygen-free conditions, this resulted in oxygen-reduction dominance in the system.

Although it was important to exclude oxygen to enable reliable quantitative assessment of the intercalation mechanism, the ability to perform exfoliation in open air systems was possible. The inclusion of residual oxygen and water in the system, although preferentially reduced as a result of the applied cathodic conditions, was found to have little effect on the exfoliation rate of the graphite source. However, electrodes were more prone to premature electrode fracture associated with harsh cathodic conditions, than in oxygen-free systems.

The complex nature of the intercalation mechanism was probed during voltammetric scanning at sufficiently small scan rates, revealing several current responses during intercalation and de-intercalation. These current responses, associated with charge transfer steps, have been attributed to different staging phenomena of the intercalation process, as well as deposition/reduction processes of the GIC formation.

The irreversible change in physical structure of the graphite cathode during intercalation has been investigated with the use of XRD and SEM, and regular segmented expansion was found to occur from the use of larger R_4N^+ species.

Furthermore, EIS techniques have been employed to measure the increase in capacitance of the expanded graphite cathode as a function of expansion time, as a preliminary to investigate this system as a graphene supercapacitor. It has been shown that during electrochemical intercalation, both the specific capacitance and general impedance of the graphite cathodes increased as a function of structural expansion. This increase was found to be irreversible, and was in agreement with the irreversible structural expansion also observed.

Successful isolation of graphene material has been assessed primarily with the use of Raman spectroscopy and AFM. The corresponding spectra and AFM data suggest that the material produced, that does not require re-dispersion in a pure dispersing solvent, consists of between three and five graphene layers, however the lateral size of these flakes is on the order of 400 nm^2 . Despite the small lateral sizes, statistical analysis does exhibit a narrow size distribution. It is thought that these relatively small flakes sizes persist due to their ability to remain suspended in solution, even in the presence of electrolyte, because of their small size and therefore significant contribution to ΔS_{mix} .

in situ studies of ion intercalation into graphene materials have been investigated (Appendix A), albeit in a preliminary study. The results presented therein generally adhere to setup and configuration systems for supporting graphene materials, allowing for electrical contact in an electrochemical cell, and are associated with the eventual premise of species intercalation into bi-layer and tri-layer graphene flakes, thus probing their energy storage capabilities, and structural expansion effects upon intercalation.

It was found that, in comparison to reported anionic intercalation mechanisms, the presented cationic mechanism did not produce materials of significant lateral dimensions, and in the specific case of HOPG electrodes; no exfoliation at all, despite HOPG being a suitable anode choice in other reported anodic

works.^{146,285,152} As discussed in detail, anodic methods always produce oxidised, and in some cases electrolyte-functionalised, materials and it is thought that this oxidation process, although undesirable for production of pristine/non-functionalised materials, may be a reason for the associated success, where flake oxidation encourages flake dispersion in the solution phase allowing materials to be stabilised *via* electrostatic stabilisation.

There are clear difficulties associated with graphene fabrication from cationic intercalation, typically in the form of flake re-aggregation and/or incomplete exfoliation as shown within this thesis, and for whatever reasons there is a relatively sparse amount of published work regarding cationic intercalation techniques, in contrast to the huge volume of published work surrounding anodic techniques.²⁸⁶ The reasons for the bias towards anionic studies are not known, and it seems surprising given the relative simplicity of cathodic exploration during an electrochemical study.

Finally, it was found towards the end of the project that the presence of electrolyte within this system severely restricted graphene material dispersibility in NMP, and it is possible that the reason for the small flake sizes is due to the inability for larger flakes to be readily dispersed in NMP whilst in the presence of R_4N^+ electrolytes. This is arguably one of the more striking discoveries presented, since it is particularly damaging to the route's viability towards producing graphene materials, without re-dispersal of the exfoliated materials in a pure solvent. However it does highlight some interesting further work to be explored; studies into the optimum electrolyte concentration for graphene exfoliation/solution stability, and investigations towards possible alternative solvents.

7.2 Future work

Since it has been found that the presence of electrolyte has drastic effects upon the exfoliation process, it would be of interest to determine the optimum electrolyte concentration in order to permit successful dispersion. By keeping the concentration below the critical coagulation concentration, but still allowing intercalation to occur, the minimal concentration could allow for successful flake dispersion. Additionally, it might be the case that although the presence of electrolyte inhibits the good dispersion properties of NMP, other solvents may not be affected in the same manner. As such, a simple solution to improve the degree of flake dispersion would be to find alternative solvents of which their dispersion properties are unaffected by electrolyte dissolution. Alternatively, it might be the case that an already tested solvent does not exhibit good graphene dispersibility when pure, but the addition of a specific electrolyte may enhance the solvent's dispersion properties allowing it to be a potential candidate for electrochemical exfoliation studies.

There is a vast selection of cationic species that may be employed as the intercalating species, such as ammonium, other group 1 metals such as cesium, and other IL-based cations for example 1-ethyl-3-methylimidazolium. However it would appear that there are no clear advantages of using R_4N^+ species with alkyl chains larger than eight carbons; shown by the severe electrode deformation caused when attempting to intercalate TOA⁺. The size of the cationic species does need to be of a comparable size to graphite's interplanar spacing, even when considering ion flexibility. Nonetheless there are many other species to be considered.

Another further area to pursue is the *in situ* characterisation techniques such as Raman spectroscopy and XRD. These methods allow a much more detailed insight as to the mechanism, as well as a more accurate analysis of the observed

effects. Although *in situ* Raman spectroscopic investigations were introduced towards the end of this thesis, they were by no means fully explored. Future investigations would be primarily based within this area of research, beginning with the study of how the Raman spectrum of graphite alters as a function of intercalation; this has been studied by Hardwick and co-workers,²²⁷ though interestingly only the Raman *D* and *G* bands were monitored. Focus would be placed on the *2D* band, as well as investigations with few-layered graphene materials. Indeed, preliminary investigations regarding this idea were begun in Chapter seven, with the isolation of a few-layer graphene flake proving difficult. It would be of interest to see whether exfoliation of few-layered materials under Raman spectroscopic observation produces a change in the observed *2D* band, and whether this change can be reversible.

Similarly, could XRD be employed as an *in situ* technique to probe the structural deformation under intercalation conditions caused by R_4N^+ species?

The need to characterise the initial surface area of the initial graphite electrode material would be valuable, since this would allow measured current to be treated as a current density. This could be achieved through the use of Brunauer, Emmett and Teller (BET) gas adsorption.

The impedance data presented in section 5.2.6 acts as a preliminary study to a future, particularly electrochemical, graphene application; that of graphene based electrochemical capacitors. The specific capacitances measured for expanded graphite electrodes were measured on the order of $\mu F\ g^{-1}$, and admittedly offer poor degrees of charge storage when compared to theoretical graphene predictions of *ca.* $500\ F\ g^{-1}$. Work remains to intercalate few-layer materials, for this purpose, as mentioned previously with respect to *in situ* characterisation.

Appendix A

in situ electrochemical studies and on-going investigations

Appendix A: *in situ* electrochemical studies and on-going investigations

A1 Introduction

This final experimental Appendix outlines the details regarding development of a particularly complex *in situ* investigation, in which the degree of graphene sheet exfoliation was to be probed with the use of XRD and Raman spectroscopy. The ultimate intention of this work was to utilise a cationic intercalation mechanism into bi-layer and few-layer graphene materials, to measure structural and bonding transformations within the graphene materials. This would also provide valuable preliminary information about the charge storage capabilities of graphene based supercapacitor devices.

Two different approaches were outlined to proceed with this study; the first approach (Approach A) employs a micromanipulator injector to deposit a droplet of electrolyte onto the edge site of an electrically contacted graphene/FLG flake, on a Si/SiO₂ support. (Figure A1)

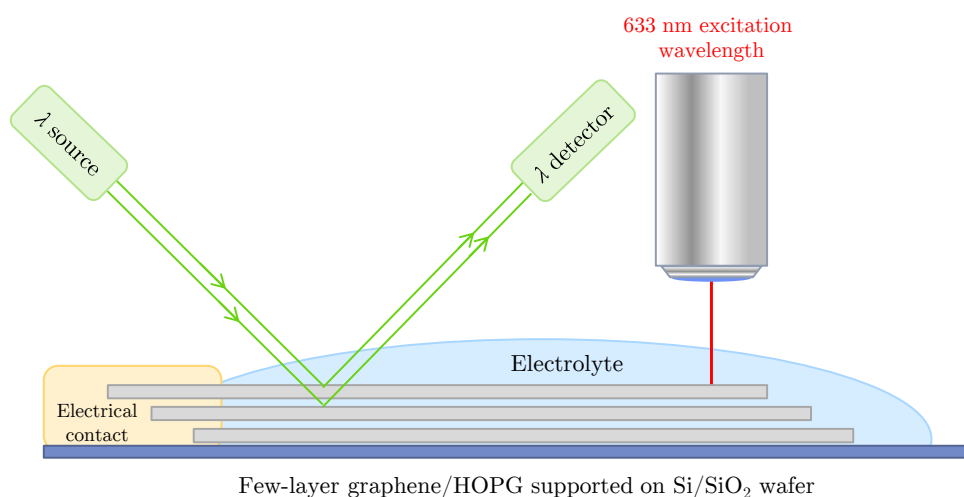


Figure A1) Schematic showing Approach A: micromechanical injector setup

This setup allows for the controlled location and precise electrolyte deposition onto bi-layer graphene, and has been shown to be an effective method of employing graphene as a working electrode in electrochemical investigations.²⁸⁷ By coupling the micromanipulator and injector with both Raman spectroscopy and XRD, it would be possible to probe the exfoliation mechanism *in situ*. Indeed, this work was inspired by several other works in which *in situ* XRD was employed to study SEI formation on graphene-based electrodes in battery work, and Raman spectroscopy to probe lithium intercalation into graphitic materials.^{227,256,258,288}

The limitations of this setup involve the difficulties of excluding oxygen from the system, since preparation and experimental procedure in an argon saturated glove box are challenging. Nonetheless, this system was investigated in parallel with a secondary approach.

Approach 2 employs the use of a specially designed *in situ* electrochemical cell (EL-Cell ECC-Opto, Hamburg, Germany, Figure A2) in which the graphene/HOPG working electrode is supported between a transparent quartz window and a holed aluminium disc current collector. This setup allows the contact of a working electrode of interest with exact known mass and dimensions, without the introduction of contacting clips or tweezers, allowing for observed currents and measured charge to be directly attributed to the WE of choice. The cell exploits the use of lithium metal as both the CE and RE.

The cell is filled with the selected electrolyte and sealed from the atmosphere, and can therefore easily be performed under oxygen free conditions. The clear disadvantage with this set up involves the graphene placement; whereas a HOPG sample can be easily placed, graphene electrode placement is much more challenging since graphene materials require a substrate in order to be transported. Micromechanically exfoliated graphene is relatively easily

transferred onto Si/SiO₂ substrates, offering graphene visibility *via* contrast from the 300 nm thick oxide layer. However since the oxide layer acts as an electrical insulator between the silicon and the graphene, contacting from below *via* the WE Contact Pin proved problematic.

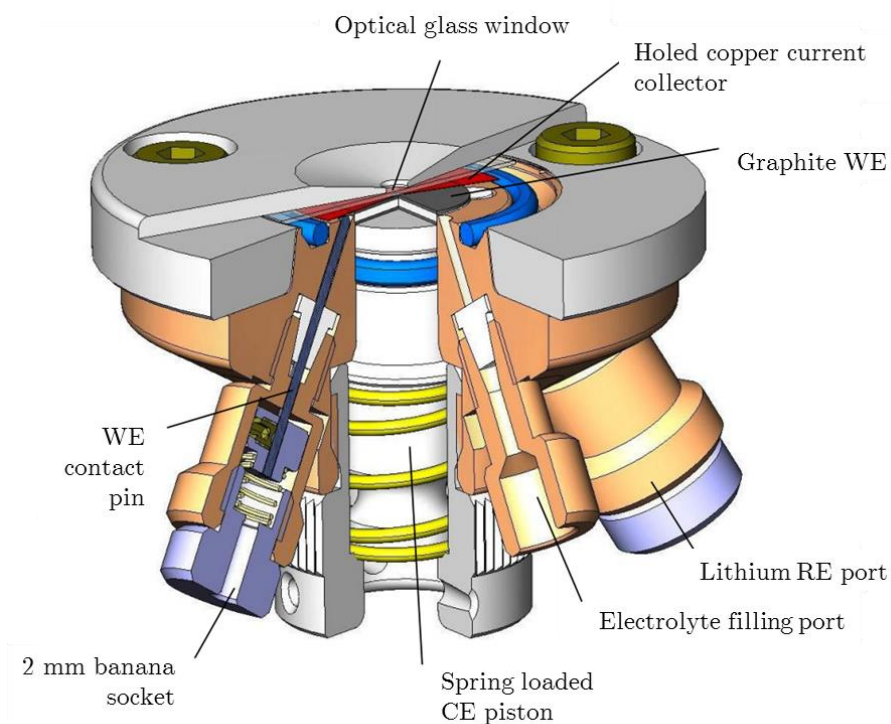


Figure A2) Schematic of Approach B: *in situ* electrochemical cell obtained from EL-Cell GmbH, Hamburg, Germany, showing placement of WE between quartz window and copper current collector, lithium CE and lithium RE

A2 Results

A2.1 Graphite pellet electrode: Approach A

Approach A utilises a simpler WE setup, and the suitability of various graphitic materials was investigated. To begin, graphitic based electrodes were optically investigated with the aim to move on to graphene materials alongside spectroscopic coupling when system familiarity was achieved.

A graphite pellet was constructed by pressing of graphite flakes, with an average lateral diameter measuring 200 μm . A droplet of solution was deposited onto the surface such that the droplet covered the entire surface. A stable droplet of solution is required to act as the electrochemical cell such that analysis can be conducted over extended periods of time. Significantly, this solution needs to have the ability to intercalate effectively between the graphene layers within the graphite cathode and the droplet needs to sufficiently wet the electrode surface, such that a large enough meniscus can form to allow a practical working area for both the CE and RE.

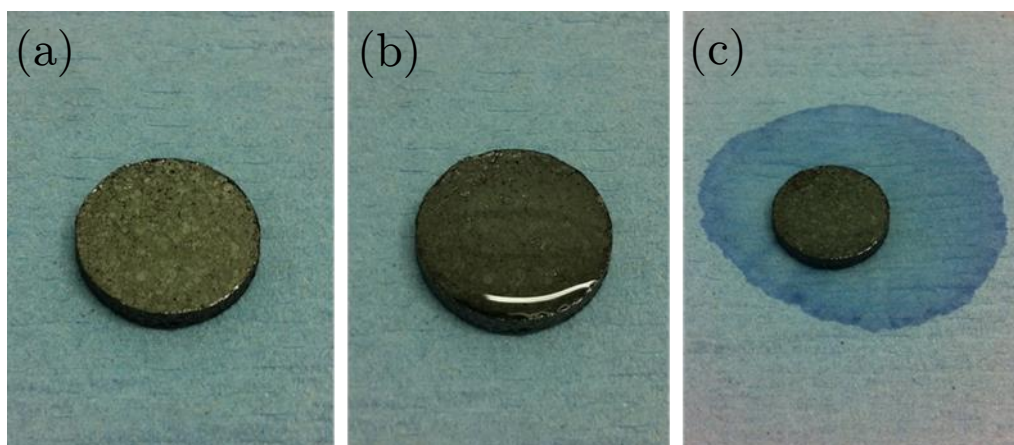


Figure A3) Photographs of a) graphite (200 μm) pellet, b) graphite pellet supporting a solution of TMAClO_4 (0.1 M) in NMP after initial deposition, and c) wetting effects of TMA^+ containing electrolyte solution on graphite pellet displaying instability after as little as 10 minutes.

TMAClO_4 (0.1M) in NMP was initially dropped onto the surface such that the droplet covered the entire surface. It can be seen in the above figures that after an initial period of as little as 10 minutes, the solution had sufficiently wet the graphite to an extent where solution had fully penetrated the graphite and absorbed into the supporting paper. This can be overcome by either one of two methods; by increasing the viscosity of the solution such that the rate of surface wetting/and solvent absorption is decreased, or by using a less porous electrode such as HOPG.

To increase the viscosity of the electrolyte, BMIM BF_4 was added to NMP in a 1:1 volume ratio. However although addition of BMIM BF_4 to NMP did increase the viscosity of the droplet, thus decreasing the rate at which surface wetting equilibrium was established, the solvent was eventually found to penetrate the graphite thereby wetting the blue towelling below. The time taken for this to occur was longer than in the absence of BMIM BF_4 ; *ca.* 20 min *cf.* 10 min. Additionally, given the limited success using graphite pellet

electrodes in earlier electrochemistry, focus was switched to using a less porous graphite source.

A2.2 HOPG support electrode: Approach A (continued)

HOPG was found to be an effective support for the drop of electrolyte and was stable for $t > 30$ mins. (Figure A4)

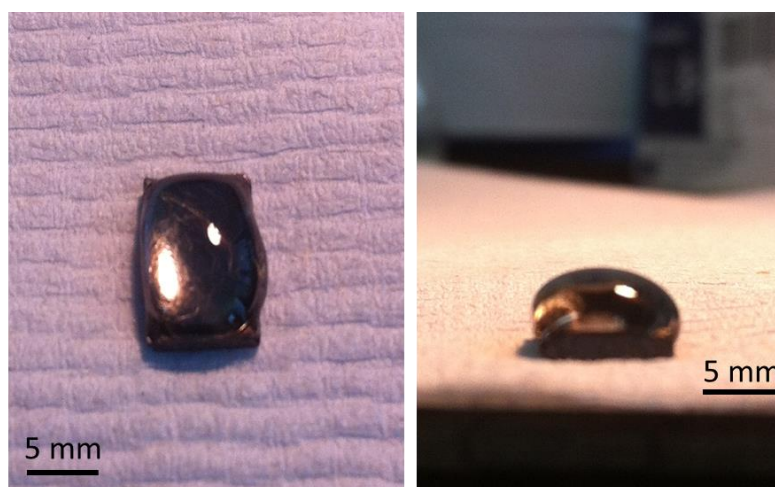


Figure A4) Photograph of HOPG sample supporting electrolyte drop taken after ca. 30 minutes, showing successful HOPG-support of a solution of TMAClO_4 (0.1 M) in NMP with no effects of wetting.

Using a two electrode setup and micromanipulator glass injector, a 50 μm diameter droplet of electrolyte (0.1 M TMAClO_4 in NMP) was placed onto a HOPG surface acting as the working electrode. The HOPG was connected to the potentiostat *via* a copper wire attached to the reverse of the HOPG using silver epoxy, and the droplet was placed on a region of the HOPG displaying a high proportion of visible edge sites and surface defects (Figure A5).

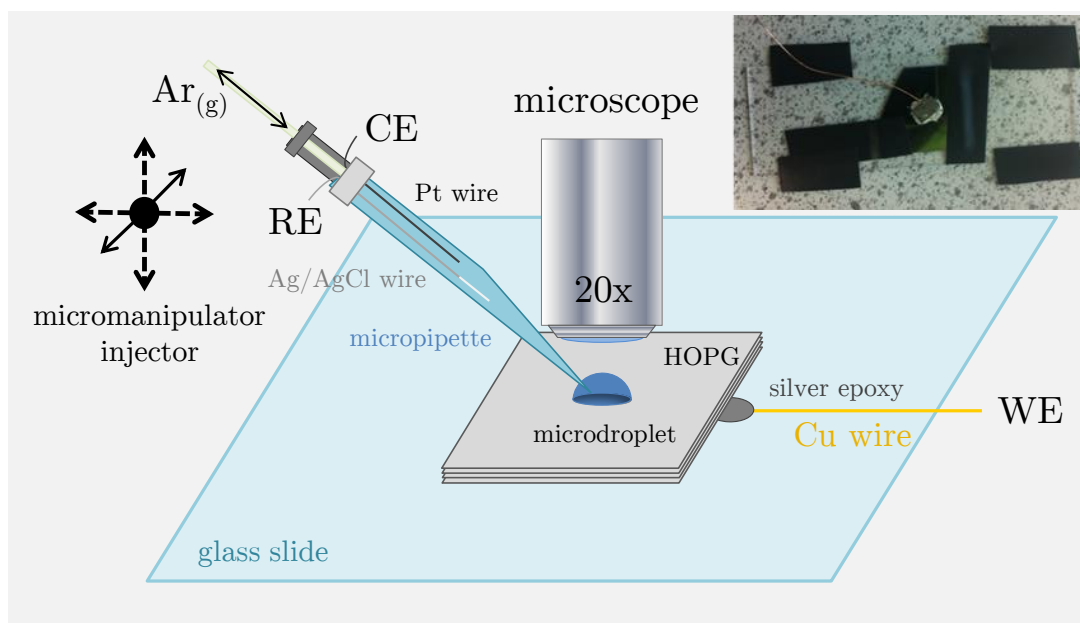


Figure A5) Schematic and photograph of HOPG support electrode using micromanipulator injector setup

However, on sweeping of the potential between 0V and -3.5 V, no voltammetric peaks were observed in the initial scans, other than a steady increase in background current, as seen previously, after *ca.* -2.0 V *vs.* Ag/AgCl. This indicates that although the HOPG surface was sufficiently conductive (shown by the observed current response) no intercalation/reversible reduction of TMA^+ was evident from the voltammetry. This is the first time in this work that intercalation was directly restricted to graphite's basal plane, and unsurprisingly it appears much more difficult than *via* the edge plane of graphite. Even so, a small degree of observable intercalation was expected *via* defects/edge sites in the basal plane, though admittedly if the fraction is very low, Faradaic currents associated with intercalation are probably not very resolvable from the background charging current. Solvent evaporation did prove to be a minor concern, occurring at a rate such that only several CVs were recordable before an insufficient volume of electrolyte remained. This may have been a reason for the lack of observed intercalation, since one would expect

intercalation *via* basal plane defects to take a longer period of time than at edge sites, due to the energetic implications associated with the lack of exposed edge sites by which intercalation can proceed. This study exemplifies the clear issues of working in an open-air system through solvent evaporation, though oxygen presence did not seem to cause any obvious voltammetry effects.

A2.3 Inert atmosphere electrochemical cell: Approach B

Due to the resistance caused by the Si/SiO₂ oxide layer, graphene was directly transferred to a more conductive, non-oxidised silicon substrate. However because the visibility of graphene is highly reliant on the 300 nm oxide layer, it was found that location of the graphene when placed within the cell was extremely difficult. Despite this, few-layer flakes were faintly visible through the optical microscope, and Raman spectroscopy was able to confirm this (Figure A6). This does highlight the importance of the oxide layer for graphene visibility.

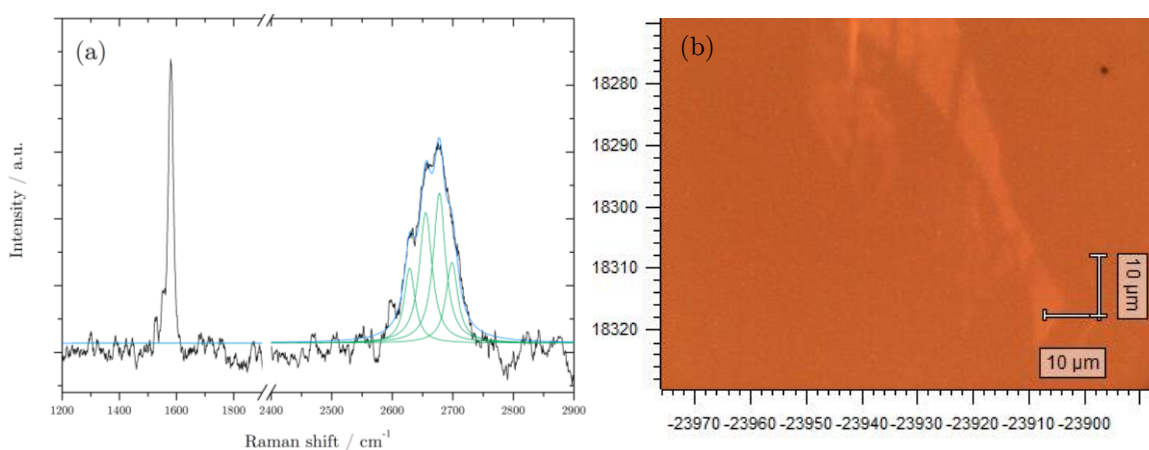


Figure A6) (a) Raman spectrum of few-layer graphene material on pure silicon wafers, and (b) optical image of analysed flake faintly visible through solution

However the difficulty in flake identification, not surprisingly, was amplified when exposed to the solvent and the addition of a quartz cell window, resulting in no successful flake identification. However, theoretically the visibility of the graphene flake is not completely necessary, so long as the flake can be observed spectroscopically. With this in mind, Raman mapping of the substrate was performed, but revealed no graphene-related spectra, likely due to masking from the solvent. Therefore, the search for another graphene support/system is currently under investigation.

A2.4 Approach B: HOPG working electrode

HOPG (3mm diameter disc, SPI-1) was employed as the supported graphite WE in the *in situ* cell, alongside a lithium metal CE and RE. TEABF₄ (0.1M) was selected as the initial electrolyte, and the cell was assembled under an oxygen free atmosphere, after which it was removed from the glove box and connected externally for ease of use. The OCP measured +2.9 V *vs.* Li/Li⁺ and the potential was swept surrounding this potential at a scan rate of 0.1 mV s⁻¹ between +5 V and 0 V *vs.* Li/Li⁺, since Hardwick and co-workers show cationic (TEA⁺) intercalation/de-intercalation taking place within this potential region.²²⁷

However, it was difficult to obtain current responses corresponding to TEA⁺ intercalation/de-intercalation in the potential region shown by Hardwick *et al.* and although a large reduction peak was visible at *ca.* 0 V, the potential at which the reduction occurred was attributed to Li⁺ reduction, from the CE/RE. The Li⁺ reduction current response decreased in magnitude during consecutive scanning (Figure A7a) indicating depletion in the concentration of dissolved lithium through SEI formation.

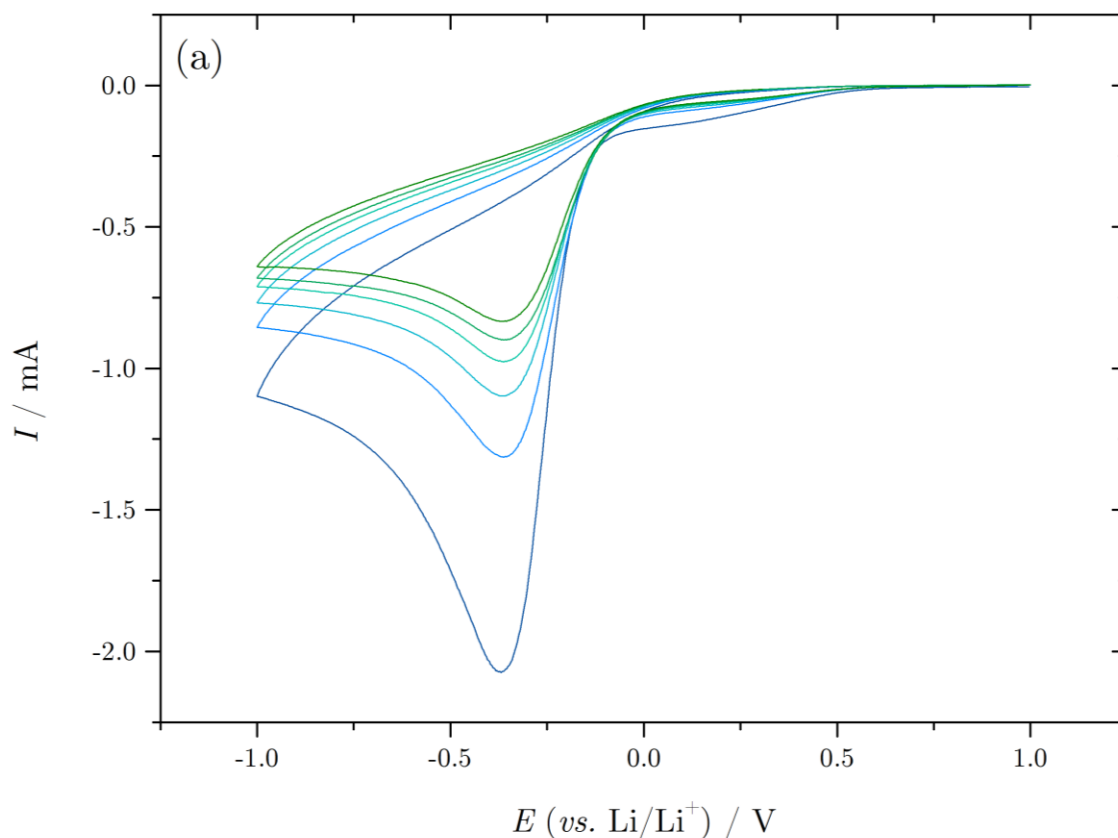


Figure A7(a) Consecutive CVs showing non-reversible Li^+ reduction at a HOPG electrode

Interestingly, prominent current responses corresponding to TEA^+ intercalation at *ca.* +1.5 V were only visible when thicker HOPG samples (*ca.* 0.5 mm thick) were employed; exposing a larger degree of edge sites to the electrolyte solution.

(Figure 7.7b) This has been attributed to a greater possible degree of intercalation, since TEA^+ GIC formation can only occur *via* intercalation at graphite edge sites. Hardwick and co-workers present CVs with extremely prominent TEA^+ redox current responses, though it should be noted that graphite powder was employed as the working electrode in their work, with the working electrode having a substantially increased proportion of accessible edge sites.

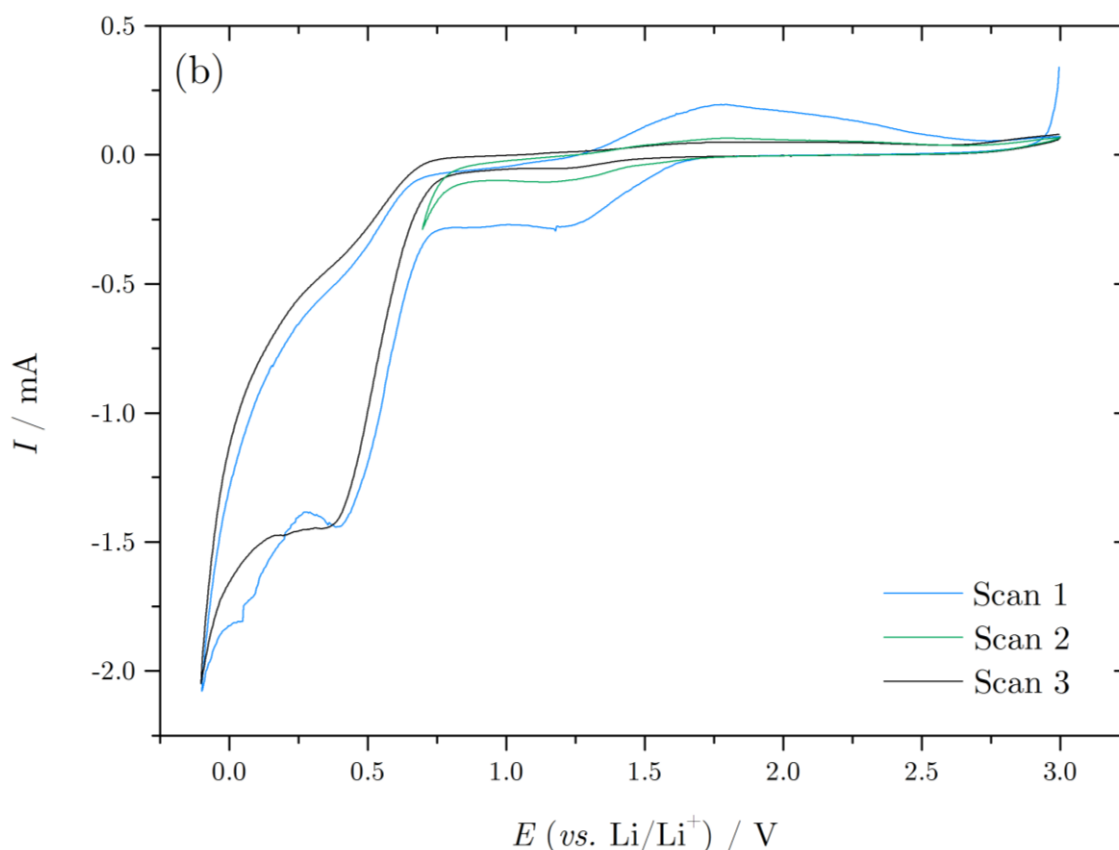


Figure A7(b) CVs showing non-reversible TEA^+ intercalation/de-intercalation into a HOPG electrode after as little as three CV scans

Finally, it was found that the intensity of the TEA^+ current responses decreased dramatically whilst cycling to 0 V. The reason for this was initially attributed to irreversible electrolyte and solvent decomposition, as seen in previous experimental investigation, and since the total volume of electrolyte in the cell is less than 1 mL, this effect is amplified in the voltammetry. However, since the inclusion of lithium reference and counter electrodes, it is possible that dissolved lithium results in the formation of an SEI layer.

Because of the suspected relationship of peak current with amount of accessible edge planes, a much thicker HOPG sample (*ca.* 2 mm thickness, 14.8 mg) was employed as the working electrode and the potential sweep was contained

within the region corresponding to TEA⁺ intercalation/de-intercalation. (Figure A8)

Despite employment of a relatively thick (*ca.* 1 mm) working electrode with a sufficient edge plane exposure, and maintaining the potential within the limits of little electrolyte/solvent reduction; the redox peaks were only prominent during the initial voltammetric sweep, after which they decreased substantially on the second scan, and barely visible in the fourth scan. This was unexpected, since extreme potentials were not applied to the system during this study; however it would appear the small *ca.* 0.3 cm³ electrolyte volume cannot compensate for even residual solvent/electrolyte decomposition, and a significant decrease in the magnitude of the recorded peak currents was observed.

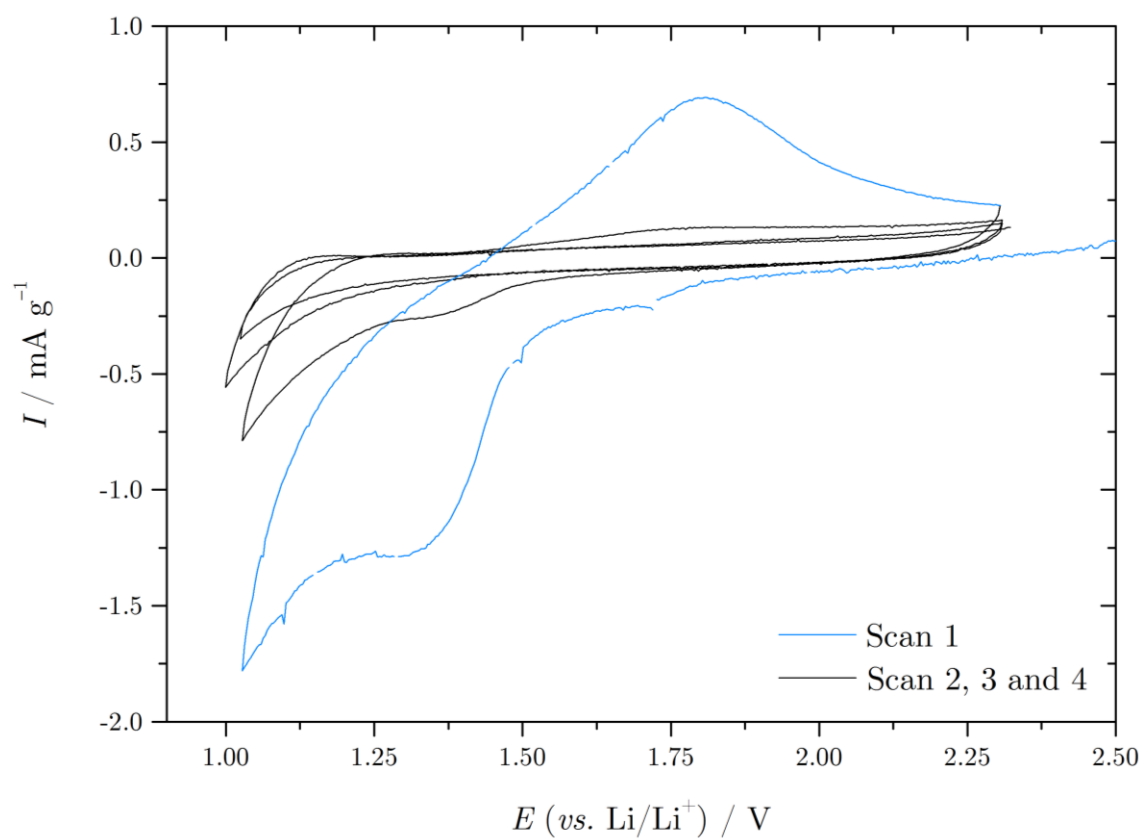


Figure A8) CVs showing current response (current density) at a HOPG (14.8 mg) working electrode displaying prominent TEA^+ redox peaks on the initial scan with significantly reduced intensities on the successive scans

A3 Conclusions

Despite this unfinished investigation, some important advances have been established in the experimental setup for and *in situ* study of ion intercalation into few-layer graphene. The next rational step would be to implement a graphene-based electrode into Approach 2, possibly in the form of CVD bi-layer graphene grown on a copper substrate, thus providing a current collector on which the graphene is supported. The nature of the setup is difficult, since the success of the investigation heavily relies on the construction of a graphene-based electrode. Still, there are systems that can be tried; including the use of both mechanically exfoliated graphene and CVD. Whereas CVD systems would be easier to construct, their inability to produce few-layer flakes makes the study short lived, only allowing the investigation of monolayer and possibly bi-layer flakes.

It was found that ion intercalation does not occur easily, if at all, *via* basal plane defects in HOPG. However, the studies were only recorded over several initial CV sweeps, after which analysis was prevented due to solvent evaporation. This study would need to be repeated with the use of either a humidity chamber to control solvent evaporation, or through the use of more viscous media.

Finally, Raman spectroscopy, with the aid of a fibre optic probe, could be employed to study the intercalation mechanism without the need for a specially designed setup. By employing the setup used throughout the majority of this thesis (Figure 2.17), it could be possible to directly focus the Raman laser directly on the graphite cathode. A simple study could easily be investigated when such a system is accessible.

References

- 1 A.-L. de Lavoisier, "Traité élémentaire de chimie " (1789).
- 2 D. Mendeleev, *Zeitschrift fur Chemie*. (1869).
- 3 R. A. Higgins, *The Properties of Engineering Materials*. (Hodder and Stoughton, 1977).
- 4 J. d. P. P. Atkins, *Physical Chemistry for the Life Sciences*. (Oxford University Press, 2006).
- 5 G. E. Harlow, *The Nature of Diamonds*. (Cambridge University Press, 1998).
- 6 J. H. T. Luong, K. B. Male, and J. D. Glennon, "Boron-doped diamond electrode: synthesis, characterization, functionalization and analytical applications," *Analyst* 134 (10), 1965-1979 (2009).
- 7 K. Kinoshita, *Carbon, Electrochemical and Physicochemical Properties*. (John Wiley & Sons, Inc., 1988).
- 8 <http://www.2spi.com/catalog/new/hopgsub.php>.
- 9 G. S. Bezruchko, G. I. Kanel, and K. V. Khishchenko, "Influence of Structure and Orientation of Graphite on its Polymorphic Transformation Under Shock Compression", in *Shock Compression of Condensed Matter - Pts 1 and 2* (Amer Inst Physics, Melville, 2009), Vol. 1195, pp. 1179-1182.
- 10 M. A. Edwards, P. Bertoncello, and P. R. Unwin, "Slow Diffusion Reveals the Intrinsic Electrochemical Activity of Basal Plane Highly Oriented Pyrolytic Graphite Electrodes," *J. Phys. Chem. C* 113 (21), 9218-9223 (2009).
- 11 P. J. F. Harris, "Fullerene-related structure of commercial glassy carbons," *Philos. Mag.* 84 (29), 3159-3167 (2004).
- 12 http://www.nobelprize.org/nobel_prizes/physics/laureates/2010
- 13 J.-H. Chen, C. Jang, S. Xiao *et al.*, "Intrinsic and extrinsic performance limits of graphene devices on SiO₂," *Nature Nanotechnology* 3 (4), 206-209 (2008).
- 14 P. N. Nirmalraj, T. Lutz, S. Kumar *et al.*, "Nanoscale Mapping of Electrical Resistivity and Connectivity in Graphene Strips and Networks," *Nano Letters* 11 (1), 16-22 (2010).

- 15 F. Xia, D. B. Farmer, Y.-m. Lin, and P. Avouris, "Graphene Field-Effect Transistors with High On/Off Current Ratio and Large Transport Band Gap at Room Temperature," *Nano Letters* 10 (2), 715-718 (2010).
- 16 R. R. a. J. W. David Halliday, *Fundamentals of Physics, 6th Edition*. (Wiley, 2000).
- 17 E. P. O'Reilly, "The electronic structure of amorphous carbon," *Journal of Non-Crystalline Solids* 97–98, Part 2 (0), 1095-1102 (1987).
- 18 W. Kotlensky and H. Martens, "Tensile properties of glassy carbon to 2,900 C," (1965).
- 19 F. C. Cowlard and J. C. Lewis, "Vitreous carbon — A new form of carbon," *J Mater Sci* 2 (6), 507-512 (1967).
- 20 R. R. Saxena and R. H. Bragg, "Electrical conduction in glassy carbon," *Journal of Non-Crystalline Solids* 28 (1), 45-60 (1978).
- 21 <http://www.mateck.com>.
- 22 N. García, P. Esquinazi, J. Barzola-Quiquia, and S. Dusari, "Evidence for semiconducting behavior with a narrow band gap of Bernal graphite," *New Journal of Physics* 14 (5), 053015 (2012).
- 23 http://www.engineeringtoolbox.com/metal-alloys-densities-d_50.html.
- 24 M. Lazar, *Let's Review: Physics, the Physical Setting Third Edition*. (United States: Barrons, 2007).
- 25 P. E. Lewis and P. M. Lee, "Band Structure and Electronic Properties of Silver," *Physical Review* 175 (3), 795-804 (1968).
- 26 <http://www.ktzmy-us.com/2011/Molybdenum-disulfide-5240.html>.
- 27 <http://www.khck.hk/adgoogle/Molybdenum-Disulfide.htm>.
- 28 R. Schlaf, O. Lang, C. Pettenkofer, and W. Jaegermann, "Band lineup of layered semiconductor heterointerfaces prepared by van der Waals epitaxy: Charge transfer correction term for the electron affinity rule," *Journal of Applied Physics* 85 (5), 2732-2753 (1999).
- 29 K. F. Mak, C. Lee, J. Hone *et al.*, "Atomically thin MoS 2: a new direct-gap semiconductor," *Physical Review Letters* 105 (13), 136805 (2010).
- 30 H. W. Kroto and R. E. Smalley, "C60: Buckminsterfullerene," *Nature* 318 (6042), 162-163 (1985).
- 31 C. E. S. Houscroft, A. G., *Inorganic Chemistry*. (Pearson Education Limited, 2005), 2nd ed.
- 32 S. Iijima, "Helical Microtubules of Graphitic Carbon," *Nature* 354 (6348), 56-58 (1991).

- 33 R. L. McCreery, "Advanced Carbon Electrode Materials for Molecular Electrochemistry," *Chem. Rev.* 108, 2646-2687 (2008).
- 34 V. a. L. Radushkevich, V. M., *Soviet Journal of Physical Chemistry* 26, 88-95 (1952).
- 35 M. Monthieux and V. L. Kuznetsov, "Who should be given the credit for the discovery of carbon nanotubes?," *Carbon* 44 (9), 1621-1623 (2006).
- 36 L. D. Landau, "Zur Theorie der phasenumwandlungen II," *Phys. Z. Sowjetunion* 11, 26-35 (1937).
- 37 R. E. Peierls, "Quelques proprietes typiques des corps solides," *Ann. I. H. Poincare* 5, 177-222 (1935).
- 38 A. K. Geim and K. S. Novoselov, "The rise of graphene," *Nat Mater* 6 (3), 183-191 (2007).
- 39 N. D. Mermin, "Crystalline Order in Two Dimensions," *Physical Review* 176 (1), 250-254 (1968).
- 40 L. D. L. Landau, E. M., "Statistical Physics, Part I", (Pergamon Press, Oxford, 1980).
- 41 N. K. S. Geim A K, *Nat. Mater.* 6 (3), 183 (2007).
- 42 A. K. Geim, "Graphene: Status and Prospects," *Science* 324 (5934), 1530-1534 (2009).
- 43 K. S. Novoselov, A. K. Geim, S. V. Morozov *et al.*, "Two-dimensional gas of massless Dirac fermions in graphene," *Nature* 438 (7065), 197-200 (2005).
- 44 K. S. Novoselov, Z. Jiang, Y. Zhang *et al.*, "Room-Temperature Quantum Hall Effect in Graphene," *Science* 315 (5817), 1379 (2007).
- 45 J. R. Williams, L. DiCarlo, and C. M. Marcus, "Quantum Hall Effect in a Gate-Controlled p-n Junction of Graphene," *Science* 317 (5838), 638-641 (2007).
- 46 Y. B. Zhang, Y. W. Tan, H. L. Stormer, and P. Kim, "Experimental observation of the quantum Hall effect and Berry's phase in graphene," *Nature* 438 (7065), 201-204 (2005).
- 47 Y. Zhu, S. Murali, M. D. Stoller *et al.*, "Carbon-based supercapacitors produced by activation of graphene," *Science* 332 (6037), 1537-1541 (2011).
- 48 C. Biswas and Y. H. Lee, "Graphene Versus Carbon Nanotubes in Electronic Devices," *Adv. Funct. Mater.* 21 (20), 3806-3826 (2011).

- 49 H. Li, Q. Zhang, C. Liu *et al.*, "Ambipolar to Unipolar Conversion in Graphene Field-Effect Transistors," ACS Nano 5 (4), 3198-3203 (2011).
- 50 H. Pfleiderer, "Elementary Ambipolar Field-Effect Transistor Model," IEEE Transactions on Electron Devices ED-33 (1) (1986).
- 51 S. A. Stauth and B. A. Parviz, "Self-assembled single-crystal silicon circuits on plastic," Proc. Natl. Acad. Sci. U. S. A. 103 (38), 13922-13927 (2006).
- 52 A. Balandin, S. Ghosh, and W. Bao, "Superior Thermal Conductivity of Single-Layer Graphene," Nano Letters 8 (3), 902-907 (2008).
- 53 C. Lee and J. Hone, "Measurement of the Elastic Properties and Intrinsic Strength of Monolayer Graphene," Science 321 (5887), 385-388 (2008).
- 54 A. C. Fisher, *Electrode Dynamics (Oxford Chemistry Primers)*. (Oxford Science Publications, 1996).
- 55 R. Kundu, P. Mishra, B. R. Sekhar *et al.*, "Electronic structure of single crystal and highly oriented pyrolytic graphite from ARPES and KRIPEs," Physica B: Condensed Matter 407 (5), 827-832 (2012).
- 56 Y. Akai and S. Saito, "Electronic structure, energetics and geometric structure of carbon nanotubes: A density-functional study," Physica E: Low-dimensional Systems and Nanostructures 29 (3-4), 555-559 (2005).
- 57 <http://large.stanford.edu/courses/2008/ph373/laughlin2/>.
- 58 S. Park and R. S. Ruoff, "Chemical methods for the production of graphenes," Nature Nanotechnology 4 (4), 217-224 (2009).
- 59 M. D. Stoller, S. Park, Y. Zhu *et al.*, "Graphene-Based Ultracapacitors," Nano Letters 8 (10), 3498-3502 (2008).
- 60 D. Chen, L. Tang, and J. Li, "Graphene-based materials in electrochemistry," Chemical Society Reviews 39 (8), 3157-3180 (2010).
- 61 M. J. Allen and V. C. Tung, "Honeycomb Carbon: A Review of Graphene," Chem. Rev. 110 (1), 132-145 (2009).
- 62 T. J. Davies, M. E. Hyde, and R. G. Compton, "Nanotrench Arrays Reveal Insight into Graphite Electrochemistry," Angewandte Chemie International Edition 44 (32), 5121-5126 (2005).
- 63 S. C. S. Lai, A. N. Patel, K. McKelvey, and P. R. Unwin, "Definitive Evidence for Fast Electron Transfer at Pristine Basal Plane Graphite from High-Resolution Electrochemical Imaging," Angewandte Chemie International Edition 51 (22), 5405-5408 (2012).

- 64 T. J. Davies, R. R. Moore, C. E. Banks, and R. G. Compton, "The cyclic voltammetric response of electrochemically heterogeneous surfaces," *Journal of Electroanalytical Chemistry* 574 (1), 123-152 (2004).
- 65 D. A. C. Brownson, D. K. Kampouris, and C. E. Banks, "Graphene electrochemistry: Fundamental concepts through to prominent applications," *Chemical Society Reviews* 41 (21), 6944-6976 (2012).
- 66 E. C. Walter and R. M. Penner, "Metal nanowire arrays by electrodeposition," *ChemPhysChem* 4 (2), 131-138 (2003).
- 67 L. L. Zhang, R. Zhou, and X. S. Zhao, "Graphene-based materials as supercapacitor electrodes," *Journal of Materials Chemistry* 20 (29), 5983-5992 (2010).
- 68 Y. Wang, Z. Shi, Y. Huang *et al.*, "Supercapacitor Devices Based on Graphene Materials," *The Journal of Physical Chemistry C* 113 (30), 13103-13107 (2009).
- 69 H. Choi, H. Kim, S. Hwang *et al.*, "Graphene counter electrodes for dye-sensitized solar cells prepared by electrophoretic deposition," *Journal of Materials Chemistry* 21 (21), 7548-7551 (2011).
- 70 Y. Wang, X. Chen, Y. Zhong *et al.*, "Large area, continuous, few-layered graphene as anodes in organic photovoltaic devices," *Applied Physics Letters* 95 (6) (2009).
- 71 D. Zheng, S. K. Vashist, M. M. Dykas *et al.*, "Graphene versus multi-walled carbon nanotubes for electrochemical glucose biosensing," *Materials* 6 (3), 1011-1027 (2013).
- 72 Y. Zhang, Y. Zhao, S. Yuan *et al.*, "Electrocatalysis and detection of nitrite on a reduced graphene/Pd nanocomposite modified glassy carbon electrode," *Sensors and Actuators, B: Chemical* 185, 602-607 (2013).
- 73 B. Yuan, X. Zeng, C. Xu *et al.*, "Electrochemical modification of graphene oxide bearing different types of oxygen functional species for the electro-catalytic oxidation of reduced glutathione," *Sensors and Actuators, B: Chemical* 184, 15-20 (2013).
- 74 B. Yuan, C. Xu, L. Liu *et al.*, "Cu₂O/NiO_x/graphene oxide modified glassy carbon electrode for the enhanced electrochemical oxidation of reduced glutathione and nonenzyme glucose sensor," *Electrochimica Acta* 104, 78-83 (2013).

- 75 Y. Yang, J. Zhou, H. Zhang *et al.*, "Electrochemical evaluation of total antioxidant capacities in fruit juice based on the guanine/graphene nanoribbon/glassy carbon electrode," *Talanta* 106, 206-211 (2013).
- 76 S. M. Majd, H. Teymourian, and A. Salimi, "Fabrication of an electrochemical l-cysteine sensor based on graphene nanosheets decorated manganese oxide nanocomposite modified glassy carbon electrode," *Electroanalysis* 25 (9), 2201-2210 (2013).
- 77 Y. Li, J. Liu, G. Song *et al.*, "Sensitive voltammetric sensor for bergenin based on poly(l-lysine)/graphene modified glassy carbon electrode," *Analytical Methods* 5 (16), 3895-3902 (2013).
- 78 Y. Li, K. Li, G. Song *et al.*, "Electrochemical behavior of codeine and its sensitive determination on graphene-based modified electrode," *Sensors and Actuators, B: Chemical* 182, 401-407 (2013).
- 79 S.-H. Lee, S.-D. Seo, Y.-H. Jin *et al.*, "A graphite foil electrode covered with electrochemically exfoliated graphene nanosheets," *Electrochemistry Communications* 12 (10), 1419-1422 (2010).
- 80 K. J. Huang, L. Wang, J. Li *et al.*, "Electrochemical sensing of catechol using a glassy carbon electrode modified with a composite made from silver nanoparticles, polydopamine, and graphene," *Microchimica Acta* 180 (9-10), 751-757 (2013).
- 81 C. Yu, W. Ji, Y. Wang *et al.*, "Graphene oxide-modified electrodes for sensitive determination of diethylstilbestrol," *Nanotechnology* 24 (11) (2013).
- 82 J. Peng, C. Hou, and X. Hu, "A graphene-based electrochemical sensor for sensitive detection of vanillin," *International Journal of Electrochemical Science* 7 (2), 1724-1733 (2012).
- 83 A. Navaee, A. Salimi, and H. Teymourian, "Graphene nanosheets modified glassy carbon electrode for simultaneous detection of heroine, morphine and noscapine," *Biosensors and Bioelectronics* 31 (1), 205-211 (2012).
- 84 Y. Li, G. Ran, W. J. Yi *et al.*, "A glassy carbon electrode modified with graphene and poly(acridine red) for sensing uric acid," *Microchimica Acta* 178 (1-2), 115-121 (2012).
- 85 X. Xie, K. Zhao, X. Xu *et al.*, "Study of Heterogeneous Electron Transfer on the Graphene/Self-Assembled Monolayer Modified Gold Electrode by

- Electrochemical Approaches," *The Journal of Physical Chemistry C* 114 (33), 14243-14250 (2010).
- 86 M. Arvand and M. Anvari, "A graphene-based electrochemical sensor for sensitive detection of quercetin in foods," *J IRAN CHEM SOC* 10 (5), 841-849 (2013).
- 87 X. Kang, J. Wang, H. Wu *et al.*, "A graphene-based electrochemical sensor for sensitive detection of paracetamol," *Talanta* 81 (3), 754-759 (2010).
- 88 G. P. Keeley, A. O'Neill, N. McEvoy *et al.*, "Electrochemical ascorbic acid sensor based on DMF-exfoliated graphene," *Journal of Materials Chemistry* 20 (36), 7864-7869 (2010).
- 89 W. Li and D. C. Ralph, "Electrochemistry of Individual Monolayer Graphene Sheets," *ACS Nano* 5 (3), 2264-2270 (2011).
- 90 A. T. Valota, I. A. Kinloch, K. S. Novoselov *et al.*, "Electrochemical Behavior of Monolayer and Bilayer Graphene," *ACS Nano* 5 (11), 8809-8815 (2011).
- 91 G. A. K. Novoselov K S, Morozov S V, Jiang D, Zhang Y, Dubonos S V, Grigorieva I V, Firsov A A, *Science* 306 (5696), 666 (2004).
- 92 P. Blake, E. W. Hill, A. H. Castro Neto *et al.*, "Making graphene visible," *Applied Physics Letters* 91 (6), - (2007).
- 93 Z. Sun, Z. Yan, J. Yao *et al.*, "Growth of graphene from solid carbon sources," *Nature* 468 (7323), 549-552 (2010).
- 94 A. Reina, X. Jia, J. Ho *et al.*, "Large area, few-layer graphene films on arbitrary substrates by chemical vapor deposition," *Nano Letters* 9 (1), 30-35 (2009).
- 95 X. Li, C. W. Magnuson, A. Venugopal *et al.*, "Graphene films with large domain size by a two-step chemical vapor deposition process," *Nano Letters* 10 (11), 4328-4334 (2010).
- 96 A. Ismach, C. Druzgalski, S. Penwell *et al.*, "Direct chemical vapor deposition of graphene on dielectric surfaces," *Nano Letters* 10 (5), 1542-1548 (2010).
- 97 L. Gomez De Arco, Y. Zhang, C. W. Schlenker *et al.*, "Continuous, highly flexible, and transparent graphene films by chemical vapor deposition for organic photovoltaics," *ACS Nano* 4 (5), 2865-2873 (2010).

- 98 S. J. Chae, F. Güneş, K. K. Kim *et al.*, "Synthesis of large-area graphene layers on poly-nickel substrate by chemical vapor deposition: Wrinkle formation," *Advanced Materials* 21 (22), 2328-2333 (2009).
- 99 J. Ryu, Y. Kim, D. Won *et al.*, "Fast synthesis of high-performance graphene films by hydrogen-free rapid thermal chemical vapor deposition," *ACS Nano* 8 (1), 950-956 (2014).
- 100 Z. Luo, Y. Lu, D. W. Singer *et al.*, "Effect of substrate roughness and feedstock concentration on growth of wafer-scale graphene at atmospheric pressure," *Chem. Mat.* 23 (6), 1441-1447 (2011).
- 101 T. Kobayashi, M. Bando, N. Kimura *et al.*, "Production of a 100-m-long high-quality graphene transparent conductive film by roll-to-roll chemical vapor deposition and transfer process," *Applied Physics Letters* 102 (2) (2013).
- 102 Z. J. Fan, J. Yan, T. Wei *et al.*, "Nanographene-constructed carbon nanofibers grown on graphene sheets by chemical vapor deposition: High-performance anode materials for lithium ion batteries," *ACS Nano* 5 (4), 2787-2794 (2011).
- 103 C. Berger, Z. Song, T. Li *et al.*, "Ultrathin Epitaxial Graphite: 2D Electron Gas Properties and a Route toward Graphene-based Nanoelectronics," *The Journal of Physical Chemistry B* 108 (52), 19912-19916 (2004).
- 104 D. Wei, L. Grande, V. Chundi *et al.*, "Graphene from electrochemical exfoliation and its direct applications in enhanced energy storage devices," *Chemical Communications* 48 (9), 1239-1241 (2012).
- 105 S. Bae, H. Kim, Y. Lee *et al.*, "Roll-to-roll production of 30-inch graphene films for transparent electrodes," *Nature Nanotechnology* 5 (8), 574-578 (2010).
- 106 "RSC Chemistry World: First graphene touchscreen", (2010).
- 107 I. Forbeaux, J. M. Themlin, and J. M. Debever, "Heteroepitaxial graphite on 6H-SiC(0001): Interface formation through conduction-band electronic structure," *Physical Review B - Condensed Matter and Materials Physics* 58 (24), 16396-16406 (1998).
- 108 J. N. Coleman, "Liquid Exfoliation of Defect-Free Graphene," *Accounts of Chemical Research* 46 (1), 14-22 (2012).
- 109 A. A. Ameen, A. N. Giordano, J. R. Alston *et al.*, "Aggregation kinetics of single-walled carbon nanotubes investigated using mechanically

- wrapped multinuclear complexes: probing the tube-tube repulsive barrier," *Physical Chemistry Chemical Physics* 16 (12), 5855-5865 (2014).
- 110 S. D. Bergin, V. Nicolosi, P. V. Streich *et al.*, "Towards Solutions of Single-Walled Carbon Nanotubes in Common Solvents," *Advanced Materials* 20 (10), 1876-1881 (2008).
 - 111 S. D. Bergin, Z. Sun, D. Rickard *et al.*, "Multicomponent Solubility Parameters for Single-Walled Carbon Nanotube–Solvent Mixtures," *ACS Nano* 3 (8), 2340-2350 (2009).
 - 112 J. N. Coleman, "Liquid-phase Exfoliation of Nanotubes and Graphene," *Adv. Funct. Mater.* 19, 3680-3695 (2009).
 - 113 T. Hasan, F. Torrisi, Z. Sun *et al.*, "Solution-phase exfoliation of graphite for ultrafast photonics," *physica status solidi (b)* 247 (11-12), 2953-2957 (2010).
 - 114 Y. Hernandez and J. N. Coleman, "High-yield production of graphene by liquid-phase exfoliation of graphite," *Nat Nano* 3 (9), 563-568 (2008).
 - 115 Y. Hernandez, M. Lotya, D. Rickard *et al.*, "Measurement of Multicomponent Solubility Parameters for Graphene Facilitates Solvent Discovery," *Langmuir* 26 (5), 3208-3213 (2009).
 - 116 D. Nuvoli, V. Alzari, R. Sanna *et al.*, "The production of concentrated dispersions of few-layer graphene by the direct exfoliation of graphite in organosilanes," *Nanoscale Res Lett* 7 (1), 1-7 (2012).
 - 117 S. L. Chin-Jen Shih, Michael S. Strano, and Daniel Blankschtein, "Understanding the Stabilization of Liquid-Phase-Exfoliated Graphene in Polar Solvents: Molecular Dynamics Simulations and Kinetic Theory of Colloid Aggregation," *J. Am. Chem. Soc.* 132 (41), 14638-14648 (2010).
 - 118 Z. Y. S. S. D Bergin, D. Rickard, P. V. Streich, J. P. Hamilton, J. N. Coleman, *ACS Nano* 3, 2340 (2009).
 - 119 J. Lyklema, "The Surface Tension of Pure Liquids - Thermodynamic Components and Corresponding States," *Colloids Sur., A* 156, 413-421 (1999).
 - 120 S. R. Z. Wang, Y.; Abidi, N.; Cabrales, L., "Wettability and Surface Free Energy of Graphene Films," *Langmuir* 25, 11078-11081 (2009).
 - 121 H. Buqa, A. Würsig, J. Vetter *et al.*, "SEI film formation on highly crystalline graphitic materials in lithium-ion batteries," *Journal of Power Sources* 153 (2), 385-390 (2006).

- 122 U. Khan, A. O'Neill, H. Porwal *et al.*, "Size selection of dispersed, exfoliated graphene flakes by controlled centrifugation," *Carbon* 50 (2), 470-475 (2012).
- 123 M. J. Yuhong Jin, Mei Zhang, Qianqian Wen, "Preparation of stable aqueous dispersion of graphene nanosheets and their electrochemical capacitive properties," *Applied Surface Science* 264, 787-793 (2013).
- 124 O. C. C. Bong Jin Hong, Zhi An, Abraham Eryazici, and SonBinh T. Nguyen, "Successful Stabilisation of Graphene Oxide in Electrolyte Solutions: Enhancement of Biofunctionalization and Cellular Uptake," *ACS Nano* 6 (1), 63-73 (2012).
- 125 W.-W. Liu, B.-Y. Xia, X.-X. Wang, and J.-N. Wang, "Exfoliation and dispersion of graphene in ethanol-water mixtures," *Front. Mater. Sci.* 6 (2), 176-182 (2012).
- 126 A. O'Neill, U. Khan, P. N. Nirmalraj *et al.*, "Graphene Dispersion and Exfoliation in Low Boiling Point Solvents," *The Journal of Physical Chemistry C* 115 (13), 5422-5428 (2011).
- 127 J. Shen, Y. Hu, M. Shi *et al.*, "Fast and Facile Preparation of Graphene Oxide and Reduced Graphene Oxide Nanoplatelets," *Chem. Mat.* 21 (15), 3514-3520 (2009).
- 128 C. Gómez-Navarro, R. T. Weitz, A. M. Bittner *et al.*, "Electronic Transport Properties of Individual Chemically Reduced Graphene Oxide Sheets," *Nano Letters* 7 (11), 3499-3503 (2007).
- 129 A. B. Bourlinos, D. Gournis, D. Petridis *et al.*, "Graphite Oxide: Chemical Reduction to Graphite and Surface Modification with Primary Aliphatic Amines and Amino Acids," *Langmuir* 19 (15), 6050-6055 (2003).
- 130 H.-J. Shin, K. K. Kim, A. Benayad *et al.*, "Efficient Reduction of Graphite Oxide by Sodium Borohydride and Its Effect on Electrical Conductance," *Adv. Funct. Mater.* 19 (12), 1987-1992 (2009).
- 131 O. Akhavan and E. Ghaderi, "Photocatalytic Reduction of Graphene Oxide Nanosheets on TiO₂ Thin Film for Photoinactivation of Bacteria in Solar Light Irradiation," *The Journal of Physical Chemistry C* 113 (47), 20214-20220 (2009).
- 132 Y. Shao, J. Wang, M. Engelhard *et al.*, "Facile and controllable electrochemical reduction of graphene oxide and its applications," *Journal of Materials Chemistry* 20 (4), 743-748 (2010).

- 133 G. Wang and J. Yao, "Facile Synthesis and Characterization of Graphene Nanosheets," *The Journal of Physical Chemistry C* 112 (22), 8192-8195 (2008).
- 134 W. Chen, L. Yan, and P. R. Bangal, "Preparation of graphene by the rapid and mild thermal reduction of graphene oxide induced by microwaves," *Carbon* 48 (4), 1146-1152 (2010).
- 135 "Preparation and examination of multilayer graphene nanosheets by exfoliation of graphite in high efficient attritor mill," *Central European Journal of Chemistry* 9 (1), 47 (2011).
- 136 U. Khan and J. N. Coleman, "High-Concentration Solvent Exfoliation of Graphene," *Small* 6 (7), 864-871 (2010).
- 137 P. K. Ang, S. Wang, Q. Bao *et al.*, "High-Throughput Synthesis of Graphene by Intercalation–Exfoliation of Graphite Oxide and Study of Ionic Screening in Graphene Transistor," *ACS Nano* 3 (11), 3587-3594 (2009).
- 138 D. V. Kosynkin, A. L. Higginbotham, A. Sinitskii *et al.*, "Longitudinal unzipping of carbon nanotubes to form graphene nanoribbons," *Nature* 458 (7240), 872-876 (2009).
- 139 Y. Hernandez, V. Nicolosi, M. Lotya *et al.*, "High-yield production of graphene by liquid-phase exfoliation of graphite," *Nat Nano* 3 (9), 563-568 (2008).
- 140 W. W. Liu and J. N. Wang, "Direct exfoliation of graphene in organic solvents with addition of NaOH," *Chemical Communications* 47 (24), 6888-6890 (2011).
- 141 A. B. Bourlinos, V. Georgakilas, R. Zboril *et al.*, "Liquid-Phase Exfoliation of Graphite Towards Solubilized Graphenes," *Small* 5 (16), 1841-1845 (2009).
- 142 A. Ciesielski and P. Samori, "Graphene via sonication assisted liquid-phase exfoliation," *Chemical Society Reviews* 43 (1), 381-398 (2014).
- 143 N. Behabtu, J. R. Lomeda, M. J. Green *et al.*, "Spontaneous high-concentration dispersions and liquid crystals of graphene," *Nature Nanotechnology* 5 (6), 406-411 (2010).
- 144 S. Vadukumpully, J. Paul, and S. Valiyaveetil, "Cationic surfactant mediated exfoliation of graphite into graphene flakes," *Carbon* 47 (14), 3288-3294 (2009).

- 145 X. Wang and S. Dai, "Direct exfoliation of natural graphite into micrometre size few layers graphene sheets using ionic liquids," *Chemical Communications* 46 (25), 4487-4489 (2010).
- 146 C.-Y. Su, A.-Y. Lu, Y. Xu *et al.*, "High-Quality Thin Graphene Films from Fast Electrochemical Exfoliation," *ACS Nano* 5 (3), 2332-2339 (2011).
- 147 M. Lotya, P. J. King, U. Khan *et al.*, "High-concentration, surfactant-stabilized graphene dispersions," *ACS Nano* 4 (6), 3155-3162 (2010).
- 148 M. Alanyalıoğlu, J. J. Segura, J. Oró-Solè, and N. Casañ-Pastor, "The synthesis of graphene sheets with controlled thickness and order using surfactant-assisted electrochemical processes," *Carbon* 50 (1), 142-152 (2012).
- 149 G. M. Morales, P. Schifani, G. Ellis *et al.*, "High-quality few layer graphene produced by electrochemical intercalation and microwave-assisted expansion of graphite," *Carbon* 49 (8), 2809-2816 (2011).
- 150 G. Wang, B. Wang, J. Park *et al.*, "Highly efficient and large-scale synthesis of graphene by electrolytic exfoliation," *Carbon* 47 (14), 3242-3246 (2009).
- 151 N. Liu, F. Luo, H. Wu *et al.*, "One-Step Ionic-Liquid-Assisted Electrochemical Synthesis of Ionic-Liquid-Functionalized Graphene Sheets Directly from Graphite," *Adv. Funct. Mater.* 18 (10), 1518-1525 (2008).
- 152 J. Lu and K. P. Loh, "One-Pot Synthesis of Fluorescent Carbon Nanoribbons, Nanoparticles, and Graphene by the Exfoliation of Graphite in Ionic Liquids," *ACS Nano* 3 (8), 2367-2375 (2009).
- 153 J. Wang, K. K. Manga, Q. Bao, and K. P. Loh, "High-Yield Synthesis of Few-Layer Graphene Flakes through Electrochemical Expansion of Graphite in Propylene Carbonate Electrolyte," *Journal of the American Chemical Society* 133 (23), 8888-8891 (2011).
- 154 Y. Yang, F. Lu, Z. Zhou *et al.*, "Electrochemically cathodic exfoliation of graphene sheets in room temperature ionic liquids N-butyl, methylpyrrolidinium bis(trifluoromethylsulfonyl)imide and their electrochemical properties," *Electrochimica Acta* 113 (0), 9-16 (2013).
- 155 A. J. Cooper, N. R. Wilson, I. A. Kinloch, and R. A. W. Dryfe, "Single stage electrochemical exfoliation method for the production of few-layer

- graphene via intercalation of tetraalkylammonium cations," *Carbon* 66 (0), 340-350 (2014).
- 156 E. Bourelle, B. Claude-montigny, and A. Metrot, "Electrochemical Exfoliation of HOPG in Formic - Sulfuric Acid Mixtures," *Molecular Crystals and Liquid Crystals Science and Technology. Section A. Molecular Crystals and Liquid Crystals* 310 (1), 321-326 (1998).
- 157 M. Sima, I. Enculescu, and A. Sima, "Preparation of graphene and its application in dye-sensitized solar cells," *Optoelectronics and Advanced Materials, Rapid Communications* 5 (4), 414-418 (2011).
- 158 V. V. Singh, G. Gupta, A. Batra *et al.*, "Greener Electrochemical Synthesis of High Quality Graphene Nanosheets Directly from Pencil and its SPR Sensing Application," *Adv. Funct. Mater.* 22 (11), 2352-2362 (2012).
- 159 K. W. Hathcock, J. C. Brumfield, C. A. Goss *et al.*, "Incipient Electrochemical Oxidation of Highly Oriented Pyrolytic Graphite: Correlation between Surface Blistering and Electrolyte Anion Intercalation," *Analytical Chemistry* 67 (13), 2201-2206 (1995).
- 160 B. Qi, L. He, X. Bo *et al.*, "Electrochemical preparation of free-standing few-layer graphene through oxidation–reduction cycling," *Chemical Engineering Journal* 171 (1), 340-344 (2011).
- 161 V. V. Pavlishchuk and A. W. Addison, "Conversion constants for redox potentials measured versus different reference electrodes in acetonitrile solutions at 25°C," *Inorganica Chimica Acta* 298 (1), 97-102 (2000).
- 162 A. J. Bard and L. R. Faulkner, *Electrochemical Methods Fundamentals and Applications*. (John Wiley & Sons, Inc., 2001), 2nd ed.
- 163 P. M. S. Monk, *Fundamentals of Electroanalytical Chemistry*. (John Wiley and Sons Ltd, 2001).
- 164 J. R. M. Evgenij Barsoukov, *Impedance Spectroscopy, Theory, Experimental, and Applications*. (John Wiley & Sons, Inc., 2005).
- 165 C. H. Lui, Z. Li, Z. Chen *et al.*, "Imaging Stacking Order in Few-Layer Graphene," *Nano Letters* 11 (1), 164-169 (2010).
- 166 M. F. Craciun, S. Russo, M. Yamamoto *et al.*, "Trilayer graphene is a semimetal with a gate-tunable band overlap," *Nature Nanotechnology* 4 (6), 383-388 (2009).

- 167 F. Guinea, A. H. Castro Neto, and N. M. R. Peres, "Electronic states and Landau levels in graphene stacks," *Physical Review B* 73 (24), 245426 (2006).
- 168 M. Aoki and H. Amawashi, "Dependence of band structures on stacking and field in layered graphene," *Solid State Communications* 142 (3), 123-127 (2007).
- 169 A. A. Avetisyan, B. Partoens, and F. M. Peeters, "Stacking order dependent electric field tuning of the band gap in graphene multilayers," *Physical Review B* 81 (11), 115432 (2010).
- 170 P. Y. Huang, C. S. Ruiz-Vargas, A. M. Van Der Zande *et al.*, "Grains and grain boundaries in single-layer graphene atomic patchwork quilts," *Nature* 469 (7330), 389-392 (2011).
- 171 Y. Wu, Y. Hao, H. Y. Jeong *et al.*, "Crystal structure evolution of individual graphene islands during CVD growth on copper foil," *Advanced Materials* 25 (46), 6744-6751 (2013).
- 172 K. Kim, Z. Lee, W. Regan *et al.*, "Grain Boundary Mapping in Polycrystalline Graphene," *ACS Nano* 5 (3), 2142-2146 (2011).
- 173 P. Nemes-Incze, Z. Osváth, K. Kamarás, and L. P. Biró, "Anomalies in thickness measurements of graphene and few layer graphite crystals by tapping mode atomic force microscopy," *Carbon* 46 (11), 1435-1442 (2008).
- 174 A. Gupta, G. Chen, P. Joshi *et al.*, "Raman Scattering from High-Frequency Phonons in Supported n-Graphene Layer Films," *Nano Letters* 6 (12), 2667-2673 (2006).
- 175 K. S. Novoselov, A. K. Geim, S. V. Morozov *et al.*, "Electric Field Effect in Atomically Thin Carbon Films," *Science* 306 (5696), 666-669 (2004).
- 176 N. S. Anton, M. Y. Mehdi, J. Romaneh *et al.*, "Electrostatic deposition of graphene," *Nanotechnology* 18 (13), 135301 (2007).
- 177 C. Casiraghi, A. Hartschuh, E. Lidorikis *et al.*, "Rayleigh Imaging of Graphene and Graphene Layers," *Nano Letters* 7 (9), 2711-2717 (2007).
- 178 Z. Chen, Y.-M. Lin, M. J. Rooks, and P. Avouris, "Graphene nanoribbon electronics," *Physica E: Low-dimensional Systems and Nanostructures* 40 (2), 228-232 (2007).
- 179 R. Erni, M. D. Rossell, C. Kisielowski, and U. Dahmen, "Atomic-resolution imaging with a sub-50-pm electron probe," *Physical Review Letters* 102 (9) (2009).

- 180 M. Haider, H. Rose, S. Uhlemann *et al.*, "Towards 0.1 nm resolution with the first spherically corrected transmission electron microscope," *Journal of Electron Microscopy* 47 (5), 395-405 (1998).
- 181 L. C. Gontard, L. Y. Chang, C. J. D. Hetherington *et al.*, "Aberration-corrected imaging of active sites on industrial catalyst nanoparticles," *Angewandte Chemie - International Edition* 46 (20), 3683-3685 (2007).
- 182 A. W. Robertson and J. H. Warner, "Atomic resolution imaging of graphene by transmission electron microscopy," *Nanoscale* 5 (10), 4079-4093 (2013).
- 183 E. Dervishi, Z. Li, J. Shyaka *et al.*, "The role of hydrocarbon concentration on the synthesis of large area few to multi-layer graphene structures," *Chemical Physics Letters* 501 (4-6), 390-395 (2011).
- 184 J. d. P. P. Atkins, *Atkins' Physical Chemistry*. (Oxford University Press, 2006), 8th ed.
- 185 A. C. Ferrari, "Raman spectroscopy of graphene and graphite: Disorder, electron-phonon coupling, doping and nonadiabatic effects," *Solid State Communications* 143 (1-2), 47-57 (2007).
- 186 A. C. Ferrari and D. M. Basko, "Raman spectroscopy as a versatile tool for studying the properties of graphene," *Nature Nanotechnology* 8 (4), 235-246 (2013).
- 187 L. M. Malard, M. A. Pimenta, G. Dresselhaus, and M. S. Dresselhaus, "Raman spectroscopy in graphene," *Physics Reports* 473 (5-6), 51-87 (2009).
- 188 L. Kavan and L. Dunsch, "Spectroelectrochemistry of Carbon Nanostructures," *ChemPhysChem* 8 (7), 974-998 (2007).
- 189 <http://www.physics.umd.edu>.
- 190 I. Kupčić, "Triple-resonant two-phonon Raman scattering in graphene," *Journal of Raman Spectroscopy* 43 (1), 1-5 (2012).
- 191 M. Pimenta, G. Dresselhaus, M. S. Dresselhaus *et al.*, "Studying disorder in graphite-based systems by Raman spectroscopy," *Physical Chemistry Chemical Physics* 9 (11), 1276-1290 (2007).
- 192 D. Graf, F. Molitor, K. Ensslin *et al.*, "Spatially Resolved Raman Spectroscopy of Single- and Few-Layer Graphene," *Nano Letters* 7 (2), 238-242 (2007).

- 193 A. C. Ferrari, K. S. Novoselov, and A. K. Geim, "Raman Spectrum of Graphene and Graphene Layers," *Physical Review Letters* 97 (18), 187401 (2006).
- 194 M. S. Dresselhaus, A. Jorio, and R. Saito, "Characterizing graphene, graphite, and carbon nanotubes by Raman spectroscopy," *Annual Review of Condensed Matter Physics* 1, 89-108 (2010).
- 195 A. Das, B. Chakraborty, and A. K. Sood, "Raman spectroscopy of graphene on different substrates and influence of defects," *Bull. Mat. Sci.* 31 (3), 579-584 (2008).
- 196 D. Yoon, H. Moon, H. Cheong *et al.*, "Variations in the Raman spectrum as a function of the number of graphene layers," *Journal of the Korean Physical Society* 55 (3), 1299-1303 (2009).
- 197 Y. K. Koh, M. H. Bae, D. G. Cahill, and E. Pop, "Reliably counting atomic planes of few-layer graphene ($n > 4$)," *ACS Nano* 5 (1), 269-274 (2011).
- 198 Y. Hao, Y. Wang, L. Wang *et al.*, "Probing layer number and stacking order of few-layer graphene by Raman Spectroscopy," *Small* 6 (2), 195-200 (2010).
- 199 C. Cong, T. Yu, K. Sato *et al.*, "Raman Characterization of ABA- and ABC-Stacked Trilayer Graphene," *ACS Nano* 5 (11), 8760-8768 (2011).
- 200 D. Graf and L. Wirtz, "Spatially Resolved Raman Spectroscopy of Single- and Few-Layer Graphene," *Nano Letters* 7 (2), 238-242 (2007).
- 201 S. Lee, K. Lee, and Z. Zhong, "Wafer Scale Homogeneous Bilayer Graphene Films by Chemical Vapor Deposition," *Nano Letters* 10 (11), 4702-4707 (2010).
- 202 A. C. Ferrari, J. C. Meyer, V. Scardaci *et al.*, "Raman Spectrum of Graphene and Graphene Layers," *Physical Review Letters* 97 (18), 187401 (2006).
- 203 N. Fairley, *Introduction to XPS and AES - CasaXPS Manual 2.3.15*. (Casa Software Ltd, 2009).
- 204 M. Velicky, K. Y. Tam, and R. A. W. Dryfe, "On the stability of the silver/silver sulfate reference electrode," *Analytical Methods* 4 (5), 1207-1211 (2012).
- 205 K. Zaghib and K. Kinoshita, *Overview of carbon anodes for lithium-ion batteries*. (2002).

- 206 X. Xia, M. N. Obrovac, and J. R. Dahn, "Comparison of the Reactivity of Na_xC_6 and Li_xC_6 with Non-Aqueous Solvents and Electrolytes," *Electrochemical and Solid State Letters* 14 (9), A130-A133 (2011).
- 207 S. I. Pyun and Y. G. Ryu, "Lithium transport through graphite electrodes that contain two stage phases," *Journal of Power Sources* 70 (1), 34-39 (1998).
- 208 J. Li, J. Fang, H. Su, and S. Sun, "Interfacial Processes of Lithium Ion Batteries by FTIR Spectroscopy," *Progress in Chemistry* 23 (2-3), 349-356 (2011).
- 209 K. Kinoshita and K. Zaghib, "Negative electrodes for Li-ion batteries," *Journal of Power Sources* 110 (2), 416-423 (2002).
- 210 Y. Nishi, "Lithium ion secondary batteries; past 10 years and the future," *Journal of Power Sources* 100 (1-2), 101-106 (2001).
- 211 D. Aurbach, "Review of selected electrode-solution interactions which determine the performance of Li and Li ion batteries," *Journal of Power Sources* 89 (2), 206-218 (2000).
- 212 K. Xu, "Nonaqueous liquid electrolytes for lithium-based rechargeable batteries," *Chem. Rev.* 104 (10), 4303-4417 (2004).
- 213 M. S. Whittingham, "Lithium batteries and cathode materials," *Chem. Rev.* 104 (10), 4271-4301 (2004).
- 214 J. M. Tarascon and M. Armand, "Issues and challenges facing rechargeable lithium batteries," *Nature* 414 (6861), 359-367 (2001).
- 215 H. Zheng, K. Jiang, T. Abe, and Z. Ogumi, "Electrochemical intercalation of lithium into a natural graphite anode in quaternary ammonium-based ionic liquid electrolytes," *Carbon* 44 (2), 203-210 (2006).
- 216 S. Zhang and P. Shi, "Electrochemical impedance study of lithium intercalation into MCMB electrode in a gel electrolyte," *Electrochimica Acta* 49 (9-10), 1475-1482 (2004).
- 217 C. Wang, A. J. Appleby, and F. E. Little, "Electrochemical impedance study of initial lithium ion intercalation into graphite powders," *Electrochimica Acta* 46 (12), 1793-1813 (2001).
- 218 B. Veeraraghavan, J. Paul, B. Haran, and B. Popov, "Study of polypyrrole graphite composite as anode material for secondary lithium-ion batteries," *Journal of Power Sources* 109 (2), 377-387 (2002).

- 219 M. Umeda, K. Dokko, Y. Fujita *et al.*, "Electrochemical impedance study of Li-ion insertion into mesocarbon microbead single particle electrode: Part I. Graphitized carbon," *Electrochimica Acta* 47 (6), 885-890 (2001).
- 220 M. N. Richard and J. R. Dahn, "Accelerating rate calorimetry study on the thermal stability of lithium intercalated graphite in electrolyte. I. Experimental," *Journal of The Electrochemical Society* 146 (6), 2068-2077 (1999).
- 221 R. Kostecki and F. McLarnon, "Microprobe study of the effect of Li intercalation on the structure of graphite," *Journal of Power Sources* 119-121, 550-554 (2003).
- 222 L. J. Fu, H. Liu, C. Li *et al.*, "Surface modifications of electrode materials for lithium ion batteries," *Solid State Sciences* 8 (2), 113-128 (2006).
- 223 Y. Ein-Eli, "New perspective on the foundation and structure of the solid electrolyte interface at the graphite anode of Li-ion cells," *Electrochemical and Solid-State Letters* 2 (5), 212-214 (1999).
- 224 A. M. Andersson, M. Herstedt, A. G. Bishop, and K. Edström, "The influence of lithium salt on the interfacial reactions controlling the thermal stability of graphite anodes," *Electrochimica Acta* 47 (12), 1885-1898 (2002).
- 225 J. E. Owejan, J. P. Owejan, S. C. DeCaluwe, and J. A. Dura, "Solid Electrolyte Interphase in Li-Ion Batteries: Evolving Structures Measured In situ by Neutron Reflectometry," *Chem. Mat.* 24 (11), 2133-2140 (2012).
- 226 V. P. Oleshko, D. Ruzmetov, P. M. Haney *et al.*, "In Situ and Ex Situ Diagnosis of Nanoscale Electrochemical Processes Using Miniature All-Solid-State Li-Ion Batteries," *Microscopy and Microanalysis* 18 (SupplementS2), 1322-1323 (2012).
- 227 L. J. Hardwick, M. Hahn, P. Ruch *et al.*, "An in situ Raman study of the intercalation of supercapacitor-type electrolyte into microcrystalline graphite," *Electrochimica Acta* 52 (2), 675-680 (2006).
- 228 R. Kötz and M. Carlen, "Principles and applications of electrochemical capacitors," *Electrochimica Acta* 45 (15-16), 2483-2498 (2000).
- 229 X. Zhao, B. M. Sanchez, P. J. Dobson, and P. S. Grant, "The role of nanomaterials in redox-based supercapacitors for next generation energy storage devices," *Nanoscale* 3 (3), 839-855 (2011).

- 230 F. Du, D. Yu, L. Dai *et al.*, "Preparation of Tunable 3D Pillared Carbon Nanotube–Graphene Networks for High-Performance Capacitance," *Chem. Mat.* 23 (21), 4810-4816 (2011).
- 231 H. Shioyama, "Interactions of two chemical species in the interlayer spacing of graphite," *Synthetic Metals* 114 (1), 1-15 (2000).
- 232 M. S. Dresselhaus and G. Dresselhaus, "Intercalation compounds of graphite," *Advances in Physics* 51 (1), 1-186 (2002).
- 233 J. E. Fischer and T. E. Thompson, "GRAPHITE INTERCALATION COMPOUNDS," *Physics Today* 31 (7), 36-& (1978).
- 234 M. S. Dresselhaus and G. Dresselhaus, "Intercalation compounds of graphite," *Advances in Physics* 30 (2), 139-326 (1981).
- 235 T. Abe, Y. Yokota, Y. Mizutani *et al.*, "X-ray diffraction and Raman scattering studies of FeCl₃-SbCl₅-graphite bi-intercalation compounds," *Journal of Materials Research* 11 (12), 3039-3044 (1996).
- 236 H. Shioyama, K. Tatsumi, R. Fujii, and Y. Mizutani, "Electrochemical preparation of the graphite bi-intercalation compound with H₂SO₄ and FeCl₃," *Carbon* 28 (1), 119-123 (1990).
- 237 M. Zhou, T. Tian, X. Li *et al.*, "Production of graphene by liquid-phase exfoliation of intercalated graphite," *International Journal of Electrochemical Science* 9 (2), 810-820 (2014).
- 238 H. Shioyama, Y. Yamada, A. Ueda, and T. Kobayashi, "Graphite intercalation compounds as PEMFC electrocatalyst supports," *Carbon* 43 (11), 2374-2378 (2005).
- 239 T. Maluangnont, G. T. Bui, B. A. Huntington, and M. M. Lerner, "Preparation of a homologous series of graphite alkylamine intercalation compounds including an unusual parallel bilayer intercalate arrangement," *Chem. Mat.* 23 (5), 1091-1095 (2011).
- 240 W. Sirisaksoontorn, A. A. Adenuga, V. T. Remcho, and M. M. Lerner, "Preparation and Characterization of a Tetrabutylammonium Graphite Intercalation Compound," *Journal of the American Chemical Society* 133 (32), 12436-12438 (2011).
- 241 M. J. Stephenson, A. J. King, S. M. Holmes, and R. A. W. Dryfe, "Size Selective and Volume Exclusion Effects on Ion Transfer at the Silicalite Modified Liquid–Liquid Interface," *The Journal of Physical Chemistry B* 109 (41), 19377-19384 (2005).

- 242 T. Osakai and K. Ebina, "Non-Bornian Theory of the Gibbs Energy of Ion Transfer between Two Immiscible Liquids," *The Journal of Physical Chemistry B* 102 (29), 5691-5698 (1998).
- 243 C. E. Dahm and D. G. Peters, "Electrochemical reduction of tetraalkylammonium tetrafluoroborates at carbon cathodes in dimethylformamide," *Journal of Electroanalytical Chemistry* 402 (1-2), 91-96 (1996).
- 244 J. Simonet and H. Lund, "Electrochemical behaviour of graphite cathodes in the presence of tetraalkylammonium cations," *Journal of Electroanalytical Chemistry and Interfacial Electrochemistry* 75 (2), 719-730 (1977).
- 245 J. Simonet, Y. Astier, and C. Dano, "On the cathodic behaviour of tetraalkylammonium cations at a platinum electrode," *Journal of Electroanalytical Chemistry* 451 (1-2), 5-9 (1998).
- 246 H. Tokuda, K. Hayamizu, K. Ishii *et al.*, "Physicochemical Properties and Structures of Room Temperature Ionic Liquids. 1. Variation of Anionic Species," *The Journal of Physical Chemistry B* 108 (42), 16593-16600 (2004).
- 247 T. Maluangnont, M. M. Lerner, and K. Gotoh, "Synthesis of Ternary and Quaternary Graphite Intercalation Compounds Containing Alkali Metal Cations and Diamines," *Inorganic Chemistry* 50 (22), 11676-11682 (2011).
- 248 W. Sirisaksoontorn and M. M. Lerner, "Preparation of a Homologous Series of Tetraalkylammonium Graphite Intercalation Compounds," *Inorganic Chemistry* 52 (12), 7139-7144 (2013).
- 249 A. Takenaka, T. Tsumura, and M. Toyoda, "Synthesis of ternary intercalation compounds of carbon fiber," *Synthetic Metals* 160 (11-12), 1247-1251 (2010).
- 250 Y. Mizutani, T. Abe, K. Ikeda *et al.*, "Graphite intercalation compounds prepared in solutions of alkali metals in 2-methyltetrahydrofuran and 2,5-dimethyltetrahydrofuran," *Carbon* 35 (1), 61-65 (1997).
- 251 J. O. Besenhard, "The electrochemical preparation and properties of ionic alkali metal-and NR₄-graphite intercalation compounds in organic electrolytes," *Carbon* 14 (2), 111-115 (1976).

- 252 J. O. Besenhard and H. P. Fritz, "Cathodic reduction of graphite in organic solutions of alkali and NR₄⁺ salts," *Journal of Electroanalytical Chemistry and Interfacial Electrochemistry* 53 (2), 329-333 (1974).
- 253 G. Bernard and J. Simonet, "Irreversible cathodic behavior of graphite in the presence of some mixtures of onium salts," *Journal of Electroanalytical Chemistry and Interfacial Electrochemistry* 96 (2), 249-253 (1979).
- 254 J. O. Besenhard, H. Möhwald, and J. J. Nickl, "Electronic conductivity and structure of DMSO-solvated A⁺ - and NR₄⁺-graphite intercalation compounds," *Carbon* 18 (6), 399-405 (1980).
- 255 C. J. Shih, A. Vijayaraghavan, R. Krishnan *et al.*, "Bi- and trilayer graphene solutions," *Nature Nanotechnology* 6 (7), 439-445 (2011).
- 256 S. Chattopadhyay, A. L. Lipson, H. J. Karmel *et al.*, "In Situ X-ray Study of the Solid Electrolyte Interphase (SEI) Formation on Graphene as a Model Li-ion Battery Anode," *Chem. Mat.* 24 (15), 3038-3043 (2012).
- 257 Y. NuLi, J. Yang, and Z. Jiang, "Intercalation of lithium ions into bulk and powder highly oriented pyrolytic graphite," *Journal of Physics and Chemistry of Solids* 67 (4), 882-886 (2006).
- 258 L. J. Hardwick, H. Buqa, M. Holzapfel *et al.*, "Behaviour of highly crystalline graphitic materials in lithium-ion cells with propylene carbonate containing electrolytes: An in situ Raman and SEM study," *Electrochimica Acta* 52 (15), 4884-4891 (2007).
- 259 P. Verma, P. Maire, and P. Novák, "A review of the features and analyses of the solid electrolyte interphase in Li-ion batteries," *Electrochimica Acta* 55 (22), 6332-6341 (2010).
- 260 H. J. Ploehn, P. Ramadass, and R. E. White, "Solvent Diffusion Model for Aging of Lithium-Ion Battery Cells," *Journal of The Electrochemical Society* 151 (3), A456-A462 (2004).
- 261 M. Levi, E. Markevich, and D. Aurbach, "NUCLEATION AND GROWTH OF SOLID PHASES FORMED DURING ELECTROCHEMICAL LITHIATION OF GRAPHITE: EXPERIMENTAL STUDIES AND MODELING."
- 262 A. Funabiki, M. Inaba, T. Abe, and Z. Ogumi, "Stage Transformation of Lithium-Graphite Intercalation Compounds Caused by Electrochemical

- Lithium Intercalation," Journal of The Electrochemical Society 146 (7), 2443-2448 (1999).
- 263 E. C. Walter, M. P. Zach, F. Favier *et al.*, "Metal nanowire arrays by electrodeposition," ChemPhysChem 4 (2), 131-138 (2003).
 - 264 P. Schoderböck and H. P. Boehm, "Observations of staging in the electrochemical intercalation of lithium into graphite from dimethyl sulfoxide solutions," Synthetic Metals 44 (3), 239-246 (1991).
 - 265 J. Morales, C. Perez-Vicente, and J. L. Tirado, "Chemical and electrochemical lithium intercalation and staging in $2H\text{-}SnS_2$," Solid State Ionics 51 (3-4), 133-138 (1992).
 - 266 J. Rodríguez-López and M. Videa, "Study of the Ion Transfer of Quaternary Ammonium Ions by SWV," Journal of the Mexican Chemical Society 56 (4), 417-425 (2012).
 - 267 M. Hoyles, V. Krishnamurthy, M. Siksik, and S.-H. Chung, "Brownian Dynamics Theory for Predicting Internal and External Blockages of Tetraethylammonium in the KcsA Potassium Channel," Biophysical Journal 94 (2), 366-378 (2008).
 - 268 H. Mo and T. C. Pochapsky, "Self-Diffusion Coefficients of Paired Ions," The Journal of Physical Chemistry B 101 (23), 4485-4486 (1997).
 - 269 A. Tokranov, B. W. Sheldon, P. Lu *et al.*, "The origin of stress in the solid electrolyte interphase on Carbon electrodes for Li ion batteries," Journal of The Electrochemical Society 161 (1), A58-A65 (2014).
 - 270 C. Xiu-Yun, "Graphene-like nanosheets synthesized by natural flaky graphite in Shandong, China," Int Nano Lett 3 (1), 1-5 (2013).
 - 271 G. Sun, X. Li, Y. Qu *et al.*, "Preparation and characterization of graphite nanosheets from detonation technique," Materials Letters 62 (4-5), 703-706 (2008).
 - 272 A. Funabiki, M. Inaba, Z. Ogumi *et al.*, "Impedance study on the electrochemical lithium intercalation into natural graphite powder," Journal of The Electrochemical Society 145 (1), 172-178 (1998).
 - 273 A. Ehsani, M. G. Mahjani, and M. Jafarian, "Electrochemical impedance spectroscopy study on intercalation and anomalous diffusion of $AlCl_4^-$ ions into graphite in basic molten salt," Turkish Journal of Chemistry 35 (5), 735-743 (2011).
 - 274 D. Aurbach, K. Gamolsky, B. Markovsky *et al.*, "Study of surface phenomena related to electrochemical lithium intercalation into Li_xMO_y

- host materials (M = Ni, Mn)," Journal of The Electrochemical Society 147 (4), 1322-1331 (2000).
- 275 A. Funabiki, M. Inaba, and Z. Ogumi, "A.c. impedance analysis of electrochemical lithium intercalation into highly oriented pyrolytic graphite," Journal of Power Sources 68 (2), 227-231 (1997).
- 276 <http://www.consultrsr.com/resources/eis/diff-o.htm>.
- 277 M. F. El-Kady, V. Strong, S. Dubin, and R. B. Kaner, "Laser Scribing of High-Performance and Flexible Graphene-Based Electrochemical Capacitors," Science 335 (6074), 1326-1330 (2012).
- 278 J. Xia, F. Chen, J. Li, and N. Tao, "Measurement of the quantum capacitance of graphene," Nature Nanotechnology 4 (8), 505-509 (2009).
- 279 J. R. Miller, R. A. Outlaw, and B. C. Holloway, "Graphene double-layer capacitor with ac line-filtering performance," Science 329 (5999), 1637-1639 (2010).
- 280 Y. Zhu, S. Murali, M. D. Stoller *et al.*, "Carbon-Based Supercapacitors Produced by Activation of Graphene," Science 332 (6037), 1537-1541 (2011).
- 281 <http://nanoprobe.aist-nt.com/apps/HOPG%20info.htm>.
- 282 U. r. i. c. w. M. T. Campos-Hernandez, (2013).
- 283 U. Khan, A. O'Neill, M. Lotya *et al.*, "High-Concentration Solvent Exfoliation of Graphene," Small 6 (7), 864-871 (2010).
- 284 <http://www3.imperial.ac.uk/pls/portallive/docs/1/7276131.PDF>.
- 285 W. Zhang, Y. Zeng, N. Xiao *et al.*, "One-step electrochemical preparation of graphene-based heterostructures for Li storage," Journal of Materials Chemistry 22 (17), 8455-8461 (2012).
- 286 C. T. J. Low, F. C. Walsh, M. H. Chakrabarti *et al.*, "Electrochemical approaches to the production of graphene flakes and their potential applications," Carbon 54 (0), 1-21 (2013).
- 287 P. S. Toth, A. T. Valota, M. Velický *et al.*, "Electrochemistry in a drop: A study of the electrochemical behaviour of mechanically exfoliated graphene on photoresist coated silicon substrate," Chemical Science 5 (2), 582-589 (2014).
- 288 P. W. Ruch, M. Hahn, F. Rosciano *et al.*, "In situ X-ray diffraction of the intercalation of (C₂H₅)₄N⁺ and BF₄[−] into graphite from acetonitrile and propylene carbonate based supercapacitor electrolytes," Electrochimica Acta 53 (3), 1074-1082 (2007).

